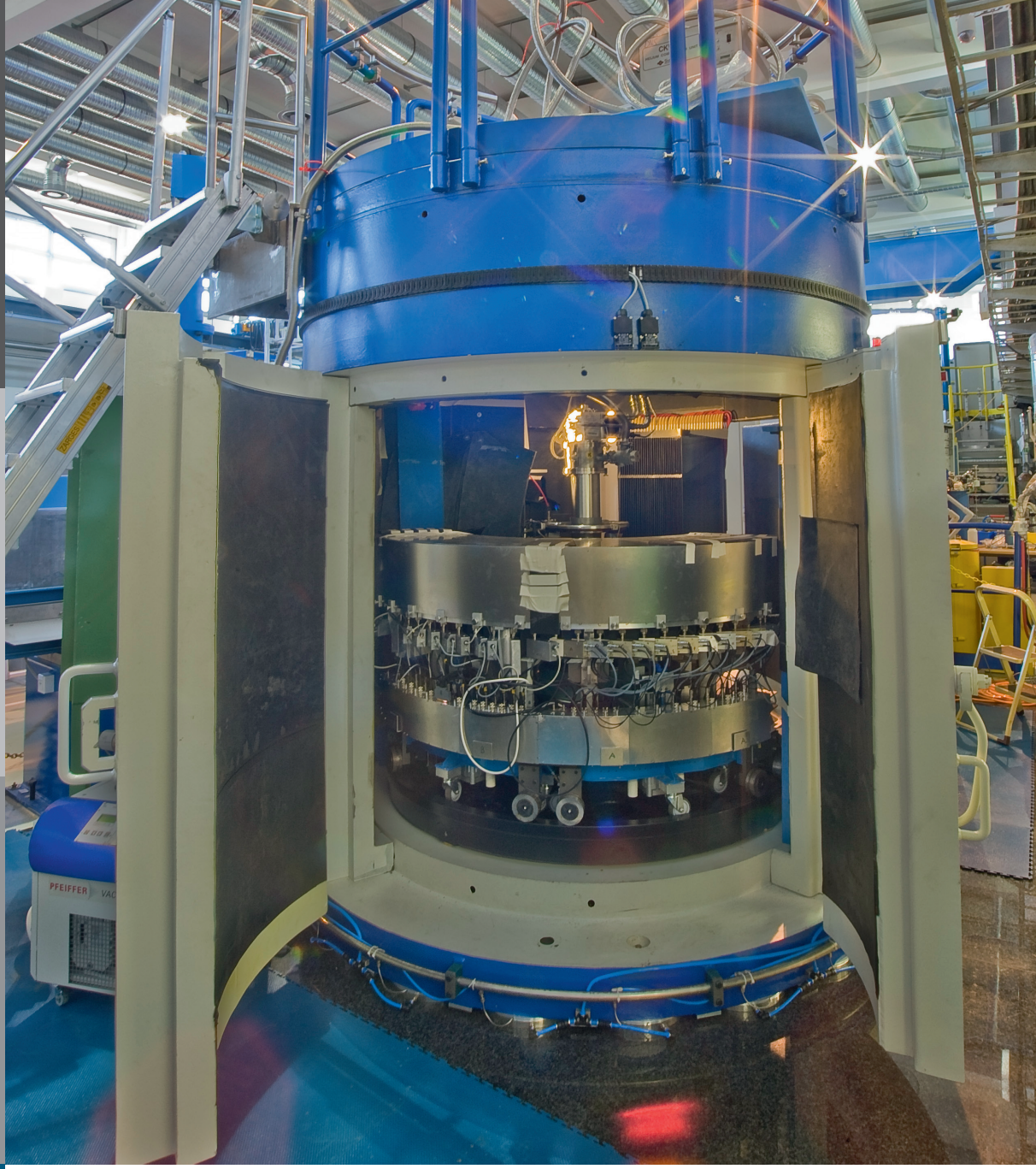

Laboratory Course

Neutron Scattering

Lectures

Thomas Brückel, Gernot Heger, Dieter Richter,
Georg Roth and Reiner Zorn (Editors)

RWTH Aachen
University Münster

JÜLICH
FORSCHUNGSZENTRUM

Schriften des Forschungszentrums Jülich
Reihe Schlüsseltechnologien / Key Technologies Band / Volume 27

Forschungszentrum Jülich GmbH
Jülich Centre For Neutron Science (JCNS)

Thomas Brückel, Gernot Heger, Dieter Richter,
Georg Roth and Reiner Zorn (Editors)

Neutron Scattering

Lectures of the JCNS Laborator Course held at
Forschungszentrum Jülich and the research reactor
FRM II of TU Munich
In cooperation with
RWTH Aachen and University of Münster

Schriften des Forschungszentrums Jülich
Reihe Schlüsseltechnologien / Key Technologies Band / Volume 27

ISSN 1866-1807 ISBN 978-3-89336-725-2

Bibliographic information published by the Deutsche Nationalbibliothek.
The Deutsche Nationalbibliothek lists this publication in the Deutsche Nationalbibliografie; detailed bibliographic data are available in the Internet at http://dnb.d-nb.de.

Publisher and Distributor:	Forschungszentrum Jülich GmbH Zentralbibliothek 52425 Jülich Phone +49 (0) 24 61 61-53 68 · Fax +49 (0) 24 61 61-61 03 e-mail: zb-publikation@fz-juelich.de Internet: http://www.fz-juelich.de/zb
Cover Design:	Grafische Medien, Forschungszentrum Jülich GmbH
Printer:	Grafische Medien, Forschungszentrum Jülich GmbH
Copyright:	Forschungszentrum Jülich 2010

Schriften des Forschungszentrums Jülich
Reihe Schlüsseltechnologien / Key Technologies Band / Volume 27

ISSN 1866-1807
ISBN 978-3-89336-725-2

The complete volume ist freely available on the Internet on the Jülicher Open Access Server (JUWEL) at http://www.fz-juelich.de/zb/juwel

Contents

1 Introduction: Neutron Scattering in Contemporary Research

Th. Brückel
Jülich Centre for Neutron Science 2
Forschungszentrum Jülich GmbH

Contents

1.1 Introduction: Why Scattering?

In this chapter, we will start with a very gentle qualitative introduction entirely without formula to give you an idea what the course is all about. The details will follow in subsequent chapters.

Imagine you leave this lecture hall, some mean looking guys dressed entirely in black follow, kidnap and take you to the medieval castle of Nideggen in the close-by Eifel mountains. There you are being thrown into a pitch dark dungeon. You cannot see anything, but you hear some noises. Are there rats? Are there other prisoners? Are there dragons? Luckily you remember that you have some matches in your pocket. You light a match, you can see everything around you and everything becomes clear to you…

What I have just described is essentially like a scattering experiment: figuratively it sheds light into darkness and helps us understand the world around us. Let's analyse what you did in the dungeon: first when you light the match, you start a source of radiation. Here the radiation is light. This light then gets scattered (reflected, transmitted) from the surrounding objects. In a scientific scattering experiment, we will call this object a "sample". Back to the dungeon: some of this radiation gets scattered into your eye. Your eye serves as very special radiation detector: with its lens, it is able to even make an image of the objects on the retina, which in the language of a physicist would be called an "area position sensitive pixel detector". This image contains lots of information: the colour of the backscattered light tells you something about the absorption of certain components of the light and therefore gives information about the material the light is scattered from. The position of the signal on the retina gives you information about the spatial arrangement of the objects around you. And finally the time dependence of the signal tells you that the monster is actually crawling towards you, ready to attack. All this information has to be treated and interpreted. This is done by our brain, an extremely powerful computer to analyse this wealth of data.

This little example shows you the importance of scattering for our understanding of the world: nearly all information that we as individuals have about the world in which we live comes from light scattering and imaging through our eyes. It is only natural that scientists mimic this process of obtaining information in well controlled scattering experiments: they build a source of radiation, direct a beam of radiation towards a sample, detect the radiation scattered from a sample, i. e. convert the signal into an electronic signal, which they can then treat by means of computers. In most cases one wants an undisturbed image of the object under investigation and therefore chooses the radiation, so that it does not influence or modify the sample. Scattering is therefore a non-destructive and very gentle method, if the appropriate type of radiation is chosen for the experiment.

1.2 X-Ray Scattering in Condensed Matter Research

What other requirements must the radiation fulfill to be useful for scattering experiments? In condensed matter science we want to go beyond our daily experience and understand the microscopic atomic structure of matter, i. e. we want to find out where the atoms are located inside our samples and also how they move. This cannot be done by light scattering. Why? Well in general light is scattered from the surface and does not penetrate enough into many materials, such as metals, for example. On the other hand, if it penetrates like in the case of glass it is normally just being transmitted except if we have a very bad glass with lots of inhomogeneities, but the main reason is actually that light has too long of the wavelength, see figure 1.1.

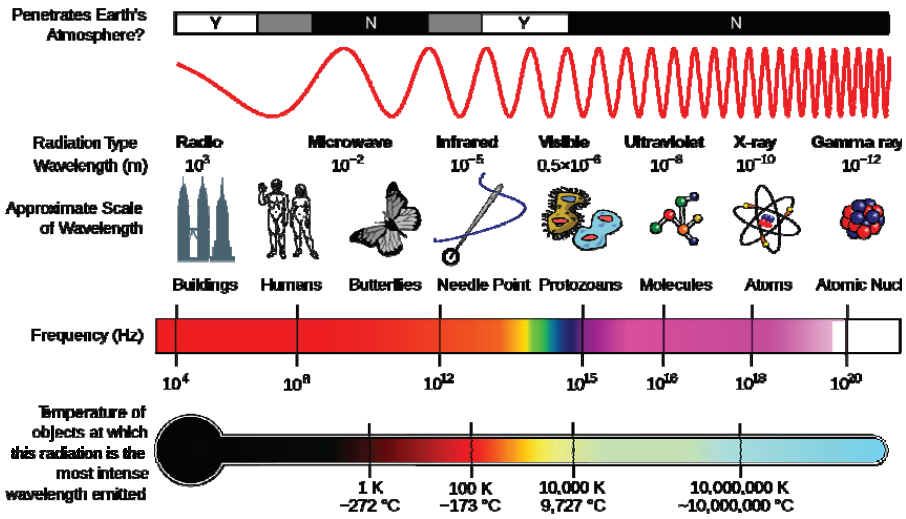

Fig. 1.1: *Electromagnetic spectrum; shown is the wavelength and frequency of electromagnetic waves, which have different names for different wavelength regions. Also given are examples for objects with sizes comparable to the wavelength. (from WIKIPEDIA).*

It is quite intuitive to understand that if we want to measure the distance between the atoms, we need a "ruler" of comparable lengths. Now the distance between atoms is in the order of 0.1 nm = 10^{-10} m = 0.0000000001 m. Since the distance between atoms is such an important length scale in condensed matter science, it has been given its own unit: 0.1 nm = 1 Ångstrøm = 1 Å. If we compare the wavelength of light with this characteristic length scale, it is 4000 to 7000 times longer and therefore not appropriate to measure distances on an atomic lengthscale. In the electromagnetic spectrum, x-rays

have a well adapted wavelength of about 1 Å for studies on such a microscopic scale. They also have a large penetration power as everybody knows from the medical x-ray images.

Classical physics describes electromagnetic radiation as propagation of electromagnetic waves. For a scattering experiment, we select waves of a certain wavelength and propagation direction, so-called plane waves, since all points on a plane in space have the same phase. If such a wave impinges on two point-like scattering centers (in a solid these could be atoms), spherical waves are being emitted from these scattering centers. This is nothing but Huygens principle for wave propagation. The emitted waves can superimpose and lead to either enhancement or cancellation of the signal in certain directions as depicted in figure 1.2.

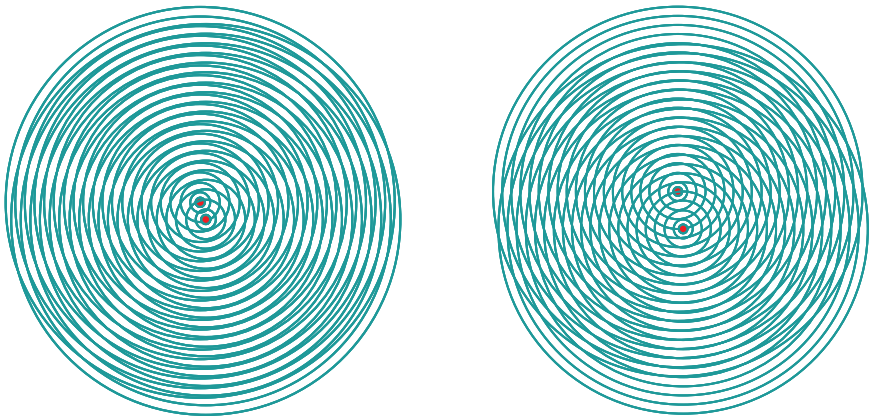

Fig. 1.2: *Moiré pattern for concentric circles with equal distances representing a planar cut through spherical waves emitted from two scattering centers. The circles represent surfaces of constant phase relationship. Linear superposition of the waves gives enhancement or cancellation of the wave amplitudes along certain directions. This interference effect is mimicked by the depicted Moiré pattern. If the distance between the scattering centers is increased, the distance in the interference maxima decreases and vice versa: distances in the image created by scattering are inverse proportional – or reciprocal - to distances in the original objects which motivates the introduction of a reciprocal space to describe scattering events compared to the real space of the object under investigation.*

As becomes clear from figure 1.2, scattering can be described as an interference phenomenon of the radiation waves. However, since de Broglie and Einstein, we know that quantum objects have a dual nature: the particle-wave-dualism. In the case of electromagnetic waves, the quanta carrying certain energy are called photons and in the detector, which registers the scattering pattern, we count single x-ray photons. This is characteristic for the quantum mechanical description: during propagation of radiation a wave picture is appropriate, while for the interaction with matter a particle is the

description of choice. Wave and particle picture are connected by the fact that the magnitude square of the wave at a certain position in space gives the probability density of finding the quantum particle at the corresponding position. Within this particle-wave-dualism it therefore becomes natural to use elementary particles as probes for scattering investigations of condensed matter systems. This was realised for the first time by Rutherford in 1909 in his famous experiment, where he directed a beam of α-particles onto a gold foil and registered the transmitted and scattered particles. He found that many particles were backscattered and from the ratio between transmitted and backscattered α-particles he could conclude on the model of an atom, which is now generally accepted, namely consisting of a positively charged nucleus of size about 10 femtometer = 10 fm = 10 x 10^{-15} m surrounded by a cloud of negatively charged electrons with an extension of about 1 Å = 10^{-10} m = 100000 fm, see figure 1.3.

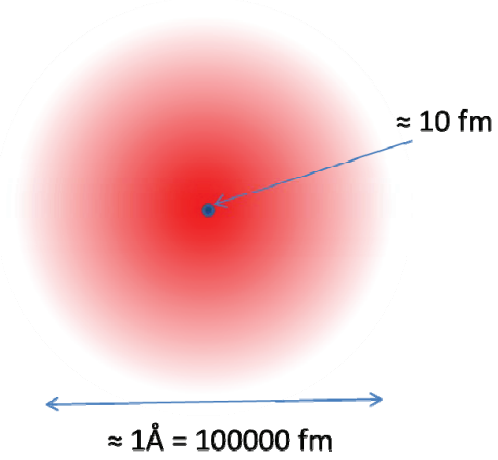

Fig. 1.3: *Schematic model of an atom with the atomic nucleus consisting of neutrons and protons having a size of about 10 fm surrounded by electrons in a cloud of a size of about 1 Å.*

The real breakthrough for structure studies of condensed matter systems came with the idea of Max von Laue to use x-rays as scattering probes. Wilhelm Conrad Röntgen discovered x-rays in 1895 and soon it was concluded that x-rays were electromagnetic waves. Arnold Sommerfeld suggested that the wavelength of x-rays was about 1 Å. At the time of Max von Laue, after the experiments of Rutherford, it was accepted that matter consisted of atoms but their periodic arrangement in crystals was maybe suggested by the regular facets of the crystals but could not be really proven by experiment. Max von Laue was a theoretician, who derived the famous Laue equation describing scattering from a regular three-dimensional periodic arrangement of scattering centers. He convinced the two experimentalists Friedrich and Knipping to perform an x-ray diffraction experiment. The result is shown in figure 1.4.

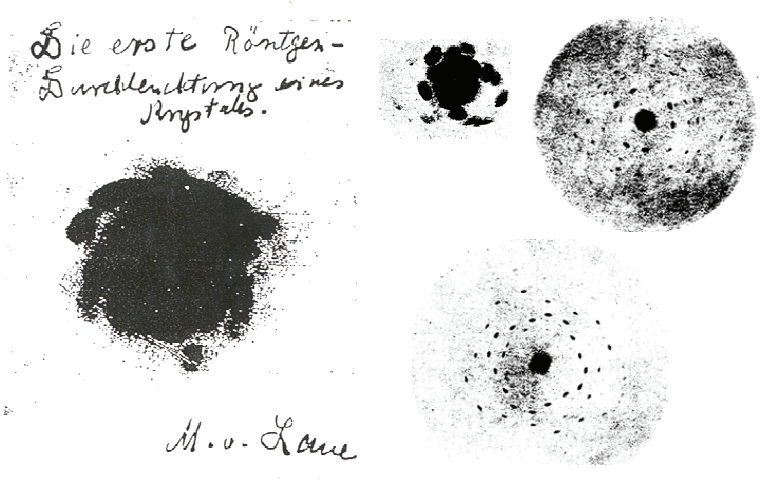

Fig. 1.4: *Early x-ray diffraction diagrams recorded by a film from copper sulphite single crystals [1].*

While the first transmission Laue photograph showed more or less just a fat plop, the quality of these images was soon refined and clear so-called Laue-spots could be identified. The impact of this discovery cannot be over-emphasized: it was the definite proof that solids consist of atoms, which are arranged in a regular three-dimensional periodic array and that x-rays were scattered as electromagnetic waves from such an arrangement of atoms. It is therefore natural that Max von Laue received the Nobel prize in 1914 for this breakthrough discovery. However, the experimentalists Friedrich and Knipping were left empty-handed.

Nearly everything we know today about the atomic structure of matter is based on this discovery which took place nearly 100 years ago. Of course the techniques were significantly refined and nowadays x-ray diffraction is heavily being used to resolve complex structures of biological macromolecules in the field of protein crystallography. Such investigations need very intense and bright x-ray beams, which are provided from large accelerators, so-called synchrotron radiation sources. Many thousands of reflections are being recorded in a few seconds. As electromagnetic waves, x-rays are mainly scattered from the electronic charge distribution around the atoms and thus x-ray diffraction allows one to determine the electron density in solids.

1.3 Impact of Scattering in other Fields of Science

It should be pointed out that scattering is a much more general method in science, which is not only used by condensed matter scientists. The world's largest accelerator is located close to Geneva at the border between Switzerland and France in the CERN research center. CERN stands for *Centre Européenne pour la Recherche Nucléaire*, i. e.

the European organisation for nuclear research. Many accelerators are located on the CERN site of which the LHC, the Large Hadron Collider, is the world's largest and highest energy particles accelerator. The LHC lies in a tunnel 27 km in circumference as deep as 175 m beneath ground level. This huge accelerator serves nothing but a scattering experiment, where opposing particle beams e. g. protons at energy of 7 TeV collide in certain interaction points, which are surrounded by huge detectors built by large international collaborations. In inelastic scattering events, new particles can be created and the hope is that this huge investment helps us to address some of the most fundamental questions of physics advancing the understanding of the deepest laws of nature. At Research Centre Jülich we have a smaller version of such a particle accelerator, the so-called COSY synchrotron for Hadron physics. These large accelerators are needed to achieve high particles energies corresponding to short wavelengths, which allow one to study fine structures within nucleons. Large detectors are needed because at these scales no imaging is possible but if all scattered particles are being traced a reconstruction of the scattering event in the computer can take place. While at the LHC new particles are being created during deep inelastic scattering events, the connection to x-ray diffraction is more evident for the former HERA accelerator, which had been in operation at DESY in Hamburg until a few years ago. There, electrons were being scattered from protons in head-on collisions and the inner structure of the proton consisting of quarks and gluons could be resolved.

1.4 Why Neutrons?

Coming back to condensed matter science: if x-rays are so successful for structure determination, why do we need neutrons? Neutrons have some very specific properties which make them extremely useful for condensed matter studies:

1. Neutrons are neutral particles. They are thus highly penetrating, can be used as non-destructive probes and to study samples in severe environment such as cryomagnets or furnaces.
2. The wavelengths of neutrons are similar to atomic spacings - just as is the case for x-rays. Therefore they can provide structural information from the picometer to the 100 μm range.
3. The energies of thermal neutrons are similar to the energies of elementary excitations in solids. Therefore neutrons can determine molecular vibrations, lattice excitations and the dynamics of atomic motion.
4. Neutrons interact with the nuclei in contrast to x-rays or electrons which interact with the electron cloud, see Figure 1.5. They are very sensitive to light atoms like hydrogen, which is difficult to detect by x-rays since hydrogen in bonds has often less than one surrounding electron. They can also distinguish between neighbouring elements in the periodic table like manganese, iron and chromium, for which x-rays are insensitive since these elements have nearly the same number of electrons. Also one can exploit isotopic substitution. A famous example is contrast variation in soft matter or biological macromolecules by replacing deuterium for hydrogen in certain molecules or functional groups.

Similar to tinting in light microscopy, the location and movement of these functional groups can then be observed on the background of the other molecules.

5. Neutrons have a magnetic moment. This dipolar moment is due to the nuclear spin. Therefore neutrons can be used to study microscopic magnetic structures but also the magnetic excitations in solids, which have similar energies than the neutrons.

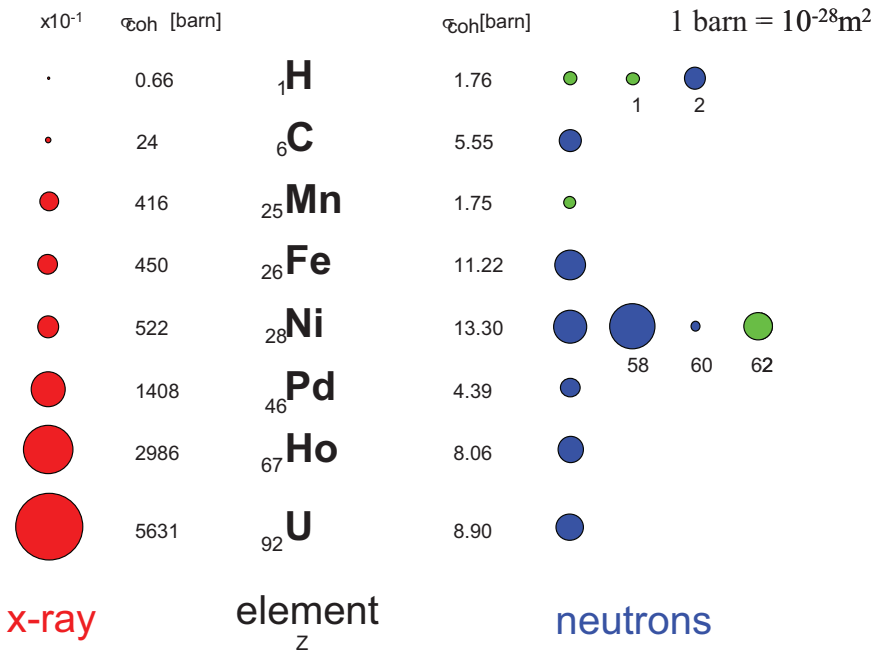

Fig. 1.5: *Comparison of x-ray and neutron scattering from single atoms for a few elements of the periodic table. The filled circles represent a measure of the total cross section, i.e. of the probability for scattering. For x-rays, which are scattered from the electron cloud, this probability goes up with the number square of electrons. Therefore Hydrogen is hardly visible for x-rays in the presence of heavier atoms. The situation is quite different for neutrons, which are scattered from the atomic nucleus. Here the scattering varies not monotonically throughout the periodic table and is different for different isotopes of the same atom. Blue and green circles distinguish scattering with and without 180° phase shift, respectively.*

Figure 1.6 shows the extreme range of applicability of neutrons for condensed matter studies based on these special properties. Different scattering techniques have to be used for different applications, as indicated in the figure.

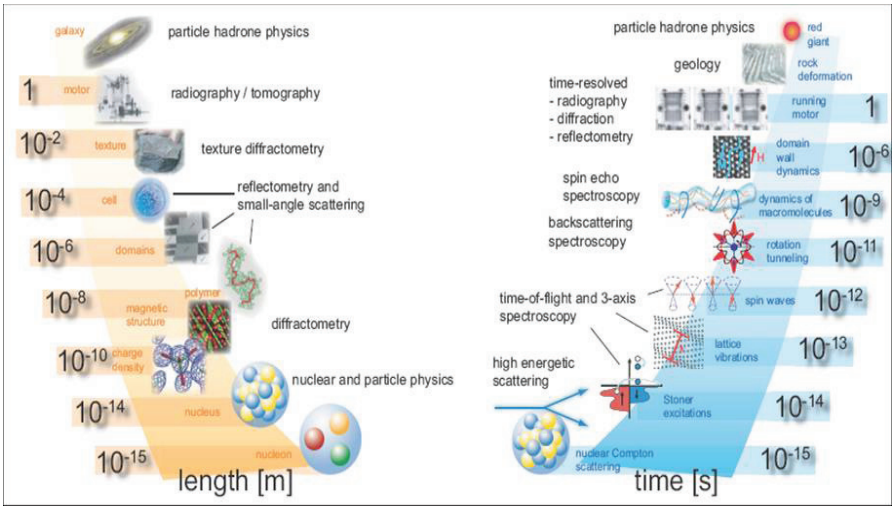

Fig. 1.6: *Huge range of length (left side) and time (right side) scales covered by research with neutrons. Also indicated is the corresponding neutron technique.*

Due to the huge impact of neutron scattering for condensed matter studies, it is no surprise that the Nobel prize in physics was awarded to two of the pioneers of neutron diffraction and inelastic neutron scattering, which Clifford G. Shull and Bertram Brockhouse received in 1994. The famous quote “neutrons tell us where atoms are and how they move” is due to Clifford Shull.

If you got the impression so far that neutrons are the ideal and most universal probe for condensed matter studies on an atomic scale, you are right in principle. However, as with everything in life, there are also some drawbacks. While neutrons are everywhere - without neutrons we would not exist - they are extremely difficult to produce as free particles not bound in nuclei. Free neutrons are produced by nuclear physics reactions, which require rather large and high-tech installations. Two main routes to produce free neutrons are being followed today:

(1) **Fission** of the uranium 235 nuclei in a chain reaction; this process happens in research reactors.

(2) Bombarding heavy nuclei with high energetic protons; the nuclei are “heated up” when a proton is absorbed and typically 20 - 30 neutrons are being evaporated. This process is called **spallation** and requires a spallation source with a proton accelerator and a heavy metal target station.

Since installations to produce free neutrons are rather expensive to build and to operate, there exist only a few sources worldwide. JCNS is present in some of the world best sources as shown in figure 1.7.

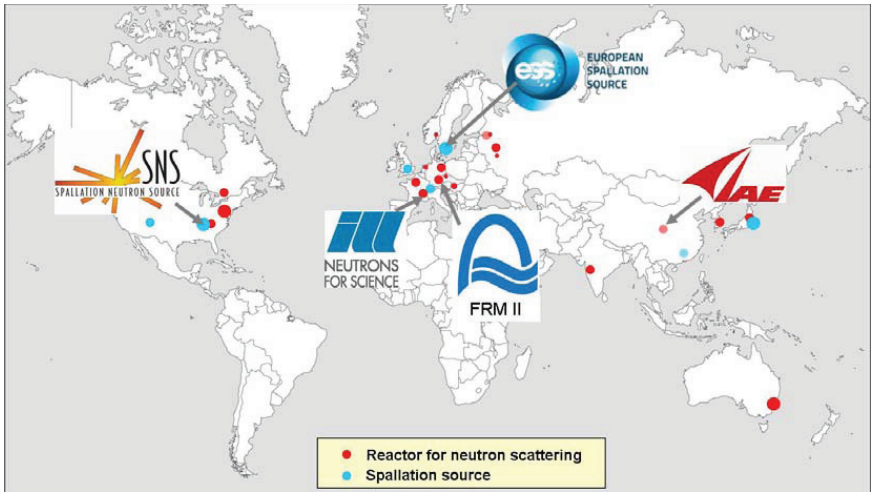

Fig. 1.7: *Major neutron research centres worldwide which have sources of appreciable flux and a broad instrumentation suite for condensed matter research. JCNS is present at four of the leading sources worldwide: the neutron research reactor FRM II in Garching, Germany, the Institute Laue-Langevin ILL in Grenoble, France, the Spallation Neutron Source SNS in Oak Ridge, USA and the Chinese Advanced Research Reactor CARR close to Beijing, China. JCNS also has a leading involvement in the European Spallation Source project, Lund, Sweden.*

The fact that there are only a few sources worldwide implies that neutron scattering experiments have to be organised quite different from normal lab-based experiments. Users have to be trained in special schools (our JCNS school is one of them) and access to the experiments has to be organised (see below).

Not only the neutron research centres are rare but also free neutrons by themselves are rare. In a high flux reactor the neutron flux i. e. the number of neutrons passing through a given area in a given time is in the order of 10^{15} neutrons/cm^2·s. If one compares this value with particle fluxes in gases, the neutron density in high flux sources corresponds to high vacuum conditions of about 10^{-6} mbar pressure. The neutrons have to be transported from the source to the experimental areas, which can either be done by simple flight tubes or so called neutron guides. These are evacuated tubes with glass walls (often covered with metal layers to increase the performance), where neutrons are transported by total reflection from the side, top, and bottom walls in a similar manner like light in glass fibers. The neutron flux downstream at the scattering experiments is then even much lower than in the source itself and amounts to typically 10^6 - 10^8 neutrons/cm^2·s. This means that long counting times have to be taken into account to achieve reasonable statistics in the neutron detector. Just for comparison: the flux of photons of a small Helium-Neon laser with a power of 1 mW (typical for a laser pointer) amounts to some 10^{15} photons/s in a beam area well below 1 mm^2.

However, it is not only the low flux that limits neutron scattering experiments, but also the fact that neutron sources are not very bright, i. e. neutron beams are rather large in the order of a few cm^2 and therefore require in general rather large samples. Typical sample sizes are again in the order of a few cm^2 and have masses of a few grams. However, this does not mean that we cannot study nanosized objects with neutrons as you will see in the subsequent lectures. However, for neutron scattering techniques, we have to have many of such objects and we will obtain ensemble averages.

1.5 The Social Practice of Neutron Scattering

The fact that neutron sources are rare leads to a particular social practice for neutron scattering: there are only a few major sources in Europe and worldwide and the operation of each one of these sources costs several million Euro per year. Therefore efforts have to be made to use the existing sources as efficient as possible. This means (i) continuous and reliable operation of the source during a large fraction of the year; (ii) many highly performing instruments, which can run in parallel, located around every source; (iii) professional instrument operation with highly qualified staff and a stringent risk management to keep the downtime of instruments and auxiliary equipment as low as possible; (iv) and access for as many scientists as possible.

There is no commercial market for neutron scattering instruments. Therefore these instruments are being built by research centres, where usually one or a few staff scientists work closely with engineers and technicians to realise an instrument for a certain application of research with neutrons. These highly experienced scientists will then later-on operate the instruments located at a certain neutron source. The Jülich Centre for Neutron Science JCNS has such staff scientists located at the outstations at FRM II, ILL and SNS. However, neutron facilities are way too expensive to be operated just for a small number of scientists. Beamtime is offered to external users from universities, research organisations (such as Max-Planck or Fraunhofer in Germany) and industry. In order for these users to obtain access to a neutron scattering instrument, the user will obtain information from the internet on available instruments, contact the instrument scientist and discuss the planned experiments with the instrument scientist. Once a clear idea and strategy for an experiment has been worked out, the user will write a beamtime proposal where he describes in detail the scientific background, the goal of the planned experiment, the experimental strategy and the prior work. The facility issues a call for proposals in regular intervals, typically twice a year. The proposals received are distributed to members of an independent committee of international experts, which perform a peer review of the proposals and establish a ranking. Typically overload factors between 2 to 3 on the neutron instruments exist, i. e. 2 to 3 times the available beam time is being demanded by external users. Once the best experiments have been selected, the beamtime will be allocated through the facility, where the directors approves the ranking of the committee, the beamline scientist schedules the experiments on her or his instrument and the user office sends out the invitations to the external users. Many facilities will pay travel and lodging for 1 up to 2 users per experiment. It is now up to the user to prepare his experiment as well as possible. If the experiment fails because it was not well prepared, it will be very

difficult to get more beamtime for the same scientific problem. Typical experiments last between 1 day and up to 2 weeks. In this time lots of data will be collected which users take home and usually spend several weeks or months to treat the data and model it.

A typical neutron scattering facility will run about 200 days a year with a few hundred visits of user from all over the world. This is also what makes research with neutrons so attractive to young scientists: early-on in their career they will learn to work in large international collaborations, get the opportunity to work on state-of-the-art high-tech equipment and learn to organise their research as efficient as possible. You have therefore chosen well to attend this laboratory course!

After this simple introduction, you can now look forward to many interesting lectures, where more details will be explained and where you will learn the basic principles to enable you to perform neutron experiments. Have lots of fun and success working with this special gift of nature, the free neutron!

References

[1] W. Friedrich, P. Knipping, M. von Laue(1912). "Interferenz-Erscheinungen bei Röntgenstrahlen". Sitzungsberichte der Mathematisch-Physikalischen Classe der Königlich-Bayerischen Akademie der Wissenschaften zu München 1912: 303.

Some useful links for research with neutrons:
German Committee for Research with Neutrons: www.neutronenforschung.de
European Neutron Portal: http://www.neutron-eu.net/
Neutron scattering reference material: http://www.neutron.anl.gov/reference.html
Neutron scattering web: http://www.neutron.anl.gov/
Jülich Centre for Neutron Science: http://www.fz-juelich.de/jcns/

Exercises

E1.1 Scattering probes

Neutron scattering allows us to determine "where the atoms are and how the atoms move" in a condensed matter system. Other scattering probes include: light, x-rays, electrons, α-particles.

a) Discuss qualitatively the strengths and weakness of these probes in comparison to neutron scattering.

b) CO_2 has a bad reputation as green-house gas in the atmosphere. Could it, however, be useful as a scattering probe to replace neutrons? (A high flux of CO_2 molecules could e.g. be obtained by an expansion of pressurised CO_2 gas from a gas bottle through a nozzle - a flux many orders of magnitude higher than the neutron fluxes used in neutron scattering experiments!)

E1.2 Huygens principle and coherence

A plane wave of wavelength λ is incident on a pair of identical scatterers, which are separated by a distance L perpendicular to the wave propagation, see figure:

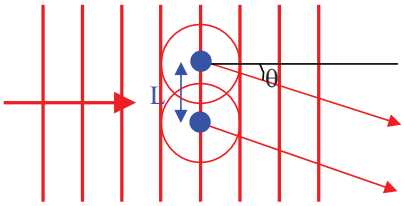

According to the Huygens principle, spherical waves will be emitted from the two scatterers. In certain directions, these waves interfere constructively, i.e. the two scattered waves are in phase.

a) Calculate the angles θ, where interference maxima occur in the far field limit.

b) What happens to the interference maxima, if there is a broad distribution of wavelength in the incident wave, but the propagation direction remains well defined?

c) What happens to the interference maxima, if the wavelength of the incident wave is well defined, but there are many waves of different directions impinging on our scatterers?

d) How would you design an instrument to measure the distance L between the two scatterers, if light from a normal light bulb is being used as radiation? Which requirement does L have to fulfill in this case?

e) According to b) and c) monochromatisation and collimation are important to obtain well resolved interference pattern. The corresponding requirements for the radiation are called longitudinal (b) and transverse (c) coherence, respectively. Discuss qualitatively the relation between coherence and resolution, i.e. in our example the ability of the apparatus designed in d) to determine the distance L between the scatterers.

2 Neutron Sources

J. Voigt
Jülich Centre for Neutron Science 2
Forschungszentrum Jülich GmbH

Contents

Lecture Notes of the JCNS Laboratory Course Neutron Scattering

2.1 Introduction

Neutrons are an extremely versatile probe to investigate the fundamental properties of matter. The possible applications range from fundamental questions (e.g. electrical dipole moment of the neutron) over condensed matter physics and chemistry to material science and life sciences. The reason for this is threefold:

- The neutron is electrically neutral: hence it can penetrate deeply into matter and prove truly the bulk properties. If you use other massive particles to investigate the properties of matter such as α particles or electrons, you probe usually only the regions close to the surface. Even for x-ray, which is also considered as an bulk technique in general, you penetrate only several hundreds of nm, if you use wavelength delivered by an laboratory x-ray tube.
- The neutron interacts with the sample via nuclear forces: hence the interaction cross section depends on the internal structure of the nuclei in your sample and not on the mass or electric charge of the whole atom. Neutrons are sensitive more or less equally to heavy and light atoms, making them an ideal probe for samples containing hydrogen, carbon or oxygen next to any other heavier atom.
- The neutron has a large magnetic moment: hence it is extremely sensitive to the magnetic properties of your sample. The magnetic field created by the sample scatters the neutron and the analysis of the direction, into which the neutrons are scattered, and the number of scattered neutrons provides the information about the magnetic structure, the size of the magnetic moments and the coupling between different magnetic sites.

Neutrons are in particular useful, because their energy and wavelength corresponds very well with the interatomic distances and the typical excitations in condensed matter problems. We calculate the kinetic energy of a free neutron

$$\begin{aligned} E_{kin} &= \tfrac{1}{2} m \mathbf{v}^2 && (2.1)\\ &= \tfrac{\mathbf{p}^2}{2m} && (2.2)\\ &= \tfrac{h^2}{2m\lambda^2}, && (2.3) \end{aligned}$$

using the de Broglie relation, that expresses the wavelength of a quantum mechanical particle with momentum $\mathbf{p}$:

$$\lambda = \frac{h}{|\mathbf{p}|} \tag{2.4}$$

If we insert the natural constants, we get

$$\begin{aligned} E(\lambda) &= 81.805 \text{ meV}\text{Å}^2 \times \lambda^{-2} && (2.5)\\ v(\lambda) &= 3956 \text{ ms}^{-1}\text{Å} \times \lambda^{-1} && (2.6) \end{aligned}$$

In other words, if we provide neutrons with a wavelength $0.8 < \lambda < 20$ Å suitable for resolving interatomic distances in condensed matter, these neutrons are also ideally suited to study the dynamics in the energy range $0.001 < E < 100$ meV.

Apparently the properties of the neutrons make them a attractive probe for a wide variety of applications. In the reminder of the lecture I will try to answer the question, what the providers of neutrons, e.g. JCNS, FRM II, ILL, SNS..., can do to make their users happy. Therefore we first need do understand, what users want. We consider an generic neutron spectrometer, that allows to measure transfer of energy and momentum between neutron and the sample, see Fig. 2.1. How this is done, you will learn in the other lectures of the course and mainly during the practical part. The signal you get finally at the detector of your instrument can be expressed in

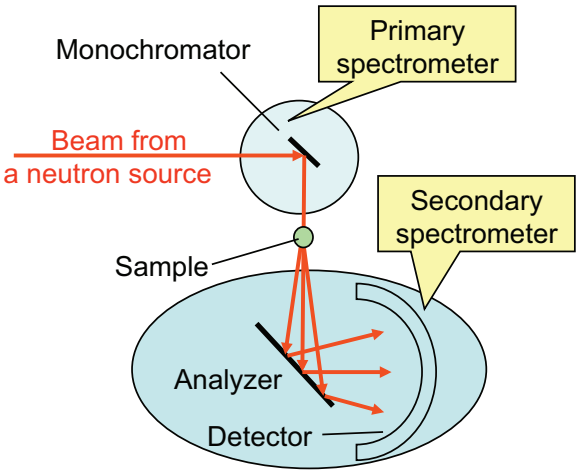

Fig. 2.1: *Generic layout of a neutron spectrometer*

the following way:

$$I_{det} = I_0 \epsilon_{pr} \epsilon_{sec} \epsilon_{det} \sigma_{sample} V_{sample} + \text{background} \tag{2.7}$$

I_0 is the incident neutron flux, ϵ_x denotes the efficiencies of the primary and the secondary spectrometer and the detector, $\sigma_{sample}, V_{sample}$ is the cross section and the Volume of the sample, respectively. If you have an interesting scientific question that has not been answered yet, usually the both the cross section and volume are small. Hence to get good data, you need first an efficient instrument with a good signal to noise ratio, which detects ideally all and only the neutrons scattered by the sample. Second you need a low background that allows you to distinguish also tiny signals. And last but not least you need an intense source of neutrons, that brings a lot of useful neutrons to the instrument.

2.2 How do we get free neutrons?

The free neutron has a mean lifetime of about 900 s, hence it is necessary to produce the free neutrons as you run your experiment. While most nuclei are constituted to more then 50 % by neutrons, nuclear forces confine them and hence it is rather difficult to set neutrons free. Nowadays free neutron for scientific applications are released by nuclear reactions mainly in fission reactors or in spallation sources. Both routes require large scale facilities, that operate the source and provide state-of-art instrumentation. One example for the nuclear research reactor is the FRM II, where you will perform the practical part of the Laboratory Course. The most

powerful spallation source is the SNS installed at the Oak Ridge National Laboratory in the USA. The neutron as a free particle was discovered by James Chadwick in 1932, when he investigated the radiation from Beryllium illuminated with α particles. Finally he described the ongoing reaction as

$$ {}^{4}_{2}\alpha + {}^{9}_{4}Be \rightarrow {}^{12}_{6}C + {}^{1}_{0}n. \tag{2.8} $$

The uncharged particle in this equation was called neutron. The flux of free neutrons released by the reaction was about 10^0 n cm^{-2}s^{-1}. Such a small number would prevent any scattering experiment.

2.2.1 Nuclear fission reactors

With the development of nuclear fission reactors in the 1940ies the situation changed. Using the fission reaction

$$ {}^{235}U + {}^{1}_{0}n \rightarrow \text{fission fragments} + 2.52 \times {}^{1}_{0}n + 180\text{MeV} \tag{2.9} $$

the first experimental reactors released about 10^7 n cm^{-2}s^{-1}. Beside the investigation of the nuclear reaction, such a flux enabled the first scattering experiments with neutrons. In the following the thermal neutron flux increased dramatically until it saturated in the mid fifties. The still most powerful research reactor at the ILL became critical in 1974. The modern FRM II reactor has 0.5 $\times$ the flux of the ILL, but the thermal reactor power is lower by a factor 0.33 due to special core design. Furthermore, the flux of cold neutrons (see Sec. 2.3) is more or less the same. In the nuclear fission reaction eq. (2.9) a slow neutron is captured by an ^{235}U

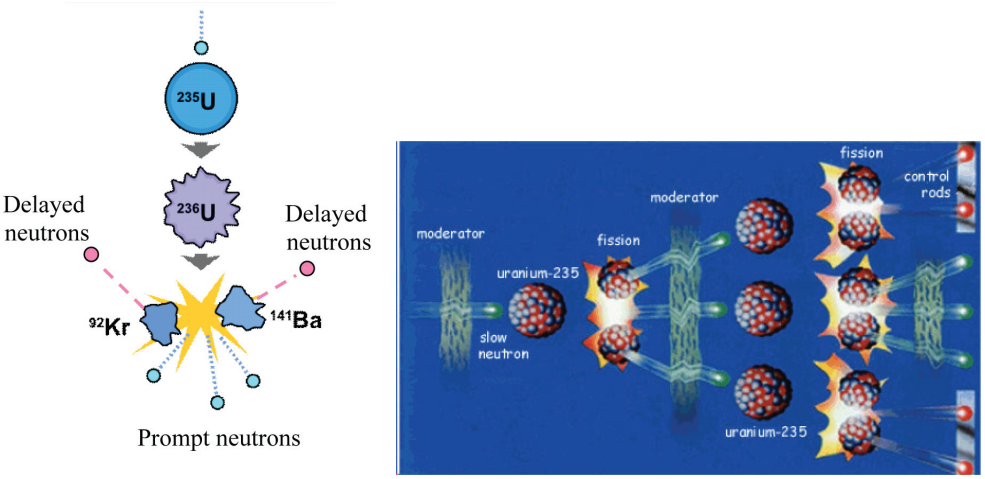

Fig. 2.2: *Left) Schematic presentation of the fission process of ^{235}U. Right) Controlled chain reaction in the nuclear reactor. Control rods reduce the number of slow neutrons to the amount just as necessary for the selfsustaining chain reaction. By the proper adjustment of the control rods position, the reaction may remains critical only with the inclusion of the delayed by a few seconds neutrons.*

nucleus, which then splits into two fragments releasing 2 or 3 prompt neutrons, which carry an

energy of 1.29 MeV. Each of this instantaneously (within 10 ns) emitted neutrons can fission another nuclei so that each of them will emit another 2 to 3 neutrons. The process is called chain reaction If the mass of the fissile material is larger than the so called critical mass M_C the number of neutron will increase exponentially, leading to an uncontrollable reaction. If the mass of the fissile material is smaller than M_C the number of neutrons will decrease over time and the nuclear chain reaction stops. If you want to sustain the nuclear reaction for a long time it is necessary to control the neutron flux such that the number of neutrons that drive the chain reaction remains constant. The control of the reactor is possible, if the nuclear reaction is not only triggered by the prompt neutrons. The fission fragments are also highly excited nuclei and relax to their ground state by the emission of neutrons among other nuclear reactions. Concerning only the prompt neutrons, the reactor is operated below its critical mass M_C, but the delayed neutrons, which are comprised by the prompt neutrons, which are moderated in the cooling medium and the secondary neutrons from the fission fragments, sustain the chain reaction. The number of delayed neutrons is controlled by rods of neutron absorbing material (usually Boron), which can be inserted in the reactor core. Beside the control rods, which are used to steer the reactor, additional rods exist to fully stop the flux of neutrons and shut down the reactor.

With the development of the nuclear research reactors the thermal neutrons flux increased rapidly until it reached a flux $\Phi = 10^{15}$ n/cm^2/s at the end of the 1960ties. An increase in neutron flux goes simultaneously with an increase in the thermal power of the reactor. However, the installations for extracting the neutrons suffers strongly by heat and radiation damage. Therefore the development of more powerful research reactors has stopped with the design of ILL reactor. The modern FRM II reactor has a very compact reactor core, which provides half of the thermal neutron flux using only one third of reactor power as compared to the ILL.

2.2.2 Spallation neutron source

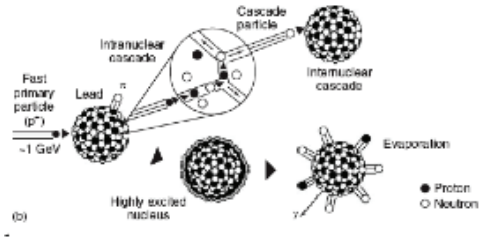

Fig. 2.3: *Schematic presentation of the spallation reaction*

As an alternative to nuclear fission reactors neutrons can be released from the nucleus via spallation reactions, see Fig. 2.3. Here, high energy protons are accelerated onto a target made of a neutron rich material. Due to the large energy, the de Broglie wavelength

$$\lambda = \sqrt{\frac{h^2}{2mE}} \tag{2.10}$$

is so short, that the protons interacts with the single nucleons instead of the nucleus as a whole. The kicked nucleon may either leave the nucleus leading to an inter-nuclear cascade or may

be scattered by other nucleons leading to an intra-nuclear cascade. However, as a result of stage 1 of the spallation process, the nucleus is in a highly excited state. In stage 2 this energy is released by evaporation of a whole particle zoo, including neutrons. The neutron yield per spallation event depends on the target material. For typical materials 20-50 neutrons are released per spallation event. The deposited heat depends on the target material, too, and is on the order of 20 to 50 MeV/$^1_0$n.

Concerning safety, the spallation source can never run out of control as no chain reaction is running. Neutrons are only produced, as long as the protons are accelerated onto the target. Even better, this feature can be used to impose a precise time structure on the neutron spectrum. The spallation process happens on a time scale of 10^{-15} s. Therefore the length of the proton pulse determines the length of the neutron pulse. If one measures the time of flight of a neutron from the source to the detector at your instrument, the neutron velocity can be determined, as the flight path is also known. You will learn more about time-of-flight spectroscopy and diffraction in the remaining lectures. Among the spallation source on distinguishes so called long pulse

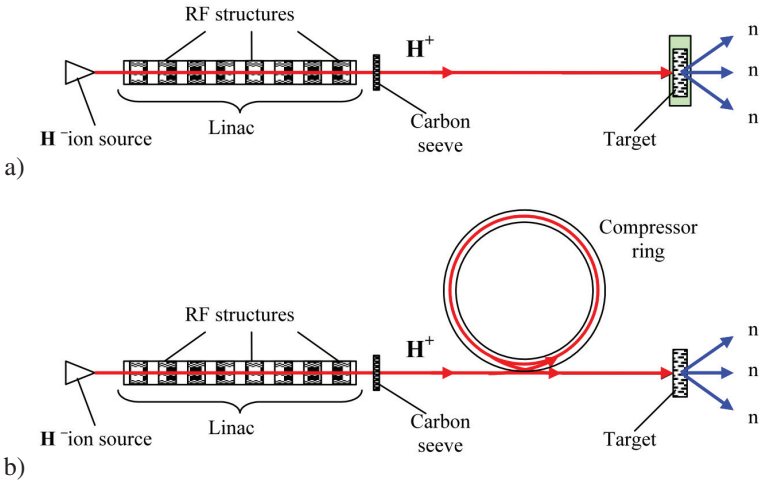

Fig. 2.4: *Schematic of a long pulse and a short pulse spallation source.*

spallation sources (LPSS) and short pulse spallation sources. Using a linear accelerator a proton bunch with a width of several ms can be tailored. If the neutron pulse should be shorter, the protons have to be compressed. This is done by feeding the protons from the Linear accelerator into a synchrotron. The next bunch is then feed in, when the former one has revolved once, to make a denser proton bunch. Using the compressor, the 1μs duration pulses. While the latter type provides a higher peak flux, i. e., more neutrons in a short time intervall, the former type yields a significantly higher average neutron flux, in particular in the energy range that is typically used for diffraction experiments. Therefore certain experiments are better of at a SPSS, while the LPSS provides a more versatile spectrum and clearly is superior for 'slow' neutrons. The most powerful existing spallation source, the 1 MW SNS at Oak Ridge is a SPSS,

while the planned ESS in Lund, Sweden, will be a LPSS with 5 MW power.

2.2.3 Comparison of reactor and spallation sources

Comparing the different sources, we have to consider a number of features:

Neutron Flux Nowadays reactor source still provide the highest average neutron flux. This flux is still higher as the flux at the 1.4 MW SPSS. The 5 MW spallation source wil actually reach a similar average flux. However, for most experiments it is necessary, to select only a narrow range in energy or wavelength, respectively. At a pulsed source this can be done natively using time-of-flight monochromatization. Then not the average flux, but the peak flux, i. e., the flux during the proton pulse, counts. In that case, the monochromatic intensity at the spallation source can be higher.

Safety While the fissile material inside the reactor core of a research reactor is only a small fraction of the amount in a nuclear power plant, there is still a nuclear chain reaction ongoing, which in principle can run out of control. The spallation reaction is not possible without the operation of the accelerator and is therefore inherently safe.
As both source use nuclear reactions and create high energy particles, they both produce radioactive waste, which must be treated or stored after the operation of the facility. In case of the spallation source the waste has generally shorter life times.

Stability In fact, the operation of a proton accelerator is quite delicate. As already mentioned this makes the source very safe. On the other hand, sometimes it may also happen, that the proton beam is not available for quite some time during your allocated beam time. The neutron reactor runs usually very stable without interruption. Additionally the neutron flux is more stable at the reactor making it easier to compare individual measurements.

Technical feasibility The source neutron flux at a reactor could be increased only by an increase of the thermal power. There have been attempts to build a more powerful reactor in the US in the nineties, which has been abandoned for economical reasons. The heat removal from the core becomes extremely complex and also the radiation damage to the installations necessary for the extraction of the neutron is a severe issue. Therefore is unlikely, that higher power research reactors will be realized. At a spallation source the deposited heat For the SPSS exist similar arguments. The intense proton beam implants a large amount of heat in a very short time interval. Again the major problem is the removal of this heat. There seem to be a technological limit also for the short pulse spallation sources to increase their power far beyond the present state. For the long pulse spallation sources, the situation seems to be slightly relaxed. Since the heat is implanted during a longer time interval, the heat removal is facilitated. The 5 MW of power for the ESS could possibly increased up to 10 MW. There exist even estimates, that one could design a long pulse spallation target running at 20 MW. However, these are plans for the very far future, as already the ESS will be operational in the 2020ies only.

So far I have not considered the nuclear fusion reaction as a source for neutrons. Technologically this could be a technique at least as far in the future as a 20 MW spallation source. However, as seen from table 2.1 the deposited heat makes this reaction also a candidate for the over next generation of neutron sources.

Reaction	Energy (GeV) per event	Neutron yield per event	Deposited heat (MeV) per neutron
(T,d) fusion		1	3
^{235}U fission		1	180
Pb spallation	1	20	23
^{238}U spallation	1	40	50

Table 2.1: *Comparison of neutron producing reactions*

2.3 How do we make free neutrons useful?

The neutrons as the are released from the nucleus have energies in the MeV range corresponding to a wavelength according to eq. (2.10) $\lambda \approx 10^{-5}$ Å. The energies we are interested in solid state physics, chemistry or biology rather range from the μeV range for relaxation phenomena to the eV range for the bonding of the valence electrons in molecules. One my also compare the energy scale to the corresponding temperatures via

$$E_{\text{therm}} = k_B T. \tag{2.11}$$

From here we see that 1 meV is equivalent to a temperature of 11.6 K or vice versa 300 K are equivalent to 25.6 meV.

The distances we want to resolve in a neutron scattering experiment are on a atomic or molecular length scale and range from 1 Å to 1μm and therefore the neutrons should have comparable wavelength to have an appropriate resolution. If we use again the expression for the de Broglie wavelength eq. (2.10), we find that a neutron with an energy $E = 25.6$ meV has a wavelength $\lambda = 1.8$ Å, fulfilling both requirements simultaneously. This is also the reason, why neutron scattering is so versatile for studies of the dynamics of crystalline materials, because all atoms in a crystal show coherent motions due to their arrangement and bonding.

How can the neutrons now slowed down to the energies we are interested in? The best way is, if they collide elastically with other partners of much lower energy and spread this energy in a large volume (don't forget, that 1 MeV$= 1.6 \times 10^{-13}$ J). The energy loss per collision depends on the mass of the colliding partners: The highest energy transfer is achieved, if the mass of both partners is equal. Therefore ^1H or ^2H are the best partners, making water an ideal choice for the moderator. Since protons like to react with neutrons, the moderator often contains heavy water, i.e. D_2O, which has a smaller absorption cross section. For the FRM II the reactor core is surrounded by the heavy water tank. The outer area of the water tank is filled with light water, hence the flux of neutrons hitting the biological shielding outside the tank is already reduced.

Typically it takes several μs to moderate the neutron to the temperature of the surrounding water. This process is therefore called thermalization. Within this time the neutron travel away from the reactor core, where they are produced. On the other hand, there is a finite probability for the absorption of a neutron, if the flight path inside the water is too long. The maximum of the thermal neutron flux density is displaced from the reactor core with the fuel element by 10 to 15 cm, as shown in Fig. 2.5 a).

For an experiment it is now of main interest to collect as many useful neutrons from the reactor, but not to get the fast neutrons or the Γ radiation that are created in the nuclear reactions into the

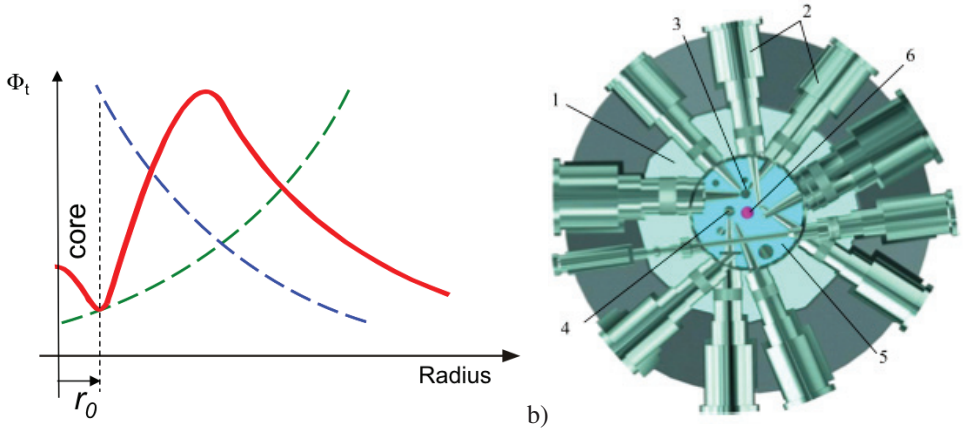

Fig. 2.5: *a) Radial distribution of the thermal neutron flux density in the reactor vessel. The green line indicates the distribution, where the full thermalization is reached, the blue line indicates that the absorption decreases the neutron flux. b) Schematic of the reactor vessel of the FRM II showing the reactor core and the beam tubes extracting the neutrons to the experiments. The reactor tank with internal diameter approx. 5m is filled with light water (1). In the centre of the arrangement the reactor core is situated. The experimental installations as horizontal beam tubes (2), a cold (3) and a hot (4) neutron source are arranged in the heavy water tank (5) around the fuel element (6).*

experimental area. Therefore the beam tubes, as indicated in Fig. 2.5 b) don't face the reactor core , but tangentially look onto the maximum of the thermal flux distribution.

In the end of the thermalization process the neutrons are in thermal equilibrium with the surrounding medium. The energy distribution takes the form of the Maxwellian distribution:

$$\Phi(E) = \frac{2\sqrt{E}}{\sqrt{\pi k^3 T_M}} \exp -\frac{E}{k_b T_M} \tag{2.12}$$

The neutrons are commonly classified for certain energy and wavelength ranges according to the position of the maximum of the Maxwell distribution for a given moderator temperature T_M:

	Energy range(meV)	Wavelength range (Å)
Ultra cold	$E < 0.0005$	$\lambda > 400$
Very cold	$0.0005 < E < 0.005$	$40 < \lambda < 400$
Cold	$0.05 < E < 5$	$4 < \lambda < 40$
Thermal	$5 < E < 100$	$0.9 < \lambda < 4$
Hot	$100 < E < 1000$	$0.3 < \lambda < 0.9$

To access the respective energy range the moderator should again effectively moderate the neutrons but also be transparent for the neutrons. A liquid hydrogen vessel fulfills the requirements for cold neutrons. A more effective but also more difficult technique employs solid methan as a moderator. A carbon block heated to a temperature above 1000 K is used in reactors to provide an intense source of hot neutrons. In Fig. 2.6 the spectra for the different moderator temperatures show clearly, that the maximum is shifted towards shorter wavelength, when

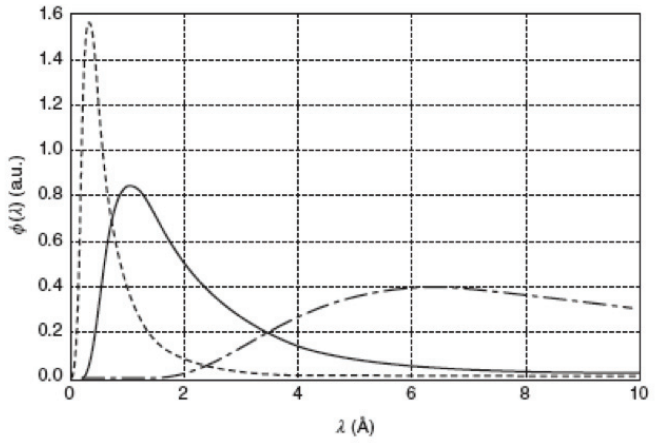

Fig. 2.6: *Neutron wavelength distribution for different moderator temperatures.Cold spectrum,* $T = 50$ *K, dot dashed line, thermal spectrum,* $T = 300$ *K, solid line, hot spectrum,* $T = 1000$ *K, dashed line.*

the temperature is increased. In a spallation source usually a different route is used to yield an intense beam of hot neutrons: The moderator is made thin enough to not fully moderate the neutrons. Therefore epithermal neutrons still exist in the energy distribution of the source. The time structure of the source might then be used to discriminate the eventually increased background.

2.4 How do we bring the neutrons to the experiment?

The angular distribution of the thermal flux distribution at the end of the thermalization process is fully isotropic. To calculate the flux at the exit of a beam tube approximately one has to divide the thermal flux at the maximum by the surface area of the sphere with the respective radius, in the case of the FRM II 2.5 m, see Fig. 2.5 b). Already at this distance the flux is reduced already by 6 orders of magnitude. If the distance required to build an actual instrument is added, the flux is lowered by 8 orders of magnitude.

To overcome this problem, neutron guides are used. These consist of 4 neutron mirrors, enclosing the flight path of a neutron. The principle of the neutron guide is similar to light wave guides: External total reflections prevents the neutrons from leaving the guide and they are transported to the end of the guide. In the case of the light wave guide, the fibre has a larger index of refraction than the surrounding air, giving rise to typical critical angles $\theta_C \approx 45°$. For the neutron guide, the vacuum inside has a larger index of refraction and the critical angle is given by

$$\theta_C = \lambda\sqrt{\frac{2\rho b_c}{\pi}} \tag{2.13}$$

with the particle density ρ and the coherent scattering length b_c. The element with the largest critical angle is Nickel and for the element the critical angle can simply be approximated $\theta_C = 0.1°\text{Å}^{-1}$. If we install such a neutron guide behind a beam tube, all neutrons, that impinge on the Ni surface under a shallower angle than the critical angle, will be guided to the instrument. If we calculate for $\lambda = 5$ Å neutrons we loose only 4 orders of magnitude independent of

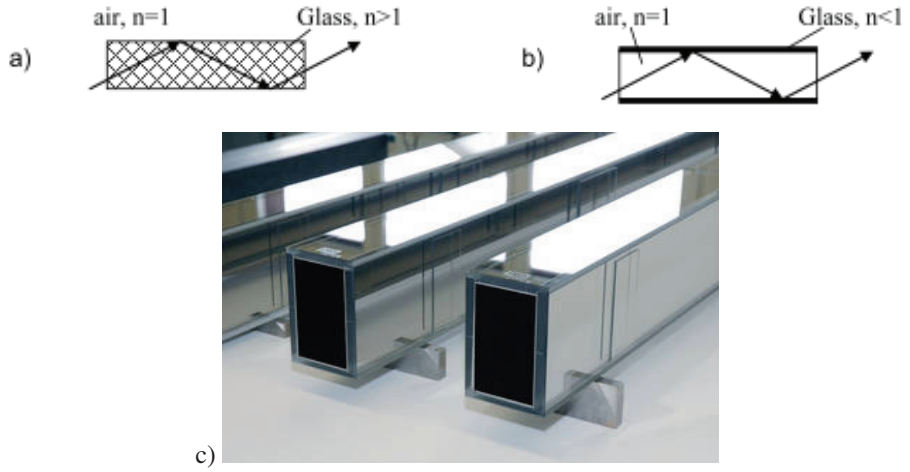

Fig. 2.7: *a) Schematic of a light wave guide. External total reflection occurs, because the fibre is optically denser than the air. b) Schematic of a neutron guide. Total reflection occurs, because the index of refraction of the mirror coating is smaller than 1. c) Picture of a super mirror neutron guide, taken from www.swissneutronics.ch.*

the distance from the reactor core. Hence such a neutron guide can be used to provide more space for instruments by going further away from the reactor. Nowadays so called supermirrors consisting of thin layers of e.g. Ni and Ti increase the critical angle of Ni by a factor up to 7. In that case it becomes possible to build neutron guides not only for cold neutrons but also for thermal neutrons. Furthermore complex focusing optics can be realized by neutron guides to increase the number of useful neutrons at the spectrometer and simultaneously keep the background low

At least as important as gaining space is the fact, that the direct sight from the instrument onto the reactor core can be omitted. Fast neutrons and Γ radiation is leaving through the holes for the neutron beamlines. They go mainly in a straight line from where they have been created, because their scattering cross section is very small. These particles contribute mainly to the radiation background around the instruments. They can of course also contribute to the background in your detector. The particles are kept away from users and detectors by massive shielding, containing a lot of concrete (for fast neutrons) or lead (for Γ radiation). If such a neutron guide is bend with a large radius, the direct line of sight hits the wall of the neutron guide and the background of the instrument can be further suppressed. Of course your shielding must then be strongest in the direct line of sight.

2.5 How do we detect neutrons?

On of the strongest advantages of the neutrons is their neutrality. It allows to probe deeply into matter. On the other hand, this makes the detection of the neutrons difficult, as it penetrates large volumes of matter without interaction. Luckily there exists a hand full of isotopes that have a large absorption cross section for thermal or cold neutrons, such as ^{3}He ^{10}B, Gd or ^{235}U.

The nuclear reactions create charged particles, which can be analyzed by interaction with the electric fields. Since the absorption cross section in the thermal to cold energy range increases more or less linearly with the wavelength, the detection of cold neutrons is more effective than the absorption of thermal neutrons

One type of detector is the gas proportional counter filled either with ^{3}He gas or gaseous $^{10}BF_3$. The absorption process releases a certain number of photons, which create secondary electrons by Compton scattering or the photo effect, or high energetic charged particles. The particles are accelerated onto the cathode or anode according to their charge and the resulting current can be related to the neutron absorption event. A refinement of the apparatus allows also the localization of the absorption event yielding a position sensitive detector. Features of the gas proportional counter are a high detection probability, which can be tuned by the filling pressure, and a low sensitivity to Γ radiation. Disadvantages are a limited count rate before the detector saturates and a position sensitivity > 1 cm.

A szintillation detector provides a much higher spatial resolution. Here the neutron absorption at a neutron absorber embedded in the solid szintillation material yields Γ photons that are detected by the photo electric effect. This detectors provides a higher spatial and timing resolution but has also a larger Γ sensitivity.

2.6 The take home messages

Today, intense neutron beams are available a nuclear research reactors and spallation sources. Reactors deliver a very stable continuous beam, while spallation sources provide a very high peak flux that can be effectively used by time-of-flight methods.

Neutrons are extremely useful for condensed matter research, if the wavelength and kinetic energy match the length scale and energy scale of e.g. magnetic compounds, polymers or biological samples. These is realized by moderating the fast neutrons released in the nuclear reaction in a volume containing a lot light elements, e.g. water for thermal neutrons, liquid hydrogen or solid methan for cold neutrons or heated graphite for hot neutrons.

Neutron guides are used to transport neutrons with only small losses quite far away from the actual neutron source. This gives more space for instruments, improves the background conditions and may even be used to tailor the neutron beam properties using complex optics similar to light optics.

Further reading

1. G.R. Bauer (1993) Neutron sources. In: A.Furrer (ed.) *Neutron Scattering*, pp. 331–357. PSI-Proceedings No. 93-01, ISSN 1019-6447, Paul Scherrer Institute, Villigen.

2. J.M. Carpenter and W.B. Yelon (1986) Neutron sources. In: K. Sköld and D.L. Price (eds.) *Methods of Experimental Physics*, vol. 23A, pp. 99196. London: Academic Press.

3. K. Clausen (2001) *Neutron sources.* Office for Official Publications of the European Communities, Luxembourg, ISBN 92-894-0037-4.

4. Utsuro, Masahiko and Ignatovich, Vladimir, *Handbook of Neutron Optics.* ISBN-13: 978-3-527-40885-6 - Wiley-VCH, Berlin.

Exercises

E2.1 How are neutrons characterized?*

Write down the kinetic energy of a free neutron as a function of its momentum!
What is the velocity in ms^{-1} and energy in meV of neutrons with a wavelength $\lambda = 1, 1.8, 5$ Å, respectively?

$$\begin{aligned} m_n &= 1.675 \times 10^{-27}\mathrm{kg} \\ h &= 6.626 \times 10^{-34}\mathrm{Js} \\ e &= 1.602 \times 10^{-19}\mathrm{As} \end{aligned}$$

E2.2 How many neutrons are produced?**

Calculate the neutron flux density of a 20 MW reactor, assuming that the flux maximum is displaced 10 cm from a point-like reactor core! What would be the flux density of a hypothetical spallation source with the same thermal power?

E2.3 How do the neutrons come to your experiment?

Why is the neutron flux reduced, when you build the diffractometer/spectrometer at larger distance without a neutron transport system? When is it advantageous to have the instrument close to the neutron source? What reasons can you imagine to separate the instrument from the neutron source?

3 Symmetry of Crystals

G. Heger
RWTH Aachen

Contents

Lecture Notes of the JCNS Laboratory Course Neutron Scattering

3.1 Introduction

The term “crystal” comes from the Greek κρύσταλλος , which was first used as description of ice and later on - more general - of transparent minerals with regular morphology (regular crystal faces and edges).

Fig. 3.1: *Example: rock crystal – quartz (SiO_2), mineral from the Gotthard-Massif.*

Matter is usually classified into three states: gaseous – liquid – solid. Crystals are representatives of the solid state. **Crystalline solids are thermodynamically stable** in contrast to glasses and are **characterised by a regular three-dimensional periodic arrangement of atoms (ions, molecules) in space**.

3.2 Crystal lattices

The three-dimensional periodicity of crystals can be represented by the so-called crystal lattice. The repeat unit in form of a parallelepiped - known as the **unit cell** – is defined by 3 non-linear basis vectors $\boldsymbol{a}_1$, $\boldsymbol{a}_2$, and $\boldsymbol{a}_3$, whose directions form the reference axes *X*, *Y*, and *Z* of the corresponding right-handed crystallographic coordination system. The 6 lattice parameters are given as the lengths of the basis vectors $a = |\boldsymbol{a}_1|$, $b = |\boldsymbol{a}_2|$, $c = |\boldsymbol{a}_3|$ and the angles between the basis vectors: angle $(\boldsymbol{a}_1,\boldsymbol{a}_2) = \gamma$, angle $(\boldsymbol{a}_2,\boldsymbol{a}_3) = \alpha$, angle $(\boldsymbol{a}_3,\boldsymbol{a}_1) = \beta$. The faces of the unit cell are named as face $(\boldsymbol{a}_1,\boldsymbol{a}_2)$ = C**,** face $(\boldsymbol{a}_2,\boldsymbol{a}_3)$ = A**,** face $(\boldsymbol{a}_3,\boldsymbol{a}_1)$ = B.

If the vertices of all repeat units (unit cells) are replaced by points, there results the crystal lattice in the form of a **point lattice**. Each lattice point is given by a vector $\boldsymbol{a} = u\boldsymbol{a}_1+v\boldsymbol{a}_2+w\boldsymbol{a}_3$, with *u*, *v*, *w* being integers. As a symmetry operation of parallel displacement, $\boldsymbol{a}$ – also known as **translation vector** – maps the atomic arrangement of the crystal (crystal structure) onto itself.

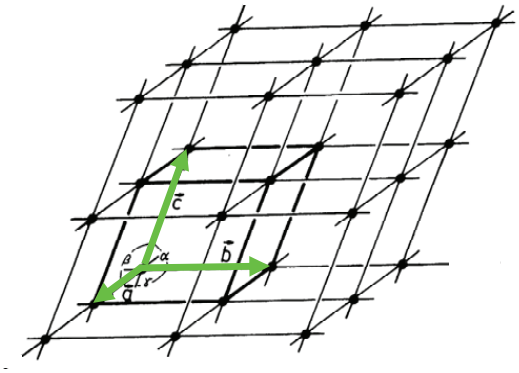

Fig. 3.2: *Notation for a unit cell and a point lattice.*

A **lattice point** is named "*uvw*", according to the coefficients (integers) of the translation vector $\boldsymbol{a} = u\boldsymbol{a_1}+v\boldsymbol{a_2}+w\boldsymbol{a_3}$ from the origin to the lattice point. A **lattice direction** - given by the symbol [*uvw*] - is defined by the direction of the corresponding translation vector.

A plane passing through three lattice points is known as a **lattice plane**. Since all lattice points are equivalent (by translation symmetry) there will be infinitely many parallel planes passing through all the other points of the lattice. Such a set of equally spaced planes is known as a **set of lattice planes**. If the first plane from the origin of a set of lattice planes makes intercepts a/h, b/k, c/l on the X, Y, Z axes, respectively, where h, k, l are integers, then the **Miller indices** of this set of lattice planes are (hkl), the three factors h, k, l being enclosed in parentheses.

The equation of lattice planes can be written in intercept form as

$$(hx/a) + (ky/b) + (lz/c) = n, \tag{3.1}$$

where n is an integer. If n = 0 the lattice plane passes through the origin; if n = 1 the plane makes intercepts a/h, b/k, c/l on the X, Y, Z axes respectively; if n = 2 the intercepts are $2a/h$, $2b/k$, $2c/l$; and so on.

The line of intersection of any two non-parallel lattice planes is a row of lattice-points common to both planes. This lattice point row defines a lattice direction [*uvw*] which is known as **zone axis**. All lattice planes intersecting in a common lattice-point row are said to lie in the same **zone**. The condition for lattice planes to be parallel to a lattice vector $\boldsymbol{a} = u\boldsymbol{a_1}+v\boldsymbol{a_2}+w\boldsymbol{a_3}$ is the **zone equation**

$$uh + vk + wl = 0 \tag{3.2}$$

The zone axis symbol [*uvw*] for the zone containing the two planes ($h_1k_1l_1$) and ($h_2k_2l_2$) is obtained by solving the simultaneous equations $uh_1 + vk_1 + wl_1 = 0$ and $uh_2 + vk_2 + wl_2 = 0$,

$$[uvw] = [k_1l_2-k_2l_1,\ l_1h_2-l_2h_1,\ h_1k_2-h_2k_1] \tag{3.3}$$

3.3 Crystallographic coordinate systems

The description of a crystal structure consists first of the choice of a unit cell as smallest repeat unit of the crystal with its basis vectors. In this way a crystal-specific coordinate system is defined which is used to localize all the atoms in the unit cell. Whereas in physics and chemistry usually Cartesian coordinate systems are used, in crystallography quite different systems are applied. The conventional crystallographic coordinate systems are based on the symmetry of the crystals. In three dimensions there exist 7 different crystal systems and hence 7 crystallographic coordinate systems:

system name	minimum symmetry	conventional unit cell
triclinic	1 or $\bar{1}$	$a \neq b \neq c$; $\alpha \neq \beta \neq \gamma$
monoclinic (unique axis b)	one diad – 2 or m ($\parallel Y$)	$a \neq b \neq c$; $\alpha=\gamma=90°$, $\beta>90°$
orthorhombic	three mutually perpendicular diads – 2 or m ($\parallel X$, Y and Z)	$a \neq b \neq c$; $\alpha=\beta=\gamma=90°$
tetragonal	one tetrad – 4 or $\bar{4}$ ($\parallel Z$)	$a = b \neq c$; $\alpha=\beta=\gamma=90°$
trigonal (hexagonal cell)	one triad – 3 or $\bar{3}$ ($\parallel Z$)	$a = b \neq c$; $\alpha=\beta=90°$, $\gamma=120°$
hexagonal	one hexad – 6 or $\bar{6}$ ($\parallel Z$)	$a = b \neq c$; $\alpha=\beta=90°$, $\gamma=120°$
cubic	four triads – 3 or $\bar{3}$ ($\parallel$space diagonals of cube)	$a = b = c$; $\alpha=\beta=\gamma=90°$

The choice of the origin of the coordinate system is free in principle, but for convenience it is usually chosen in a centre of symmetry (inversion centre), if present, otherwise in a point of high site symmetry of the space group.

In order to complete the symmetry conventions of the coordinate systems it is necessary to add to the 7 so-called primitive unit cells of the crystal systems (primitive lattice types with only one lattice point per unit cell) 7 centred unit cells with two, three or four lattice points per unit cell (centred lattice types). These centred unit cells are consequently two, three or four times larger than the smallest repeat units of the crystals. The resulting 14 **Bravais lattice types** with their centring conditions are collected in figure 3.3.

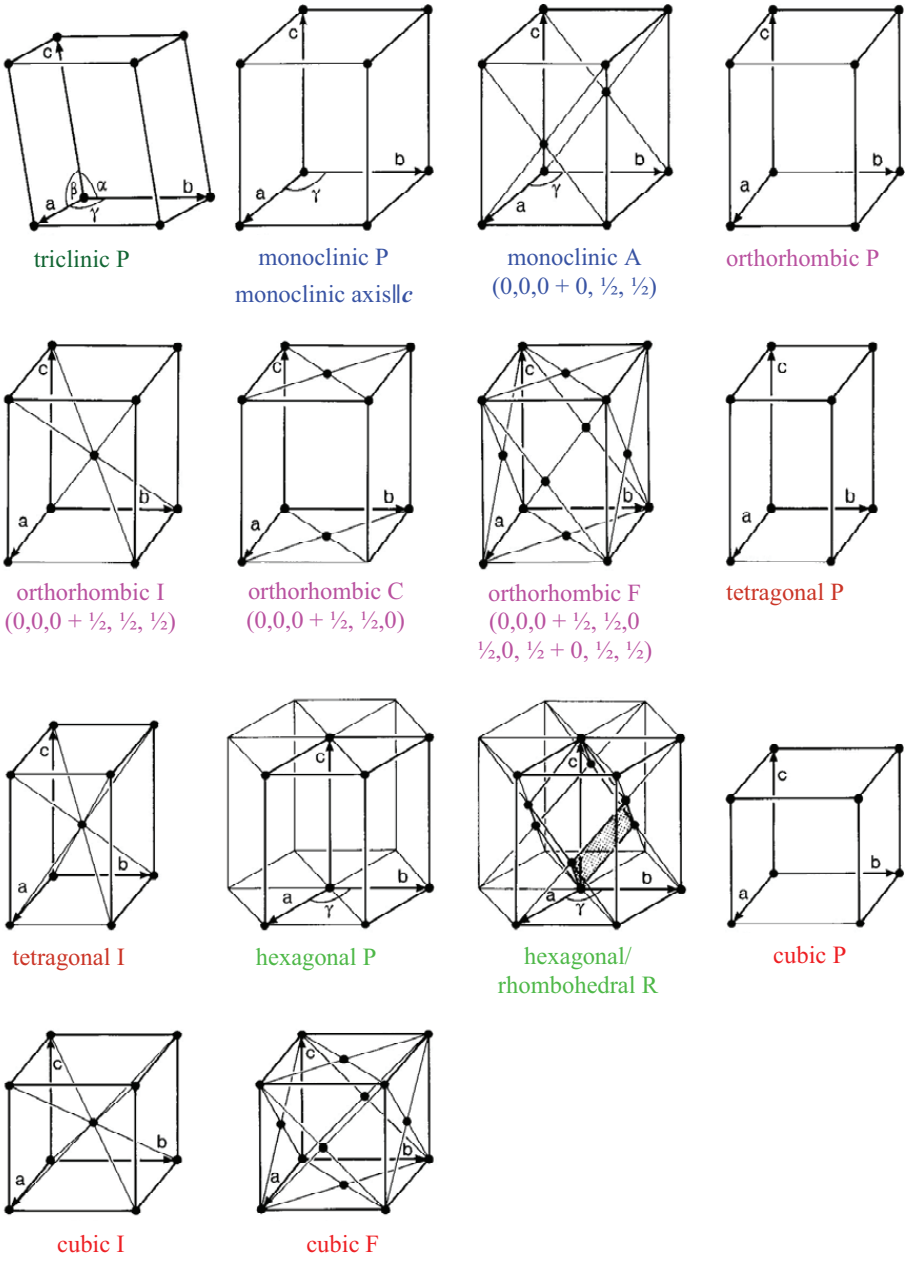

Fig. 3.3: *The 14 Bravais lattices consisting of the 7 primitive lattices P for the 7 crystal systems with only one lattice point per unit cell + the 7 centred (multiple) lattices A, B, C, I, R and F with 2, 3 and 4 lattice points per unit cell.*

A set of lattice planes (*hkl*) is separated by a characteristic interplanar spacing *d*(*hkl*). According to the different crystallographic coordinate systems these *d*(*hkl*) values are calculated in a specific manner:

For the cubic lattice ($a = b = c$, $\alpha = \beta = \gamma = 90°$), ex. NaCl

$$d(hkl) = a \cdot \left(h^2 + k^2 + l^2\right)^{-\frac{1}{2}} \tag{3.4}$$

For the hexagonal lattice ($a = b, c$, $\alpha = \beta = 90°$, $\gamma = 120°$), ex. Graphite

$$d(hkl) = \left(\frac{4}{3}\frac{h^2 + k^2 + hk}{a^2} + \frac{l^2}{c^2}\right)^{-\frac{1}{2}} \tag{3.5}$$

For the tetragonal lattice ($a = b, c$, $\alpha = \beta = \gamma = 90°$)

$$d(hkl) = \left(\frac{h^2 + k^2}{a^2} + \frac{l^2}{c^2}\right)^{-\frac{1}{2}} \tag{3.6}$$

For the orthorhombic lattice (a, b, c, $\alpha = \beta = \gamma = 90°$)

$$d(hkl) = \left(\frac{h^2}{a^2} + \frac{k^2}{b^2} + \frac{l^2}{c^2}\right)^{-\frac{1}{2}} \tag{3.7}$$

For the monoclinic lattice (a, b, c, $\alpha = \gamma = 90°$, $\beta > 90°$)

$$d(hkl) = \left(\frac{h^2}{a^2\sin^2\beta} + \frac{k^2}{b^2} + \frac{l^2}{c^2\sin^2\beta} - \frac{2hl\cos\beta}{ac\sin^2\beta}\right)^{-\frac{1}{2}} \tag{3.8}$$

For the triclinic lattice ($a, b, c, \alpha, \beta, \gamma$), the most general case,

$$\begin{aligned} d(hkl) = {} & \left(1 - \cos^2\alpha - \cos^2\beta - \cos^2\gamma + 2\cos\alpha \cdot \cos\beta \cdot \cos\gamma\right)^{\frac{1}{2}} \\ & \left(\frac{h^2}{a^2}\sin^2\alpha + \frac{k^2}{b^2}\sin^2\beta + \frac{l^2}{c^2}\sin^2\gamma \right. \\ & \left. + \frac{2kl}{bc}\left(c \cdot \cos^2\beta - \cos\alpha\right) + \frac{2lh}{ca}\left(c \cdot \cos^2\gamma - \cos\beta\right) + \frac{2hk}{ab}\left(c \cdot \cos^2\alpha - \cos\gamma\right)\right)^{-\frac{1}{2}} \end{aligned} \tag{3.9}$$

3.4 Crystallographic symmetry operations and symmetry elements

The **symmetry operations** of a crystal are isometric transformations or motions, i.e. mappings which preserve distances and, hence, also angles and volumes. An object and its transformed object superpose in a perfect manner, they are indistinguishable.

The simplest crystallographic symmetry operation is the **translation**, which is a parallel displacement of the crystal by a translation vector $\boldsymbol{a}$ (see chapt. 3.2). There is no fixed point, the entire lattice is shifted and therefore, theoretically, the crystal lattice is considered to be infinite.

Crystallographic **rotations** n around an axis by an angle $\varphi = 360°/n$ (n-fold rotations) and **rotoinversions** (combination of rotations and inversions) $\bar{n}$ are called point symmetry operations because they leave at least one point of space invariant (at least one fixed point). An important fact of crystallographic symmetry is the restriction of the rotation angles by the three-dimensional crystal lattice to $\varphi = 360°$ (n = 1), 180° (n = 2), 120° (n = 3), 90° (n = 4), 60° (n = 6). Only for these crystallographic rotations the space can be covered completely without gaps and overlaps. The rotoinversion $\bar{n} = \bar{1}$ is an **inversion** in a point, $\bar{n} = \bar{2} \equiv m$ (mirror) describes a **reflection** across a plane.

The combination of n-fold rotations with $m/n \cdot \boldsymbol{a}$ translation components (m < n) ∥ to the rotation axis leads to the so-called **screw rotations** n_m, e.g. 2_1, 3_2, 4_2, 6_5. These symmetry operations have no fixed points.

The combination of a reflection through a plane (glide plane) with translation components (glide vectors) of $\boldsymbol{a_1}/2$, $\boldsymbol{a_2}/2$, $\boldsymbol{a_3}/2$, $(\boldsymbol{a_1}+\boldsymbol{a_2})/2$, … ∥ to this plane are known as **glide reflections** a, b, c, n, …, d. Again no fixed points exist for these symmetry operations.

In addition to the symmetry operations which represent isometric motions of an object, symmetry can also be described in (static) geometrical terms by **symmetry elements**. They form the geometrical locus, oriented in space, on which a symmetry operation is performed (line for a rotation, plane for a reflection, and point for an inversion) together with a description of this operation. Symmetry elements are mirror planes, glide planes, rotation axes, screw axes, rotoinversion axes and inversion centres. The geometrical descriptions of the crystallographic symmetry operations are illustrated in Figs. 3.4-3.6.

A symmetry operation transforms a point X with coordinates x, y, z (according to a position vector $\boldsymbol{X} = x\boldsymbol{a_1} + y\boldsymbol{a_2} + z\boldsymbol{a_3}$) into a symmetrically equivalent point X' with coordinates x', y', z' mathematically by the linear equations

$$\begin{aligned} x' &= W_{11}x + W_{12}y + W_{13}z + w_1 \\ y' &= W_{21}x + W_{22}y + W_{23}z + w_2 \\ z' &= W_{31}x + W_{32}y + W_{33}z + w_3 \end{aligned} \qquad (3.10)$$

or, in matrix notation:

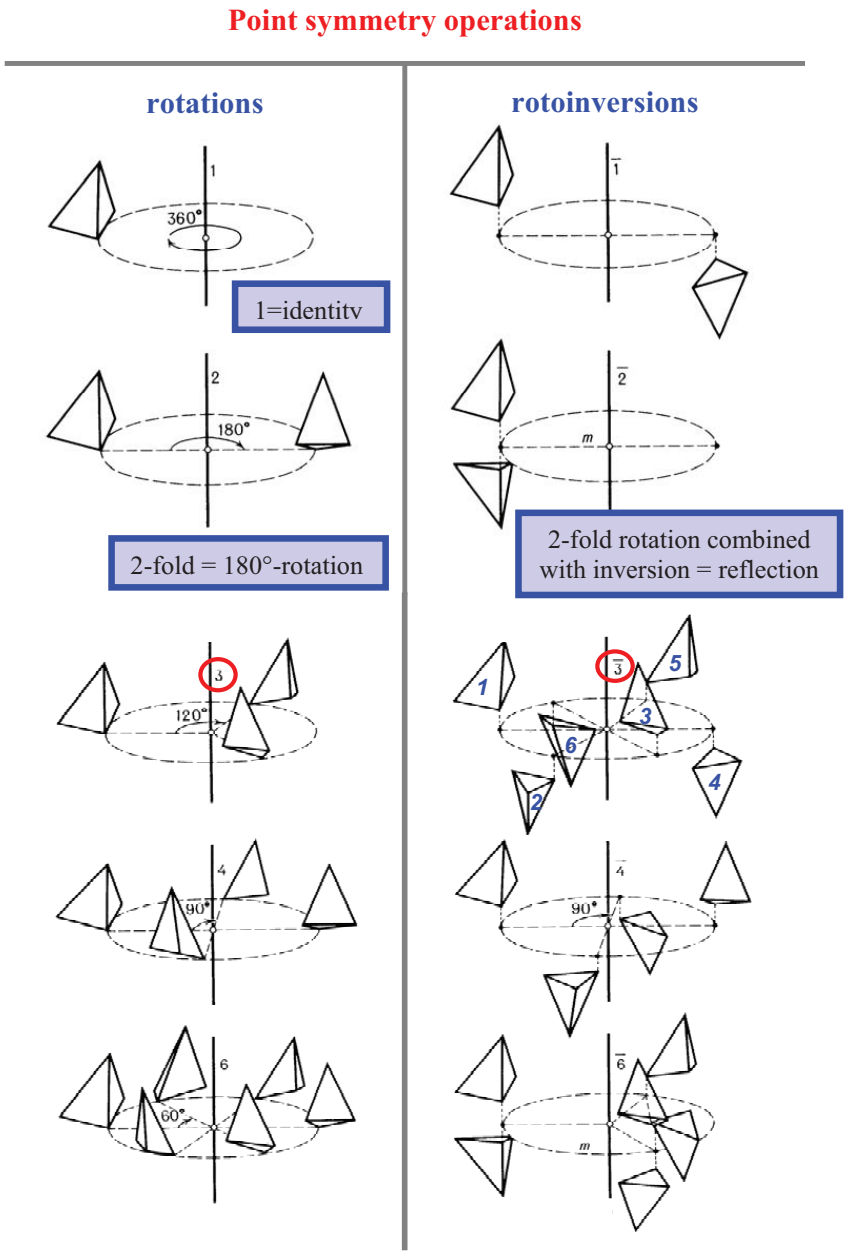

Fig. 3.4: *Rotations: n=1 (identity), n=2 (rotation angle 180°), n=3 (120°), n=4 (90°), n=6 (60°).*
Rotoinversions: $\bar{1}$ *(inversion),* $\bar{2} \equiv m$ *(reflection),* $\bar{3} = 3 + \bar{1}$, $\bar{4}$, $\bar{6} = 3/m$.

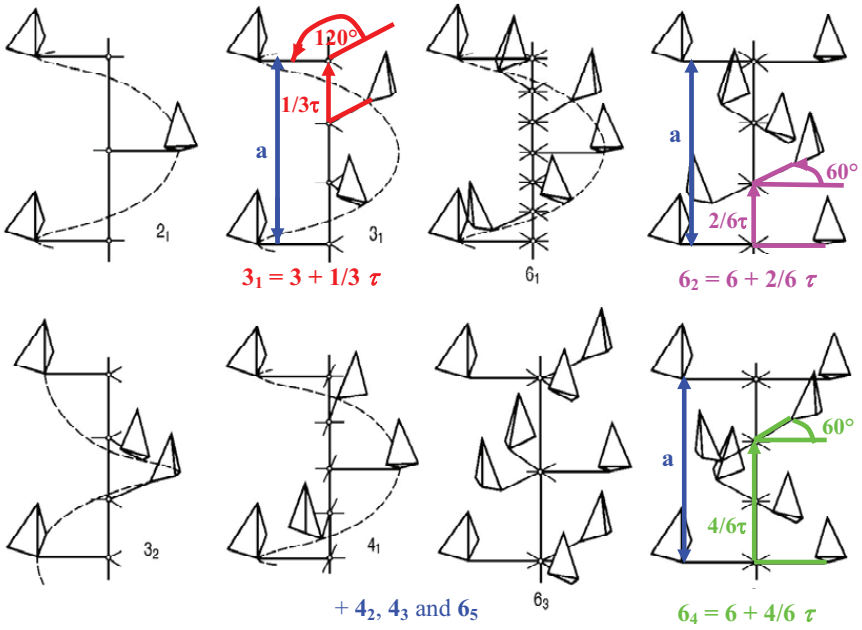

Fig. 3.5: *Screw rotations n_m: combination of rotations n and translation components m/n·a ∥ to the rotation axis.*

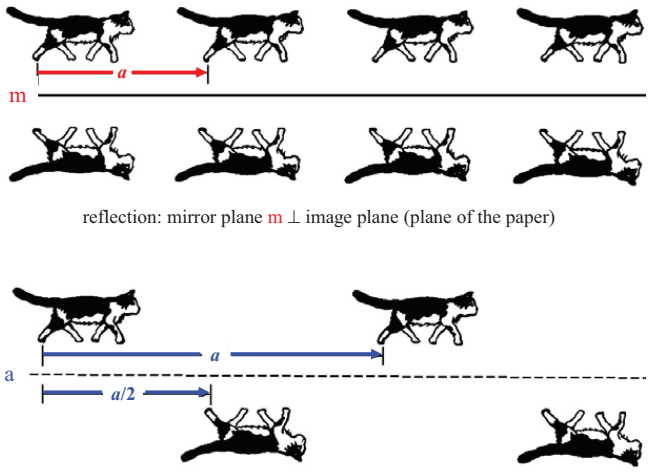

Fig. 3.6: *Examples of reflections and glide reflections.*

$$\begin{pmatrix} x' \\ y' \\ z' \end{pmatrix} = \begin{pmatrix} W_{11} & W_{12} & W_{13} \\ W_{21} & W_{22} & W_{23} \\ W_{31} & W_{32} & W_{33} \end{pmatrix} \circ \begin{pmatrix} x \\ y \\ z \end{pmatrix} + \begin{pmatrix} w_1 \\ w_2 \\ w_3 \end{pmatrix}; \quad \boldsymbol{X}' = \mathbf{W} \circ \boldsymbol{X} + \boldsymbol{w} = (\mathbf{W}, \mathbf{w}) \circ \boldsymbol{X} \tag{3.11}$$

The (3×3) matrix **W** is the rotation part and the (3×1) column matrix $\boldsymbol{w}$ the translation part of the symmetry operation. The two parts **W** and $\boldsymbol{w}$ can be assembled into an augmented (4×4) matrix $\boldsymbol{W}$ according to

$$\begin{pmatrix} x' \\ y' \\ z' \\ 1 \end{pmatrix} = \begin{pmatrix} W_{11} & W_{12} & W_{13} & w_1 \\ W_{21} & W_{22} & W_{23} & w_2 \\ W_{31} & W_{32} & W_{33} & w_3 \\ 0 & 0 & 0 & 1 \end{pmatrix} \circ \begin{pmatrix} x \\ y \\ z \\ 1 \end{pmatrix} = \boldsymbol{W} \circ \boldsymbol{X} \tag{3.12}$$

Since every symmetry transformation is a “rigid-body” motion, the determinant of all matrices **W** and $\boldsymbol{W}$ is det **W** = det $\boldsymbol{W}$ = ± 1 (+ 1: preservation of handedness; - 1: change of handedness of object).

The sequence of two symmetry operations (successive application) is given by the product of their matrices $\boldsymbol{W_1}$ and $\boldsymbol{W_2}$:

$$\boldsymbol{W_3} = \boldsymbol{W_1} \circ \boldsymbol{W_2} \tag{3.13}$$

whereby $\boldsymbol{W_3}$ is again a symmetry operation.

3.5 Crystallographic point groups and space groups

The symmetry of a crystal and of its crystal structure can be described by mathematical group theory. The symmetry operations are the group elements of a crystallographic group G and the combination of group elements is the successive execution of symmetry operations. All possible combinations of crystallographic point-symmetry operations in three-dimensional space lead to exactly 32 crystallographic point groups (≡ crystal classes) which all are of finite order (the maximum order is 48 for the cubic crystal class $m\bar{3}m$). For the different crystal systems they are represented by stereographic projections in figure 3.7. There are two types of group symbols in use: for each crystal class the corresponding Schoenflies symbol is given at the bottom left and the Hermann-Mauguin (international) symbol at the bottom right. A maximum of 3 independent main symmetry directions (“Blickrichtungen”) is sufficient to describe the complete symmetry of a crystal. These Blickrichtungen are specifically defined for the 7 crystal systems (Hermann-Mauguin symbols). As an example the Blickrichtungen of the cubic system are shown in figure 3.8.

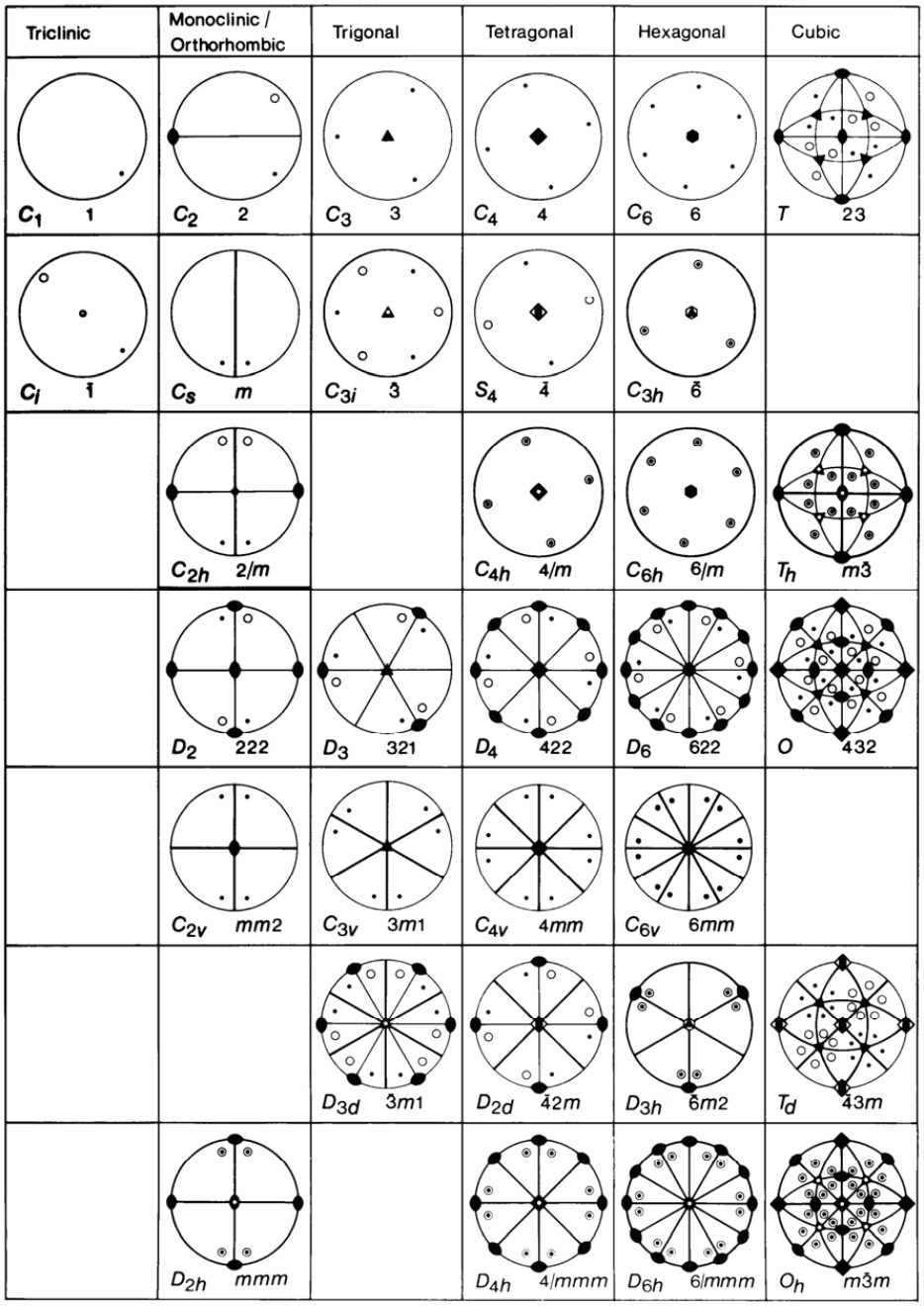

Fig. 3.7: *The 32 crystallographic point groups (crystal classes) in three-dimensional space represented by their stereographic projections. The group symbols are given according to Schoenflies (bottom left) and to Hermann-Mauguin (bottom right).*

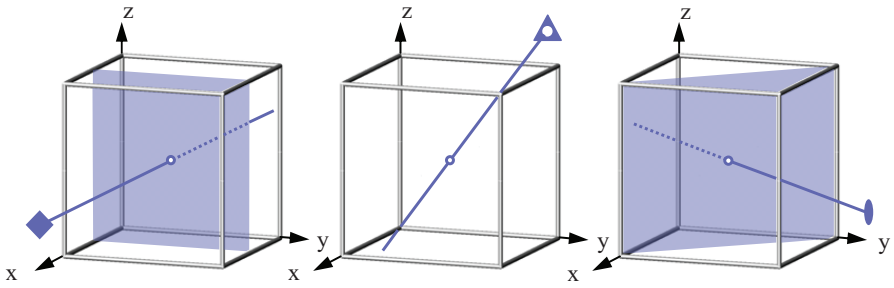

Fig. 3.8: *Symmetry directions ("Blickrichtungen") of the cubic lattice (a=b=c, α=β=γ=90°). Along [100]: 4/m, along [111]: $\bar{3}$, along [110]: 2/m.*

The point-group symmetries determine the anisotropic (macroscopic) physical properties of crystals, i. e. mechanical, electrical, optical and thermal properties. By diffraction methods normally only the 11 centrosymmetric Laue classes can be determined:

crystal system	Laue class
triclinic	$\bar{1}$
monoclinic	1 2/m 1 = 2/m
orthorhombic	2/m 2/m 2/m = m m m
tetragonal	4/m 4/m 2/m 2/m = 4/m m m
trigonal	$\bar{3}$ $\bar{3}$ 2/m = $\bar{3}$ m
hexagonal	6/m 6/m 2/m 2/m = 6/m m m
cubic	2/m $\bar{3}$ = m $\bar{3}$ 4/m $\bar{3}$ 2/m = m $\bar{3}$ m

In three dimensions all possible combinations of the point symmetries of the 32 crystallographic point groups with the lattice translations of the 14 Bravais lattices lead to exactly 230 space groups, all of infinite order. As already mentioned, there result new symmetry operations: screw rotations and glide reflections. The conventional graphical symbols for the symmetry elements according to the International Tables for Crystallography Vol. A (ITA, 2002 [1]) are shown in figure 3.9.

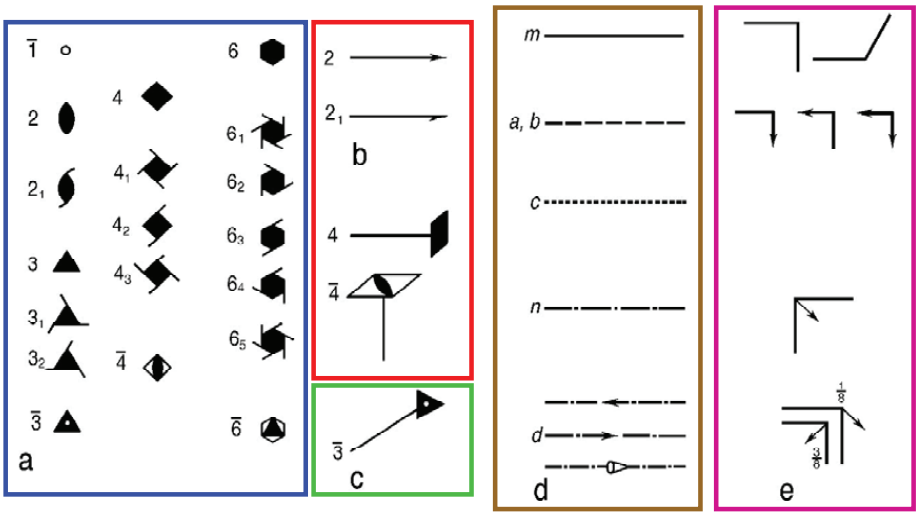

Fig. 3.9: *Conventional graphical symbols for symmetry elements:*
- symmetry axes: (a) perpendicular, (b) parallel, and (c) inclined to the image plane;
- symmetry planes: (d) perpendicular and (e) parallel to the image plane.

In the International Tables for Crystallography Vol. A [1] all space groups are described in detail with their Hermann-Mauguin symbols and corresponding crystal classes, the relative locations and orientations of the symmetry elements with respect to a chosen origin and the crystal-specific basis vectors, a listing of the general and all special positions (with their symmetrically equivalent points) and the related reflection conditions.

3.6 Example of the crystal structure description of $YBa_2Cu_3O_{7-\delta}$ using the ITA

The crystal structure determination with atomic resolution is achieved by diffraction experiments with X-rays, electron or neutron radiation. As an example, the results of a structure analysis by neutron diffraction on a single crystal of the ceramic high-T_C superconductor $YBa_2Cu_3O_{7-\delta}$ with T_C = 92 K are presented. The atomic arrangement of the orthorhombic structure, space group Pmmm, and the temperature-dependent electrical resistivity is shown in figure 3.10.

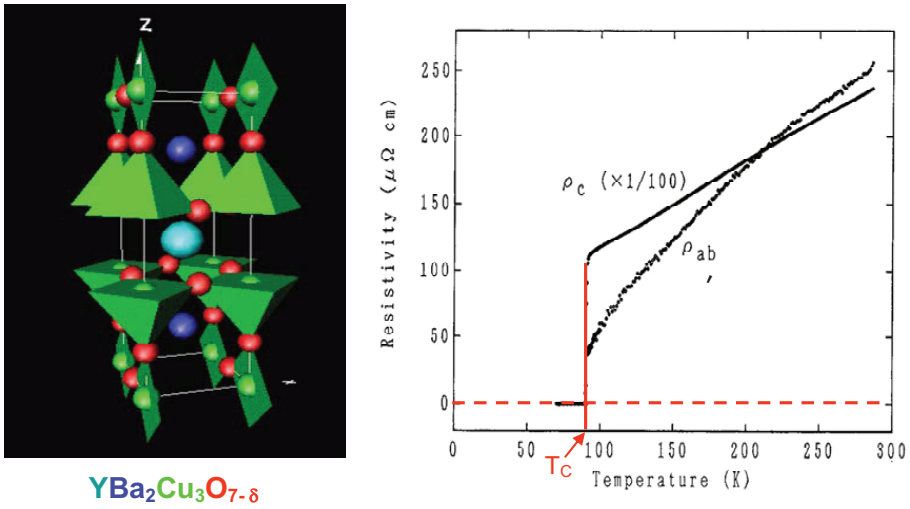

Fig. 3.10: *Crystal structure (unit cell) of $YBa_2Cu_3O_{7-\delta}$ with the CuO_x-polyhedra (left) and the electrical resistivity as a function of temperature ∥ and ⊥ to the [001] direction (right).*

Information from ITA on the relative locations and orientations of the symmetry elements (symmetry operations 1, 2_z, 2_y, 2_x, $\bar{1}$, m_z, m_y, m_x) of the orthorhombic space group Pmmm, together with the choice of the origin (in an inversion centre), is shown in figure 3.11. The general position (site symmetry 1) of multiplicity 8 and all special positions with their site symmetries are listed in figure 3.12. There are no special reflection conditions for this space group.

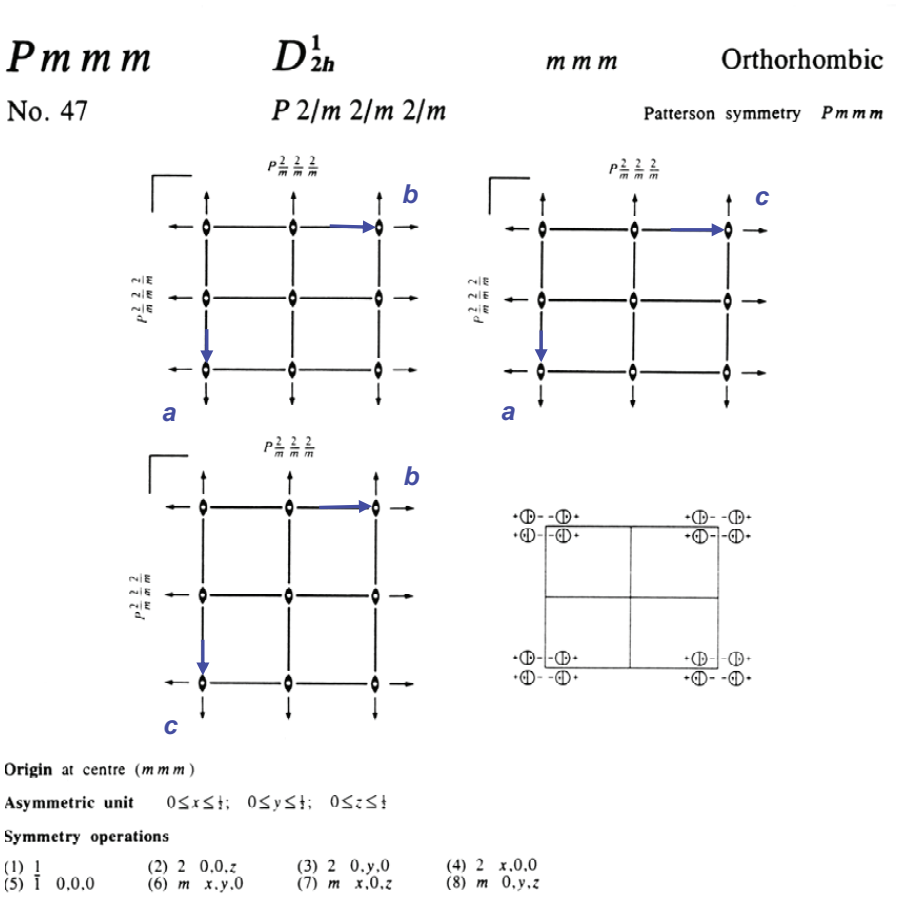

Fig. 3.11: *Description of the orthorhombic space group Pmmm in ITA (2002).*

CONTINUED $YBa_2Cu_3O_{7-\delta}$ No. 47 *Pmmm*

Generators selected (1); $t(1,0,0)$; $t(0,1,0)$; $t(0,0,1)$; (2); (3); (5)

Positions

Multiplicity, Wyckoff letter, Site symmetry			Coordinates				Reflection conditions
8	α	1	(1) x,y,z	(2) $\bar{x},\bar{y},z$	(3) $\bar{x},y,\bar{z}$	(4) $x,\bar{y},\bar{z}$	General: no conditions
			(5) $\bar{x},\bar{y},\bar{z}$	(6) $x,y,\bar{z}$	(7) $x,\bar{y},z$	(8) $\bar{x},y,z$	
4	z	$..m$	$x,y,\frac{1}{2}$	$\bar{x},\bar{y},\frac{1}{2}$	$\bar{x},y,\frac{1}{2}$	$x,\bar{y},\frac{1}{2}$	Special: no extra conditions
4	y	$..m$	$x,y,0$	$\bar{x},\bar{y},0$	$\bar{x},y,0$	$x,\bar{y},0$	
4	x	$.m.$	$x,\frac{1}{2},z$	$\bar{x},\frac{1}{2},z$	$\bar{x},\frac{1}{2},\bar{z}$	$x,\frac{1}{2},\bar{z}$	
4	w	$.m.$	$x,0,z$	$\bar{x},0,z$	$\bar{x},0,\bar{z}$	$x,0,\bar{z}$	
4	v	$m..$	$\frac{1}{2},y,z$	$\frac{1}{2},\bar{y},z$	$\frac{1}{2},y,\bar{z}$	$\frac{1}{2},\bar{y},\bar{z}$	
4	u	$m..$	$0,y,z$	$0,\bar{y},z$	$0,y,\bar{z}$	$0,\bar{y},\bar{z}$	
2	t	$mm2$	$\frac{1}{2},\frac{1}{2},z$	$\frac{1}{2},\frac{1}{2},\bar{z}$			
2	s	$mm2$	$\frac{1}{2},0,z$	$\frac{1}{2},0,\bar{z}$			
2	r	$mm2$	$0,\frac{1}{2},z$	$0,\frac{1}{2},\bar{z}$			
2	q	$mm2$	$0,0,z$	$0,0,\bar{z}$			
2	p	$m2m$	$\frac{1}{2},y,\frac{1}{2}$	$\frac{1}{2},\bar{y},\frac{1}{2}$			
2	o	$m2m$	$\frac{1}{2},y,0$	$\frac{1}{2},\bar{y},0$			
2	n	$m2m$	$0,y,\frac{1}{2}$	$0,\bar{y},\frac{1}{2}$			
2	m	$m2m$	$0,y,0$	$0,\bar{y},0$			
2	l	$2mm$	$x,\frac{1}{2},\frac{1}{2}$	$\bar{x},\frac{1}{2},\frac{1}{2}$			
2	k	$2mm$	$x,\frac{1}{2},0$	$\bar{x},\frac{1}{2},0$			
2	j	$2mm$	$x,0,\frac{1}{2}$	$\bar{x},0,\frac{1}{2}$			
2	i	$2mm$	$x,0,0$	$\bar{x},0,0$			
1	h	mmm	$\frac{1}{2},\frac{1}{2},\frac{1}{2}$				
1	g	mmm	$0,\frac{1}{2},\frac{1}{2}$				
1	f	mmm	$\frac{1}{2},\frac{1}{2},0$				
1	e	mmm	$0,\frac{1}{2},0$				
1	d	mmm	$\frac{1}{2},0,\frac{1}{2}$				
1	c	mmm	$0,0,\frac{1}{2}$				
1	b	mmm	$\frac{1}{2},0,0$				
1	a	mmm	$0,0,0$				

Fig. 3.12: *General and special positions (coordinates of all symmetrically equivalent positions) of space group Pmmm with their site symmetries and multiplicities as well as reflection conditions. The special positions of the $YBa_2Cu_3O_{7-\delta}$ structure are indicated by frames.*

The atomic parameters of the structure refinement of $YBa_2Cu_3O_{6..96}$ at room temperature [2] are given in the following Table:

Atomic positions of $YBa_2Cu_3O_{6.96}$
orthorhombic, space group type P *2/m 2/m 2/m*
a = 3.858 Å, b = 3.846 Å, c = 11.680 Å (at room temperature)

atom/ion	multiplicity	site symmetry	x	y	z
$Cu1/Cu^{2+}$	1	*2/m 2/m 2/m*	0	0	0
$Cu2/Cu^{2+}$	2	*m m 2*	0	0	0.35513(4)
Y/Y^{3+}	1	*2/m 2/m 2/m*	½	½	½
Ba/Ba^{2+}	2	*m m 2*	½	½	0.18420(6)
$O1/O^{2-}$	2	*m m 2*	0	0	0.15863(5)
$O2/O^{2-}$	2	*m m 2*	0	½	0.37831(2)
$O3/O^{2-}$	2	*m m 2*	½	0	0.37631(2)
$O4/O^{2-}$	1	*2/m 2/m 2/m*	0	½	0

References

[1] International Tables for Crystallography Vol. A, Space-group Symmetry, edited by Th. Hahn, Dordrecht: Kluwer Academic Publishers (5. Edition, 2002)

[2] P. Schweiss, W. Reichardt, M. Braden, G. Collin, G. Heger, H. Claus, A. Erb, Phys. Rev. **B49**, 1387 – 1396 (1994)

Exercises

E3.1 Lattice points, lattice directions and lattice planes

A projection of an orthorhombic lattice on the lattice plane (001) is given in the following figure (this means a projection parallel to the **c**-axis). The dots represents the lattice points (not atoms) according to the translation symmetry of a crystal with the general translation vector $\boldsymbol{a} = u\boldsymbol{a}_1+v\boldsymbol{a}_2+w\boldsymbol{a}_3$ ($\boldsymbol{a}_1$, $\boldsymbol{a}_2$, and $\boldsymbol{a}_3$ are the basis vectors of the unit cell and u, v, w being integers)

Please indicate in the figure

a) the lattice points uvw = 030, -120, 1-20, and 450,

b) the lattice directions [uvw] = [100], [210], [-2-10] and [-250],

c) and the traces of the lattice planes (hkl) = (100), (300), (210), (-210), and (140).

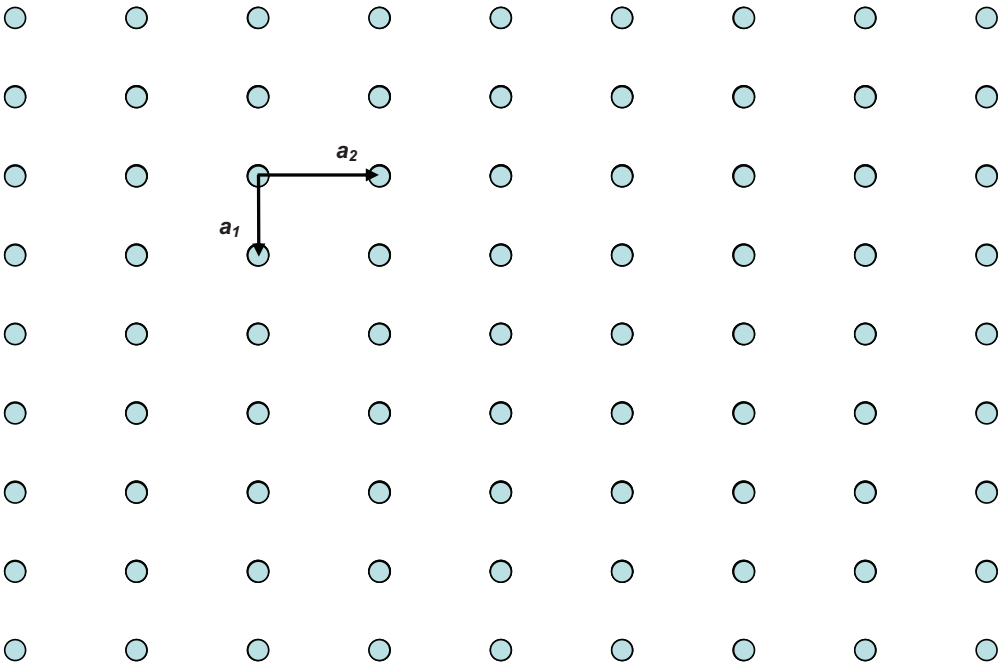

d) Which conditions of the crystallographic coordinate system must be fulfilled

for [100] ⊥ (100),

for [110] ⊥ (110),

and for [111] ⊥ (111)?

Please give the conditions for the lattice parameters. Indicate for each case the possible corresponding crystal systems.

e) Which is the zone axis for the lattice planes (110), (111), and (001) in the cubic system?

E3.2 Crystal structure of La_2MnO_4

La_2MnO_4 crystallizes in the so-called T-phase with the space group *I4/mmm*. The lattice parameters are $a_1 = 3.787$ and $a_3 = 13.154$ Å. The atoms occupy the following positions in the asymmetric unit (given by the *x*, *y*, and *z* coordinates according to the positional vector of the atom j $\boldsymbol{r_j} = x\boldsymbol{a_1}+y\boldsymbol{a_2}+z\boldsymbol{a_3}$):

Mn: 0, 0, 0

La: 0, 0, 0.356

O(1): 0, 0.5, 0

O(2): 0, 0, 0.174

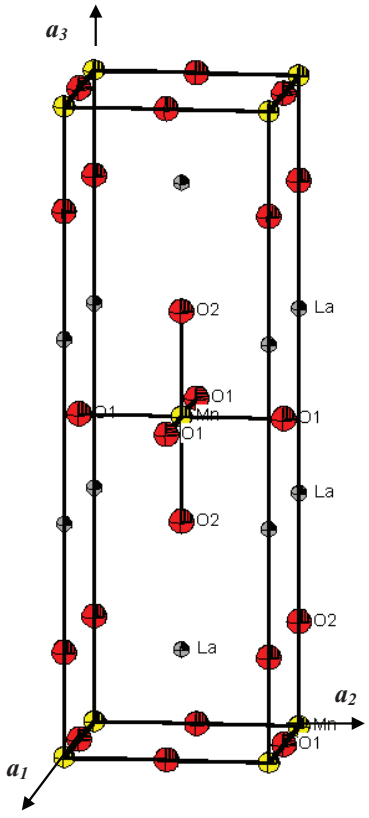

Unit cell of La_2MnO_4.

a) Indicate the crystal system and the Bravais lattice type of La_2MnO_4. How many formula units are in one unit cell?

b) Calculate the interplanar spacings *d(hkl)* for the lattice planes (200), (310), (-130), (-224), (4-22), and (24-2).

c) List all symmetry equivalent lattice planes with equal d-spacing (including all different orientation possibilities) of
(h00), *(00l)*, *(hh0)*, *(h0l)*, *(hhh)*, and *(hkl)*
for the tetragonal crystal system; example: *d(h00) = d(-h00) = d(0h0) = d(0-h0)*.
How many symmetry equivalent lattice planes result in each case (multiplicity factor of powder diffraction)?

d) Plot in the given projection on (001), i. e. on the ($\boldsymbol{a_1}$, $\boldsymbol{a_2}$)-plane, for the marked manganese in 0, 0, 0 the positions of the nearest neighbour oxygen-atoms and indicate their *z*-parameters.

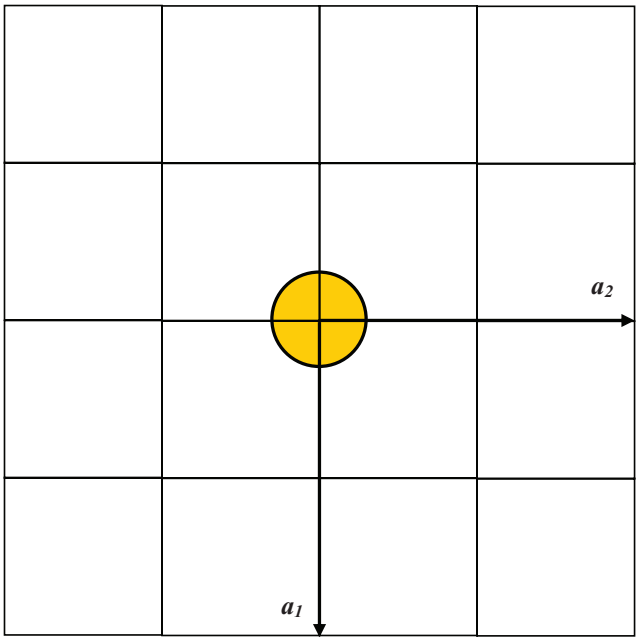

e) Determine the coordination number and coordination geometry of Mn by the surrounding O-atoms.

Please draw the symmetry elements (rotation axes and mirror planes), which you can identify.

Which is the site symmetry (one of the 32 crystallographic point groups) of the Mn position? Give the Hermann-Mauguin symbol according to the Blickrichtungen of the tetragonal crystal system.

f) Which are the site symmetries (the crystallographic point groups) of the La-, O(1)-, and O(2)-positions?

g) Indicate which of the atomic positions: Mn, La O(1), and O(2) is situated on an inversion point $\bar{1}$, i.e. which of the related crystallographic point groups is centrosymmetric.

h) Combine the following point symmetry operations:
4 with m (parallel to 4),
4 with m ($\perp$ 4).
Please list all symmetry operations of the resulting crystallographic point groups (remember that the identity 1 is always a group member) and give the corresponding Hermann-Mauguin symbol.

Example:

The combination of two mirror operations with their planes perpendicular to each other, $m_a \perp m_b$, gives rise to a two-fold rotation whose axis is just situated along the intersection line of the two mirror planes. The resulting crystallographic point group of index 4 (4 group members) belong to the orthorhombic crystal system and consists of the symmetry operations 1 m_a, m_b, and 2_c. The Hermann-Mauguin symbol of this crystal class is mm2.

The interrelationships in 3 dim. space between lattice planes and lattice directions as well as symmetry operations can be represented in two dimensions by means of the so-called stereographic projection. The above mentioned combination $m_a \perp m_b$ is shown by means of the stereographic projection as follows:

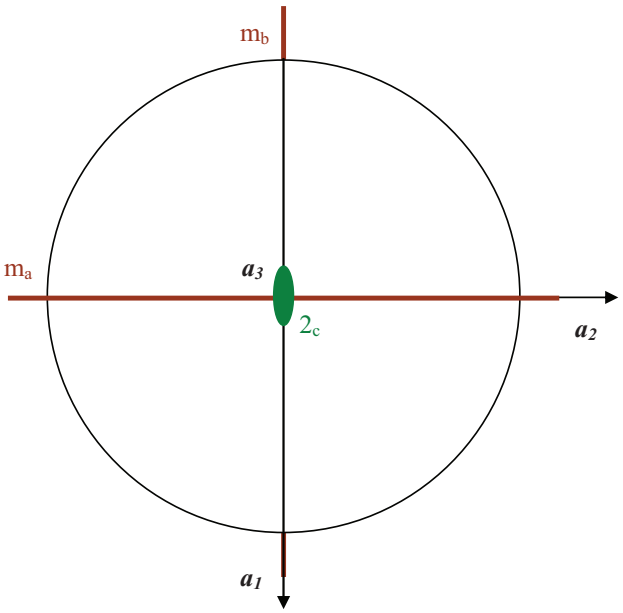

4 Diffraction

G. Roth
Institute of Crystallography
RWTH Aachen University

Contents

Lecture Notes of the JCNS Laboratory Course Neutron Scattering

4.1 Introduction

Each scattering experiment performed with any type of radiation - regardless of whether it involves massive particles like neutrons and electrons or electromagnetic waves like x-rays or visible light - has a total of four attributes which altogether characterize the type of the scattering experiment as well as the information that can be obtained from such an experiment. These attributes and their characteristics are:

Elastic scattering, which involves the conservation of the energy of the particle or quantum during the scattering process, *inelastic* scattering, corresponding to a loss or gain of particle or quantum energy during the scattering event, *coherent* scattering which involves the interference of waves (recall that, according to the particle-wave dualism first stated by de Broglie (1924), each particle may also be described by wave which can interfere with other particle waves) and finally *incoherent* scattering which is scattering without interference.

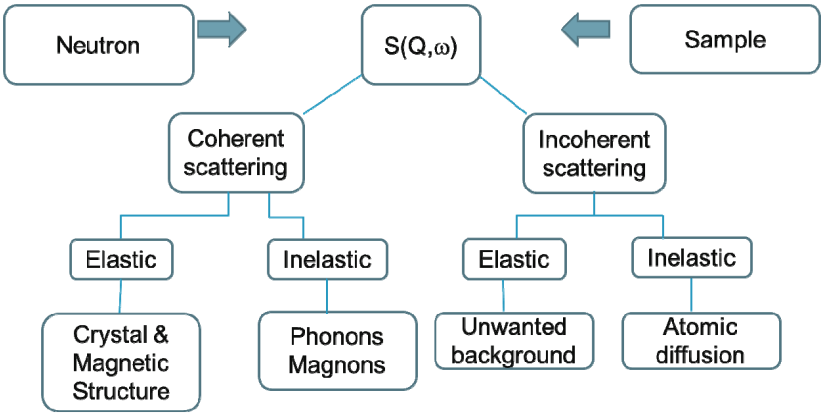

Fig. 4.1: Scattering function S(Q,ω) of a general scattering experiment (Q: scattering vector, ω: frequency), its different contributions and information that can be obtained from them.

This chapter will deal mostly with neutron *diffraction* which is, in the above nomenclature of a general scattering experiment, equivalent to *elastic coherent scattering* of neutrons.

Most of the readers of this chapter will be more or less familiar with x-ray diffraction from crystals, which has been demonstrated for the first time by Laue in 1912 and, since then, has developed into the most powerful method for obtaining structural information on crystalline materials. Diffraction - in sharp contrast to imaging techniques like optical or electron microscopy - has no principal limitation as to the spatial resolution, expressed in units of the wavelength of the radiation used for diffraction or imaging: While the resolution of imaging is limited to half the wavelength (recall the Abbe diffraction limit) diffraction can yield useful information, for instance, on bond distances between atoms on a length scale that is by two to three orders of magnitude smaller than the wavelength. On the other hand, diffraction, other than imaging,

requires 3-dimensional periodicity that is underlying the concept of the crystalline state (see chapter 3, symmetry in crystals).

This chapter will discuss the basics and peculiarities of neutron diffraction from either single- or polycrystalline matter. We will start by discussing scattering of neutrons from individual atoms, then turn to the geometry of diffraction from crystals, treat the subject of diffraction intensities and end with a discussion of a few experimental issues connected to the instruments which will be used in the practical part of the course. Examples of applications of these methods will be given in chapter 8 "structural analysis". The subject of magnetic neutron diffraction and scattering will be discussed separately in chapter 7.

4.2 Neutron waves & neutron scattering

The three major probes for investigating condensed matter are photons, electrons and neutrons. While photons are the (massless) quanta of electromagnetic radiation (e.g. x-rays, including synchrotron radiation, but also visible light, gamma-rays etc.) electrons and neutrons are massive particles. Owing to the wave-particle-duality, a central concept of quantum mechanics that states that all particles exhibit both wave- and particle-properties, the formal description of a scattering experiment does not differ for these different probes. However, the relation between energy and wavelength of the probes and also the mechanisms by which they interact with matter are vastly different.

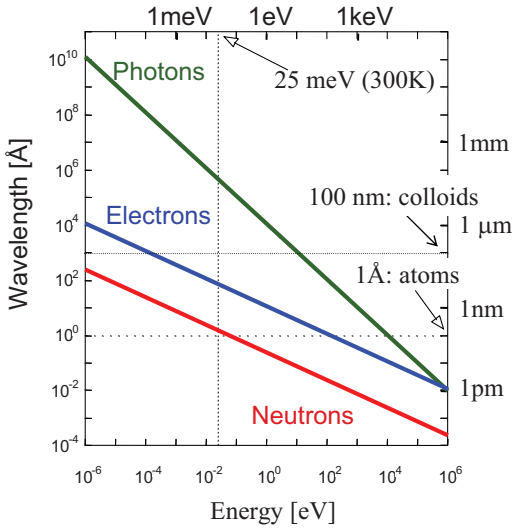

Fig. 4.2: *Comparison of the three probes - neutrons, electrons and photons - in a double logarithmic energy-wavelength diagram. Added to the figure are the typical size of objects to be studied and the energy of thermal neutrons.*

As the horizontal line at a wavelength of 1 Å shows, neutrons of this wavelength have an energy as low as about 80 meV, while 1 Å electrons correspond to about 150 eV and 1 Å photons (x-rays) have energies in excess of 12 keV. All three types of radiation

with this wavelength are well suited for scattering experiments on objects like atoms, molecules and crystals. The investigation (by scattering) of larger objects like colloids (in the 100 nm size range) requires, correspondingly, much lower energy probes like, for instance, photons in the ultraviolet range (about 12 eV).

The scattering process

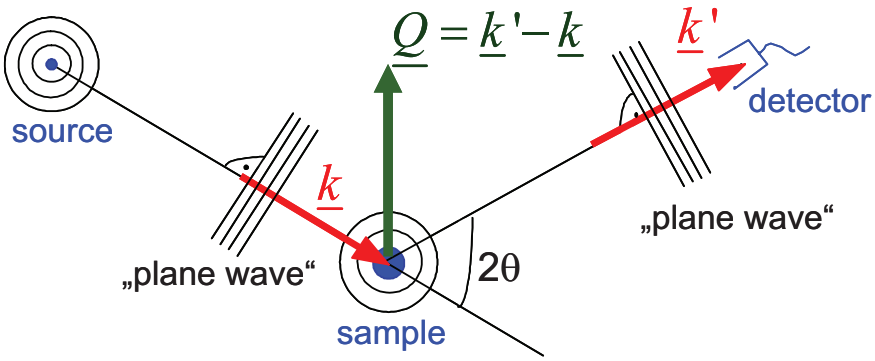

Fig. 4.3: *Sketch of the scattering process with the incoming wave characterized by wavevector k, diffracted wave by k' and the sample by scattering vector Q, assumed: plane waves, (Fraunhofer approximation, source-sample and sample-detector distances much larger than sample size), also assumed: monochromatic radiation (single wavelength)*

In the case of elastic scattering (diffraction) we have

$$k = |\underline{k}| = |\underline{k}'| = k' = \frac{2\pi}{\lambda} \qquad (4.1)$$

k is also called the wave number of the neutron and is conserved during scattering because the neutron energy and therefore the wavelength does not change.

The so-called *scattering vector* is defined by

$$\underline{Q} = \underline{k}' - \underline{k} \qquad (4.2)$$

The units of k, k' and Q are Å^{-1}.

$\hbar\underline{Q}$ represents the momentum transfer during scattering, since according to de Broglie, the momentum of the particle corresponding to the wave with wave vector $\underline{k}$ is given by $\underline{p}=\hbar\underline{k}$. The magnitude of the scattering vector can be calculated from wavelength λ and scattering angle 2θ as follows

$$Q = |\underline{Q}| = \sqrt{k^2 + k'^2 - 2kk'\cos 2\theta} \Rightarrow Q = \frac{4\pi}{\lambda}\sin\theta \qquad (4.3)$$

A scattering experiment comprises the measurement of the intensity distribution as a function of the scattering vector $I(\underline{Q})$. The scattered intensity is proportional to the so-

called *cross section*, where the proportionality factors arise from the detailed geometry of the experiment. For a definition of the scattering cross section see Figure 4.4.

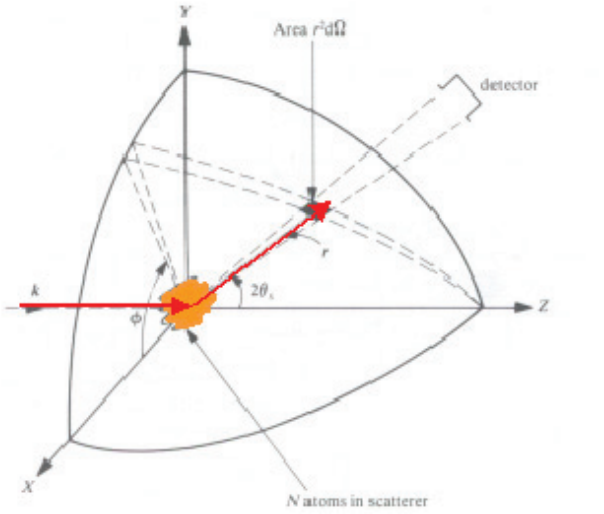

Fig. 4.4: *Geometry used for the definition of the scattering cross section.*

This is in close analogy to the absorption cross section derived in chapter 2.

Let us drop, for a moment, the assumption of strictly elastic scattering and treat the universal case of a general scattering experiment (will be needed in other chapters):
If n' particles are scattered per second into the solid angle $d\Omega$ seen by the detector under the scattering angle 2θ and into the energy interval between E' and $E' + dE'$, then we can define the so-called *double differential cross section* by:

$$\frac{d^2\sigma}{d\Omega dE'} = \frac{n'}{j d\Omega dE'} \tag{4.4}$$

Here j refers to the incident beam flux in terms of particles per area and time. If we are not interested in the change of the energy of the radiation during the scattering process, or if our detector is not able to resolve this energy change, then we will describe the angular dependence by the so-called *differential cross section:*

$$\frac{d\sigma}{d\Omega} = \int_0^\infty \frac{d^2\sigma}{d\Omega dE'} dE' \tag{4.5}$$

Finally the so-called *total scattering cross section* gives us a measure for the total scattering probability independent of changes in energy and scattering angle:

$$\sigma = \int_0^{4\pi} \frac{d\sigma}{d\Omega} d\Omega \tag{4.6}$$

All the information about the scattering matter is contained in the (double differential) scattering cross section. This includes positions and possible motions of scatterers in the

sample volume. Note that in most diffraction experiments (with x-rays in particular, but also with electrons and neutrons), the actual measurement is energy-integrated because the detectors used are energy-insensitive. Consequently, the inelastic scattering also contributes to the measured intensity, but it is usually much weaker than the purely elastic scattering. Neutron scattering, however, offers the unique opportunity to set a very narrow energy window and study purely elastic scattering as well as inelastic scattering at arbitrary energies.

If we go back to elastic scattering the information on the positions of the scatterers is contained in the differential cross section $d\sigma / d\Omega$. The relationship between scattered intensity and the structure of the sample is particularly simple in the so-called *Born approximation*, which is often also referred to as *kinematic scattering approximation*. In this case, refraction of the beam entering and leaving the sample, multiple scattering events and the extinction of the primary beam due to scattering within the sample are being neglected. According to Figure 4.5, the phase difference between a wave scattered at the origin of the coordinate system and at position $\underline{r}$ is given by

$$\Delta\Phi = 2\pi \cdot \frac{\left(\overline{AB} - \overline{CD}\right)}{\lambda} = \underline{k}' \cdot \underline{r} - \underline{k} \cdot \underline{r} = \underline{Q} \cdot \underline{r} \tag{4.7}$$

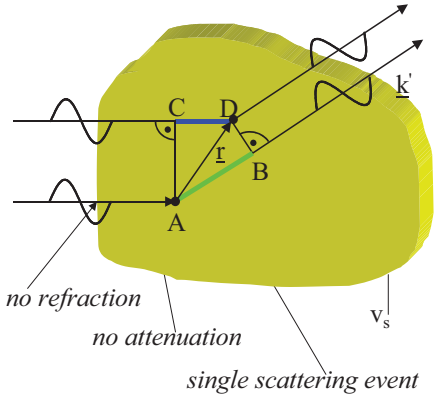

Fig. 4.5: *Elastic scattering from a non-periodic object, illustrating the phase difference between a beam scattered at the origin of the coordinate system (A) and a beam scattered at the position r. Additional caption: underlying assumptions of the kinematic scattering approximation.*

The scattered amplitude at position $\underline{r}$ is proportional to the scattering density $\rho_s(\underline{r})$ at this position. ρ_s depends on the type of radiation used and the interaction of this radiation with the sample. In fact, ρ_s is directly proportional to the interaction potential, as will be shown in the next paragraph. Assuming a laterally coherent beam, the total scattering amplitude is given by a coherent superposition of the scattering from all points within the sample, i. e. by the integral

$$A = A_0 \cdot \int_{V_S} \rho_S\left(\underline{r}\right) \cdot e^{i\underline{Q}\cdot\underline{r}} d^3r \tag{4.8}$$

Here A_0 denotes the amplitude of the incident wave field. (4.8) demonstrates that the scattered amplitude is connected with the scattering density $\rho_s(\underline{r})$ by a simple Fourier

transform. Knowledge of the scattering amplitude for all scattering vectors $\underline{Q}$ allows us to determine via a Fourier transform the scattering density uniquely. This is the complete information on the sample, which can be obtained by the scattering experiment. Unfortunately, nature is not so simple. On one hand, there is the technical problem that one is unable to determine the scattering cross section for all values of momentum transfer $\hbar\underline{Q}$. The more fundamental problem, however, is that normally the amplitude of the scattered wave is not measurable. Instead only the scattered intensity

$$I \sim |A|^2 \tag{4.9}$$

can be determined. Therefore the phase information is lost and the simple reconstruction of the scattering density via a reverse Fourier transform is no longer possible. This is the so-called *phase problem* of scattering. There are ways to overcome the phase problem, either experimentally, e. g. by use of reference waves (holography) or by using *a priori* information about the scattering density function (like positiveness or peakedness) which is the basis of the so called *direct methods of structure determination* that is very frequently used in x-ray crystallography. The question, which information we can obtain from a conventional scattering experiment despite the phase problem will be addressed below.

Which wavelength do we have to choose to obtain the required real space resolution? For information on a length scale L, a phase difference of about $Q \cdot L \approx 2\ \pi$ has to be achieved. Otherwise $\underline{k}'$ and $\underline{k}$ will not differ significantly (see eqn. (4.7)). According to (4.3) $Q \approx 2\pi/\lambda$ for typical scattering angles $(2\theta \sim 60°)$. Combining these two estimates, we end up with the requirement that the wavelength λ has to be on the order of the real space length scale L under investigation. To give an example: with the wavelength in the order of 0.1 nm, atomic resolution can be achieved in a scattering experiment.

Coherence

In the above derivation, we assumed plane waves as initial and final states. For a real scattering experiment, this is an unphysical assumption. In the incident beam, a wave packet is produced by collimation (defining the direction of the beam) and monochromatization (defining the wavelength of the incident beam). Neither the direction $\hat{\underline{k}}$, nor the wavelength λ have discrete values but rather have a distribution of non-vanishing width about their respective mean values. This wave packet can be described as a superposition of plane waves. As a consequence, the diffraction pattern will be a superposition of patterns for different incident wavevectors $\underline{k}$ and the question arises, which information is lost due to these non-ideal conditions. This *instrumental resolution* is intimately connected with the *coherence* of the beam. Coherence is needed, so that the interference pattern is not significantly destroyed. Coherence requires a phase relationship between the different components of the beam. Two types of coherence can be distinguished:

Temporal or longitudinal coherence due to a wavelength spread:

A measure for the longitudinal coherence is given by the length, on which two components of the beam with largest wavelength difference (λ and $\lambda+\Delta\lambda$) become fully out of phase.

According to the following figure, this is the case for $l_{\parallel} = n \cdot \lambda = \left(n - \frac{1}{2}\right)(\lambda + \Delta\lambda)$.

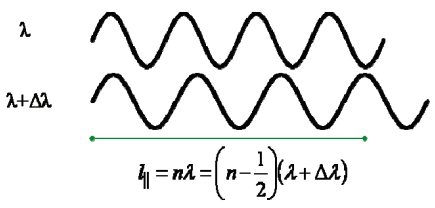

Fig. 4.6: *Sketch illustrating the longitudinal coherence due to a wavelength spread.*

From this, we obtain the *longitudinal coherence length* $l_{\parallel}$ as

$$l_{\parallel} = \frac{\lambda^2}{2\Delta\lambda} \tag{4.10}$$

Transverse coherence due to source extension:
Due to the extension of the source (transverse beam size), the phase relation is destroyed for large source size or large divergence. According to the following figure, a first minimum occurs for $\frac{\lambda}{2} = d \cdot \sin\theta \approx d \cdot \theta$.

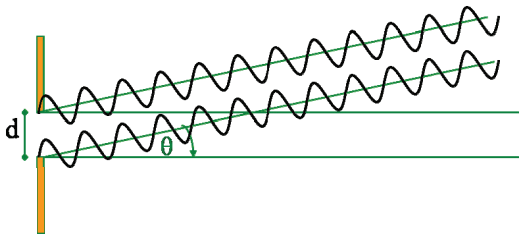

Fig. 4.7: *Sketch illustrating the transverse coherence due to source extension and beam divergence.*

From this, we obtain the *transversal coherence length* $l_{\perp}$ as

$$l_{\perp} = \frac{\lambda}{2\Delta\theta} \tag{4.11}$$

Here $\Delta\theta$ is the divergence of the beam. Note that $l_{\perp}$ can be different along different spatial directions: in many instruments, the vertical and horizontal collimations are different.
Together, the longitudinal and the two transversal coherence lengths (in two directions perpendicular to the beam propagation) define a *coherence volume*. This is a measure for a volume within the sample, in which the amplitudes of all scattered waves superimpose to produce an interference pattern. Normally, the coherence volume is

significantly smaller than the sample size, typically a few *100 Å* for neutron scattering, up to *μm* for synchrotron radiation. Scattering between different coherence volumes within the sample is no longer coherent, i. e. instead of the amplitudes the intensities of the contributions to the scattering pattern have to be summed up. This limits the real space resolution of a scattering experiment to the extension of the coherence volume.

Neutron scattering from atomic nuclei

Neutrons interact with the nuclei of the atoms by potential scattering as well as with the magnetic moment of unpaired electrons in the electron shells of the atoms. Here we focus on the so-called nuclear scattering contribution. As the wavelength of thermal neutrons (approx. 10^{-10} m) is much larger than the diameter of the atomic nucleus (10^{-14} ...10^{-15} m), the atom is essentially a point scatterer. As the construction of Fig. 4.5 and equation (4.7) shows, this means that the length of the vector r (now a vector within the nucleus) is very small compared to the wavelength of the neutron and therefore the phase difference of waves from different parts of the nucleus is essentially zero. This is in sharp contrast to x-ray diffraction, where the scattering occurs from the electron cloud and the size of the scatterer and the wavelength of the radiation are similar. This results in the well-known formfactor falloff of the scattered intensity with increasing scattering angle. The same holds true for the magnetic formfactor for thermal neutrons. Magnetic neutron scattering will be the subject of chapter 7. For neutron scattering from the atomic nuclei, the formfactor is a constant. This is one big advantage of neutrons over x-rays because there is still an appreciable amount of scattered intensity even at very high scattering angles, where an x-ray experiment will yield hardly any useful information.

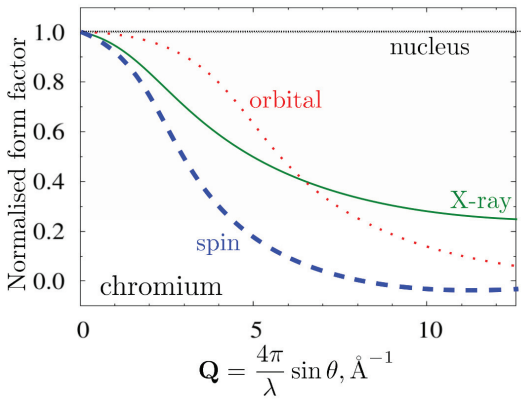

Fig. 4.8: *Form-factor of Cr [1]. On the Å length scale of the thermal neutron wavelength, the nucleus is point-like, therefore, nuclear scattering is independent of the scattering angle. For x-rays and magnetic neutron scattering, the form factor falls off with increasing scattering angle. For more details on magnetic neutron scattering see chapter 7.*

The interaction that governs nuclear neutron scattering (essentially potential scattering) is the strong nuclear force. Note that, despite the fact that the strong interaction of high

energy physics is responsible for the scattering of the neutron with the nucleus, the scattering probability is very small due to the small nuclear radius.
The quantity that describes the interaction between neutrons and matter is the scattering length b, it is usually expressed in units of a Fermi (1 fm = 10^{-15} m). Another frequently used quantity is the total cross section of a given nucleus $\sigma = 4\pi |b|^2$ corresponding to the surface area of a sphere with radius *b*. σ is usually expressed in barns, 1 barn = 10^{-24} cm^2. A simple description of potential scattering predicts the smooth increase of the scattering length with increasing atomic weight depicted in Figure 4.9 by the dashed line. Obviously, this description is rather crude as resonance effects play an important role and, consequently, there are pronounced deviations from this line. As the interaction potential depends on the details of the nuclear structure, scattering lengths *b* can be very much different for different isotopes of the same element and also for different nuclear spin states (see chapter 7). In fact, neutron nuclear scattering lengths are still very hard to calculate (in contrast to x-ray scattering where the scattering power of any atom can be calculated to a very high precision) illustrating our still quite limited knowledge of the nuclear structure of atoms as opposed to the very well understood electronic structure of atoms. Consequently, the tabulated values of *b* which can be found in [2] or at http://www.ncnr.nist.gov/resources/n-lengths/ are experimentally measured quantities, not calculated ones. The scattering length is mostly positive but can also adopt negative values, this negative sign corresponds to a phase shift of π (or 180°) during the scattering process. The fact that different isotopes of the same element have different scatterings lengths also gives rise to the appearance of so-called *incoherent scattering* (see below).

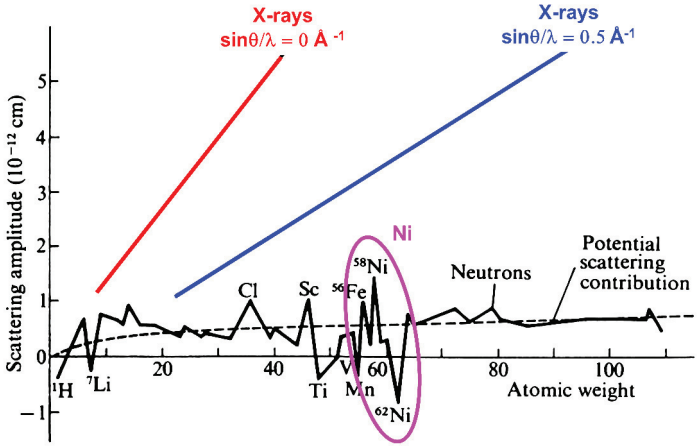

Fig. 4.9: *Scattering length as a function of atomic weight throughout the periodic table (from Research, London 7 (1954), 257). Note the two different curves for x-rays at low- and high scattering angles, illustrating the formfactor falloff that is typical for x-rays but doesn't exist for nuclear neutron scattering.*

In Figure 4.10, the scattering cross sections for x-rays and neutrons are compared. Note that the x-ray scattering cross sections are in general a factor of 10 larger as compared to the neutron scattering cross sections. This means that the signal for x-ray scattering is stronger for the same incident flux and sample size. For x-rays, the

cross section depends on the number of electrons and thus varies in a monotonic fashion throughout the periodic table. Clearly it will be difficult to determine hydrogen positions with x-rays in the presence of heavy elements such as metal ions. Moreover, there is a very weak contrast between neighboring elements as can be seen for the transition metals Mn, Fe and Ni in Figure 4.10. However, this contrast can be enhanced by anomalous scattering, if the photon energy is tuned close to the absorption edge of an element. For neutrons the cross section depends on the details of the nuclear structure and thus varies in a non-systematic fashion throughout the periodic table. As an example, there is a very high contrast between Mn and Fe. With neutrons, the hydrogen atom is clearly visible even in the presence of such heavy elements as Uranium. Moreover there is a strong contrast between the two Hydrogen isotopes H and D. This fact can be exploited for soft condensed matter investigations by selective deuteration of certain molecules or functional groups. This will vary the contrast within the sample.

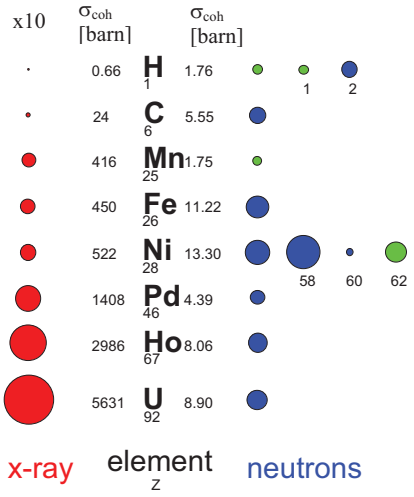

Fig. 4.10: *Comparison of the (coherent) scattering cross-sections σ for x-rays and neutrons for a selection of elements. The area of the colored circles represent the scattering cross section, where in the case of x-rays a scale factor 10 has to be applied. For neutrons, the blue and green circles distinguish the cases where the scattering occurs with or without a phase shift of π. For $_1$H and $_{28}$Ni, scattering cross sections for certain isotopes are given in addition to the averaged values for the natural abundances.*

Coherent and incoherent scattering

As mentioned above, the scattering length *b* is different for different isotopes of a given element and also for different nuclear spin states. This gives rise to an additional contribution to the total intensity, the *incoherent scattering*. In this chapter, we will

focus on *isotope-incoherence* and leave the detailed discussion of *spin-incoherence* for other chapters.

Figure 4.11 shows a 2-D model crystal with atoms of two isotopes of the same element with two different scattering lengths b_i sitting on fixed positions $\underline{R}_i$ in a crystal lattice. As stated above, the scattering amplitude is obtained from a Fourier transform:

$$A(\underline{Q}) = \sum_i b_i e^{i\underline{Q}\cdot\underline{R}_i} \tag{4.12}$$

When we calculate the scattering cross section, we have to take into account that the different isotopes are distributed randomly over all sites. Therefore, we have to average over the random distribution of the scattering length in the sample:

$$\frac{d\sigma}{d\Omega}(\underline{Q}) \sim \left|A(\underline{Q})\right|^2 = \left\langle \sum_i b_i \; e^{i\underline{Q}\cdot\underline{R}_i} \cdot \sum_j b_j^* e^{-i\underline{Q}\underline{R}_j} \right\rangle \tag{4.13}$$

As isotopes of the same element are chemically undistinguishable, the distribution of the scattering lengths b_i and b_j on the different sites is completely uncorrelated. This implies that for $i \neq j$, the expectation value of the product equals to the product of the expectation values. Only for $i = j$ a correlation occurs, which gives an additional term describing the mean quadratic deviation from the average:

$$\left\langle b_i b_j \right\rangle = \begin{cases} \langle b\rangle\langle b\rangle = \langle b\rangle^2 & i \neq j \\ \left\langle b^2 \right\rangle = \langle b\rangle^2 + \left\langle \left(b - \langle b\rangle\right)^2 \right\rangle & i = j \end{cases} \tag{4.14}$$

The line for i = j results from the identity:

$$\left\langle \left(b - \langle b\rangle\right)^2 \right\rangle = \left\langle b^2 - 2b\langle b\rangle + \langle b\rangle^2 \right\rangle = \left\langle b^2 \right\rangle - \langle b\rangle^2 \tag{4.15}$$

Therefore, we can write the cross section in the following form:

$$\begin{aligned} \frac{d\sigma}{d\Omega}(\underline{Q}) = \langle b\rangle^2 \left| \sum_i e^{i\underline{Q}\cdot\underline{R}_i} \right|^2 \quad & \text{"}coherent\text{"} \\ + N\left\langle \left(b - \langle b\rangle\right)^2 \right\rangle \quad & \text{"}incoherent\text{"} \end{aligned} \tag{4.16}$$

The scattering cross section is a sum of two terms. Only the first term contains the phase factors $e^{i\underline{Q}\cdot\underline{R}}$, which result from the coherent superposition of the scattering from pairs of scatterers. This term takes into account interference effects and is therefore named *coherent scattering*. The scattering length averaged over the isotope- and nuclear spin-distribution enters this term. This is in complete analogy to the "isotope insensitive" x-ray-diffraction. The second term in (4.16) does not contain any phase information and is proportional to the number N of atoms (and not to N^2). This term is not due to the interference of scattering from different atoms and it has no direct counterpart in x-ray scattering. As we can see from (4.14) (line $i = j$), this term corresponds to the scattering from single atoms, which subsequently superimpose in an incoherent manner (adding intensities, not amplitudes!). This is the reason for the intensity being proportional to the number N of atoms. Therefore the second term is called *incoherent scattering*.

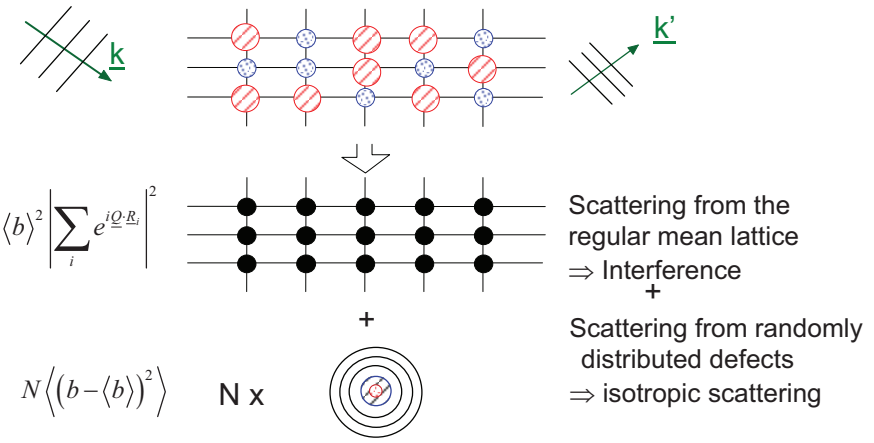

Fig. 4.11: *Upper panel: Sketch of the scattering process from a 2-D lattice of N chemically identical atoms with two isotopes (small dotted circles and large hatched circles). The area of the circle represents the scattering cross section of the single isotope. Middle panel: The incident wave is scattered coherently only from the average structure. This gives rise to Bragg peaks in certain directions. Lower panel: Additionally, an isotropic background (incoherent scattering) is observed, which is proportional to the number N of atoms and to the mean quadratic deviation from the average scattering length.*

The most prominent example for *isotope incoherence* is elementary nickel. The scattering lengths of the nickel isotopes are listed together with their natural abundance in Table 4.1 [2]. The differences in the scattering lengths for the various nickel isotopes are enormous. Some isotopes even have negative scattering lengths. This is due to resonant bound states, as compared to the usual potential scattering.

Isotope	Natural Abundance	Nuclear Spin	Scattering Length [fm]
^{58}Ni	68.27 %	0	14.4(1)
^{60}Ni	26.10 %	0	2.8(1)
^{61}Ni	1.13 %	$^3/_2$	7.60(6)
^{62}Ni	3.59 %	0	-8.7(2)
^{64}Ni	0.91 %	0	-0.37(7)
Ni			10.3(1)

Tab. 4.1: *The scattering lengths of the nickel isotopes and the resulting scattering length of natural $_{28}$Ni [2], see also fig. 4.9.*

Neglecting the less abundant isotopes ^{61}Ni and ^{64}Ni, the average scattering length is calculated as:

$$\langle b \rangle \approx \left[0.68 \cdot 14.4 + 0.26 \cdot 2.8 + 0.04 \cdot (-8.7)\right] fm \approx 10.2\, fm \qquad (4.17)$$

which gives the total coherent cross section of:

$$\Rightarrow \sigma_{coherent} = 4\pi\langle b\rangle^2 \approx 13.1\,barn\ (exact: 13.3(3)barn) \tag{4.18}$$

The incoherent scattering cross section per nickel atoms is calculated from the mean quadratic deviation:

$$\sigma_{incoherent}^{Isotope} = 4\pi\left[0.68\cdot(14.4-10.2)^2 + 0.26\cdot(2.8-10.2)^2 + 0.04\cdot(-8.7-10.2)^2\right] fm^2 \tag{4.19}$$
$$\approx 5.1 barn\ (exact: 5.2(4)barn)$$

Values in parentheses are the exact values taking into account the isotopes ^{61}Ni and ^{64}Ni and the nuclear spin incoherent scattering (see chapter 7). From (4.18) and (4.19), we learn that the incoherent scattering cross section in nickel amounts to more than one third of the coherent scattering cross section.

The most prominent example for *nuclear spin incoherent scattering* is elementary hydrogen. The nucleus of the hydrogen atom, the proton, has the nuclear spin $I = ½$. The total nuclear spin of the system H + n can therefore adopt two values: $J = 0$ and $J = 1$. Each state has its own scattering length: b_- for the singlet state $(J = 0)$ and b_+ for the triplet state $(J = 1)$.

Total Spin	Scattering Length	Abundance
J = 0	b_- = - 47.5 fm	$\frac{1}{4}$
J = 1	b_+ = 10.85 fm	$\frac{3}{4}$
<b> = - 3.739(1) fm		

Tab. 4.2: *Scattering lengths for hydrogen [2].*

As in the case of isotope incoherence, the average scattering length can be calculated:

$$\langle b\rangle = \left[\frac{1}{4}(-47.5) + \frac{3}{4}\cdot(10.85)\right] fm = -3.74\,fm \tag{4.20}$$

This corresponds to a coherent scattering cross section of about ≈ 1.76 barn [2]:

$$\Rightarrow \sigma_{coherent} = 4\pi\langle b\rangle^2 = 1.7568(10)\ barn \tag{4.21}$$

The nuclear spin incoherent part is again given by the mean quadratic deviation from the average:

$$\sigma_{incoherent}^{nuclear\ spin} = 4\pi\left[\frac{1}{4}(-47.5+3.74)^2 + \frac{3}{4}(10.85+3.74)^2\right] fm^2 = 80.2\ barn$$

$$(exact\ value:\ 80.26(6)\ barn) \tag{4.22}$$

Comparing (4.21) and (4.22), it is immediately clear that hydrogen scatters mainly incoherently. As a result, we observe a large background for all samples containing hydrogen. We should avoid all hydrogen containing glue for fixing our samples to a sample stick. Finally, we note that deuterium with nuclear spin $I = 1$ has a much more favorable ratio between coherent and incoherent scattering:

$$\sigma_{coh.}^{D} = 5.592(7)barn; \quad \sigma_{inc.}^{D} = 2.05(3)barn$$

The coherent scattering lengths of hydrogen (-3.74 fm) and deuterium (6.67 fm) are significantly different. This can be used for contrast variation by isotope substitution in all samples containing hydrogen, i. e. in biological samples or soft condensed matter samples, see the corresponding chapters.

A further important element, which shows strong nuclear incoherent scattering, is vanadium. Natural vanadium consists to 99,75 % of the isotope ^{51}V with nuclear spin 7/2. By chance, the ratio between the scattering lengths b_+ and b_- of this isotope are approximately equal to the reciprocal ratio of the abundances. Therefore, the coherent scattering cross section is very small and the incoherent cross section dominates [2]:

$$\sigma_{coh}^{V} = 0.01838(12)\ barn; \quad \sigma_{incoh}^{V} = 5.08(6)\ barn$$

For this reason, Bragg scattering of vanadium is difficult to observe above the large incoherent background. On the other hand, this fact can be turned into an advantage: By using vanadium metal, one can make sample containers which are practically invisible for (coherent) neutron scattering: They produce almost no reflections but rather a diffuse background (since incoherent scattering is isotropic) which usually doesn't cause severe problems in diffraction experiments.

4.3 Diffraction geometry

For purely elastic scattering, the scattering function $S(\underline{Q},\omega)$ reduces to the special case without energy transfer ($E_0 = E_1$ and $\hbar\varpi = E_0 - E_1 = 0$) and equal length of the wave vectors of the incident and scattered beams ($|\underline{k}_0| = |\underline{k}_1|$). $S(\underline{Q},\omega = 0)$ and the scattering intensity then only depends on the scattering vector $\underline{Q} = \underline{k}_0 - \underline{k}_1$. The *coherent elastic* neutron scattering (≡ neutron *diffraction*) yields information on the positions (distribution) of the atomic nuclei and the arrangement of the localised magnetic spins in crystalline solids, the pair correlation function of liquids and glasses, and the conformation of polymer chains.

Figure 4.12 shows a sketch of a general diffraction experiment. More specifically, it is a typical setup of a constant wavelength, angular dispersive diffraction experiment. There are other methods to perform a diffraction experiment (e.g. time of flight- (TOF-), Laue-, energy-dispersive diffractometers etc.) but these are outside the scope of this introductory lecture.

For constant wavelength diffraction, the energy (wavelength) and direction (collimation) of the incident neutron beam needs to be adjusted. For that purpose, the diffractometer is equipped with a crystal monochromator to select a particular wavelength band ($\lambda \pm \Delta\lambda/\lambda$) out of the "white" beam. Collimators are used to define the beam direction and divergence pretty much as is done in x-ray diffraction.

In the case of a crystalline sample, the diffraction geometry is most conveniently described by the concepts of the *reciprocal lattice* and the *Ewald construction* which are both well-known from x-ray-diffraction.

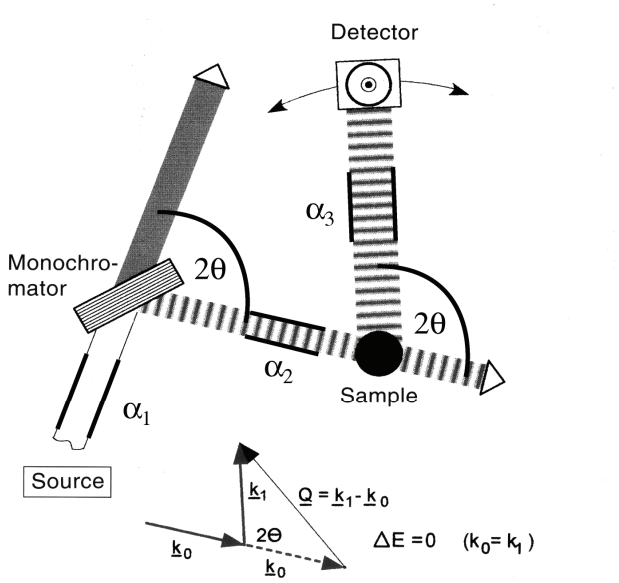

Fig. 4.12: *Schematic representation of a constant wavelength diffractometer.*

Reciprocal lattice

The characteristic feature of the crystalline state (see chapter 3) is its periodic order, which may be represented by a (translation) lattice. In the 3D case, three basis vectors $\boldsymbol{a_1}$, $\boldsymbol{a_2}$, $\boldsymbol{a_3}$ define a parallelepiped, called unit cell. Each lattice node of the crystal lattice can be addressed by a general lattice vector

$$\boldsymbol{a} = u\,\boldsymbol{a_1} + v\,\boldsymbol{a_2} + w\,\boldsymbol{a_3}. \tag{4.23}$$

which results from a linear combination of the basis vectors with coefficients u, v, and w (positive or negative integers, including 0).

The position of atom j in the unit cell is given by the vector

$$\boldsymbol{r_j} = x_j\,\boldsymbol{a_1} + y_j\,\boldsymbol{a_2} + z_j\,\boldsymbol{a_3}. \tag{4.24}$$

The coefficients x_j, y_j, and z_j are called atomic coordinates ($0 \le x_j < 1$; $0 \le y_j < 1$; $0 \le z_j < 1$).

For an ideal crystal and an infinite lattice with the basis vectors $\boldsymbol{a_1}$, $\boldsymbol{a_2}$, $\boldsymbol{a_3}$ there is only diffraction intensity $I(\boldsymbol{\tau})$ at the vectors

$$\boldsymbol{\tau} = h\,\boldsymbol{\tau_1} + k\,\boldsymbol{\tau_2} + l\,\boldsymbol{\tau_3}. \tag{4.25}$$

of the reciprocal lattice. h,k,l are the integer Miller indices and $\boldsymbol{\tau_1}$, $\boldsymbol{\tau_2}$, $\boldsymbol{\tau_3}$ are the basis vectors of the reciprocal lattice, satisfying the two conditions

$$\boldsymbol{\tau_1}\cdot\mathbf{a_1} = \boldsymbol{\tau_2}\cdot\mathbf{a_2} = \boldsymbol{\tau_3}\cdot\mathbf{a_3} = 1 \text{ and } \boldsymbol{\tau_1}\cdot\mathbf{a_2} = \boldsymbol{\tau_1}\cdot\mathbf{a_3} = \boldsymbol{\tau_2}\cdot\mathbf{a_1} = \ldots = 0,$$

or in terms of the Kronecker symbol with i, j and k = 1, 2, 3

$$\delta_{ij} = 0 \text{ for } i \neq j \text{ and } \delta_{ij} = 1 \text{ for } i = j \text{ with } \delta_{ij} = \boldsymbol{\tau_i}\cdot\boldsymbol{\tau_j}. \tag{4.26}$$

The basis vectors of the reciprocal lattice can be calculated from those of the unit cell in real space

$$\boldsymbol{\tau}_i = (\mathbf{a_j} \times \mathbf{a_k})/V_c, \tag{4.27}$$

where × means the cross product, and $V_c = \mathbf{a_1}\cdot(\mathbf{a_2}\times\mathbf{a_3})$ is the volume of the unit cell.

In solid state physics,

$$\boldsymbol{Q} = 2\pi\ \boldsymbol{\tau} \tag{4.28}$$

is used instead of $\boldsymbol{\tau}$

Here is a compilation of some properties of the reciprocal lattice:

- Each reciprocal lattice vector is perpendicular to two real space vectors: $\boldsymbol{\tau}_i \perp \mathbf{a_j}$ and $\mathbf{a_k}$ (for $i \neq j, k$)
- The lengths of the reciprocal lattice vectors are $|\boldsymbol{\tau}_i| = 1/V_c \cdot |\mathbf{a_j}| \cdot |\mathbf{a_k}| \cdot \sin\angle(\mathbf{a_j},\mathbf{a_k})$.
- Each point *hkl* in the reciprocal lattice refers to a set of planes (*hkl*) in real space.
- The direction of the reciprocal lattice vector $\boldsymbol{\tau}$ is normal to the (*hkl*) planes and its length is reciprocal to the interplanar spacing d_{hkl}: $|\boldsymbol{\tau}| = 1/d_{hkl}$.
- Duality principle: The reciprocal lattice of the reciprocal lattice is the direct lattice.

Performing a diffraction experiment on a single crystal actually means doing a Fourier transform of the 3D-periodic crystal (see chapter on symmetry in crystals) followed by forming the square of the resulting (complex) amplitude function. The Fourier transform of the (infinite) crystal lattice is essentially the reciprocal lattice derived above and yields directly the positions of the reflections in space (directions of the diffracted beams). The atomic arrangement within the unit cell determines the reflection intensities which may be envisaged as a weight attached to the nodes of the reciprocal lattice.

Doing a (single crystal) diffraction experiment therefore corresponds to measuring the positions and weights of the reciprocal lattice points. Their position yields information on the lattice parameters and the orientation of the crystal on the diffractometer while the weights (the reflection intensities) allow reconstructing the atomic positions within the unit cell.

Ewald construction

The concept of the reciprocal space also provides a handy tool to express geometrically the condition for Bragg scattering in the so-called Ewald construction. In this way the different diffraction methods can be discussed.

We consider the reciprocal lattice of a crystal and choose its origin 000. In Fig. 4.13 the wave vector $\underline{k}_0$ (defined in the crystallographers' convention with $|\underline{k}_0| = 1/\lambda$) of the incident beam is marked with its end at 000 and its origin P. We now draw a sphere of radius $|\underline{k}_0| = 1/\lambda$ around P passing through 000. Now, if any point *hkl* of the reciprocal lattice lies on the surface of this "Ewald sphere", then the diffraction condition for the (*hkl*) set of lattice planes is fulfilled: The wave vector of the diffracted beam $\underline{k}$ (with its origin also at P) for the set of planes (*hkl*), is of the same length as $\underline{k}_0$ ($|\underline{k}| = |\underline{k}_0|$) and the resulting vector diagram satisfies $\underline{k} = \underline{k}_0 + \boldsymbol{\tau}$. Introducing the scattering angle 2θ (and

hence the Bragg angle θ_{hkl}), we can deduce immediately from $2|\underline{k}|\cdot\sin\theta = |\boldsymbol{\tau}|$ the Bragg equation $2d_{hkl}\cdot\sin\theta_{hkl} = \lambda$.

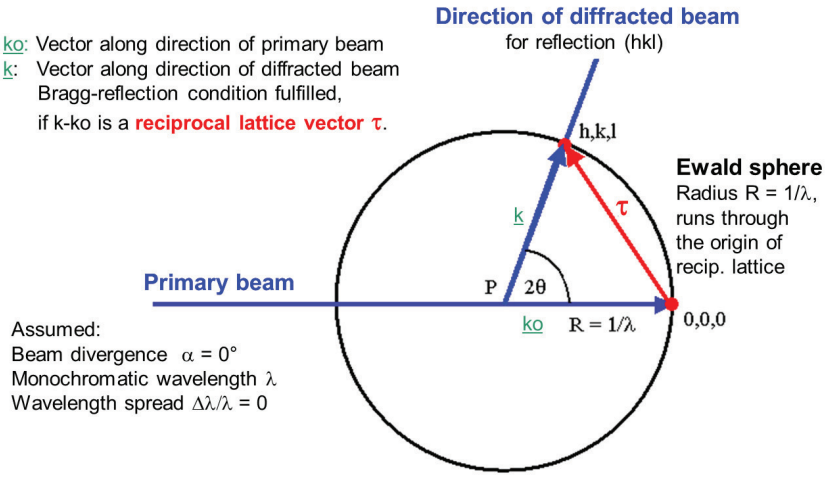

Fig. 4.13: *Ewald construction in reciprocal space, showing the diffraction condition for reflection (hkl).*

In the case of single crystal diffraction a rotation of the crystal and therefore also of the corresponding reciprocal lattice (which is rigidly attached to the crystal) is often used to set the diffraction conditions for the measurement of intensities $I(\boldsymbol{\tau})$.

If $|\boldsymbol{\tau}| > 2/\lambda$ (then $d_{hkl} < \lambda/2$) the reflection *hkl* cannot be observed. This condition defines the so called limiting sphere, with center at 000 and radius $2/\lambda$: only the points of the reciprocal lattice inside the limiting sphere can be rotated into diffraction positions. Vice versa if $\lambda > 2d_{max}$, where d_{max} is the largest interplanar spacing of the unit cell, then the diameter of the Ewald sphere is smaller than $|\boldsymbol{\tau}|_{min}$. Under these conditions no node of the reciprocal lattice can intercept the Ewald sphere. That is the reason why diffraction of visible light (wavelength ≅ 5000 Å) can never be obtained from crystals. λ_{min} determines the amount of information available from a diffraction experiment. In ideal conditions λ_{min} should be short enough to measure all points of the reciprocal lattice with significant diffraction intensities.

For a real crystal of limited perfection and size the infinitely sharp diffraction peaks (delta functions) evolve into broadened reflections. One reason can be the local variation of the orientation of the crystal lattice (mosaic spread) implying some angular splitting of the vector $\boldsymbol{\tau}$. A spread of interplanar spacings $\Delta d/d$, which may be caused by some inhomogeneities in the chemical composition of the sample, gives rise to a variation of its magnitude $|\boldsymbol{\tau}|$. The ideal diffraction geometry on the other hand also needs to be modified: In a real experiment the primary beam has a non-vanishing divergence and wavelength spread. The detector aperture is also finite. A gain of intensity, which can be accomplished by increasing the angular divergence and wavelengths bandwidth, has to be paid for by some worsening of the resolution function

(see below) and hence by a limitation of the ability to separate different Bragg reflections.

All of these influences can be studied by the Ewald construction. The influence of a horizontal beam divergence on the experimental conditions for a measurement of Bragg-intensities of a single crystal is illustrated in Fig. 4.14 where strictly monochromatic radiation (only one wavelength λ with $\Delta\lambda/\lambda = 0$) is assumed. To collect the complete intensity contained in the spread out reflection, a so-called ω-scan, where the crystal is rotated around the sample axis perpendicular to the diffraction plane, may be used. The summation over the whole reflection profile yields the so-called integral diffraction intensities.

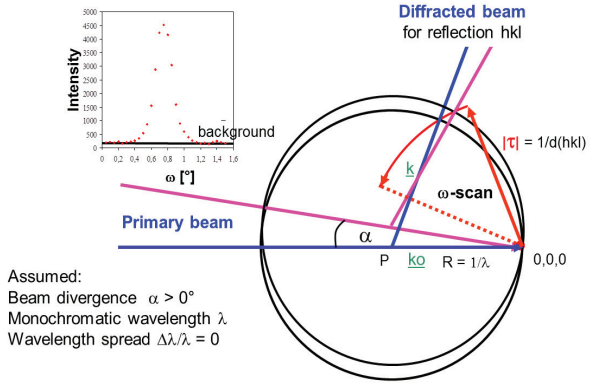

Fig. 4.14: *Ewald-construction: Influence of the horizontal beam divergence on the experimental conditions for the measurement of Bragg-intensities.*

Finally, the geometry of powder diffraction experiments can also be discussed in terms of the Ewald-construction:

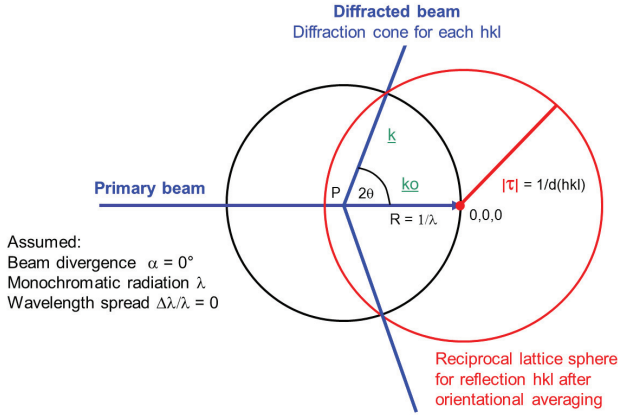

Fig. 4.15: *Ewald construction for a powder diffraction experiment.*

An ideal polycrystalline sample is characterised by a very large number of arbitrarily oriented small crystallites. Therefore, the reciprocal lattice point hkl is smeared out on a sphere and the 3D-information contained in vector $\boldsymbol{\tau}$ is reduced to only 1D-information contained in $|\boldsymbol{\tau}|$. In Figure 4.15 the corresponding sphere with radius $|\boldsymbol{\tau}| = 1/d_{hkl}$ is drawn around the origin of the reciprocal lattice at 0,0,0. For each Bragg-reflection the circle of intersection of the "reciprocal lattice sphere" with the Ewald-sphere yields a diffraction cone. These cones are recorded on a point or position sensitive detector. And the resulting information is plotted as a intensity vs. diffraction angle (or Q) diagram. All reflections with equal interplanar spacing d_{hkl} are perfectly superimposed and cannot be separated experimentally.

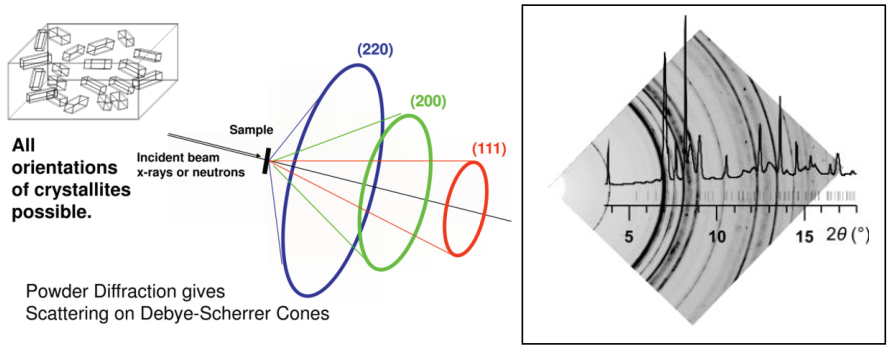

Fig. 4.16: *Sketch of a powder diffraction experiment, diffraction cones are recorded on a 2D- or 1D- detector (reproduced from [3]).*

4.4 Diffraction intensities

As stated in chapter 4.2, a scattering experiment is equivalent to performing a Fourier transform of the scattering object (eqn. 4.8) followed by taking the square of the resulting complex amplitude (eqn. 4.9). The latter step is very simply due to the fact, that our detectors can measure the magnitude (the absolute value) of a diffracted wave but are completely insensitive to its phase. This results in an intrinsic loss of information and poses the so-called "phase problem of crystallography". There are methods to reconstruct the missing phase information from the measured magnitudes and from a-priori information about the scattering object (e.g. the so-called direct methods of *structure determination*), but these methods are again outside the scope of this lecture. The first step of a diffraction experiment - the Fourier transform - needs some further elaboration: In a diffraction (elastic, coherent scattering) experiment we can safely ignore time as a variable and concentrate only on the spatial Fourier transform of the scattering object (here: the crystal). For those who are not particularly familiar with the Fourier transform, figure 4.17 shows a very simple one-dimensional analogue. The transformation from A to E (labelled FT, ||) corresponds to the diffraction experiment: Fourier-transform (harmonic analysis) plus calculation of the absolute value. If we could also retrieve the phases φ, the inverse Fourier transform (labelled FT^{-1}, φ) would lead directly to the structure of the scattering object A (harmonic synthesis).

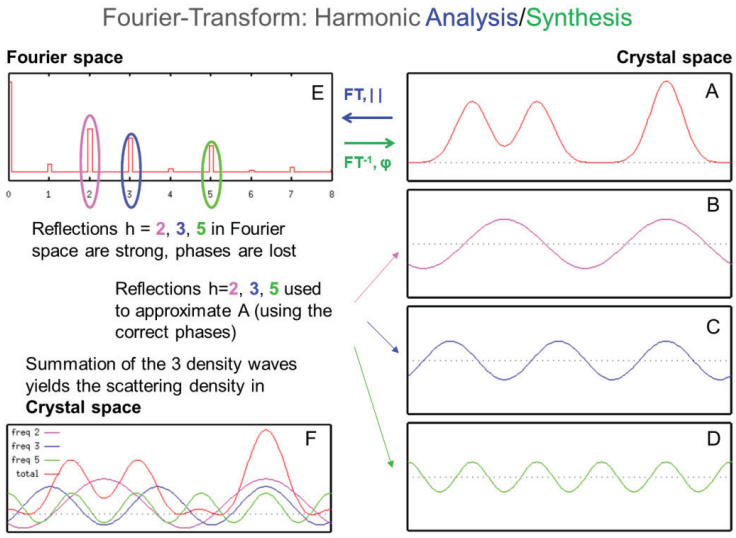

Fig. 4.17: *1D illustration of the Fourier transform, A: scattering object: 1D-density function, assumed: periodic in 1D, B-D: decomposition of A into 3 harmonic (co-)sine waves, F: synthesis of A (red curve) via summation of B-D with the correct phases, E: "diffractogramm" of A: Fourier transform, only the magnitudes of waves in B to D are plotted, figures taken from[4].*

Without the phase information, we need an approximate model of the crystal structure and a formula to calculate diffraction intensities from the model. In the kinematical approximation (see above) we use the so called structure factor formula for that purpose (see below). The model is then iteratively improved to give an optimum match between observed and calculated intensities. This is referred to as the *structure refinement*.

Structure factor and Bragg intensities

In the kinematical approximation, which assumes that the magnitude of the incident wave amplitude is the same at all points in the specimen (this implies a small sample size, weak scattering intensities, no multiple diffraction and negligible absorption), the diffracted intensity is proportional to the square of the amplitude of the scattered wave for each individual reflection; it can be regarded as a weight ascribed to the reciprocal-lattice nodes (see eqn. 4.25).

$$I(\boldsymbol{\tau}) \sim |\boldsymbol{F}(\boldsymbol{\tau})|^2. \tag{4.29}$$

The structure factor $\mathbf{F}(\boldsymbol{\tau})$ is the Fourier transform of the scattering density within the unit cell. For a 3D-periodic scattering density function composed of discrete atoms (the crystal), the integral in (4.8) describing the Fourier transform in its most general form, simplifies to a sum over all atoms j in the unit cell The structure factor $\mathbf{F}(\boldsymbol{\tau})$ contains the complete structural information, including the atomic coordinates $\boldsymbol{r_j} = x_j\, \boldsymbol{a_1} + y_j\, \boldsymbol{a_2} + z_j\, \boldsymbol{a_3}$ (see eqn. 4.24), site occupations and the thermal vibrations contained in T_j.

$$\boldsymbol{F}(\boldsymbol{\tau}) = \sum_j bj \cdot \exp[2\pi i(\boldsymbol{\tau}\boldsymbol{r}_j)] \cdot T_j(\boldsymbol{\tau}) = |\boldsymbol{F}(\boldsymbol{\tau})| \cdot \exp[i\varphi(\boldsymbol{\tau})]. \quad (4.30)$$

In the case of nuclear scattering of neutrons the structure factor has the dimension of a length, as has the scattering length $b_j(\boldsymbol{\tau}) = b_j$ = const. of nucleus j. $T_j(\boldsymbol{\tau})$ is the Debye-Waller factor which takes into account dynamical and static displacements of the nucleus j from its average position $\boldsymbol{r}_j$ in the unit cell. With the fractional coordinates x_j, y_j and z_j, the scalar product in the exponential function can be written as

$$\boldsymbol{\tau} \cdot \boldsymbol{r}_j = hx_j + ky_j + lz_j \quad (4.31)$$

In a diffraction experiment normally only relative Bragg intensities are measured. A scale factor SCALE takes into account all parameters which are constant for a given set of diffraction intensities. Additional corrections have to be applied, which are a function of the scattering angle. For nuclear neutron diffraction from single crystals the integrated relative intensities are given by

$$I(\boldsymbol{\tau}) = \text{SCALE} \cdot L \cdot A \cdot E \cdot |\boldsymbol{F}(\boldsymbol{\tau})|^2 \quad (4.32)$$

The Lorentz factor L is instrument specific. The absorption correction A depends on the geometry and linear absorption coefficient of the sample and the extinction coefficient E takes into account a possible violation of the assumed conditions for the application of the kinematical diffraction theory.

Information on the crystal system, the Bravais lattice type and the basis vectors $\boldsymbol{a}_1$, $\boldsymbol{a}_2$, $\boldsymbol{a}_3$ of the unit cell (lattice parameters a, b, c, α, β, γ) may be directly deduced from the reciprocal lattice. The $|\boldsymbol{F}(\boldsymbol{\tau})|^2$ values associated as weights to the nodes of the reciprocal lattice give the diffraction symbol and hence valuable information on the space-group symmetry (see chapter 3). Here, systematic absences (zero structure factors) can be used to determine non-primitive Bravais lattices or detect the presence of non-symmorphic symmetry operations (symmetry operations with translation components).

As an example, consider a *body centered cubic* lattice with atoms at 0,0,0 and ½,½,½. Using eqn. 4.31 and dropping the Debye-Waller factor for the moment, eqn. 4.30 may be rewritten as:

$$\boldsymbol{F}(hkl) = \sum_j bj \cdot \exp[2\pi i(hx_j + ky_j + lz_j)] \cdot T_j(\boldsymbol{\tau}) = |\boldsymbol{F}(\boldsymbol{\tau})| \cdot \exp[i\varphi(\boldsymbol{\tau})]. \quad (4.33)$$

For a centrosymmetric structure, F is a real quantity (instead of complex), the exponentials in (4.33) reduce to cosines and the phase factor assumes only the values + or -. For this simple structure, index j just runs over the two equivalent atoms with scattering length b within the unit cell. Thus we get:

$$F(hkl) = b \cdot \cos\left[2\pi(h \cdot 0 + k \cdot 0 + l \cdot 0\right] + b \cdot \cos\left[2\pi(h/2 + k/2 + l/2)\right] \quad (4.34)$$

The first term cos(0) = 1 and we therefore have:

$$F(hkl) = b + b \cdot \cos\left[2\pi(h/2 + k/2 + l/2)\right] = b \cdot (1 + \cos[\pi(h + k + l)]) \quad (4.35)$$

If h+k+l is even, the cosine term is +1, otherwise it is -1.

Reflections with h+k+l=2n+1 are therefore *systematically absent*.

These statements apply equally well to x-ray and neutron diffraction and to powder as well as to single crystal diffraction data.

In the case of a powder sample, orientational averaging leads to a reduction of the dimensionality of the intensity information from 3D to 1D: Diffraction intensity I is recorded as a function $|\boldsymbol{\tau}| = 1/d_{hkl}$ or, by making use of Bragg's law, of $\sin(\theta)/\lambda$ or just as a function of 2θ. For powders, two additional corrections (M and P in eqn. 4.36) need to be applied in order to convert between the measured intensities I and the squared structure factor magnitudes F^2:

$$I(|\boldsymbol{\tau}|) = \text{SCALE} \cdot \text{L} \cdot \text{A} \cdot \text{E} \cdot \text{M} \cdot \text{P} \cdot |\boldsymbol{F}(|\boldsymbol{\tau}|)|^2 \qquad (4.36)$$

M is the multiplicity of the individual reflections and takes into account how many symmetrically equivalent sets of lattice planes correspond to a given hkl. In the cubic crystal system, for instance, $M_{111}=8$ (octahedron) while $M_{100}=6$ (cube). P is the so-called preferred orientation parameter which corrects the intensities for deviations from the assumption of randomly oriented crystals in the powder sample.

4.5 Diffractometers

Single Crystal Neutron Diffractometry

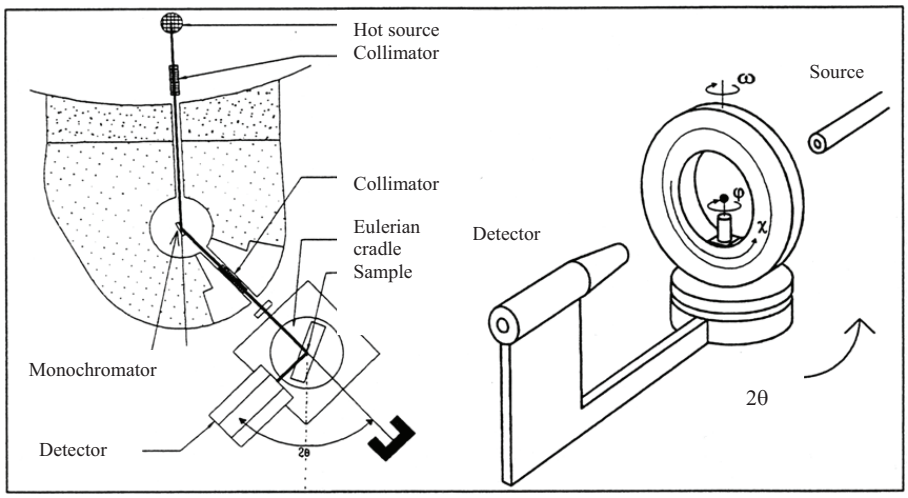

Fig. 4.18: *Principle components of a constant wavelength single crystal diffractometer.*

Monochromator and collimator

For constant wavelength diffraction, the energy (wavelength) and direction (collimation) of the incident neutron beam needs to be adjusted. For that purpose, the diffractometer is equipped with a crystal monochromator to select a particular wavelength band ($\lambda \pm \Delta\lambda/\lambda$) out of the "white" beam according to the Bragg condition for its scattering plane (*hkl)*

$$2d_{hkl} \cdot \sin\theta_{hkl} = \lambda, \qquad (4.37)$$

with the interplanar spacing d_{hkl} and the monochromator scattering angle $2\theta_{hkl} = 2\theta_M$. The width of the wavelengths band $\Delta\lambda/\lambda$, which is important for the Q-resolution, depends on the divergences of the beam before and after the monochromator (collimations α_1 and α_2), on the mosaic spread of the monochromator crystal ΔM, and on the monochromator angle $2\theta_M$. In order to increase the intensity of the monochromatic beam at the sample position the monochromator crystal is often bent in vertical direction perpendicular to the diffraction plane of the experiment. In this way the vertical beam divergence is increased leading to a loss of resolution in reciprocal space. The diffracted intensity from the sample is measured as a function of the scattering angle 2θ and the sample orientation (especially in case of a single crystal). 2θ is again defined by collimators. As there is no analysis of the energy of the scattered beam behind the sample, the energy resolution $\Delta E/E$ of such a 2-axes diffractometer is not well defined (typically of the order of some %). In addition to the dominant elastic scattering also quasi-elastic and some inelastic scattering contributions are collected by the detector.

Neutron filters and the problem of λ/2 contamination

Unfortunately, the monochromator crystals not only "reflect" the desired wavelength λ by diffraction from the set of lattice planes (hkl) but also the higher orders of λ/2 or λ/3 etc. from 2h,2k,2l or 3h,3k,3l to the same diffraction angle:

$$\sin\theta = \lambda/d_{hkl} = (\lambda/2)/d_{2h\,2k\,2l} = (\lambda/3)/d_{3h\,3k\,3l} \qquad (4.38)$$

The only requirement is, that the higher order reflection (2h,2k,2l) or (3h,3k,3l) has a reasonably large structure factor (see chapter 4). Higher order contamination causes measurable reflection intensities at "forbidden" reflection positions and in addition to that can modify intensities at allowed positions. Thus it can very much affect the correct determination of the unit cell as well of the symmetry (from systematically absent reflections). The solution to this problem is to minimize the λ/2 contamination by using filters which suppress the higher orders stronger than the desired wavelength. One such type of filters uses resonance absorption effects - completely analogous to the suppression of the K_β line in x-ray diffractometers. Another way to attenuate short wavelengths is to use the scattering from materials like beryllium or graphite. These filters use the fact that there is no Bragg diffraction if $\lambda > 2d_{max}$, where d_{max} is the largest interplanar spacing of the unit cell. As we have shown above, for such long wavelengths the Ewald sphere is too small to be touched by any reciprocal lattice point. Below this critical wavelength, the neutron beam is attenuated by diffraction and this can be used to suppress higher order reflections very effectively. Frequently used materials are polycrystalline beryllium and graphite. Due to their unit cell dimensions, they are particularly suitable for experiments with cold neutrons because they block wavelengths smaller than about 3.5 A and 6 A respectively.

Resolution function:

An important characteristic of any diffractometer is its angular resolution. Fig. 4.19 shows (on the right) the resolution function (reflection half width as a function of scattering angle) for the four circle single crystal neutron diffractometer HEiDi at FRM II shown on the left. The resolution depends on a number of factors, among them the

collimation, the monochromator type and quality, the 2θ and (hkl) of the reflection used for monochromatization etc.

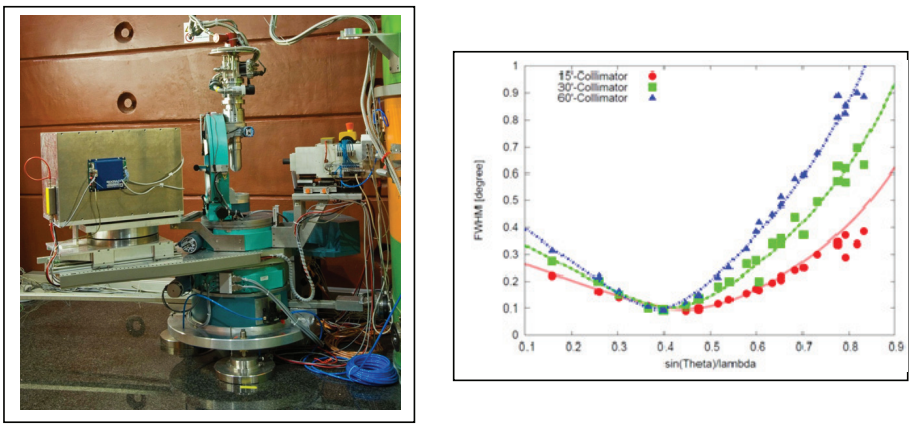

Fig. 4.19: *Left: Experimental setup of the four circle single crystal diffractometer HEiDi at FRM II. Right: Resolution function of HEiDi for different collimations, monochromator: Cu (220), 2ΘMono = 40° → λ = 0.873 Å.*

Powder Neutron Diffractometry:

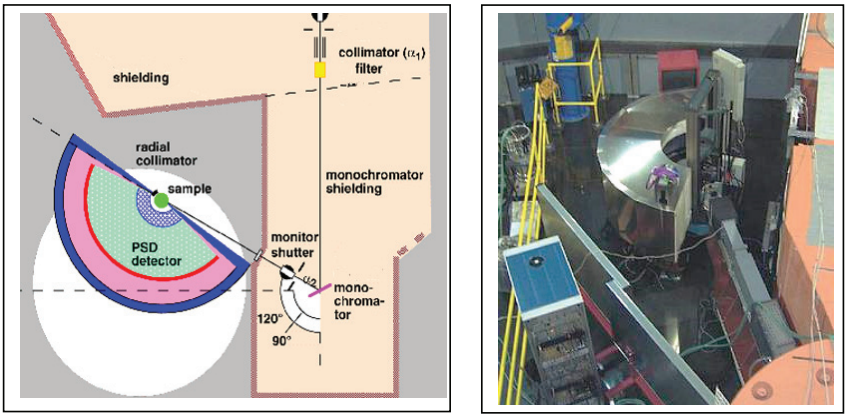

Fig. 4.20: *Left: Typical setup of a (constant wavelength) powder neutron diffractometer with position sensitive detector (PSD). Right: Neutron powder diffractometer SPODI at FRM II*

Neutron Rietveld analysis:

The conversion from 3D- to 1D-intensity data caused by the averaging over all crystallite orientations in a powder sample severely restricts the informative value of

powder neutron (or x-ray) diffraction experiments and makes the resolution function of the instrument even more important than in the single crystal case. Even with optimized resolution, the severe overlap of reflections on the 2θ-axis often prohibits the extraction of reliable integrated intensities from the experiment. Instead, the Rietveld method, also referred to as *full pattern refinement*, is used to refine a given structural model against powder diffraction data. The method, which is widely used in powder x-ray diffraction, has actually been invented by Hugo Rietveld in 1966 for the structural analysis from powder neutron data. Full pattern refinement means that along with the structural parameters (atomic coordinates, thermal displacements, site occupations) which are also optimized in a single crystal structure refinement, additional parameters like the shape and width of the reflection profiles and their 2θ-dependence, background parameters, lattice parameters etc. need to be refined.

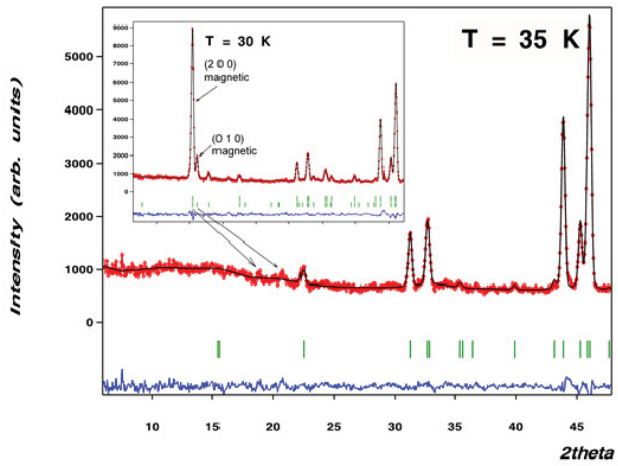

Fig. 4.21: *Results of a Rietveld refinement at the magnetic phase transition of $CoGeO_3$ [5], red: measured intensity, black: calculated from model, blue: difference, green: tick-marks at allowed reflection positions. The figure shows the low-angle part of two diffractograms measured at SPODI at 35K and 30K. Note the strong magnetic reflection appearing below the magnetic ordering transition (in the inset).*

References

[1] J. Strempfer et al. Eur. Phys. J B **14**, 63 – 72, (2000).
J. Strempfer et al. Physica B **267 - 268**, 56 – 59, (1999).
[2] A. Dianoux, G. Lander (Eds.) "Neutron Data Booklet",
Institute Laue-Langevin (2002)
[3] Reproduced from: Braggs world, talk by Th. Proffen
http://ebookbrowse.com/proffen-talk-bragg-pdf-d59740269
[4] Courtesy of Kevin Cowtan , http://www.ysbl.york.ac.uk/~cowtan/
[5] G. Redhammer et al. Phys. Chem. Min. **37**, 311-332, (2010) .

Exercises

E4.1 Types of Scattering Experiments

Discuss/define the following terms:

A. Elastic scattering, **B.** Inelastic scattering, **C.** Coherent scattering, **D.** Incoherent scattering

What is the major source of incoherent elastic scattering that is specific to neutrons?

E4.2 Energy and Wavelength

Give orders of magnitudes for the energy [eV] and the wavelength [Å] of the following types of radiation which are being used for diffraction experiments:

A. Thermal neutrons, **B.** x-ray photons, **C.** Electrons

E4.3 Scattering Length

Discuss the terms *(units, similarities, differences):*
A. Elastic scattering length, **B.** Elastic scattering cross section,
C. Atomic form factor (for x-rays)

E4.4 The Phase Problem

Describe, in simple terms, the "phase problem of crystallography"

A. Formulate the diffraction experiment in terms of the Fourier transform with subsequent squaring of the modulus of the Fourier coefficients

B. Discuss in how far these operations may be inverted.

C. Describe qualitatively how the phase problem is solved.

E4.5 Ewald Construction

Sketch the Ewald-construction for a single crystal experiment.

What is this geometric construction useful for?

E4.6 Intensity Corrections

The experimental Bragg-reflection intensity $I(\boldsymbol{\tau})$ and the squared modulus of the calculated structure factor $|\boldsymbol{F}(\boldsymbol{\tau})|^2$ (from the structure factor formula) are proportional to each other.
A number of corrections have to be made to get from $I(\boldsymbol{\tau})$ to $|\boldsymbol{F}(\boldsymbol{\tau})|^2$ or vice versa.

A. Recall *(from your experience with x-rays)* and discuss the physical origin of these intensity corrections:

SCALE: Scalefactor; L: Lorentz factor; A: Absorption correction, E: Extinction correction.
For powder methods also: M: Multiplicity, P: Preferred orientation.

B. Discuss the relative importance of these factors for neutrons and x-rays.

C. The polarisation correction, which is important in x-ray scattering, is missing in the neutron case: Discuss this fact in terms of the different physical meaning of "polarization" for x-rays and neutrons.

E4.7 Fourier Transform

A. Define the terms "Fourier-analysis" and "Fourier-synthesis" in the context of a diffraction experiment *(formula and description)*

B. What is the purpose of calculating a Fourier synthesis in crystallography?

E4.8 Filtering

A. How does a beryllium filter work? What is it used for?

B. Discuss why filters are also used in laboratory x-ray diffraction.

E4.9 Systematic absences

Calculate (from the structure factor formula) the systematic absences of reflections for an orthorhombic C-centered lattice.

5 Nanostructures Investigated by Small Angle Neutron Scattering

H. Frielinghaus
Jülich Centre for Neutron Science
Forschungszentrum Jülich GmbH

Contents

Lecture Notes of the JCNS Laboratory Course Neutron Scattering

5.1 Introduction

Small angle neutron scattering aims at length scales ranging from nanometers to micrometers [1, 2]. This is the typical mesoscale where often atomistic properties can be neglected but structurally systems self-organize, i.e. self-assemble. The structural information about the mesoscale is therefore indispensible for the understanding of the macroscopic behavior. Fundamental concepts of many materials are verified by small angle neutron scattering which supports the finding of new materials for the future. Especially for formulations with many substances the individual role of each of them is often unclear. The use of theoretical models helps to understand the mechanism of additives. Using these concepts the system behavior for remote parameter ranges can be predicted which overcomes tedious trial and error concepts.

The simplest molecules which leave the atomistic scale are chain like. Model polymers chemically string identical monomers linearly. These macromolecules have a lot of internal degrees of freedom which practically leads to the formation of coils. Studying the structure of these coils is a typical application for small angle neutron scattering. In this way, the coil size can be related to the monomer structure. The high entropy of polymers is responsible for rubber elasticity. The deformation of polymers under stress is an important question of nowadays research. The often used solid filler particles complicate the physical behavior of the polymers and not all details are finally understood. The larger particles strengthen the mechanical behavior, but there are also nanoparticles which cause the opposite behavior.

Proteins are important building blocks of biological systems. Often they are characterized as crystals by x-ray scattering. These structures are roughly corresponding to the natural state, but often specific properties cannot be explained completely. It is known that the aqueous environment changes the structure of proteins. The parallel structural characterization of dissolved proteins in water is a typical application for small angle neutron scattering. Another point of criticism is the dynamics of proteins. While the crystalline structures are rather rigid and do not reflect the highly dynamical properties, the dissolved proteins include such effects. In combination with neutron spin echo spectroscopy aiming at the dynamics explicitly the fluctuations of protein shapes are also explained on the basis of small angle neutron scattering experiments. All these details explain the function of proteins in their natural environment of biological systems.

When molecules include groups which tend to separate often microdomains are formed. While macroscopic phase separation is inhibited the self-organization of the molecules leads to highly ordered structures. Examples are liquid crystals – more generally one speaks of liquid crystalline order. The microdomains are again of nanometer size and are well characterized by small angle neutron scattering. Aligned single crystals and ‘powder’ samples are also of interest. Important questions range from optical to mechanical properties.

Membranes represent the field of surface science. In biology many questions arise about the function of cell membranes. The major molecules are lipids with a hydrophilic head and a hydrophobic tail. These molecules form bilayers with the hydrophobic moiety in the middle. The bilayer has a thickness of a few nanometers and, thus, fits perfectly to small angle neutron scattering. On larger scales the membranes form closed vesicles or membrane stacks for example. Biologically embedded proteins and smaller molecules such as cholesterol enrich the behavior of the simple membranes. While these examples are rather biologically motivated, surfactant molecules resemble the lipids, but are often used as soaps and detergents. A microemulsion

dissolves oil and water macroscopically by adding certain amounts surfactant. Microscopically oil and water stay demixed and form microdomains which ideally suit the length scales of a neutron small angle scattering experiment. Certain polymers as additives allow for increasing the surfactant efficiency dramatically. This application is environmentally friendly and saves resources.

So small angle neutron scattering experiments connect fundamental physics with chemical and biological aspects and finally lead to industrial applications. May the reader find enlightening ideas for new applications of small angle neutron scattering.

5.2 Survey about the SANS Technique

At the research reactor FRM 2 in Garching, the neutron radiation is used for experiments. In many cases, materials are examined in terms of structure and dynamics. The word neutron radiation already contains the wave-particle duality, which can be treated theoretically in quantum mechanics. By neutron we mean a corpuscle usually necessary for the construction of heavier nuclei. The particle properties of the neutron become visible when classical trajectories are describing the movement. The equivalent of light is obtained in geometrical optics, where light rays are described by simple lines, and are eventually refracted at interfaces. However, for neutrons the often neglected gravity becomes important. A neutron at a (DeBroglie) wavelength of 7Å ($= 7 \times 10^{-10}$m) has a velocity of $v = h/(m_n\lambda) = 565$m/s. Over a distance of 20m this neutron is therefore falling by 6.1mm. Thus, the design of neutron instruments is oriented to straight lines with small gravity corrections. Only very slow neutrons show significant effects of gravitation, such as the experiment of H. Meier-Leibnitz described at the subway station 'Garching Forschungszentrum'. The wave properties of neutrons emerge when there is an interaction with materials and the structural size is similar to the neutron wavelength. For the neutron wavelength 7Å these are about 5 atomic distances of carbon. For a Small Angle Neutron Scattering (SANS) experiment we will see that the typical structural sizes investigated are in the range of 20 to 3000Å. The coherence of the neutron must, therefore, be sufficient to examine these structural dimensions. Classically this consideration will be discussed in terms of resolution (see below). The scattering process appears only due to the wave properties of the neutron.

A scattering experiment is divided into three parts. First, the neutrons are prepared with regard to wavelength and beam alignment. The intensity in neutron experiments is much lower than in experiments with laser radiation or x-rays at the synchrotron. Therefore, an entire wavelength band is used, and the divergence of the beam is limited only as much as necessary. The prepared beam penetrates the sample, and is (partly) scattered. For every neutron scattering experiment elastic and inelastic scattering processes occur. The typical length scales of small angle scattering focus on the nanometer (up to micrometer). The corresponding movements of such large volumes are slow and the scattering processes are called quasi elastic in this Q-range. For simplicity, we assume elastic scattering processes as the idealized condition. So, there is virtually no energy transferred to the neutron. However, the direction changes in the scattering process. The mean wave vector of the prepared beam $\mathbf{k}_i$ (with $|\mathbf{k}_i| = 2\pi/\lambda$) is deflected according to the scattering process to the final wave vector $\mathbf{k}_f$. The scattered neutrons are detected with an area detector. The experimental information is the measured intensity as a function of the solid

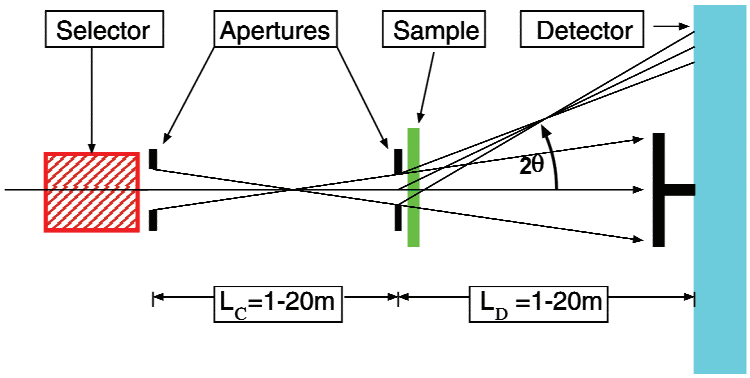

Fig. 5.1: *Principle of a small-angle neutron scattering diffractometer. The neutrons pass through the neutron velocity selector. The divergence is determined by the two apertures (entrance and sample aperture of the collimation). Then, the neutrons penetrate the sample. The unscattered neutrons are absorbed at the beam stop, while the scattered neutrons are detected by the position sensitive detector.*

angle Ω. This solid angle is defined relatively to an ideally small sample and for large detector distances.

In practice, the classical small-angle neutron scattering apparatus including the source looks like this: In the reactor a nuclear chain reaction takes place. A uranium nucleus ^{235}U captures a free neutron, and fission to smaller nuclei takes place. Additionally, 2.5 neutrons (on average) are released, which are slowed down to thermal energy by the moderator. One part of the neutrons keeps the chain reaction going, while the remaining part can be used for neutron experiments. The cold source is another moderator, which cools the neutrons to about 30K. Here, materials with light nuclei (deuterium at FRM 2) are used to facilitate the thermalization. The cold neutrons can easily be transported to the instruments by neutron guides. Rectangular glass tubes are used with a special mirror inside. The neutron velocity selector works mechanically (Fig. 5.1 shows scheme). A rotating cylinder with tilted lamellae allows only neutrons with a certain speed to pass. The wavelengths distribution is ideally triangular with a relative half-width of $\pm 5\%$ or $\pm 10\%$. The collimation determines the divergence of the beam. The entrance aperture and the sample aperture have a distance L_C, and restrict the divergence of the beam. The sample is placed directly behind the sample aperture. Many unscattered neutrons leave the sample and will be blocked by an absorber at the front of the detector. Only the scattered neutrons are detected by the detector at a distance L_D. The sensitive detector detects about 93% of the scattered neutrons, but the huge primary beam cannot be handled, and, therefore, is absorbed by an absorber. In the instruments KWS-1 and KWS-2 the beam stop contains a small counter to measure the unscattered neutrons in parallel. The classic small-angle neutron scattering apparatus is also known as pinhole camera, because the entrance aperture is imaged to the detector by the sample aperture. The sample aperture may be opened further if focusing elements maintain (or improve) the quality of the image of the entrance aperture. By focusing elements the intensity of the experiment may be increased on the expense of needing large samples. Focusing elements can be either curved mirrors or neutron lenses made of MgF_2. Both machines KWS-1 & KWS-2 have neutron lenses, but for this lab course they will not be used.

5.2.1 The Scattering Vector Q

In this section, the scattering vector **Q** is described with its experimental uncertainty. The scattering process is schematically shown in Fig. 5.3, in real space and momentum space. In real space the beam hits the sample with a distribution of velocities (magnitude and direction). The neutron speed is connected to the wavelength, whose distribution is depending on the velocity selector. The directional distribution is defined by the collimation. After the scattering process, the direction of the neutron is changed, but the principal inaccuracy remains the same. The scattering angle 2θ is the azimuth angle. The remaining polar angle is not discussed further here. For samples with no preferred direction the scattering is isotropic and, thus, does not depend on the polar angle. In reciprocal space the neutrons are defined by the wave vector **k**. The main direction of the incident beam is defined as the z-direction, and the modulus is determined by the wavelength, so $|\mathbf{k}_i| = 2\pi/\lambda$. Again, **k** is distributed due to the selector and the collimation inaccuracies. The wave vector of the (quasi) elastic scattering process has the same modulus, but differs in direction, namely by the angle 2θ. The difference between both wave vectors is given by the following value:

$$Q = \frac{4\pi}{\lambda} \sin\theta \tag{5.1}$$

For isotropic scattering samples, the measured intensity depends only on the absolute value of the scattering vector $Q = |\mathbf{Q}|$. For small angles, the common approximation of small angle (neutron) scattering is valid:

$$Q = \frac{2\pi}{\lambda} \cdot 2\theta \tag{5.2}$$

The typical Q-range of a small angle scattering instrument thus follows from the geometry. The detector distances L_D vary in the range from 1.5m to 20m. The area detector is active between $\varnothing_D = 4$cm and 35cm from the center. The angle 2θ is approximated by the ratio $\varnothing_D/L_D$ and the wavelength λ is 7Å. For the instruments KWS-1 and KWS-2, a typical Q-range from 2×10^{-3} to 0.2Å^{-1} is obtained.

The Q-vector describes which length scales ℓ are observed, following the rule $\ell = 2\pi/Q$. If a Bragg peak is observed, the lattice parameters can be taken directly from the position of the peak. If the scattering shows a sudden change at a certain Q-value, we obtain the length scale of the structural differences. There are characteristic scattering behaviors that can be described by so called scattering laws that are simple power laws Q^α with different exponents α.

5.2.2 Measurement of the Macroscopic cross section

In this section, the macroscopic scattering cross section is connected to the experimentally measured intensity. The experimental intensity is dependent on the instrument at hand, while the macroscopic scattering cross section describes the sample properties independent of instrumental details. The absolute calibration allows to compare experimental data between different measurements. In theory, the intensity and the cross section are connected by:

Fig. 5.2: *Setup of the SANS instrument KWS-2 in the neutron guide hall of FRM 2, Garching. In the middle of the picture is the sample position (A collaborator mounts a sample). The neutrons are coming from the left through the collimation. On the right is the detector tank with its entry window. The neutrons are transported largely in vacuum due to absorption by air.*

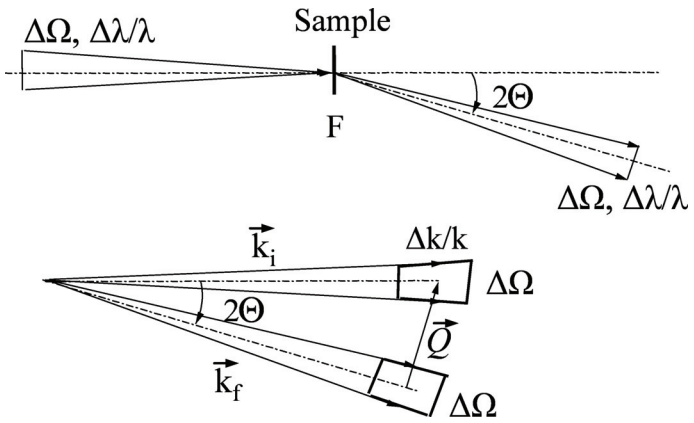

Fig. 5.3: Above: *the neutron speed and its distribution in real space, before and after the scattering process.* Bottom: *The same image expressed by wave vectors (reciprocal space). The scattering vector is the difference between the outgoing and incoming wave vector.*

$$\frac{\Delta I}{\Delta\Omega}(\mathbf{Q}) = I_0 \cdot A \cdot T_r \cdot t \cdot \frac{d\Sigma}{d\Omega}(\mathbf{Q}) \tag{5.3}$$

The intensity ΔI for one detector channel is measured as a function of the scattering angle. Each detector channel covers the solid angle $\Delta\Omega$. The experimental intensity is proportional to: (a) the intensity at the sample position I_0 (in units of neutrons per second per area), (b) of the irradiated area A, (c) the transmission of the sample (the relative portion of non-scattered neutrons), (d) of the sample thickness t, and (e) the macroscopic scattering cross section $d\Sigma/d\Omega$. In most practical cases, the primary intensity cannot be detected by the same detector. By a calibration measurement of a substance with known scattering strength the primary intensity is measured indirectly. At KWS-1 and KWS-2 we often use plexiglass, which scatters only incoherently (due to the hydrogen content). The two measurements under the same conditions will be put in relation, which thereby eliminates the identical terms. One writes:

$$\frac{\left.\frac{\Delta I(\mathbf{Q})}{\Delta\Omega}\right|_{\text{sample}}}{\left.\frac{\Delta I(\mathbf{Q})}{\Delta\Omega}\right|_{\text{plexi}}} = \frac{I_0 \cdot A \cdot T_{r,\text{sample}} \cdot t_{\text{sample}}}{I_0 \cdot A \cdot T_{r,\text{plexi}} \cdot t_{\text{plexi}}} \cdot \frac{\left.\frac{d\Sigma(\mathbf{Q})}{d\Omega}\right|_{\text{sample}}}{\left.\frac{d\Sigma(\mathbf{Q})}{d\Omega}\right|_{\text{plexi}}} \tag{5.4}$$

The macroscopic scattering cross section of the plexiglass measurement does not depend on the scattering vector. The measured intensity of the plexiglass is also a measure of the detector efficiency, as different channels can have different efficiency. The plexiglass specific terms are merged to $\mu_{\text{plexi}} = T_{r,\text{plexi}} \cdot t_{\text{plexi}} \cdot (d\Sigma/d\Omega)_{\text{plexi}}$. So, finally the macroscopic scattering cross-section reads:

$$\left.\frac{d\Sigma(\mathbf{Q})}{d\Omega}\right|_{\text{sample}} = \frac{\mu_{\text{plexi}}}{T_{r,\text{sample}} \cdot t_{\text{sample}}} \frac{\Delta I(\mathbf{Q})|_{\text{sample}}}{\Delta I(\mathbf{Q})|_{\text{plexi}}} \cdot \left(\frac{L_{D,\text{sample}}}{L_{D,\text{plexi}}}\right)^2 \tag{5.5}$$

Essentially, formula 5.5 follows directly from equation 5.4. The last factor results from the solid angles of the two measurements, which in principle can be done at different detector distances L_D. Plexiglass is an incoherent scatterer, and therefore can be measured at smaller detector distances to obtain an increased intensity. Nonetheless, the collimation setting must be the same as for the sample measurement.

5.2.3 Incoherent Background

The macroscopic cross section usually has two contributions: the coherent and incoherent scattering. For small angle neutron scattering the incoherent scattering is mostly Q-independent and does not contain important information:

$$\left.\frac{d\Sigma}{d\Omega}(\mathbf{Q})\right|_{\text{total}} = \left.\frac{d\Sigma}{d\Omega}(\mathbf{Q})\right|_{\text{coh}} + \left.\frac{d\Sigma}{d\Omega}\right|_{\text{incoh}} \tag{5.6}$$

We therefore tend to subtract the incoherent scattering. It is well determined at large Q when the coherent scattering becomes small. The origin of the incoherent scattering is the spin-dependent scattering length. Especially for hydrogen ^{1}H the neutron spin and the nuclear spin

form a singlet or triplet state with different scattering lengths. The average scattering length of these two states contributes to the coherent scattering. The variance of the scattering length gives rise to the incoherent scattering. Here, each of the nuclei appears as an independent point scatterer which in reciprocal space means a Q-independent scattering signal. The dependence of the scattering on the neutron spin means that neutron spin polarization and analysis yields another method to determine the incoherent scattering independently from the coherent signal.

5.2.4 Resolution

The simple derivatives of equation 5.2 support a very simple view on the resolution of a small angle neutron scattering experiment. We obtain:

$$\left(\frac{\Delta Q}{Q}\right)^2 = \left(\frac{\Delta\lambda}{\lambda}\right)^2 + \left(\frac{2\Delta\theta}{2\theta}\right)^2 \tag{5.7}$$

The uncertainty about the Q-vector is a sum about the uncertainty of the wavelength and the angular distribution. Both uncertainties result from the beam preparation, namely from the monochromatization and the collimation. The neutron velocity selector selects a wavelength band of either $\pm 5\%$ or $\pm 10\%$. The collimation consists of an entrance aperture with a diameter d_C and a sample aperture of a diameter d_S. The distance between them is L_C.

One property of eq. 5.7 is the changing importance of the two contributions at small and large Q. At small Q the wavelength spread is nearly negligible and the small terms Q and θ dominate the resolution. This also means that the width of the primary beam is exactly the width of the resolution function. More exactly, the primary beam profile describes the resolution function at small Q. Usually, the experimentalist is able to change the resolution at small Q. At large Q the resolution function is dominated by the wavelength uncertainty. So the experimentalist wants to reduce it – if possible – for certain applications. This contribution is also an important issue for time-of-flight SANS instruments at spallation sources. The wavelength uncertainty is determined by the pulse length of the source and cannot be reduced without intensity loss.

A more practical view on the resolution function includes the geometrical contributions explicitely [5]. One obtains:

$$\left(\frac{\sigma_Q}{Q}\right)^2 = \frac{1}{8\ln 2}\left(\left(\frac{\Delta\lambda}{\lambda}\right)^2 + \left(\frac{1}{2\theta}\right)^2 \cdot \left[\left(\frac{d_C}{L_C}\right)^2 + d_S^2\left(\frac{1}{L_C}+\frac{1}{L_D}\right)^2 + \left(\frac{d_\mathrm{D}}{L_D}\right)^2\right]\right) \tag{5.8}$$

Now the wavelength spread is described by $\Delta\lambda$ being the full width at the half maximum. The geometrical terms have contributions from the aperture sizes d_C and d_S and the spatial detector resolution d_D. The collimation length L_C and detector distance L_D are usually identical such that all geometric resolution contributions are evenly large ($d_C = 2d_S$ then). This ideal setup maximizes the intensity with respect to a desired resolution.

The resolution function profile is another topic of the correction calculations. A simple approach assumes Gaussian profiles for all contributions, and finally the overall relations read:

$$\left.\frac{d\Sigma(\bar{Q})}{d\Omega}\right|_{\text{meas}} = \int_0^\infty dQ\; R(Q-\bar{Q}) \cdot \left.\frac{d\Sigma(Q)}{d\Omega}\right|_{\text{theo}} \tag{5.9}$$

$$R(Q-\bar{Q}) = \frac{1}{\sqrt{2\pi}\sigma_Q} \exp\left(-\frac{1}{2}\frac{(Q-\bar{Q})^2}{\sigma_Q^2}\right) \tag{5.10}$$

The theoretical macroscopic cross section is often described by a model function which is fitted to the experimental data. In this case the computer program only does a convolution of the model function with the resolution function $R(\Delta Q)$. Alternatively, there are methods to deconvolute the experimental data without modeling the scattering at first hand.

The here described resolution function is given as a Gaussian. This is true for relatively narrow distributions. The reason for using a Gaussian function although the original distributions of λ and θ are often triangular is: The central limit theorem can be applied to this problem because we have seen from eq. 5.8 that there are four contributions to the resolution function, and the radial averaging itself also smears the exact resolution function further out. Thus, the initial more detailed properties of the individual distributions do not matter anymore. Equations 5.9 and 5.10 are a good approximation for many practical cases.

We now want to describe the connection between the resolution function and the coherence of the neutron beam at the sample position. From optics we know about the transverse coherence length:

$$\ell_{\text{coh,transv}} = \frac{\lambda L_C}{2d_C} \qquad \text{is similar to} \qquad \Delta Q_\theta^{-1} = \frac{\lambda L_C}{\pi d_C} \tag{5.11}$$

It can be compared well with the geometric resolution contribution that arises from the entrance aperture only. Small differences in the prefactors we can safely neglect. For the longitudinal coherence length we obtain:

$$\ell_{\text{coh,long}} = \frac{1}{4}\lambda\left(\frac{\Delta\lambda}{\lambda}\right)^{-1} \qquad \text{is similar to} \qquad \Delta k^{-1} = \frac{1}{2\pi}\lambda\left(\frac{\Delta\lambda}{\lambda}\right)^{-1} \tag{5.12}$$

This coherence length can be well compared to the wavevector uncertainty of the incoming beam. If we look back on Figure 5.3 we see that the coherence volume exactly describes the uncertainty of the incoming wave vector. The two contributions are perpendicular which supports the vectorial (independent) addition of the contributions in eq. 5.8 for instance. The coherence volume describes the size of the independent wave packages which allow for wave-like properties such as the scattering process. So the coherence volume describes the maximum size of structure that is observable by SANS. If larger structures need to be detected the resolution must be increased.

5.2.5 Focusing Instruments

We have described the resolution function of the pin-hole SANS instrument very well. This design comes to its limits if very large structures (of $\sim \mu$m) need to be resolved. Usually focusing instruments take over because they provide higher intensities at higher resolutions.

Focusing instruments have the same motivation as photo cameras. When the pin-hole camera does not provide proper intensities any more, focusing elements – such as lenses – allow for opening the apertures. Then the resolution is good while the intensity increases to a multiple of its original value. For focusing SANS instruments this means that the sample sizes must be increased accordingly to the lens or mirror size.

There are two possible ways for focusing elements: Neutron lenses are often made of MgF_2. Large arrays of lenses take an overall length of nearly one meter. This is due to the low refractive index of the material for neutrons. A disadvantage of the lenses is the dispersion relation which leads to strong chromatic aberrations. So it is hardly possible to focus the full wavelength band of classical neutron velocity selectors on the detector. Other ways like magnetic neutron lenses have to deal with similar problems.

The focusing mirror does not show chromatic aberration. So this focusing element provides the highest possible resolution at highest intensities. The small angle scattering instrument KWS-3 is a unique instrument which uses this technique. The mirror technique was motivated by satellite mirrors. The roughness needs to stay below a few Ångström over large areas.

Practically the entrance aperture may be closed to a few millimeters while the sample aperture takes a few square centimeters accordingly to the mirror size. This setup images the entrance aperture on the detector. So, the primary beam profile has sharp edges in comparison to the triangular shapes of the pin-hole camera. This narrower distribution of intensity means that the beam stop might be slightly smaller than for a similar pin-hole instrument and so the focusing instrument improves the intensity-resolution problem by a rough factor of two.

5.3 The Theory of the Macroscopic Cross Section

We have seen that the SANS instrument aims at the macroscopic cross section which is a function of the scattering vector $\mathbf{Q}$. In many examples of isotropic samples and orientationally averaged samples (powder samples) the macroscopic cross section depends on the modulus $|\mathbf{Q}| \equiv Q$ only. This measured function has to be connected to important structural parameters of the sample. For this purpose model functions are developed. The shape of the model function in comparison with the measurement already allows to distinguish the validity of the model. After extracting a few parameters with this method, deeper theories – like thermodynamics – allow to get deeper insight about the behavior of the sample. Usually, other parameters – like concentration, temperature, electric and magnetic fields, ... – are varied experimentally to verify the underlying concepts at hand. The purpose of this section is to give some ideas about model functions.

When the Born approximation was developed several facts and assumptions came along. The scattering amplitudes of the outgoing waves are derived as perturbations of the incoming plane wave. The matrix elements of the interaction potential with these two wave fields as vectors

describe the desired amplitudes. The interaction potential can be simplified for neutrons and the nuclei of the sample by the Fermi pseudo potential. This expresses the smallness of the nuclei ($\sim$1fm) in comparison to the neutron wavelength ($\sim$Å). For the macroscopic cross section we immediately obtain a sum over all nuclei:

$$\frac{d\Sigma}{d\Omega}(\mathbf{Q}) = \frac{1}{V}\left|\sum_j b_j \exp(\mathrm{i}\mathbf{Q}\cdot\mathbf{r}_j)\right|^2 \tag{5.13}$$

This expression is normalized to the sample volume V because the second factor usually is proportional to the sample size. This simply means: The more sample we put in the beam the more intensity we obtain. The second factor is the square of the amplitude because we measure intensities. While for electromagnetic fields at low frequencies one can distinguish amplitudes and phases (without relying on the intensity) the neutrons are quantum mechanical particles where experimentally such details are hardly accessible. For light (and neutrons) for instance holographic methods still remain. The single amplitude is a sum over each nucleus j with its typical scattering length b_j and a phase described by the exponential. The square of the scattering length b_j^2 describes a probability of a scattering event taking place for an isolated nucleus. The phase arises between different elementary scattering events of the nuclei for the large distances of the detector. In principle, the scattering length can be negative (for hydrogen for instance) which indicates an attractive interaction with a phase π. Complex scattering lengths indicate absorption. The quadrature of the amplitude can be reorganized:

$$\frac{d\Sigma}{d\Omega}(\mathbf{Q}) = \frac{1}{V}\sum_{j,k} b_j b_k \exp\left(\mathrm{i}\mathbf{Q}(\mathbf{r}_j - \mathbf{r}_k)\right) \tag{5.14}$$

Here we find then self-terms with identical indices j and k without any phase and cross terms with phases arising from distances between different nuclei. Here it becomes obvious that only relative positions of the nuclei matter which is a result of the quadrature. The overall phase of the sample does not matter because of the modulus in eq. 5.13. We will use this expression for the polymer scattering.

Apart from this detailed expression a simplified view is allowed for small angle scattering experiments. Firstly, we know that the wavelength is typically 7Å which is much larger than the atom-atom distance of ca. 1.5Å. Secondly, the SANS experiment aims at structures at the nanoscale. So the scattering vector aims at much larger distances compared to the atomistic distances (i.e. $2\pi Q^{-1} \gg 1$Å). This allows for exchanging sums by integrals as follows:

$$\sum_j b_j \cdots \quad \longrightarrow \quad \int_V d^3r\ \rho(\mathbf{r}) \cdots \tag{5.15}$$

Such methods are already known for classical mechanics, but reappear all over physics. The meaning is explained by the sketch of Figure 5.4. The polymer polyethylene oxide (PEO) contains many different nuclei of different species (hydrogen, carbon and oxide). However, the SANS method does not distinguish the exact places of the nuclei. The polymer appears rather like a homogenous worm. Inside, the worm has a constant scattering length density which reads:

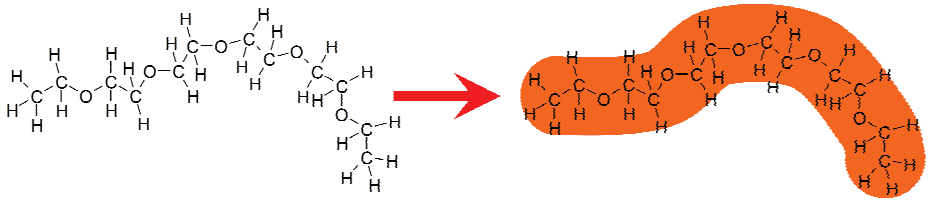

Fig. 5.4: *The concept of the scattering length density. On the left the atomic structure of a polyethylene oxide polymer (PEO) is depicted. For small angle scattering the wavelength is much larger than the atomic distance. So for SANS the polymer appears like a worm with a constant scattering length density inside.*

$$\rho_{\mathrm{mol}} = \frac{1}{V_{\mathrm{mol}}} \sum_{j \in \{\mathrm{mol}\}} b_j \tag{5.16}$$

So, for each molecule we consider all nuclei and normalize by the overall molecule volume. Of course different materials have different scattering length densities ρ. The initial equation 5.13 reads then:

$$\frac{d\Sigma}{d\Omega}(\mathbf{Q}) = \frac{1}{V}\left|\int_V d^3r\ \rho(\mathbf{r}) \exp(\mathrm{i}\mathbf{Q}\mathbf{r})\right|^2 \tag{5.17}$$

$$= \frac{1}{V}\Big|\mathcal{F}\left[\rho(\mathbf{r})\right]\Big|^2 \quad = \quad \frac{1}{V}\Big|\rho(\mathbf{Q})\Big|^2 \tag{5.18}$$

The single amplitude is now interpreted as a Fourier transformation of the scattering length density $\rho(\mathbf{r})$ which we simply indicate by $\rho(\mathbf{Q})$. The amplitude simply is defined by:

$$\rho(\mathbf{Q}) = \int_V d^3r\ \rho(\mathbf{r}) \exp(\mathrm{i}\mathbf{Q}\mathbf{r}) \tag{5.19}$$

Again, equation 5.17 loses the phase information due to the modulus. While we focused on the scattering experiment so far, another view on this function will provide us with further insight. We define the correlation Γ as follows:

$$\Gamma(\mathbf{Q}) = \frac{1}{V}\Big|\rho(\mathbf{Q})\Big|^2 \quad = \quad \frac{1}{V}\rho^*(\mathbf{Q})\rho(\mathbf{Q}) \quad = \quad \frac{1}{V}\rho(-\mathbf{Q})\rho(\mathbf{Q}) \tag{5.20}$$

The modulus is usually calculated via the complex conjugate $\rho^*(\mathbf{Q})$ which in turn can be obtained by changing the sign of the argument $\mathbf{Q}$. Now the correlation function is a simple product of two Fourier transformed functions. They can be interpreted on the basis of a convolution in real space:

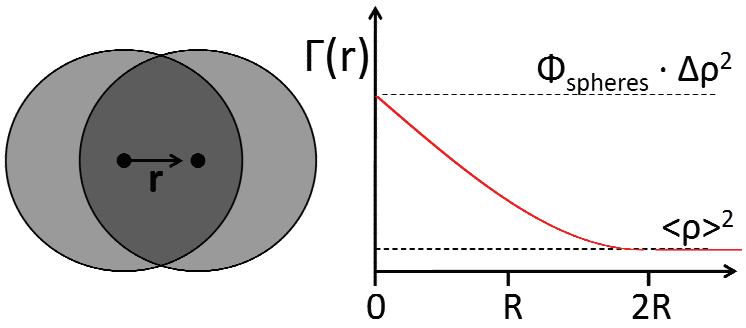

Fig. 5.5: *On the left the meaning of the convolution is depicted. Two identical shapes are displaced by a vector* $\mathbf{r}$*. The convolution volume is the common volume (dark grey). This consideration leads for three-dimensional spheres to the linear correlation function* $\Gamma(\mathbf{r})$ *shown on the right.*

$$\Gamma(\mathbf{r}) = \frac{1}{V}\rho(\mathbf{r}) \otimes \rho(\mathbf{r}) \quad = \quad \frac{1}{V}\int_V d^3r'\ \rho(\mathbf{r}+\mathbf{r}') \cdot \rho(\mathbf{r}') \tag{5.21}$$

The underlying correlation function $\Gamma(\mathbf{r})$ arises from the convolution of the real space scattering length density with itself. The mathematical proof is carried out in Appendix A. For imagining the convolution assume you have two foils with the same pattern printed on. The vector $\mathbf{r}$ describes the relative displacement of the two foils. Then you calculate the product of the two patterns and integrate over V. For patterns of limited size it becomes clear that the function turns to 'zero' at a finite distance $\mathbf{r}$. For simple compact patterns the function monotonically decays. The example of spheres is depicted in Fig. 5.5. In the left the meaning of the convolution is indicated. The darkest area in the center is the considered volume of the convolution for the vector $\mathbf{r}$. In three dimensions this consideration leads to the correlation function (see also Appendix A and references [3,4]):

$$\Gamma(\mathbf{r}) = \phi_{\text{spheres}} \cdot \Delta\rho^2 \cdot \left\{ \begin{array}{ll} 1 - \frac{3}{2}|\mathbf{r}|/(2R) + \frac{1}{2}|\mathbf{r}|^3/(2R)^3 & \text{for } |\mathbf{r}| \le 2R \\ 0 & \text{for } |\mathbf{r}| > 2R \end{array} \right\} + \langle\rho\rangle^2 \tag{5.22}$$

The concentration ϕ_{spheres} accounts for many independent, but diluted spheres. The value $\Delta\rho$ is the scattering length density difference between the sphere and the surrounding matrix (i.e. solvent). The constant $\langle\rho\rangle^2$ is the average scattering length density of the overall volume. Apart from these simple rationalizations we can formally calculate the limits for small and large distances $\mathbf{r}$:

$$\Gamma(\mathbf{r} \to 0) = \langle\rho^2\rangle \qquad \Gamma(\mathbf{r} \to \infty) = \langle\rho\rangle^2 \tag{5.23}$$

At this stage the reasons for the limits are based on mathematics. The brackets $\langle\cdots\rangle$ indicate an averaging of a locally defined function $\rho^2(\mathbf{r}),\ \rho(\mathbf{r})$ over the whole volume. For small

distances the averaging over squares of the scattering length density usually leads to higher values compared to the average being squared afterwards. So the correlation function often is a monotonically decaying function. A very simple realization is given by:

$$\Gamma(\mathbf{r}) = \left\langle \left(\rho - \langle\rho\rangle\right)^2 \right\rangle \exp\left(-|\mathbf{r}|/\xi\right) + \langle\rho\rangle^2 \tag{5.24}$$

The shape of the decay is usually described by an exponential decay and can be motivated further in detail [1]. The first addend is proportional to the fluctuations of the scattering length density. This finding already indicates that scattering experiments are sensitive to fluctuations. The correlation length ξ indicates over which distance the correlations are lost. The current picture does not allow for a complete decay (in comparison to the single sphere which finds $\Gamma(r) = 0$ for $r > 2R$). This means that the current discussion treats scattering length density fluctuations which fill the full 3-dimensional space. The Fourier transformation of eq. 5.24 leads to the following expression:

$$\Gamma(\mathbf{Q}) \propto \left(\rho - \langle\rho\rangle\right)^2 \frac{\xi^3}{1 + \xi^2\mathbf{Q}^2} \tag{5.25}$$

The scattering intensity in this case is proportional to the scattering length density fluctuations, to the coherence volume ξ^3 and the Q-dependent Lorentz peak. The latter has to be interpreted as a kind of expansion. So different details of the decaying correlation function (eq. 5.24) might lead to differently decaying scattering functions. The current Lorentz function is typical for Ornstein-Zernicke correlation functions. Further discussions of the correlation function are given in Appendix A.

For the fluctuations of the scattering length density we would like to consider a two phase system, i.e. the whole space is taken by either component 1 or 2. The concentration of phase 1 is ϕ_1, and the scattering length density is ρ_1 (correspondingly ρ_2 is defined). For the average scattering lenght density we clearly obtain $\langle\rho\rangle = \phi_1\rho_1 + (1-\phi_1)\rho_2$. For the scattering length density fluctuations we obtain similarly $\langle(\rho - \langle\rho\rangle)^2\rangle = \phi_1(1-\phi_1)(\rho_1 - \rho_2)^2$. The latter result describes the concentration fluctuations of the two phase system and the scattering length density contrast. For the following considerations the contrast will reappear in many examples.

5.3.1 Spherical Colloidal Particles

In this section we will derive the scattering of diluted spherical particles in a solvent. These particles are often called colloids, and can be of inorganic material while the solvent is either water or organic solvent. Later in the manuscript interactions will be taken into account.

One important property of Fourier transformations is that constant contributions will lead to sharp delta peaks at $Q = 0$. This contribution is not observable in the practical scattering experiment. The theoretically sharp delta peak might have a finite width which is connected to the overall sample size, but centimeter dimensions are much higher compared to the largest sizes observed by the scattering experiment ($\sim \mu$m). So formally we can elevate the scattering density level by any number $-\rho_{\mathrm{ref}}$:

$$\rho(\mathbf{r}) \longrightarrow \rho(\mathbf{r}) - \rho_{\mathrm{ref}} \qquad \text{leads to} \qquad \rho(\mathbf{Q}) \longrightarrow \rho(\mathbf{Q}) - 2\pi\rho_{\mathrm{ref}}\delta(\mathbf{Q}) \tag{5.26}$$

The resulting delta peaks can simply be neglected. For a spherical particle we then arrive at the simple scattering length density profile:

$$\rho_{\mathrm{single}}(\mathbf{r}) = \begin{cases} \Delta\rho & \text{for } |\mathbf{r}| \leq R \\ 0 & \text{for } |\mathbf{r}| > R \end{cases} \tag{5.27}$$

Inside the sphere the value is constant because we assume homogenous particles. The reference scattering length density is given by the solvent. This function will then be Fourier transformed accordingly:

$$\rho_{\mathrm{single}}(\mathbf{Q}) = \int_0^{2\pi} d\phi \int_0^{\pi} d\vartheta \, \sin\vartheta \int_0^{R} dr \, r^2 \, \Delta\rho \, \exp\left(\mathrm{i}|\mathbf{Q}| \cdot |\mathbf{r}| \cos(\vartheta)\right) \tag{5.28}$$

$$= 2\pi \, \Delta\rho \int_0^{R} dr \, r^2 \left[\frac{1}{\mathrm{i}Qr} \exp\left(\mathrm{i}QrX\right)\right]_{X=-1}^{X=+1} \tag{5.29}$$

$$= 4\pi \, \Delta\rho \int_0^{R} dr \, r^2 \, \frac{\sin(Qr)}{Qr} \tag{5.30}$$

$$= \Delta\rho \, \frac{4\pi}{3} R^3 \left(3\frac{\sin(QR) - QR\cos(QR)}{(QR)^3}\right) \tag{5.31}$$

In the first line 5.28 we introduce spherical coordinates with the vector $\mathbf{Q}$ determining the z-axis for the real space. The vector product $\mathbf{Qr}$ then leads to the cosine term. In line 5.29 the azimutal integral is simply 2π, and the variable $X = \cos\vartheta$ is introduced. Finally, in line 5.30 the kernel integral for spherically symmetric scattering length density distributions is obtained. For homogenous spheres we obtain the final result of eq. 5.31. Putting this result together for the macroscopic cross section (eq. 5.18) we obtain:

$$\frac{d\Sigma}{d\Omega}(\mathbf{Q}) = \frac{N}{V} \cdot \left|\rho_{\mathrm{single}}(\mathbf{Q})\right|^2 = (\Delta\rho)^2 \, \phi_{\mathrm{spheres}} \, V_{\mathrm{sphere}} \, F(\mathbf{Q}) \tag{5.32}$$

$$F(\mathbf{Q}) = \left(3\frac{\sin(QR) - QR\cos(QR)}{(QR)^3}\right)^2 \tag{5.33}$$

We considered N independent spheres in our volume V, and thus obtained the concentration of spheres ϕ_{spheres}. Furthermore, we defined the form factor $F(Q)$, which describes the Q-dependent term for independent spheres (or the considered shapes in general). The function is shown in Figure 5.6. The first zero of the form factor is found at $Q = 4.493/R$. This relation

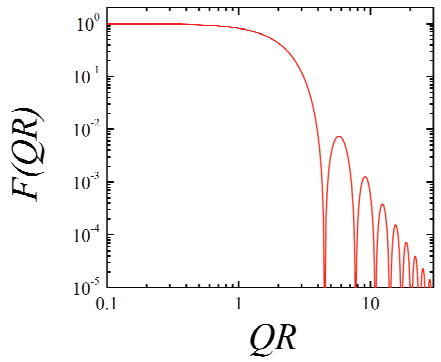

Fig. 5.6: *The form factor of a homogenous sphere in a double logarithmic plot.*

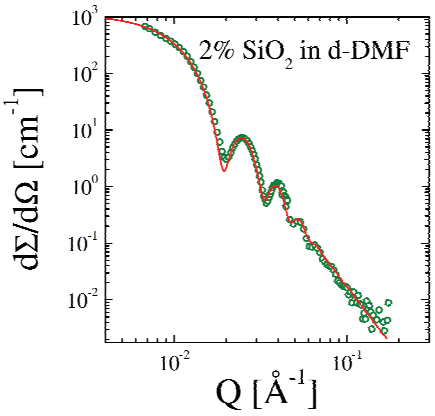

Fig. 5.7: *Experimental scattering curve of spherical SiO_2 colloids in the deuterated solvent DMF. The resolution function (eq. 5.9) is included in the fit (red line).*

again makes clear why the reciprocal space (Q-space) is called reciprocal. We know the limit for small scattering angles is $F(\mathbf{Q}\to 0) = 1 - \frac{1}{5}Q^2R^2$. So the form factor is normalized to 1, and the initial dependence on Q^2 indicates the size of the sphere. For large scattering angles the form factor is oscillating. Usually the instrument cannot resolve the quickest oscillations and an average intensity is observed. The asymptotic behavior would read $F(\mathbf{Q}\to\infty) = \frac{9}{2}(QR)^{-4}$. The obtained power law Q^{-4} is called Porod law and holds for any kind of bodies with sharp interfaces. So sharp interfaces are interpreted as fractals with $d = 2$ dimensions, and the corresponding exponent is $6 - d$.

When comparing the theoretical description of the spherical form factor with measurements one finds a good agreement (Fig. 5.7). Many fringes are seen, but after the third or fourth peak the function does not indicate any oscillation any more. Furthermore, the sharp minima are washed out. All of this is a consequence of the resolution function (eq. 5.9) which has been taken into account for the fitted curve. For many other examples one also needs to take the polydispersity into account. The synthesis of colloids usually produces a whole distribution of different radii. In our example the polydispersity is very low which is the desired case. Polydispersity acts in a similar way compared to the resolution function. The sharp minima are washed out. While the resolution appears as a distribution of different Q-values measured at a certain point the polydispersity integrates over several radii.

Another general scattering law for isolated (dilute) colloids is found for small scattering angles. The general appearance of the Guinier scattering law is:

$$\frac{d\Sigma}{d\Omega}(\mathbf{Q}\to 0) = \frac{d\Sigma}{d\Omega}(0)\cdot\exp\left(-\frac{1}{3}Q^2R_g^2\right) \tag{5.34}$$

When comparing the scattering law of a sphere and the Guinier formula we obtain $R_g = \sqrt{\frac{3}{5}}R$. The radius of gyration R_g can be interpreted as a momentum of inertia normalized to the total

mass and specifies the typical size of the colloid of any shape. The Guinier formula can be seen as an expansion at small scattering angles of the logarithm of the macroscopic cross section truncated after the Q^2 term. Further details are discussed in Appendix B.

Another general appearance for independent colloids shall be discussed now using equation 5.32. The macroscopic cross section is determined by several important factors: The contrast between the colloid and the solvent given by $\Delta\rho^2$, the concentration of the colloids, the volume of a single colloid, and the form factor. Especially for small Q the latter factor turns to 1, and the first three factors dominate. When knowing two factors from chemical considerations, the third factor can be determined experimentally using small angle neutron scattering. Below, we will discuss a fifth factor – the structure factor – arising due to interactions between the colloids.

When comparing this expression for isolated colloids with the Ornstein-Zernicke result we see in parallel: The contrast stays for both kinds of interpretations. The particle volume corresponds to the correlation volume (i.e. $V \sim \xi^3$). The concentration of the correlation volumes comes close to 1 (i.e. $\phi \sim 1$). Finally, F is a measure for the correlations inside the correlation volume. So, for independent colloids the correlation volume must fully cover the single particle but two neighbored particles are found in distinct correlation volumes. Finally, the overall experimental correlation length is limited by the sample and the radiation coherence. So for the transversal correlation length one would obtain $\xi^{-2}_{\mathrm{eff,transv}} = \xi^{-2} + \ell^{-2}_{\mathrm{coh,transv}}$.

5.3.2 Contrast Variation

For neutron scattering the method contrast variation opens a wide field of possible experiments. For soft matter research the most important labelling approach is the exchange of hydrogen ^{1}H by deuterium ^{2}H. Since in a single experiment the phase information is lost completely the contrast variation experiment retrieves this information partially. Relative positions of two components are obtained by this method.

The scattering length density of the overall sample is now understood to originate from each component individually. So the specific $\rho_j(\mathbf{r})$ takes the value of the scattering length density of component j when the location points to component j and is zero otherwise. We would then obtain the following:

$$\rho(\mathbf{Q}) = \int_V d^3r \left(\sum_{j=1}^{n} \rho_j(\mathbf{r})\right) \exp(\mathrm{i}\mathbf{Q}\mathbf{r}) \tag{5.35}$$

n specifies the number of components. The assumption of incompressibility means that on every place there is one component present, and so all individual functions $\rho_j(\mathbf{r})$ fill the full space. Furthermore, we would like to define component 1 being the reference component, i.e. $\rho_{\mathrm{ref}} = \rho_1$ (see eq. 5.26). This means that on each place we have a $\Delta\rho_j(\mathbf{r})$ function similar to eq. 5.22. Then, we arrive at:

$$\rho(\mathbf{Q}) = \sum_{j=2}^{n} \Delta\rho_{j1}(\mathbf{Q}) \tag{5.36}$$

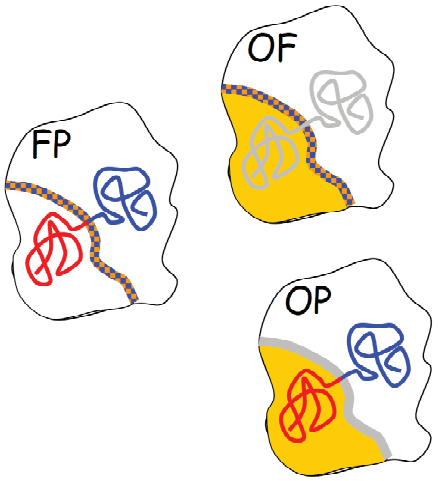

Fig. 5.8: *Scheme of scattering functions for the cross terms within the microemulsion. There are the film-polymer scattering S_{FP}, the oil-film scattering S_{OF}, and the oil-polymer scattering S_{OP}. The real space correlation function means a convolution of two structures.*

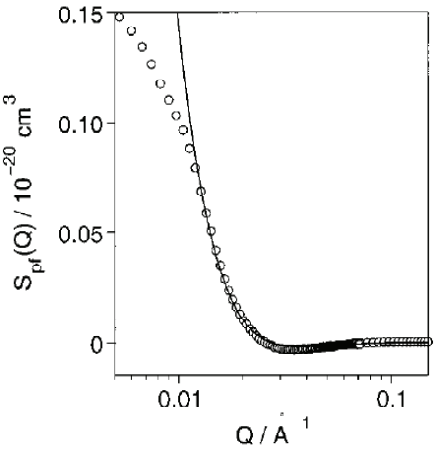

Fig. 5.9: *A measurement of the film-polymer scattering for a bicontinuous microemulsion with a symmetric amphiphilic polymer. The solid line is described by a polymer anchored in the film. The two blocks are mushroom-like in the domains. At low Q the overall domain structure (or size) limits the idealized model picture.*

The macroscopic cross section is a quadrature of the scattering length density $\rho(\mathbf{Q})$, and so we arrive at:

$$\frac{d\Sigma}{d\Omega}(\mathbf{Q}) = \frac{1}{V}\cdot\sum_{j,k=2}^{n}\Delta\rho^{*}_{j1}(\mathbf{Q})\cdot\Delta\rho_{k1}(\mathbf{Q}) \tag{5.37}$$

$$= \sum_{j,k=2}^{n}(\Delta\rho_{j1}\Delta\rho_{k1})\cdot S_{jk}(\mathbf{Q}) \tag{5.38}$$

$$= \sum_{j=2}^{n}(\Delta\rho_{j1})^2\cdot S_{jj}(\mathbf{Q}) \;+\; 2\sum_{2<j<k\leq n}(\Delta\rho_{j1}\Delta\rho_{k1})\cdot\Re\, S_{jk}(\mathbf{Q}) \tag{5.39}$$

In line 5.38 the scattering function $S_{jk}(\mathbf{Q})$ is defined. By this the contrasts are separated from the Q-dependent scattering functions. Finally, in line 5.39 the diagonal and off-diagonal terms are collected. There are $n-1$ diagonal terms, and $\frac{1}{2}(n-1)(n-2)$ off-diagonal terms. Formally, these $\frac{1}{2}n(n-1)$ considerably different terms are rearranged (the combinations $\{j,k\}$ are now simply numbered by j), and a number of s different measurements with different contrasts are considered.

$$\left.\frac{d\Sigma}{d\Omega}(\mathbf{Q})\right|_s = \sum_j (\Delta\rho \cdot \Delta\rho)_{sj} \cdot S_j(\mathbf{Q}) \tag{5.40}$$

In order to reduce the noise of the result, the number of measurements s exceeds the number of independent scattering functions considerably. The system then becomes over-determined when solving for the scattering functions. Formally one can nonetheless write:

$$S_j(\mathbf{Q}) = \sum_s (\Delta\rho \cdot \Delta\rho)^{-1}_{sj} \cdot \left.\frac{d\Sigma}{d\Omega}(\mathbf{Q})\right|_s \tag{5.41}$$

The formal inverse matrix $(\Delta\rho \cdot \Delta\rho)^{-1}_{sj}$ is obtained by the singular value decomposition method. It describes the closest solution of the experiments in context of the finally determined scattering functions.

An example case is discussed for a bicontinuous microemulsion with an amphiphilic polymer [6]. The microemulsion consists of oil and water domains which have a sponge structure. So the water domains host the oil and vice versa. The surfactant film covers the surface between the oil and water domains. The symmetric amphiphilic polymer position and function was not clear beforehand. From phase diagram measurements it was observed that the polymer increases the efficiency of the surfactant dramatically. Much less surfactant is needed to solubilize equal amounts of oil and water. Fig. 5.8 discusses the meaning of the cross terms of the scattering functions. Especially the film-polymer scattering is highly interesting to reveal the polymer role inside the microemulsion (see Fig. 5.9). By the modeling it was clearly observed that the amphiphilic polymer is anchored in the membrane and the two blocks describe a mushroom inside the oil and water domains. So basically, the polymer is a macro-surfactant. The effect of the polymer on thermodynamics and the microscopic picture is discussed in chapter 5.3.5.

5.3.3 Scattering of a Polymer

In this section we derive the scattering of a single (isolated) polymer coil. This model is the basis for many more complicated models of polymers in solution, polymeric micelles, polymer melts, diblock and multiblock copolymers and so on. So the understanding of these concepts is rather important for scattering experiments on any kind of polymer systems.

This example starts apart from many other calculations from point-like monomers (see eq. 5.14). These monomers are found along a random walk with an average step width of ℓ_K. We try to argue for non-ideal chain segments, but finally will arrive at an expression for rather ideal polymers. For the scattering function we obtain:

$$S(\mathbf{Q}) \propto \frac{1}{N}\sum_{j,k=0}^{N}\left\langle \exp\left(\mathrm{i}\mathbf{Q}\cdot(\mathbf{R}_j-\mathbf{R}_k)\right)\right\rangle \tag{5.42}$$

$$\propto \frac{1}{N}\sum_{j,k=0}^{N}\exp\left\langle -\tfrac{1}{2}\left(\mathbf{Q}\cdot(\mathbf{R}_j-\mathbf{R}_k)\right)^2\right\rangle \tag{5.43}$$

$$\propto \frac{1}{N}\sum_{j,k=0}^{N}\exp\left\langle -\tfrac{1}{6}\mathbf{Q}^2\cdot(\mathbf{R}_j-\mathbf{R}_k)^2\right\rangle \tag{5.44}$$

At this stage we use statistical arguments (i.e. statistical physics). The first rearrangement of terms (line 5.43) moves the ensemble average of the monomer positions (and distances $\Delta\mathbf{R}_{jk}$) from the outside of the exponential to the inside. This is an elementary step which is true for polymers. The underlying idea is, that the distance $\Delta\mathbf{R}_{jk}$ arises from a sum of $|j-k|$ bond vectors which all have the same statistics. So each sub-chain with the indices jk is only distinguished by its number of bond vectors inside. The single bond vector $\mathbf{b}_j$ has a statistical average of $\langle\mathbf{b}_j\rangle = 0$ because there is no preferred orientation. The next higher moment is the second moment $\langle\mathbf{b}_j^2\rangle = \ell_K^2$. This describes that each bond vector does a finite step with an average length of ℓ_K. For the sub-chain we then find an average size $\langle\Delta\mathbf{R}_{jk}^2\rangle = |j-k|\ell_K^2$. The reason is that in the quadrature of the sub-chain only the diagonal terms contribute because two distinct bond vectors show no (or weak) correlations.

Back to the ensemble average: The original exponential can be seen as a Taylor expansion with all powers of the argument $\mathrm{i}\mathbf{Q}\Delta\mathbf{R}_{jk}$. The odd powers do not contribute with similar arguments than for the single bond vector $\langle\mathbf{b}_j\rangle = 0$. Thus, the quadratic term is the leading term. The reason why the higher order terms can be arranged that they finally fit to the exponential expression given in line 5.43 is the weak correlations of two distinct bond vectors. The next line 5.44 basically expresses the orientational average of the sub-chain vector $\Delta\mathbf{R}_{jk}$ with respect to the Q-vector in three dimensions.

This derivation can be even simpler understood on the basis of a Gaussian chain. Then every bond vector follows a Gaussian distribution (with a center of zero bond length). Then the ensemble average has the concrete meaning $\langle\cdots\rangle = \int\cdots\exp\left(-\frac{3}{2}\Delta\mathbf{R}_{jk}^2/(|j-k|\ell_K^2)\right)d^3\Delta R_{jk}$. This distribution immediately explains the rearrangement of line 5.43. The principal argument is the central limit theorem: When embracing several segments as an effective segment any kind of distribution converges to yield a Gaussian distribution. This idea came from Kuhn who formed the term Kuhn segment. While elementary bonds still may have correlations at the stage of the Kuhn segment all correlations are lost, and the chain really behaves ideal. This is the reason why the Kuhn segment length ℓ_K was already used in the above equations.

In the following we now use the average length of sub-chains (be it Kuhn segments or not), and replace the sums by integrals which is a good approximation for long chains with a large number of segments N.

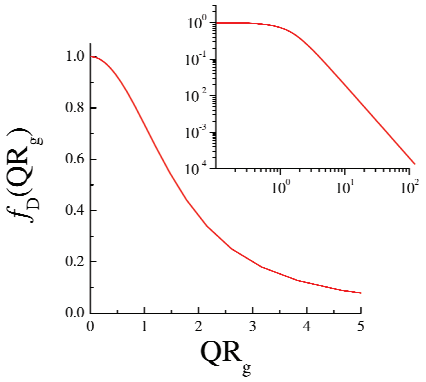

Fig. 5.10: *The theoretical Debye function describes the polymer scattering of independent polymers without interaction. The two plots show the function on a linear and double logarithmic scale.*

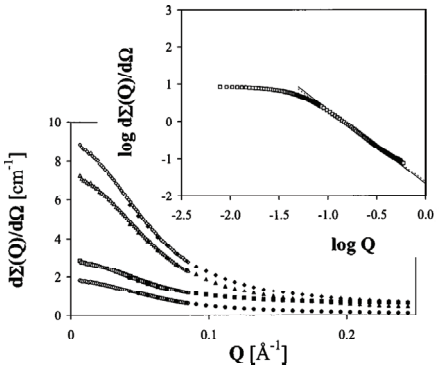

Fig. 5.11: *Scattering of a h/d-PDMS polymer blend. The linear scale shows different compositions of hydrogenous polymer (from bottom to top: 0.05, 0.94, 0.27, 0.65) while the double logarithmic plot shows the 0.65 sample only [7].*

$$S(\mathbf{Q}) \propto \frac{1}{N}\int_0^N dj \int_0^N dk \exp\left(-\tfrac{1}{6}\mathbf{Q}^2 \cdot |j-k| \cdot \ell_K^2\right) \tag{5.45}$$

$$= N \cdot f_D(Q^2 R_g^2) \tag{5.46}$$

$$f_D(x) = \tfrac{2}{x^2}\left(\exp(-x) - 1 + x\right) \tag{5.47}$$

In this integral one has to consider the symmetry of the modulus. The result is basically the Debye function which describes the polymer scattering well from length scales of the overall coil down to length scales where the polymer becomes locally rigid (see Fig. 5.10). The covalent bonds of a carbon chain effectively contribute to a certain rigidity which will not be treated here. The radius of gyration describes the overall dimension of the chain and is $R_g = \sqrt{N/6}\,\ell_K$. The limits of the polymer scattering are found to be:

$$S(\mathbf{Q}) \propto N(1 - \tfrac{1}{3}Q^2 R_g^2) \qquad \text{for small } Q \tag{5.48}$$

$$\propto N \cdot 2/(Q^2 R_g^2) \qquad \text{for large } Q \tag{5.49}$$

The line 5.48 describes the conventional Guinier scattering of the overall polymer (compare eq. 5.34). The second line 5.49 describes a power law. At these length scales the sub-chains of different lengths are self-similar and so they reveal a fractal behavior. The prefactor is connected to the magnitude R_g^2/N which is the effective segment size. From this magnitude one can calculate back to the local rigidity which is responsible for the effective segments.

When we want to compare experiments with this theory the best examples are obtained from polymer blends (Fig. 5.11). One could come to the conclusion that diluted polymer solutions must provide the ideal conditions for such an experiment but practically the interactions of the solvent molecules with the monomers lead to a deviating behavior: The good solvent conditions lead to energetic violations of monomer-monomer contacts and so the polymer swells and displays a different fractal behavior. The high Q power law in good solvents comes close to $Q^{-1.7}$. The Flory theory was the first attempt to describe this behavior while many refinements find small corrections. The theoretically most precise Flory exponent is $\nu = 0.588$ which is the reciprocal value of the given exponent 1.7 above.

So polymer blends are often better examples for weakly interacting chains. This finding is supported by the low entropy of mixing which enforces small interactions. The discussed example of Fig. 5.11 [7] considers the isotopic mixture of hydrogenous and deuterated polydimethylsiloxane (PDMS). This practically leads to one of the lowest possible interactions even though they are not completely zero. The theoretical concept of the random phase approximation is able to deal with interactions and describes phase diagrams and the scattering in this way. At high temperatures the polymers usually mix well, and the scattering comes closer to the weakly interacting case. Closer to the demixing temperature at lower temperatures the scattering intensity increases dramatically. This indicates strong composition fluctuations. The system loses the tendency to form a homogenous mixture and so local enrichments of species A or B are possible. While the random phase approximation is a mean field concept which describes weak fluctuations there are other concepts for strong fluctuations close to the phase boundary: The 3-dimesional Ising model – known for ferromagnets – describes the strong fluctuations of the two component polymer system.

5.3.4 The Structure Factor

In this section we develop the ideas about the structure factor – an additional factor for the scattering formula (eq. 5.32) – which describes the effect of interactions between the colloids or particles. We start from a rather simple interaction for colloids. It simply takes into account that the particles cannot intersect. This interaction is called excluded volume interaction. Then the general case will be discussed briefly and conceptually.

We start from the scattering length density for two spheres with different origins $\mathbf{R}_1$ and $\mathbf{R}_2$. In this case the formula reads:

$$\Delta\rho(\mathbf{Q}) = \Delta\rho \cdot V_{\text{sphere}} \cdot \left(\exp(\mathrm{i}\mathbf{Q}\mathbf{R}_1) + \exp(\mathrm{i}\mathbf{Q}\mathbf{R}_2)\right) \cdot K(Q,R) \tag{5.50}$$

$$K(Q,R) = 3 \cdot \frac{\sin(QR) - QR\cos(QR)}{(QR)^3} \tag{5.51}$$

The main difference arises from the phases of the two origins of the two colloids. Otherwise the result is known from eq. 5.31. For the macroscopic cross section we rearrange the amplitudes in the following way:

$$\frac{d\Sigma}{d\Omega}(\mathbf{Q}) = (\Delta\rho)^2 \cdot \frac{2V_{\text{sphere}}}{V_{\text{tot}}} \cdot V_{\text{sphere}} \cdot \left|\exp(\mathrm{i}\mathbf{Q}\mathbf{R}_1)\right|^2 \cdot \left\langle \frac{1}{2}\left|1+\exp(\mathrm{i}\mathbf{Q}\Delta\mathbf{R})\right|^2 \right\rangle_{\Delta\mathbf{R}} \cdot K^2(Q,R) \tag{5.52}$$

There are factors for the contrast, the concentration, the single particle volume, one phase factor which results in 1, one factor for the relative phases, and the form factor. In comparison to eq. 5.32 all factors are known except for the factor about the relative phases. The brackets describe an ensemble average known from statistical physics. We have to consider all possible relative positions $\Delta\mathbf{R}$. This is done in the following:

$$\begin{aligned} S(Q) &= \left\langle \frac{1}{2}\left|1+\exp(\mathrm{i}\mathbf{Q}\Delta\mathbf{R})\right|^2 \right\rangle_{\Delta\mathbf{R}} = \left\langle 1+\cos(\mathbf{Q}\Delta\mathbf{R}) \right\rangle_{\Delta\mathbf{R}} && (5.53)\\ &= \frac{1}{V_{\text{tot}}}\left(V_{\text{tot}} + 2\pi\delta(\mathbf{Q}) - \frac{4\pi}{3}(2R)^3 K(Q,2R)\right) && (5.54) \end{aligned}$$

The main result is found in line 5.54 which is obtained from the ensemble average. The prefactor arises from the normalization. The constant term arises from integrating over the whole volume. To be more precise the vector $\mathbf{R}$ has to omit a volume of a sphere with the radius $2R$, because this is the minimum distance of the two centers. For the integral of the constant contribution we neglect this small difference. For the integral over the cosine function we have to do a trick which is called the Babinet principle: The really allowed volume is the sum of the full volume minus the sphere with the radius $2R$. The cosine function integrated over the full volume is again a delta function, and the subtracted term is the Fourier transformation of a sphere, i.e. $K(Q,2R)$. We obtain the same result for the cosine-Fourier transformation and the complex Fourier transformation because the volume is centro-symmetric. The Babinet principle actually uses the inversion of the volume and states for squares of amplitudes, i.e. intensities, exactly the same result as for the original structure. For the structure factor we have to keep in mind: It arises from a single Fourier transformation and is not squared. The final result in brief is (neglecting the delta function again):

$$\begin{aligned} S(\mathbf{Q}) &= 1 - \phi_{2R} \cdot K(Q,2R) && (5.55)\\ \frac{d\Sigma}{d\Omega}(\mathbf{Q}) &= (\Delta\rho)^2 \cdot \phi_{\text{sphere}} \cdot V_{\text{sphere}} \cdot S(\mathbf{Q}) \cdot K^2(Q,R) && (5.56) \end{aligned}$$

So we obtain the well known factors for the macroscopic cross section – now with a structure factor. The form and structure factor are compared in Fig. 5.12. The reduced intensity at small scattering vectors due to the structure factor appears for repulsive interactions and means that the possible fluctuations of the particles are reduced because they have less freedom. The first maximum indicates a preferred distance between the colloids. Such a maximum becomes more pronounced with higher concentrations. Note that for this example the maximum appears at a Q where the form factor already has a downturn. There are many examples in the literature where the form factor is still relatively close to 1 and then the structure factor is exposed very clearly.

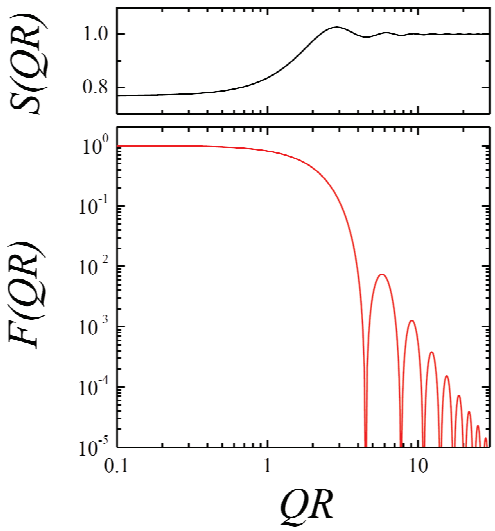

Fig. 5.12: *The structure factor $S(Q)$ on top of the form factor $F(Q) = K^2(Q)$. Note that the structure factor is smaller than 1 for small Q. This indicates a repulsive interaction. The first maximum of the structure factor expresses a certain tendency for preferred distances. Of course it only appears for rather strong concentrations.*

So far we have derived the excluded volume structure factor for very dilute systems. The method of Ornstein-Zernicke allows for a simple refinement by describing higher order correlations on the basis of the simple pair correlation. Then – in the simplest way – one would obtain the following expression:

$$S_2(\mathbf{Q}) = \left(1 + \phi_{2R} \cdot K(Q, 2R)\right)^{-1} \tag{5.57}$$

It describes the probability for finding two particles at a distance $\mathbf{r}_2 - \mathbf{r}_1$. A more rigorous treatment of the Ornstein-Zernicke formalism results in the Perkus-Yevick structure factor [8] which is the best known approximation for hard spheres. On the basis of this structure factor as the dominating term small corrections for additional interactions can be included [9]. For colloidal systems this is the strategy of choice.

Nonetheless, we would like to understand the structure factor more generally. From equation 5.53 we have seen that the phases of two centers have to be considered. The ensemble average finally took the distribution of possible distance vectors $\Delta\mathbf{R}$ into account. So we can understand the structure factor on the basis of a pair correlation function for the centers of the particles.

$$S(\mathbf{Q}) = 1 + \phi \int_V d^3r \, \left(g(\mathbf{r}) - 1\right) \exp(\mathrm{i}\mathbf{Q}\mathbf{r}) \tag{5.58}$$

The function $g(\mathbf{r})$ is the pair correlation function and describes the probabilities for certain distance vectors $\mathbf{r}$, and the exponential function accounts for the phases. Again, for centrosymmetric $g(\mathbf{r})$ there is no difference between a cosine and a complex Fourier transformation.

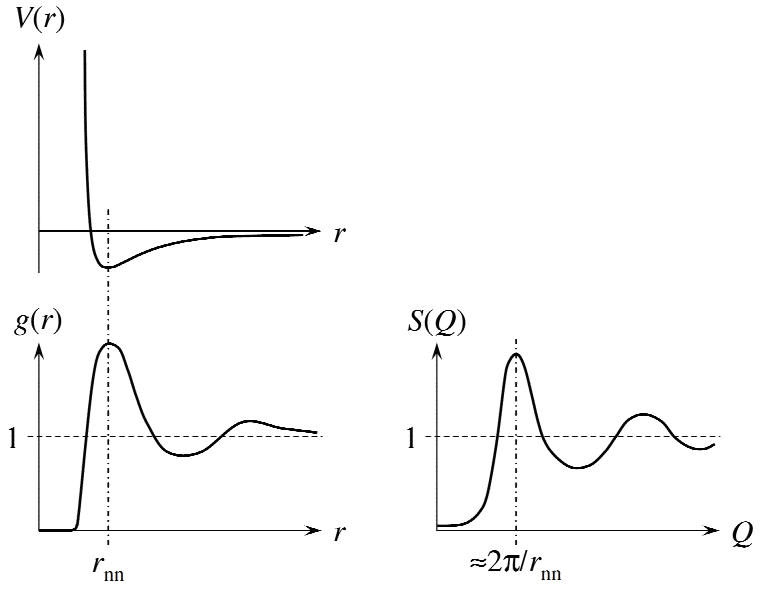

Fig. 5.13: *The relation between the interaction potential $V(r)$, the pair correlation function $g(r)$ in real space, and the structure factor $S(Q)$.*

The subtraction of the constant 1 accounts for delta peak contributions which we also obtained in line 5.54. The added term 1 we also obtained in the beginning (line 5.53). It arises from the self correlation of the particle with itself. For the pair distribution function we now can write:

$$g(\mathbf{r}_2 - \mathbf{r}_1) = \frac{P(\mathbf{r}_1, \mathbf{r}_2)}{P(\mathbf{r}_1) \cdot P(\mathbf{r}_2)}, \qquad \text{and } \phi = P(\mathbf{r}_1) \tag{5.59}$$

and can be obtained theoretically with methods from statistical physics. A rather elementary example is discussed in Fig. 5.13 starting from an interaction potential $V(\mathbf{r})$. It has a repulsive short range interaction, a weak minimum at a distance $r_{\rm nn}$, and a quickly decaying tail to long distances. The distance $r_{\rm nn}$ indicates the preferred distance of nearest neighbors. The pair correlation function then shows an inhibited range at short distances – similar to an excluded volume interaction. The following peak at $r_{\rm nn}$ indicates a preferred nearest neighbor distance. The following oscillations for larger distances indicate more remote preferred places. The limit of $g(\mathbf{r})$ at large distances is 1 indicating the average concentration of particles. For the structure factor we obtain a rather strong suppression at small Q. This means that the repulsive interactions lead effectively to a more homogenous distribution of particles. The peak of the structure factor at $Q = 2\pi/r_{\rm nn}$ indicates the preferred distance of the nearest neighbors. Strong oscillations at higher Q indicate a narrow distribution of the actual neighbor distances. The limit at high Q is again 1, and arises from the self correlation of identical particles. This example describes a liquid-like behavior which has historically been developed for liquids. In soft matter research this concept applies for many systems ranging from colloids, over micelles to star-polymers. While the liquid-like structure describes a near order, a perfect crystal would lead to a different behavior: The correlation function $g(\mathbf{r})$ would contain a lattice of separated delta peaks. The

structure factor would describe the reciprocal lattice with the well known Bragg peaks. In soft matter research there exist many examples with liquid crystalline order. Very often they display a finite size of crystalline domains – so there is a grain structure – and the real state takes an intermediate stage between the perfect crystalline and liquid-like order.

5.3.5 Microemulsions

In this section we will follow a very successful way of deriving the scattering formula for bicontinuous microemulsions (see Fig. 5.14). Bicontinuous microemulsions consist of equal amounts of oil and water. A certain amount of surfactant is needed to solubilize all components, and a one phase system is obtained. The domain structure of the oil is a continuous sponge structure which hosts the water and vice versa. The surfactant forms a film at the surface between the oil and water domains.

The starting point is a thermodynamic model for such kind of system. The Landau approach takes mesoscopic sub-volumes and assumes that the internal degrees of freedom are integrated out, and there is a small number of order parameters describing the state of the sub-volume very accurately. For microemulsions we stay with a single (scalar) order parameter $\phi(\mathbf{r})$ which takes the values -1 for oil, 0 for surfactant, and $+1$ for water. Now the order parameter can still be treated like a continuous function since the physical effects take place on larger length scales than the sub-volume size. The (free) energy of the overall volume is now expressed as a function of the order parameter. One still cannot be perfectly accurat, so an expansion with respect to the order parameter is used. The expansion for microemulsions looks like:

$$F_0\big(\phi(\mathbf{r})\big) = \int d^3r \big[c(\nabla^2\phi)^2 + g_0(\nabla\phi)^2 + \omega_2\phi^2\big] \tag{5.60}$$

This expansion does not only contain the order parameter itself, but there are derivatives included. These appear since this expression of the free energy is a functional expansion. Certain orders (especially the odd orders) of the order parameter and its derivatives have been ruled out due to the symmetry of the system. One important symmetry is the restriction to equal amounts of oil and water. Another facilitating property is that the functional form only considers local contributions in the functional form. For this free energy expression one can apply statistical physics methods and derive a scattering function (done in Appendix C). In comparison with the real space correlation function one can identify two important parameters: the correlation length ξ and the wavevector of the domain spacing $k = 2\pi/d$. The obtained scattering function looks like:

$$\left.\frac{d\Sigma}{d\Omega}(\mathbf{Q})\right|_{\mathrm{TS}} = (\Delta\rho_{\mathrm{oil\text{–}water}})^2 \frac{8\pi\phi_{\mathrm{oil}}\phi_{\mathrm{water}}/\xi}{(k^2+\xi^{-2})^2 - 2(k^2-\xi^{-2})\mathbf{Q}^2 + \mathbf{Q}^4} \tag{5.61}$$

This function is also known as the Teubner-Strey formula [10]. While the applied concept approaches the reality as a long wavelength description, there are details missing. The described domains have rather plain walls while in reality the domain walls also fluctuate quite heavily. An empirical approach for the scattering function for the full Q-range is the following:

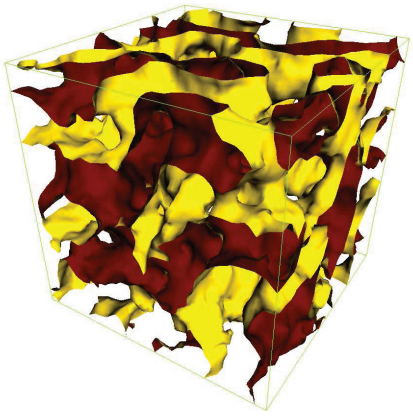

Fig. 5.14: *A real space picture of the bicontinuous microemulsion according to computer simulations [11]. Actually the surfactant film is shown with the surface color being red for oil facing surface and yellow for water facing surface.*

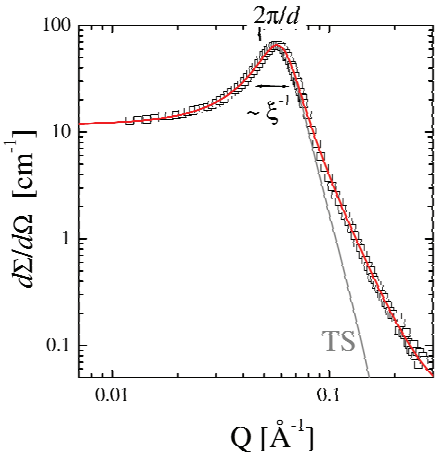

Fig. 5.15: *The macroscopic cross section of a bicontinuous microemulsion. The peak indicates an alternating domain structure with the spacing d. The peak width is connected to the correlation length ξ. The grey line is the simple Teubner-Strey fitting while the red line corresponds to eq. 5.62.*

$$\frac{d\Sigma}{d\Omega}(\mathbf{Q}) = \left[\frac{d\Sigma}{d\Omega}(\mathbf{Q})\Big|_{\mathrm{TS}} + \frac{G\ \mathrm{erf}^{12}(1.06 \cdot QR_g/\sqrt{6})}{1.5 \cdot Q^4 R_g^4}\right] \cdot \exp\left(-\sigma^2 Q^2\right) \tag{5.62}$$

The error function $\mathrm{erf}(x)$ in the overall context describes a peak with a Porod behavior at large Q. This additional Porod term accounts for the larger surface of the fluctuating membranes. The final Gaussian factor describes a roughness of the surfactant film and often is not that clearly observed due to the high incoherent background. An example fit of this function to scattering data is discussed in Fig. 5.15. The pure Teubner-Strey function clearly shows a downturn at higher Q and the real Porod scattering is not well described. Only the additional Porod scattering allows for a realistic estimation of the averge surface of the domain structure.

From the structural parameters $k = 2\pi/d$ and ξ one can make connections to the microscopic parameters of the microemulsion. The Gaussian random field theory describes the thermodynamics of a microemulsion by using a wave field that places the surfactant film at the zero surfaces of the field. The theory makes a connection of the structural parameters to the bending rigidity:

$$\frac{\kappa}{k_B T} = \frac{5\sqrt{3}}{64} \cdot k\xi \tag{5.63}$$

The bending rigidity κ is an elastic modulus of the surfactant membrane. The overall underlying concept only relies on the elastic properties of the membrane to describe the thermodynamics

of bicontinuous microemulsions. For symmetric amphiphilic polymers it was found that the bending rigidity increases [6]. The reason is that the mushroom conformation (obtained by the contrast variation measurements from chapter 5.3.2) exerts a pressure on the membrane. This makes the membrane stiffer which in turn allows to form larger domains with a better surface to volume ratio. So the much lower demand for surfactant is explained on the basis of small angle neutron scattering experiments.

5.4 Summary

We have seen that small angle neutron scattering is a powerful tool to characterize nanostructures. Examples included colloidal dispersions and microemulsions. The structural parameters are connected to thermodynamics and therefore the behavior is understood microscopically.

In many cases, small angle x-ray scattering can obtain the same results. Nonetheless, x-ray samples need to be thinner due to the low transmission, amd radiation damage has to be taken into account. The powerful method of contrast variation is restricted to heavier atoms, and is, therefore, barely used in soft matter research.

Transmission electron microscopy (TEM) measures the structures in real space, and is as such much easier to understand. Nowadays microscopes provide a spatial resolution of nanometers and better. Nonetheless, usually surfaces or thin layers are characterized and the volume properties need to be extrapolated. For statistics about polydispersity single particles need to be counted while the scattering experiment averages over macroscopic volumes. The sample preparation for TEM does not always produce reliable conditions and results.

The beauty of small angle neutron scattering has convinced in many applications ranging from basic research to applied sciences. The heavy demand for SANS is documented by the large over-booking factors at all neutron facilities. So, even in future we have to expect exciting results obtained by this method.

Appendices

A Further details about the correlation function

In this appendix we consider further details about the correlation function Γ. The first interesting property is the convolution theorem. In equation 5.21 it was stated that the correlation function in real space is a convolution while in reciprocal space the correlation function is a product (eq. 5.20). We simply calculate the Fourier transformation of $\Gamma(\mathbf{r})$:

$$\begin{aligned}
\Gamma(\mathbf{Q}) &= \mathcal{F}\left[\Gamma(\mathbf{r})\right] && (5.64)\\
&= \frac{1}{V}\int_V d^3r \int_V d^3r'\ \rho(\mathbf{r}+\mathbf{r}')\cdot\rho(\mathbf{r}')\cdot\exp(\mathrm{i}\mathbf{Q}\mathbf{r}) && (5.65)\\
&= \frac{1}{V}\int_V d^3r \int_V d^3r'\ \rho(\mathbf{r}+\mathbf{r}')\cdot\rho(\mathbf{r}')\cdot\exp(-\mathrm{i}\mathbf{Q}\mathbf{r}')\exp(\mathrm{i}\mathbf{Q}(\mathbf{r}'+\mathbf{r})) && (5.66)\\
&= \frac{1}{V}\int_V d^3u\ \rho(\mathbf{u})\exp(-\mathrm{i}\mathbf{Q}\mathbf{u})\int_V d^3u'\ \rho(\mathbf{u}')\exp(\mathrm{i}\mathbf{Q}\mathbf{u}') && (5.67)\\
&= \frac{1}{V}\rho^*(\mathbf{Q})\rho(\mathbf{Q}) \qquad \text{with } \mathbf{u}=\mathbf{r}',\ \mathbf{u}'=\mathbf{r}'+\mathbf{r} && (5.68)
\end{aligned}$$

In line 5.66 we split the exponential according to the two arguments of the scattering length density. These variables are finally used for the integration. For extremely large volumes V the integration limits do not really matter and stay unchanged – otherwise surface effects would play a role. Finally we arrive at the already known product of the scattering amplitudes.

The overlap of two displaced spheres has a lens shape and is calculated as a spherical segment being proportional to the solid angle minus a cone. So the lens has the following volume:

$$\begin{aligned}
V_{\text{lens}} &= \frac{4\pi}{3}R^3\cdot 2\cdot\left(\frac{1}{4\pi}\int_0^{2\pi}d\phi\int_0^{\alpha}d\vartheta\ \sin\vartheta\ \ -\frac{1}{4}\cos\alpha\ \sin^2\alpha\right) && (5.69)\\
&= \frac{4\pi}{3}R^3\left(1-\frac{3}{2}\frac{r}{2R}+\frac{1}{2}\left(\frac{r}{2R}\right)^3\right) \qquad \text{with } \cos\alpha=\frac{r}{2R} && (5.70)
\end{aligned}$$

The displacement is given by r and the radius of the sphere is R. The result is finally used in equation 5.22.

The next topic aims at the real space correlation function with the model exponential decay in one dimension (eq. 5.24). We simply consider the variable z. The Fourier transformation is done in the following explicitly:

$$\Gamma(Q_z) = \int_{-\infty}^{\infty} dz \ \left(\left\langle \left(\rho - \langle\rho\rangle\right)^2 \right\rangle \exp\left(-|z|/\xi\right) + \langle\rho\rangle^2 \right) \exp(\mathrm{i}Q_z z) \tag{5.71}$$

$$= \left\langle \left(\rho - \langle\rho\rangle\right)^2 \right\rangle \cdot \frac{2\xi}{1+\xi^2 Q_z^2} \quad + \quad 2\pi\langle\rho\rangle^2 \delta(Q_z) \tag{5.72}$$

We obtain a product of the scattering length density fluctuations, a size of the correlation 'volume', and a Lorentz function which is typical for Ornstein-Zernicke correlation functions. A second addend appears due to the Q-independent term $\langle\rho\rangle^2$. Constants Forier-transform to delta functions which are infinitely sharp peaks at $Q = 0$. In the scattering experiment they are not observable. The same calculation can be done in three dimensions (with similar results):

$$\Gamma(\mathbf{Q}) = \left\langle \left(\rho - \langle\rho\rangle\right)^2 \right\rangle \cdot \int_V d^3r \ \exp\left(-|\mathbf{r}|/\xi\right) \exp(\mathrm{i}\mathbf{Q}\mathbf{r}) \quad + \quad \cdots \tag{5.73}$$

$$= \left\langle \left(\rho - \langle\rho\rangle\right)^2 \right\rangle \cdot \int_0^{2\pi} d\phi \int_0^{\pi} d\vartheta \ \sin\vartheta \int_0^{\infty} dr \ r^2 \ \exp\left(-r/\xi\right) \frac{\sin(Qr)}{Qr} \tag{5.74}$$

$$= \left\langle \left(\rho - \langle\rho\rangle\right)^2 \right\rangle \cdot 4\pi \cdot \frac{2\xi^3}{(1+\xi^2\mathbf{Q}^2)^2} \tag{5.75}$$

This functional form appears for polymer gels on large length scales. The density of the polymer network tends to fluctuations which are described by eq. 5.75. To make the looking of eq. 5.75 more similar to the Lorentz function the denominator is seen as a Taylor expansion which will be truncated after the Q^2 term. Then the Q-dependent term is $\Gamma(\mathbf{Q}) \sim (1 + 2\xi^2\mathbf{Q}^2)^{-1}$. Finally, we can state that the functional form of eq. 5.25 is 'always' obtained.

B Guinier Scattering

The crucial calculation of the Guinier scattering is done by a Taylor expansion of the logarithm of the macroscopic cross section for small scattering vectors Q. Due to symmetry considerations there are no linear terms, and the dominating term of the Q-dependence is calculated to be:

$$R_g^2 = -\frac{1}{2} \cdot \frac{\partial^2}{\partial Q^2} \ln\Big(\rho(\mathbf{Q})\rho(-\mathbf{Q})\Big)\Big|_{\mathbf{Q}=0} \tag{5.76}$$

$$= -\frac{1}{2} \cdot \frac{\partial}{\partial Q} \frac{2\Re\big(\rho(\mathbf{Q}) \int d^3r \ \rho(\mathbf{r})(-\mathrm{i}\mathbf{r}) \exp(-\mathrm{i}\mathbf{Q}\mathbf{r})\big)}{\rho(\mathbf{Q})\rho(-\mathbf{Q})}\Bigg|_{\mathbf{Q}=0} \tag{5.77}$$

$$
\begin{aligned}
&= -\Re\frac{\rho(\mathbf{Q})\int d^3r\ \rho(\mathbf{r})(-\mathbf{r}^2)\exp(-\mathrm{i}\mathbf{Q}\mathbf{r})}{\rho(\mathbf{Q})\rho(-\mathbf{Q})}\bigg|_{\mathbf{Q}=0} \\
&\quad -\Re\frac{\int d^3r\ \rho(\mathbf{r})(\mathrm{i}\mathbf{r})\exp(\mathrm{i}\mathbf{Q}\mathbf{r})\int d^3r\ \rho(\mathbf{r})(-\mathrm{i}\mathbf{r})\exp(-\mathrm{i}\mathbf{Q}\mathbf{r})}{\rho(\mathbf{Q})\rho(-\mathbf{Q})}\bigg|_{\mathbf{Q}=0} + 0 \qquad (5.78)\\
&= \langle\mathbf{r}^2\rangle - \langle\mathbf{r}\rangle^2 \qquad (5.79)\\
&= \left\langle \big(\mathbf{r}-\langle\mathbf{r}\rangle\big)^2 \right\rangle \qquad (5.80)
\end{aligned}
$$

The first line 5.76 contains the definition of the Taylor coefficient. Then, the derivatives are calculated consequently. Finally, we arrive at terms containing the first and second momenta. The last line 5.80 rearranges the momenta in the sense of a variance. So the radius of gyration is the second moment of the scattering length density distribution with the center of 'gravity' being at the origin. We used the momenta in the following sense:

$$
\begin{aligned}
\langle\mathbf{r}\rangle &= \int d^3r\ \mathbf{r}\rho(\mathbf{r}) \Big/ \int d^3r\ \rho(\mathbf{r}) \qquad (5.81)\\
\langle\mathbf{r}^2\rangle &= \int d^3r\ \mathbf{r}^2\rho(\mathbf{r}) \Big/ \int d^3r\ \rho(\mathbf{r}) \qquad (5.82)
\end{aligned}
$$

So far we assumed an isotropic scattering length density distribution. In general, for oriented anisotropic particles, the Guinier scattering law would read:

$$
\frac{d\Sigma}{d\Omega}(\mathbf{Q}\to 0) = \frac{d\Sigma}{d\Omega}(0)\cdot\exp\left(-Q_x^2\left\langle\big(x-\langle x\rangle\big)^2\right\rangle - Q_y^2\left\langle\big(y-\langle y\rangle\big)^2\right\rangle - Q_z^2\left\langle\big(z-\langle z\rangle\big)^2\right\rangle\right) \qquad (5.83)
$$

Here, we assumed a diagonal tensor of second moment. This expression allows for different widths of scattering patterns for the different directions. In reciprocal space large dimensions appear small and vice versa. Furthermore, we see that R_g is defined as the sum over all second momenta, and so in the isotropic case a factor $\frac{1}{3}$ appears in the original formula 5.34.

C Details about Scattering of Microemulsions

The first step for the derivation of the scattering formula for microemulsions takes place on the level of the free energy (and the order parameter). The overall free energy is an integral over the whole volume, and contains only second order of the order parameter. So the derivatives in expression 5.60 can be understood as an operator acting on the order parameter, and the overall free energy is a matrix element of this operator – like in quantum mechanics. The wave functions can now be tranferred to the momentum space, i.e. the reciprocal space:

$$
F_0\big(\phi(\mathbf{k})\big) = \int d^3k\ \phi^*(\mathbf{k})\big[c\mathbf{k}^4 + g_0\mathbf{k}^2 + \omega_2\big]\phi(\mathbf{k}) \qquad (5.84)
$$

Now the order parameter appears with its Fourier amplitudes $\phi(\mathbf{k})$ and the operator becomes a simple polynomial as a wavevector $\mathbf{k}$. So the operator takes a diagonal form, because different states are not mixed anymore. The macroscopic cross section for the scattering vector $\mathbf{Q}$ is simply the expected value of the corresponding Fourier amplitude $\phi(\mathbf{Q})$. The statistical physics simply consider all possible Fourier amplitudes:

$$\frac{d\Sigma}{d\Omega}(\mathbf{Q}) \quad \propto \quad \frac{\int d^n\phi(\mathbf{k})\ \phi^*(\mathbf{Q})\phi(\mathbf{Q}) \exp\left(-\frac{1}{k_BT}F_0\big(\phi(\mathbf{k})\big)\right)}{\int d^n\phi(\mathbf{k})\ \exp\left(-\frac{1}{k_BT}F_0\big(\phi(\mathbf{k})\big)\right)} \tag{5.85}$$

$$= \quad -k_BT\frac{\partial}{\partial\omega_2}\ln\int d^2\phi(\mathbf{Q})\ \exp\left(-\frac{1}{k_BT}F_0\big(\phi(\mathbf{Q})\big)\right) \tag{5.86}$$

$$= \quad -k_BT\frac{\partial}{\partial\omega_2}\ln\left(\frac{1}{\sqrt{\frac{1}{k_BT}(c\mathbf{Q}^4+g_0\mathbf{Q}^2+\omega_2)}}\right)^2 \tag{5.87}$$

$$= \quad \frac{k_BT}{c\mathbf{Q}^4+g_0\mathbf{Q}^2+\omega_2} \quad \propto \quad \Gamma(\mathbf{Q}) \tag{5.88}$$

In line 5.86 the considered space of Fourier amplitudes has been reduced to the single important one. There are only two amplitudes left, which can be understood as the real and imaginary part of the complex amplitude. So the residual integral is 2-dimensional. The integral is Gaussian, and the result is known well. In line 5.87 the important dependencies are kept and all constant factors cancel out. The final result is the scattering function which is basically the reciprocal operator of line 5.84. This derivation is an explicit example of the fluctuation dissipation theorem.

To interpret the meaning of the scattering function the real space correlation function is calculated. While before the absolute value of the scattering intensity stayed rather undefined, in this representation absolute values have a meaning:

$$\Gamma(\mathbf{r}) = \left\langle\big(\rho-\langle\rho\rangle\big)^2\right\rangle \cdot \exp\big(-|\mathbf{r}|/\xi\big) \cdot \frac{\sin(kr)}{kr} \quad + \quad \langle\rho\rangle^2 \tag{5.89}$$

Furthermore the coefficients get a meaning: There is a correlation length ξ describing the decay of the correlations with the distance $\mathbf{r}$. The oscillating term describes the alternating appearance of oil and water domains. The domain spacing d is connected to the wavevector $k = 2\pi/d$. The connection to the original coefficients is given by:

$$k = \left[\frac{1}{2}\sqrt{\frac{\omega_2}{c}} - \frac{1}{4}\frac{g_0}{c}\right]^{\frac{1}{2}} \qquad \text{and} \qquad \xi = \left[\frac{1}{2}\sqrt{\frac{\omega_2}{c}} + \frac{1}{4}\frac{g_0}{c}\right]^{-\frac{1}{2}} \tag{5.90}$$

So the overall scattering formula takes the expression given in eq. 5.61. This example shows clearly that the real space correlation function supports the interpretation of scattering formulas obtained from a Landau approach with coefficients that are hard to connect to microscopic descriptions.

References

[1] R.-J. Roe, *Methods of X-ray and Neutron Scattering in Polymer Science* (Oxford University Press, New York, 2000).

[2] J.S. Higgins, H.C. Benoît, *Polymers and Neutron Scattering* (Clarendon Press, Oxford, 1994).

[3] O. Glatter, *J. Appl. Cryst.* **10**, 415 (1977).

[4] O. Glatter, *J. Appl. Cryst.* **12**, 166 (1979).

[5] J. Skov Pedersen, D. Posselt, K. Mortensen, *J. Appl. Cryst.* **23**, 321 (1990).

[6] H. Endo, M. Mihailescu, M. Monkenbusch, J. Allgaier, G. Gompper, D. Richter, B. Jakobs, T. Sottmann, R. Strey, I. Grillo, *J. Chem. Phys.* **115**, 580 (2001).

[7] S. Gagliardi, V. Arrighi, R. Ferguson, A.C. Dagger, J.A. Semlyen, J.S. Higgins, *J. Chem. Phys.* **122**, 064904 (2005).

[8] X. Ye, T. Narayanan, P. Tong, J.S. Huang, M.Y. Lin, B.L. Carvalho, L.J. Fetters, *Phys. Rev. E* **54**, 6500 (1996).

[9] S. Maccarrone, H. Frielinghaus, J. Allgaier, D. Richter, P. Lindner, *Langmuir* **23**, 9559 (2007).

[10] M. Teubner, R. Strey, *J. Chem. Phys.* **87**, 3195 (1987).

[11] Internal communication with M. Kraus, G. Goos, and G. Gompper; see also G. Gompper, M. Kraus, *Phys. Rev. E* **47**, 4301 (1993). and G. Gompper, G. Goos, *Phys. Rev. E* **50**, 1325 (1994).

Exercises

E5.1 Contrasts for SAXS and SANS

Our model nanocomposite is made of clay dispersed in polyethyleneoxide. What is the physical reason for the dominating contrasts of a small angle x-ray (SAXS) experiment? Would deuterated polymers change the contrast? For small angle neutron scattering we would like to use a mixture of normal and deuterated polymer in order to observe the chain dimensions. What is the optimal condition to suppress the clay scattering? The chemical formulas are approximately SiO_2 and $[\text{-}CH_2\text{-}CH_2\text{-}O\text{-}]_N$.

E5.2 Contrast Variation Experiment on Micelles

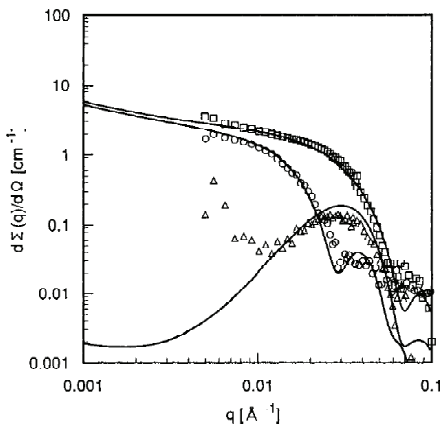

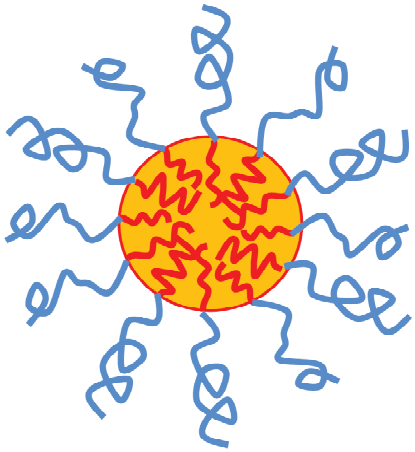

The three symbols □, ○, and △ indicate the characteristic small angle scattering of spherical polymer micelles under different important contrast conditions. There are three conditions called: shell contrast, core contrast and zero average contrast. What do these terms specify? Which condition can be connected to which symbol (or curve)? Why?

E5.3 The Pin-Hole Camera

The condition for the pinhole geometry is that the solid angle of the pin-hole observed from the position of the detector is equal or smaller than the solid angle of the object, here: the entrance aperture. Assume a symmetric SANS instrument with equal distances between the entrance aperture and the pin-hole (and sample), and between the pin-hole and the detector. What are the relative dimensions of the entrance aperture and the pin-hole? What are the relative areas?

Assume that the eye operated as a pin-hole camera. The sizes may be for the aperture 1mm, for the retina distance 2cm, and for the object 1km. What would be the minimal object size that could be resolved at this distance? Why do we see better?

E5.4 Spherical Form Factor

In microemulsions the topology of spherical droplets is quite frequent. We would like to assume a deuterated oil droplet of radius R surrounded by the protonated surfactant film and normal water (H_2O). For simplicity, the oil is assumed to be homogenous with a scattering length density ρ, and the surrounding materials are assumed to have an average zero scattering length density (which is nearly true). So the amplitude $\rho(Q)$ is calculated by the Fourier transform of a homogenous sphere. The macroscopic scattering cross section is normalized to the overall volume.

Calculate the three dimensional Fourier transformation of a solid sphere. Use spherical coordinates, and integrate in the order ϕ, ϑ, r. What is the simplicity of the integral over ϕ? How can the integral over ϑ be simplified (what is the variable X)? What does the kernel of the integral mean before the integration over r is performed? How would the integral be generalized for a scattering length density profile $\rho(r)$ with spherical symmetry? What is the meaning of the term $\sin(Qr)/(Qr)$?

The formulas 5.28 to 5.33 already show the solution of the problem. Nonetheless, the student should be motivated to rationalize each step of the derivation. The highly motivated student might also derive the sphere scattering from eq. 5.22.

E5.5 A Simple Structure Factor for Diluted Hard Spheres

Rationalize the derivation of the very simple structure factor from eq. 5.50 to 5.56! Follow the different stages of the phases from the two spheres from eq. 5.50 to 5.53! What does each individual term in eq. 5.54 mean? Why does the cosine Fourier transformation yield the same result as the complex Fourier transformation? Why is the radius of the avoided volume $2R$? What are the essential assumptions and what does the result mean? What does the additional Ornstein-Zernicke approach (eq. 5.57) improve?

6 Macromolecules (structure)

J. Stellbrink
Jülich Centre for Neutron Science 1
Forschungszentrum Jülich GmbH

Contents

Lecture Notes of the JCNS Laboratory Course Neutron Scattering

6.1 Introduction

Macromolecules are an integral part of Soft and Living Matter. In *Living Matter*, macromolecule-based functional systems are built from molecular units consisting of only a few different building blocks: amino acids are assembled into proteins, which in turn function individually, or cooperatively in nano- and micro-machines. The secret of success is the intrinsic hierarchical structuring over a large range of length scales. In *Soft Matter*, synthetic macromolecules are of much simpler structure. Nevertheless, there is a vast variety of material properties that can be realized with synthetic macromolecules. Theoretical concepts have been developed, and are essential for the rational design of soft materials, that are of paramount importance in a multitude of technical applications.

Synthetic polymers have crucially changed daily life since its development in the 1930ies. Modern polymers can be divided into two major classes (i) commodity polymers for daily life use which are produced in millions of tons per year and (ii) specialty polymers for high-performance applications which are niche products but highly profitable [1]. Typical commodity polymers are polyolefines like polyethylene (PE) or polypropylene (PP) used for packaging, films etc. Examples for specialty polymers are polydimethylsiloxane (PDMS) derivatives used in dental implants.

Currently, both classes of polymers in use are based on petrochemical feedstock, thus considered not “carbon-neutral” and “environment-friendly”. Due to changing global conditions and growing concerns about the mounting disposal problems, research on sustainable commodity polymers has been intensified during the last decade, both on the level of fundamental research and applied science [2]. To find the required balance between material properties and bioavailability/-degradability is the key for establishing sustainable polymers on a large scale industrial level and therefore a major challenge of future polymer science.

The development of new biomimetic specialty polymers is another major challenge. Biopolymers, like spider silk, are high-performance materials with material properties superior to any synthetic polymer. To transfer these properties to artificial biomimetic polymers, one has to fully understand, on the molecular level, the structure-property-relationships and enzymatic synthesis processes in living organisms.

In this lecture some recent applications of neutron scattering methods to characterize quantitatively on a microscopic length scale structure and interactions of synthetic macromolecules and its hierarchical structuring are given. A more comprehensive overview is found e.g. in [3].

6.2 Polymers in dilute solution

6.2.1 Linear polymers

A linear polymer is a sequence of molecular repetition units, the monomers, continuously linked by covalent bonds. The degree of polymerisation, D_p, i.e. the number of monomers constituting the polymer, the (weight average) molecular weight, $M_w=D_p\,M_m$, with M_m the molecular weight of the monomer, and the radius of gyration, $R_g \sim M_w^{\nu}$, are the most important structural parameters of a polymer. On a coarse grained level, structural details arising from the explicit chemical composition of the

polymer like bond lengths and angles can be neglected and what remains is the so called scaling relation given above that links molecular weight to size and which is generally valid for all polymers [4]. The numerical value of the scaling exponent v depends on the strength of interactions. In the so called θ-state, when monomer-monomer interactions are as strong as monomer solvent interactions, the polymer structure can be described by a random walk, therefore Gaussian chain statistics are valid and v=1/2, see Chapter 5.3.3. When monomer solvent interactions are stronger than monomer-monomer interactions, so called excluded volume forces are effective, the polymer chain is "swollen" and v=3/5.

Here one has to emphasize that synthetic polymers, unlike biopolymers, always have an intrinsic polydispersity, i.e. there is a distribution of molecular weights. The polydispersity is given usually in terms of M_w/M_n, with M_n the number average molecular weight. Its precise number depends on the polymerisation reaction by which the polymer was synthesized. For a (theoretical) monodisperse polymer M_w/M_n=1 holds, the most monodisperse synthetic polymers with M_w/M_n=1.02 can be synthesized by "living" anionic polymerisation, classical polycondensation yields M_w/M_n =2, radical polymerisation can even result in extremely broad distributions, M_w/M_n >10.

Although in technical applications polymers are mostly used as bulk materials, polymer characterisation is usually performed in (dilute) solution. Historically, light scattering was the method of choice to characterise synthetic polymers [5], but nowadays size exclusion chromatography (SEC), also called gel permeation chromatography (GPC), is the standard technique to characterize routinely polymers [6].

Neutron scattering, due do its limited accessibility and high experimental costs, usually is found in basic academic research, but here it played a crucial role in confirming fundamental theoretical concepts of polymers [3].

As explained in detail in Chapter 5.3.4 the measured intensity $I(Q)=P(Q)\,S(Q)$ is in first approximation a product of particle form factor $P(Q)$ given by the *intra*molecular structure, i.e. the particle shape, and structure factor $S(Q)$ given by the *inter*molecular structure arising due to particle-particle interactions. To characterize properly the *intra*molecular form factor $P(Q)$ one has therefore to investigate a concentration series in the dilute regime and extrapolate finally to infinite dilution. The form factor of a Gaussian chain (Debeye function) has been derived in Chapter 5.3.3.

Particle-particle interactions as seen in $S(Q)$ are weak in the dilute regime, but still effective, so that one can apply the virial expansion.

$$\phi / I(Q=0) = 1/V_w + 2A_2\phi + \ldots \tag{6.1}$$

Here ϕ is the polymer volume fraction and $V_w = M_w/d$ is the molecular volume and d the polymer density in [g/cm^3]. The value of the second virial coefficient A_2 directly reflects particle-particle interactions, i.e. a positive A_2 is found for repulsive interactions (good solvent), a negative one for attractive interactions (marginal/bad solvent) and finally A_2=0 characterizes no interactions (θ-solvent). Without any data fitting this distinction can easily be made by plotting the intensity data $I(Q)$ of a concentration series normalized to the corresponding volume fractions $I(Q)/\phi$ (Since scattering arises due to an exchange of a volume element of solvent by a volume element of polymer with different scattering contrast, the natural concentration unit for any scattering

experiment should be volume fraction ϕ). This is schematically shown in Figure 6.1. If no particle-particle interactions are present all data for all Q-vectors exactly fall on top of each other.

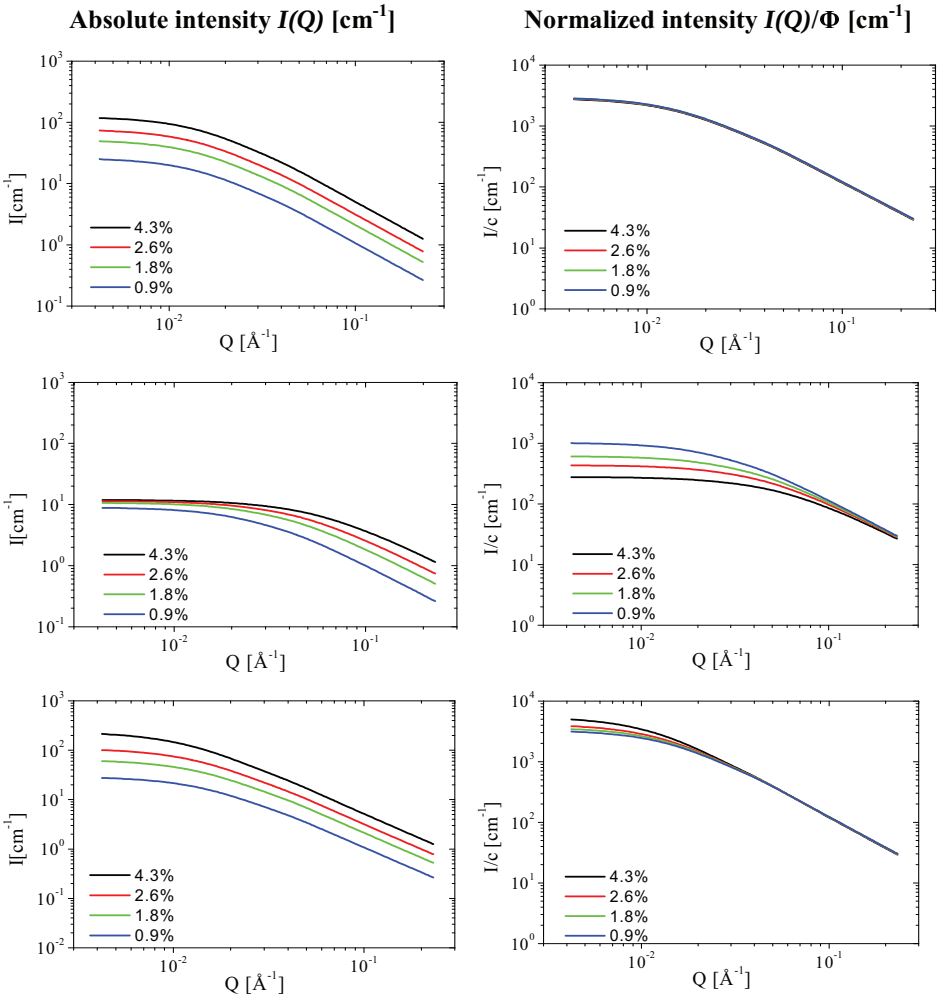

Fig. 6.1: Calculated scattering intensities in absolute units I(Q) (left) and normalized to polymer volume fraction I(Q)/ ϕ (right) for solutions of a linear polymer at different volume fractions given in percent, see legends, assuming a virial ansatz for particle interactions. From top to bottom: No interactions A_2=0 (θ solvent, repulsive interactions A_2>0 good solvent, attractive interactions A_2<0 marginal or bad solvent).

Irrespective what kind of interactions are present this also holds for high Q-vectors, since high Q-vectors mean small length scales and the local (*intra*molecular) structure is not affected by particle-particle interaction ($S(Q)$=1). In contrary, at low Q-vectors there are crucial differences between the individual concentrations in this representation. For

repulsive interactions the forward scattering is reduced by *S(Q)* therefore the lowest concentration shows the highest normalized intensity. For attractive interactions, on the other hand, the forward scattering is increased by *S(Q)*, therefore the lowest concentration shows the lowest normalized intensity. This sequence can be easily understood, because attractive interactions finally result in clustering of the individual particles.

For more details about synthesis and characterisation of macromolecules the interested reader is referred to standard textbooks e.g. [7][8].

6.2.2 Branched polymers

Branching crucially influences the mechanical properties of polymers therefore characterisation and control of branching reactions during polymerisation processes are of vital interest not only for polymer industry to tune semi-empirically material properties, but also for fundamental research to derive a proper quantitative structure property relationship.

The simplest branched polymer is a regular star polymer, where *f* arms, each of same molecular weight $M_{w,arm}$, are emanating from a microscopic central branch point, the star core. Experimentally, such regular star polymers are nowadays most precisely realized by using chlorosilane dendrimers as branch points. The arms forming the star corona or shell are grafted to the dendrimer core by "living" anionic polymerisation [9]. The precise control of the dendrimer generation is reflected in the precise functionality of the final star polymer so that functionalities as high as *f*=128 can be achieved. However, with increasing functionality there is a polydispersity in functionality since the last arms are extremely difficult to graft since they have to diffuse through the already very crowded star polymer corona to react at the star core [10].

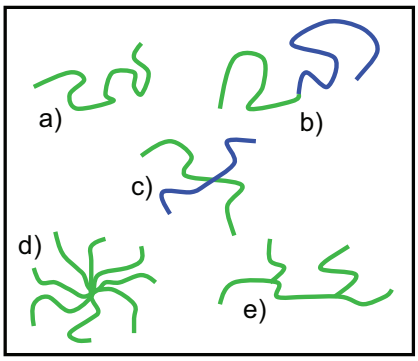

Fig. 6.2: *Schematic illustration of different polymer architectures: a) linear homopolymer, b) linear block copolymer, c) regular mikto-arm star polymer (f=4), d) regular star polymer(f=8), and e) comb polymer.*

The form factor of a regular star polymer with Gaussian chain statistics has been derived by Benoit already in 1953 [11].

$$P_{star}(Q) = \frac{2}{f_w Q^4 R_{g,arm}^4} \times \left[Q^2 R_{g,arm}^2 - \left(1 - e^{-Q^2 R_{g,arm}^2}\right) + \frac{f_w - 1}{2} \left(1 - e^{-Q^2 R_{g,arm}^2}\right)^2 \right] \quad (6.2)$$

The overall size of the star polymer $R_{g,star}$ is related to the size of the individual arm by $R_{g,star} = \sqrt{\frac{(3f-2)}{f}} R_{g,arm}$.

There is no rigorous analytical formula for a star polymer with swollen chain statistics, but experimental data for star polymers in a good solvent can be nicely described either by the Dozier function [12] or the approach derived by Beaucage [13]. His equation can be viewed as a "universal form factor" for an arbitrary mass fractal that can also be applied to many other polymeric systems:

$$P(Q) = G \cdot \exp(-Q^2 R_g^2 / 3) + B \left(\frac{1}{Q^*} \right)^P \quad (6.3)$$

with $Q^* = Q/[erf(QkR_g/\sqrt{6})]^3$. Here *erf* is the error function and G and B are amplitudes, which for mass fractals can be related to each other by $B = G \cdot P / R_g^P \cdot \Gamma(P)$ (polymeric constraint). P is the fractal dimension of the internal substructure, k an empirical constant found to be ≈ 1.06 and Γ is the Gamma function. The fractal dimension is related to the scaling exponent by P=1/ν. The Beaucage expression can be nicely extended to describe hierarchically structures over multiple levels *i* $P(Q) = \sum_i P_i(Q)$ where $P_i(Q)$ are given by Equation (6.3).

Fig. 6.3: shows form factors obtained for polybutadiene (PB) star polymers with varying functionality *f* but same R_g≈50nm in d-cis-decalin.

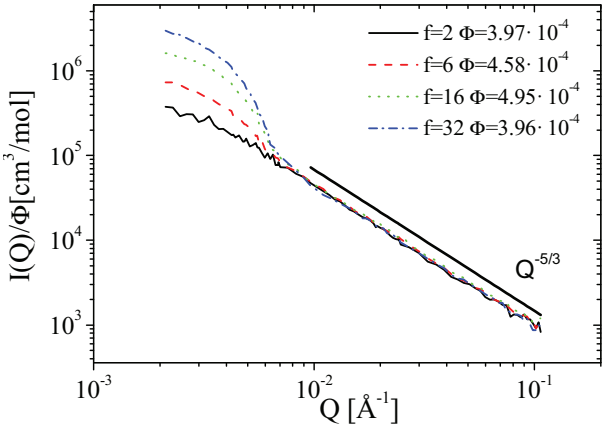

Fig. 6.3: *SANS intensity I(Q) normalized by volume fraction ϕ for regular polybutadiene star polymers with varying functionality f but same radius of gyration R_g≈50nm. The asymptotic power law observed at high scattering vectors $I \sim Q^{-5/3}$ clearly indicates excluded volume interactions relevant in a good solvent , i.e. swollen chain statistics; figure taken from [14].*

At low *Q*-vectors, $Q \leq 8\times10^{-3}$ Å^{-1}, data could be modelled using the Benoit form factor, Equation (6.2) for a Gaussian star, which gives the explicit dependence on functionality *f*. For describing the complete data sets we used the Beaucage form factor, Equation (6.3), which describes also the observed power law at high *Q*-vectors. One should note that this power law extends over more than one order of magnitude in *Q* and starts at the same *Q*-value of $\approx 8\times10^{-3}$ Å^{-1} for all *f* due to the same R_g. The observed power law slope of $I(Q) \sim Q^{-5/3}$ reflects the good solvent quality of cis-decaline for polybutadiene and decreases slightly with increasing *f* , indicating increasing arm stretching due to the increasing monomer density in the star corona.

The effect of branching becomes easily visible by using a so called Kratky representation, $I(Q)\ Q^2$ vs. *Q*. Whereas a linear polymer with Gaussian chain statistics reaches monotonically an asymptotic plateau, any branched structure shows a maximum. For the here discussed regular star polymer the height quantitatively depends on the arm number or functionality *f*, see Fig. 6.4:

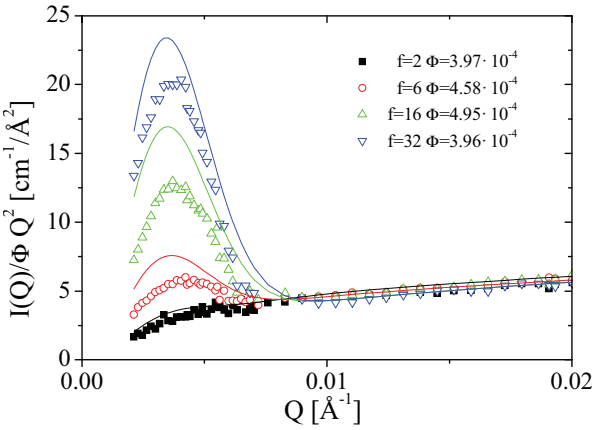

Fig. 6.4: *Kratky representation $I(Q)\ Q^2$ vs. Q for same data as in Fig. 6.3. The increasing peak height with increasing functionality f due to branching becomes clearly visible as well as the discrepancy between experimental data (symbols) and Beaucage function used to model the data. The fact that no asymptotic plateau is observed results from the excluded volume interactions relevant in a good solvent, i.e. swollen chain statistics.*

6.2.3 In-situ experiments during polymerisation

For understanding and controlling any chemical reaction a detailed understanding of reaction mechanism, type and role of intermediate species as well as reaction kinetics are prerequisite. How the microscopic structure of a growing polymer chain is evolving in the different steps of polymerisation reactions has to be resolved by non-invasive, real-time measurements. The ideal tool is small angle neutron scattering (SANS), since the microscopic structure of polymer-based materials can be resolved on a micrometer-to- nanometer-level by modern neutron scattering techniques. In addition, contrast variation, i.e. H/D exchange, can even “stain” certain parts of the polymers giving

access to unprecedented structural information. So neutron scattering is a unique and outstanding technique to investigate polymerising systems in real-time, in particular since new, more powerful neutron sources became available worldwide (FRM-2, SNS, J-PARC). But for a complete description of the polymerisation process additional information in terms of reaction kinetics etc. are prerequisite. Thus, in-situ SANS experiments have to be supported by complementary methods like NMR, SEC, UV/VIS and IR spectroscopy, favourably also in real-time mode.
Recently we investigated reaction mechanism and kinetics of different polymerisation techniques like "living" anionic polymerisation [15] or post-metallocene catalyzed olefin polymerisation [16] by such an in-situ multi technique approach. Fig. 6.5: shows time resolved SANS intensities *I(Q)* in absolute units obtained during the polymerisation of 1-octene by a pyridylamidohafnium catalyst in toluene at 20°C. Experiments have been performed using the KWS-1 instruments at the former FRJ-2 reactor in Jülich which allowed a temporal resolution of about several minutes.

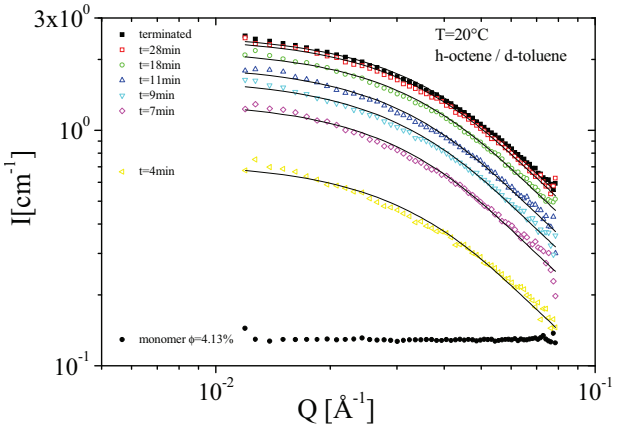

Fig. 6.5: *Time resolved SANS intensities I(Q) in absolute units obtained during the polymerisation of 1-octene by a pyridylamidohafnium catalyst in toluene at 20°C; figure taken from [16].*

Whereas the monomer solution shows a *Q*-independent intensity over the whole accessible SANS *Q*-range typical for small molecules ("incoherent scatterers"), after 4 minutes a polymer is already formed and the *Q*-dependence of the intensity can be described by a Beaucage form factor, Equation (6.3). With ongoing polymerisation, increasing polymerisation time *t* the general shape of *I(Q)* does not change any further, only the forward scattering *I(Q=0)* is increasing due to the increasing molecular weight and concentration of the growing polymer chain. Finally, the polymerisation is almost finished after half an hour as can be seen by comparison with the terminated polymer. A detailed quantitative analysis of *I(Q,t)* reveals that during this type of polymerisation reaction no aggregation phenomena of the growing polymer chain are relevant. Similar experiments at high flux sources allow today temporal resolutions smaller than 1 second if experiments are repetitively performed using a stopped flow mixer.

6.3 Block copolymer Micelles

When amphiphilic block copolymers are dissolved in a selective solvent, i.e. a solvent which is good for one block but a precipitant for the other, they spontaneously self-assemble into supramolecular aggregates known as micelles, in which the insoluble block forms the inner part or core, whereas the soluble block forms a solvent-rich shell or corona. The general behaviour of block copolymers in selective solvents has been subject of copious theoretical and experimental studies during the past decades. They are reviewed in several books [17] [18] and review articles [19][20] related to this topic.
Extensive studies demonstrated that the micellar morphology can be tuned (going from spheres, cylinders, worms and vesicles) by varying the block-copolymer molecular weight, the chemical nature and the ratio of the blocks. One of the most extensively studied block-copolymers is poly(butadiene-ethylene oxide) (PB-PEO). As a function of the hydrophilic block length (in term of PEO weight fraction w_{PEO}) spherical micelles (w_{PEO} >0.6), worm-like micelles, WLM (0.47 ≤w_{PEO} ≤ 0.59) or bilayers (w_{PEO} <0.47) are formed. Different theoretical studies contributed to define the scaling laws for the parameters of equilibrium structures. Among them, a quantitative theory defining the thermodynamic stability of different morphologies in selective solvents has been recently developed [21]. The theory expresses the free energy contributions of the core, the corona and the interface as a function of the blocks structural parameters and the interfacial tension between the solvent and the insoluble block for different micellar morphologies. Solvent selectivity can be more easily tuned than the above mentioned parameters (molecular weight, block ratio etc) and moreover in a continuous way by varying the solvent composition. Therefore solvent composition is a very natural and easy parameter to control the micellar structures. The change in the morphology of the self-assembled structures can be attributed to a change of solvent selectivity, which influences the different energy contributions responsible for the morphology: core-chain stretching, corona-chain repulsion and interfacial tension between the core and the solution.
The interest is to relate changes on the smallest relevant length scale, i.e. diameter and aggregation number per unit length, density profile in the corona, to changes in the macroscopic structure, i.e. the contour and persistence length of wormlike micelles and the transition from wormlike-to-spherical micelles etc. This molecular level understanding can help to elucidate the mechanisms involved in non equilibrium conditions. Besides, it is expected that these quantities have a pronounced effect on the rheological behavior of the systems, and as such solvent composition could be used to tune the flow properties of micellar solutions.

6.3.1 Form factor

Figure 6.6 (left) shows the partial form factor normalized to volume fraction Φ, $P(Q)/\Phi$, in shell and core contrast for micelles formed by a symmetric amphiphilic block copolymer poly(ethylene-alt-propylene)–poly(ethylene oxide), h-PEP4-dh-PEO4 (the numbers denote the block molecular weight in kg/mol) [22]. Already, a qualitative discussion of the data reveals important features of the micellar architecture. First, the forward scatterings, $I\ (Q = 0)$, in the two contrasts are the same. This is expected for micelles formed by a symmetric diblock copolymer in shell and core contrast (we should note that the two blocks have the same molar volume V_w) and is in this sense a

proof of the applied contrast conditions. This means that the scattering profiles shown in figure 2 are directly reflecting pure shell and core properties. Second, both scattering profiles show well defined maxima and minima, up to 4 in core contrast, which arise from sharp interfaces typical for a monodisperse, compact particle. Also shown is Porod's law $I \sim Q^{-4}$, which describes the limiting envelope of all form factor oscillations. (We should note that one has to consider that these oscillations are already smeared by the instrumental resolution function, so the data shown offer even more confirmation of the strong segregation between the core and corona and the low polydispersity of the micelles.) We should emphasize that in core contrast no *blob* scattering is visible [22]. This also corroborates the compact PEP core. A quantitative analysis in terms of a core–shell model gave the following micellar parameters: aggregation number P = 1600, core radius R_{core} = 145 Å and shell radius R_m = 280 Å with a polydispersity of ≈5%. The solvent fraction in the swollen shell is Φ_{solv} = 60%.
Figure 6.6 (right) shows the corresponding partial form factor data, $P(Q)/\Phi$, in shell and core contrast for an asymmetric h-PEP1-dh-PEO20. The differences compared to figure 6.6. (left) are obvious: the difference in forward scattering of the two contrasts is reflecting the asymmetry of the block copolymer. Moreover, no maxima or minima are visible (also not at high Q in core contrast) and the power law observed in shell contrast has a slope of only $I \sim Q^{-5/3}$, which is typical for a polymer chain in a good solvent and arises from the swelling of the PEO in the shell (*blob* scattering). A quantitative analysis gives the following micellar parameters: aggregation number P = 130, core radius R_{core} = 34 Å and shell radius R_m = 260 Å.

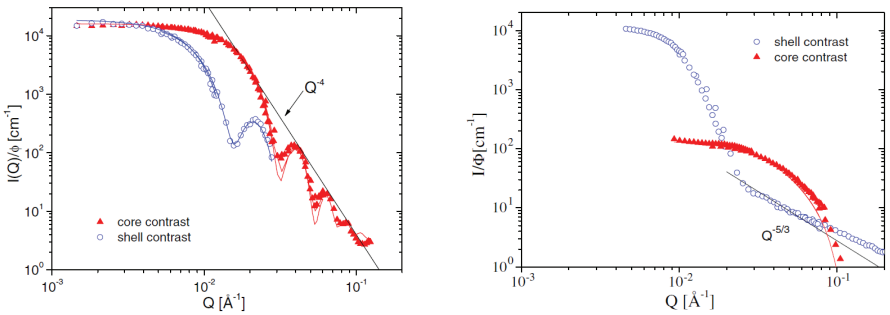

Fig. 6.6: *Form factors of block copolymer micelles with varying architecture in core (red) and shell contrast(blue). Left symmetric PEP4-PEO;right asymmetric PEP1-PEO20, the numbers denote the block molecular weight in kg/mole. Figure taken from [22].*

6.3.2 Micellar exchange dynamics

Polymeric micelles are macromolecular analogues of well-known low-molecular surfactant micelles. As a consequence of random stochastic forces, the constituting chains will continuously exchange between the micelles. From the theory of Halperin and Alexander (HA), this exchange kinetics is expected to be dominated by a simple expulsion or insertion mechanism where single chains (unimers) are required to overcome a defined potential barrier [23]. Higher order kinetics including fusion and

fission is not expected to take place since these mechanisms are neither favored energetically nor entropically [24]. Experimentally, relatively few studies have been devoted to the exchange kinetics of polymeric micelles in equilibrium. This is most likely related to the associated experimental difficulties. Recently, we used a newly developed time resolved small angle neutron scattering (TR-SANS) technique [25]. This technique is perfectly suited for determination of exchange kinetics in equilibrium as, unlike other techniques; virtually no chemical or physical perturbations are imposed on the system. The labeling is restricted to a simple hydrogen/deuterium (H=D) substitution using fully hydrogenated (h) and fully deuterated (d) polymers with identical molar volumes and compositions. By mixing the corresponding H- and D-type micelles in a solvent with a scattering length corresponding to the average between the two, the kinetics can be determined. The average excess fraction of labeled chains residing inside the micelles is then simply proportional to the square root of the excess SANS intensity. The corresponding correlation function is given by $R(t) = \{[I(t) - I_\infty]/[I(t=0) - I_\infty]\}^{1/2}$ was measured from a reference sample where the polymers have been completely randomized and $I(t=0)$ from the scattering of the reservoirs at low concentrations.

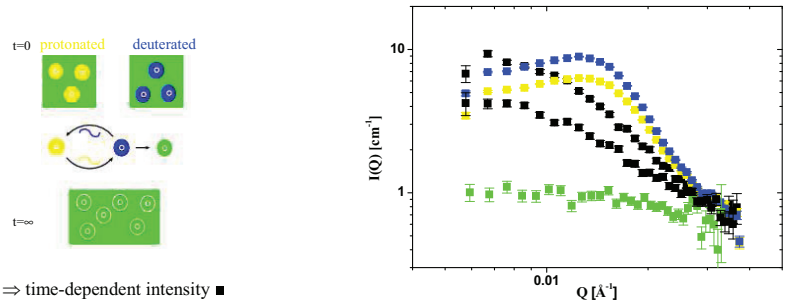

Fig. 6.7: *Left: Schematic illustration of the TR-SANS technique to follow micellar exchange kinetics. Right: Corresponding time-resolved SANS data forPEP1-PEO20 micelles in H2O/DMF 7:3 showing slow exchange (5min, 2h @ 50°C).*

6.3.3 Structure factor

How the structure factor *S(Q)* can be derived from the pair correlation function *g(r)* by liquid state theory has been shown in Chapter 5.3.4. *g(r)* finally results from the effective pair potential *V(r)*, which describes the direct interactions between the solute only, after eliminating the rapidly moving degrees of freedom of the solvent molecules.
We recently showed that micelles formed by the amphiphilic block copolymer poly(ethylene-alt-propylene)– poly(ethylene oxide) (PEP–PEO) provide an interesting system to conveniently tune the 'softness' in terms of particle interactions (intermolecular softness) and the deformability of the individual particle (intramolecular softness). This is achieved by changing the ratio between hydrophobic and hydrophilic blocks from symmetric (1:1, Hard Sphere-like) to very asymmetric (1:20, star-like). One must emphasize that to approach the star-like regime is not a trivial task.
Figure 6.6 compares the effective interaction potential for soft colloids to those of the limiting cases Gaussian Chain, i.e. no interactions, and Hard Spheres, i.e. infinite strength of the potential at contact. The explicit form of *V(r)* for star polymers, the

limiting ultra-soft colloids, was derived by Likos et al. [26] and is explained in detail in Appendix 6.1.

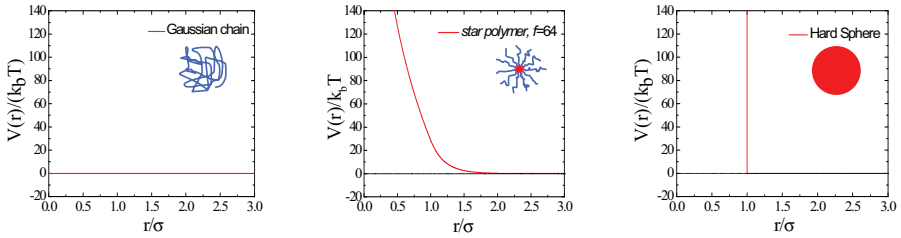

Fig. 6.8: *Different effective interaction potentials. The one for star polymers, i.e. soft colloids, is in-between the two limits Gaussian Chain (left) and Hard Spheres (right).*

Figure 6.9 shows the corresponding experimental structure factors S(Q) for Hard Sphere and Soft interactions and its comparison with theoretical predictions.

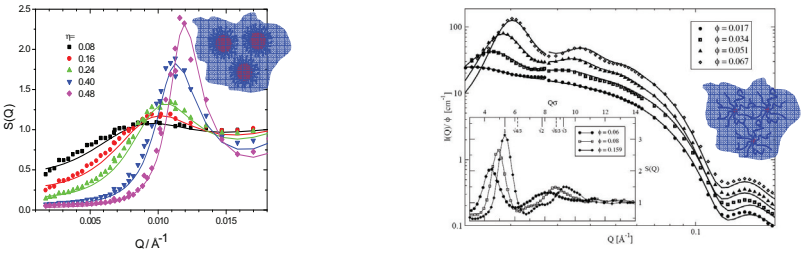

Fig. 6.9: *Experimental structure factor S(Q) of block copolymer micelles with varying architecture obtained by SANS in core contrast (symbols) and the theoretical description (lines) resulting from the corresponding interaction potentials: Symmetric PEP4-PEO4 / Hard Sphere potential left, asymmetric PEP1-PEO20/ ultra soft potential right, see text and [22].*

6.4 Soft Colloids

Soft colloids in general, e.g. polymer-coated silica particles, block copolymer micelles, star polymers etc., are hybrids between (linear) polymer chains and (hard sphere) colloids. Due to this hybrid nature, soft colloids macroscopically show interesting (phase) behaviour resulting from its unique microscopic structure. The combination of polymer-like properties, i.e. the formation of (transient) geometric constraints due to overlapping polymeric coronas and direct colloidal interactions due to the (hard) core in particular affects flow properties and nonequilibrium behaviour of soft colloids. Therefore soft colloids are frequently used in many technical applications (paints, shampoos, motor oils, polymer nano-composites etc.).

More recently, the interest of colloid scientists in fundamental science has shifted towards the study of soft particles, among which star polymers have emerged as a

model system for a wide class of soft spheres. For a star polymer, softness can be controlled by varying its number of arms (or functionality *f*), allowing to bridge the gap between linear polymer Gaussian chains ($f = 2$) and Hard Spheres ($f = \infty$). Therefore, star polymers feature tuneable softness, which is responsible for the observation of anomalous structural behaviour and for the formation of several crystal structures [28]. Hence, mixtures of soft particles offer an even higher versatility with respect to their hard counterparts, both in terms of structural and rheological properties and of effective interactions. Recently, we confirmed experimentally by combining SANS and rheology the theoretical phase diagram of soft colloids [29] and mixtures of soft colloids with linear polymers [29]. As experimental realization again the previously described PEP-PEO star-like micelles have been used. Figure 6.10 shows the phase diagram in the functionality vs. packing fraction representation. We have to point out that quantitative agreement starting from experimental parameters is achieved without any adjustable parameter. For this the determination of the interaction length σ by SANS in core contrast was inevitable.

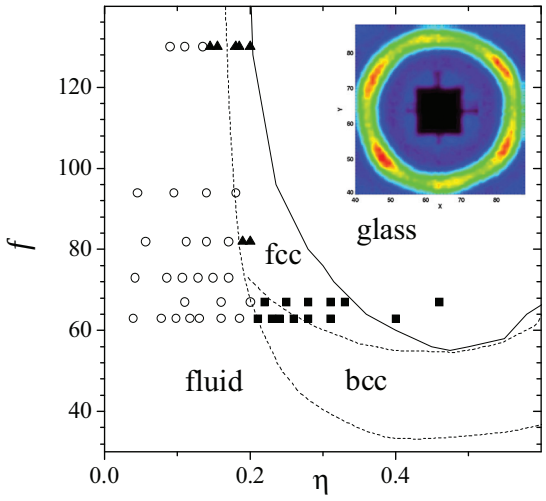

Fig. 6.10: *Phase diagram of ultra soft colloids (symbols experiment: ○ fluid, ■ bcc ▲ amorphous solid;, lines theory). Figure taken from.*

Appendices

A6.1 The ultra-soft potential (Likos-Potential)

The effective potential $V(r)/k_bT$ between star polymers as a function of functionality f and interaction length σ was derived by by Likos et al. [26]. The interaction length σ is the distance between two star centres when the outermost blob overlaps. For larger distances two stars interact via a screened Yukawa-type potential whereas at distances smaller than σ when there is overlap of the star coronas, the potential has an ultra-soft logarithmic form.

$$\frac{V(r)}{k_bT} = \begin{cases} \frac{5}{18} f^{3/2} \left(1+\sqrt{f}/2\right)^{-1} (\sigma/r) \exp\left[-\sqrt{f}\,(r-\sigma)/2\sigma\right] & (r>\sigma) \\ \frac{5}{18} f^{3/2} \left[-\ln(r/\sigma) + \left(1+\sqrt{f}/2\right)^{-1}\right] & (r \le \sigma) \end{cases} \tag{6.4}$$

All numerical factors have been chosen in such a way that the potential as wells as its first derivative are smooth at crossover. Figure 6.11 shows the Likos-potential for different functionalities. At $f = \infty$ the Hard Sphere potential is recovered.

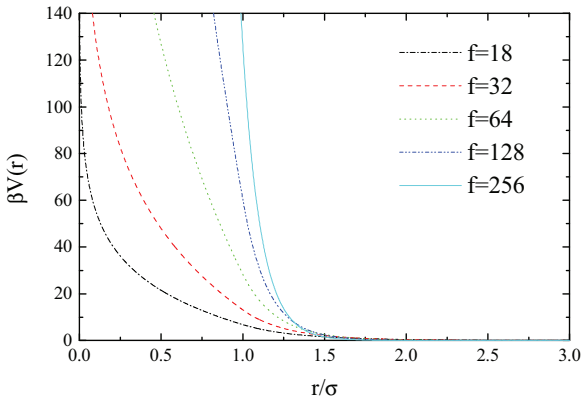

Fig. 6.11: *Effective potential $V(r)/k_bT$ between star polymers with varying functionality f.*

References

[1] C J.R. Severn and J.C. Chadwick, Tailor-Made Polymers, (Wiley-VCH, Weinheim, 2008)
[2] G.W. Coates and M.A. Hillmyer, Polymers from Renewable Resources, Macromolecules, VI2, 7987 (2009); C.K. Williams, M.A. Hillmyer, Polymer Rev. 48, 1 (2008)
[3] J. S. Higgins and H. C. Benoit, Polymers and Neutron Scattering; (Clarendon Press, Oxford, U.K., 1994).
[4] P.G. De Gennes, Scaling Concepts in Polymer Physics, (Cornell University Press, 1979)
[5] W. Brown, Light Scattering: Principles and development, (Oxford University Press, 1996)
[6] S. Mori and H.G. Barth, Size Exclusion Chromatography, (Springer, 1999)
[7] P.J. Flory, Principles of Polymer Chemistry, (Cornell University Press, 1953)
[8] H.G. Elias, Macromolecules, (Wiley-VCH, Weinheim, 2009)
[9] G. S. Grest, L. J. Fetters, J. S. Huang, and D. Richter, Adv. Chem. Phys. 94, 67 (1996)
[10] J. Allgaier, K. Martin, H. J. Räder, and K. Müllen, Macromolecules 32, 3190 (1999)
[11] H.J. Benoît, J. Polym. Sci., 11**,** 507 (1953).
[12] William D. Dozier, John S. Huang, Lewis J. Fetters, Macromolecules 24 2810 (1991)
[13] G. Beaucage, J. Appl. Crystallogr. 28, 717(1995)
[14] J. Stellbrink et al., Applied Physics A 74, S355 (2002)
[15] J. Stellbrink et al. Macromolecules, 31, 4189 (1998)
[16] A.Z. Niu et al., Macromolecules 42 1083 (2009)
[17] I.W. Hamley, The Physics of Block Copolymers; (Oxford University Press: New York, 1998)
[18] M. Antonietti and S. Förster, Vesicles and Liposomes: A Self-Assembly Principle Beyond Lipids, Vol. 15, (WILEY-VCH Weinheim, , 2003)
[19] G. Riess, *Prog. Polym. Sci.* 28, 1107 (2003)
[20] A. Halperin, M. Tirell and T.P. Lodge, *Adv. Polym. Sci.* 100, p31 (1990).
[21] E.B. Zhulina, M. Adam, I. LaRue, S.S. Sheiko, M. Rubinstein, Macromolecules 38, 5330 (2005)
[22] J. Stellbrink, G. Rother, M. Laurati, R. Lund, L. Willner and D. Richter, J. Phys.: Cond. Matter, 16, S3821 (2004)
[23] A. Halperin and S. Alexander, Macromolecules 22, 2403 (1989)
[24] E. Dormidontova, Macromolecules 32, 7630 (1999)
[25] L. Willner, A. Poppe, J. Allgaier, M. Monkenbusch, and D. Richter, Europhys. Lett. 55, 667 (2001)
[26] C.N. Likos et al., Phys. Rev. Letters, 80, 4450, (1998)
[27] M. Watzlawek, C. N. Likos, and H. Lowen, Phys. Rev. Lett. 82, 5289 (1999).
[28] M. Laurati, Phys. Rev. Letters, 94 195504 (2005)
[29] B. Lonetti et al. Phys. Rev. Letters, 106, 228301 (2011)

Exercises

E6.1 Contrast or no contrast?

Due to synthetic (and financial) limitations only protonated material is available for a SANS experiment, for both polymer (poly(ethylene propylene), PEP, and solvent dimethyl-formamide, DMF.

a) Calculate the contrast factor $\frac{\Delta\rho^2}{N_A}$.

b) What is the necessary molecular weight M_w to achieve a signal-to-background ratio of 5 at Q=0 for a given polymer volume fraction ϕ_p =0.01? (Remember: Also the incoherent scattering contributes to the background and there is an empirical "rule of thumb" that the experimental incoherent scattering is twice the theoretical value due to inelastic and multiple scattering!)

c) At which Q-value the signal vanishes in the background?

(Assuming good-solvent conditions with a prefactor 0.01 [nm] for the R_g-M_w-relation and assuming the Guinier approximation for $P(Q)$)

d) For which combination of molecular weight and volume fraction ϕ_p the experiment could be performed in the dilute regime, i.e. $\phi_p \leq 0.1\phi^*$?

Given are sum formulae and densities

h-PEP = C_5H_{10}, d_{PEP}=0.84g/cm^3

h-DMF = C_3H_7NO, d_{PEO}=0.95g/cm^3

and coherent and incoherent scattering lengths b_{coh} and b_{inc} in units [cm]:

C: b_{coh} =6.65E-13, b_{inc} = 0

H: b_{coh} =-3.74E-13, b_{inc} = 2.53E-12

D: b_{coh} =6.67E-13, b_{inc} = 4.04E-13

O: b_{coh} =5.80E-13, b_{inc} = 0

N: b_{coh} =9.36E-13, b_{inc} = 0

E6.2 Contrast factors for Micelles

In aqueous solution, the diblock copolymer poly(ethylene propylene-block-ethylene oxide), PEP-PEO, forms spherical micelles, with PEP the non-soluble and PEO the soluble block. Using SANS combined with contrast variation the micellar structure should be investigated. To prepare the corresponding samples the following parameters have to be calculated

a.) the coherent scattering length densities ρ_{PEP} and ρ_{PEO} in units of [cm^{-2}]:

Known are the monomer sum formulae and densities
h-PEP = C_5H_{10}, d_{PEP}=0.84g/cm^3
h-PEO = C_2H_4O, d_{PEO}=1.12g/cm^3
the degree of polymerisation, D_p, of the blocks:
$D_{p,PEP}$ = 15
$D_{p,PEO}$ = 40
and the coherent scattering lengths b_{coh} in units [cm]:
C=6.65E-13
H=-3.741E-13
D=6.671E-13
O=5.803E-13
b.) the isotopic solvent mixture (H2O/D2O) that match the scattering length density of either PEP and PEO.
Given: d_{D2O}=1.1g/cm^3

E6.3 Aggregation number of micelles

For the same PEP-PEO micelles as in E6.2, in dilute solution using core contrast, i.e. the scattering length density of the solvent is matched to the scattering length density of the micellar shell (formed by the soluble block PEO), the first form factor minimum is observed at Q=0.12 Å^{-1}.
Calculate
a.) the aggregation number N_{agg}, i.e. the number of diblock copolymers forming a single micelle, assuming full segregation, i.e. a non-swollen micellar core.
b.) How can N_{agg} derived in this way be cross-checked without performing another experiment?

E6.4 Reduced forward scattering (virial expansion)

For the same PEP-PEO micelles as in E6.2 at finite concentration using core contrast the corresponding forward scattering *I(Q=0)* for volume fractions ϕ_1=1x10^{-3}, ϕ_2=5x10^{-3} and ϕ_3=7.5x10^{-3} assuming a second virial coefficient A_2=2x10^{-4} should be calculated.

E6.5 Peak position in *S(Q)*

A solution of compact spherical colloids, R=250Å, with volume fraction 0.25 should be characterised by SANS. At which Q-vector do you expect the first peak in the structure factor *S(Q)* to appear?

7 Spin Dependent and Magnetic Scattering

R. P. Hermann
Jülich Centre for Neutron Science 2
Forschungszentrum Jülich GmbH

Contents

Lecture Notes of the JCNS Laboratory Course Neutron Scattering

7.1 Introduction

Among the properties that make neutrons such powerful probes for investigating condensed matter, the neutron spin and magnetic moment are of essential importance not only for investigating magnetic properties, but also, in a maybe unexpected way, for investigating soft matter. Interesting consequences that can be used in scattering experiments arise from these two properties. First, because the neutron has a spin $S = \pm 1/2$ and the scattering process is fundamentally governed by quantum mechanics, the scattering length of a nucleus will in general be dependent on the spin states of both the nucleus and the neutron; the nuclear interaction is thus spin dependent. Second, because the nucleus possesses a magnetic moment, it will also interact with magnetic moments in the probed sample or with magnetic fields; modeling this additional magnetic interaction is thus required for a detailed description. Third, as the neutron spin and its magnetic moment are tied, we further expect that any magnetic interaction that will influence the magnetic moment of the neutron will also influence its spin state; manipulation of the neutron spin with magnetic interactions is thus a powerful technique to add to our toolkit.

The properties of the neutron have been discussed in previous lectures and the aspects relevant to the present lecture are briefly developed below. The neutron is a particle, a nucleon, with no electrical charge, and a mass close to that of a proton. Similarly to the proton, the neutron possesses an internal structure and is comprised of three quarks. This quark structure is uud and udd, for the proton and neutron, respectively. How the electrical neutrality of a neutron comes about can be understood from the electrical charges of these quarks, which are $2e/3$ and $-e/3$ for u and d, respectively. The internal structure of the neutron is in principle of no further practical consequence for scattering applications, except that both the u and d quarks also possess a spin 1/2. As a consequence, both the neutron and the proton have a non-zero spin, which can after a lengthy calculation, be shown to be 1/2. Associated with this spin, both particles also possess a magnetic dipolar spin moment. The natural unit to express this moment is the nuclear magneton $\mu_N = \frac{e\hbar}{2m_\mathrm{p}}$, where m_p is the mass of the proton. Note that this moment contrasts with the electronic Bohr magneton, $\mu_\mathrm{B} = \frac{e\hbar}{2m_\mathrm{e}}$, where m_e is the mass of the electron, as it is much smaller, $\mu_\mathrm{N}/\mu_\mathrm{B} = m_\mathrm{e}/m_\mathrm{p} \simeq 1/1836$. Exactly as for the electron, there is a proportionality constant, the g-factor, which relates the magneton to the magnetic moment. For the electron, this constant $g_\mathrm{e} = 2{\cdot}(1{+}1/137{+}\cdots)$ is very close to 2, which has as a consequence that for the electron, with a spin $s = 1/2$, the magnetic moment $\mu_\mathrm{e} = g_\mathrm{e} \cdot s \cdot \mu_\mathrm{B} \simeq 1\mu_\mathrm{B}$. For the neutron and the proton, these constants are somewhat different, and can also be obtained from the lengthy calculation related to their internal structure mentioned above. With the spin $S = \pm 1/2$, the moments are:

$$\begin{aligned} \mu_\mathrm{p} &= g_\mathrm{p} \cdot S \cdot \mu_\mathrm{N} \simeq \pm 2.793 \mu_\mathrm{N}, \\ \mu_\mathrm{n} &= g_\mathrm{n} \cdot S \cdot \mu_\mathrm{N} \simeq \mp 1.913 \mu_\mathrm{N} = \pm \gamma_\mathrm{n} \mu_\mathrm{N}. \end{aligned} \tag{7.1}$$

where $\gamma_\mathrm{n} = -1.913$ is the gyromagnetic *factor* for the neutron. Note that γ_n is negative, $i.e.$ the magnetic moment is antiparallel to the spin. The spin and magnetic moment are thus intrinsically tied to each other, but in fact these properties lead to quite different behavior: the spin is relevant for the nuclear interaction and scattering of the neutron with other nuclei, whereas the magnetic moment is relevant for the interaction of the neutron with electronic magnetic moments in samples and with magnetic fields.

This lecture will give an introduction in the spin dependence of neutron scattering processes.

The nuclear spin dependent scattering length and how this dependence leads to spin incoherent scattering will first be introduced. Secondly, a first insight into magnetic interactions and scattering will be given. Thirdly, the different approaches to manipulate the neutron spin and the polarization of a neutron beam will be reviewed. Finally, some instrumental realizations for polarized neutron scattering will be presented. At the end of this lecture, understanding how the spin and magnetic properties of the neutron can be used in order to gain deeper insight in the materials under study must be achieved, in particular, how the nuclear coherent, spin incoherent, and magnetic scattering contributions can be experimentally separated. The readers should refer to Refs. [1–6] for more detailed insights and derivations. Essentially the discussion herein will be restricted to elastic scattering of the neutrons, and inelastic scattering will be mentioned only briefly when relevant.

7.2 Spin Dependent Interactions

The pseudo-potential for the scattering of a neutron by a single nucleus located at $\mathbf{R}$ describes the interaction with a point-like nucleus and is proporptional to the scattering length, b,

$$V(\mathbf{r}) = \frac{2\pi\hbar^2}{m} b\delta(\mathbf{r} - \mathbf{R}). \tag{7.2}$$

The matrix elements for scattering from the wavevector state $|\mathbf{k}\rangle$ to $\langle\mathbf{k}'|$ with this pseudo-potential for an ensemble of l nuclei with position $\mathbf{R}_l$ and scattering length b_l are

$$\langle\mathbf{k}'|V|\mathbf{k}\rangle = \frac{2\pi\hbar^2}{m} \sum_l b_l e^{\mathrm{i}\mathbf{Q}\mathbf{R}_l}, \tag{7.3}$$

and lead to the scattering law, see Chapter 4,

$$\frac{d\sigma}{d\Omega} = N\left(\overline{b^2} - \bar{b}^2\right) + \bar{b}^2 \sum_{ll'} e^{\mathrm{i}\mathbf{Q}(\mathbf{R}_l - \mathbf{R}'_l)} \tag{7.4}$$

where the first term on the right hand side is the isotope incoherent scattering that contain no phase information and the second term is the coherent scattering that contains the phase information.

We will now investigate the spin dependent scattering. For this purpose, we first consider a single isotope, with a nuclear spin $I \neq 0$. Before the scattering event, the spin of the neutron and the nucleus are in general randomly distributed. During the scattering process, the spin state J of the compound system comprised of the neutron and the nucleus must be considered, and there are (only) two possibilities for this spin state: either $J = J_+ = I + 1/2$ or $J = J_- = I - 1/2$, the former if the neutron and nuclear spins are parallel, the latter if they are antiparallel. As usual, the multiplicity for a spin state is $2J + 1$, and thus the multiplicities are $2I + 2$ and $2I$ for the J_+ and J_- compound states, respectively. The total number of configurations is the sum of the multiplicities and is thus $4I + 2$. Again assuming the statistical equiprobable distribution of all states, we obtain the probabilities p_+ and p_- for realizing the J_+ and J_- compound states:

$$p_+ = \frac{I+1}{2I+1}, \quad p_- = \frac{I}{2I+1}. \tag{7.5}$$

Distinguishing these two cases would be pointless if the scattering cross sections, or the scattering length, for both cases were identical. This is however not the case and for all isotopes with nuclei that have $I \neq 0$ the scattering length b_+ and b_- are found to be different [7]. As a consequence, for any such isotope the average and mean square average scattering lengths, $\overline{b}$ and $\overline{b^2}$ become (see pp. 4.11-4.15):

$$\begin{aligned} \overline{b} &= p_+ b_+ + p_- b_- = \frac{(I+1)b_+ + I b_-}{2I+1} = A, \\ \overline{b^2} &= \textstyle\sum_i p_i b_i^2 = p^+ b_+^2 + p^- b_-^2. \end{aligned} \tag{7.6}$$

For the scattering from an ensemble of particles, if this ensemble is comprised of a single isotope that possess a non-zero nuclear spin, the spin dependent scattering length has to be considered. The difference between b_+ and b_- will give rise to a new type of incoherent scattering, namely spin incoherent scattering, even for an ensemble comprised of a single isotope. This specific spin incoherent differential scattering cross section is obtained by combining Eqs. 7.4 and 7.6,

$$\frac{d\sigma}{d\Omega}_{\text{spin inco}} = N\frac{I(I+1)(b_+ - b_-)^2}{(2I+1)^2} = NB^2 I(I+1) = N b_{\text{inc}}^2, \tag{7.7}$$

where $B = (b_+ - b_-)/(2I+1)$ and we introduce b_{inc} the spin incoherent scattering amplitude. The specific (spin) coherent differential scattering cross section is in contrast,

$$\frac{d\sigma}{d\Omega}_{\text{coh}} = \overline{b}^2 \sum_{ll'} e^{i\mathbf{Q}(\mathbf{R}_l - \mathbf{R}'_l)} = A^2 \sum_{ll'} e^{i\mathbf{Q}(\mathbf{R}_l - \mathbf{R}'_l)} = b_{\text{coh}}^2 \sum_{ll'} e^{i\mathbf{Q}(\mathbf{R}_l - \mathbf{R}'_l)}, \tag{7.8}$$

where we introduce b_{coh} the (spin) coherent scattering amplitude. As usual, the total scattering cross sections are obtained as $\sigma_{\text{coh}} = 4\pi b_{\text{coh}}^2$ and $\sigma_{\text{inc}} = 4\pi b_{\text{inc}}^2$ for the (spin) coherent and spin incoherent scattering, respectively.

A first simple and important example to consider from the point of view of instrumentation is the scattering by vanadium. There is two stable vanadium isotopes, ^{50}V, with I=6 and 0.25% natural abundance, which we neglect in what follows, and ^{51}V, with I=7/2 and 99.75% natural abundance. For ^{51}V, $b_+ = 4.93(25)$ and $b_- = -7.58(28)$ fm. The probabilities for the two cases are $p_+ = 9/16$ and $p_- = 7/16$ and thus, we obtain the scattering lengths $b_{\text{coh}} = -0.54$ (exact: -0.4) and $b_{\text{inc}} = 6.21$ fm (exact: 6.35). The corresponding cross sections are $\sigma_{\text{coh}} = 2\,\text{fm}^2 = 0.02\,\text{barn}$, and $\sigma_{\text{inc}} = 5.07\,\text{barn}$. Bragg scattering from vanadium is hence difficult to observe, as the incoherent scattering provides a large background. However this large isotropic background is very useful to calibrate the detector efficiency and solid angle, in particular in multi detector instruments. A second important example is scattering from hydrogen, which has been detailed in Chapter 4. Hydrogen has the largest incoherent scattering cross section of all elements, ~ 80 barn, and this large cross section can be exploited for spectroscopy in hydrogen containing materials.

The spin incoherent scattering, exactly as the (spin coherent) isotopically incoherent scattering, does not contain any phase information. This however does not mean that no useful information can be extracted. Incoherent scattering always gives only information about single particle behavior, $i.e.$ the self-correlation function, see for example Chapter 11.2, and not about specific arrangement of atoms, $i.e.$ the pair-correlation function. The spin incoherent scattering can thus be used in order to gain insight for example about diffusion of single atoms, in particular hydrogen. A second use is, that in samples that contain both spin incohrent and coherent scattering,

the spin incoherent scattering can be used as internal calibration for absolute intensity measurements, provided these contributions can be determined separately by polarization analysis, see below and Section 4.

Summarizing, there is thus two sources for incoherent scattering, namely isotopic and spin incoherent scattering, and one might wonder why it is important to differentiate them, as both give rise to isotropic scattering that contains no phase information. A first difference is that it is possible to reduce or enhance isotopic incoherent scattering by isotopic substitution, whereas this is impossible for spin incoherent scattering (unless one were able to align all nuclear spins in the sample which is a daunting but not impossible task [8]). The second difference concerns the effect of the scattering of a neutron by a nucleus with $I \neq 0$ on the *neutron* spin. In order to investigate this effect we need to consider the scattering amplitude and matrix elements for spin dependent scattering

$$A(\mathbf{Q}) = \langle \mathbf{k}' S'_z | A + B\hat{\boldsymbol{\sigma}} \cdot \hat{\mathbf{I}} | \mathbf{k} S_z \rangle, \tag{7.9}$$

with A and B as defined in 7.6 and 7.7, and with $\hat{\boldsymbol{\sigma}}$ and $\hat{\mathbf{I}}$ the neutron and nuclear spin operators. In what follows, we will not explicitly write out the wave vector dependence of these elements. We can use the z projected spin states for the neutron, which we write $\langle + |$ and $\langle - |$ without sacrificing generality. For nuclei with $I = 0$ we see that $A(\mathbf{Q}) = \langle S'_z | \overline{b} | S_z \rangle = \overline{b} \langle S'_z | S_z \rangle$. Only the terms with same initial and final neutron spin state are non zero, as $\langle + | + \rangle = \langle - | - \rangle = 1$ and $\langle + | - \rangle = \langle - | + \rangle = 0$. This is not surprising, considering the conservation of total angular momentum.

In the general case, $I \neq 0$, angular momentum can be exchanged between the nucleus and the neutron, and the non zero matrix elements are

$$\begin{array}{ll} A(\mathbf{Q})^{\text{NSF}} = A + BI_z & \text{for the ++ and -- case,} \\ A(\mathbf{Q})^{\text{SF}} = B(I_x + \mathrm{i}I_y) & \text{for the +- and -+ case,} \end{array} \tag{7.10}$$

where NSF and SF denote the spin-flip and non spin-flip scattering amplitude, and I_x, I_y, and I_z are the x, y, and z components of the spin of the nucleus. The derivation of Eq. 7.10 is based on the Pauli spin matrix algebra used for the neutron spin operator, see Appendix A. Note that a flip of the neutron spin occurs only if the nuclear spin is not parallel to the neutron spin, which, as will be discussed later, can be exploited to separate spin incoherent scattering experimentally.

A final question concerns the spin-flip process. As mentioned above, in such a process angular momentum is exchanged. But is there also an exchange in energy? In general this is not the case because the nuclear spin states have all the same energy. However, at low temperature and in some magnetic materials, there might be a splitting in the nuclear spin states through hyperfine interactions. In this case the spin-flip scattering will involve a small transfer in energy between the nucleus and the neutron, and inelastic scattering in the μeV range is observed. This provides an elegant method to measure hyperfine fields [9, 10].

7.3 Magnetic Interactions

We will now consider the interaction of the neutron with magnetic fields and thus also the magnetic dipolar moments originating from unpaired electronic spins. For this purpose, the magnetic dipole moment of the neutron $\boldsymbol{\mu}$ will be considered. The existence of this purely

magnetic, $i.e.$ non nuclear, interaction of the neutron is extremely useful both in order to manipulate the polarization of a neutron beam and in order to determine the magnetic structure of a material, $i.e.$ the arrangements of the magnetic moments in a sample. Neutron scattering can thus be used as a microscopic magnetometer, with a resolution comparable to the wavelength, that reveals, for example, the onset of magnetic order or the distribution of magnetic moments within nanoparticles.

The dipolar interaction potential of a neutron with the magnetic field is given by $V_M = -\boldsymbol{\mu} \cdot \mathbf{B}$ where $\mathbf{B}$ is the magnetic induction, generated $e.g.$ by electrons in a sample or by magnetic coils. The magnetic interaction *tends* to align the neutron moment within the magnetic induction in order to minimize the interaction energy. However, we know from classical mechanics that the magnetic moment is related to $\mathbf{L}$, the angular momentum as $\boldsymbol{\mu} = \gamma \mathbf{L}$, where γ is the gyromagnetic ratio. Thus, the torque $\mathbf{G} = \boldsymbol{\mu} \times \mathbf{B}$, which is equal to the time derivative of the angular momentum $\mathbf{G} = \dot{\mathbf{L}}$, will lead to precession of the angular momentum and of the magnetic moment and the spin. Accordingly

$$\dot{\boldsymbol{\mu}} = \gamma \boldsymbol{\mu} \times \mathbf{B}. \tag{7.11}$$

The gyromagnetic *ratio* for the neutron, not to be confused with the gyromagnetic factor, is given by

$$\gamma = 2\gamma_{\mathrm{n}}\mu_{\mathrm{N}}/\hbar = -1.83 \cdot 10^{8}\,\mathrm{s}^{-1}\mathrm{T}^{-1} \tag{7.12}$$

or, in cgs units,

$$\gamma/2\pi = -2916\,\mathrm{Hz/Oe}. \tag{7.13}$$

The Larmor precession rate is given by $\boldsymbol{\omega} = -\gamma \mathbf{B}$. Note that in Eq. 7.11, the time derivative of the moment is always perpendicular to the moment, which indeed indicates a precession, as only the direction but not the magnitude of the moment changes with time. In contrast, the force exerted on a dipole is given by $\mathbf{F} = (\boldsymbol{\mu} \cdot \nabla)\mathbf{B}$ and is zero if the magnetic field is homogeneous.

In order to establish how the presence of magnetic moments in a sample leads to magnetic neutron scattering we must now consider the magnetic induction generated by the spin and orbital moment of an electron, see Fig. 7.1. The dipole field of the electronic spin moment, $\boldsymbol{\mu}_e = -2\mu_B \cdot \hat{\mathbf{s}}$, is

$$\mathbf{B}_S = \boldsymbol{\nabla} \times \left(\frac{\boldsymbol{\mu}_e \times \mathbf{R}}{R^3} \right) \tag{7.14}$$

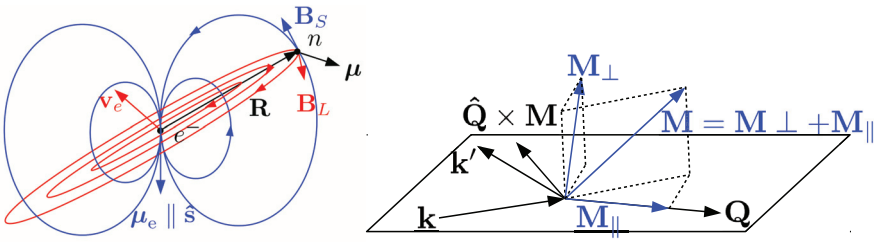

Fig. 7.1: *Left: electronic dipolar field lines and the corresponding induction,* $\mathbf{B}_S$*, in blue, and the field lines and induction,* $\mathbf{B}_L$*, associated with the orbital motion, in red. Right: decomposition of the magnetization vector* $\mathbf{M}$ *in its components parallel and perpendicular to the scattering vector* $\mathbf{Q}$*.*

whereas the magnetic induction generated by the electronic current related tothe orbital motion of the electron is obtained from the Biot and Savard law

$$\mathbf{B}_L = -\frac{e}{\mathrm{c}}\frac{\mathbf{v}_e \times \mathbf{R}}{R^3}. \tag{7.15}$$

The scattering potential to consider is thus

$$V_M = -\boldsymbol{\mu}\cdot(\mathbf{B}_S + \mathbf{B}_L) = -\boldsymbol{\mu}\cdot\left[\boldsymbol{\nabla}\times\left(\frac{\boldsymbol{\mu}_e\times\mathbf{R}}{R^3}\right) - \frac{e}{\mathrm{c}}\frac{\mathbf{v}_e\times\mathbf{R}}{R^3}\right]. \tag{7.16}$$

The derivation of the scattering law is quite lengthy and the reader is referred to Ref. [1] for details. It leads to

$$\frac{d\sigma}{d\Omega}_{\mathrm{mag}} = (\gamma_{\mathrm{n}} r_0)^2 \left|\frac{1}{2\mu_{\mathrm{B}}}\langle S_z'|\hat{\boldsymbol{\sigma}}\cdot\mathbf{M}_\perp(\mathbf{Q})|S_z\rangle\right|^2, \tag{7.17}$$

where r_0 is the classical electron radius, and the important quantity to consider is the magnetization, $i.e.$ the density of magnetic moments, in reciprocal space, $\mathbf{M}(\mathbf{Q})$, which is obtained as the Fourier transformation of the magnetization in real space $\mathbf{M}(\mathbf{R})$,

$$\mathbf{M}(\mathbf{Q}) = \int_{-\infty}^{\infty} \mathbf{M}(\mathbf{R}) e^{\mathrm{i}\mathbf{Q}\cdot\mathbf{R}} d\mathbf{R}. \tag{7.18}$$

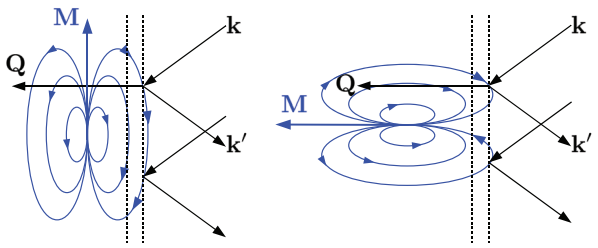

Fig. 7.2: *The magnetic field line configuration for* $\mathbf{M}$ *perpendicular, left, and parallel, right, to the scattering vector* $\mathbf{Q}$ *give rise to constructive and destructive interference, respectively.*

According to Eq. 7.17, only the component of the magnetization which is perpendicular to the scattering vector contributes to the scattering cross section. The geometrical construction in the right of Fig. 7.1 indicates how this component is obtained as

$$\mathbf{M}_\perp = \hat{\mathbf{Q}}\times\mathbf{M}(\mathbf{Q})\times\hat{\mathbf{Q}}, \tag{7.19}$$

where $\hat{\mathbf{Q}} = \mathbf{Q}/Q$ is the unitary scattering vector. This a priori somewhat surprising scattering cross section can be understood as illustrated in Fig. 7.2, because the components of any magnetic dipole field parallel to the scattering vector will cancel out. In contrast to spin or isotope incoherent scattering, the magnetic scattering is fundamentally anisotropic with respect to $\mathbf{M}$, and only the component perpendicular to $\mathbf{Q}$ is observable. Fig. 7.3 beautifully illustrates this. The intensity is collected on an area detector and is given by the product of the magnetic and nuclear scattering amplitude. Because the sample was magnetized in the horizontal direction,

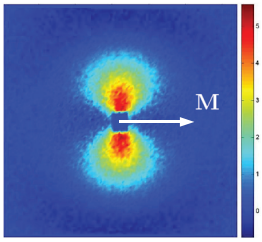

Fig. 7.3: *The product of the magnetic and nuclear scattering amplitude was obtained in a polarized small angle scattering experiment on a collection of magnetized nanoparticles. In the direction parallel to the sample magnetization the magnetic scattering vanishes. (Adapted from Ref. [11]; data obtained at the ILL D22 instrument from the (I^+-I^-) term in a half-polarized experiment.)*

the magnetic scattering vanishes in this direction and intensity is observed only for scattering vectors that have a vertical component.

According to Eqs. 7.17 and 7.18 it is thus in principle possible to determine the magnetization $\mathbf{M}(\mathbf{R})$ microscopically, which goes beyond the informations that can be obtained by macroscopic magnetometry measurements.

Before investigating the detailed consequences of the magnetic scattering, it is important to estimate its order of magnitude. If we consider a single unpaired electron with spin $s = 1/2$ and thus replace the matrix element in Eq. 7.17 by a $1\,\mu_\mathrm{B}$ moment, we obtain a scattering length of $\gamma_\mathrm{n} r_0/2 = 2.696$ fm and a cross section $\sigma_\mathrm{mag} = 0.91$ barn. These values are quite comparable to typical nuclear scattering lengths and cross sections. For x-ray scattering the magnetic scattering cross section is between 6 and 9 orders of magnitude smaller than the structural or charge scattering, and although this can be partly mitigated by using resonance scattering techniques, magnetic neutron scattering thus clearly appear at first glance as being at an advantage for investigating magnetism.

We now need to consider the scattering from an ensemble of atoms, or more precisely, here, only their unpaired electrons. First, we neglect the orbital moment ($L = 0$) and consider pure spin scattering such as for spherically symmetric ions, Fe^{3+}, Mn^{2+}, or ions with fully quenched orbital moment. Ignoring itinerant electrons, we simplify further to an ionic crystal where the electrons are in direct vicinity of the atoms and model these atoms as illustrated in Fig. 7.4. The spin magnetization, *i.e.* the spin moment density, is

$$\mathbf{M}(\mathbf{R}) = -2\mu_\mathrm{B} \cdot \hat{\mathbf{s}}(\mathbf{R}) = -2\mu_\mathrm{B} \sum_{ik} \delta\left(\mathbf{R} - \mathbf{r}_{ik}\right) \cdot \hat{\mathbf{s}}_{ik}. \tag{7.20}$$

where $\hat{\mathbf{s}}_{ik}$ is the spin operator of the k^{th} electron of the i^{th} atom, located at $\mathbf{r}_{ik}$ in the coordinate system, and at $\mathbf{t}_{ik}$ with respect to the nucleus. The Fourier transform of the magnetization is

$$\mathbf{M}(\mathbf{Q}) = -2\mu_\mathrm{B} \sum_{ik} e^{\mathrm{i}\mathbf{k}\cdot\mathbf{r}_{ik}} \cdot \hat{\mathbf{s}}_{ik} = -2\mu_\mathrm{B} \sum_{i} e^{\mathrm{i}\mathbf{Q}\cdot\mathbf{R}_i} \sum_{k} e^{\mathrm{i}\mathbf{Q}\cdot\mathbf{t}_{ik}} \cdot \hat{\mathbf{s}}_{ik}, \tag{7.21}$$

Because the electrons are described by a probability density, the expectation value for the quantum mechanical state must be considered, as well as an averaging over the thermodynamic

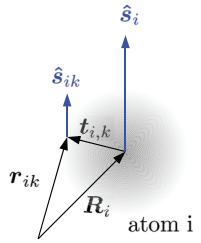

Fig. 7.4: *The electrons of atom i are located around its position $\mathbf{R}_i$ and contribute to the total spin $\hat{\mathbf{s}}_i$.*

ensemble representative for the sample. Thus, the spin density, $\rho_s(\mathbf{R})$, must be Fourier transformed and the magnetic (spin) from factor $f_m(\mathbf{Q})$ is obtained as $f_m(\mathbf{Q}) = \int_{atom} \rho_s(\mathbf{R}) e^{\mathrm{i}\mathbf{Q}\cdot\mathbf{R}} d\mathbf{R}$ and the magnetization is

$$\mathbf{M}_s(\mathbf{Q}) = -2\mu_\mathrm{B} \cdot f_m(\mathbf{Q}) \cdot \sum_i e^{\mathrm{i}\mathbf{Q}\cdot\mathbf{R}_i} \cdot \langle \hat{\mathbf{s}}_i \rangle \tag{7.22}$$

where we again simplified and considered a single type of atoms in order to factorize the form factor.

Finally, using Eq. 7.17 the differential cross section is given by

$$\frac{d\sigma}{d\Omega}_{\mathrm{mag}} = (\gamma_\mathrm{n} r_0)^2 \left| f_m(\mathbf{Q}) \sum_i \langle \hat{\mathbf{s}}_{i\perp} \rangle e^{\mathrm{i}\mathbf{Q}\cdot\mathbf{R}_i} \right|^2 . \tag{7.23}$$

In sharp contrast with nuclear scattering, magnetic neutron scattering depends on a form factor in a similar way than for x-ray scattering. This form factor comes about because the scattering no longer occurs on a point-like nucleus but on an extended electronic (spin) cloud, and the larger this cloud is, the faster the form factor drops in reciprocal space. The form factor thus reveals the distribution of the spin and orbital magnetization. Because the unpaired electrons are typically in the outer electronic shells, such as the 3d shell for the first row of transition metal or the 4f shell for the rare earth elements, the magnetic form factor drops faster than for the whole electronic cloud as seen by x-ray scattering, see Fig. 7.5. If an orbital moment is present the magnetic form factor is significantly more complicated, see Appendix B.

Exactly as for spin dependent scattering in the previous section, the spin of the neutron explicitly enters the magnetic scattering cross section. It is thus also important to establish how angular momentum can be exchanged between the sample and the neutron through magnetic scattering, $i.e.$ understand in what conditions the spin of the neutron is flipped by magnetic interactions. For this purpose we consider the magnetic scattering amplitude:

$$A(\mathbf{Q}) = \langle S'_z | - \frac{\gamma_\mathrm{n} r_0}{2\mu_\mathrm{B}} \hat{\boldsymbol{\sigma}} \cdot \mathbf{M}_\perp(\mathbf{Q}) | S_z \rangle = -\frac{\gamma_\mathrm{n} r_0}{2\mu_\mathrm{B}} \sum_\alpha \langle S'_z | \underline{\hat{\boldsymbol{\sigma}}}_\alpha | S_z \rangle \mathbf{M}_{\perp\alpha}(\mathbf{Q}), \tag{7.24}$$

where the sum over α stands for the x, y, and z directions, and $\underline{\hat{\boldsymbol{\sigma}}}_\alpha$ are the Pauli matrices, see Appendix A. Considering all possibilities for the neutron spin state before and after the

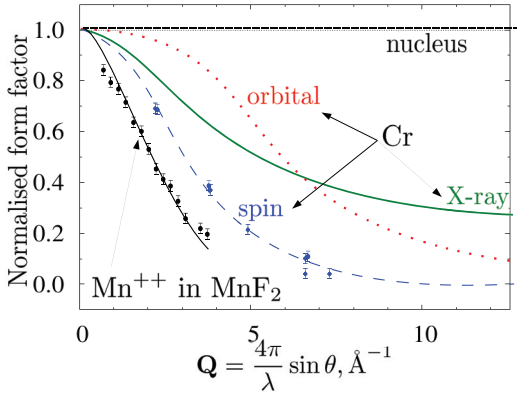

Fig. 7.5: *The form factor of Cr metal for nuclear, spin moment, and orbital moment neutron scattering, and for x-ray charge scattering, adapted from Ref. [12] and of Mn^{2+} ions in MnF_2 adapted from Ref. [2]. Curves and points indicate theory and experiment, respectively.*

scattering process, and by decomposing $\mathbf{M}_\perp(\mathbf{Q})$ in its components we obtain

$$A(\mathbf{Q}) = -\frac{\gamma_\mathrm{n} r_0}{2\mu_\mathrm{B}} \cdot \begin{cases} \mathbf{M}_{\perp\mathbf{Q},z} & \text{for the ++ NSF case,} \\ -\mathbf{M}_{\perp\mathbf{Q},z} & \text{for the -- NSF case,} \\ \mathbf{M}_{\perp\mathbf{Q},x} - \mathrm{i}\mathbf{M}_{\perp\mathbf{Q},y} & \text{for the +- SF case,} \\ \mathbf{M}_{\perp\mathbf{Q},x} + \mathrm{i}\mathbf{M}_{\perp\mathbf{Q},y} & \text{for the -+ SF case.} \end{cases} \tag{7.25}$$

Note that exactly as for spin incoherent scattering, a flip of the neutron spin occurs only if there is a component of $\mathbf{M}_{\perp\mathbf{Q}}$ which is not parallel to the neutron spin. Again, as will be discussed later, this can be exploited in order to separate magnetic scattering experimentally. A simple, interesting, and important case is achieved when the neutron spin is parallel to the scattering vector: in this case $\mathbf{M}_{\perp\mathbf{Q}}$ is always perpendicular to the spin, and thus all magnetic scattering will involve a spin flip.

The total scattering amplitude $A(\mathbf{Q})$ thus consist of two parts, the nuclear and the magnetic scattering and can be simply written as

$$A(\mathbf{Q}) = N(\mathbf{Q}) + \hat{\boldsymbol{\sigma}} \cdot M_\perp(\mathbf{Q}) \tag{7.26}$$

where $N(\mathbf{Q})$ is the nuclear scattering amplitude and contains the nuclear coherent, the isotope incoherent, and the spin incoherent part. The derivation of the resulting scattering cross sections in the general case of a polarized neutron beam is given in Appendix C.

A final question concerns the spin-flip process, and again, in such a process angular momentum is exchanged and potentially there is also an exchange in energy. In ordered magnetic materials, whenever the neutron undergoes a spin-flip, $\Delta S = \mp 1$, there must also be a change in the total electronic angular momentum, J, given by $\Delta J = \pm 1$, which typically creates a magnetic excitation, a so called magnon. Inelastic magnetic scattering can thus be used in order to map out the spectrum of magnetic excitations. In paramagnets a similar process is possible, but the excitations are not well defined in energy and the spectrum is strongly broadened out. Generally

speaking, inelastic magnetic scattering will reveal any magnetic fluctuation perpendicular to the scattering vector.

7.4 Polarization and Separation Rules

We have seen in the two previous sections that both spin incoherent and magnetic scattering can lead specifically to a flip of the neutron spin upon scattering. It is possible to take advantage of this specificity if this spin flip process can be experimentally measured. In order to do so, devices are required to detect and manipulate the neutron spin. For a schematic instrument, this is solved by measuring the polarization of the neutrons scattered by the sample impinged upon by an initially polarized neutron beam. An example of such instrument is given in Fig. 7.6.

The polarization of a neutron beam, $\mathbf{P}$, is defined by the expectation value of the neutron spin operator, $\hat{\mathbf{S}}$,

$$\mathbf{P} = \langle 2\hat{\mathbf{S}} \rangle. \tag{7.27}$$

An equivalent alternative definition is that the polarization, P, with respect to the quantization axis is given by the number of neutrons with spin up and down states, $n_\uparrow$ and $n_\downarrow$, respectively, as

$$P = \frac{n_\uparrow - n_\downarrow}{n_\uparrow + n_\downarrow}. \tag{7.28}$$

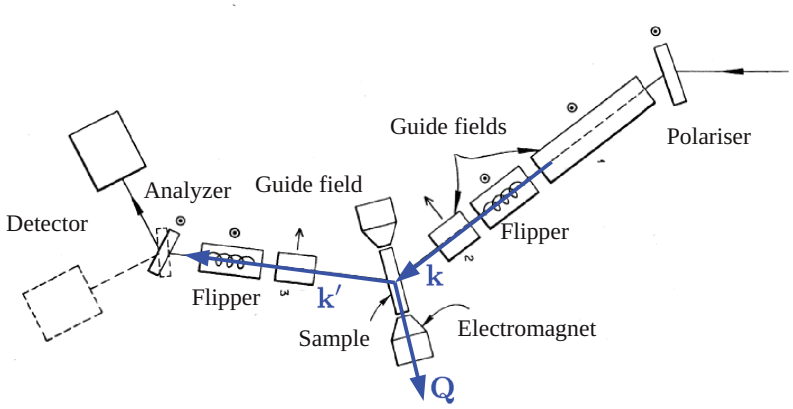

Fig. 7.6: *Schematic setup for a triple axis polarized neutron scattering experiment with polarization analysis. The field generated by the electromagnet could be used to align a sample either in a horizontal or vertical magnetic field (Adapted from Ref. [2]).*

In order to experimentally realize a polarized neutron beam a polarizing device is required, as the neutrons extracted from the moderator, see Chapter 2.3, are initially unpolarized, *e.g.* $P = 0$. In analogy with optics, there are two important ways to polarize the beam; either the neutrons with the 'wrong' polarization are absorbed, or these neutrons are separated and directed to another direction. In practice, there are three types of polarizing devices:

a) filters that absorb the neutrons in one of the spin states and transmit the others. In practice this can be realized with polarized ^{3}He gas cells, where the nuclear spins are kept aligned. The absorption cross section is very large for neutrons with the spin anti-parallel to the nuclear spin, and thus only the neutrons with the spin parallel to the ^{3}He nuclear spins are transmitted.

b) super-mirrors, which show total reflection for one spin state only. These mirrors are realized as magnetic layered structures, see Chapters 9 and 10.

c) Bragg scattering from a crystal monochromator, $e.g.$ Heusler alloy crystals, where a reflection is chosen such that the magnetic and nuclear scattering interfere destructively for one spin state and constructively for the other, see Appendix C.

When constructing a neutron scattering instrument, the choice of the polarizer will depend on the specific design. Bragg scattering monochromators reach excellent polarization but often transport only a small wavelength band and divergence of the neutron beam. Super mirrors achieve excellent polarization in a wider band but perform best only for long wavelength, $i.e.$ cold neutrons. ^{3}He filters perform very well for thermal neutrons and their efficiency is tunable by adjusting the pressure in the cell. At the end of the day, however, a compromise must always be found between the degree of polarization that is required and the intensity of the neutron beam. As will be discussed below, it is not necessary to have a perfect polarization, as corrections can be made to account for $P < 1$.

Having now achieved the polarization process, the beam must be transported to the sample while preserving the polarization. In principle, establishing a zero field region by screening any magnetic field disturbance would work, see Fig. 7.9, but in practice, it is customary to use a magnetic guide field, the field being parallel or antiparallel to $\mathbf{P}$. The field should be fairly homogeneous in order to avoid precession with unwanted angular components. Such guide fields are typically weak enough not to modify the sample magnetization, but strong enough, typically $\sim$1 mT, to avoid adverse effects from the earth magnetic field or other stray fields. Depending on whether the polarizer is located far or near from the sample, one would use polarized neutron guides, adding to the cost of the instrument, or simple guide fields generated by magnetic coils. The advantage of the former is that the neutrons with the wrong polarization are absorbed far from the sample and do not contribute to neutron and radiation background.

In order to manipulate the direction of the polarization, as required for measuring polarization components in different directions, variations of the guide field can be used. If the field changes slowly, the neutrons, moving with a velocity

$$v(\lambda) = 3956\,\text{m/s} \cdot \text{Å}/\lambda, \tag{7.29}$$

will keep their precession motion along a magnetic field that varies slowly in space. This slow precession should be smaller than the Larmor precession in the guide field. The slow field change is used to align the polarization in a particular direction at the sample position. If the field changes rapidly, the polarization does not follow and the neutrons will start to precess in the new field. A specific case of interest is when two guide fields have opposite directions, as can be achieved by separating the fields by strong currents in a metallic sheet. The polarization that was originally parallel to the first guide field would then end up antiparallel to the second guide field.

An alternative way for modifying the direction of the polarization is the use of flippers, see Fig. 7.7. The neutrons will start to precess immediately if they are subject to a field (or a field com-

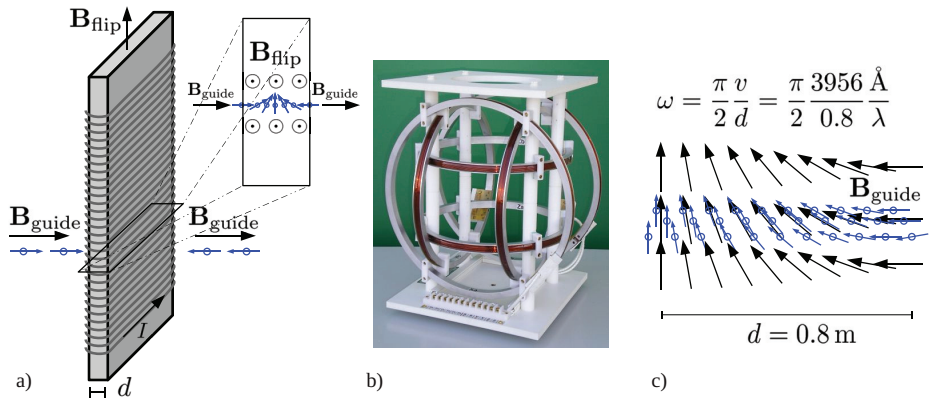

Fig. 7.7: *(a) A neutron spin flipper. Wires are typically Al in order to minimize absorption. Adapted from Ref. [3]. (b) A set of xyz Helmholtz coils used for adiabatically guiding the neutron polarization in an arbitrary direction at the sample position [Source: http://www.serviciencia.es]. (c) Neutrons adiabatically follow a field which rotates by $\pi/2$.* $\mathbf{B}$ *must be sufficient strong so that $\omega \ll \omega_L$ [3].*

ponent) perpendicular to their polarization. By defining a region in space where the neutrons are subject to a perpendicular field, it is thus possible to have them precess by a defined angle. One can, for example, use a long rectangular coil, with thickness d to make a homogeneous field, $H = n \cdot I$ where n is the linear wire density and I the current, parallel to the coil axis and perpendicular to the neutron polarization. During the time the neutrons spend in the coil, $t = d/v$, they precess around this field. A rotation of 180° or π radian is realized when

$$\omega \cdot t = -\gamma B \cdot d/v = \pi. \tag{7.30}$$

Accordingly for such a π-flipper, by combining Eqs. 7.13, 7.29, and 7.30,

$$B = \frac{\pi}{d}(\,\text{m/s} \cdot \text{Å}/\lambda)/(2916 \cdot 2\pi\,\text{Hz/Oe}) = \frac{67.83}{d\lambda}\,\text{cm Å Oe}. \tag{7.31}$$

For a 1 cm coil and a wavelength of 2.2 Å, a field of 30 Oe or 3 mT is thus required for a rotation of 180°. It is crucial to note that for a given width of the coil and a given field the π-flip is perfect only for one particular wavelength, $i.e.$ for a monochromatic beam. Using the same approach, it is also possible to generate a π/2-flip. After such a flipper the polarization will be perpendicular to the guide field, and thus precess in a plane perpendicular to the guide field. Such precession mode can be use for example in spin echo spectrometers, see Fig. 7.12. Spin flippers can also be build by using radio frequency resonators, where the time dependence of the fields is the control parameter.

A final element in our schematic instrument is the detector for the polarization of the neutron beam. Again in analogy to optics, this is easily solved by combining a polarizer, which we simply call analyzer as it comes second, with a general (unpolarized) detector. Possible physical realizations are a Heusler alloy crystal that both selects a polarization and deflect the beam towards the detector, see Fig. 7.6, a ^{3}He cell placed in front of the detector, or a set of supermirrors that only transmits a given polarization, as in Figs. 7.10 and 7.11.

We now need to link what we have learned about the scattering cross sections with what is measured in an experiment. The experimentally accessible quantities are the intensities $\frac{d\sigma}{d\Omega}^{\text{NSF}}_{x,y,z}$ and $\frac{d\sigma}{d\Omega}^{\text{SF}}_{x,y,z}$, which can be obtained $e.g.$ by using a beam polarized in z direction, passing through a π-flipper that can be on or off, then having a guide field (slowly) bring the polarization in either x, y, or z direction at the sample and back to the z direction after the scattering, and finally measuring the intensity after an analyzer.

For soft matter investigations or when there is no magnetism, two measurements are sufficient: NSF and SF in one direction. For colinear magnetism, three measurements at least are required, but often six are done for completeness (SF and NSF in x,y, and z). In the most general case more terms, up to 18, that involve mixing the initial and final polarization directions can be obtained ($e.g.$ from z to y), for example by using zero field sample environment [13] or a spin precession technique [14].

Having established a workable idealized instrument, that allows one to measure the polarization of the scattered neutrons, we can use the relations Eqs. 7.10 and 7.25 in order to experimentally separate the different contributions and thus measure the spin incoherent, the coherent ($i.e.$ isotopically incoherent and nuclear coherent), and the magnetic scattering.

For the spin incoherent scattering, the expectation values and squared expectation values of I_x, I_y, and I_z are relevant. The nuclear spin orientation is in general random, with two notable exceptions, namely (dynamic) nuclear polarization [8] at low temperature and polarized ^{3}He cells, exceptions that we will neglect in what follows. Accordingly, the expectation values for stochastic nuclear spin orientation are

$$\langle I_x\rangle = \langle I_y\rangle = \langle I_z\rangle = 0, \tag{7.32}$$

and for the square operators:

$$\langle I_x^2\rangle = \langle I_y^2\rangle = \langle I_z^2\rangle = \frac{1}{3}\langle I(I+1)\rangle. \tag{7.33}$$

By considering separately the case for the z, x, and y nuclear spin orientations, and then summing up the x and y cases that give rise to spin flip scattering, we obtain that

$$\frac{d\sigma}{d\Omega}^{\text{NSF}}_{\text{spin inco}} = \tfrac{1}{3}NB^2\langle I(I+1)\rangle, \quad \frac{d\sigma}{d\Omega}^{SF}_{\text{spin inco}} = \tfrac{2}{3}NB^2\langle I(I+1)\rangle. \tag{7.34}$$

First, we consider the case when there is no magnetic scattering involved, $i.e$ isotropic scattering from the point of view of polarization. The measurement of $\frac{d\sigma}{d\Omega}^{\text{NSF}}_{z}$ and $\frac{d\sigma}{d\Omega}^{\text{SF}}_{z}$ is sufficient (consider that the background has been subtracted). The NSF differential cross section corresponds to the coherent scattering plus one third of the spin incoherent scattering, whereas the SF differential cross section corresponds to two thirds of the spin incoherent scattering, see Eqs. 7.10 and 7.34. The different contributions can thus be obtained by

$$\begin{aligned} \frac{d\sigma}{d\Omega}_{\text{spin inco}} &= \frac{3}{2}\frac{d\sigma}{d\Omega}^{\text{SF}}, \\ \frac{d\sigma}{d\Omega}_{\text{coh}} &= \frac{d\sigma}{d\Omega}^{\text{NSF}} - \frac{1}{2}\frac{d\sigma}{d\Omega}^{\text{SF}}. \end{aligned} \tag{7.35}$$

Second, considering now the possibility for magnetic scattering, it is required to distinguish the cases where the magnetization is perpendicular and parallel to the scattering vector. We will chose the coordinates such that the scattering vector is in a horizontal plane and in the x direction, and the z direction is vertical. Obviously, according to Eq. 7.17, the component of the sample magnetization parallel to the scattering vector will not contribute to the scattering, that is, in this case $\mathbf{M}_x$ is not accessible. As further simplification we will consider that if the material is ferromagnetic, a sufficiently strong field is applied in order to saturate the moments and to remove domain boundaries that would depolarize the beam, and we neglect possible magnetic chirality.

A first method to determine the magnetic scattering is the so-called $\|$-$\perp$ method. Consider the spin-flip and non spin-flip intensities for the two cases where the polarization (or the applied guide field) is first parallel to $\mathbf{Q}$, $i.e$ in x direction and parallel to $\mathbf{M}_\perp(\mathbf{Q})$, and second perpendicular to $\mathbf{Q}$ and in z direction. The scattering intensities are then

Polarization/Field	Spin-flip	Non spin-flip
$\mathbf{P} \parallel x \parallel Q$	$\frac{2}{3}\frac{d\sigma}{d\Omega}_{\text{inc}} + bg + \frac{d\sigma}{d\Omega}^{\mathbf{M}_y^\perp}_{\text{mag}} + \frac{d\sigma}{d\Omega}^{\mathbf{M}_z^\perp}_{\text{mag}}$	$\frac{d\sigma}{d\Omega}_{\text{coh}} + \frac{1}{3}\frac{d\sigma}{d\Omega}_{\text{inc}} + bg$
$\mathbf{P} \parallel z \perp Q$	$\frac{2}{3}\frac{d\sigma}{d\Omega}_{\text{inc}} + bg + \frac{d\sigma}{d\Omega}^{\mathbf{M}_y^\perp}_{\text{mag}}$	$\frac{d\sigma}{d\Omega}_{\text{coh}} + \frac{1}{3}\frac{d\sigma}{d\Omega}_{\text{inc}} + bg + \frac{d\sigma}{d\Omega}^{\mathbf{M}_z^\perp}_{\text{mag}}$

(7.36)

The z component of the magnetization is thus readily obtained by

$$\frac{d\sigma}{d\Omega}^{\mathbf{M}_z^\perp}_{\text{mag}} = \frac{d\sigma}{d\Omega}^{\text{NSF}}_{\perp} - \frac{d\sigma}{d\Omega}^{\text{NSF}}_{\parallel} = \frac{d\sigma}{d\Omega}^{\text{SF}}_{\parallel} - \frac{d\sigma}{d\Omega}^{\text{SF}}_{\perp} . \tag{7.37}$$

where interestingly all contributions that are not of magnetic origin cancel out, as they do not depend on the direction of the guide field or the neutron polarization [15]. This relation is particularly useful for single crystals when the sample is placed in the beam with the moments in z direction, or for powder samples. In powders $|\mathbf{M}_x| = |\mathbf{M}_y| = |\mathbf{M}_z| = \frac{1}{3}|\mathbf{M}|$. Note that the magnetic scattering intensities are proportional to the $square$ of the $\mathbf{M}$ components, and that in the above derivation we have omitted to explicitly write out the magnetic form factor. The total paramagnetic magnetic scattering cross section is actually given by $\sigma_{\text{mag}} = \sigma_{\text{mag}}^{\mathbf{M}_y^\perp} + \sigma_{\text{mag}}^{\mathbf{M}_z^\perp} = 2 \cdot \sigma_{\text{mag}}^{\mathbf{M}_z^\perp}$ and not $3 \cdot \sigma_{\text{mag}}^{\mathbf{M}_z^\perp}$, as one component is always hidden. This $\|$-$\perp$ method was developed, see Fig. 7.13 of Exercise 7.6, by Moon *et al.* in a seminal paper [2] and used to separate the paramagnetic scattering of MnF_2.

A second method to determine the magnetic scattering is used in the case of multi-detector instruments where the condition of $\mathbf{P} \parallel \mathbf{Q}$ cannot be fulfilled simultaneously for all detector angles. We assume here that $\mathbf{P} \perp \mathbf{Q}$ can be fulfilled by choosing $\mathbf{P} \parallel z$, $i.e.$ all detectors are in the horizontal scattering plane. An expression similar to Eq. 7.36 can be obtained [16] for paramagnetic scattering, $i.e.$ with $\langle M_x^2 \rangle = \langle M_y^2 \rangle = \langle M_z^2 \rangle$, but requires to measure the polarization both in the x and y directions with the strict condition that $x \perp y$, so that $\cos^2\alpha + \sin^2\alpha = 1$, where α is the angle between x and $\mathbf{Q}$. Both for the spin-flip and non spin-flip channel we have

$$\frac{d\sigma}{d\Omega}_{\perp} + \frac{d\sigma}{d\Omega}_{\parallel} = \frac{d\sigma}{d\Omega}_{x} + \frac{d\sigma}{d\Omega}_{y} . \tag{7.38}$$

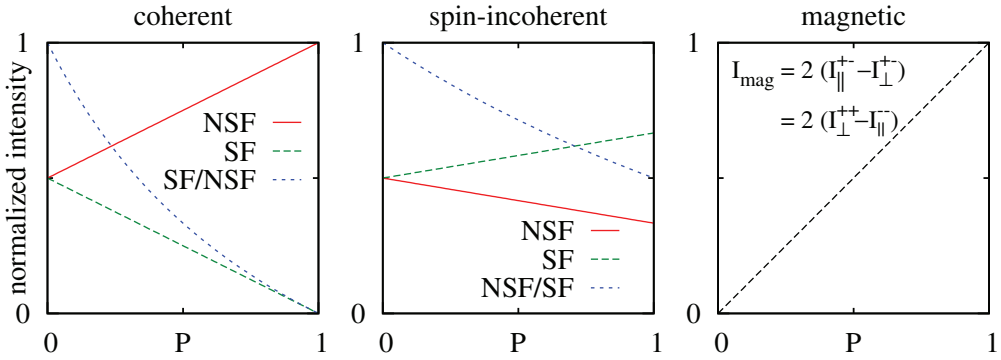

Fig. 7.8: *Dependence of the spin-flip (SF) and non spin-flip (NSF) scattering and the magnetic scattering upon the initial polarization. If the flipping ratio from a known scatterer, i.e. the polarization, has been measured it is possible to extrapolate to ideal conditions with* $P = 1$.

Provided the measured intensities have been corrected for background, all contributions can thus be separated by a set of rules:

$$\begin{aligned}
\frac{d\sigma}{d\Omega}_{\text{para}} &= 2\left(\frac{d\sigma}{d\Omega}^{\text{SF}}_x + \frac{d\sigma}{d\Omega}^{\text{SF}}_y - 2\frac{d\sigma}{d\Omega}^{\text{SF}}_z\right) \\
&= -2\left(\frac{d\sigma}{d\Omega}^{\text{NSF}}_x + \frac{d\sigma}{d\Omega}^{\text{NSF}}_y - 2\frac{d\sigma}{d\Omega}^{\text{NSF}}_z\right), \\
\frac{d\sigma}{d\Omega}_{\text{inc}} &= \tfrac{3}{2}\left(3\frac{d\sigma}{d\Omega}^{\text{SF}}_z - \frac{d\sigma}{d\Omega}^{\text{SF}}_x - \frac{d\sigma}{d\Omega}^{\text{SF}}_y\right), \\
\frac{d\sigma}{d\Omega}_{\text{coh}} &= \frac{d\sigma}{d\Omega}^{\text{SF}}_z - \tfrac{1}{2}\frac{d\sigma}{d\Omega}_{\text{para}} - \tfrac{1}{3}\frac{d\sigma}{d\Omega}_{\text{inc}}.
\end{aligned} \tag{7.39}$$

All derivations above for the separation rules have assumed that the polarization of the neutrons is perfect, which is not the case in practice. The first question that then arises is how to determine the degree of polarization of a neutron beam, or, more generally, the quality of the ensemble comprised by the polarizer, flipper, and analyzer. Because coherent scattering is purely non spin-flip and the ratio of spin-flip to non spin-flip is exactly 2 for purely spin incoherent scattering the polarization can readily be determined by the flipping ratios, f_{NSF} or f_{SF}, obtained as the intensity ratios for the flipper off and on setting $f_{\text{NSF}} = I^{++}/I^{+-}$ or $f_{\text{SF}} = I^{+-}/I^{++}$. For purely coherent scattering and perfect polarization $f_{\text{NSF}} = \infty$ and for unpolarized neutrons $f_{\text{NSF}} = 1$. A recommended and easy exercise is to show that

$$P = \frac{f_{\text{NSF}} - 1}{f_{\text{NSF}} + 1}, \quad P = 3\frac{f_{\text{SF}} - 1}{f_{\text{SF}} + 1}. \tag{7.40}$$

It is much more advisable to obtain the polarization from a coherent scatterer than from a spin incoherent scatterer, because if multiple scattering occurs, multiple spin flip will also occur, which is more difficult to handle. In order to obtain the flipping ratio for different scattering angles it is however required to either interpolate between Bragg peaks, or, better, to use a strong isotopically incoherent scatterer that does not produce spin incoherent scattering, such as ZrTi alloys (see Exercise 7.5).

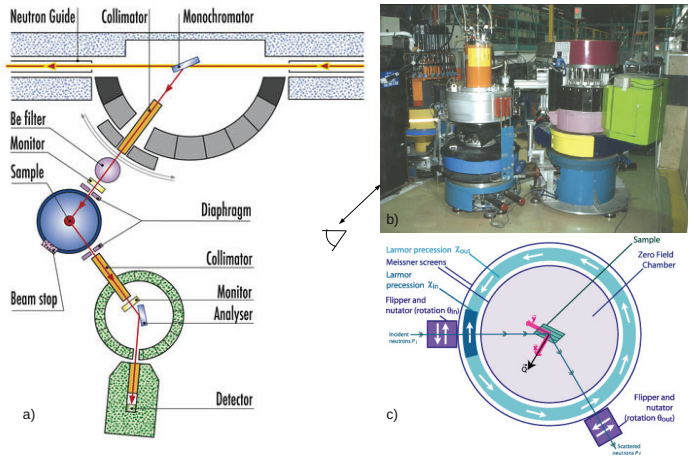

Fig. 7.9: *(a,b) The IN12 triple axis spectrometer at ILL, Grenoble. Helmholtz coils or a magnet can be placed at the sample position. (c) Schematic drawing of Cryopad, a zero-field sample environment based on superconducting shielding that allows to measure the flipping ratios in all relative directions of* $\mathbf{P}$ *and* $\mathbf{P}'$ *.*

The second question that arises is how to correct for imperfections in the instrument and the polarization. This can be done by calibrating with a sample with known flipping ratio, measuring the real flipping ratio and then, by inverting Eq. 7.40 and solving for $f(P)$. A useful visualization of the required corrections is given in Fig. 7.8, where the relative non spin-flip and spin-flip intensities are represented.

7.5 Instrumentation

Armed with a set of relations and devices we can now have a first glance at basic techniques that provide us insight into the materials under study, as well as some typical instrument designs that take advantage of polarization analysis.

The probably easiest method for studying magnetic scattering is diffraction of an unpolarized neutron beam. By measuring the scattering above and below the ordering temperature of the material, that is in the magnetically ordered and in the paramagnetic state, and building the difference in the scattering intensities, one can obtain $|\mathbf{M}_{\mathbf{Q}}^{\perp,\mathrm{order}}|^2 - |\mathbf{M}_{\mathbf{Q}}^{\perp,\mathrm{para}}|^2$, see Appendix C. Under the assumption that in the ordered state strong magnetic Bragg scattering occurs, whereas in the paramagnetic state only weak diffuse scattering is observed, the magnetic structure can in most cases be solved. A minor complication of this technique is that often the nuclear Bragg scattering is not perfectly subtracted, as the lattice constants might be slightly different in the ordered and paramagnetic state due to magnetostrictive effects.

A second elegant method is the so-called half polarized experiment, in which a polarized neutron beam is scattered by the sample but the polarization of the scattered neutrons is not analyzed. By applying a magnetic field parallel and antiparallel to the polarization, it is possible to

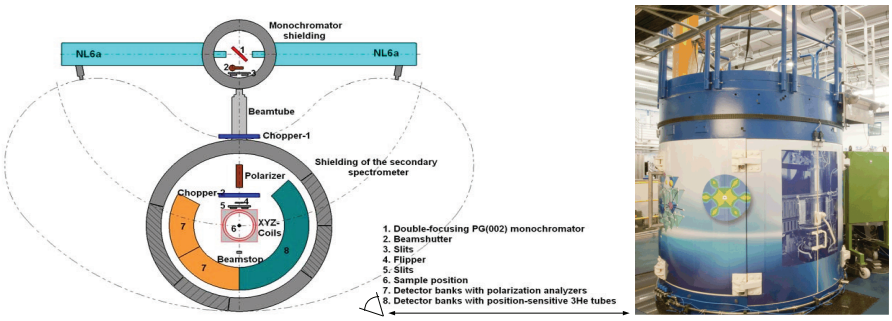

Fig. 7.10: *The JCNS diffuse neutron spectrometer DNS with polarization analysis and time of flight option, at the FRM-II, Munich.*

obtain the product of the nuclear and magnetic scattering *amplitudes* (see details in Appendix C, Eq. 7.45, by setting $P = 1$ and $P = -1$ and building the difference). The purely nuclear scattering can also be obtained by taking into account that the scattering in the direction parallel to the field is purely nuclear. The method works best if the magnetic moment can be saturated in field direction. This was illustrated in Fig. 7.3 for a half polarized small angle neutron scattering experiment on magnetically saturated nanoparticles [11].

A host of other methods exist and require more or less specialized instrumental setups. The conceptually simplest instrument is the triple axis spectrometer with polarizer and analyzer. A schematic representation is given in Fig. 7.6. In the basic version, with this instrument it is possible to measure the scattering intensities for one particular scattering vector. By using a spin flipper before (or after) the sample the spin-flip and non spin-flip intensities can be recorded. Further, the background can be efficiently measured by rocking the analyzer crystal by a few degrees, see for example Fig. 7.13 in Exercise 7.6. Depending on the requirements, a set of Helmholtz coils, see Fig. 7.7(b,c), can be placed around the sample in order to adiabatically bring the neutron polarization at the sample from the original direction of the polarizer to either x, y, or z direction and then back in the direction of the analyzer. Such instruments are very efficient for precise measurements in small regions of reciprocal space, but the measurement must be done step by step.

Multi detector instruments are more efficient when large volumes in reciprocal space must be probed. Examples of such instruments are D7, at the ILL in Grenoble, see Fig. 7.11, or DNS, at the FRM-II, in Munich, see Fig. 7.10. These instruments feature a bank of detectors for polarization analysis mounted in the horizontal scattering plane. The polarizer and the analyzers are magnetic multilayers separated by a layer of absorbing material, in which only one polarization is transported by total reflection. As there is a large number of detectors for polarization analysis, see right panel in Fig. 7.11, large amounts of multilayers had to be produced. A π-flipper is located in the incident beam between the polarizer and the sample. A particular challenge is to have a large area with a controlled guide field between the sample and the analyzers. As for the triple axis instruments, a set of Helmholtz coils can be located at the sample position in order to measure the spin-flip and non spin-flip scattering in different directions. Both of these instruments also feature a time-of-flight mode for separating the elastic and inelastic scattering, however inelastic polarized experiments are time consuming, as they require a factor $\sim$10 more

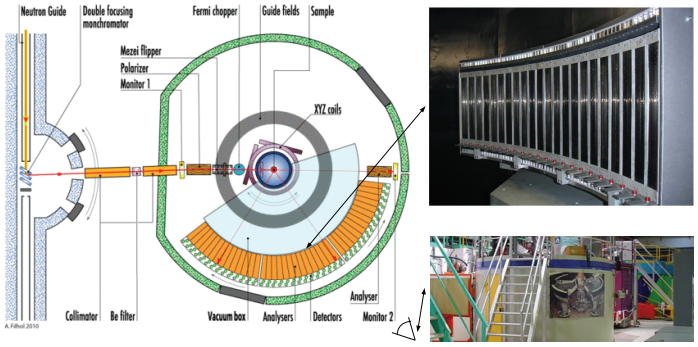

Fig. 7.11: *The D7 spectrometer at ILL, Grenoble, and its analyzer bank (top right) [17].*

time for the 6 polarization components, and a factor ∼10-50 more due to the chopper duty cycle. For only two components and H spin incoherent scattering this is however nicely feasible.

Finally, polarized neutrons can also be used in a very clever way in order determine the energy transferred during the process of neutron scattering, in particular for quasielastic scattering studies. In general, quasi- or inelastic scattering instruments rely upon a determination of the wavelength of the neutrons before and after the scattering process. This can be bypassed by encoding this wavelength on the neutron itself, by using its spin. In such a so called neutron spin echo experiment, a polychromatic beam obtained by a velocity selector ($\Delta\lambda/\lambda \sim 10 - 20\%$) is polarized longitudinally, $i.e.$ the spin is parallel to $\mathbf{k}$. At the entrance of a first magnetic precession coil with field in z, the neutron spin is flipped perpendicular to $\mathbf{k}$ and starts to precess for a distance l until reaching the sample. The precession rate depends on the field strength and the number of precession depends on the time spent in the coils, that is, on the neutron velocity or wavelength.

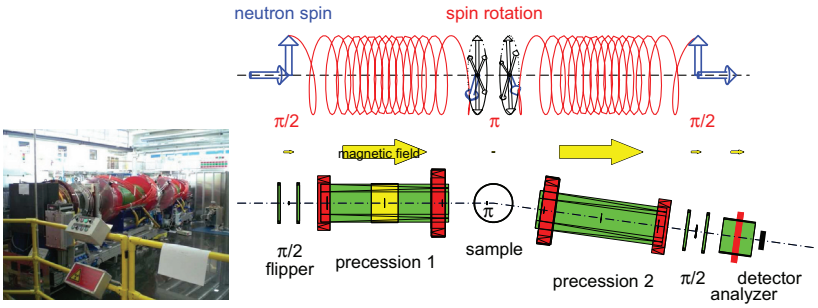

Fig. 7.12: *The JCNS J-NSE neutron spin-echo spectrometer at FRM II, left. Diagram of a neutron spin-echo spectrometer, right.*

Neglecting scattering, if after the sample, the neutron travels in an exactly opposite magnetic field for the same distance l, the spin at the exit of this second magnetic precession coil will be exactly in the same direction as at the entrance of the first coil. More importantly, all neutrons, regardless of their wavelength will have recovered the same polarization as initially. Thus, the

spin polarization produces an echo of the initial state. In practice, in order to avoid regions of null magnetic field where the beam could get depolarized, the neutron spins are flipped by π just before the sample and the field in the second coil is in the same direction as in the first. If elastic scattering occurs, the amplitude of the echo will not be affected; however, if some neutrons lose energy when scattered, the number of precessions before and after the scattering will be different, and the amplitude of the echo reduced. The gist of this trick is to use the spin of the neutron as an internal individual clock. The neutron spin echo technique gives the best dynamic resolution typically, $\sim 0.1\mu$eV, and with the new JCNS instrument NSE at the SNS spallation source, measurements with time resolutions between 1 ps (0.7 meV) and 1 μs (0.7 neV) will be possible.

Appendices

A Pauli Spin Operators

The vector spin operator can be represented in terms of its x, y, and z components:

$$\hat{\boldsymbol{\sigma}} = \{\underline{\hat{\boldsymbol{\sigma}}}_x, \underline{\hat{\boldsymbol{\sigma}}}_y, \underline{\hat{\boldsymbol{\sigma}}}_z\}$$

where the $\hat{\boldsymbol{\sigma}}_\alpha$ are the Pauli matrices

$$\underline{\hat{\boldsymbol{\sigma}}}_x = \begin{pmatrix} 0 & 1 \\ 1 & 0 \end{pmatrix} \quad \underline{\hat{\boldsymbol{\sigma}}}_y = \begin{pmatrix} 0 & -\mathrm{i} \\ \mathrm{i} & 0 \end{pmatrix} \quad \underline{\hat{\boldsymbol{\sigma}}}_z = \begin{pmatrix} 1 & 0 \\ 0 & -1 \end{pmatrix}$$

for a spin 1/2 particle, we can use the spin state representations

$$|+\rangle = \begin{pmatrix} 1 \\ 0 \end{pmatrix} \quad |-\rangle = \begin{pmatrix} 0 \\ 1 \end{pmatrix}$$

and accordingly, the algebra for applying the Pauli matrices to these spin states are simply given by

$$\begin{aligned} \underline{\hat{\boldsymbol{\sigma}}}_x|+\rangle &= |-\rangle \quad \underline{\hat{\boldsymbol{\sigma}}}_x|-\rangle = |+\rangle \\ \underline{\hat{\boldsymbol{\sigma}}}_y|+\rangle &= \mathrm{i}|-\rangle \quad \underline{\hat{\boldsymbol{\sigma}}}_y|-\rangle = -\mathrm{i}|+\rangle \\ \underline{\hat{\boldsymbol{\sigma}}}_z|+\rangle &= |+\rangle \quad \underline{\hat{\boldsymbol{\sigma}}}_z|-\rangle = -|-\rangle. \end{aligned}$$

B Combined Spin and Orbital Momentum Form Factor

When the considered ions have an orbital angular momentum next to the spin angular momentum, the cross section is significantly more complicated [1]. We have to consider the total angular momentum $\mathbf{J} = \mathbf{L} + \mathbf{S}$ and we will assume weak spin-orbit interaction, $e.g.$ the L-S or Russel-Saunders coupling, which is valid provide the atomic number is not too large. If the momentum transfer is then small, compared to the size of the Fourier transform of the electron orbits, a simplified expression is obtained in the dipole approximation

$$\frac{d\sigma}{d\Omega}_{\text{mag}} = (\gamma_{\text{n}} r_0)^2 \left| \frac{\mathrm{g}_J}{2} f_m(Q) \sum_i \langle \hat{\mathbf{J}}_{i\perp} \rangle e^{\mathrm{i}\mathbf{Q}\cdot\mathbf{R}_i} \right|^2 . \tag{7.41}$$

where $g_J = \frac{3}{2} + \frac{S(S+1)-L(L+1)}{2J(J+1)}$ is the Landé g-factor, and the form factor is

$$f_m(Q) = \langle j_0(Qr)\rangle + C_2\langle j_2(Qr)\rangle \tag{7.42}$$

with $C_2 = \frac{2}{g_J} - 1$ and

$$\langle j_l(Qr)\rangle = 4\pi \int_0^\infty j_l(Qr) R^2(r) r^2 dr \tag{7.43}$$

where the $j_l(Qr)$ are the spherical Bessel functions and $R(r)$ the radial density distribution. For isolated atoms, the functions $\langle j_0(Q)\rangle$ and $\langle j_2(Q)\rangle$ have been tabulated [18] and the $R(r)$ have been determined by Hartree-Fock calculations.

C Scattering Cross Section for Polarized Neutrons

A full derivation of the magnetic scattering of neutrons has been obtained by Blume [5] and Maleyev [6] and accordingly the scattering process is described by two equations, one for the scattering cross-section, $\sigma(\mathbf{Q}) = \sigma_\mathbf{Q}$, and one for the final polarization, $\mathbf{P}'$:

$$\begin{aligned} \sigma_\mathbf{Q} &= \sigma^N_{\mathbf{Q},\text{coh}} + \sigma^N_{\text{isotope inc}} + \sigma^N_{\text{spin inc}} \\ &+ |\mathbf{M}^\perp_\mathbf{Q}|^2 + \mathbf{P}(N_{-\mathbf{Q}}\mathbf{M}^\perp_\mathbf{Q} + \mathbf{M}^\perp_{-\mathbf{Q}}N_\mathbf{Q}) \\ &+ \mathrm{i}\mathbf{P}(\mathbf{M}^\perp_{-\mathbf{Q}} \times \mathbf{M}^\perp_{+\mathbf{Q}}) \end{aligned} \tag{7.44}$$

$$\begin{aligned} P'\sigma_\mathbf{Q} &= \mathbf{P}(\sigma^N_{\mathbf{Q},\text{coh}} + \sigma^N_{\text{isotope inc}}) - \tfrac{1}{3}\mathbf{P}\sigma^N_{\text{spin inc}} \\ &+ \mathbf{M}^\perp_\mathbf{Q}(\mathbf{P}\mathbf{M}^\perp_{-\mathbf{Q}}) + \mathbf{M}^\perp_{-\mathbf{Q}}(\mathbf{P}\mathbf{M}^\perp_\mathbf{Q}) - \mathbf{P}\mathbf{M}^\perp_\mathbf{Q}\mathbf{M}^\perp_{-\mathbf{Q}} \\ &+ \mathrm{i}(\mathbf{M}^\perp_{-\mathbf{Q}}N_\mathbf{Q} - \mathbf{M}^\perp_\mathbf{Q}N_{-\mathbf{Q}}) \times \mathbf{P} \\ &+ \mathrm{i}\mathbf{M}^\perp_\mathbf{Q} \times \mathbf{M}^\perp_{-\mathbf{Q}} \\ &+ \mathbf{M}^\perp_\mathbf{Q}N_{-\mathbf{Q}} + \mathbf{M}^\perp_{-\mathbf{Q}}N_\mathbf{Q} \end{aligned} \tag{7.45}$$

where $N_\mathbf{Q}$ and $M^\perp_\mathbf{Q}$ stands for the nuclear magnetic scattering amplitudes for a given $\mathbf{Q}$.

For $\mathbf{P} = 0$ only the square of the nuclear and magnetic scattering can be measured, $\sigma_\mathbf{Q} = |N_\mathbf{Q}|^2 + |\mathbf{M}^\perp_\mathbf{Q}|^2$ and the other terms do not contribute to the total scattering cross section. Interestingly, as indicated by the last term in Eq. 7.45, polarization can be generated in collinear structures by magnetic scattering through the interference of the nuclear and magnetic terms. For $\mathbf{P} = 0$, and neglecting chiral terms, we obtain that

$$\mathbf{P}' = \frac{\mathbf{P}'\sigma_\mathbf{Q}}{\sigma_\mathbf{Q}} = \frac{M^\perp_\mathbf{Q}N_{-\mathbf{Q}} + M^\perp_{-\mathbf{Q}}N_\mathbf{Q}}{|N_\mathbf{Q}|^2 + |\mathbf{M}^\perp_\mathbf{Q}|^2} \tag{7.46}$$

which yields $\mathbf{P}' = 1$ if $N_\mathbf{Q} = \mathbf{M}^\perp_\mathbf{Q}$. Chiral magnetism also can lead to polarization, as indicated by the next to the last term in Eq. 7.45.

Acknowledgements

I am grateful to Th. Brückel and W. Schweika for the material in their lecture notes of the schools Neutron Scattering (2000), Chapter 3 and 4, Neutron Scattering (2008), Chapter 2 and 3, as well as Polarized Neutron Scattering (2002), material which these notes are based upon, and to W. Schweika, A. Möchel, D. Bessas, and P. Zakalek for the proofreading.

References

[1] S. W. Lovesey, *Theory of neutron scattering from condensed matter, Volume 2: Polarisation effects and magnetic scattering* (Clarendon Press, Oxford, 1987).

[2] R. M. Moon, T. Riste , and W. C. Koehler, *Phys. Rev.* **181**, 920-931 (1969).

[3] O. Schärpf, in *Neutron Spin Echo* (Lectures Notes in Physics **128**, Springer, 1980). See also O. Schärpf, The spin of the Neutron as a measuring probe, `http://82.135.31.182/neutronpol.pdf`

[4] O. Halpern and M. R. Johnson, *Phys. Rev.* **55**, 898 (1939).

[5] M. Blume, *Phys. Rev.* **130**, 1670 (1963); *Phys. Rev.* **133**, A1366 (1964).

[6] S. V. Maleyev, *Zh. Eksperim. i Teor. Fiz.* **33**, 129 (1958); *Zh. Eksperim. i Teor. Fiz.* **33**, 129 (1958). [English translation: *Soviet Phys.-JETP* **34**, 89 (1958); *Soviet Phys.-JETP* **13**, 860 (1961)]

[7] A. Dianoux, G. Lander (Eds.), *Neutron Data Booklet* (Institute Laue-Langevin, Grenoble, 2002).

[8] A. Abragam and M. Goldman, *Rep. Prog. Phys.* **41**, 395-467 (1978).

[9] T. Chatterji and G. Schneider, *Phys. Rev. B* **79**, 212409 (2009).

[10] A. Heidemann, *Z. Phys.* **238**, 208 (1970).

[11] S. Disch, *The Spin Structure Of Magnetic Nanoparticles And In Magnetic Nanostructures* (Schriften des Forschungszentrum Jülich, Key Technology Vol. 21, Jülich, 2011).

[12] J. Strempfer, *et al.*, *Eur. Phys. J B* **14**, 63 (2003); J. Strempfer, *et al.*, *Physica B* **267-268**, 56 (1999).

[13] Poole A., *J. Phys.: Condens. Matter* **19**, 452201 (2007).

[14] W. Schweika, *Neutron News* **16**, 14-17 (2005); *Physica B-Cond. Matter* **335**, 157-163 (2003); *Journal of Physics Conference Series, PNSXM 2009* **211**, 012025 (2009)

[15] G. Shirane, *et al.*, *Phys. Rev. B* **31**, 1227 (1985).

[16] O. Schärpf and H. Capellmann, *Phys. Stat. Sol. (a)* **135**, 359 (1993).

[17] J. R. Stewart, *J. Appl. Cryst.* **42**, 69-84 (2009).

[18] E. Prince (Ed.), *International Tables for Crystallography, Volume C* (International Union for Crystallography, Chester CH1 2HU, England, 2004).

Exercises

Exercises marked with * have priority, others are optional.

E7.1 Coherent and incoherent scattering cross section*

The values for coherent and incoherent neutron scattering length and cross section are tabulated in several references. An excerpt from the ILL Neutron Data Booklet [7] is given below for several elements and isotopes. Fill in the missing values indicate by XX in the table below (optional: YY).

Table 7.1: *Selected scattering lengths and cross-sections. p: abundance in %; $b_{c,+,-}$: bound coherent, spin dependent I+1/2 and I-1/2 scattering lengths, respectively, in fm; $\sigma_{\mathrm{coh,inc,abs}}$: coherent, incoherent, and absorption (at 25.3 meV) cross-section in barn.*

$_Z$Symb^A	p	I	b_c	b_+	b_-	σ_{coh}	σ_{inc}	σ_{abs}
$_1$H			-3.7409(11)			1.7568(10)	XX	0.3326(7)
$_1$H^1	99.885	1/2	-3.7423(12)	10.817(5)	-47.420(14)	XX	XX	0.3326(7)
$_1$H^2	0.0149	1	6.674(6)	9.53(3)	0.975(60)	XX	2.05(3)	0.000519(7)
$_{21}$Ti			-3.370(13)			1.485(2)	2.87(3)	6.09(13)
$_{25}$Mn^{55}	100	5/2	-3.750(18)	-4.93(46)	-1.46(33)	YY	XX	13.3(2)
$_{27}$Co^{59}	100	7/2	XX	-9.21(10)	3.58(10)	XX	XX	37.18(6)
$_{28}$Ni			XX			13.3(3)	XX	YY
$_{28}$Ni^{58}	67.88	0	14.4(1)			26.1(4)	0	4.6(3)
$_{28}$Ni^{60}	26.23	0	2.8(1)			0.99(7)	0	2.9(2)
$_{28}$Ni^{61}	1.19	3/2	7.60(6)	YY	YY	7.26(11)	1.9(3)	2.5(8)
$_{28}$Ni^{62}	3.66	0	-8.7(2)			9.5(4)	0	14.5(3)
$_{28}$Ni^{64}	1.08	0	-0.37(7)			0.017(7)	0	1.52(3)
$_{40}$Zr			7.16(3)			6.44(5)	0.02(15)	0.185(3)

E7.2 Neutron contrast*

The scattering length averaged over all Zr and Ti isotopes are given in Table 7.1. $\mathrm{Zr}_{1-x}\mathrm{Ti}_x$ alloys, with a hexagonal crystalline structure can be prepared for continuous values of x. Which x would you choose if you had to construct a sample chamber from such an an alloy? Why? What would be the disadvantage?

E7.3 Precession*

A fully polarized beam of cold neutrons with a wavelength of 5.4 Å enters the primary coil of a spin echo spectrometer. The coil have a length of 2.2 m, and the 1000 Oe field inside the coil is along the horizontal flight path. The initial direction of the neutron spins is in the vertical direction. What is the direction of the neutron spins at the exit of the coil? Spin echo spectrometers typically work with a 10 % or 20 % bandwidth in $\Delta\lambda/\lambda$. What polarization of the neutron beam do you expect at the exit of the coil considering the full bandwidth?

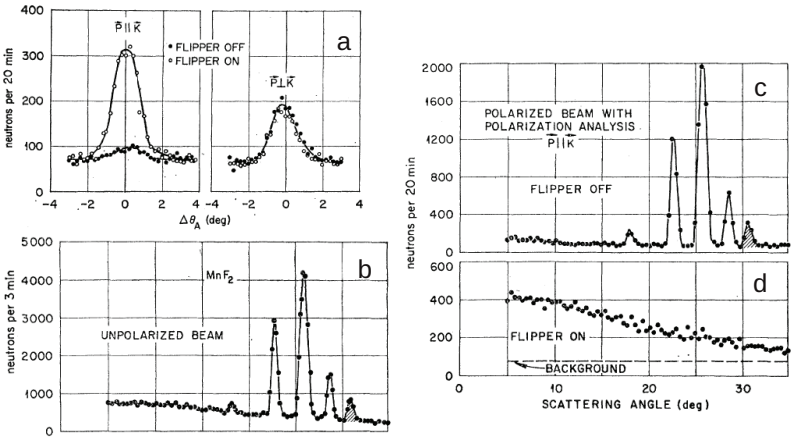

Fig. 7.13: *Polarization analysis of the scattering by MnF_2. Note that K stands for* Q *[Source: Ref. [2]].*

E7.4 Flipping**

A Mezei coil with 1 cm total thickness is used as a spin flipper. The field inside the coil is perpendicular to both the polarization of the beam and the travel direction of the neutron. What field would you chose for carrying out a π-flip of the neutron polarization, considering a monochromatic beam with λ=3.4 Å? Is this solution unique? If not, what solution would you choose for a neutron bandwidth of 5 %?

E7.5 Flipping ratio and corrections*

Using an ideal $Zr_{1-x}Ti_x$ alloy scatterer with purely isotopic incoherent scattering, the spin-flip and non-spin-flip intensities, $I_{\rm SF} = 1000$ and $I_{\rm NSF} = 19000$ counts, respectively, were determined at Q = 2 Å^{-1} (the background is subtracted). What is the flipping ratio and what is the polarization of the neutron beam? What flipping ratio would you obtain using a purely spin incoherent scatterer (such as, in good approximation, vanadium)? Is it preferable to determine the flipping ratio with V or with $Zr_{1-x}Ti_x$? Why?

E7.6 Magnetic scattering***

Determine the relative spin-incoherent, spin-coherent, and magnetic scattering by MnF_2 from the data in Fig. 7.13a . How do you interpret Fig. 7.13d: a) what type of scattering is seen? b) why does this scattering decrease with increasing angle? c) what information could you extract from this data?

8 Structural Analysis

G. Roth
Institute of Crystallography
RWTH Aachen University

Contents

Lecture Notes of the JCNS Laboratory Course Neutron Scattering

8.1 Introduction

The analysis of crystal structures and magnetic ordering is usually based on diffraction phenomena caused by the interaction of matter with x-rays, neutrons or electrons. Even though modern electron microscopy (HRTEM) can achieve atomic resolution, more detailed and quantitative information on the 3D atomic arrangement in crystals and on 3D magnetic structures and spin densities requires diffraction methods. In a more general nomenclature, diffraction is equivalent to coherent, elastic scattering. The basic theory of diffraction used for structural analysis (the so called kinematical theory) is similar for all types of radiation. Due to the different properties of x-rays, neutrons and electrons and their specific interaction with matter, complementary information is obtained from experiments with different types of radiation.

Considering only x-rays and thermal neutrons one finds that their wavelengths are similar (0.5 Å < λ < 2.4 Å) but they are scattered very differently by matter: While the electromagnetic x-radiation is scattered from the electrons and yields the total electron density distribution in the crystal, the nuclear scattering of neutrons is sensitive to the density distribution of the nuclei and the magnetic neutron scattering probes the magnetisation density of unpaired electrons.

x-ray diffraction using conventional laboratory equipment and/or synchrotron installations is the most frequently used method for structure analysis. Neutrons are, however, indispensable in a number of applications. The purpose of this chapter is to discuss a few typical examples of structural analysis, for which, instead of or complementary to x-rays, neutrons are required to solve structural problems.

8.2 Diffraction Contrast Variation

A great advantage of neutrons over x-rays in the context of structural analysis is the very much different variation of the scattering length of atoms within the periodic system of the elements: The contrast in conventional x-ray diffraction is directly related to the ratio of the number of electrons Z_j of the different atoms or ions j involved. The atomic scattering factor f_j in the structure-factor formula, which represents the Fourier transform of the atomic electron density distribution, is proportional to Z_j ($f_j = Z_j$ for $\sin\theta/\lambda = 0$). Standard x-ray techniques can hardly differentiate between atoms/ions with a similar number of electrons (like Si and Al or Cr and Mn). Even if the atoms are fully ordered on different sites, x-ray diffraction just 'sees' the average structure.
For neutrons the atomic scattering factor f_j is replaced by the nuclear scattering length (or coherent scattering amplitude) b_j, which is of the same order of magnitude for all nuclei but varies from nucleus to nucleus in a non-systematic way. b_j values can be either positive or negative and depend on the isotopes and nuclear spin states of the element j (see chapter 4).

Crystal structure and site occupation of $(Mn_{1-x}Cr_x)_{1+\delta}Sb$.

As an example of contrast variation, the combination of x-ray and neutron diffraction information is demonstrated for the intermetallic compounds $(Mn_{1-x}Cr_x)_{1+\delta}Sb$, with

$0 \le x \le 1$ [1]. This solid solution system is interesting for its magnetic properties: One end member of the solid solution series ($Mn_{1+\delta}Sb$) shows isotropic ferromagnetic behaviour while the other one ($Cr_{1+\delta}Sb$) is a uniaxial antiferromagnet. Intermediate compositions are characterized by competing magnetic interactions leading to a complex magnetic phase diagram. The crystal structure is closely related to the hexagonal NiAs-type structure (space group: $P6_3/mmc$) with some additional partial occupation (≤ 0.14) of the interstitial site 2(d) (see Fig. 8.1):

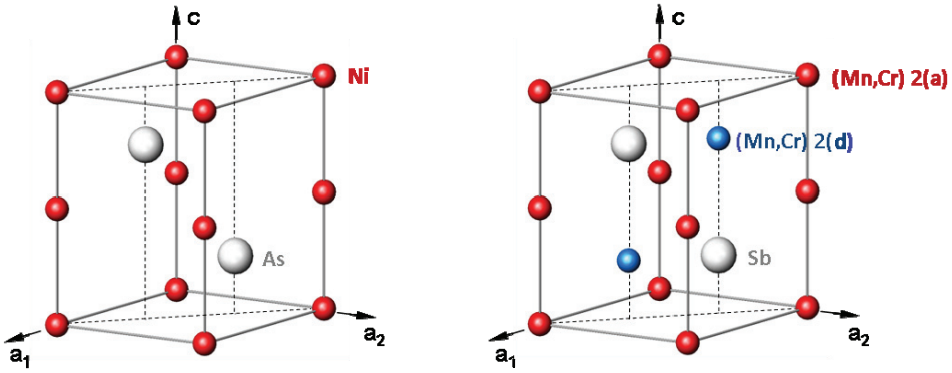

Fig. 8.1: *Left: NiAs structure, right: $(Mn_{1-x}Cr_x)_{1+\delta}Sb$ structure*

Conventional x-ray diffraction can hardly differentiate between chromium (Z_{Cr}= 24) and manganese (Z_{Mn}= 25) but still yields information on the overall occupation probabilities by (Mn,Cr) for site 2(a) (denoted as a) and site 2(d) (denoted as d). The Sb position is assumed to be fully occupied, thus serving as an internal standard for the scattering power.
The compound formula can now be reformulated site-specifically as:

$$\underset{\textit{site 2(a)}}{(Mn_{1-y}\,Cr_y)_a}\;\underset{\textit{site 2(d)}}{(Mn_{1-z}\,Cr_z)_d}\;Sb$$

corresponding to a chemical composition of $Mn_{[(1-y)a\,+\,(1-z)d]}\,Cr_{[ya\,+zd]}\,Sb$.

On the other hand, the nuclear scattering lengths of Cr and Mn for neutron diffraction are extremely different with b_{Cr} = +3.52 fm and b_{Mn} = -3.73 fm (see also chapter 4).
In the structure analysis of the neutron data, site-specific effective scattering lengths b_{eff} (2a) and b_{eff} (2d) are refined, which in turn are expressed as:

$b_{eff}(2a) = a\cdot[(1-y)\cdot b_{Mn} + y\cdot b_{Cr}]$ and $b_{eff}(2d) = d\cdot[(1-z)\cdot b_{Mn} + z\cdot b_{Cr}]$

solving for the unknown parameters y and z gives:

$y = [b_{eff}(2a)/a - b_{Mn}] / [b_{Cr} - b_{Mn}]$ and $z = [b_{eff}(2d)/d - b_{Mn}] / [b_{Cr} - b_{Mn}]$.

The combination of the overall occupation probabilities a and d - from conventional x-ray studies – with the effective scattering lengths b_{eff}(2a) and b_{eff}(2d) determined in a neutron diffraction experiment allows the evaluation of the Cr and Mn concentrations on the different sites 2(a) and 2(d).

It is evident, that the individual (Cr,Mn) distributions on the two crystallographically different sites 2(a) and 2(d) are not accessible merely by a chemical analysis. For most of the samples studied, the site 2(a) was found to be fully occupied: a ≈ 1.0. But the formula $(Mn_{1-x}Cr_x)_{1+\delta}Sb$ used normally is only correct for the special case of equal Cr : Mn ratios on both sites:

$$x = y = z \quad \text{and} \quad 1 + \delta = a + d.$$

Note that, in general, a statistical occupation of one crystallographic site with three kinds of scatterers - e.g. Mn, Cr and "vacancies" - requires at least two independent experiments with sufficiently different relative scattering power of the atoms involved to determine the fractional occupancies.
The detailed information on the (Cr,Mn) distribution is needed to explain the magnetic properties of these intermetallic compounds, but we will not further elaborate on this.

8.3 The hydrogen problem in structural analysis

The determination of the structural parameters (coordinates, displacement parameters) of hydrogen atoms in crystals is a special problem involving again the different properties of x-rays and neutrons. It is obvious that H or D atoms with Z = 1 give only a small contribution to the electron density and, therefore, they are hardly visible in x-ray structure analysis, particularly if heavy atoms are also present in the structure. However, there is an even more fundamental problem: The single electron of H or D is engaged in the chemical bonding and is by no means localised at the proton/deuteron position. Therefore, bond distances from x-ray diffraction involving hydrogen are notoriously wrong and any comparison with quantum mechanical calculations is quite hard to perform. This lack of sound experimental information is in sharp contrast to the importance of hydrogen bonding in solids, particularly in biological molecules like proteins, where hydrogen bonds govern to a large extent structures and functionalities of these ‘bio-catalysts’. A combination with neutron diffraction experiments is important to determine the structural parameters of the H/D atoms properly. More generally, the structure analysis by neutron diffraction yields separately and independently from the x-ray data the structure parameters of all atoms including the mean square displacements due to static and dynamic (even anharmonic) effects.

H/D ordering in ferroelectric RbH_2PO_4 (RDP):

The hydrogen problem in crystal structure analysis is of special importance for structural phase transitions driven by proton ordering. KH_2PO_4 (KDP) is the most well-known representative of hydrogen-bonded ferroelectrics. Here, we discuss the isotypic RbH_2PO_4 (RDP). The crystal structure consists of a three-dimensional network of PO_4-groups linked by strong hydrogen bonds (Fig. 8.2).

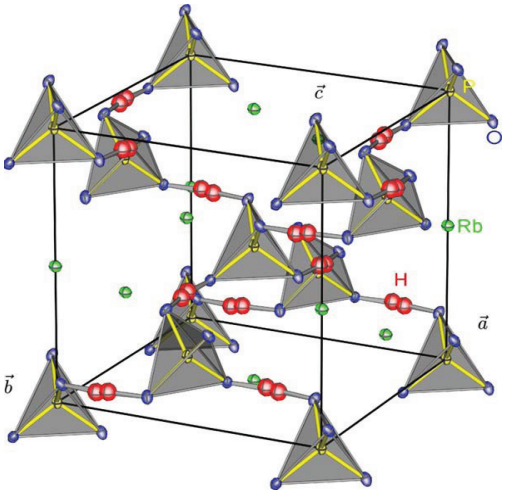

Fig. 8.2: *Crystal structure of the paraelectric phase of RDP (RbH_2PO_4) with a split-model representation of the hydrogen disorder [3].*

In the paraelectric phase at room temperature KDP as well as RDP crystallise in the tetragonal space group I $\bar{4}$2d, where the H-atoms are dynamically disordered in symmetric O···H···O bonds, which are almost linear with short O–O distances, typically in the range of 2.5 Å. The disordered H-distribution may be interpreted as corresponding to a double-well potential [2].
Figures 8.3 and 8.4 show the corresponding results for RDP, obtained from single crystal neutron diffraction [3].

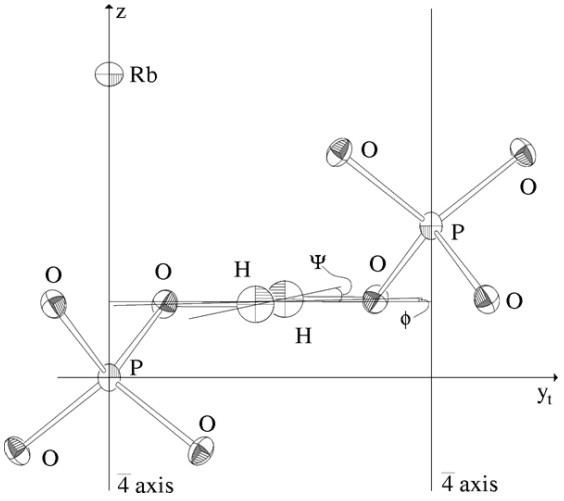

Fig. 8.3: *Local configuration of two PO_4-tetrahedra in the paraelectric phase of RDP (RbH_2PO_4)(at T_c + 4 K) linked by a strong, disordered hydrogen bond [3].*

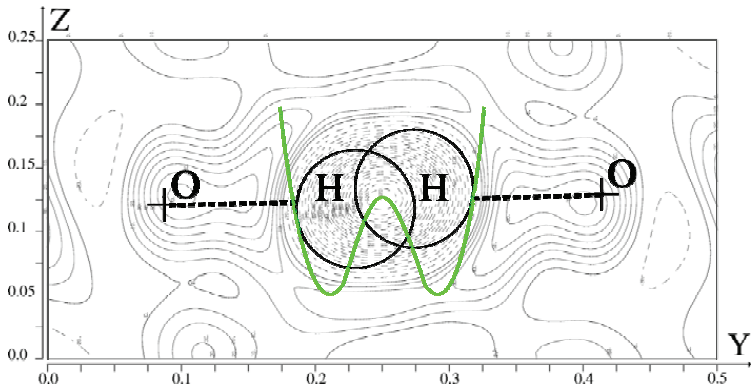

Fig. 8.4: *Difference-Fourier-plot of the negative proton density in the hydrogen bond of paraelectric RDP indicated by broken contour line [3]. The double-well potential model used to describe this density is inscribed in green.*

The two very close hydrogen positions with 50% occupation probability are, of course, an artefact of the time-space averaging that is inherent to diffraction. In this case, the hydrogen disorder is assumed to be a dynamic hopping process between the two energetically degenerate sites.
At T_c = 147 K, RDP transforms to a ferroelectric phase of orthorhombic symmetry (space group: Fdd2) in which the protons order in short asymmetric O-H···O bonds (Fig. 8.5). The PO4-tetrahedra show a characteristic deformation with two shorter and two longer P-O distances due to a transfer of electron density to the covalent O–H bonds. The electrical dipole moments are oriented ||z which give rise to a polarisation along the ***c***-direction.

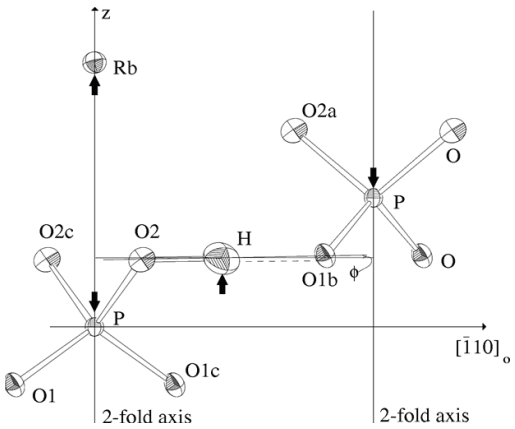

Fig. 8.5: *Ferroelectric, hydrogen-ordered structure of RDP close to the phase transition at T_C – 1 K (major changes indicated by arrows, presentation as in Figure 8.3) [3].*

The phase transition temperatures of KDP-type compounds change drastically when H is substituted by D. For $K(H,D)_2PO_4$, for instance, the para- to ferroelectric T_C changes from 122 K in the protonated to 229 K in the deuterated compound. This huge H/D-isotope effect proves that hydrogen-ordering and -dynamics is the major factor controlling this phase transition. Another type of H/D-isotope effect was found for $Tl(H,D)_2PO_4$ (TDP/DTDP) and $Rb(H,D)_2PO_4$ (RDP/DRDP), where a different polymorphism between the protonated and deuterated phases exists.
Clearly, the use of neutron diffraction is detrimental to a better understanding of these compounds and their interesting physical properties.

8.4 Atomic coordinates and displacement parameters

As discussed above, neutron diffraction is very useful for obtaining precise atomic coordinates and displacement parameters. The improved accuracy (compared to x-rays) stems mainly from the absence of the form-factor fall-off. We will use measurements on Cobalt-olivine, Co_2SiO_4, (crystal size 3 x 2 x 2 mm) taken at the four-circle diffractometer HEiDi at the hot-neutron source of the FRM II reactor (λ = 0.552 Å) for demonstrating this advantage for the thermal displacements:

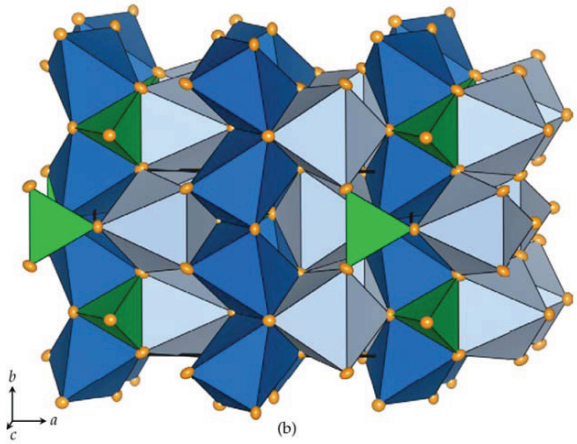

Fig. 8.6: *Structure of Co_2SiO_4 olivine at room temperature, projected along c. Green: SiO_4-tetrahedra, Dark blue: $Co(1)O_6$-octahedra, light blue: $Co(2)O_6$-octahedra. Displacement ellipsoids are plotted at the 95% probability level (from [4]).*

The olivine structure (fig. 8.6) consists of chains of two types of edge-sharing CoO_6-octahedra connected by SiO_4-tetrahedra. A large data set with 1624 independent reflections up to sin θ/λ = 1.05 $Å^{-1}$ had been measured. The data were then successively cut off in shells of sin θ/λ and the resulting partial data sets were used to analyse the displacement parameters. Figure 8.7 shows two interesting observations: First of all, the precision improves significantly with increasing $(\sin \theta/\lambda)_{max}$, as is evident from the decreasing size of the error bars. In the x-ray case, high angle reflections are usually very weak and their measurement does often not lead to improved precision. Secondly,

there is a systematic change of the displacement values themselves, resulting from systematic errors that vary with $(\sin \theta/\lambda)_{max}$.

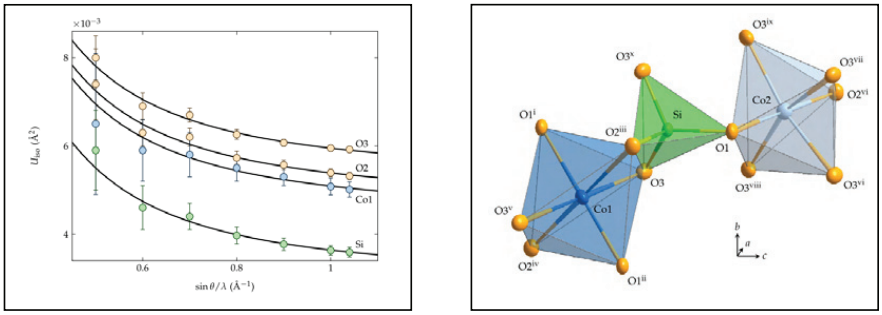

Fig. 8.7: *Left: Statistical (error bars) and systematic errors of isotropic displacements parameters in Co_2SiO_4 as a function of measured sin θ/λ range from single-crystal neutron diffraction data at room temperature [4]. Right: Clinographic view of the CoO_6 and SiO_4 polyhedra in Co_2SiO_4 at room temperature [4].*

High d_{hkl}-value resolution data from neutron diffraction is also useful to derive precise temperature dependent displacement parameters (fig. 8.8):

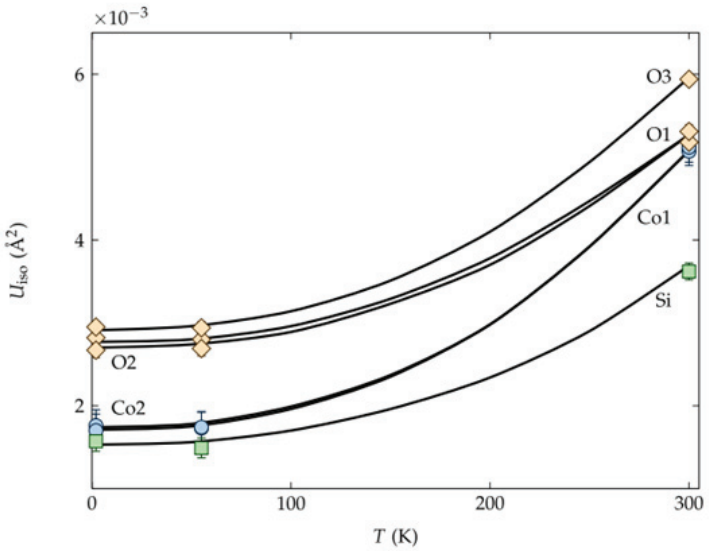

Fig. 8.8: *Temperature dependence of the isotropic displacement parameters of Co_2SiO_4 [4].*

Just as in the case of high quality single crystal x-ray diffraction data, anisotropic displacement parameters can be determined as well. In addition to that, the quality of single crystal neutron data also often allows refining anharmonic displacement parameters. Anharmonic oscillations of atoms in crystals occur if the atoms are vibrating in a non-parabolic potential well. In such cases, the harmonic approximation,

which is the basis of the description of thermal displacements by the Debye-Waller factor, fails. Analysis of the anharmonic displacements allows to reconstruct the non-parabolic potential at the site of the vibrating atom.

8.5 Magnetic structures from neutron diffraction

Cobalt-Olivine, Co_2SiO_4, orders magnetically below about 50 K. The magnetic moments of the Co^{2+}-ions turn from a paramagnetic phase with no long range order of the magnetic moments into an antiferromagnetically ordered arrangement. We use Co_2SiO_4 again to briefly demonstrate the application of neutron diffraction to the structural analysis of magnetic structures. This time, a powder neutron diffraction experiment has been performed at the diffractometer D20 (ILL, France) in its high-resolution mode, at temperatures between 70K and 5K, with a neutron wavelength of λ = 1.87 Å and approximately 2 g of powdered Co_2SiO_4 [4].

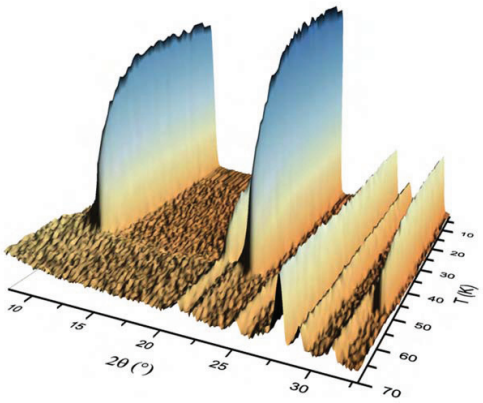

Fig. 8.9: *Thermal evolution of the neutron powder diffraction pattern (low angle part) of Co_2SiO_4 [4].*

At about 50 K, new magnetic reflections (001), (100), (110), (300) etc. appear (fig. 8.9). The nuclear reflections don't change much at the magnetic phase transition. The new reflections can be indexed with the same unit cell as the nuclear reflections, but they were forbidden in the paramagnetic phase with space group P n m a. Obviously, the symmetry has changed at the magnetic ordering transition. The task is then - just as in 'ordinary' structure determination - to find a structural model (that is: magnetic moments and their orientation on the magnetic ions, here Co^{2+}) that fits the observed positions and intensities of the magnetic Bragg peaks. Magnetic structure determination is outside the scope of this chapter, but assumed such a model has been constructed, it can be refined - in the case of powder data by the Rietveld method (fig. 8.10).

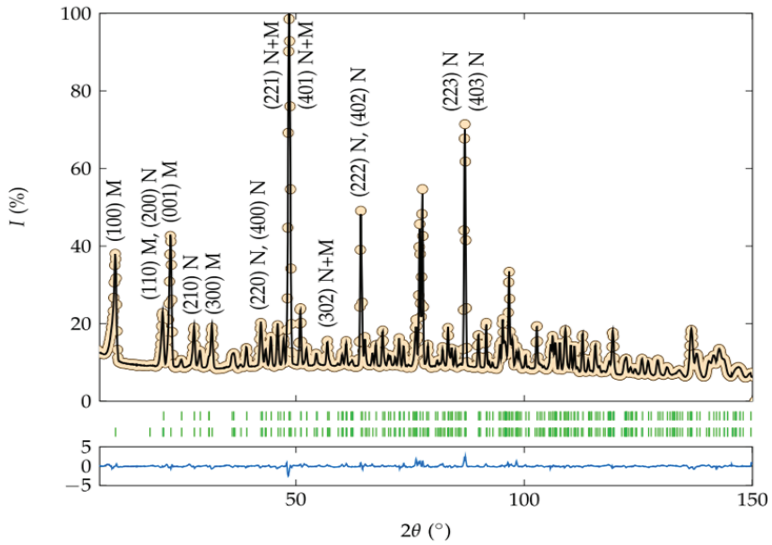

Fig. 8.10: *Neutron powder diffraction pattern (dots), Rietveld fit (black line) and allowed Bragg reflections (green marks) at 5 K of Co_2SiO_4 [4].*

The lower trace (blue) is the difference *Iobs - Icalc* on the same scale. The upper row of the green marks shows Bragg reflections corresponding to the nuclear phase and the lower row represents the allowed positions of the magnetic peaks. Some of the Bragg peaks are indexed. 'N' and 'M' denote the nuclear and magnetic contributions, respectively [4]. Note that the magnetic Bragg peaks are only visible at low diffraction angles.

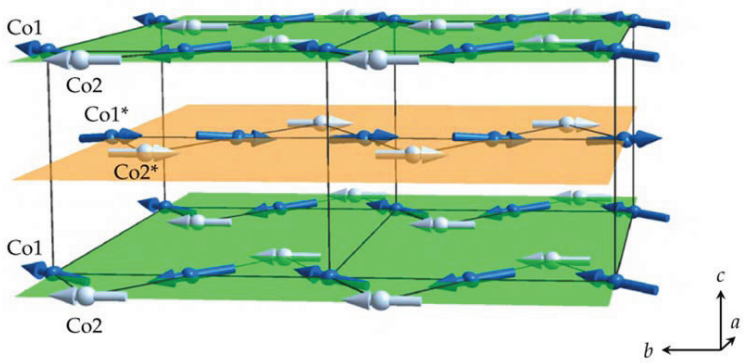

Fig. 8.11: *Graphical representation of the magnetic structure of Co_2SiO_4 below 50 K. The non-magnetic atoms (Si and O) are excluded for simplicity. The figure shows the zigzag chains of Co(1) and Co(2) in layers perpendicular to the c axis [4].*

From the Rietveld refinements, one can derive the exact spin orientation (fig. 8.11) as well as parameters describing quantitatively the magnetic moments on the two symmetrically non-equivalent Co^{2+}-sites (see table below). However, magnetic neutron diffraction from single crystals often gives additional and more accurate information:

	Co1 (0,0,0)	Co2 (x,1/4,z)
M_x (μ_B)	1.18 ± 0.05	—
M_y (μ_B)	3.61 ± 0.04	3.37 ± 0.04
M_z (μ_B)	0.66 ± 0.18	—
M (μ_B)	3.86 ± 0.05	3.37 ± 0.04
ϕ (°)	71.9 ± 0.7	90
θ (°)	80.2 ± 2.7	90

$\chi^2 = 2.23$, $R[F^2 > 2\sigma(F^2)] = 0.033$, $wR(F^2) = 0.044$.

The table shows cartesian (M_x, M_y and M_z) and spherical (M, φ and θ) components of the Co1 and Co2 magnetic moments according to the single-crystal neutron diffraction data at 2.5 K. The directions of the magnetic moments for other cobalt ions in the unit cell can be obtained by applying the symmetry operations of the magnetic space group (Schubnikov group) Pnma.

8.6 Electron densities from x-rays and neutrons

Another advanced application of neutron diffraction in structural analysis is the determination of 3-dimensional high resolution maps of the electron density in the unit cell to study, for instance, details of the chemical bonding. The most involved method of electron density studies (called x-N-synthesis) uses a combination of high quality single crystal neutron and x-ray diffraction experiments. In the present case, a single crystal of Co_2SiO_4 with dimensions 3 x 2 x 2 mm, was measured on the four-circle diffractometer HEiDi at the hot-neutron source of the FRM II reactor (Garching) at λ = 0.552 Å, the single crystal x-ray (synchrotron) experiment was performed on Diffractometer D3 at the synchrotron facility HASYLAB/DESY (Hamburg) with a Co_2SiO_4-sphere, diameter 150 μm as the sample and an x-ray wavelength of λ = 0.5 Å. The next step is to take the x-ray-data, do a Fourier-transform (Fourier-synthesis) to obtain the electron density map:

$$\rho(\boldsymbol{r}) = 1/V \cdot \sum_{\tau} \boldsymbol{F}(\boldsymbol{\tau}) \cdot \exp[2\pi i(\boldsymbol{\tau}\boldsymbol{r})], \quad \text{with } \boldsymbol{F}(\boldsymbol{\tau}) = |\boldsymbol{F}(\boldsymbol{\tau})| \cdot \exp[i\varphi(\boldsymbol{\tau})].$$

The phases $\varphi(\boldsymbol{\tau})$ are calculated from the atomic model (structure factor equation, see ch. 4), the moduli $|\boldsymbol{F}(\boldsymbol{\tau})|$ are taken from the measured x-ray intensities. The result is a 3-dimensional map of the total electron density $\rho(\boldsymbol{r})$ within the unit cell:

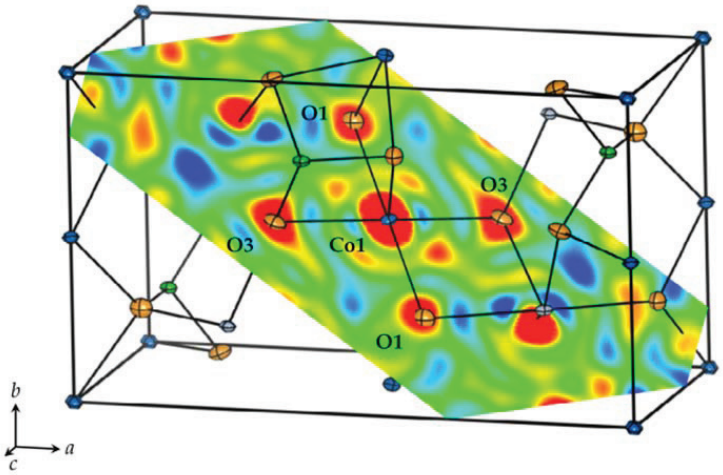

Fig. 8.12: *Electron density distribution ρ(r) of Co_2SiO_4 at 12 K from Fourier synthesis of x-ray data. Contours range from −8 e/Å^3 (blue) to 10 e/Å^3 (red). A plane which intersects the $Co1O_6$ octahedron and contains the Co1, O1 and O3 atoms is shown together with a sketch of the crystal structure [4].*

In favourable cases, such a map already shows interesting features of the (anisotropic) bonding electron density, however, the information content of the map can be very significantly improved by taking the coordinates and displacement parameters from the more accurate neutron diffraction experiment (see above for the reasons) and calculate, in a second step, the so called deformation density. This is done by subtracting from the total electron density $\rho(\boldsymbol{r})$ the density $\rho(\boldsymbol{r})_{\text{spherical}}$ corresponding to a superposition of spherical atoms at the nuclear positions. More specifically: atomic positions x_j, y_j, z_j and thermal displacements T_j of atoms j derived from the neutron experiment, 'decorated' with the calculated spherical single atom electron densities.

$\rho(\boldsymbol{r})_{\text{deform}} = \rho(\boldsymbol{r}) - \sum \rho(\boldsymbol{r})_{\text{spherical}}$, where the sum runs over all atoms in the unit cell.

$\rho(\boldsymbol{r})_{\text{spherical}}$ corresponds to the expectation value of the electron density within the unit cell without any effects which are due to chemical bonding. The deformation density then represents the deformation of the charge distribution as a result of the formation of chemical bonds. Figure 8.13 shows such a deformation density map for Co_2SiO_4. In favourable cases, the electron density in the hybridized bonding orbitals (in this case of Co3d- and O2p character) can be directly observed.

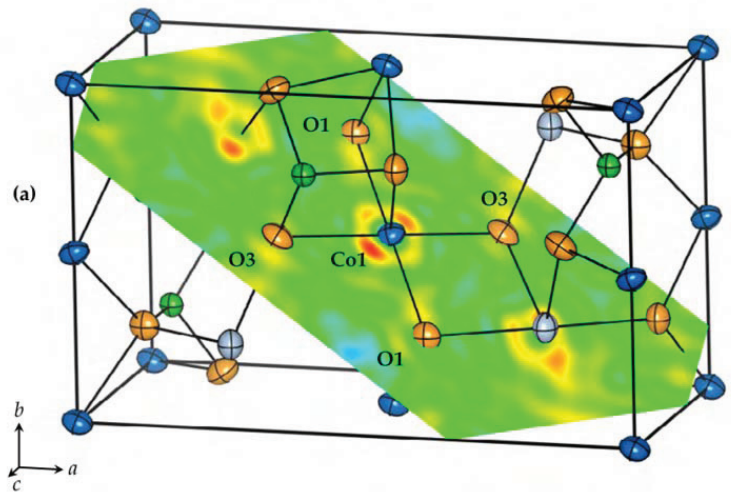

Fig. 8.13: *Deformation density from the x-N-difference Fourier map of Co_2SiO_4 at 300 K: Section through the O1–Co1–O3 plane The difference density varies from −1.25 e/Å^3 (blue) to 1.15 e/Å^3 (red) [4].*

8.7 Magnetization densities from neutron diffraction

As a final example for the application of neutron diffraction in structural analysis, we briefly sketch how a 3-dimensional map of the magnetization density, that is: the density of magnetic moments (spin- as well as orbital-moments) within the unit cell can be determined. These maps are sometimes lucidly called 'spin density maps', but in systems with non-vanishing orbital moments, the term magnetization density is really the correct one.

The experiment is performed by polarized neutron diffraction on a single crystal using the flipping ratio method For details on the experimental method see the chapter on magnetic scattering. The flipping ratio method allows to separate nuclear and magnetic contributions to the diffracted intensities. It is performed *above* the magnetic phase transition in the paramagnetic state (in the case of Co_2SiO_4 above T_N=50K) and the sample is in a strong external magnetic field (here: 7 T). 207 Bragg reflection flipping ratios were measured at diffractometer 5C1 of the ORPHÉE reactor (Laboratory Léon Brillouin, CEA Saclay, France) for Co_2SiO_4 at 70K up to $\sin\theta/\lambda \approx 0.62$ Å^{-1} at a neutron wavelength of λ = 0.845 Å. Given the flipping ratios and the nuclear structure factors, the magnetic structure factors can be calculated which are then Fourier transformed to give the spatially resolved magnetization density shown in figure 8.14 in a section through the unit cell of Co_2SiO_4.

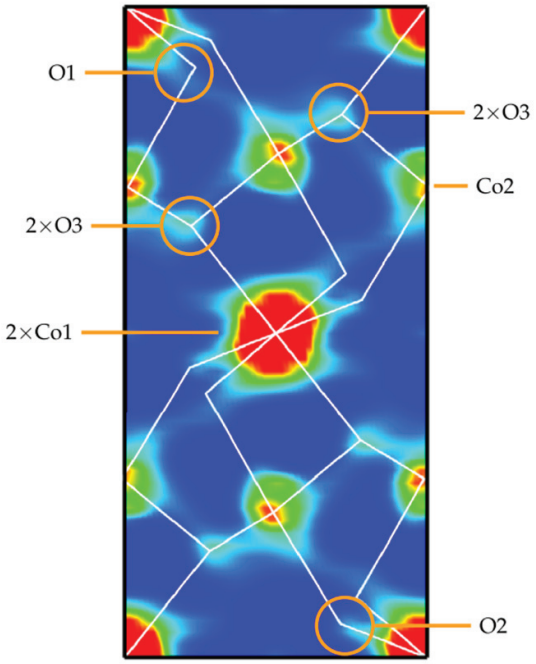

Fig. 8.14: *Reconstruction of the density (projected along the b axis) corresponding to the observed magnetization distribution of Co_2SiO_4 at 70 K with contours ranging from 0 $\mu_B/Å^3$ (blue) to 2 $\mu_B/Å^3$ (red) [4].*

Among the interesting features of this map is the observation of magnetization density on the, nominally non-magnetic, oxygen atoms coordinating the Co^{2+}-ions. These 'transferred moments' are direct experimental evidence for the hybridization of the oxygen 2p- with Co-3d-orbitals which is not only responsible for covalent bonding but also for the magnetic exchange interaction along the Co-O-Co-bond network.

References

[1] W. Reimers, E. Hellner, W. Treutmann and G. Heger, J. Phys. C: Solid State Phys. **15**, 3597 (1982).

[2] R. J. Nelmes, W. F. Kuhs, C. J. Howard, J. E. Tibballs and T. W. Ryan, J. Phys. C: Solid State Phys. **18**, L711 (1985).

[3] S. Mattauch, G. Heger, and K. H. Michel, Cryst. Res. Technol. **39**, 1027 (2004)

[4] A. Sazonov, Ph.D.-thesis, RWTH Aachen (2009)
A. Sazonov et al., Acta Cryst. **B65**, 664-675 (2009).

Exercises

E8.1 Rietveld refinement

A. What is the basic problem in refining crystal structures from powder diffraction data?

B. Sketch the fundamental idea to solve this problem.

C. What kind of data can be obtained from a Rietveld refinement?
(collect a list and sort into categories: Structural parameters, instrumental parameters, others)
D. Can powder diffraction data be used for structure determination? *(yes or no plus arguments)*

E8.2 Thermal displacement Parameters

A. Write down the (isotropic) displacement factor ("Debye-Waller-factor") that enters the structure factor formula (for x-rays)

B. Discuss the physical origin of this factor.

C. Describe the overall effect of this displacement factor on the diffracted intensities.

D. Do you expect the formal description to be fundamentally different for neutron diffraction as compared to x-ray diffraction?

E. It is generally said, that neutron diffraction yields much more precise displacement parameters than x-ray diffraction. Correct? If so: Why?

F. What are anisotropic displacement parameters and how can they be visualized?

G. Is it correct, that all atoms in cubic crystals have to vibrate isotropically?

H. Discuss the symmetry restrictions (shape and orientation of the ellipsoid) following from the point symmetry at the atomic sites for the following cases: **-1**, **2/m**, **4/m -3 2/m**

E8.3 Displacements at low temperatures

A. Discuss the reduction of the displacement parameters with decreasing temperature (fig.8.8): Is this effect real or an artefact? Arguments?

B. Discuss the non-zero values of the displacements factors for T => 0 K in the same figure and the different values for different atom types.

E8.4 Choice of neutron wavelengths

A. Magnetic neutron diffraction experiments are usually done with rather long wavelengths (see chapter 8.7: $\lambda = 1.87$ Å): Why?

B. Diffraction experiments aiming at obtaining precise atomic coordinates and displacements are done with much shorter wavelengths (see chapter 8.8: $\lambda = 0.552$ Å): Why?

C. Powder diffraction experiments usually use longer wavelengths than single crystal experiments: Why?
(Discuss this issue in terms of the competition between angular and direct space resolution.)

E8.5 Density maps from diffraction experiments

A. How can one obtain (from diffraction) the bonding electron density map?
(discuss the experiment(s), the necessary calculations and the information obtained)

B. Discuss the difference between the bonding electron density map and a magnetization density map. *(which kind of data is used, what is the specific information?)*

E8.6 Hydrogen bonded crystals

Assume you have grown a new hydrogen-bonded compound in the form of a single crystal and you want to know how the hydrogen bonds are arranged within the structure.

A. Collect arguments pro & con the usage of single crystal x-ray- vs. neutron diffraction experiment to study your new crystal.
(Discuss availability / costs of the experiment, required size of the crystal, scattering power of hydrogen, absorption & incoherent scattering, additional effort to deuterate etc.)

9 Neutron reflectometry

E. Kentzinger
Jülich Centre for Neutron Science 2
Forschungszentrum Jülich GmbH

Contents

Lecture Notes of the JCNS Laboratory Course Neutron Scattering

9.1 Introduction

Neutron reflectometry is a relatively new technique that allows determining the nuclear and magnetization profile along the depth of a nanometric thin film system. It has been extensively used for solving soft matter problems like polymer mixing, the structure of air-water, liquid-solid or oil-water interfaces, or the structure of bio-mimetic membranes [1]. The key property of neutrons for soft matter studies is their large contrast in nuclear scattering length between hydrogen and deuterium which allows selective labeling by deuteration.

In the mid 1980's, a new field of neutron reflectometry emerged. Following the discovery of new magnetic phenomena in ultra-thin films, interlayer exchange coupling and giant magneto-resistance effect in multilayered films [2], there has been an interest in the precise measurement of the magnetic moment direction in each layer of a multilayer and at the interface between layers. The large magnetic coupling between the neutron spin and the magnetic moment makes neutron reflectometry a powerful tool for obtaining information about these magnetic configurations and for measuring magnetic depth profiles (see lecture 10 of this book).

In this lecture, we will concentrate on neutron reflectometry for the determination of nuclear profiles. Section 9.2 shows the calculation of specular reflection at flat and homogeneous surfaces, introducing the concepts of scattering length density, index of refraction and total external reflection. It then describes the reflectivity from various types of layered structures and the effect of interfacial roughness and interdiffusion. The two types of reflectometers one can encounter and the practical aspects of a reflectometry experiment are discussed in section 9.3. Finally, two examples are given, one in the field of polymer science (section 9.4), the other one in biology (section 9.5).

9.2 Description of specular reflection

A monochromatic, well collimated beam impinges under a well defined, small angle $\alpha_i = \theta$ (in most cases $\theta \ll 5^o$) onto the surface of the sample. It is then partly reflected specularly from the surface, i.e. the outgoing angle $\alpha_f = \theta$ as well, and partly refracted into the material (See Fig. 9.1). As we will derive below, the reflection from a laterally homogeneous medium can be treated according to classical optics. Only the proper index of refraction n has to be used.

For most material, the index of refraction for neutrons is slightly smaller than 1, leading to total external reflection for small angles of incidence $\theta < \theta_c$, where θ_c depends on the material.

In the case of a single layer on the substrate, reflection and refraction take place at both the surface and the interface (Fig. 9.2). Then, the reflected beams from the different interfaces interfere with each other. Maximum intensity is received, when the path length difference between the two reflected beams is an integer multiple of the wavelength.

For the case of perfectly smooth surface and interfaces, an exact description of the reflected and transmitted intensity can be deduced from quantum theory.

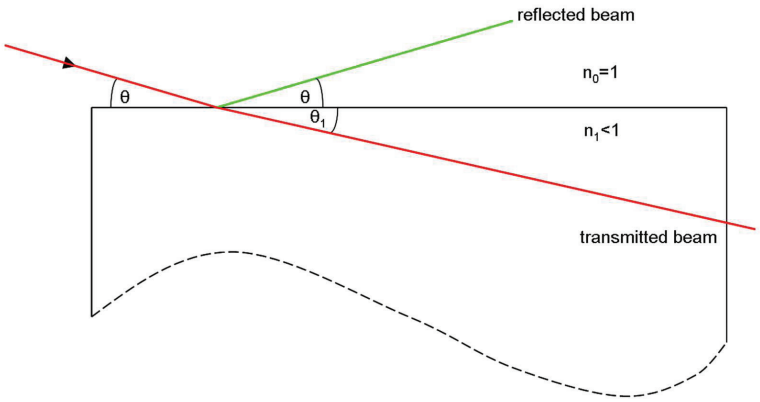

Fig. 9.1: *Reflection and refraction from a free surface*

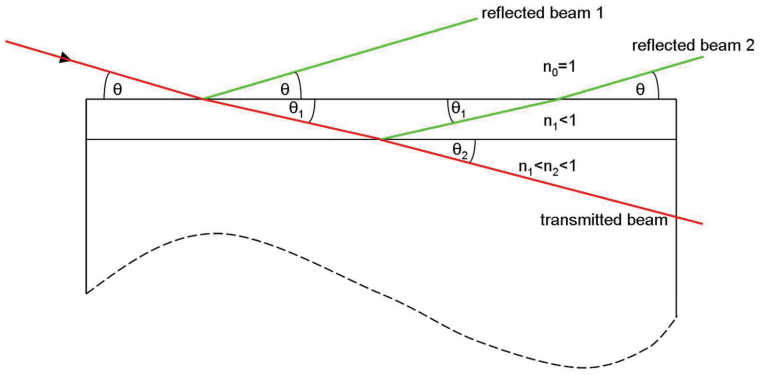

Fig. 9.2: *Reflection and refraction from a single layer on a substrate*

9.2.1 Wave equation in homogeneous medium. Optical index

The starting point is the Schrödinger equation for the wave function of the neutron:

$$\left[-\frac{\hbar^2}{2m}\Delta + V(\mathbf{r})\right]\psi(\mathbf{r}) = E\psi(\mathbf{r}) \tag{9.1}$$

The kinetic energy of the neutron is given by $E = \hbar^2 k^2/(2m)$ with the modulus $k = 2\pi/\lambda$ of the wave vector $\mathbf{k}$.

Due to the small $|\mathbf{Q}|$ values that are probed, a reflectometry experiment does not resolve the atomic structure of the sample in any of the three directions. Therefore, it is a valid approximation to describe the potential V_1 of the homogeneous material as

$$V_1 = \frac{2\pi\hbar^2}{m}\rho \tag{9.2}$$

where ρ if the scattering length density (SLD) defined by

$$\rho = \sum_j N_j b_j \tag{9.3}$$

where N_j is the number of nuclei per unit volume and b_j is the coherent scattering length of nucleus j. With that we receive

$$\left[\Delta + \left(k^2 - 4\pi\rho\right)\right]\psi(\mathbf{r}) = \left[\Delta + k^2\left(1 - \frac{\lambda^2}{\pi}\rho\right)\right]\psi(\mathbf{r}) = \left[\Delta + k_1^2\right]\psi(\mathbf{r}) = 0 \tag{9.4}$$

with the wave vector k_1 inside the medium. From this equation, it is justified to introduce the index of refraction in the material

$$n = \frac{k_1}{k} \qquad\qquad n \simeq 1 - \frac{\lambda^2}{2\pi}\rho \tag{9.5}$$

It is a number very close to 1 for thermal and cold neutrons. The quantity $1 - n$ is of the order of 10^{-6} to 10^{-5}. For most materials it is positive (because the coherent scattering length b_j is positive for most isotopes), so that n is smaller than 1. This means that the transmitted beam is refracted towards the sample surface, which is opposite to the daily experience with light refracted at a glass or liquid surface.

9.2.2 Solution for a sharp surface. Fresnel's formulas

In analogy to classical optics, we can derive e.g. Fresnel's formulas. For the solution of the wave equation at a sharp surface between air and a semi-infinite medium, we assume the surface of the sample to be at $z = 0$. The potential is then

$$V(z) = \begin{cases} 0 & for \quad z > 0 \\ V_1 & for \quad z \leq 0 \end{cases} \tag{9.6}$$

As the potential V is independent of the in-plane coordinates x and y, the wave function in the Schrödinger equation (9.4) is of the form

$$\psi(\mathbf{r}) = e^{i(k_x x + k_y y)}\psi_z(z) \tag{9.7}$$

with the in plane components k_x and k_y of $\mathbf{k}$ independent of z. The Schrödinger equation then reduces to the one dimensional equation

$$\frac{d^2\psi_z(z)}{dz^2} + k_z^2(z)\psi_z(z) = 0 \tag{9.8}$$

with $k_z(z)$ depending on the medium. The general solution is given by

$$\psi_{zl}(z) = t_l e^{ik_{zl}z} + r_l e^{-ik_{zl}z}, \tag{9.9}$$

where the index l distinguishes between vacuum (l=0) and medium (l=1). The unique solution is determined by the boundary conditions. The incoming wave in the vacuum before interaction with the sample is a plane wave of norm 1, i.e. t_0 is equal to 1. In a half-infinite medium, there is no reflected wave, because there is nothing to reflect from, i.e. r_1 vanishes. In addition, the wave function and its first derivative must be continuous at the interface. So we receive the following boundary conditions:

$$t_0 = 1 \ ; \ r_1 = 0 \ ; \ \psi_{z0}(z=0) = \psi_{z1}(z=0) \ ; \ \frac{d\psi_{z0}}{dz}(z=0) = \frac{d\psi_{z1}}{dz}(z=0). \tag{9.10}$$

When we insert (9.9) into (9.10) we receive the continuity equations for the wave function:

$$1 + r_0 = t_1 \ ; \ k_{z0}(1 - r_0) = k_{z1}t_1. \tag{9.11}$$

t_1 is the amplitude of the transmitted wave and r_0 is the amplitude of the reflected wave. The reflectivity R is defined as the modulus squared of the ratio of the amplitudes or reflected and incoming waves, the transmissivity T is defined as the modulus squared of the ratio of the amplitudes or transmitted and incoming waves.

$$R = |r_0|^2 \ ; \ T = |t_1|^2 \tag{9.12}$$

In conclusion, we arrive at the Fresnel's formulas for the reflection and the refraction at a flat interface

$$\text{Reflectivity :} \qquad R = \left| \frac{k_{z0} - k_{z1}}{k_{z0} + k_{z1}} \right|^2 \tag{9.13}$$

$$\text{Transmissivity :} \qquad T = \left| \frac{2k_{z0}}{k_{z0} + k_{z1}} \right|^2 \tag{9.14}$$

9.2.3 Snell's law of refraction. Total external reflection

Taking into account the continuity relation for the wave vector component tangential to the surface

$$k_{x0} = k_{x1} \qquad k_{y0} = k_{y1} \tag{9.15}$$

together with $k_1 = k_0 n_1$ (Eq. 9.5), Snell's law for refraction follows from trigonometry:

$$\frac{\cos\theta}{\cos\theta_1} = \frac{k_1}{k_0} = n_1 \tag{9.16}$$

The fact that in most cases the index of refraction is $n_1 < 1$ means that the transmitted beam is refracted towards the sample surface ($\theta_1 < \theta$ in Fig. 9.1). For angles of incidence θ below the so called critical angle θ_c with

$$n_1 = \cos\theta_c \qquad \theta_c \simeq \lambda\sqrt{\frac{\rho}{\pi}} \tag{9.17}$$

total reflection is observed, i.e. all intensity is reflected and no wave propagating in z-direction exists in the sample. Only an evanescent wave in the z-direction with propagation parallel to the surface is induced. For angle of incidence above θ_c, the beam can partially penetrate the sample and is only partly reflected.

From Snell's law (Eq. 9.17) and the definition of the index of refraction in Eq. (9.4) one can relate the normal components of the incoming and refracted wave vectors

$$k_{z1}^2 = k_{z0}^2 - k_{z0,c}^2 \quad \text{with} \quad k_{z0,c} = \frac{2\pi}{\lambda}\sin\theta_c = \sqrt{4\pi\rho}. \tag{9.18}$$

This confirms that, for angles of incidence θ below θ_c, k_{z1} becomes purely imaginary and the refracted wave is an evanescent wave in the z-direction.

The last relation allows to express the Fresnel coefficients (Eq. 9.13 and 9.14) as a function of one variable only. In general the measured reflectivity is represented as a function of θ or the magnitude of the scattering wave vector $Q = 2k_{z0}$:

$$R = \left|\frac{Q - \sqrt{Q^2 - Q_c^2}}{Q + \sqrt{Q^2 - Q_c^2}}\right|^2 \tag{9.19}$$

When $Q \gg Q_c$, the preceding equation reduces to:

$$R \simeq \frac{1}{16}\frac{Q_c^4}{Q^4} \tag{9.20}$$

which is the formula for the reflectivity within the Born approximation [3]. This shows that the reflectivity above the critical angle decreases sharply with Q.

Once again, coming back to the wave function inside the surface, one finds using Eq. (9.18) that, when $\theta < \theta_c$:

$$\psi_{z1}(z) = t_1 e^{i\left(k_{z0}^2 - k_{z0,c}^2\right)^{1/2} z} = t_1 e^{-\frac{1}{2}\left(Q_c^2 - Q^2\right)^{1/2} z}. \tag{9.21}$$

This result is very important, because it shows that when the energy of the particle normal to the surface is smaller than the potential barrier, the wave still can penetrate the medium on a characteristic depth of $2/\sqrt{Q_c^2 - Q^2}$. This evanescent wave propagates itself along the surface

with a wave vector equal to (k_x, k_y) and then leaves the volume in the specular direction. For example for Ni ($\rho = 9.41 \times 10^{-6}$ Å^{-2}), the penetration depth is of the order of 200 Å at $Q = 0$; if one neglects absorption, it raises rapidly to infinity at $Q = Q_c$. No conservation rule is broken: the reflectivity equals 1 because this wave represent no transmitted flux in the medium.

Fig. 9.3 represents, on a linear scale, the reflectivity and the transmissivity of a substrate as a function of the angle of incidence θ. The reflectivity equals 1 for angles smaller than the critical angle θ_c and decreases rapidly above this value (Eq. 9.20). The transmissivity increases monotonously up to a value of 4 at θ_c and decreases to 1 at large angles. This result might look very surprising at first sight. The value of 4 for the transmissivity comes from the fact that the incident and the reflected waves in vacuum superpose to form a stationary wave of amplitude exactly equal to 2 at the interface with the medium. For the intensity, we obtain a factor of 4.

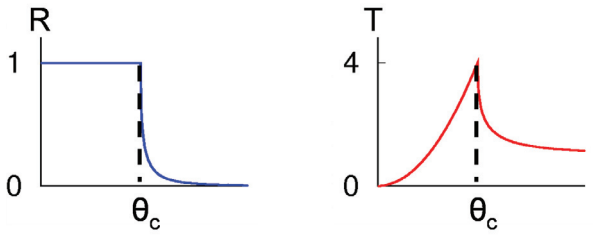

Fig. 9.3: *Reflectivity and transmissivity of a substrate as a function of the angle of incidence*

9.2.4 Reflectivity from layered systems

In a layered system, the same Ansatz as in Eq. (9.9) can be written in each layer l. The coefficients of reflection r_l and transmission t_l can be deduced recursively from the continuity relations of the wave function and its derivative at each interface. If N is the number of layers, and considering the vacuum on top of the multilayer and the substrate below, 2(N+2) coefficients have to be calculated. The number of interfaces being N+1, the continuity relations lead to 2(N+1) equations. Two other equations are obtained considering that the transmission into the vacuum is equal to one ($t_0 = 1$) and that, in the substrate, there is no reflected wave ($r_{N+1} = 0$), leading in total to a number of equations equal to the number of coefficients to determine. The calculation of the coefficients of reflection and transmission in each layer and, in particular, the calculation of the reflectivity in air are therefore possible [4].

Here we just want to demonstrate with very simple arguments how interference effects from layered structures arise and how the intensity modulations in Q-space are related to real space length scales.

Fig. (9.2) shows how interference can occur in a system composed of a single layer of thickness d deposited on a substrate. Interference occurs between beams reflected from the surface and those first transmitted in the layer, reflected from the interface between layer and substrate and then leaving the layer into vacuum. To a good approximation, refraction at the top surface can be neglected for incident angles twice the critical angle or total reflection. In this case $\theta = \theta_1$ in Fig. (9.2) holds. Since the index of refraction of the neutrons is very close to one, this

approximation is valid even for rather small angles of incidence. Then the optical path length difference between the two beams is:

$$\Delta = 2d \sin\theta \tag{9.22}$$

We can now determine the distance between interference maxima from the condition that the path length difference has to differ by one wavelength: $\lambda = 2d \cdot \delta(\sin\theta) \simeq 2d \cdot \delta\theta$. With $Q = \frac{4\pi}{\lambda}\sin\theta \simeq \frac{4\pi}{\lambda}\theta$ we final obtain:

$$\delta Q \simeq \frac{2\pi}{d} \tag{9.23}$$

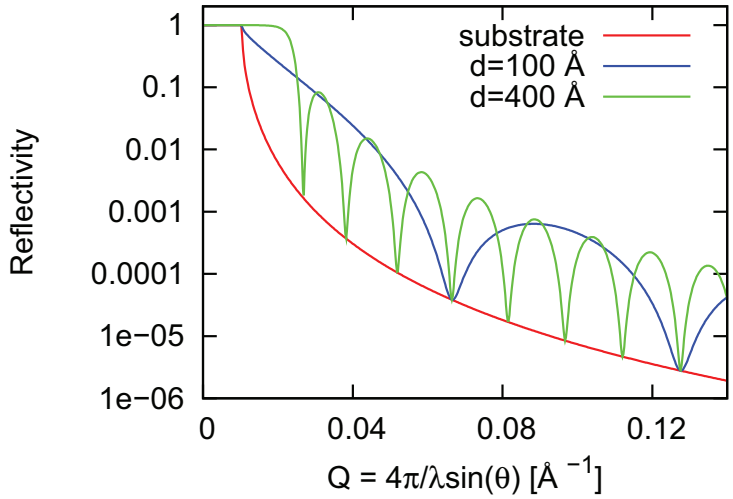

Fig. 9.4: *Reflectivity of a Si substrate and reflectivity of a Ni layer ($\rho = 9.41 \times 10^{-6}$ Å^{-2}) on Si substrate ($\rho = 2.15 \times 10^{-6}$ Å^{-2}). Simulations are performed for two layer thicknesses d.*

We can see that the interference phenomena in Q-space are connected with real space length scales in a reciprocal way. (9.23) tells us that there will be a number of interference maxima at a distance in Q of $\frac{2\pi}{d}$. These interference phenomena are called "Kiessig fringes". Fig. 9.4 shows calculations of the reflectivity of a Ni layer deposited on a Si substrate. One observes that the reflectivities above the critical angle for total reflection decrease rapidly, therefore the ordinate is on a logarithmic scale. The oscillations of the reflectivity due to the above described interference effect can be observed. At small angles, due to the effect of refraction, the interference maxima are a bit denser distributed than at higher angles where formula (9.23) can be used to determine the layer thickness from the distance between the interference maxima. The thinner layer corresponds to an interference scheme with a bigger period. In both cases the minima of the interference scheme lay on the reflectivity of the Si substrate.

Note that for a 100 Å thick layer of Ni, that has a scattering length density (SLD) approximately 4 times larger than the one of Si, the critical angle of total reflection is determined by the SLD

of Si and not by the one of Ni. This comes from the penetration depth of the neutrons that is bigger than 100 Å. For a 400 Å thick Ni layer, the θ_c approaches the one of Ni and the total reflection plateau is somewhat rounded.

Fig. 9.5 shows the simulation of the neutron reflectivity from a multilayer on a Si substrate. This multilayer is composed of 10 double layers of 70 Å Ni and 30 Å Ti. On can clearly see the pronounced maxima due to the periodicity of the Ni/Ti double layer of thickness 100 Å. In between, one observes many weaker oscillation (be attentive to the logarithmic scale) with a period given by the total thickness of the multilayer.

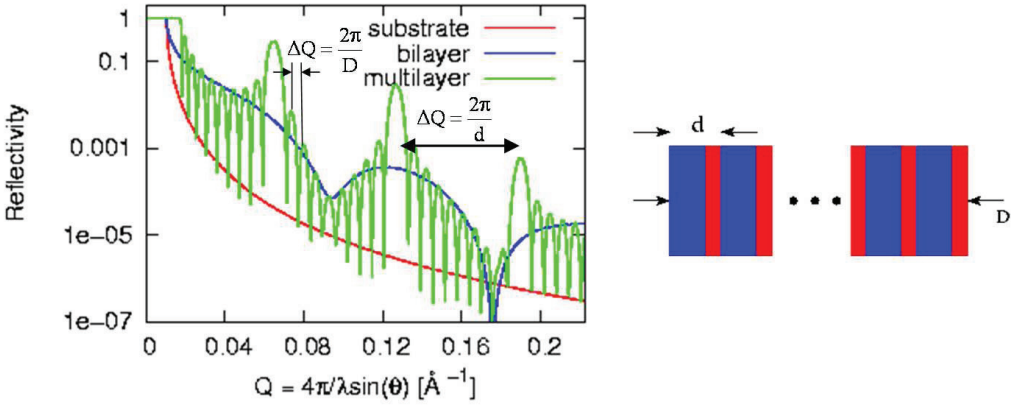

Fig. 9.5: *Reflectivities of a Ni/Ti bilayer and of a Ni/Ti multilayer on Si substrate. Simulations are performed for Ni and Ti thicknesses of 70 and 30 Å respectively.*

9.2.5 Roughness and interdiffusion

Until now we assumed perfectly flat interfaces. A real interface will, however, always show a certain roughness at the atomic level, as shown in Fig. 9.6. The height profile of the interface is completely described by the parametrization $z(x, y)$. Such a detailed information is not at all interesting. Much more interesting are parameters that statistically describe the interface, such as the mean squared deviation from an ideally flat interface, or the lateral correlation length. Those parameters can be determined from reflectometry and scattering under grazing incidence [5].

As simplest model, we assume that the height coordinate z follows a random distribution of values around the nominal value z_j of the flat interface. The random distribution being described by a Gaussian function

$$P(\Delta z) = \frac{1}{\sigma\sqrt{2\pi}} \exp\left(-\frac{\Delta z^2}{2\sigma^2}\right), \tag{9.24}$$

the profile of index of refraction between layers j and $j+1$ takes the form:

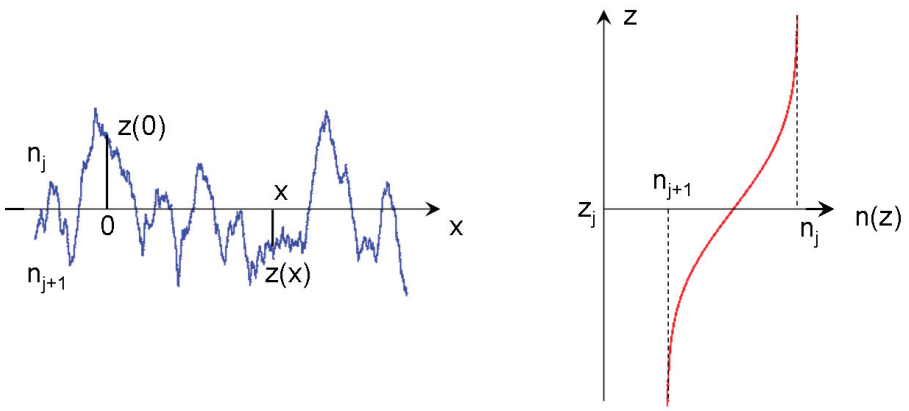

Fig. 9.6: *Roughness of a real interface, characterized by the parametrization $z(x, y)$ and dependency of the refractive index on z.*

$$n(z) = \frac{n_j + n_{j+1}}{2} - \frac{n_j - n_{j+1}}{2}\mathrm{erf}\left(\frac{z - z_j}{\sqrt{2}\sigma_j}\right) \tag{9.25}$$

with the "Error" function:

$$\mathrm{erf}(z) = \frac{2}{\sqrt{\pi}} \int_0^z e^{-t^2} dt. \tag{9.26}$$

The reflectivity from such a rough interface is obtained from the average of the reflectivities from a sequence of layers that describe the profile of refraction index. This average is performed in detail in Ref. [6]. As a result one obtains that the Fresnel coefficient for an ideally flat interface has to be modified by an exponential damping factor in the following way:

$$R_{rough} = R_{flat} \cdot \exp\left(-4\sigma_j^2 k_{zj} k_{zj+1}\right). \tag{9.27}$$

In this equation, σ_j is the root mean squared deviation from the nominal position of the flat interface.

The effects of interfacial roughness on the neutron reflectivity from a Si substrate and from a Ni layer on Si substrate have been simulated in Fig. 9.7. On the left side of Fig. 9.7 one can observe that the effect of roughness is to decrease the reflectivity at large wave vector transfers. The effect of roughness will be seen, if the value of the scattering wave vector gets bigger than $1/\sigma$. Therefore, if one wants to determine very small roughness amplitudes, one has to measure the reflectivity till very large reflection angles and over a large dynamical range.

The right side of Fig. 9.7 shows the effect of the roughness of a single layer. The simulations have been performed for ideally flat interfaces, for a rough surface of the layer, for a rough interface between layer and substrate and for the case where both interfaces are rough. One can

see that the four cases can be well differentiated. When only one of the two interfaces is rough, the interference pattern due to the reflection on the top and bottom interfaces is suppressed at large wave vectors. If both interfaces are rough, a faster decrease of the averaged reflectivity takes place.

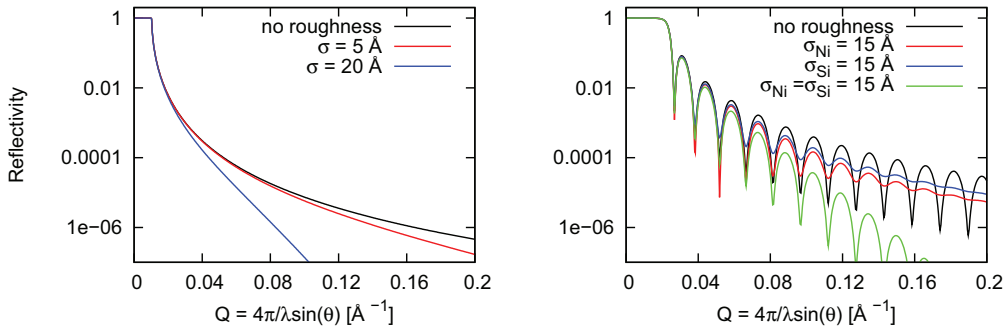

Fig. 9.7: *Left: Neutron reflectivity at the interface between vacuum and Si. Right: Neutron reflectivity from a 400 Å thick Ni layer on Si substrate. Effect of interfacial roughness.*

Finally, one should point out that a specular reflectivity measurement can only describe the profile of scattering length density normal to the interface. This means that a reflectivity measurement can not differentiate between interfacial roughness and interdiffusion, as interdiffusion will induce the same profile of refraction index as in Fig. 9.6. But what happens to the intensity loss described by the exponential factor of Eq. (9.27)? In the case of a diffuse interface, this intensity goes into the transmitted beam because there is no potential gradient in a direction different than the one normal to the interface. On the other hand, in the case of a rough interface, the intensity loss comes from scattering by lateral fluctuations of the potential, leading to intensities that can be observed in directions other than the specular direction: this is off-specular diffuse scattering. A statistical function like the height-height pair correlation function can be determined from the measurement of off-specular scattering [5].

9.3 Neutron reflectivity measurement and data analysis

The principal components of a reflectivity experiment are (i) a radiation source, (ii) a wavelength selector (monochromator, choppers), (iii) a collimation system, (iv) the sample and (v) a detection system.

The aim of a neutron specular reflectivity experiment is to measure the reflectivity as a function of the scattering wave vector Q perpendicular to the sample surface:

$$Q = \frac{4\pi}{\lambda} \sin\theta \tag{9.28}$$

The measurement can be done by changing either the angle of incidence θ on the sample or the wavelength λ, or both.

9.3.1 Monochromatic instruments

At a nuclear reactor source, the measurements are usually performed at a fixed value of λ, using θ-2θ scans (2θ being the detector angle). The wavelength selection can be obtained by Bragg scattering on a monochromator crystal or by using a velocity selector. Fig. 9.8 describes such an instrument. This is the MARIA reflectometer of the JCNS located at the FRM-II source in Garching [7]. The neutrons are brought from the cold source to the instrument using a supermirror coated guide (see lecture 2 of this book). A certain wavelength with a spread of 10 % is chosen by adjusting the rotation speed of a velocity selector. The wavelength spread can be reduced by using a Fermi chopper and time-of-flight detection. The neutron beam is then collimated by a pair of slits in order to define the angle of incidence of the neutrons relative to the sample surface with a certain precision. The neutrons are then detected on a two dimensional position sensitive detector. Such a detector allows to record at the same time not only the specular reflectivity signal but also the signals of off-specular scattering and grazing incidence small angle scattering. The projection of the spin of the neutron on a quantization axis can be selected before interaction with the sample by using a polarizer and after interaction with the sample by using a polarization analyzer, allowing to retrieve information about the norm and angle of the layer magnetizations in a magnetic sample (see lecture 10). The polarizer uses magnetic supermirrors and the analyzer uses a nuclear polarized ^{3}He gas to select the spin projection.

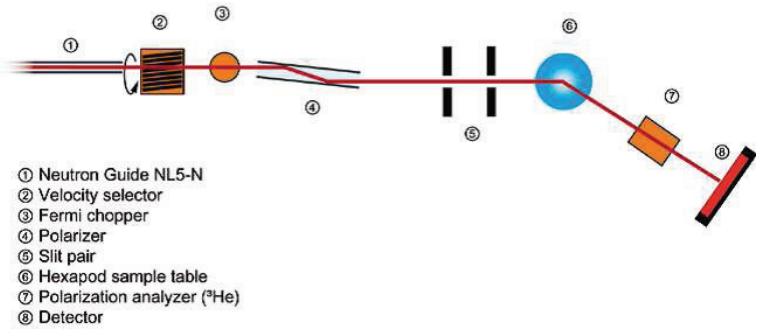

Fig. 9.8: *A monochromatic instrument: MARIA of the JCNS at FRM-II [7].*

9.3.2 Time-of-flight instruments

At a spallation source, the measurements are performed at fixed values of θ and as a function of λ. This is the time-of-flight technique, that consists in sending a pulsed white beam on the sample. Since the speed of the neutron varies as the inverse of the wavelength, the latter is directly related to the time taken by the neutron to travel from the pulsed source to the detector (over the distance L) by:

$$\lambda = \frac{h}{mL}t. \tag{9.29}$$

For a reflectivity measurement, the angle is fixed and the reflectivity curve is obtained by measuring the reflectivity signal for each wavelength of the available spectrum, each wavelength corresponding to a different scattering wave-vector magnitude. Sometimes it is necessary to use several angles of incidence because the Q range is not large enough.

An example of time-of-flight reflectometer is presented in Fig. 9.9. This is the magnetism reflectometer of the Spallation Neutron Source (SNS) in Oak Ridge, USA [8]. Neutrons coming from the moderator are first deflected by 2.5^o using a channel beam bender, composed of a stack of supermirrors, in order to achieve enough separation with the neighbour instrument (a liquid reflectometer) and in order to deliver to the sample a "clean" neutron beam, essentially free of fast neutrons and γ radiation. As much useful neutrons as possible are transported to the sample by using a supermirror coated tapered neutron guide that focuses the beam horizontally and vertically to a size comparable to usual sample sizes, i.e. several cm^2. The bandwidth choppers are used to select a wavelength width (λ from 2 to 5 Å), in order to avoid frame overlap. A chopper is a rotating disk with windows transparent to neutrons. When two choppers are mounted at a certain distance one with respect to the other, the delay between the window openings and the width of the windows can be chosen to achieve a transmission of only those neutrons having speeds contained in a certain range. The phenomenon of frame overlap happens when the slow neutrons of a pulse are overtaken by the fast neutrons of the next pulse. A time-of-flight detection cannot differentiate between those neutrons. Therefore, frame overlap has to be avoided. The function of the second of the three choppers is to absorb the very slow neutrons. This instrument has also collimation slits, a position sensitive detector and polarizing and analyzing devices whose functions are the same as the ones explained in the preceding section.

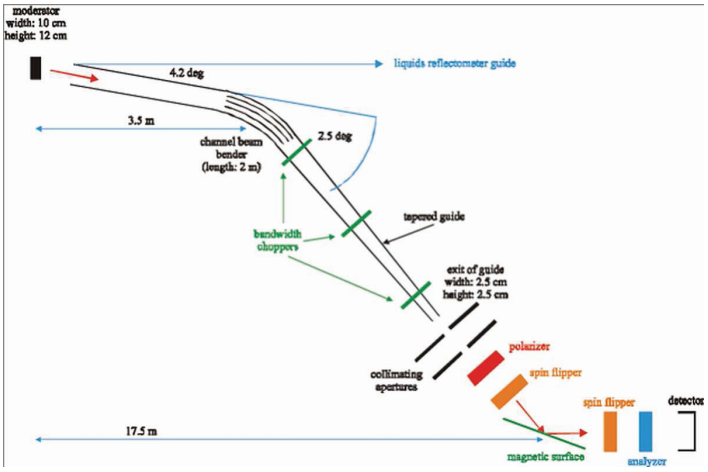

Fig. 9.9: *A time-of-flight instrument: The magnetism reflectometer of the SNS [8].*

9.3.3 Resolution

The reflectivity signal decreases very rapidly above the critical angle of total reflection when Q increases (see Eq. (9.20), $R \propto 1/Q^4$). In order to win some intensity, either the collimation slits can be opened or the wavelength spread $\delta\lambda$ can be increased, at the price of a loss in resolution in scattering wave vector. The dispersion in Q is given by (for $\theta \ll 1$):

$$\delta Q \simeq \sqrt{\left(\frac{4\pi}{\lambda}\frac{\delta\lambda}{\lambda}\theta\right)^2 + \left(\frac{4\pi}{\lambda}\delta\theta\right)^2} \tag{9.30}$$

where $\delta\theta$ is the beam angular divergence. The divergence of the incident beam is usually determined by the two collimation slits if the beam is smaller than the effective width of the sample seen by the neutron beam, or by the first slit and the sample itself if the sample is small enough to be totally illuminated by the neutron beam. The experimental reflectivity is then the calculated reflectivity convoluted by a resolution function whose width is given by δQ. Experience shows that Gaussian function works well to reproduce the resolution effects. In Fig. 9.10 the reflectivity is calculated for a perfect instrument and by taking into account the effects of angular divergence and wavelength spread. As can be inferred from Eq. (9.30), angular divergence induces a loss of resolution independent of θ, and wavelength spread degrades the resolution as θ increases. This example shows that, when preparing a reflectometry experiment and depending on the sample under study, a good compromise between intensity and resolution has to be found.

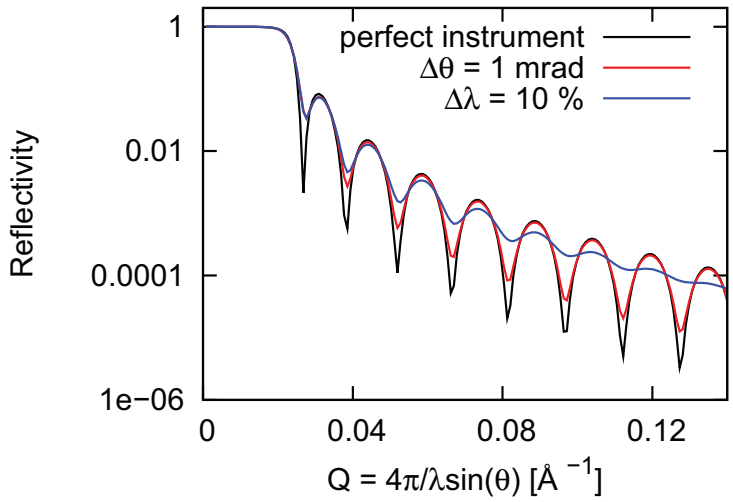

Fig. 9.10: *Effect of $\delta\theta$ and $\delta\lambda$. Comparison between a perfect instrument, an instrumental $\delta\theta$, and a $\delta\lambda$ for a measurement on a 400 Å thick Ni layer on Si substrate*

9.3.4 Data analysis

The method of analysis often used for specular reflection data involves the construction of a model of the multilayer consisting of a series of parallel layers of homogeneous material. Each layer is characterized by a scattering length density ρ and a thickness d, which are used to calculate a model reflectivity profile by means of the recursion method introduced in section 9.2.4 and taking into account the resolution in Q (section 9.3.3). The interfacial roughness or interdiffusion between two consecutive layers, σ, may also be included as described in section 9.2.5. The calculated profile is compared to the measured profile and the quality of the fit is assessed either visually or by using χ^2 in the least-square method. By variation of ρ, d and σ in each layer and interface, the calculated profile may be compared with the measured profile until optimum fit to the data is found. Any one profile may not provide a unique solution. This is because only the intensity, and not also the phase of the reflection amplitude is measured. In soft matter, the use of different isotopic contrasts can usually ensure an unambiguous model of the system. Contrast variation relies on the fact that different nuclear isotopes scatter neutrons with different amplitudes, and sometimes, as in the case of protons and deuterons, with opposite phases. By using several combinations of hydrogenated and deuterated materials the reflectivity profile of a layered system can be substantially changed while keeping the same chemical structure. An example where contrast variation is used is given in section 9.5.

9.4 Interdiffusion between diblock copolymer layers under annealing

Diblock copolymers are made up of two blocks of different polymerized monomers. Block copolymers are interesting because they can ”microphase separate” to form periodic nanostructures. Microphase separation is a situation similar to that of oil and water. Oil and water are immiscible - they phase separate. Due to incompatibility between the blocks, block copolymers undergo a similar phase separation. Because the blocks are covalently bonded to each other, they cannot demix macroscopically as water and oil. In ”microphase separation” the blocks form nanometer-sized structures. Depending on the relative lengths of each block, several morphologies can be obtained. In diblock copolymers, sufficiently different block lengths lead to nanometer-sized spheres of one block in a matrix of the second (for example PMMA in polystyrene). Using less different block lengths, a ”hexagonally packed cylinder” geometry can be obtained. Blocks of similar length form layers (often called lamellae in the technical literature) [9].

In the study presented in this chapter, a diblock copolymer of the type polystyrene - polybutylmetacrylate (PS-PBMA), with similar lengths of the two blocks, has been deposited on a substrate by spin-coating, forming a self-organized multilayer of a fixed thickness parallel to the surface. The initial system consists in a layer of partially deuterated PS-PBMA copolymer deposited on a trilayer of totally hydrogenated copolymer. The reflectivity of the system is shown on the left picture of Fig. 9.11. The numerical fit shows a large index at the top of the system corresponding to the deuterated copolymer. The system has then been annealed for 12 hours at 400 K and then remeasured (right picture of Fig. 9.11). On this reflectivity curve, one can observe a clear “Bragg” peak at the position $q_1 = 0.11$ nm^{-1}, and a second

one at $q_2 = 0.29$ nm^{-1}. This indicates the diffusion of the deuterated polymer to the inner layers. Since the diblock copolymers are ordered in multilayers, a periodic variation of the index appears (see insert in Fig. 9.11), whose period is approximately given by $2\pi/(q_2 - q_1)$. (After [10])

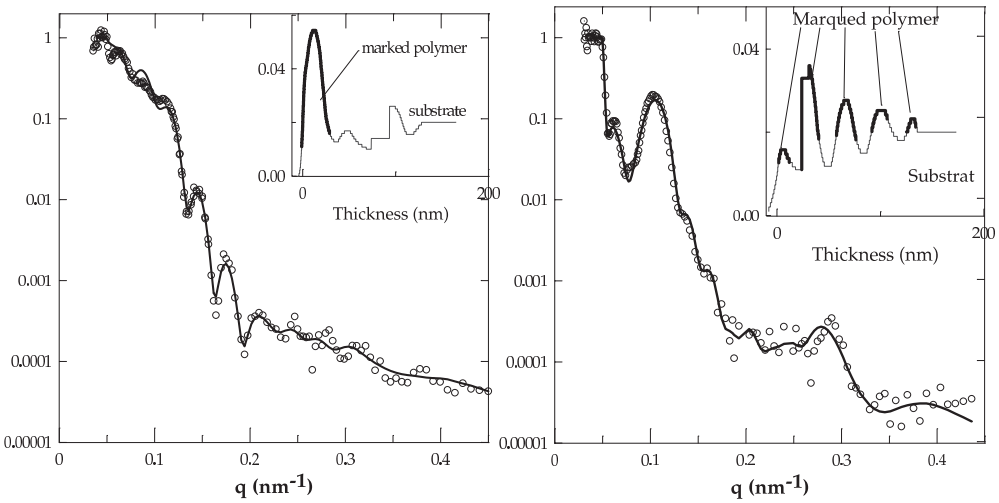

Fig. 9.11: *Left: Reflectivity of a quadrilayer consisting in a partially deuterated PS-PBMA copolymer layer deposited on a trilayer of totally hydrogenated polymer. Right: Reflectivity of the quadrilayer after annealing for 1 hour at 115 C. (After [10]). Measurements performed on the time-of-flight reflectometer EROS at the Laboratoire Léon Brillouin [11]*

9.5 Structural characterization of sparsely tethered bilayer lipid membranes

All cells are enclosed by biological membranes that define their boundaries and regulate their interactions with the environment. The biological membrane consists of assemblies of lipid and protein molecules. The lipid molecules form a continuous double layer, or bilayer, which acts as a barrier to water-soluble molecules and provides the framework for the incorporation of the protein molecules. The intrinsic complexity of the cell membrane system often precludes direct access to these features, thus driving the development of simpler model systems that are more amenable to a detailed characterization. One generic approach involves supports for the stabilization of biomimetic membranes. The work shown here focuses on a membrane system, illustrated in Fig. 9.12, that is chemically tethered to a gold support through a tether lipid.

Tethered membranes are systems designed for the incorporation of membrane-associated proteins. In order to be useful as a biomembrane model, such membranes need to retain their fluid in-plane organization and at the same time remain separated from the supporting solid interface by a molecularly thin hydration layer. In order to create space for hydration, the tether lipid

is co-adsorbed with a smaller "backfiller" molecule (see Fig. 9.12). The resulting "sparsely-tethered membrane" has been characterized by ellipsometry, electrochemical impedance spectroscopy and neutron reflectometry [12].

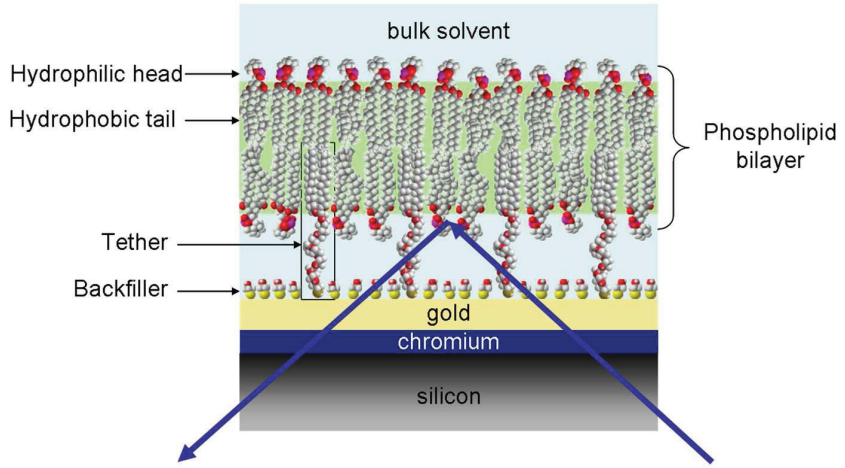

Fig. 9.12: *Sparsely tethered biomimetic membrane. The arrows show the geometry of the neutron reflection experiment: the neutrons hit the sample from the side of the silicon substrate.*

Neutron reflection is uniquely capable of characterizing in molecular detail the resulting membrane structure, particularly with respect to the thin hydration layer. Fig. 9.13 shows data sets measured on the system discussed above in three distinct solvent contrasts (pure D_2O, pure H_2O and a H_2O/D_2O mixture with SLD 4×10^{-6} $\AA^{-2}$ called CM4). The three measurements used the same sample, with the exchange of the isotopically distinct water solutions performed *in-situ*, and were co-refined on the assumption that the sample is identical except for the distinct solvent contrasts. As is evident from the differences in the SLD profiles, the spacer region containing the tethers is highly hydrated while the bilayer membrane covers the substrate homogeneously: only a minimal hydration of the inner leaflet is present. Such a system thus constitutes a biomimetic membrane that is very well suited to understand the interaction between lipid bilayer and membrane proteins [13, 14].

The top graph of Fig. 9.13 shows measurements performed on a system with a molar proportion of tether to backfiller at the gold surface equal to 30 to 70 and the bottom graph shows measurements performed with this proportion equal to 15 to 85. The SLD profiles show that the aqueous reservoir for the system containing 30 % of tether at the gold surface is 21 Å thick, the one for the system containing 15 % of tether being slighlty thinner, i.e. 19 Å thick. This slight difference in thicknesses is revealed by slight shifts in the positions of the intensity maxima and minima in the region of scattering wave vectors around $Q_z = 0.2$ $\AA^{-1}$. This comparison gives an idea of the high resolution of the neutron reflection technique.

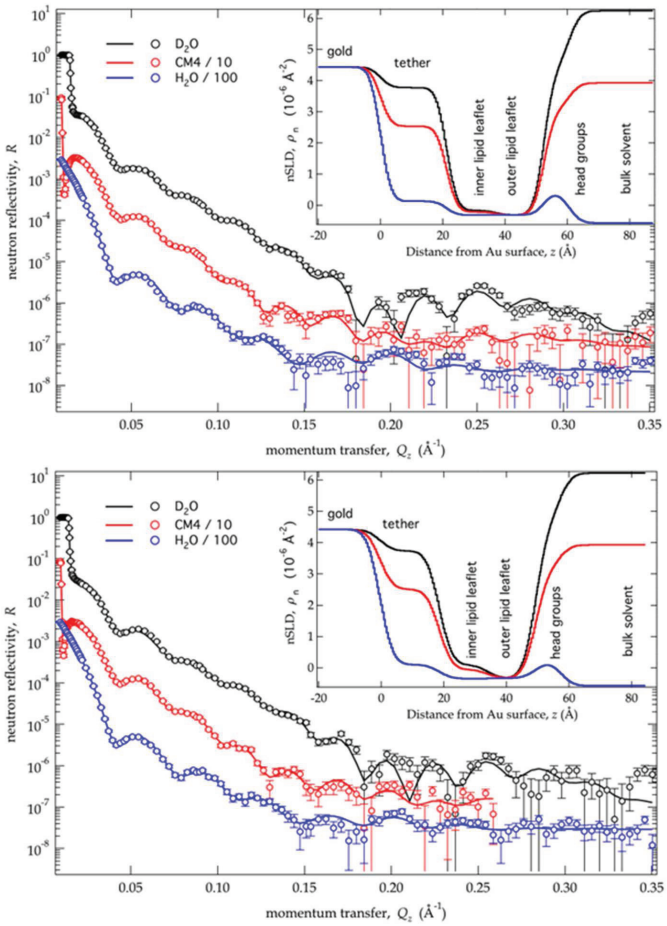

Fig. 9.13: *Neutron reflectometry on sparsely tethered bilayer lipid membranes. The two graphs represent measurements performed on two different samples with two different molar proportions of tether and backfiller molecules anchored at the gold surface. Top graph: 30 % of tether. Bottom graph: 15 % of tether. Those measurements were performed on the Advanced Neutron Diffractometer/Reflectometer (AND/R) [15] at the NIST Center for Neutron Research (NCNR).*

9.6 Conclusion and outlook

This chapter has given an overview of neutron reflectometry as a tool for the investigation of surfaces and interfaces. We have presented a formalism which makes it possible to describe the specular reflectivity on non-magnetic systems. Neutron reflectivity is especially suited for polymer and magnetic thin film systems. This has been illustrated with two examples. The formalism of neutron reflectometry for the investigation of the magnetic moment orientations in magnetic multilayers is presented in the next chapter of this book, together with several application examples.

Recently, the neutron reflectometry technique has been extended to study nuclear and magnetic structures in the sample surface. At grazing incidence, it is possible to distinguish three scattering geometries: specular reflection, scattering in the incidence plane of the neutrons (off-specular scattering) and scattering perpendicular to the incidence plane (grazing incidence SANS). These different scattering geometries probe different mesoscopic length scales and directions in the sample surface [16–19].

References

[1] A special issue of *Langmuir* covers a broad range of applications of this technique for the characterization of surfaces and interfaces in the fields of soft matter and biology: *Lamgmuir* **25(7)**, (2009).

[2] P. Grünberg, *J. Phys. Condens. Matter* **13**, 7691 (2001).

[3] M. Born and E. Wolf, *Principles of Optics* (Pergamon Press, Oxford, 1989).

[4] L.G. Parratt, *Phys. Rev.* **95**, 359 (1954).

[5] S.K. Sinha, E.B. Sirota, S. Garoff, H.B. Stanley, *Phys. Rev. B* **38:4**, 2297 (1988).

[6] L. Névot, P. Croce, *Rev. de Phys. Appl.* **15**, 761 (1980).

[7] http://www.jcns.info/MARIA_new

[8] http://neutrons.ornl.gov/instruments/SNS/MR/

[9] I.W. Hamley, *The Physics of Block Copolymers* (Oxford University Press, Oxford, 1998).

[10] C. Fermon, F. Ott, A. Menelle: "Neutron Reflectometry" in J. Daillant, A. Gibaud (eds), *X-Ray and Neutron Reflectivity: Principles ans Applications* (Springer, Berlin, 1999).

[11] http://www-llb.cea.fr/en/fr-en/spectros_p.php

[12] F. Heinrich, T. Ng, D.J. Venderah, P. Shekar, M. Mihailescu, H. Nanda, M. Lösche, *Langmuir* **25**, 4219 (2009).

[13] D.J. McGillivray, G. Valincius, F. Heinrich, J.W.F. Robertson, D.J. Vandrah, W. Febo-Ayala, I. Ignatjev, M. Lösche, J.J. Kasianowicz, *Biophysical Journal* **96:4**, 1547 (2009).

[14] S.A.K. Datta, F. Heinrich, S. Raghunandan, S. Krueger, J.E. Curtis, A. Rein, H. Nanda, *J. Mol. Biol.* **406**, 205 (2011).

[15] J.A. Dura, D.J. Pierce, C.F. Majkrzak, N.C. Maliszewskyi, D.J. McGillivray, M. Lösche, K.V. O'Donovan, M. Mihailescu, U. Perez-Salas, D.L. Worcester and S.H. White, *Rev. Sci. Instrum.* **77**, 074301 (2006).

[16] P. Müller-Buschbaum, E. Maurer, E. Bauer, R. Cubitt, *Langmuir* **22**, 9295 (2006).

[17] E. Kentzinger, H. Frielinghaus, U. Rücker, A. Ioffe, D. Richter and Th. Brückel, *Physica B* **397**, 43 (2007).

[18] E. Kentzinger, U. Rücker, B. Toperverg, F. Ott and Th. Brückel, *Phys. Rev. B* **77**, 104435 (2008).

[19] D. Korolkov, P. Busch, L. Willner, E. Kentzinger, U. Rücker, A. Paul, H. Frielinghaus, and Th. Brückel, submitted to *J. Appl. Cryst.* (2011)

Exercises

In the following the nuclear scattering length densities (in 10^{-6} Å^{-2}) of several elements are displayed:

Cu: 6.53; Ag: 3.5; Si: 2.15; Au: 4.5

E9.1 Reflection and transmission by a flat substrate

The following figure shows the neutron reflectivity from a flat substrate.

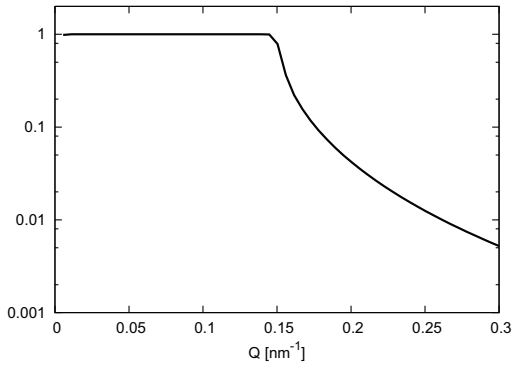

Fig. 9.14: *Reflectivity from a substrate.*

- Determine the element of which this substrate is made of
- Explain why the amplitude of the wave transmitted in the substrate is equal to 2 at an angle of incidence equal to the critical angle of total reflection

E9.2 Layers on substrate

The figure below shows two simulations of reflectivity from a Cu layer deposited on Ag substrate. Determine for both cases (red and blue curves) the thickness of the Cu layer.

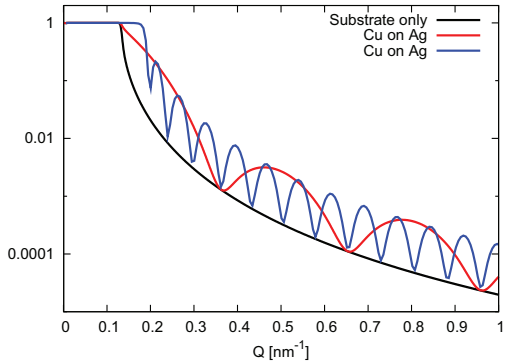

Fig. 9.15: *Layer of Cu on Ag substrate*

In the next figure, the reflectivity from a [Cu/Au]×n multilayer is depicted. Determine the [Cu/Au] thickness, the total thickness of the multilayer and the number n of bilayers the multilayer is composed of.

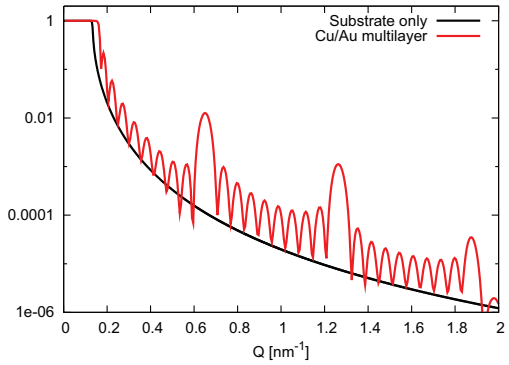

Fig. 9.16: *Cu/Au multilayer on Ag substrate*

10 Magnetic Nanostructures

U. Rücker
Jülich Centre for Neutron Science 2
Forschungszentrum Jülich GmbH

Contents

Lecture Notes of the JCNS Laboratory Course Neutron Scattering

10.1 Introduction

The physical properties of a layered structure of nanometer size, as it is shown schematically in Fig. 10.1, differs from the bulk properties of the constituents. There are several origins of new effects due to miniaturization:

The ratio between surface and volume is much higher than in bulk. Therefore, the amount of atoms with reduced coordination is significant and can change the crystalline structure as well as the electronic structure of the whole layer. Boundary conditions, e.g. for the magnetic induction **B** become important, introducing shape anisotropies. The magnetization tends to align along the long edges of the magnetic nanostructure because the dipolar fields are smaller then.

At the interface between two layers, the electronic structures and the crystal lattices have to be matched, which leads to structural stress, interfacial disorder and electronically to charge transfer (e.g. a Shottky barrier in semiconductor heterostructures) or splitting of the layers' bandstructures.

Nanostructures can be prepared in several dimensions: thin films with a thickness in the nm range are 2D nanostructures, stripes with thickness and width are 1D nanostructures and dots or nanoparticles with all three dimensions in the nm range are 0D nanostructures. The dimension number indicates, in how many directions the dimension remains macroscopic.

Magnetic nanostructures are nanostructures which contain at least one magnetic constituent. Typical systems are layered structures with ferromagnetic and nonmagnetic layers or arrays of ferromagnetic dots on a nonmagnetic substrate. The interesting aspect of magnetic nanostructures is the fact that two ferromagnetic (FM) layers with a nonmagnetic (NM) spacer in between have a connection between their electronic systems across the spacer layer. This connection influences as well the magnetic behaviour as the electron transport through the system.

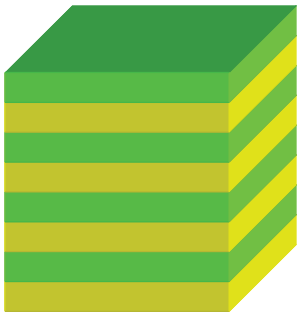

Fig. 10.1: *Sketch of a layered structure of two materials*

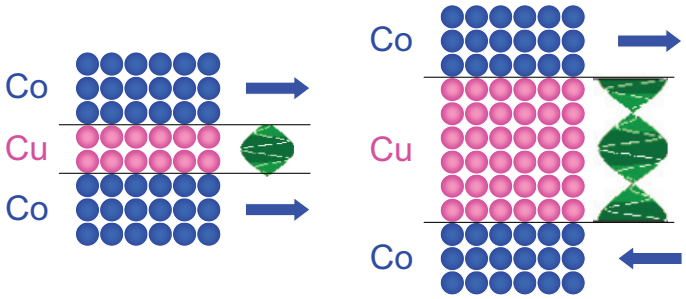

Fig. 10.2: *Oscillating interlayer coupling as a function of interlayer thickness*

The first phenomenon found in magnetic layered structures has been the oscillating magnetic interlayer coupling in FM / NM / FM trilayer structures. Depending on the NM interlayer thickness, the magnetization of the two FM layers tend to align parallel or antiparallel to each other [1]. It turned out that the coupling is mediated by electronic states in the NM interlayer close to the Fermi surface [2]. The oscillation period of the coupling is related to the length of the wavevector of the electrons at the Fermi surface, as is sketched in Fig. 10.2.

Subsequently, the most important discovery followed, the Giant Magnetoresistance Effect (GMR) [3] [4]. For this discovery, P. Grünberg and A. Fert were honoured with the Nobel Prize for Physics 2007. They have found out that the resistivity of a layered structure containing more than ferromagnetic layer depends on the mutual orientation of the magnetization directions, see Fig. 10.3. They used the antiferromagnetic coupling in Fe / Cr / Fe trilayer structures to be able to influence the mutual orientation of the magnetization of the Fe layers by changing the applied magnetic field.

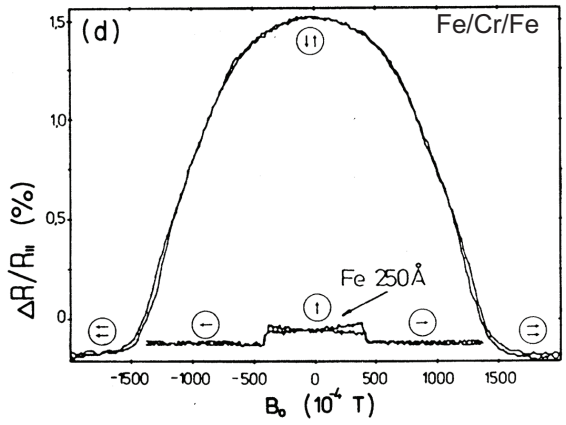

Fig. 10.3: *Giant Magnetoresistance effect in an Fe / Cr / Fe trilayer compared to the anisotropic magnetoresistance in a single Fe layer [3]*

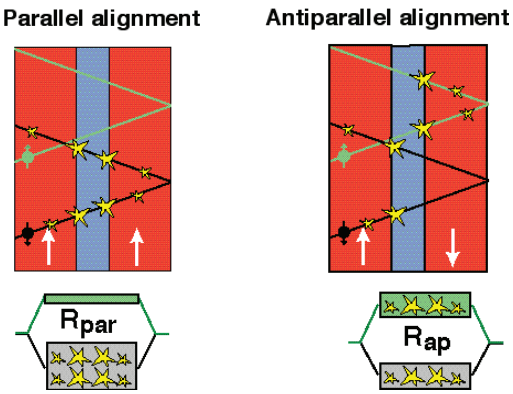

Fig. 10.4: *Different matching of the bandstructure between ferromagnetic and non-magnetic layers changes the resistivity for the different spin channels*

It turns out that the resistivity is highest in the case of antiparallel alignment of the two magnetization directions. This effect is much stronger and much more sensitive than the anisotropic magnetoresistance effect in single ferromagnetic layers, which was known before. The microscopic origin of the GMR effect is the matching between the spin-split bandstructures of the two ferromagnetic layers. The conductivity of the entire structure is the sum of the conductivities of the two spin channels. As the Fermi surface is different for the two spin channels, the matching between the FM and the NM layer is different.

As shown in Fig. 10.4, in the case of parallel alignment, the scattering probability of a conduction electron is the same at both interfaces. For one spin channel, the scattering probability is high while for the other it is low. The conductivity is then dominated by the spin channel with the smaller scattering probability. The resistivity of the entire structure, which can be described as a parallel wiring of the two resistors for the two spin channels, is small.

In the case of antiparallel alignment, the scattering probability for both spin channels is high in one of the FM layers. This results in a relatively low conductivity for every spin channel, so that the resulting resistivity is much higher than in the case of parallel magnetization.

As GMR structures are easy to prepare and easy to use, the sensor technology based on this effect quickly became standard in the readout system of computer harddisks and many other applications. Today, it has been replaced by Tunneling Magnetoresistance (TMR), where the nonmagnetic interlayer is insulating and electrons travel across this tunneling barrier while preserving their spin state. Then, the height of the tunneling barrier depends on the spin of the electron and the magnetization direction of both ferromagnetic layers. A detailed overview over the field of spin transport in layered systems is given in Ref. [5].

10.2 Why neutrons are useful for investigating magnetic nanostructures

For the investigation of magnetism, many methods are well known. In most cases the magnetization of a sample is measured. A different, but more indirect approach is the measurement of spin-dependent bandstructures by absorption and photoemission spectroscopy of polarized light / x-rays.

The first (and oldest) approach is to measure the integral magnetization of a sample by classical magnetometry, e.g. by using a Vibrating Sample Magnetometer (which measures the induction when moving the magnetic sample in a coil), a Faraday balance (which measures the force on the magnetic sample in a field gradient), or more recently a SQUID magnetometer (which measures the magnetic flux inside a superconducting loop). In case of magnetic nanostructures, the small signal coming from the nanostructure is superimposed by the signal from the substrate which is typically 10000 times larger in volume. Even if the nanostructure is ferromagnetic and the substrate only diamagnetic, the correction due to the substrate is in most cases much stronger then the signal itself.

Better adapted to thin structures are methods that are surface sensitive. The Magnetooptical Kerr-Effect (MOKE) measures magnetization with polarized light reflected from a magnetic surface. Due to magnetization of the sample the polarization direction of the light is changed. This method is surface sensitive in the range of the penetration depth of the light used (typically some 10 nanometers). At synchrotron x-ray sources one can use X-ray Magnetic Circular Dichroism (XMCD). The energy dependence of the absorption of circular polarized (soft) x-rays is measured at the absorption edges of the magnetic materials. Again the information is integrated over the penetration depth of the x-rays used, but it is element specific due to the choice of the x-ray energy in resonance with the magnetic orbitals.

Magnetic domains can be imaged using e.g. Magnetic Force Microscopy (surface sensitive, measuring stray fields above the sample), Lorentz microscopy (the transmission of electrons through a very thin sample is observed; due to the Lorentz forces the electrons are deviated according to the magnetization strength and direction), or Kerr microscopy (observing the MOKE using an optical microscope; again it integrates over the penetration depth of the light, with the lateral resolution of the optical microscope). Photoemission electron microscopy (PEEM) with soft x-rays can give an overview about the density of certain electronic states with a lateral resolution in the nanometer range and time resolution down to nanoseconds. In combination with XMCD, XMCD-PEEM can visualize the evolution of magnetic domains under variable magnetic fields. But again, the depth resolution is only determined by the penetration depth and the element specific absorption of the x-rays.

What is missing, is a method that can access the magnetism of buried layers using the depth information. Here, we need a probe that is sensitive to magnetic fields while having a spatial resolution (at least in depth) in the nm regime. Cold neutrons have a wavelength appropriate for resolving nm length scales and they carry a spin that can interact with magnetic fields. For most of the magnetic investigations, the neutron's

spin has to be prepared in a certain state, so we use polarized neutrons for the investigation of magnetic nanostructures.

Polarized neutron reflectometry with polarization analysis is a method for the depth-resolved investigation of magnetic layered structure; I will introduce this method in the following chapter. Together with the analysis of offspecular scattering, lateral structures in the µm range can be investigated, allowing to access magnetic domains in buried layers. Polarized SANS gives information about magnetic structures in the nm range perpendicular to the beam direction, while polarized GISANS (Grazing Incidence Small Angle Neutron Scattering) combines the possibilities of both methods and allows to access lateral structures in the nm range in buried layers.

10.3 Specular reflectivity of polarized neutrons

In the previous lecture, you have learned about specular reflectivity of neutrons on layered structures with nuclear scattering contrast. For the investigation of magnetic layered structures, we have to remember that the neutron is a spin ½ particle and therefore interacts with the magnetic induction **B.**

To treat the neutron's spin properly, we have to work with wave functions in the 2-dimensional quantum mechanical spin space, where the usual space-dependent functions, e.g. the potential, become operators on the neutron's spin.

In analogy to eq. (9.2), the potential of a homogeneous magnetic material can be separated into two parts

$$\hat{V}_l = V_l^N \hat{1} + \hat{V}_l^M \tag{10.1}$$

where V_l^N is the nuclear interaction from eq. (9.2), and $\hat{1}$ is the unity operator, which does not affect the spin state, so that the nuclear interaction is described independent on the neutron's spin. The magnetic dipole interaction is described by the operator $\hat{V}_l^M = -\mu_n \hat{\boldsymbol{\sigma}} \cdot \mathbf{B}_l$ which is a scalar product of the neutron magnetic moment operator $\mu_n \hat{\boldsymbol{\sigma}}$ and the magnetic induction $\mathbf{B}_l$ inside the material.

For the description in coordinates, we need to define a coordinate system which is convenient to describe the experiment. Typically, the magnetic field **H** is applied in the plane of the sample. We choose this direction to be the x-direction of the coordinate system $\mathbf{H}=H\mathbf{e}_x$ and also as the quantization axis for the neutron spin. Under this assumption, the spin operator $\hat{\boldsymbol{\sigma}} = (\sigma_x, \sigma_y, \sigma_z)$ is the following:

$$\sigma_x = \begin{pmatrix} 1 & 0 \\ 0 & -1 \end{pmatrix} \qquad \sigma_y = \begin{pmatrix} 0 & 1 \\ 1 & 0 \end{pmatrix} \qquad \sigma_z = \begin{pmatrix} 0 & -i \\ i & 0 \end{pmatrix} \tag{10.2}$$

In analogy to chapter 9.2, the Schrödinger equation can be solved in coordinate and spin space, where the eigenvectors $|+\rangle$ and $|-\rangle$ of the operator $\hat{\boldsymbol{\sigma}} \cdot \mathbf{b}_0 = \sigma_x$ with the eigenvalues +1 and -1, respectively, define states of the neutron with "spin up" and "spin down". The solution of the Schrödinger equation is the neutron state $|\Psi(\mathbf{r})\rangle$, which is again a linear combination of those two spin states.

$$|\Psi(\mathbf{r})\rangle = \Psi^+(\mathbf{r})|+\rangle + \Psi^-(\mathbf{r})|-\rangle = \begin{pmatrix} \Psi^+(\mathbf{r}) \\ \Psi^-(\mathbf{r}) \end{pmatrix} \tag{10.3}$$

After some calculation which you can find in Ref [6] we end up with a set of two coupled one-dimesional linear differential equations for every layer, which are the analogue to equation (9.8).

$$\Psi_l^{+\,\prime\prime}(z) + \left[k_{zl}^2 - 4\pi(\rho_l^N + \rho_l^M m_{xl})\right]\Psi_l^+(z) - 4\pi\rho_l^M m_{yl}\Psi_l^-(z) = 0 \tag{10.4}$$

$$\Psi_l^{-\,\prime\prime}(z) + \left[k_{zl}^2 - 4\pi(\rho_l^N - \rho_l^M m_{xl})\right]\Psi_l^-(z) - 4\pi\rho_l^M m_{yl}\Psi_l^+(z) = 0 \tag{10.5}$$

In this formulae, you find the nuclear scattering length density ρ^N that you know from eq. (9.3) together with its magnetic analogue ρ^M, the magnetic scattering length density. It is proportional to the net magnetization of the material. In case of a ferromagnetic material, the magnetization typically is aligned in some direction, which is described by the unit vector **m**.

Now, we can have a closer look at the different terms in equation (10.4) and (10.5). As Non-Spinflip (NSF) interaction, one finds in (10.4) for spin + the sum of the nuclear interaction and the magnetic interaction with the magnetization along the quantization direction and in (10.5) for spin – the difference. In case of a magnetically saturated layer (all the magnetization is aligned with the external field), the scattering length density for spin + neutrons is enhanced and for spin – neutrons is reduced compared to the nonmagnetic case.

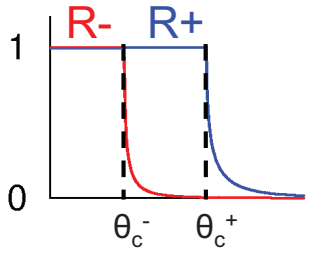

Fig. 10.5: *The total reflection angle θ_c of the surface of magnetized material is different for both spins*

This has an influence on the index of refraction, on the total reflection angle, and of course on the reflectivity, which is a function of the change of the index of refraction at a certain interface. Fig. 10.5 shows schematically the splitting of the total reflection angle.

In the case that the magnetization is not fully aligned with the field, the component along the field direction influences the scattering length density for NSF. The in-plane magnetization component perpendicular to the field induces a spin-flip (SF) interaction that is equally strong for both spin-flip channels +– and –+, as is described in the last term of eq. (10.5) or (10.4), respectively.

As en example, I would like to show the polarized neutron reflectivity of a [Co / Cu] multilayer. The respective nuclear and magnetic scattering length densities are

Co: $\rho_N = 2.30 \cdot 10^{-6}$ Å^{-2} $\rho_M = 4.24 \cdot 10^{-6}$ Å^{-2}

Cu: $\rho_N = 6.53 \cdot 10^{-6}$ Å^{-2} $\rho_M = 0$.

Obviously, the sum of the magnetic and the nuclear scattering length density of Co is almost equal to the scattering length density of Cu. In the case of magnetic saturation, spin + neutrons will not feel any contrast at the Co / Cu interfaces because they see the sum of nuclear and magnetic scattering length density in the Co layer. The multilayer structure is invisible for spin + neutrons. In contrast, spin – neutrons experience the difference of nuclear and magnetic scattering length density (which is in fact negative), so that the contrast is huge.

Fig. 10.6 makes the contrast situation visible by using colours representing the different scattering length densities.

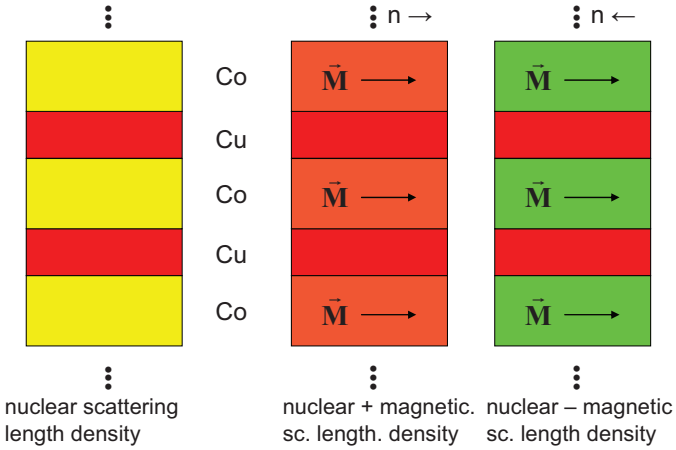

Fig. 10.6: *The contrast between Co and Cu depends on the magnetization state. It almost vanishes for spin up neutrons, but is strong for spin down.*

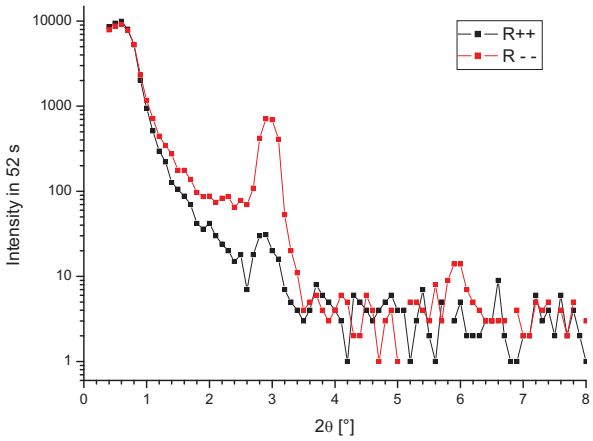

Fig. 10.7: *Specular reflectivity of polarized neutrons from a [Co/Cu] multilayer with 20 periods at magnetic saturation*

Fig. 10.7 shows the measured polarized neutron reflectivity of such a multilayer. The total reflection edge is identical for both spin channels, because the biggest scattering length density in the layered structure is the one of Cu, which is not magnetic. But the multilayer Bragg peaks at $2\theta = 3°$ and $2\theta = 6°$ are strongly spin split. For spin – neutrons, the Bragg peak is about 30 times stronger than for spin + neutrons. Here, one can see that the contrast is responsible for the reflectivity, not the strength of the scattering potential, as the scattering length density (which describes the scattering potential) is stronger for spin +, but the contrast between the layers is much stronger for spin –.

10.4 Layer-by-layer magnetometry

One important application of polarized neutron reflectometry with polarization analysis is layer-by-layer magnetometry. As an example, I present the magnetization evolution in exchange bias multilayers of the type [IrMn / CoFe] with the number of periods [7]. The exchange bias effect is the coupling between a ferromagnetic layer and a neighboring antiferromagnetic layer. If the antiferromagnet has been cooled below its Néel temperature with the ferromagnet being saturated, it has conserved the interface magnetization without being sensitive to the applied magnetic field. This induces an additional unidirectional anisotropy on the ferromagnetic layer, i.e. the original magnetization direction is preferred over all others. The hysteresis loop is shifted away from $H = 0$.

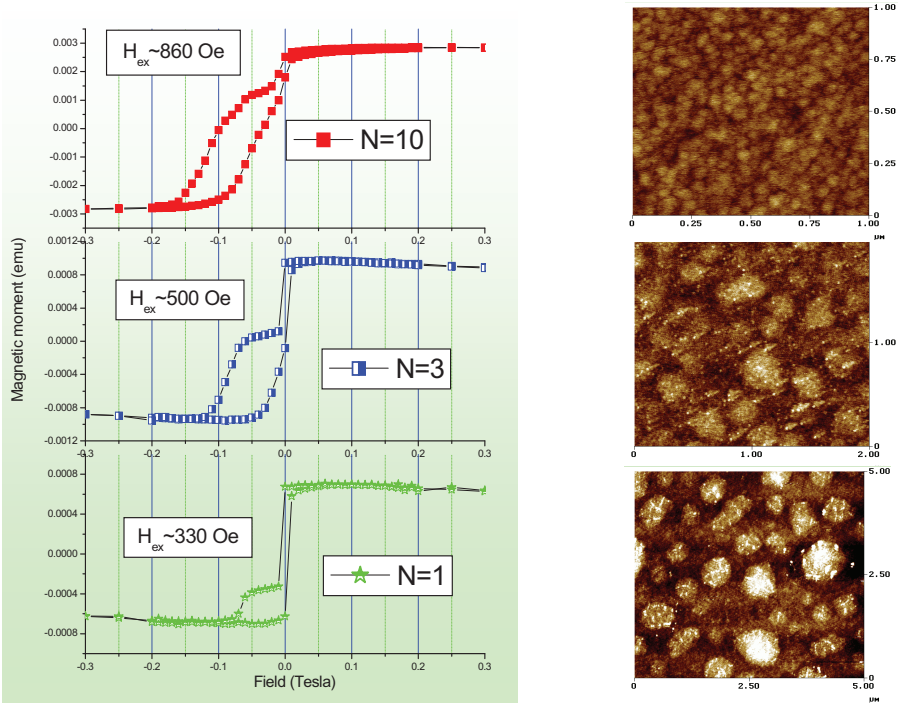

Fig. 10.8: *SQUID magnetization measurements (at room temperature, left) and AFM micrographs of the surface (right) of polycrystalline multilayers of the type SiO_2 / 10 nm NiFe / [5 nm IrMn / 3 nm CoFe]$_{x\,N}$ with N = 1, 3, or 10, resp.*

The green curve in Fig. 10.8 shows the exchange biased magnetization curve of a IrMn / CoFe double layer shifted left together with the magnetization loop of the NiFe buffer layer, which is not affected by exchange bias and therefore symmetric around H = 0 field. The CoFe layer shows a nice square hysteresis loop, indicating spontaneous magnetization flip at the coercive field.

Strangely, the shape of the magnetization loop of the exchange biased CoFe layers changes, when the number of [IrMn / CoFe]$_{xN}$ bilayers is increased. In addition, the strength of the exchange bias in increased. An AFM study of the surfaces shows that the grain size of the polycrystalline layers is reduced from layer to layer during the preparation procedure, but not information could be found that justifies the slope of the magnetization curves and that could eventually explain the origin of a magnetization rotation process responsible for the gradual evolution of the magnetization as a function of the applied field.

Therefore, a polarized neutron reflectivity study was performed, to investigate the individual behaviour of the ferromagnetic layers in the multilayer structure. As an example, Fig. 10.9 shows the specular polarized neutron reflectivity at one of the coercive fields (i.e. the net magnetization vanishes) together with the fit.

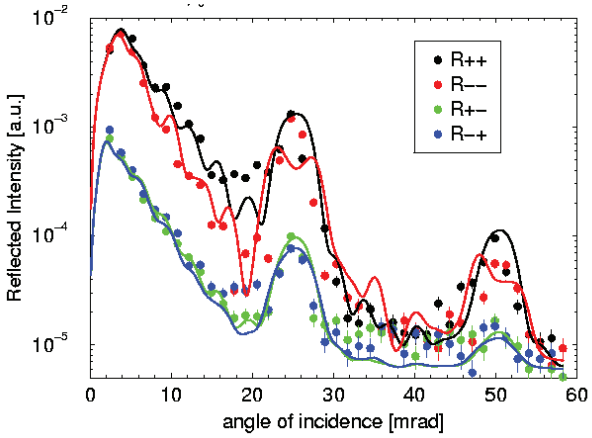

Fig. 10.9: *Polarized neutron reflectivity of the sample with N=10 at $\mu_0 H$ = -0.1 mT after positive saturation*

The polarized neutron measurement shows no spin flip signal at all, immediately excluding the idea of a magnetization rotation process. Furthermore, it shows that the magnetization of the upper 5 CoFe layers is aligned antiparallel to the field while the magnetization of the lower 5 CoFe layers is still aligned along to the field. I.e., the exchange bias on the upper layers (with smaller grains) still can hold the magnetization in the preferred direction, while the magnetization of the lower layers already has followed the field.

Together with measurements at several magnetic field values on both branches of the hysteresis loop it turned out that every single layer has a square magnetization loop, but the strength of the exchange bias effect (i.e. the shift of the centre of the loop away from H=0) increases with reduced grain size. The overlaying of the differently shifted square loops then results in the inclined net magnetization loop measured with magnetometry.

10.5 Vector magnetometry

The second important application of polarized neutron reflectometry with polarization analysis is vector magnetometry in layered structures. The ability to distinguish between SF and NSF channels offers an independent access to the in-plane magnetization components perpendicular and parallel to the field direction. As a magnetization direction perpendicular to the sample surface is rare (due to the shape anisotropy) one can determine the full magnetization vector in most cases.

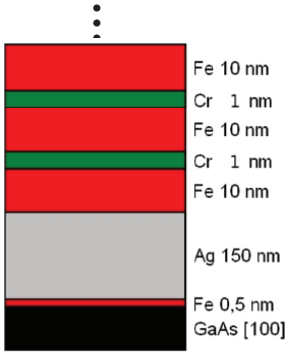

Fig. 10.10: *Layer sequence of an epitaxially grown and antiferromagnetically coupled [Fe / Cr]$_{xN}$ multilayer*

I would like to explain the power of vector magnetometry using the example of an epitaxially grown and antiferromagnetically (AF) coupled [Fe / Cr]$_{xN}$ multilayer with an odd number of Fe layers [8]. Fig. 10.10 shows the layer sequence of such a sample grown on a GaAs single crystal with a Ag buffer layer to improve the surface quality. The magnetic behaviour is determined by the competition between 3 different interactions (see. Fig. 10.11): The crystalline anisotropy in the single crystalline Fe layers tries to align the magnetization in every Fe layer along one of the in-plane [100] directions. This results in 4 equivalent easy axes. The antiferromagnetic coupling (mediated by the Cr interlayer) has the tendency to align the magnetization of two neighbouring Fe layers antiparallel to each other. The Zeeman term tries to align the magnetization along the applied field.

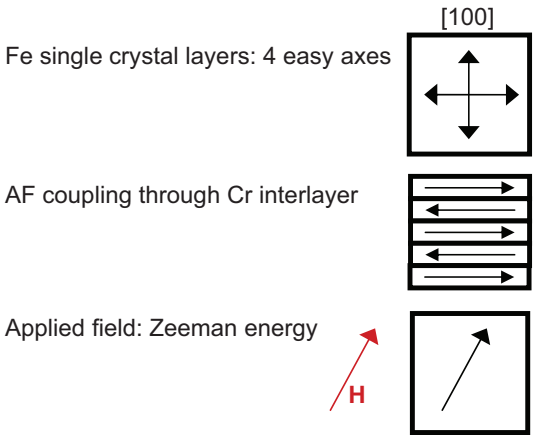

Fig. 10.11: *The magnetic behaviour in an applied magnetic field is governed by 3 competing interactions*

As the multilayer under investigation has an odd number of Fe layers, the antiparallel orientation of the magnetization in remanence (where the Zeeman term is weak) will leave the magnetization of one layer uncompensated, so that the Zeeman energy does not vanish even at very small fields. This effect is supposed to align the remanent magnetization of all layers along or antiparallel to the field direction.

Fig. 10.12 shows MOKE measurements of such samples with N=7 or N=19 Fe layers in the multilayer sequence. The MOKE signal is a function of the magnetization, but not proportional to it, because it is a superposition of the longitudinal Kerr effect (proportional to the magnetization along the field) and the transverse Kerr effect (proportional to the magnetization perpendicular to the field). Furthermore, the weight of the layers close to the surface is much higher than the weight of lower lying layers. Therefore, one should not worry about the MOKE curve not being monotonous. Nevertheless, a jump in the MOKE curve always indicates a spontaneous change of the magnetization state.

In addition, Fig. 10.12 shows a simulation of the integral magnetization component along the field based on numerical minimization of the three energy terms mentioned above. This kind of simulation cannot reproduce effects of activation barriers leading to hysteresis.

In the case of the multilayer with N=7 Fe layers, the simulation and the MOKE measurement have a good qualitative agreement. In saturation, the magnetic moment of every layer is aligned with the field. In the intermediate field range, the magnetization is alternatingly pointing left or right from the field direction, so that the magnetization component along the field is almost equal for every layer and the magnetization components perpendicular to the field fulfil as much as possible the AF coupling.

At remanence, the magnetization of all layers is turned by 90°, so that 4 layers have the magnetization along the field and 3 layers antiparallel to the field. This configuration fulfils as well the AF coupling condition as the alignment of the net magnetization along the applied field.

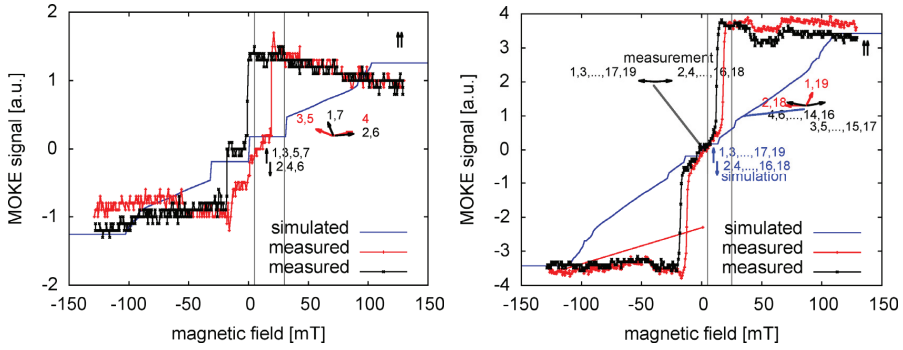

Fig. 10.12: *MOKE measurement of [Fe / Cr]$_{xN}$ multilayers with N=7 Fe layers (left) and N=19 Fe layers (right). The simulation of the magnetization curve is based on total energy minimization.*

In contrast to that, the MOKE measurement of the multilayer with N=19 Fe layers shows a smooth transition through H=0 while the simulation proposes a step comparable to the case described previously. This behaviour is known from AF coupled multilayers with even number of ferromagnetic layers, because there the net magnetization vanishes, so that there is no Zeeman energy that causes the rotation of the entire magnetic configuration at remanence. This contradiction cannot be resolved by magnetometry measurements only.

Fig. 10.13 shows the polarized neutron reflectivity together with the offspecular scattering for the two samples at saturation field. One can see a structured signal with total reflection and several Bragg peaks according to the periodicity in the multilayer structure only in the R++ channel. For spin – neutrons the contrast between fully magnetized Fe and Cr vanishes, so the R– – shows only the total reflection (with a reduced critical angle compared to R++), but no Bragg peaks. As no magnetization component perpendicular to the field direction exists, there is no real spin flip signal. What you see in R+– and R –+ is a parasitic signal due to the limited efficiency of the polarizing equipment of the instrument. The Bragg sheets crossing the specular Bragg peaks are due to vertically correlated roughness of the Fe / Cr interfaces.

No qualitative difference between the two samples can be observed except the fact that the Bragg peaks and Bragg sheets are sharper and more intense for the $[Fe / Cr]_{19}$ sample because of the bigger number of periods.

Fig. 10.14 shows the same in the intermediate field range. Additional Bragg peak of half order appear, which are stronger in SF compared to NSF. This is the indication of the alternation of the magnetization directions due to the antiferromagnetic coupling. Mainly the magnetization component perpendicular to the field oscillates while the component remaining along the field is modulated less. As the sample is no more saturated, the magnetization component in field direction is reduced, so that the contrast for spin – neutrons does not vanish any more. Therefore, the full order Bragg peaks also come up in R– –. They are now mainly induced by the nuclear structure while the magnetic contribution is collected in the half order signal. The strong off-specular signal around the half order Bragg peaks in the SF channels is a signature of magnetic domains. Again, no distinct qualitative difference between the two samples is observed.

This is very different at remanence, as shown in Fig. 10.15. The $[Fe / Cr]_7$ sample has all half order peaks in the NSF channels while the $[Fe / Cr]_{19}$ sample has all half order peaks in SF. The small contribution in the other channels can be explained due to the limited polarization of the neutron beam. This shows that the magnetization of all layers of the $[Fe / Cr]_7$ sample is aligned alternatingly parallel and antiparallel to the field direction, as has been proposed by the simulation for the MOKE measurement.

In the case of the $[Fe / Cr]_{19}$ sample, all magnetization is now concentrated perpendicular to the field, no more difference between R++ and R– – can be observed. The measurement clearly shows, that the Zeeman energy contribution equivalent to the magnetization of a single Fe layer is not sufficient to turn the entire magnetization of all 19 layers by 90° across the crystalline anisotropy barrier.

In addition to the qualitative description presented here, a quantitative analysis of the measurements allows to determine the angle of the magnetization vector of every layer independently. This analysis is presented in Ref. [8].

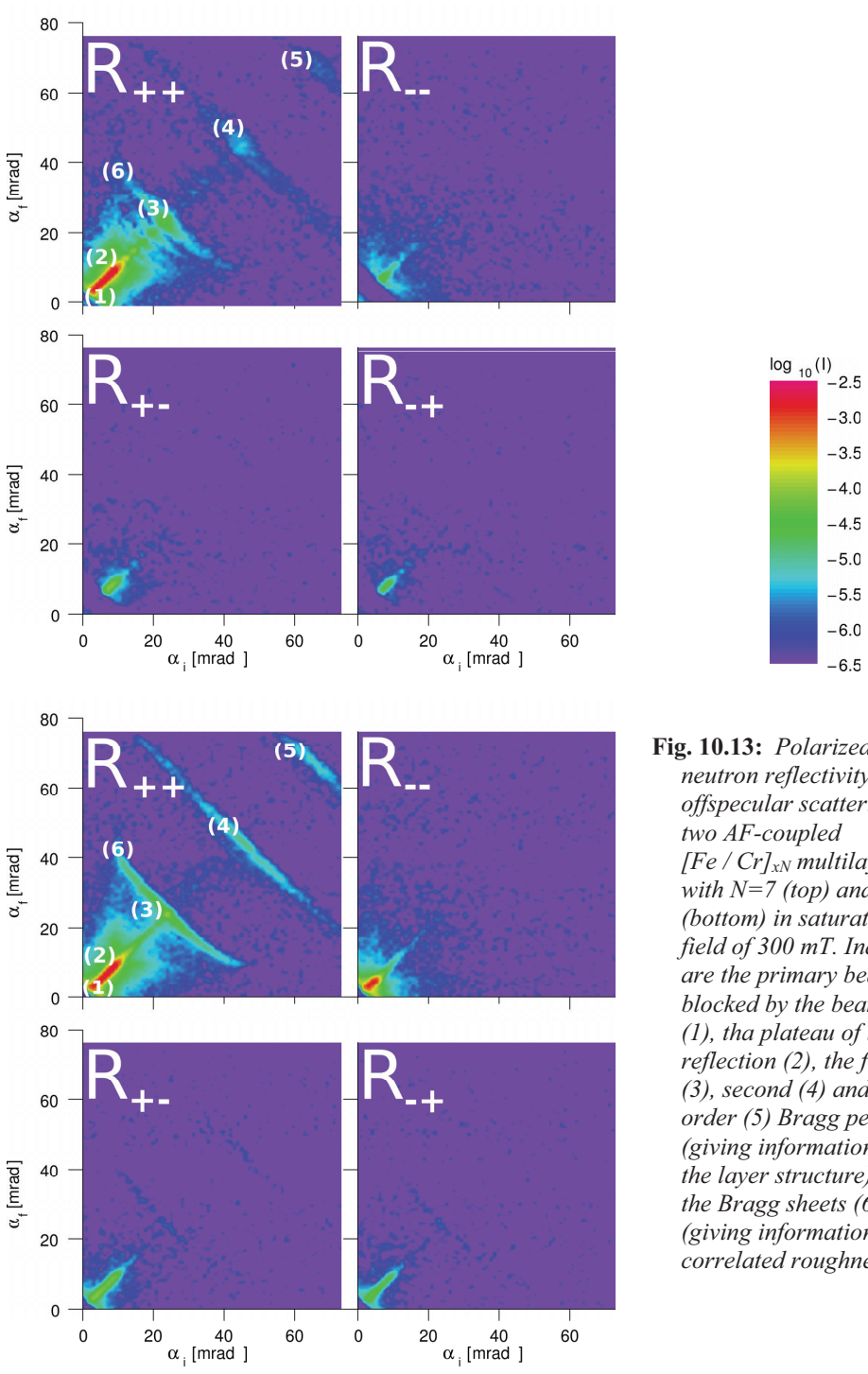

Fig. 10.13: *Polarized neutron reflectivity and offspecular scattering for two AF-coupled $[Fe / Cr]_{xN}$ multilayers with N=7 (top) and N=19 (bottom) in saturation field of 300 mT. Indicated are the primary beam blocked by the beamstop (1), tha plateau of total reflection (2), the first (3), second (4) and third order (5) Bragg peak (giving information about the layer structure) and the Bragg sheets (6) (giving information about correlated roughness).*

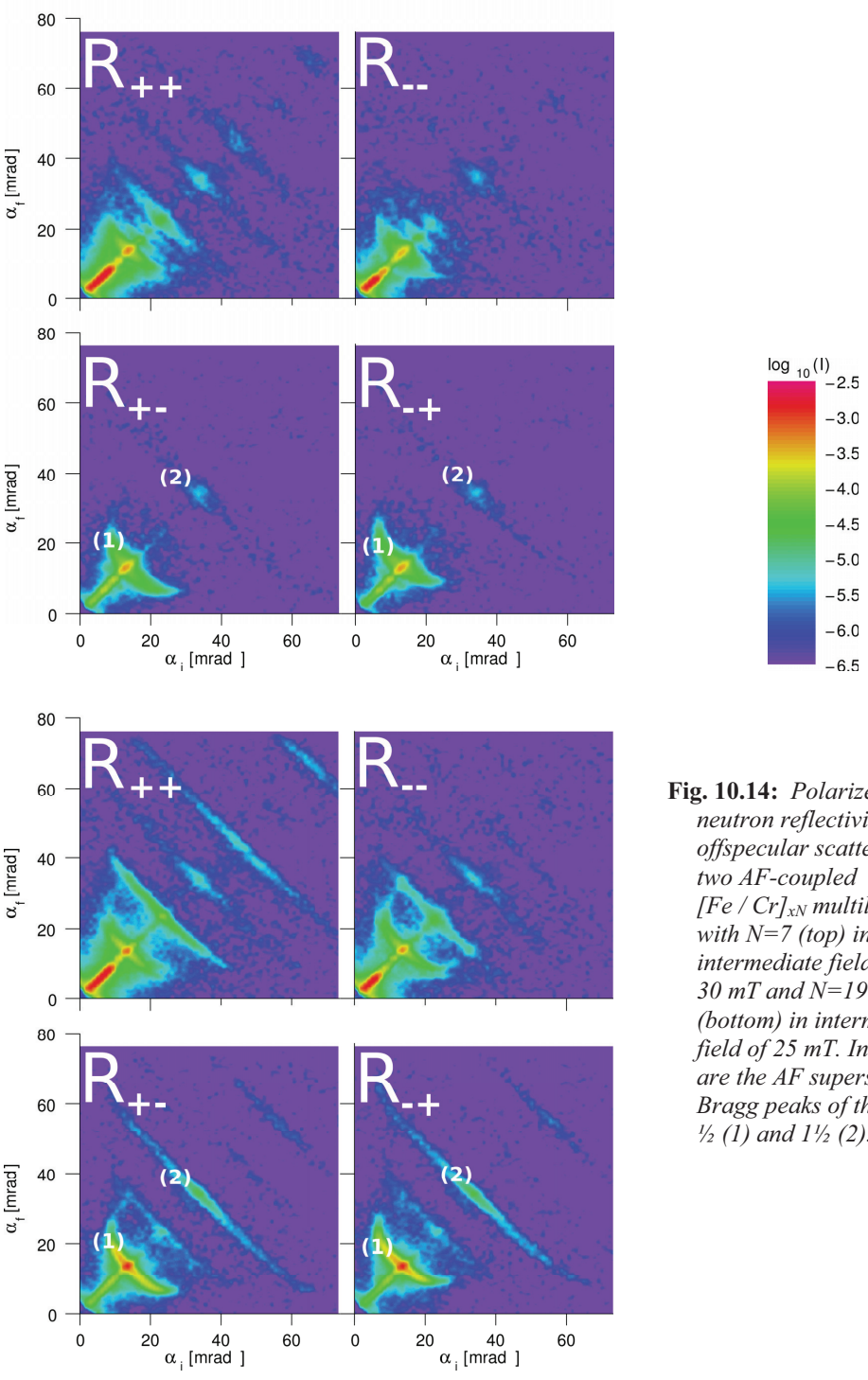

Fig. 10.14: *Polarized neutron reflectivity and offspecular scattering for two AF-coupled $[Fe / Cr]_{xN}$ multilayers with N=7 (top) in intermediate field of 30 mT and N=19 (bottom) in intermediate field of 25 mT. Indicated are the AF superstructure Bragg peaks of the order ½ (1) and 1½ (2).*

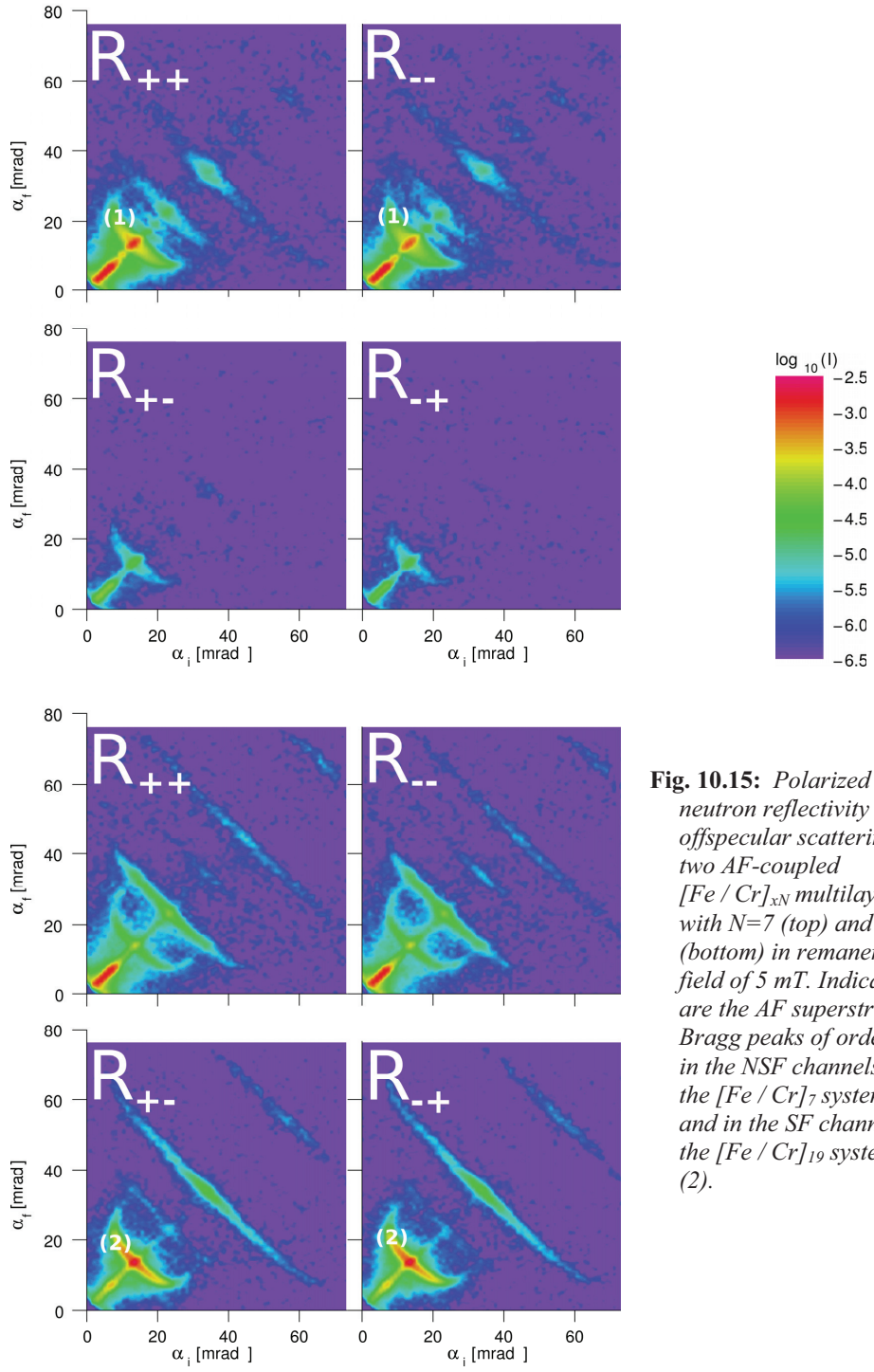

Fig. 10.15: *Polarized neutron reflectivity and offspecular scattering for two AF-coupled $[Fe / Cr]_{xN}$ multilayers with N=7 (top) and N=19 (bottom) in remanence field of 5 mT. Indicated are the AF superstructure Bragg peaks of order ½ in the NSF channels of the $[Fe / Cr]_7$ system (1) and in the SF channels of the $[Fe / Cr]_{19}$ system (2).*

References

[1] P. Grünberg, R. Schreiber, Y. Pang, M.B. Brodsky, and H. Sowers, Phys. Rev. Lett. 57 (1986), 2442
[2] P.H. Dederichs, "Interlayer Exchange Coupling", chapter C 3 in "Magnetism goes Nano", 36th IFF Spring School, Forschungszentrum Jülich, series Matter and Materials, Vol. 26 (2005)
[3] G. Binasch, P. Grünberg, F. Saurenbach, and W. Zinn, Phys. Rev. B 39 (1989), 4828
[4] M.N. Baibich, J.M. Broto, A. Fert, F. Nguyen Van Dau, F. Petroff, P. Etienne, G. Creuzet, A. Friedrich, and J. Chazelas, Phys. Rev. Lett. 61 (1988), 2472
[5] D.E. Bürgler, "Spin-Transport in Layered Systems" , chapter E 5 in "Magnetism goes Nano", 36th IFF Spring School, Forschungszentrum Jülich, series Matter and Materials, Vol. 26 (2005)
[6] U. Rücker, E. Kentzinger, "Thin Film Systems: Scattering under Grazing Incidence", chapter D4 in "Probing the Nanoworld", 38th IFF Spring School, Forschungszentrum Jülich, series Matter and Materials, Vol. 34 (2007)
[7] A. Paul, E. Kentzinger, U. Rücker, D.E. Bürgler, and P. Grünberg, Phys. Rev. B 70 (2004), 224410
[8] E. Josten, U. Rücker, S. Mattauch, D. Korolkov, A. Glavic, and Th. Brückel, J. Phys: Conf. Ser. **211** (2010), 012023

Exercises

E10.1 Magnetic contrast

We measure the polarized neutron reflectivity of a $[Ni_2Fe / Pt]_N$ multilayer structure in magnetic saturation. The Ni_2Fe alloy is ferromagnetic.

a) Calculate the nuclear and magnetic scattering length densities for the two constituents of the multilayer:

	Ni	Fe	Pt
density [g/cm³]	8.90	7.86	21.4
atomic weight [g/mol]	58.71	55.85	195.09
nuclear scattering length [1E-14 m]	1.03	0.954	0.95
magnetic scattering length density [1E-6 Å^{-2}]	1.52	5.12	0

If you do not manage to calculate the values properly, you may continue with the tabulated values of the nuclear scattering length densities: Ni: 9.41E-6 Å^{-2}, Fe: 8.09E-6 Å^{-2}, Pt: 6.29E-6 Å^{-2}.

b) Which of the 5 reflectivity curves presented below is the one measured on this alloy? Think about the critical angle (has to do with the highest scattering length density in all layers) and the contrast between adjacent layers (influences the height of the diffraction peaks) for both spin directions parallel (R+ +) and antiparallel (R– –) to the applied magnetic field (saturation!).

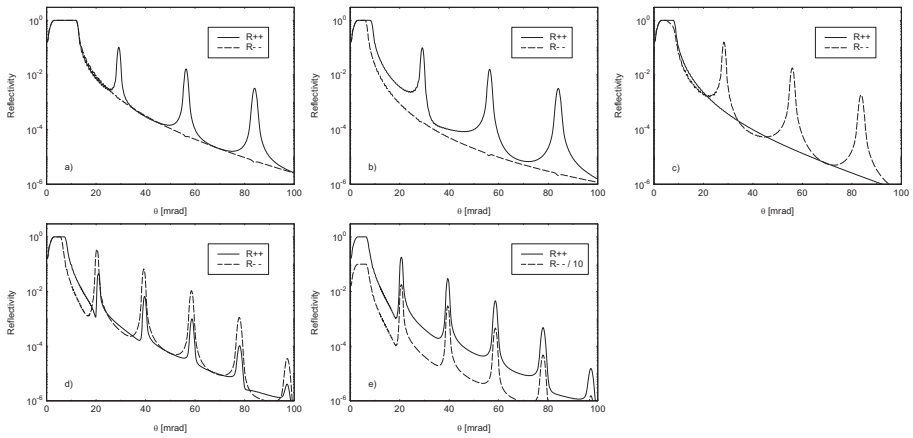

c) The other 4 curves have been measured on different samples. Which curve belongs to which sample?

I. The sum of nuclear and magnetic scattering length density of the magnetic layers is equal to the nuclear scattering length density of the nonmagnetic layers
II. The sample contains an additional nonmagnetic layer with a scattering length density higher than the sum of the magnetic and nuclear scattering length densities of Ni_2Fe on top of the $[Ni_2Fe / Pt]_N$ multilayer
III. No layer is magnetic
IV. The nuclear scattering length density of the nonmagnetic layers is somewhere between the sum and the difference of nuclear and magnetic scattering length density of the magnetic layers

E10.2 Vector magnetometry

The following figures show polarized neutron reflectivity measurements with polarization analysis from a ferromagnetic single layer on a nonmagnetic substrate. Find out which figure belongs to which magnetization state:

I. The sample is magnetized perpendicular to the field direction
II. The sample is magnetized parallel to the field direction
III. The magnetization of the sample is inclined by 45° against the field direction
IV. This set of curves is wrong. (Why?)

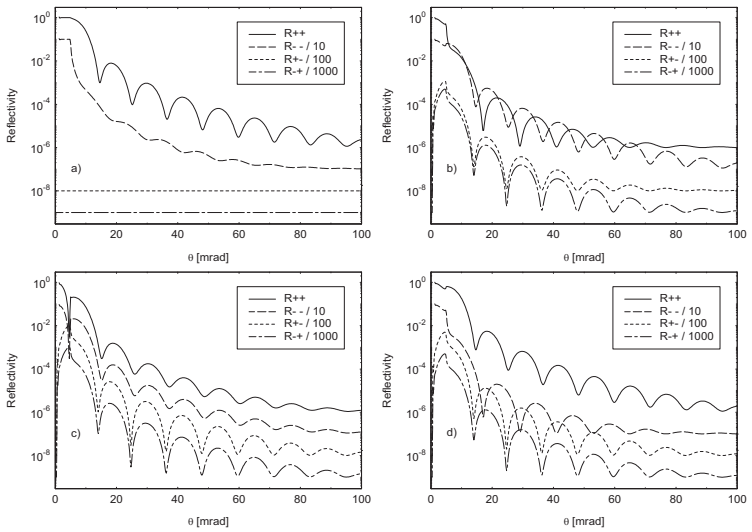

11 Inelastic Neutron Scattering

R. Zorn
Jülich Centre for Neutron Science 1
Forschungszentrum Jülich GmbH

Contents

Lecture Notes of the JCNS Laboratory Course Neutron Scattering

11.1 Introduction

One of the most important benefits of neutron scattering is the possibility to do inelastic scattering and by this way gain insight into the dynamics of materials as well as the structure. Neutrons tell us where the atoms are *and how they move* [1]. Although this feature is shared with inelastic x-ray scattering and dynamic light scattering, there is still a considerable range of slow dynamics in molecular systems which can be studied exclusively by inelastic neutron scattering.

This lecture can only present a short glimpse on the theoretical foundations and instrumental possibilities of inelastic neutron scattering. For those who are interested in more details, several textbooks can be recommended [2–6]. Also supplementary information on correlation functions [7] and Fourier transforms [8] may be found in earlier editions of this school.

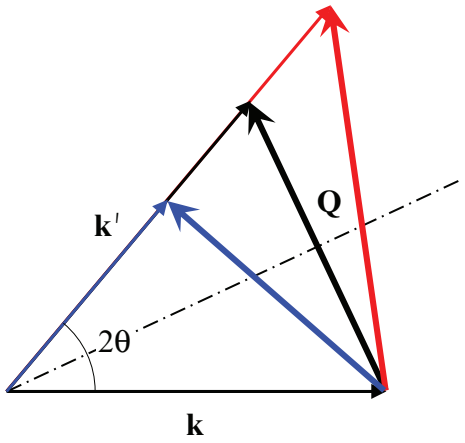

Fig. 11.1: *Definition of the scattering vector* Q *in terms of the incident and final wave vectors* k *and* k′. *The black (isosceles) triangle corresponds to elastic scattering. The blue and red ones correspond to inelastic scattering with energy loss or gain of the scattered neutron, respectively.*

11.2 Theory

11.2.1 Kinematics of neutron scattering

Up to this lecture it has always been assumed that the wavelength (or wave vector, or energy) of the neutrons is the same before and after scattering. The defining quality of *inelastic neutron scattering* is that this is not anymore the case. The neutrons may lose or gain energy in the collision with the nuclei implying that $k' \neq k$. This implies that Q now does not anymore result from the isosceles construction in Fig. 11.1 drafted in black but from scattering triangles as those in blue and red. Application of the cosine theorem leads to the following expression for

Q in the inelastic situation:

$$Q = \sqrt{k^2 + k'^2 - 2kk'\cos(2\theta)} \tag{11.1}$$

$$= \sqrt{\frac{8\pi^2}{\lambda^2} + \frac{2m\omega}{\hbar} - \frac{4\pi}{\lambda}\sqrt{\frac{4\pi^2}{\lambda^2} + \frac{2m\omega}{\hbar}}\cos(2\theta)}\,. \tag{11.2}$$

Note that there is a fundamental difference to the simpler expression for elastic scattering,

$$Q_{\mathrm{el}} = \frac{4\pi}{\lambda}\sin\theta\,, \tag{11.3}$$

used in the preceding lectures. Q now also depends on the energy transfer $\hbar\omega$ implying that Q is not anymore constant for a single scattering angle. Fig. 11.2 shows the magnitude of this effect for typical parameters of a neutron scattering experiment. It can be seen that it is by no means negligible for typical thermal energies of the sample even at temperatures as low as 100 K.

The other fundamental difference to elastic scattering to be considered is that the total scattering cross section is not identical anymore to the bound scattering cross section read from tables. In the extreme case of a free nucleus the scattering cross section is reduced to [2]

$$\sigma = \frac{4\pi b^2}{(1 + m/M)^2} \tag{11.4}$$

where M is the mass of the scattering nucleus. It can be seen that in the worst case (scattering from a gas of atomic hydrogen) this is a reduction by $1/4$.

11.2.2 Scattering from vibrating atoms

The most important case of inelastic neutron scattering from vibrating atoms is that of scattering from phonons in crystals. In this field, inelastic neutron scattering is the most important tool of research. At first, a short recapitulation of the phonon picture will be presented [9, 10].

As a simplified model for the crystal one can consider a chain of N atoms with mass M regularly spaced by a distance a and connected by springs with the spring constant K. For this system the equations of motion can readily be written down:

$$\frac{\mathrm{d}^2 u_j}{\mathrm{d}t^2} = \frac{K}{M}\left(u_{j+1} - 2u_j + u_{j+1}\right)\,. \tag{11.5}$$

In addition, it has to be specified what the equations of motions are for the first and the last atom (boundary condition). This is usually done by identifying the left neighbour of the first atom with the last and vice versa, $u_0 = u_N$ and $u_{N+1} = u_1$, as in a closed necklace rather than an open chain. This is the most natural choice for large N and called the Born-von-Kármán boundary condition. The equation system (11.5) can be solved by the ansatz

$$u_j(t) = \sum_k U_k(t)\exp\left(\mathrm{i}\frac{kj}{N}\right) \tag{11.6}$$

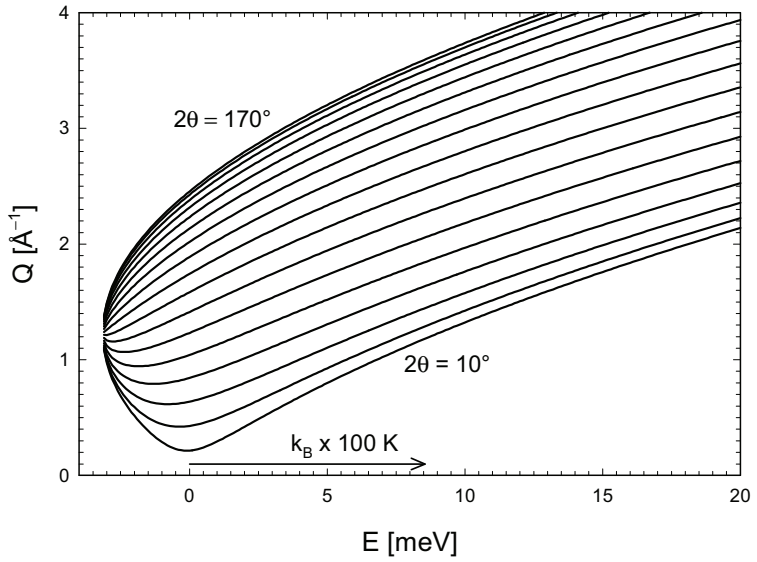

Fig. 11.2: *Scattering vectors Q accessed by a neutron scattering experiment with the detector at scattering angles $2\theta = 10 \ldots 170°$ vs. the energy transfer $\hbar\omega$ (incident wavelength $\lambda = 5.1$ Å). For comparison the thermal energy $k_{\mathrm{B}}T$ corresponding to 100 K is indicated by an arrow.*

with integer k ($k \in \mathbb{Z}$). Here, U_k are the *normal coordinates* and each of them fulfils the equation of motion of a single harmonic oscillator:

$$\frac{\mathrm{d}^2 U_k}{\mathrm{d}t^2} = \frac{2K}{M}\left(\cos\frac{2\pi k}{N} - 1\right) U_k \,. \tag{11.7}$$

By introducing these *normal coordinates*, the system of differential equations (11.5) can be *decoupled* into a set of differential equations which can be solved separately. The solutions are

$$U_k(t) = A_k \exp\left(\mathrm{i}\Omega_k t\right) \text{ with} \tag{11.8}$$

$$\Omega_k = \sqrt{\frac{2K}{M}\left(1 - \cos\frac{2\pi k}{N}\right)} = 2\sqrt{\frac{K}{M}}\left|\sin\frac{\pi k}{N}\right| \,. \tag{11.9}$$

The second equation gives a relation between the index of the oscillator k and the frequency. On the other hand, the index determines via equation (11.6) the wavelength of the vibration. One wavelength covers N/k lattice positions, corresponding to $\lambda_{\mathrm{vib}} = Na/k$ in actual length. The corresponding wave 'vector' is $q = 2\pi/\lambda_{\mathrm{vib}} = 2\pi k/Na$[1]. This implies that there is a relation between the wave vector and the frequency called the *dispersion relation* (Fig. 11.3):

$$\Omega(q) = 2\sqrt{\frac{K}{M}}\left|\sin\frac{qa}{2}\right| \,. \tag{11.10}$$

[1] As will be seen later, there is a close connection between this lower case q and the scattering vector upper case Q. Nevertheless, they are not the same and care has to be taken not to mix up both q-s.

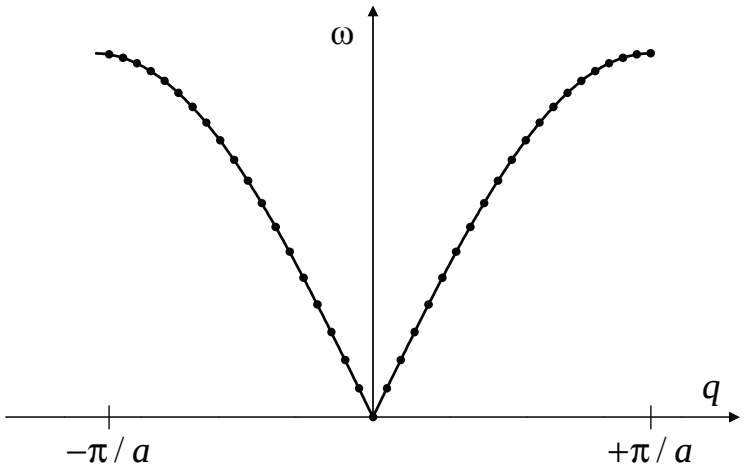

Fig. 11.3: *Dispersion relation in a linear chain with $N = 40$ atoms (Born-von-Kármán boundary condition).*

This relation does not contain the number of atoms anymore. For large N the points constituting the curve in Fig. 11.3 will get closer and closer, finally leading to the continuous function (11.10). The individual positions of these points depend on the boundary condition. But because they are getting infinitely dense for $N \to \infty$ the exact boundary conditions do not matter for a large system.

It can be seen that the dispersion relation (11.10) is periodic in q. On the other hand, there are only N normal coordinates necessary to solve the N original equations of motion. This is exactly the number of wave vectors found in a q interval of length $2\pi/a$. The usual choice is $-\pi/a \ldots \pi/a$ as a representative zone for the dispersion relation.

There are two modifications necessary when considering a real three-dimensional crystal instead of this simplified model: (1) The crystal is periodic in three dimensions. (2) The vibrations are governed by quantum mechanics. The first requirement leads to the consequence that instead of a scalar, one has to use a real wave *vector*, $q \to \mathbf{q} = (q_x, q_y, q_z)$ in reciprocal space. The interval defined in Fig. 11.3 changes into a polyhedron called the first Brillouin zone (Fig. 11.4) [9, 10]. It is constructed in the same way as the Wigner-Seitz cell in real space: The Brillouin zone contains all points which are closer to the origin than to any other lattice point. Its surfaces are the bisecting planes between the origin and its neighbours (in reciprocal space).

For every amplitude A_k equation (11.8) gives a valid solution of the equations of motion. This means that in the classical picture the vibrations can have any energy. The quantum mechanical treatment (which is too complex to be treated here in detail) leads to the result that only certain energies with a distance of $\hbar\Omega_k$ are allowed. This quantisation implies that the vibrations can be treated as *quasiparticles* with the energy $\hbar\Omega_k$ called *phonons*. The increase of the vibrational amplitude corresponding to an energy change of $+\hbar\Omega_k$ is then seen as a creation, the inverse process as an annihilation of a phonon. Then it makes sense to define $\hbar\mathbf{q}$ as the momentum of the phonon. In this way the dispersion relation $\Omega(\mathbf{q})$ is similar to the relations shown in Fig. 4.2 of lecture 4 for real particles.

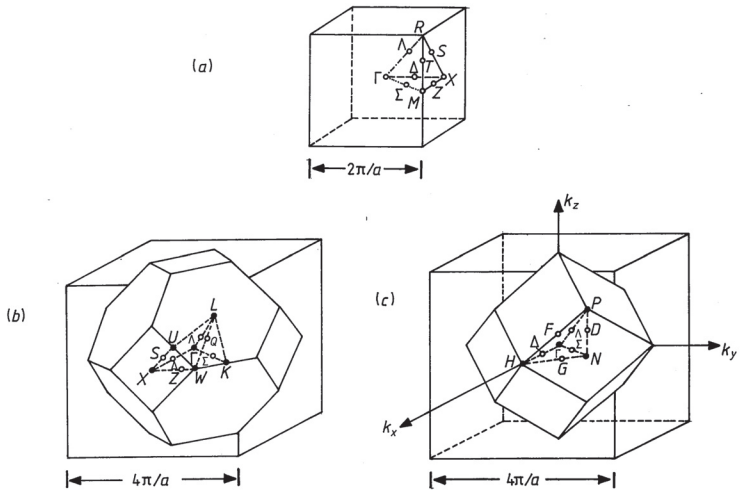

Fig. 11.4: *Brillouin zones for cubic lattices: (a) simple cubic, (b) face-centred cubic, (c) body-centred cubic. From [10].*

The introduction of the quasiparticle (phonon) concept leads to the simple interpretation of inelastic neutron scattering by vibrating lattices: The scattering process can be viewed as a collision between phonons and neutrons. In this process the energy as well as the momentum has to be conserved:

$$E' - E = \hbar\omega = \pm\hbar\Omega(\mathbf{q})\,, \tag{11.11}$$

$$\mathbf{k}' - \mathbf{k} = \mathbf{Q} = \pm\mathbf{q} + \boldsymbol{\tau}\,. \tag{11.12}$$

The second equation shows that the analogy with a two-particle collision is not complete. A wave vector, changed by a lattice vector $\boldsymbol{\tau}$ in reciprocal space, corresponds to the *same* phonon. In the one-dimensional case, this can be seen from equation (11.6): If one adds an integer multiple of N to k (corresponding to a multiple of $2\pi/a$ in q) all values of the complex exponential remain the same. Analogously, in the three dimensional case adding a lattice vector

$$\boldsymbol{\tau} = h\boldsymbol{\tau}_1 + k\boldsymbol{\tau}_2 + l\boldsymbol{\tau}_3 \quad (h, k, l \in \mathbb{Z}) \tag{11.13}$$

does not change anything and momentum has only to be conserved up to an arbitrary reciprocal lattice vector. The condition (11.12) can also be visualised by the Ewald construction as done in lecture 4 for elastic scattering.

From the conservation laws (11.11) and (11.12) one expects that the the scattering intensity has sharp peaks at the positions where both conditions are fulfilled and is zero everywhere else. This is indeed so for coherent scattering, unless effects as multi-phonon scattering and anharmonicity are strong (usually at higher temperatures). Therefore, inelastic scattering allows the straightforward determination of the phonon dispersion relation as shown in Fig. 11.5.

In this figure, it can be seen that some of the phonon 'branches' start at the origin (*acoustic phonons*), as in the simple calculation of the one-dimensional chain. Others are 'floating' around high frequencies *optical phonons*. They occur in materials with atoms of different

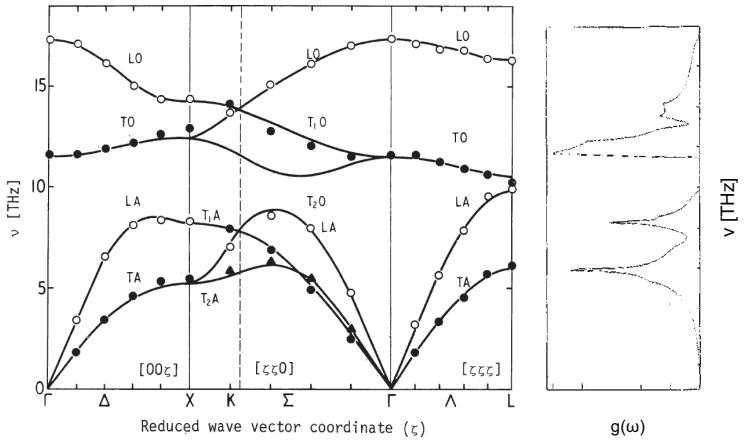

Fig. 11.5: *Left: Phonon dispersion of NiO measured by inelastic neutron scattering. Frequencies are expressed as $\nu = \omega/2\pi$ and the wave vector is expressed in units of $\zeta = \pi/a$. The lattice is simple cubic, thus the symbols below the abscissa correspond to those in Fig. 11.4(a). Right: Phonon density of states (see section 11.2.3) of NiO plotted to the same scale in frequency. From [11].*

weight or bond potential. (The one-dimensional chain would also produce these solutions if the masses were chosen differently for even and odd j.) In this case, a mode, where all atoms of a unit cell move roughly in phase, has the usual behaviour expected from the monatomic chain. In particular the dispersion relation at low $\mathbf{q}$ is a proportionality:

$$\Omega(q) = vq\,. \tag{11.14}$$

This relation is typical for sound waves. v is the sound velocity, longitudinal or transverse according to the type of phonons considered. In the polyatomic crystal or chain, there are additional modes where the atoms move in anti-phase. This implies a much higher deformation of the bonds. These vibrations constitute the optical phonon branches.

There is another difference between the one-dimensional chain and the three-dimensional crystal visible. The atomic displacements are not simply scalars u_j but vectors $\mathbf{u}_j$ which have a direction. This direction can be either parallel or perpendicular to to the wave vector $\mathbf{q}$. Depending on this, one speaks of *longitudinal* and *transverse* phonons. The usual notation is LA, TA, LO, TO, where the first letter indicates the phonon polarisation and the second whether it is acoustic or optical. An additional index as T_1A is used for $\mathbf{q}$ directions where the symmetry allows a distinction between the perpendicular orientations of $\mathbf{u}_j$. The full mathematical expression for the phonon scattering [2] includes an intensity factor proportional to $|\mathbf{Q}\cdot\mathbf{u}_j|^2$. This factor obviously vanishes if $\mathbf{Q}$ and $\mathbf{u}_j$ are perpendicular, implying that purely transverse modes are unobservable in the first Brillouin zone where $\mathbf{Q} = \mathbf{q}$.

It has to be noted, that the above arguments only hold for *coherent neutron scattering* (see equation (11.21) below) from crystalline materials. If the material is amorphous the coherent scattering will be diffuse (as it is for incoherent scattering always). The readily understandable reason for this is that the definition of the phonon wave vector $\mathbf{q}$ requires a lattice.

Finally, an indirect effect of vibrations on the elastic scattering should be mentioned. The elastic scattering (also for x-ray scattering) is reduced by the *Debye-Waller factor*. This reduction can be understood from a 'hand-waving' argument: Due to the thermal vibrations, atoms are displaced by $\mathbf{u}_j$ from their nominal lattice position. Although on the average $\langle \mathbf{u} \rangle$ is zero, there will be a finite *mean-square displacement* $\langle u^2 \rangle$. The Debye-Waller factor can be shown [2,9] to be

$$\exp\left(-\langle (\mathbf{Q} \cdot \mathbf{u}) \rangle\right) = \exp\left(-Q^2 \langle u^2 \rangle / 3\right) \tag{11.15}$$

where the second expression is only valid for isotropic conditions. It can be seen that the attenuation of diffraction peaks increases with increasing Q and increasing mean-square displacement, that is at higher temperature. Note, that this does *not* mean that elastic scattering can observe dynamics, because a permanent static displacement of the atoms would have the same effect.

The treatment of inelastic scattering by spin waves is very similar to that of deformation waves above. In analogy to the phonon the quasiparticle "magnon" is introduced. Thereby, the displacement $\mathbf{u}_j$ is replaced by the orientation of the spin. The construction of normal modes (Bloch waves) and the quantisation proceeds in the same way as for phonons. As explained in lecture 7 neutrons interact with the nuclei as well as with the magnetic moments of nuclei and electrons. Therefore, inelastic neutron scattering is also a tool for the detection of magnons and this has been one of its first applications [12].

11.2.3 Scattering from diffusive processes

For the inelastic scattering from vibrational motions it was practical to consider the scattering as a process between (quasi)particles, neutrons and phonons/magnons. But there are many types of molecular motions, mostly irregular and only statistically defined, which cannot be treated in this concept, e.g. thermally activated jumps or Brownian motion. For these motions it is more adequate to use a concept of *correlation functions* to calculate the scattering.

Because these 'diffusive' processes are usually much slower than phonon frequencies it is in most cases not necessary to treat them quantum-mechanically. Therefore, in this section, a picture of the scattering material will be used where the positions of all scatterers are given as functions of time $\mathbf{r}_j(t)$ (trajectories). In this picture the the *double differential cross-section*, defined as the probability density that a neutron is scattered into a solid angle element $\mathrm{d}\Omega$ with an energy transfer $\hbar\omega \ldots \hbar(\omega + \mathrm{d}\omega)$, is

$$\frac{\mathrm{d}\sigma}{\mathrm{d}\Omega \mathrm{d}\omega} = \frac{1}{2\pi} \frac{k'}{k} \int_{-\infty}^{\infty} \mathrm{e}^{-\mathrm{i}\omega t} \mathrm{d}t \sum_{j,k=1}^{N} b_j^* b_k \left\langle \mathrm{e}^{\mathrm{i}\mathbf{Q}\cdot(\mathbf{r}_k(t) - \mathbf{r}_j(0))} \right\rangle \,. \tag{11.16}$$

In order to derive a quantity similar to the structure factor $S(\mathbf{Q})$ in lectures 4 and 5, one assumes again a system of N *chemically* identical particles. Because the neutron scattering length is a nuclear property, there may still be a variance of scattering lengths. And even in monisotopic systems, there may be such a variance due to disorder of the nuclear spin orientations, since the scattering length also depends on the combined spin state of the scattered neutron and the scattering nucleus[2]. Therefore, it is assumed that scattering lengths are randomly distributed

[2] In this section only nuclear non-magnetic scattering will be considered. For a full treatment of magnetic scattering see lecture 7 or vol. 2 of ref. 2.

with the average $\overline{b} = (1/N)\sum_j b_i$ and the variance $\overline{|b|^2} - \left|\overline{b}\right|^2 = \overline{\left|b - \overline{b}\right|^2} = (1/N)\sum_i \left|b_j - \overline{b}\right|^2$. As will be seen later, this gives rise to the *incoherent scattering* contribution which is usually found in neutron scattering (but not in x-ray scattering). The sum in expression (11.16) can be decomposed into one over different indices and one over identical indices:

$$\sum_{j,k=1}^{N} b_j^* b_k \mathrm{e}^{\mathrm{i}\mathbf{Q}\cdot(\mathbf{r}_k(t)-\mathbf{r}_j(0))} = \sum_{j\neq k=1}^{N} b_j^* b_k \mathrm{e}^{\mathrm{i}\mathbf{Q}\cdot(\mathbf{r}_k(t)-\mathbf{r}_j(0))} + \sum_{j=1}^{N} |b_j|^2 \mathrm{e}^{\mathrm{i}\mathbf{Q}\cdot(\mathbf{r}_j(t)-\mathbf{r}_j(0))} . \tag{11.17}$$

They have to be averaged in different ways with respect to the distribution of scattering lengths. In the first term b_j^* and b_k can be averaged separately because the different particle scattering lengths are uncorrelated: $\overline{b^*}\,\overline{b} = \overline{b}^*\overline{b} = |\overline{b}|^2$. In the second term one has to average *after* taking the absolute square:

$$= \sum_{j\neq k=1}^{N} |\overline{b}|^2 \mathrm{e}^{\mathrm{i}\mathbf{Q}\cdot(\mathbf{r}_k(t)-\mathbf{r}_j(0))} + \sum_{j=1}^{N} \overline{|b|^2} \mathrm{e}^{\mathrm{i}\mathbf{Q}\cdot(\mathbf{r}_j(t)-\mathbf{r}_j(0))} . \tag{11.18}$$

In order to avoid the sum over distinct particles, the first sum is complemented by the $j = k$ terms, $|\overline{b}|^2 \mathrm{e}^{\mathrm{i}\mathbf{Q}\cdot(\mathbf{r}_j(t)-\mathbf{r}_j(0))}$, and to compensate, these terms are subtracted in the second sum:

$$= \sum_{j,k=1}^{N} |\overline{b}|^2 \mathrm{e}^{\mathrm{i}\mathbf{Q}\cdot(\mathbf{r}_k(t)-\mathbf{r}_j(0))} + \sum_{j=1}^{N} \left(\overline{|b|^2} - |\overline{b}|^2\right) \mathrm{e}^{\mathrm{i}\mathbf{Q}\cdot(\mathbf{r}_j(t)-\mathbf{r}_j(0))} . \tag{11.19}$$

With this result it is possible to express the double differential cross section as

$$\frac{\partial\sigma}{\partial\Omega\partial\omega} = N\frac{k'}{k}\left(\left|\overline{b}\right|^2 S_{\mathrm{coh}}(\mathbf{Q},\omega) + \left(\overline{|b|^2} - \left|\overline{b}\right|^2\right) S_{\mathrm{inc}}(\mathbf{Q},\omega)\right) \tag{11.20}$$

with

$$S_{\mathrm{coh}}(\mathbf{Q},\omega) = \frac{1}{2\pi N}\int_{-\infty}^{\infty} \mathrm{e}^{-\mathrm{i}\omega t}\mathrm{d}t \sum_{j,k=1}^{N} \left\langle \mathrm{e}^{\mathrm{i}\mathbf{Q}\cdot(\mathbf{r}_k(t)-\mathbf{r}_j(0))}\right\rangle \tag{11.21}$$

and

$$S_{\mathrm{inc}}(\mathbf{Q},\omega) = \frac{1}{2\pi N}\int_{-\infty}^{\infty} \mathrm{e}^{-\mathrm{i}\omega t}\mathrm{d}t \sum_{j=1}^{N} \left\langle \mathrm{e}^{\mathrm{i}\mathbf{Q}\cdot(\mathbf{r}_j(t)-\mathbf{r}_j(0))}\right\rangle . \tag{11.22}$$

The quantities defined by (11.21) and (11.22) are called *coherent* and *incoherent scattering function* or *dynamic structure factors*. It is a peculiarity of neutron scattering that there is also the incoherent term, which solely depends on the *single particle dynamics* due to the variance of the scattering lengths.

The prefactors of the scattering functions in expression (11.20) are often replaced by the scattering cross sections

$$\sigma_{\mathrm{coh}} = 4\pi\left|\overline{b}\right|^2, \quad \sigma_{\mathrm{inc}} = 4\pi\left(\overline{|b|^2} - \left|\overline{b}\right|^2\right) . \tag{11.23}$$

They give the scattering into all directions, i.e. the solid angle 4π (for the incoherent part in general and for the coherent in the limit $Q \to \infty$).

As demonstrated in ref. 2, it is also possible to use the concept of correlation functions for phonons. In this way it is possible to calculate the scattering from phonons in terms of

$S_{\mathrm{coh}}(\mathbf{Q},\omega)$ and $S_{\mathrm{inc}}(\mathbf{Q},\omega)$. The result for the coherent scattering gives non-vanishing contributions only for $(\mathbf{Q},\omega)$ combinations which fulfil the conservation laws (11.11) and (11.12). This was already shown in section 11.2.2 but the explicit calculation gives also the intensity of the phonon peaks, e.g. the mentioned result that transverse phonon peaks vanish in the first Brillouin zone. But with this mathematical approach it is also possible to calculate the incoherent scattering which is not bound to the momentum conservation (11.12). The result is for inelastic incoherent neutron scattering from cubic crystals in the one-phonon approximation [2]:

$$S_{\mathrm{inc}}(\mathbf{Q},\omega\neq 0) \quad = \quad \frac{\hbar Q^2}{2M}\exp(-2W(\mathbf{Q})\frac{g(|\omega|)}{\omega}\frac{1}{\exp(\hbar\omega/k_{\mathrm{B}}T)-1} \tag{11.24}$$

$$\xrightarrow{\text{classical limit}} \quad \frac{Q^2 k_{\mathrm{B}}T}{2M}\frac{g(|\omega|)}{\omega^2}\,. \tag{11.25}$$

(Here, $\exp(-2W(\mathbf{Q})$ is a shorthand for the Debye-Waller factor (11.15).) From this expression it can be seen that the incoherent scattering is determined by the *phonon density of states* $g(\omega)$ alone and does not depend on the full details of the phonon dispersion. The density of states $g(\omega)$ is the projection of the phonon dispersion curves onto the frequency axis, as demonstrated in Fig. 11.5. Besides nuclear inelastic scattering, which requires Mößbauer-active nuclei, inelastic incoherent neutron scattering is the most important method to determine $g(\omega)$.

In some cases it is interesting to consider the part of expression (11.21) before the time-frequency Fourier transform, called *intermediate coherent scattering function*:

$$I_{\mathrm{coh}}(\mathbf{Q},t) = \frac{1}{N}\sum_{jk}\left\langle \mathrm{e}^{\mathrm{i}\mathbf{Q}\cdot(\mathbf{r}_k(t)-\mathbf{r}_j(0))}\right\rangle\,. \tag{11.26}$$

Its value for $t=0$ expresses the correlation between atoms *at equal times*. A theorem on Fourier transforms tells that this is identical to the integral of the scattering function over all energy transfers:

$$I_{\mathrm{coh}}(\mathbf{Q},0) = \frac{1}{N}\sum_{jk}\left\langle \mathrm{e}^{\mathrm{i}\mathbf{Q}\cdot(\mathbf{r}_k-\mathbf{r}_j)}\right\rangle = S(\mathbf{Q}) = \int_{-\infty}^{\infty} S_{\mathrm{coh}}(\mathbf{Q},\omega)\mathrm{d}\omega\,. \tag{11.27}$$

($S(\mathbf{Q})$ is the structure factor as derived in lectures 4 and 5 for the static situation.) This integral relation has a concrete relevance in diffraction experiments. There, the energy of the neutrons is not discriminated: The diffraction experiment implicitly integrates over all $\hbar\omega$ [3]. Equation (11.27) shows that this integral corresponds to the instantaneous correlation of the atoms. The diffraction experiment performs a 'snapshot' of the structure. All dynamic information is lost in the integration process and therefore it is invisible in a diffraction experiment.

Similarly the *incoherent intermediate scattering function* is

$$I_{\mathrm{inc}}(\mathbf{Q},t) = \frac{1}{N}\sum_{j=1}^{N}\left\langle \mathrm{e}^{\mathrm{i}\mathbf{Q}\cdot(\mathbf{r}_j(t)-\mathbf{r}_j(0))}\right\rangle \tag{11.28}$$

[3] Strictly speaking, this is only an approximation. There are several reasons why the integration in the diffraction experiment is not the 'mathematical' one of (11.27): (1) On the instrument the integral is taken along a curve of constant 2θ in Fig. 11.2 while constant Q would correspond to a horizontal line. (2) The double differential cross-section (11.20) contains a factor k'/k which depends on ω via (11.1). (3) The detector may have an efficiency depending on wavelength which will introduce another ω-dependent weight in the experimental integration. All these effects have been taken into account in the so-called Placzek corrections [8, 13, 14].

with

$$I_{\mathrm{inc}}(\mathbf{Q},0) = \frac{1}{N}\sum_{j=1}^{N}\left\langle \mathrm{e}^{\mathrm{i}\mathbf{Q}\cdot(\mathbf{r}_j-\mathbf{r}_j)}\right\rangle = 1 = \int_{-\infty}^{\infty} S_{\mathrm{inc}}(\mathbf{Q},\omega)\mathrm{d}\omega\,. \tag{11.29}$$

Note that this result is independent of the actual structure of the sample. Integration of the double-differential cross section (11.20) over ω shows that also the static scattering contains an incoherent contribution. But because of (11.29), this term is constant in Q. It contributes as a flat background in addition to the $S(Q)$-dependent scattering. In some cases (e.g. small-angle scattering) it may be necessary to correct for this, in other cases (e.g. diffraction with polarisation analysis) it may even be helpful to normalise the coherent scattering.

In the paragraphs before it was shown, that the value of the intermediate scattering functions at $t = 0$ corresponds to the integral of the scattering function over an infinite interval. This is a consequence of a general property of the Fourier transform. There is also the inverse relation that the value of $S(\mathbf{Q},\omega)$ at $\omega = 0$ is related to the integral of $I(\mathbf{Q},t)$ over all times. The most important case is here when $I(\mathbf{Q},t)$ does not decay to zero for infinite time, but to a finite value $f(\mathbf{Q})$. In that case the integral is infinite, implying that $S(\mathbf{Q},\omega)$ has a delta function contribution at $\omega = 0$. This means that the scattering contains a strictly elastic component. Its strength can be calculated by decomposing the intermediate scattering function into a completely decaying part and a constant for the coherent and the incoherent scattering:

$$I_{[\mathrm{coh|inc}]}(\mathbf{Q},t) = I^{\mathrm{inel}}_{[\mathrm{coh|inc}]}(\mathbf{Q},t) + f_{[\mathrm{coh|inc}]}(\mathbf{Q})\,. \tag{11.30}$$

Because the Fourier transform of constant one is the delta function this corresponds to

$$S_{[\mathrm{coh|inc}]}(\mathbf{Q},\omega) = S^{\mathrm{inel}}_{[\mathrm{coh|inc}]}(\mathbf{Q},\omega) + S^{\mathrm{el}}_{[\mathrm{coh|inc}]}(\mathbf{Q})\delta(\omega)\,, \tag{11.31}$$

where $S^{\mathrm{el}}_{[\mathrm{coh|inc}]}(\mathbf{Q}) = f_{[\mathrm{coh|inc}]}(\mathbf{Q})$, the *elastic coherent/incoherent structure factor* (EISF), can be written as

$$S^{\mathrm{el}}_{\mathrm{coh}}(\mathbf{Q}) = \frac{1}{N}\sum_{j,k=1}^{N}\left\langle \mathrm{e}^{\mathrm{i}\mathbf{Q}\cdot(\mathbf{r}_k(\infty)-\mathbf{r}_j(0))}\right\rangle\,, \tag{11.32}$$

$$S^{\mathrm{el}}_{\mathrm{inc}}(\mathbf{Q}) = \frac{1}{N}\sum_{j=1}^{N}\left\langle \mathrm{e}^{\mathrm{i}\mathbf{Q}\cdot(\mathbf{r}_j(\infty)-\mathbf{r}_j(0))}\right\rangle\,. \tag{11.33}$$

Here, $t = \infty$ indicates a time which is sufficiently long that the correlation with the position at $t = 0$ is lost. For the EISF this lack of correlation implies that the terms with initial and final positions can be averaged separately:

$$\begin{aligned} S^{\mathrm{el}}_{\mathrm{inc}}(\mathbf{Q}) &= \frac{1}{N}\sum_{j=1}^{N}\left\langle \mathrm{e}^{\mathrm{i}\mathbf{Q}\cdot\mathbf{r}_j}\right\rangle\left\langle \mathrm{e}^{-\mathrm{i}\mathbf{Q}\cdot\mathbf{r}_j}\right\rangle \\ &= \frac{1}{N}\sum_{j=1}^{N}\left|\mathrm{e}^{-\mathrm{i}\mathbf{Q}\cdot\mathbf{r}_j}\right|^2 \qquad (11.34) \\ &= \frac{1}{N}\sum_{j=1}^{N}\left|\int_V \mathrm{d}^3r\,\exp\left(\mathrm{i}\mathbf{Q}\cdot\mathbf{r}\right)\rho_j(\mathbf{r})\right|^2\,. \qquad (11.35) \end{aligned}$$

Here, $\rho_j(\mathbf{r})$ denotes the 'density of particle j', i.e. the probability density of the individual particle j being at $\mathbf{r}$. From (11.34) one can see that the normalisation of the EISF is $S^{\mathrm{el}}_{\mathrm{inc}}(0) = 1$ (in contrast to that of the structure factor, $\lim_{Q\to\infty} S(Q) = 1$). One can say that the EISF is the form factor of the volume confining the motion of the particles. E.g. for particles performing any kind of motion within a sphere, the EISF would be $S^{\mathrm{el}}_{\mathrm{inc}}(Q) = 9\left(\sin(QR) - QR\cos(QR)\right)^2/Q^6R^6$ as derived in lecture 5.

As in the static situation, the scattering law can be traced back to distance distribution functions. These are now (in the treatment of inelastic scattering) time-dependent. They are called *van Hove correlation functions*:

$$G(\mathbf{r},t) = \frac{1}{N}\left\langle \sum_{j,k=1}^{N} \delta(\mathbf{r} - \mathbf{r}_k(t) + \mathbf{r}_j(0)) \right\rangle , \tag{11.36}$$

$$G_{\mathrm{s}}(\mathbf{r},t) = \frac{1}{N}\left\langle \sum_{j=1}^{N} \delta(\mathbf{r} - \mathbf{r}_j(t) + \mathbf{r}_j(0)) \right\rangle . \tag{11.37}$$

Insertion into

$$I_{[\mathrm{coh|inc}]} = \int_{V_d} G_{[\mathrm{s}]}(\mathbf{r},t)\exp(\mathrm{i}\mathbf{Q}\cdot\mathbf{r})\mathrm{d}^3r \tag{11.38}$$

directly proves that the spatial Fourier transforms of the van Hove correlation function are the intermediate scattering functions.

The two particle version can be reduced to the microscopic density,

$$\rho(\mathbf{r},t) = \sum_{j=1}^{N} \delta(\mathbf{r} - \mathbf{r}_j(t)) . \tag{11.39}$$

Its autocorrelation function in space and time is

$$\langle \rho(\mathbf{0},0)\rho(\mathbf{r},t)\rangle . \tag{11.40}$$

The $\mathbf{0}$ is showing that translational symmetry is assumed. So the correlation function can be replaced by its average over all starting points $\mathbf{r}_1$ in the sample volume:

$$\langle \rho(\mathbf{0},0)\rho(\mathbf{r},t)\rangle = \frac{1}{V}\int_V \mathrm{d}^3r_1 \langle \rho(\mathbf{r}_1,0)\rho(\mathbf{r}_1+\mathbf{r},t)\rangle . \tag{11.41}$$

Insertion of (11.39) gives

$$\langle \rho(\mathbf{0},0)\rho(\mathbf{r},t)\rangle = \frac{1}{V}\left\langle \sum_{j,k=1}^{N} \int_V \mathrm{d}^3r_1 \delta(\mathbf{r}_1 - \mathbf{r}_k(t))\delta(\mathbf{r}_1 + \mathbf{r} - \mathbf{r}_j(t)) \right\rangle \tag{11.42}$$

$$= \frac{1}{V}\left\langle \sum_{j,k=1}^{N} \delta(\mathbf{r}_k(t) + \mathbf{r} - \mathbf{r}_j(t)) \right\rangle . \tag{11.43}$$

Together with (11.36) this implies

$$G(\mathbf{r},t) = \frac{1}{\rho_0}\langle \rho(\mathbf{0},0)\rho(\mathbf{r},t)\rangle . \tag{11.44}$$

Again setting $t = 0$ results in the static scattering situation:

$$G(\mathbf{r}, 0) = \frac{\langle \rho(\mathbf{0}, 0)\rho(\mathbf{r}, 0)\rangle}{\rho_0} = \delta(\mathbf{r}) + \rho_0 g(\mathbf{r}) \tag{11.45}$$

with $g(\mathbf{r})$ as defined in lecture 5.

As in the case of static scattering there is an alternative way to derive the scattering function by Fourier-transforming the density

$$\rho_{\mathbf{Q}}(t) = \int \mathrm{d}^3 r \mathrm{e}^{\mathrm{i}\mathbf{Q}\cdot\mathbf{r}} \rho(\mathbf{r}, t) = \sum_{j=1}^{N} \mathrm{e}^{\mathrm{i}\mathbf{Q}\cdot\mathbf{r}_j(t)} \tag{11.46}$$

and then multiplying its conjugated value at $t = 0$ with that at t:

$$I_{\mathrm{coh}}(\mathbf{Q}, t) = \frac{1}{N} \left\langle \rho^*_{\mathbf{Q}}(0)\rho_{\mathbf{Q}}(t)\right\rangle \tag{11.47}$$

and

$$S_{\mathrm{coh}}(\mathbf{Q}, \omega) = \frac{1}{2\pi N} \int_{-\infty}^{\infty} \mathrm{e}^{-\mathrm{i}\omega t} \left\langle \rho^*_{\mathbf{Q}}(0)\rho_{\mathbf{Q}}(t)\right\rangle \mathrm{d}t\,. \tag{11.48}$$

(This is a consequence of the *cross-correlation theorem* of Fourier transform which is the generalisation of the Wiener-Khintchine theorem for two different correlated quantities.)

Note that a reduction of the self correlation function $G_{\mathrm{s}}(\mathbf{r}, t)$ to the density is *not* possible in the same way. The multiplication $\rho(\mathbf{0}, 0)\rho(\mathbf{r}, t)$ in equation (11.44) inevitably includes all combinations of particles j, k and not only the terms for identical particles j, j. Therefore, the incoherent scattering cannot be derived from the density alone but requires the knowledge of the motion of the individual particles.

From the definitions (11.36) and (11.37) it is immediately clear that the van Hove correlation functions are symmetric with respect to a *combined* inversion of space and time. (Note that the following relations are *not* valid in a correct quantum-mechanical treatment.):

$$G^{\mathrm{cl}}_{[\mathrm{s}]}(-\mathbf{r}, -t) = G^{\mathrm{cl}}_{[\mathrm{s}]}(\mathbf{r}, t)\,. \tag{11.49}$$

But in many cases the system is dynamically symmetric to an inversion of space (meaning that the distance between two particles is changing by $-\mathbf{r}$ in the time interval t with equal probability as changing by $\mathbf{r}$)[4]:

$$G^{\mathrm{cl}}_{[\mathrm{s}]}(-\mathbf{r}, t) = G^{\mathrm{cl}}_{[\mathrm{s}]}(\mathbf{r}, t) \tag{11.50}$$

which implies symmetry in time

$$G^{\mathrm{cl}}_{[\mathrm{s}]}(\mathbf{r}, -t) = G^{\mathrm{cl}}_{[\mathrm{s}]}(\mathbf{r}, t)\,. \tag{11.51}$$

From (11.50) and general properties of the Fourier transform it follows that $I_{[\mathrm{coh|inc}]}(\mathbf{Q}, t)$ is real and from (11.51) that it is also symmetric in time:

$$I^{\mathrm{cl}}_{[\mathrm{coh|inc}]}(\mathbf{Q}, -t) = I^{\mathrm{cl}}_{[\mathrm{coh|inc}]}(\mathbf{Q}, t)\,. \tag{11.52}$$

[4] A simple counterexample would be a solid moving at constant velocity as a car in a Doppler radar. In that case $G_{\mathrm{s}}(\mathbf{r}, t) = \delta(\mathbf{r} - \mathbf{v}t)$ but $G_{\mathrm{s}}(-\mathbf{r}, t) = \delta(\mathbf{r} + \mathbf{v}t)$ and $S(\mathbf{Q}, \omega)$ will only have a component for positive *or* negative frequency shift ω, depending on whether $\mathbf{Q}$ and $\mathbf{v}$ are parallel or antiparallel, the former arrangement usually being the choice of the police.

In turn this implies that the scattering functions are real and symmetric in energy transfer $\hbar\omega$:

$$S^{\mathrm{cl}}_{[\mathrm{coh|inc}]}(\mathbf{Q},-\omega) = S^{\mathrm{cl}}_{[\mathrm{coh|inc}]}(\mathbf{Q},\omega)\,. \tag{11.53}$$

Without the dynamical symmetry to inversion in space (11.50) from (11.49) would only follow that $S_{[\mathrm{coh|inc}]}(\mathbf{Q},\omega)$ is real.

Inelastic scattering is often also called neutron (scattering) spectroscopy. That there is indeed a relation to better-known spectroscopic methods as light spectroscopy, can be seen from the dependence of the scattering function on a frequency ω. It can be said that inelastic neutron scattering, for every $\mathbf{Q}$, produces a spectrum, understood as the frequency dependence of a quantity, here the scattering cross section. The optical methods Raman- and Brillouin spectroscopy are completely analogous in this respect, yielding the same $S(\mathbf{Q},\omega)$ but different measured double-differential cross-sections because photons interact with matter differently. Other methods, as absorption spectroscopy, impedance spectroscopy or rheology do not yield a $\mathbf{Q}$ dependence and are thus insensitive to the molecular structure. They provide only information about the overall dynamics. The deeper reason for this analogy is that scattering experiments as well as 'ordinary' spectroscopy can be explained by linear response theory (appendix B of ref. 2 or ref. 15).

Example: diffusion

For simple diffusion the density develops in time following Fick's second law,

$$\frac{\partial\rho}{\partial t} = D\Delta\rho \equiv D\left(\frac{\partial^2\rho}{\partial x^2}+\frac{\partial^2\rho}{\partial y^2}+\frac{\partial^2\rho}{\partial z^2}\right)\,. \tag{11.54}$$

The underlying mechanism is Brownian motion, i.e. random collisions with solvent molecules. Therefore, it can be concluded from the central limit theorem of statistics that the density of particles initially assembled at the origin is a Gaussian in all coordinates:

$$\begin{aligned}\rho_1 &= \frac{1}{\sqrt{2\pi}\sigma}\exp\left(-\frac{x^2}{2\sigma^2}\right)\frac{1}{\sqrt{2\pi}\sigma}\exp\left(-\frac{y^2}{2\sigma^2}\right)\frac{1}{\sqrt{2\pi}\sigma}\exp\left(-\frac{z^2}{2\sigma^2}\right)\\ &= \frac{1}{(2\pi)^{3/2}\sigma^3}\exp\left(-\frac{r^2}{2\sigma^2}\right)\,.\end{aligned} \tag{11.55}$$

The index 1 should remind that the prefactor is chosen such that the total particle number $\int\rho_1\ \mathrm{d}^3r$ is normalised to one. The width of the distribution, σ has the dimension length. The only way to construct a length out of D (dimension $\mathrm{length}^2/\mathrm{time}$) and time is $\sigma = c\sqrt{Dt}$ where c is a dimensionless constant. Inserting this into (11.55) yields:

$$\rho_1 = \frac{1}{c^3(2\pi Dt)^{3/2}}\exp\left(-\frac{r^2}{2c^2Dt}\right)\,. \tag{11.56}$$

The derivatives of this expression with respect to t and x,y,z can be calculated and inserted into (11.54):

$$\frac{\sqrt{2}\,(r^2-3c^2Dt)}{8\pi^{3/2}c^5D^{5/2}t^{7/2}}\exp\left(-\frac{r^2}{2c^2Dt}\right) = \frac{\sqrt{2}\,(r^2-3c^2Dt)}{4\pi^{3/2}c^7D^{7/2}t^{7/2}}\exp\left(-\frac{r^2}{2c^2Dt}\right)\,. \tag{11.57}$$

One can see that the right- and left-hand side are identical if $c = \sqrt{2}$. This proves that the 'guess' (11.55) is indeed a solution of Fick's second law and also determines the unknown c. With the value of c substituted, the 'single particle density' is

$$\rho_1 = \frac{1}{(8\pi Dt)^{3/2}} \exp\left(-\frac{r^2}{4Dt}\right) . \tag{11.58}$$

Diffusion-like processes are often characterised by the *mean-square displacement* $\langle r^2 \rangle$ [5]. Because of the statistical isotropy, the average displacement $\langle r \rangle$ is always zero. Therefore, the characterisation of the mobility of a diffusional process has to be done using the second moment, which is the average of the square of the displacement. For the simple Fickian diffusion this can be calculated from (11.58):

$$\langle r^2 \rangle = \int \rho_1 r^2 4\pi r^2 \mathrm{d}^3 r = 6Dt\,. \tag{11.59}$$

For incoherent scattering the starting position $\mathbf{r}(0)$ is irrelevant. Therefore, expression (11.58) is also $G_\mathrm{s}(r,t)$. Because the Fourier transform of a Gaussian function is a Gaussian itself, the corresponding incoherent intermediate scattering function is

$$I_\mathrm{inc}(Q,t) = \exp\left(-DQ^2 t\right) , \tag{11.60}$$

and because the Fourier transform of an exponential decay is a Lorentzian the incoherent scattering function is

$$S_\mathrm{inc}(Q,\omega) = \frac{1}{\pi} \frac{DQ^2}{\omega^2 + (DQ^2)^2} . \tag{11.61}$$

This function is centred around $\omega = 0$, and for that reason the scattering is called *quasielastic*. This is typical for diffusionlike processes in contrast to vibrational processes which yield (phonon) peaks at finite energy transfers. For this reason, many textbook authors distinguish between inelastic and quasielastic neutron scattering instead of subsuming the latter under the former as done here[6].

From expression (11.60) one can see that $I_\mathrm{inc}(Q,t)$ decays faster with time for larger Q and from (11.61) that $S_\mathrm{inc}(Q,\omega)$ is getting broader. This is understandable because Q defines the spatial resolution of a neutron scattering experiment in a reciprocal way. So a larger Q means observation on shorter distances which can be travelled faster by the diffusing particle.

Finally, one can see that

$$I_\mathrm{inc}(Q,t) = \exp\left(-\frac{Q^2\langle r^2 \rangle}{6}\right) . \tag{11.62}$$

[5] Here, the definition is "displacement from the position at $t = 0$" rather than "displacement from a potential minimum" on page 8. This is an obvious choice because the diffusing particle is not subjected to a potential as the atom in a crystal. Therefore, there is nothing like an 'equilibrium position'. This difference is indicated by the usage of $\langle r^2 \rangle$ instead of $\langle u^2 \rangle$. Because in the case of motion in a potential the displacement between time zero and time t can be understood as the difference of the displacements at time zero from the equilibrium position and that at time t, it follows that $\langle r^2 \rangle = 2\langle u^2 \rangle$

[6] There are two reasons for the choice made here: (1) The correlation function approach is also applicable to phonons. So, if this method is used, there is no conceptual difference between the treatment of vibrations and diffusion. (2) There are models as the damped harmonic oscillator which yield a continuous transition between inelastic scattering in the underdamped case and quasielastic scattering in the overdamped case.

Because this expression is derived independently of the specific form of $\sigma(t)$ in (11.55) it is generally valid if the distribution of displacements $G_\mathrm{s}(r,t)$ is a Gaussian. Even if this is not the case, equation (11.62) is often a good low-Q approximation called the *Gaussian approximation*[7] and is the dynamical analogue of to the Guinier approximation of static scattering.

In general, the incoherent intermediate scattering function cannot be derived from the mean-square displacement alone. Because equation (11.62) is the first term of the cumulant expansion $\exp(aQ^2 + bQ^4 + \dots)$ of $I_\mathrm{inc}(Q,t)$ [16] the mean-square displacement can be calculated as

$$\langle r^2 \rangle = -\lim_{Q\to 0} \frac{6}{Q^2} \ln I_\mathrm{inc}(Q,t) \quad \text{or} \tag{11.63}$$

$$\langle r^2 \rangle = -\left.\frac{\mathrm{d} \ln I_\mathrm{inc}(Q,t)}{\mathrm{d}Q^2}\right|_{Q=0} . \tag{11.64}$$

By replacing $I_\mathrm{inc}(Q,t)$ by its value at infinite time, the EISF $S^\mathrm{el}_\mathrm{inc}(Q)$, the limiting mean-square displacement of a confined motion can be obtained. This is the principle of the *elastic scan* technique often used on neutron backscattering spectrometers [17].

11.3 Instrumentation

11.3.1 Triple axis spectrometer

The basic objective of inelastic neutron scattering is to measure the momentum transfer $\mathbf{q} = \mathbf{k}' - \mathbf{k}$ and the energy transfer $\hbar\omega = E' - E$. This task in general requires a monochromator for the incoming neutron beam and an analyzer for the scattered neutrons. In the most straightforward setup, the triple-axis spectrometer (3AX), one uses the Bragg planes of crystals similar to the diffracting grids in an optical spectrometer (figure 11.6).

Axis 1 turns the monochromator crystal. By doing this the neutron wavelength fulfilling the Bragg condition can be changed. In this way the wave vector $k = 2\pi/\lambda$ of the neutrons impinging on the sample is determined. Axis 2 turns the the arm carrying the analyser crystal around the sample position. This defines the scattering angle 2θ. Finally, axis 3 turns the analyser crystal around its own axis such that only the desired k' is admitted to the detector.

For a given setting of axis 1 all points in the kinematically allowed (Q,ω) area (see Fig. 11.2) can be addressed by suitable settings of axis 2 and 3. E.g., for the study of phonons usually a 'constant-Q scan' is performed where $\mathbf{Q} = \mathbf{k}' - \mathbf{k}$ is held constant and only $\hbar\omega = E' - E$ is varied. For this purpose a coordinated change of the angles of axis 2 and 3 is required which is accomplished by computer control.

Historically, the triple-axis spectrometer is the first inelastic neutron scattering instrument. The first prototype was constructed in 1955 by Bertram N. Brockhouse. In 1994, Brockhouse received the Nobel prize for this accomplishment (together with Clifford G. Shull for the development of neutron diffraction).

[7] In the literature, denominators 1, 2, and 3 are also found in this expression. Most of these formulae are nevertheless correct. Some authors use $\langle r^2 \rangle$ as mean-square displacement from an average position (what is called $\langle u^2 \rangle$ here). Then, 3 is the correct denominator because of $\langle r^2 \rangle = 2\langle u^2 \rangle$ (footnote 5). If the displacement is considered only in one coordinate ($\langle x^2 \rangle$), then 2 is the right denominator.

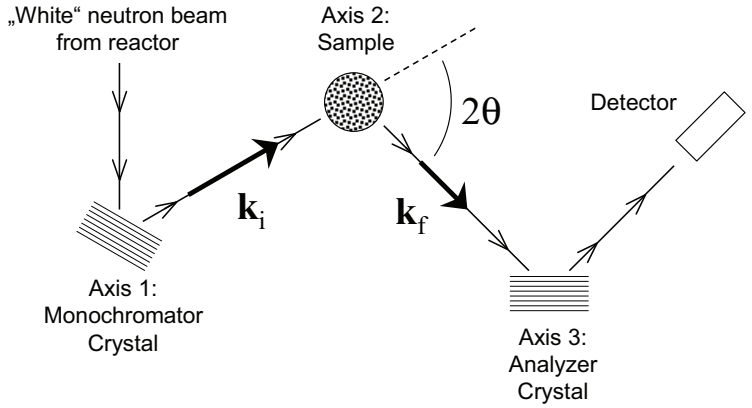

Fig. 11.6: *Schematic setup of a triple-axis spectrometer.*

The 3AX spectrometer is still widely in use for purposes where a high Q resolution is necessary and only a small region in the (Q, ω) plane has to be examined. This is mostly the study of phonons and magnons in crystals. In other fields, e.g. for 'soft matter' systems, it has been replaced by instruments showing better performance. The most important ones will be discussed here: time-of-flight (TOF) spectrometer, backscattering (BS) spectrometer, and neutron spin echo (NSE) spectrometer.

11.3.2 Time-of-flight spectrometer

The main disadvantage of the 3AX spectrometer is that it can only observe one (Q, ω) point at a time. While for samples where the scattering is concentrated into Bragg peaks this may be acceptable, for systems with diffuse scattering a simultaneous observation of a range of Q vectors and energy transfers $\hbar\omega$ is desired. This is accomplished by surrounding the sample position with an array of detectors (figure 11.7). In addition the energy of the scattered neutrons E' is here measured by their time of flight: A chopper in the incident beam defines the start time of the neutrons. The electronic pulse from their registration in the detector gives the end of their flight through the spectrometer. From the time difference the velocity of the neutrons can be calculated and from this in turn the energy transfer. The relation between time-of-flight and energy transfer is given by

$$\hbar\omega = \left(\frac{{l_1}^2}{\left(l_0 - \sqrt{E/m_\mathrm{n}}\, t_\mathrm{flight} \right)^2} - 1 \right) E \,. \tag{11.65}$$

The monochromatization of the incoming neutron beam can either be done by Bragg reflection from a crystal or by a sequence of choppers which are phased in order to transmit a single wavelength only. The former principle usually yields higher intensities while the latter is more flexible for the selection of the incident energy E and attains better energy resolution.

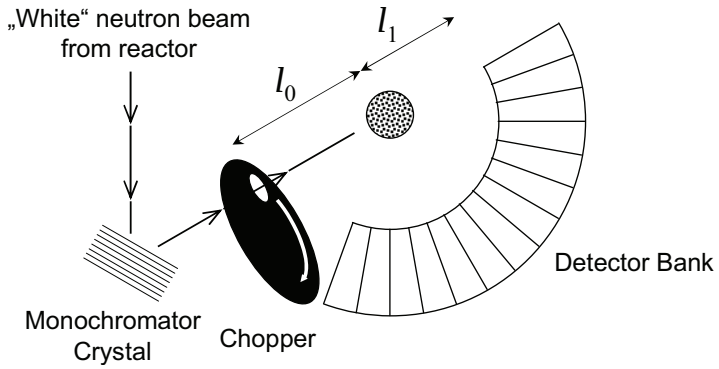

Fig. 11.7: *Schematic setup of a time-of-flight spectrometer with crystal monochromator.*

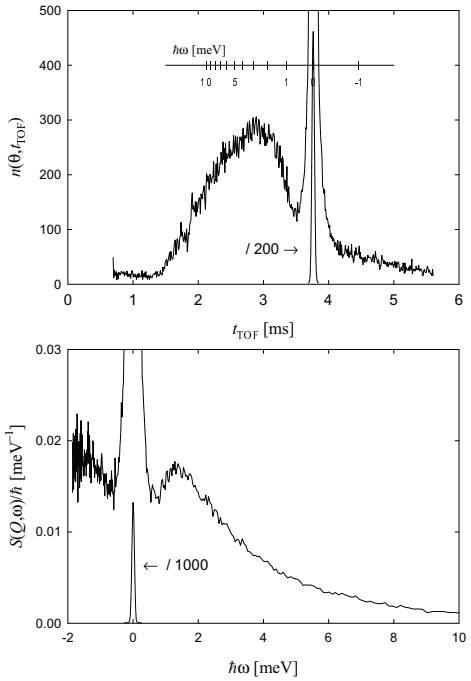

Fig. 11.8: *Top: raw data from TOF spectrometer: neutron counts in a time channel of* $10\,\mu s$ *during one hour registration time. The sample is a mesoscopically confined glass-forming liquid. The floating non-linear axis indicates the energy transfers calculated by equation (11.65). Because of the strength of the elastic scattering that part of the spectrum has been reduced by a factor of 200. Bottom: the same TOF data converted to* $S(Q,\omega)$*, elastic line reduced by factor 1000. The characteristic vibrational modes of the material at* $\hbar\omega \approx 1.7\,\mathrm{meV}$ $(14\,\mathrm{cm}^{-1})$ *become only visible after the transformation.*

Instrument	Type	λ_i [Å]	Q_max [Å^{-1}]	$\Delta\hbar\omega$ [meV]
IN4 (ILL)	TX	0.8–4	3–14	0.25–6
IN5 (ILL)	CC	2–15	0.8–5.7	0.01–6
IN6 (ILL)	CX	4.1–5.9	1.8–2.6	0.05–0.17
NEAT (HMI)	CC	1.8–19	0.6–6.5	0.006–5
IRIS (RAL)	CI	$\lambda_\mathrm{f} = 6.7$–20	0.6–1.9	0.001–0.015

Table 11.1: *Basic specifications of representative neutron time-of-flight spectrometers. Instrument types: TX–thermal, crystal; CX–cold, crystal; CC–cold, chopper; CI–cold, inverse. The maximal Q and the energy resolution $\Delta\hbar\omega$ depend on the incident wavelength; the upper limits of their ranges correspond to the lower limit of the incident wavelength λ_i and vice versa.*

Table 11.1 shows some representative TOF instruments with their basic specifications. Depending on the desired incident wavelength the instruments are constructed either using neutrons directly from the reactor moderator (thermal neutrons, $\lambda_\mathrm{max} \approx 1.8$ Å) or a cold source, where an additional moderation, e.g. by liquid hydrogen, takes place ($\lambda_\mathrm{max} \approx 4$ Å). Thermal neutrons make a larger Q range accessible while cold neutrons yield better energy resolution. Therefore, the choice of the instrument depends on the system to be observed but in general 'cold neutron' instruments are preferred for inelastic neutron scattering in soft matter systems.

A variant of the TOF spectrometer exists on spallation sources, the inverse time-of-flight spectrometer. Because the neutrons are produced in pulses by a spallation source one can use their creation time to start the TOF clock and in principle there is no need for a chopper. In this way all neutrons can be used in contrast to conventional TOF spectrometers which use only a few percent. Then usually the incident energy is measured by the time-of-flight and the final energy is kept constant by a fixed set of analyzer crystals ("inverse geometry"). By putting those crystals into near backscattering postion (see next section for details) it is possible to obtain a very good energy resolution already close to true backscattering spectrometers. Of course as a direct consequence of the good resolution function the count rates are low, especially with current spallation sources which have total neutron production rates significantly lower than reactors.

11.3.3 Backscattering spectrometer

A recurring problem of inelastic neutron scattering investigations is that processes are too slow to be observed. Without resorting to extreme setups which lead to a loss of intensity, the energy resolution of TOF spectrometers is limited to about $10\,\mu$eV, which corresponds to a maximal timescale of 200 ps. This is often not sufficient for e.g. the large scale motions in polymers or the glass transition related relaxation. Therefore, instruments with highest energy resolution are often needed, the backscattering (BS) and neutron spin echo (NSE) spectrometer.

The energy resolution of a TOF spectrometer is limited by the selectivity of the monochromator crystal[8]. If perfect crystals are used the spread of the selected wavelengths $\Delta\lambda/\lambda$ is determined by the angular divergence $\Delta\alpha$ of the reflected neutrons. Differentiating the Bragg condition

[8] For chopper spectrometers the limit is given by the pulse length which could in principle be arbitrary small. But since the counted intensity decreases quadratically with pulse length the resolution limit of an efficient experiment is in the same range.

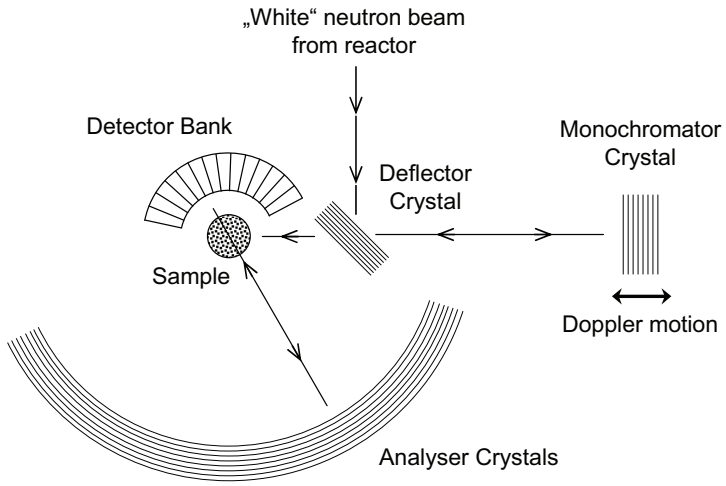

Fig. 11.9: *Schematic setup of a backscattering spectrometer.*

$\lambda = 2\sin\theta/d$ one obtains

$$\Delta\lambda/\lambda = \cot\theta \cdot \Delta\theta\,. \tag{11.66}$$

This expression becomes zero for $2\theta = 180°$. In practice this means that the wavelength spread becomes minimal if the neutron beam is reflected by $180°$, i.e. in backscattering condition.

Figure 11.9 shows schematically the instrument based on this principle. The first crystal in the beam is only a deflector with low wavelength selectivity. The actual monochromatization takes place upon the second reflection by the crystal in backscattering position. The monochromatized neutrons are then scattered by the sample which is surrounded by analyzer crystals placed on a spherical surface. There they are again scattered under backscattering condition. The reflected neutrons pass once more through the sample and finally reach the detector.

It can be seen that the backscattering condition leads to technical problems in several places: (1) The deflector must not accept all neutrons otherwise the monochromatized beam would be scattered back into the source. This can be solved by reducing its size deliberately below the neutron beam area or putting it on a rotating disk which removes it at the moment when the neutrons come back from the monochromator. Of course all these measures are taken at the expense of intensity. (2) The second passage of the scattered neutrons through the sample causes additional multiple scattering and absorption. Both problems can be avoided by leaving exact backscattering condition but with the consequence that the energy resolution degrades.

So far it seems that the backscattering instrument can only observe elastic scattering ($E' = E$) if the same crystals are used for monochromator and analyzer. In order to do inelastic scattering one has to change either E or E'. It turns out that this is much easier for the incident energy by either using a moving monochromator (Doppler effect) or a heated monochromator (thermal expansion modifying the lattice plane distance d). The latter technique usually allows larger energy transfers. For very large energy transfers, different crystals are used for monochromator and analyzer, yielding an offset of the whole $\hbar\omega$ range. Table 11.2 comprises specifications of representative BS spectrometers.

Instrument	Type	λ [Å]	$Q_{\max}$ [Å^{-1}]	$\Delta\hbar\omega$ [μeV]	$\hbar\omega_{\max}$ [μeV]
IN16 (ILL)	CD	6.27	1.9	0.2–1.0	15
IN10B (ILL)	CH	6.29	2.0	1.5	120
IN13 (ILL)	TH	2.23	5.5	8	300
SPHERES (JCNS)	CD	6.27	1.8	0.7	30

Table 11.2: *Basic specifications of representative neutron time-of-flight spectrometers. Instrument types: CD–cold, Doppler monochromator; CH–cold, heated monochromator; TH–thermal, heated monochromator. The maximal Q and the energy resolution $\Delta\hbar\omega$ depend on the incident wavelength; the upper limits of their ranges correspond to the lower limit of the incident wavelength λ_{i} and vice versa.*

11.3.4 Neutron spin echo spectrometer

In order to access even slower processes a very high resolution technique is needed allowing to reach more than 100 nanoseconds corresponding to energy transfers in the neV range. Such a technique is provided by neutron spin echo (NSE) spectrometers [18] which are able to measure directly energy *changes* of the neutron due to scattering.

This distinguishes NSE from conventional inelastic neutron scattering techniques which proceed in two steps: (1) monochromatization of the incident beam to E, (2) analysis of the scattered beam (E'). The energy transfer is then determined by taking the difference $E' - E$. In order to achieve high energy resolutions with these conventional techniques a very narrow energy interval must be selected from the relatively low-intensity neutron spectrum of the source. Conventional high-resolution techniques therefore inevitably run into the problem of low count rates at the detector.

Unlike these methods, NSE measures the individual velocities of the incident and scattered neutrons using the Larmor precession of the neutron spin in a magnetic field. The neutron spin vector acts as the hand of an internal clock, which is linked to each neutron and connects the result of the velocity measurement to the neutron itself. Thereby the velocities before and after scattering on one and the same neutron can be compared and a direct measurement of the velocity difference becomes possible. The energy resolution is thus decoupled from the monochromatization of the incident beam. Relative energy resolutions in the order of 10^{-5} can be achieved with an incident neutron spectrum of 20% bandwidth.

The motion of the neutron polarization $\mathbf{P}(t)$—which is the quantum mechanical expectancy value of the neutron spin—is described by the Bloch equation

$$\frac{\mathrm{d}\mathbf{P}}{\mathrm{d}t} = \frac{\gamma\mu}{\hbar}(\mathbf{P} \times \mathbf{B}) \tag{11.67}$$

where γ is the gyromagnetic ratio ($\gamma = -3.82$) of the neutron, μ the nuclear magneton and $\mathbf{B}$ the magnetic field. Equation (11.67) is the basis for manipulation of the neutron polarization by external fields. In particular, if a neutron of wavelength λ is exposed to a magnetic field B over a length l of its flight path, its spin is rotated by

$$\phi = \left(\frac{2\pi|\gamma|\mu\lambda m}{h^2}\right) Bl\,. \tag{11.68}$$

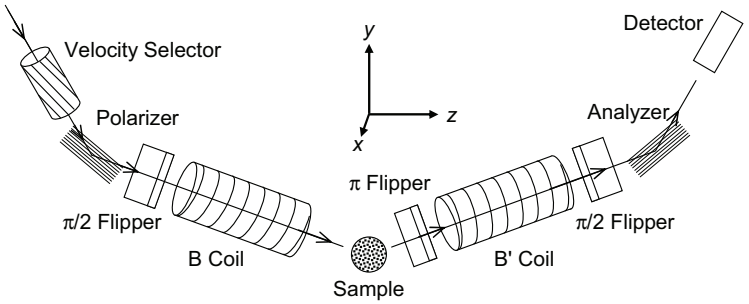

Fig. 11.10: *Schematic setup of a neutron spin echo spectrometer.*

The basic setup of an NSE spectrometer is shown in figure 11.10. A velocity selector in the primary neutron beam selects a wavelength interval of 10–20% width. In the primary and secondary flight path of the instrument precession fields B and B' parallel to the respective path are generated by cylindrical coils. Before entering the first flight path the neutron beam is polarized in forward direction[9]. Firstly, a $\pi/2$ flipper rotates the polarization to the x direction perpendicular to the direction of propagation (z). This is done by exposing the neutrons to a well defined field for a time defined by their speed and the thickness of a flat coil (Mezei coil). Beginning with this well-defined initial condition the neutrons start their precession in the field B. After being scattered by the sample the neutrons pass a π flipper and then pass the second precession field B'. Finally, the neutrons pass another $\pi/2$ coil which, under certain conditions, restores their initial polarization parallel to their flight direction. In order to understand what that condition is, one has to trace the changes of the spin vector (z always denoting the direction parallel to neutron propagation):

(n_x, n_y, n_z)	neutronic device
(0,0,1)	
	$\pi/2$ flipper
(1,0,0)	
	field B
$(\cos\phi, \sin\phi, 0)$	
	π flipper
$(\cos\phi, -\sin\phi, 0) =$ $(\cos(-\phi), \sin(-\phi), 0)$	
	field B'
$(\cos(\phi' - \phi), \sin(\phi' - \phi), 0)$	
	$\pi/2$ flipper
$(0, \sin(\phi - \phi'), \cos(\phi - \phi'))$	

In total, the spin is rotated by $\phi - \phi'$ around the x axis when a neutron passes through the spectrometer. This means that the final polarization is identical to the incident if $\phi = \phi'$ $(+2\pi n)$, especially if $\lambda_\mathrm{i} = \lambda_\mathrm{f}$ (elastic scattering) and $\int_0^l B\mathrm{d}z = \int_0^{l'} B'\mathrm{d}z$ (for homogeneous fields: $Bl = B'l'$) as follows from (11.68). This condition is called "spin echo" and is independent of the individual velocities of the neutrons because their difference alone determines $\phi - \phi'$.

Leaving spin echo condition the probability of a single neutron to reach the detector is reduced

[9] This is done by a a "polarizing supermirror" which only reflects neutrons of that spin—similar to the Nicol prism in optics.

due to the polarization analyzer by $\cos(\phi' - \phi)$. If we keep the symmetry of the instrument, $Bl = B'l'$, but consider inelastic scattering the precession angle mismatch can be approximated by

$$\begin{aligned} \phi' - \phi &= \left(\frac{2\pi|\gamma|\mu m}{h^2}\right) Bl(\lambda_\mathrm{f} - \lambda_\mathrm{i}) \\ &\approx \underbrace{\frac{|\gamma|\mu {m_\mathrm{n}}^2 \lambda^3 Bl}{h^3}}_{=t_\mathrm{NSE}(B)} \omega \end{aligned} \tag{11.69}$$

for small energy transfers where $\Delta\lambda \approx \hbar\omega \,/\, \frac{\mathrm{d}E}{\mathrm{d}\lambda}$ can be used. Because the energy transfer for inelastic scattering is not fixed but distributed as determined by the scattering function $S(Q,\omega)$ we have to average the factor $\cos(\phi' - \phi)$ weighted by $S(Q,\omega)$ to get the reduction of count rate at the detector, the effective polarization

$$P(Q, t_\mathrm{NSE}) = \frac{\int_{-\infty}^{\infty} S(Q,\omega)\cos(\omega t_\mathrm{NSE})\mathrm{d}\omega}{\int_{-\infty}^{\infty} S(Q,\omega)\mathrm{d}\omega}\,. \tag{11.70}$$

Firstly, we note that $S(Q,\omega)$ in this expression usually is the coherent scattering function. In principle, similar arguments can used for incoherent scattering because a well-defined fraction of neutrons changes its spin. This leads to a "negative echo" because the majority of neutrons invert their polarization. But because this effect is only partial (e.g. 2/3 for Hydrogen nuclei) it is much more difficult to observe. Only recently, NSE spectroscopy could be applied successfully to incoherently scattering samples.

Secondly, expression (11.70) reverses the temporal Fourier transform of equation (11.21) and therefore the result of the NSE experiment

$$P(Q, t_\mathrm{NSE}(B)) = \frac{I(Q, t_\mathrm{NSE}(B))}{I(Q,0)} \tag{11.71}$$

is the normalised *intermediate* scattering function. This function is often more understandable and easier to interpret than the frequency dependent scattering function.

In order to estimate typical Fourier times t_NSE which can be accessed by NSE we consider maximum fields of $B = B' = 500\,\mathrm{Gauss}$ in precession coils of $l = l' = 2$ m length operating at $\lambda = 8$ Å. Then (11.69) results in a time of about 10 ns which can be reached.

From this equation it also becomes clear that the most efficient way to enlarge this time is to use longer wavelengths because λ enters in the third power. This in turn reduces the accessible Q range which constitutes a drawback for studies on low molecular materials but not for the large scale properties of polymers which have to be observed at low Q anyway.

Typical NSE spectrometers with their specifications are listed in table 11.3. NSE spectrometers are very flexible instruments often used with different setups of which only "typical" ones have been included. As special features have to be mentioned that IN11 and SPAN have one-dimensional detector arrays which span $60°$ and $150°$ degrees respectively, allowing the simultaneous observation of a range of Q values. The instruments IN15 and J-NSE have two-dimensional detector arrays which can be used for studying anisotropies but cover a smaller angular range. IN15 uses a focusing mirror in order to increase neutron flux which would be otherwise very low due to its long precession coils.

Instrument	λ [Å]	$Q_{\max}$ [Å^{-1}]	$t_{\max}$ [ns]
IN11 (ILL)	4.5–12	0.9–2.4	2–45
IN15 (ILL)	8–25	0.13–0.4	30–1000
J-NSE (JCNS)	4.5–16	0.4–1.5	10–350
SPAN (HMI)	2.5–10	1.2–4.9	0.2–10

Table 11.3: *Basic specifications of representative neutron spin echo spectrometers. The maximal Q and the maximal Fourier time $t_{\max}$ depend on the incident wavelength; the upper limit of the Q range and the lower limit of $t_{\max}$ correspond to the lower limit of the incident wavelength λ and vice versa.*

Acknowledgment

The author thanks Matthias Muthmann for critical reading of the manuscript.

References

[1] This dictum is usually attributed to the Nobel prize winners B. N. Brockhouse and/or C. G. Shull. But to the knowledge of the author, no reliable quotation clarifying its true origin exists.

[2] S. W. Lovesey: "Theory of Neutron Scattering from Condensed Matter" (Clarendon Press, Oxford, 1984).

[3] G. L. Squires: "Introduction to the theory of thermal neutron scattering" (Cambridge University Press, Cambridge, 1978).

[4] G. E. Bacon: "Neutron Diffraction" (Clarendon Press, Oxford, 1975).

[5] G. E. Bacon (ed.): "Fifty Years Of Neutron Diffraction: The Advent Of Neutron Scattering" (Adam Hilger, Bristol, 1986).

[6] M. Bée: "Quasielastic neutron scattering" (Adam Hilger, Bristol, 1988).

[7] R. Zorn: "Fourier Transforms" in T. Brückel, G. Heger, D. Richter, R. Zorn (eds.): "Neutron Scattering" (Forschungszentrum Jülich, 2008, `http://hdl.handle.net/2128/37180`), chapter I.

[8] R. Zorn, D. Richter: "Correlation Functions Measured by Scattering Experiments", ibidem, chapter 4.

[9] N. W. Ashcroft, N. D. Mermin: "Solid State Physics" (Holt-Saunders, New York, 1976).

[10] G. P. Srivastava: "The physics of phonons" (Adama Hilger, Bristol, 1990).

[11] H. Bilz, W. Kress: "Phonon dispersion relations in insulators", Solid-state sciences, Vol. 10 (Springer, Berlin, 1979).

[12] B. N. Brockhouse, *Phys. Rev.* **106** 859 (1957).

[13] G. Placzek, *Phys. Rev.* **86** 377 (1952).

[14] J. L. Yarnell, M. J. Katz, R. G. Wenzel, S. H. Koenig, *Phys. Rev. A* **7** 2130 (1973).

[15] R. Zorn: "Correlations and Response of Matter to Probes" in K. Urban, C. M. Schneider, T. Brückel, S. Blügel, K. Tillmann, W. Schweika, M. Lentzen, L. Baumgarten: "Probing the Nanoworld" (Forschungszentrum Jülich, 2008).

[16] A. Rahman, K. S. Singwi, A. Sjölander, *Phys. Rev.* **126**, 986 (1962).

[17] R. Zorn, *Nucl. Instr. Meth. A* **603**, 439 (2009)

[18] Mezei, F. (ed.) (1980): *Neutron spin echo*, Springer, Heidelberg.

Exercises

Note: Exercises are labelled by stars (* through ***) indicating the level of difficulty. Try to solve the easier ones first.

E11.1 Scattering triangle*

For the feasibility of an inelastic neutron scattering experiment it is essential that the desired $Q, \hbar\omega$ combination (in the scattering function $S(Q,\omega)$ can be reached at a certain combination of incident neutron wavelength λ and angle 2θ.

1. $\lambda = 5.1$ Å, $2\theta = 90°$ and $\hbar\omega = 5$ meV, which value has Q? Which value would Q have calculated from the formula for elastic scattering?
2. $\lambda = 5.1$ Å, $Q = 1$ Å^{-1}, what is the largest energy gain and largest absolute energy loss one can reach? What do you have to do if you need larger values of $|\hbar\omega|$?
3. **: (neutron Brillouin scattering) One of the most demanding tasks of inelastic neutron scattering is the measurement of sound waves, i.e. Brillouin scattering. A typical sound velocity for a metal is $v = 2500\,\mathrm{m/s}$. If you would like to observe the Brillouin peaks at $Q = 1.5$ Å^{-1} what would be ω? Give an incident wavelength λ such that both Brillouin lines, $\pm\hbar\omega$, can be observed at certain values of 2θ. What experiment-technical challenges does your result present? Why could you be still interested to do this experiment with neutrons and not with light? Do you need coherent or incoherent scattering? Which sound will you see, longitudinal or transverse?

Hints: $\hbar = 1.0546 \times 10^{-34}$ Js, neutron mass: $m = 1.6749 \times 10^{-27}$ kg, $1\,\mathrm{eV} = 1.6022 \times 10^{-19}$ J.

E11.2 Q dependence of characteristic time**

In many cases, the incoherent intermediate scattering function can be written in the form $I_{\mathrm{inc}}(Q,t) = \exp\left(-(t/\tau(Q))^{\beta}\right)$ with $\tau(Q) \propto Q^{-x}$. E.g. in the lecture diffusion ($x = 2$, $\beta = 1$) and the ideal gas ($x = 1$, $\beta = 2$) were presented. In a later lecture you will learn that for polymers in the melt $x = 4$, $\beta = 1/2$ holds. For polymers in solution the Zimm model predicts $x = 3$, $\beta = 2/3$. In all cases $x \cdot \beta = 2$. What is the reason for this nearly universal relation?

E11.3 Jump diffusion in a confined space***

In the lecture, it was shown that for diffusion the incoherent scattering function is

$$S_{\mathrm{inc}}(Q,\omega) = \frac{1}{\pi} \frac{DQ^2}{\omega^2 + (DQ^2)^2}\,. \tag{11.72}$$

This function ('Lorentzian') has a width of $w = 2DQ^2$ at half its maximum value. The 'hand-waving' argument for this is that Q defines a length scale of observation $l \approx 2\pi/Q$. The average

time it takes a particle to diffuse out of this length scale is $\tau = l^2/D \sim D^{-1}Q^{-2}$. The Fourier transform from time to ω causes the width of $S(Q,\omega)$ to be related by $w \sim 1/\tau \sim DQ^2$.

In reality where diffusion is constituted from individual steps and on the long end may be limited by some confinement e.g. a pore wall, the dependence of the width w on Q may look like this:

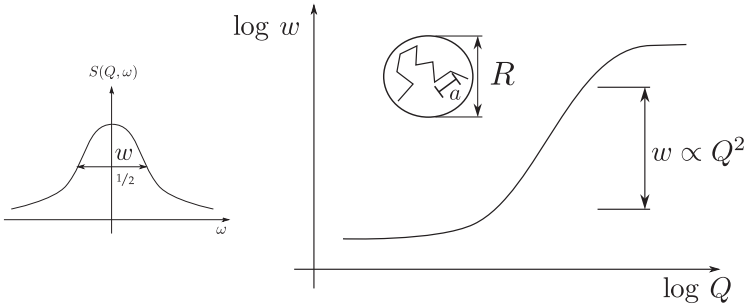

The Q^{-2} law is only valid in a small range. Can you explain this from the 'hand-waving' argument above? Where are the kinks in the double-logarithmic plot located approximately in terms of the dimensions a and R?

12 Strongly correlated electrons

M. Angst
Peter Grünberg Institut 4
Forschungszentrum Jülich GmbH

Contents

Lecture Notes of the JCNS Laboratory Course Neutron Scattering

12.1 Introduction

Materials with strong electronic correlations are materials, in which the movement of one electron depends on the positions and movements of all other electrons due to the long-range Coulomb interaction. With this definition, one would naively think that all materials show strong electronic correlations. However, in purely ionic systems, the electrons are confined to the immediate neighborhood of the respective atomic nucleus. On the other hand, in ideal metallic systems, the other conduction electrons screen the long-range Coulomb interaction. Therefore, while electronic correlations are also present in these systems and lead for example to magnetism, the main properties of the systems can be explained in simple models, where electronic correlations are either entirely neglected (e.g. the free electron Fermi gas) or taken into account only in low order approximations (Fermi liquid, exchange interactions in magnetism etc.). In highly correlated electron systems, simple approximations break down and entirely new phenomena and functionalities can appear. These so-called *emergent* phenomena cannot be anticipated from the local interactions among the electrons and between the electrons and the lattice [1]. This is a typical example of *complexity*: the laws that describe the behavior of a complex system are qualitatively different from those that govern its units [2]. This is what makes highly correlated electron systems a research field at the very forefront of condensed matter research. The current challenge in condensed matter physics is that we cannot reliably predict the properties of these materials. There is no theory, which can handle this huge number of interacting degrees of freedom. While the underlying fundamental principles of quantum mechanics (Schrödinger equation or relativistic Dirac equation) and statistical mechanics (maximization of entropy) are well known, there is no way at present to solve the many-body problem for some 10^{23} particles. Some of the exotic properties of strongly correlated electron systems and examples of emergent phenomena and novel functionalities are:

- *High temperature superconductivity*; while this phenomenon was discovered in 1986 by Bednorz and Müller [3], who received the Nobel Prize for this discovery, and since then has continually attracted the attention of a large number of researchers, there is still no commonly accepted mechanism for the coupling of electrons into Cooper pairs, let alone a theory which can predict high temperature superconductivity or its transition temperatures. High temperature superconductivity has already some applications such as highly sensitive magnetic field sensors, high field magnets, and power lines, and more are likely in the future.

- *Colossal magnetoresistance* effect CMR, which was discovered in transition metal oxide manganites and describes a large change of the electrical resistance in an applied magnetic field [4]. This effect can be used in magnetic field sensors and could eventually replace the giant magnetoresistance [5, 6] field sensors, which are employed for example in the read heads of magnetic hard discs.

- The *magnetocaloric* effect [7], a temperature change of a material upon applying a magnetic field, can be used for magnetic refrigeration without moving parts or cooling fluids.

- *Metal-insulator-transitions* as observed e.g. in magnetite (Verwey transition [8]) or certain vanadites are due to strong electronic correlations and could be employed as electronic switches.

- *Multiferroicity* [9], the simultaneous occurring of various ferroic orders, e.g. ferromagnetism and ferroelectricity, in one material. If the respective degrees of freedom are strongly coupled, one can switch one of the orders by applying the conjugate field of the other order. Interesting for potential applications in information technology is particularly the switching of magnetization by an electric field, which has been proposed to be used for easier switching of magnetic non-volatile memories [10]. Future applications of multiferroic materials in computer storage elements are apparent. One could either imagine elements, which store several bits in form of a magnetic- and electric polarization, or one could apply the multiferroic properties for an easier switching of the memory element.
- *Negative thermal expansion* [11] is just another example of the novel and exotic properties that these materials exhibit.

It is likely that many more such emergent phenomena will be discovered in the near future. This huge potential is what makes research on highly correlated electron systems so interesting and challenging: this area of research is located right at the intersection between fundamental science investigations, striving for basic understanding of the electronic correlations, and technological applications, connected to the new functionalities [12].

12.2 Electronic structure of solids

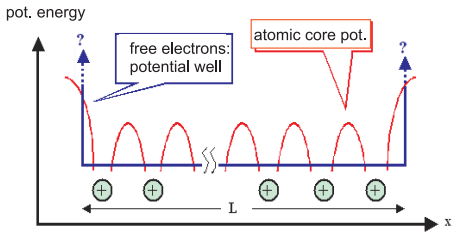

Fig. 12.1: *Potential energy of an electron in a solid.*

In order to be able to discuss the effects of strong electronic correlations, let us first recapitulate the textbook knowledge of the electronic structure of solids [13, 14]. The description of the electron system of solids usually starts with the adiabatic or Born-Oppenheimer approximation. The argument is made that the electrons are moving so quickly compared to the nuclei that the electrons can instantaneously follow the movement of the much heavier nuclei and thus see the instantaneous nuclear potential. This approximation serves to separate the lattice- and electronic degrees of freedom. Often one makes the further approximation to consider the nuclei to be at rest in their equilibrium positions. The potential energy seen by a single electron in the averaged field of all other electrons and the atomic core potential is depicted schematically for a one dimensional system in Fig. 12.1.

The following simple models are used to describe the electrons in a crystalline solid:

- *Free electron Fermi gas*: here a single electron moves in a 3D potential well with infinitely high walls corresponding to the crystal surfaces. All electrons move completely indepen-

dent, i.e. the Coulomb interaction between the electrons is considered only indirectly by the Pauli exclusion principle.

- *Fermi liquid*: here the electron-electron interaction is accounted for in a first approximation by introducing *quasiparticles*, so-called dressed electrons, which have a charge e, and a spin $\frac{1}{2}$ like the free electron, but an effective mass m^*, which can differ from the free electron mass m.

- *Band structure model*: this model takes into account the periodic potential of the atomic cores at rest, i.e. the electron moves in the average potential from the atomic cores and from the other electrons.

Considering the strength of the long-range Coulomb interaction, it is surprising that the simple models of Fermi gas – or better Fermi liquid – already are very successful in describing some basic properties of simple metals. The band structure model is particularly successful to describe semiconductors. But all three models have in common that the electron is described with a single particle wave function and electronic correlations are only taken into account indirectly, to describe phenomena like magnetism due to the exchange interaction between the electrons or BCS superconductivity [15], where an interaction between electrons is mediated through lattice vibrations and leads to Cooper pairs, which undergo a Bose-Einstein condensation.

What we have sketched so far is the textbook knowledge of introductory solid state physics courses. Of course there exist more advanced theoretical descriptions, which try to take into account the electronic correlations. The strong Coulomb interaction between the electrons is taken into account in density functional theory in the so-called "LDA+U" approximation or in so-called dynamical mean field theory DMFT or a combination of the two in various degrees of sophistication [16]. Still, all these extremely powerful and complex theories often fail to predict even the simplest physical properties, such as whether a material is a conductor or an insulator.

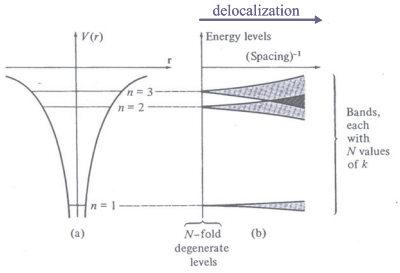

Fig. 12.2: Left*: Atomic potential of an electron interacting with the atomic core and the corresponding level scheme of sharp energy levels.* Right*: Broadening of these levels into bands upon increase of the overlap of the wave functions of neighboring atoms.*

Let us come back to the band structure of solids. In the so-called tight binding model one starts from isolated atoms, where the energy levels of the electrons in the Coulomb potential of the corresponding nucleus can be calculated. If such atoms are brought together, the wave functions of the electrons from different sites start to overlap, leading to a broadening of the atomic energy levels, which eventually will give rise to the electronic bands in solids. The closer

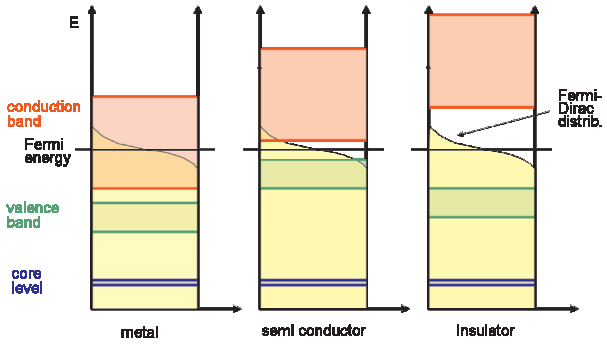

Fig. 12.3: *band structure of metals, semiconductors, and instulator.*

the atoms are brought together, the more the wave functions overlap, the more the electrons will be delocalized, and the broader are the corresponding bands (Fig. 12.2).

If electronic correlations are not too strong, the electronic properties can be described by a band structure, which allows one to predict whether a material is a metal, a semiconductor or an insulator. This is shown in Fig. 12.3. At $T = 0$ all electronic states are being filled up to the Fermi energy. At finite T the Fermi-Dirac distribution describes the occupancy of the energy levels. If the Fermi energy lies somewhere in the middle of the conduction band, the material will be metallic. If it lies in the middle between valence band and conduction band and these two are separated by a large/small gap (compared to the energy equivalent of room temperature) the material will show insulating/semiconducting behavior. However, as mentioned above this band structure model describes the electrons with single particle wave functions. Where are the electronic correlations?

12.3 Strong electronic correlations

Fig. 12.4: *Rock-salt structure of CoO.*

It turns out that electronic correlations are particularly important in materials, which have some very narrow bands. This occurs for example in transition metal oxides or transition metal chalcogenides as well as in some light rare earth intermetallics (heavy fermion systems). Consider CoO as a typical and simple example of a transition metal oxide. CoO has the rock-salt

structure shown in Fig. 12.4, with a face-centered cubic (fcc) unit cell containing four formula units. The primitive unit cell of the fcc lattice, however, is spanned by the basis vectors

$$\mathbf{a}' = \frac{1}{2}a(\mathbf{e}_x + \mathbf{e}_y); \quad \mathbf{b}' = \frac{1}{2}a(\mathbf{e}_y + \mathbf{e}_z); \quad \mathbf{c}' = \frac{1}{2}a(\mathbf{e}_z + \mathbf{e}_x). \tag{12.1}$$

Here, a is the lattice constant, and $\mathbf{e}_x$, $\mathbf{e}_y$, and $\mathbf{e}_y$, are the unit basis vectors of the original fcc unit cell. Therefore the primitive unit cell contains exactly one cobalt and one oxygen atom. The electronic configurations of these atoms are: Co: [Ar]$3d^7 4s^2$; O: [He]$2s^2 2p^4$. In the solid, the atomic cores of Co and O have the electronic configuration of Ar and He, respectively. These electrons are very strongly bound to the nucleus and we need not consider them on the usual energy scales for excitations in the solid state. We are left with nine outer electrons for the Co and six outer electrons for the O atom in the solid, so that the total number of electrons per primitive unit cell is $9 + 6 = 15$, i.e. an uneven number. According to the Pauli principle, each electronic state can be occupied by two electrons, one with spin up and one with spin down. Therefore with an uneven number of electrons, we must have at least one partially filled band and according to Fig. 12.1, CoO must be a metal.

What does experiment tell us? Well, in fact, CoO is a very good insulator with a room-temperature resistivity $\rho(300\,\mathrm{K}) \sim 10^8\,\Omega\mathrm{cm}$ (For comparison, the good conductor iron has $\rho(300\,\mathrm{K}) \sim 10^{-7}\,\Omega\mathrm{cm}$. The resistivity of CoO corresponds to activation energies of about $0.6\,\mathrm{eV}$ or a temperature equivalent of $7000\,\mathrm{K}$, which means there is a huge band gap making CoO a very good insulator. To summarize these considerations: the band theory breaks down already for a very simple oxide consisting of only one transition metal and one oxygen atom!

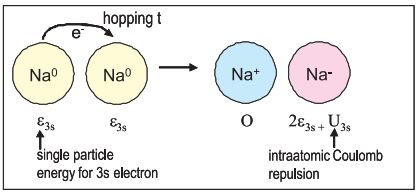

Fig. 12.5: *Illustration of (electron) hopping between two neutral Na atoms - involving charge fluctuations.*

In order to understand the reason for this dramatic breakdown of band theory, let us consider an even simpler example: the alkali metal sodium (Na) with the electronic configuration [Ne]$3s^1$=$1s^2 2s^2 2p^6 3s^1$. Following our argumentation for CoO, sodium obviously has a half-filled 3s band and is therefore a metal. This time our prediction was correct: $\rho(300\,\mathrm{K}) \sim 5 \times 10^{-6}\,\Omega\mathrm{cm}$. However, what happens if we pull the atoms further apart and increase the lattice constant continuously? Band theory predicts that for all distances sodium remains a metal, since the 3s band will always be half-filled. This contradicts our intuition and of course also the experiment: at a certain critical separation of the sodium atoms, there must be a transition from a metal to an insulator. This metal-to-insulator transition was predicted by Sir Nevill Mott (physics Nobel price 1977), which is therefore called the Mott-transition [17]. The physical principle is illustrated in Fig. 12.5: On the left, two neutral Na atoms are depicted. The atomic energy levels of the outer electrons correspond to an energy ε_{3s}. The wave functions of the 3s electrons will overlap giving rise to a finite probability that an electron can hop from one sodium atom to the other one. Such a delocalization of the electrons is favored according to the

Heisenberg uncertainty principle

$$\Delta p \cdot \Delta x \geq \frac{\hbar}{2}. \tag{12.2}$$

Eq. (12.2) shows that we can gain kinetic energy if the electrons become more delocalized. Fig. 12.5 on the right shows the situation after the electron transfer. Instead of neutral atoms, we have one Na^+ and one Na^- ion. However, we have to pay a price for the double occupation of the 3s states on the Na^- ion, namely the intra-atomic Coulomb repulsion between the two electrons denoted as U_{3s}. While this is a very simplistic picture, where we assume that the electron is either located on one or the other Na atom, this model describes the two main energy terms by just two parameters: the hopping matrix element t, connected to the kinetic energy, and the intra-atomic Coulomb repulsion U, connected with the potential energy due to the Coulomb interaction between the two electrons on one site. In this simple model, we have replaced the long range Coulomb potential proportional to $1/r$ with its leading term, an on-site Coulomb repulsion U. More realistic models would have to take higher order terms into account but already such a simple consideration leads to very rich physics. We can see from Fig. 12.5 that electronic conductivity is connected with charge fluctuations and that such charge transfer costs energy, where U is typically in the order of 1 or $10\,\mathrm{eV}$. Only if the gain in kinetic energy due to the hopping t is larger than the penalty in potential energy U can we expect metallic behavior. If the sodium atoms are now being separated more and more, the intra-atomic Coulomb repulsion U will maintain its value while the hopping matrix element t, which depends on the overlap of the wave functions, will diminish. At a certain critical value of the lattice parameter a, potential energy will win over kinetic energy and conductivity will be suppressed. This is the physical principle behind the Mott transition.

More formally, this model can be cast into a model Hamiltonian, the so-called Hubbard model [18]. In second quantization of quantum-field theory, the so-called single band Hubbard Hamiltonian is

$$\hat{\mathcal{H}} = -t \sum_{j,l,\sigma} (\hat{c}^\dagger_{j\sigma} \hat{c}_{l\sigma} + \hat{c}^\dagger_{l\sigma} \hat{c}_{j\sigma}) + U \sum_j \hat{n}_{j\uparrow} \hat{n}_{j\downarrow}. \tag{12.3}$$

The operator $\hat{c}^\dagger_{j\sigma}$ creates an electron in the tight binding (Wannier)-state $\Phi(\mathbf{r} - \mathbf{R}_j)|\sigma\rangle$ and $\hat{n}_{j\sigma} = \hat{c}^\dagger_{j\sigma} \hat{c}_{j\sigma}$ is the occupation operator of the tight-binding state. U is the Coulomb repulsion in one orbital at one site,

$$U = \int \frac{e^2 \left|\Phi(\mathbf{r}_1 - \mathbf{R}_j)\right|^2 \left|\Phi(\mathbf{r}_2 - \mathbf{R}_j)\right|^2}{4\pi\varepsilon_0 \left|\mathbf{r}_1 - \mathbf{r}_2\right|} \, d\mathbf{r}_1 d\mathbf{r}_2, \tag{12.4}$$

and t is the hopping amplitude depending on the overlap of the wavefunctions from nearest-neighbor atoms at $\mathbf{R}_1$ and $\mathbf{R}_2$:

$$t = \int \Phi(\mathbf{r} - \mathbf{R}_1) \frac{e^2}{4\pi\varepsilon_0 \left|\mathbf{r} - \mathbf{R}_2\right|} \Phi(\mathbf{r} - \mathbf{R}_2) \, d\mathbf{r}. \tag{12.5}$$

The Hubbard model is a so-called *lattice fermion model*, since only discrete lattice sites are being considered. It is the simplest way to incorporate correlations due to the Coulomb interaction since it takes into account only the strongest contribution, the on-site Coulomb interaction. Still there is very rich physics contained in this simple Hamiltonian like the physics of ferromagnetic- or antiferromagnetic metals and insulators, charge- and spin density waves and so on [18]. A

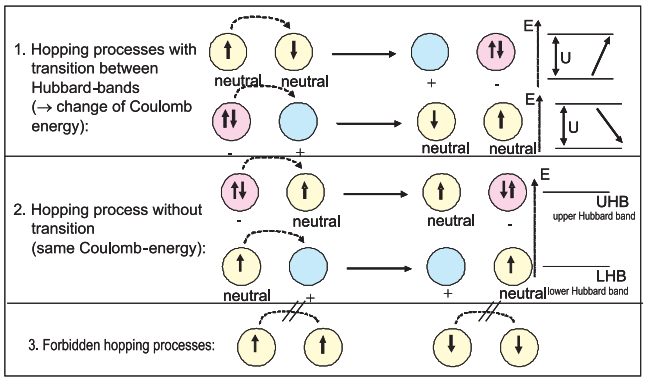

Fig. 12.6: *Illustration of hopping processes between neighboring atoms together with their corresponding energy scales.*

realistic Hamiltonian should contain many more inter-site terms due to the long-range Coulomb interaction likely to contain additional new physics.

The most direct consequence of the on-site Coulomb interaction is that additional so-called Hubbard bands are created due to possible hopping processes, illustrated in Fig. 12.6: The first row shows hopping processes involving a change of the total Coulomb energy. The second row shows hopping processes without energy change. The last row shows hopping processes forbidden due to the Pauli principle. From Fig. 12.6 we can identify two different energy states. Configurations for which the on-site Coulomb repulsion comes into play have an energy which is higher by the on-site Coulomb repulsion U as compared to such configurations where the electrons are not on the same atom. In a solid these two energy levels will broaden into bands (due to the delocalization of the electrons on many atoms driven by the hopping matrix element t), which are called the lower Hubbard band and the upper Hubbard band. If these bands are well separated, i.e. the Coulomb repulsion U dominates over the hopping term t, we will have in insulating state (only the lower Hubbard band is occupied). If the bands overlap, we will have a metallic state. Note that lower and upper Hubbard band are totally different from the usual band structure of solids as they do not arise due to the interaction of the electrons with the atomic cores but due to electronic correlations. As a result the existence of the Hubbard bands depends on the electronic occupation: the energy terms for simple hopping processes depend on the occupation of neighboring sites. The apparently simple single electron operator gets complex many body aspects.

12.4 Complex ordering phenomena: perovskite manganites as example

In what follows we will discuss ordering processes of electronic degrees of freedom in correlated electron systems, taking as an example perovskite manganites (see e.g. [19]). Their stoichiometric formula is $A_{1-x}B_x\mathrm{MnO}_3$, where A is a trivalent cation (e.g. $A =$ La, Gd, Tb, Er, Y, Bi) and B is a divalent cation ($B =$ Sr, Ca, Ba, Pb). The doping with divalent cations

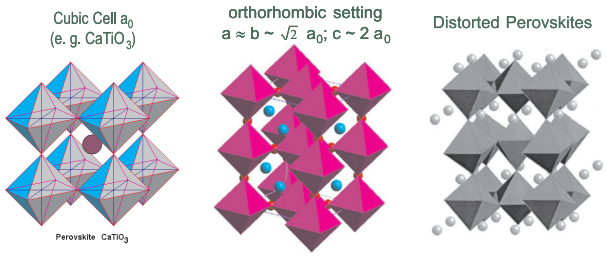

Fig. 12.7: *Perovskite structures. Left: Ideal (cubic) structure. Middle: cubic structure in orhorhombic setting. Right: distorted structure with rotated and tilted oxygen octahedra.*

leads to a mixed valence on the manganese sites. In a purely ionic model (neglecting covalency) charge neutrality requires that manganese exists in two valence states: Mn^{3+} (electronic configuration [Ar]$3d^4$) and Mn^{4+} ([Ar]$3d^3$) according to the respective doping levels: $A_{1-x}B_xMnO_3 \rightarrow \left[A^{3+}_{1-x}B^{3+}_x\right]\left[Mn^{3+}_{1-x}Mn^{4+}_x\right]O^{2-}_3$.

The structure of these mixed valence manganites is related to the perovskite structure (Fig. 12.7). Perovskite $CaTiO_3$ is a mineral, which has a cubic crystal structure, where the smaller Ca^{2+} metal cation is surrounded by six oxygen atoms forming an octahedron; these corner sharing octahedra are centered on the corners of a simple cubic unit cell and the larger Ti^{4+} metal cation is filling the interstice in the center of the cube. This ideal cubic perovskite structure is extremely rare. It only occurs when the sizes of the metal ions match to fill the spaces between the oxygen atoms ideally. Usually there is a misfit of the mean ionic radii of the A and B ions, which leads to sizeable tilts of the oxygen octahedra. The resulting structure is related to the perovskite structure as illustrated in Fig. 12.7: in the middle the cubic perovskite structure is shown in a different, orthorhombic setting. The usually observed (e.g. for $LaMnO_3$) perovskite structure is related to this structure by a tilting of the corner shared oxygen octahedra as shown on the right.

For the manganites the octahedral surrounding of the Mn ions leads to so-called crystal field effects. To explain these we stay in the ionic model and describe the oxygen atoms as O^{2-} ions. The outer electrons of the Mn ions, the 3d electrons, experience the electric field created by the surrounding O^{2-} ions of the octahedral environment. This leads to a splitting of the electronic levels by the crystal field as depicted in Fig. 12.8: The 3d orbitals with lobes of the electron density pointing towards the negatively charged oxygen ions ($3z^2 - r^2$ and $x^2 - y^2$; so-called e_g orbitals) will have higher energies with respect to the orbitals with the lobes pointing in-between the oxygen atoms (zx, yz, and xy; so-called t_{2g} orbitals). For the manganites this crystal-field splitting is typically $\sim 2\,\mathrm{eV}$. If we now consider a Mn^{3+} ion, how the electrons will occupy these crystal field levels depends on the ratio between the crystal-field splitting and the intra-atomic exchange: According to Hunds' rule, electrons tend to maximize the total spin, i.e. occupy energy levels in such a way that the spins of all electrons are parallel as far as Pauli principle permits. This is a consequence of the Coulomb interaction within a single atom and is expressed by the Hunds' rule energy J_H. If the crystal field splitting is much larger than Hunds' coupling, a *low-spin state* results, where all electrons are in the lower t_{2g} level and two of these t_{2g} orbitals are singly occupied and one is doubly occupied. Due to the Pauli principle the spins in the doubly occupied orbital have to be antiparallel, giving rise to a total spin $S = 1$ for this low spin state. Usually, however, in the manganites Hunds' rule coupling amounts to

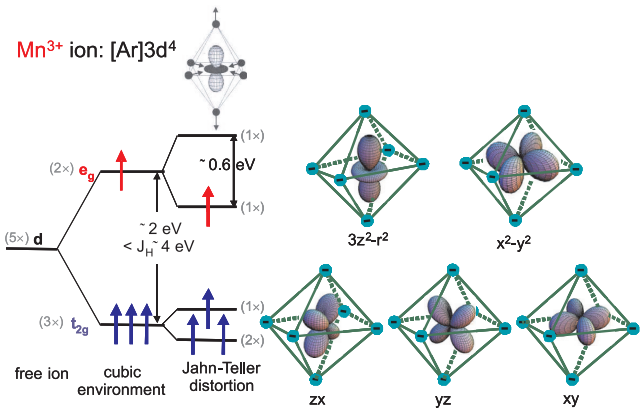

Fig. 12.8: *Energy level diagram for a MnO^{3+} ion in an oxygen octahedron. For the free ion, the four 3d electron levels are degenerate. They split in a cubic environment into t_{2g} and e_g levels. If Hunds' rule coupling is stronger than crystal field splitting, a high spin state results. The degeneracy of the e_g level is lifted by a Jahn-Teller distortion resulting in an elongation of the oxygen octahedra. On the right of the figure, the a basis set of 5* real *3d orbitals are depicted.*

$\sim 4\,\mathrm{eV}$, stronger than the crystal field splitting. In this case the *high spin state* shown in Fig. 12.8 is realized, where four electrons with parallel spin occupy the three t_{2g} orbitals plus one of the two e_g orbitals. The high spin state has a total spin of $S = 2$ and the orbital angular momentum is quenched, i.e. $L = 0$. This state has an orbital degree of freedom: the e_g electron can either occupy the $3z^2 - r^2$ or the $x^2 - y^2$ orbital. The overall energy can (and thus will) be lowered by a geometrical distortion of the oxygen octahedra that shifts the e_g levels, lifting their degeneracy This so-called *Jahn-Teller effect* (Fig. 12.8) further splits the d-electron levels. For the case shown, the c-axis of the octahedron has been elongated, thus lowering the energy of the $3z^2 - r^2$ orbital with respect to the energy level of the $x^2 - y^2$ orbital. The Jahn-Teller splitting in the manganites has a magnitude of typically $\sim 0.6\,\mathrm{eV}$.

The Jahn-Teller effect demonstrates nicely how in these transition metal oxides electronic and lattice degrees of freedom are coupled. Only the Mn^{3+} with a single electron in the e_g orbitals exhibits the Jahn-Teller effect, whereas the Mn^{4+} ion does not. A transfer of charge between neighboring manganese ions is accompanied with a change of the local distortion of the oxygen octahedron: a so-called lattice polaron. Due to the Jahn-Teller effect, charge fluctuations and lattice distortions become coupled in these mixed-valence oxides.

Having explained the Jahn-Teller effect, we can now introduce an important type of electronic order occurring in these materials: *orbital order*. Consider the structure of $LaMnO_3$: All manganese are trivalent and are expected to undergo a Jahn-Teller distortion. In order to minimize the elastic energy of the lattice, the Jahn-Teller distortions on neighboring sites are correlated. Below a certain temperature $T_{\mathrm{JT}} \sim 780\,\mathrm{K}$, a cooperative Jahn-Teller transition takes place, with a distinct pattern of distortions of the oxygen octahedra throughout the crystal lattice as shown in Fig. 12.9 left. This corresponds to a long-range orbital order of the e_g electrons, not to be confused with magnetic order of an orbital magnetic moment. In fact, the orbital magnetic moment is quenched, i.e. totally suppressed, by the crystal field surrounding the Mn^{3+} ions (this is always the case for non-degenerate states with real wave functions because such functions

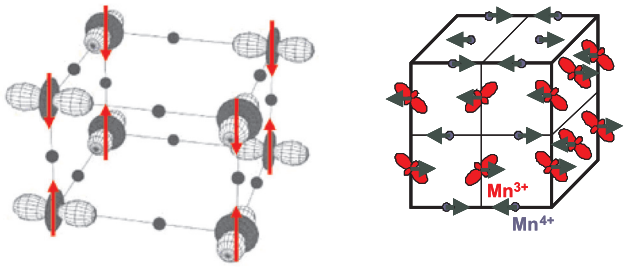

Fig. 12.9: Left*: Orbital order in $LaMnO_3$. Below the Jahn-Teller transition temperature of* $780\,\mathrm{K}$*, a distinct long range ordered pattern of Jahn-Teller distortions of the oxygen octahedra occurs leading to orbital order of the e_g orbitals of the Mn^{3+} ions as shown. Also shown is the antiferromagnetic spin order which sets in below the Néel temperature $T_\mathrm{N} \sim 145\,\mathrm{K}$. Oxygen atoms are represented by filled circles, La is not shown.* Right*: Charge-, orbital- and spin-order in half-doped manganite.*

have pure-imaginary expectation values for an angular momentum operator). Orbital ordering instead denotes a long-range ordering of an anisotropic charge distribution around the nuclei. As the temperature is further lowered, magnetic order sets in at $T_\mathrm{N} \sim 145\,\mathrm{K}$. In $LaMnO_3$ the spin degree of freedom of the Mn^{3+} ion orders antiferromagnetically in so-called A-type order: spins within the a-b plane are parallel, while spins along c are coupled antiferromagnetically. This d-type orbital ordering and A-type antiferromagnetic ordering results from a complex interplay between structural-, orbital- and spin degrees of freedom and the relative strengths of the different coupling mechanisms in $LaMnO_3$.

Doped manganites are even more complex, because the charge on the Mn site becomes an additional degree of freedom due to the two possible manganese valances Mn^{3+} and Mn^{4+}. In order to minimizes the Coulomb interaction between neighboring manganese sites, so-called charge order can develop. This is shown for the example of half-doped manganites in Fig. 12.9 on the right: These half-doped manganites show antiferromagnetic spin order, a checkerboard-type charge order with alternating Mn^{3+} and Mn^{4+} sites and a zig-zag orbital order of the additional e_g electron present on the Mn^{3+} sites. This is only one example of the complex ordering phenomena that can occur in doped mixed valence manganites. These ordering phenomena result from a subtle interplay between lattice-, charge-, orbital-, and spin degrees of freedom and can have as a consequence novel phenomena and functionalities such as colossal magnetoresistance.

How are these ordering phenomena related with the macroscopic properties of the system? To answer this question, let us look at the resistivity of doped Lanthanum-Strontium-Manganites (Fig. 12.10): The zero field resistance changes dramatically with composition. The $x = 0$ compound shows insulating behavior: the resistivity ρ increases with decreasing temperature T. The higher doped compounds, e.g. $x = 0.4$, are metallic with $\rho(T)$ decreasing. Note, however, that the resistivity of these compounds is still about three orders of magnitude higher than for typical good metals. At an intermediate composition $x = 0.15$, the samples are insulators at higher T down to about $250\,\mathrm{K}$, then a dramatic drop of the resistivity indicating an insulator-to-metal transition and again an upturn below about $210\,\mathrm{K}$ with typical insulating behavior. The metal-insulator transition occurs at the temperature where ferromagnetic long-range order sets in. Around this temperature we also observe a very strong dependence of resistivity on

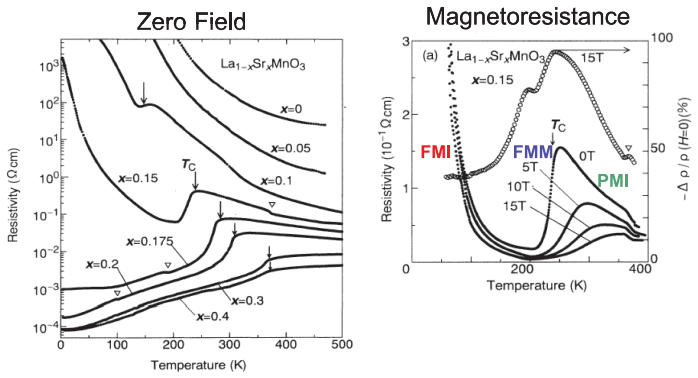

Fig. 12.10: *Resistivity in the $La_{1-x}Sr_xMnO_3$ series [20].* Left*: resistivity in zero field for various compositions from $x = 0$ to $x = 0.5$.* Right*: resistivity for $x = 0.15$ in different magnetic fields H, and magnetoresistance, defined as the change in resistivity relative to its value for $H = 0$.*

external magnetic field. This is the so-called *colossal magnetoresistance* effect. In order to appreciate the large shift in the maximum of the resistivity curve with field (Fig. 12.10 right) one should remember that the energy scales connected with the Zeeman interaction of the spin $\frac{1}{2}$ electron in an applied magnetic field are very small: the energy equivalent of 1 Tesla for a spin $\frac{1}{2}$ system corresponds to $0.12\,\mathrm{meV}$, which in turn corresponds to a temperature equivalent of $1.3\,\mathrm{K}$. The strong dependence of the resistance on an external field is partly due to the so-called *double exchange* mechanism: the electron hopping from Mn^{3+} to Mn^{4+} (associated with metallicity) can occur only if the t_{2g} spins are parallel, which is automatically fulfilled (only) in the ferromagnetic state.

It is clear that our entire discussion starting from ionic states is only a crude approximation to the real system. Therefore we now have to pose the question how can we determine the true valence state? Or more general, which experimental methods exist to study the complex ordering and excitations of the charge-, orbital-, spin- and lattice- degrees of freedom in these complex transition metal oxides?

12.5 Probing correlated electrons by scattering methods

How can these various ordering phenomena be studied experimentally? Obviously we need probes with atomic resolution, which interact with the spins as well as with the charges in the system. Therefore neutron and x-ray scattering are the ideal microscopic probes to study the complex ordering phenomena and their excitation spectra. The lattice and spin structure can be studied with neutron diffraction from a polycrystalline or single crystalline sample as detailed in chapter 8 of this course, “Structural analysis”. Fig. 12.11 shows as an example a powder spectrum of a $La_{7/8}Sr_{1/8}MnO_3$ material.

Neutrons also allow one to determine the magnetic structure from a powder diffraction pattern. As a result of such a refinement, one can show that the low temperature structure of

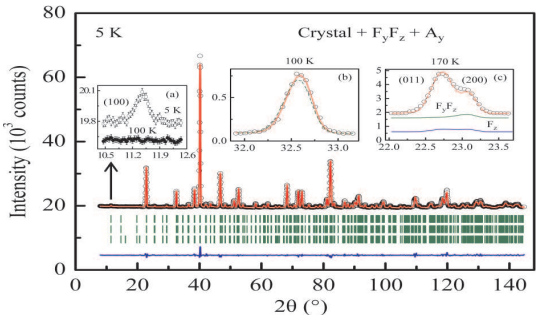

Fig. 12.11: *High resolution neutron powder diffractogram of a powdered single crystal of* $La_{\frac{7}{8}}Sr_{\frac{1}{8}}MnO_3$. ○*: data points, line: structural refinement. Structural and magnetic Bragg reflections are located at the 2 values indicated by the vertical lines below the spectrum. The solid line underneath shows the difference between the observed and simulated spectra. Insets show details in certain regions e.g. a magnetic Bragg reflection at very low* q.

this compound is monoclinic or even triclinic (for solving the metric of the cell, complementary synchrotron x-ray diffraction data is often useful because of the higher achievable q-resolution), i.e. there exists an additional distortion from the Pnma structure introduced in Sec. 12.4. Ferromagnetic order becomes visible by intensity on top of the structural Bragg peak. Antiferromagnetic order is usually (but not always!) connected with an increase in the unit cell dimension, which in turn shows up in the diffractogram by additional superstructure reflections between the main nuclear reflections. It is beyond the scope of this lecture to discuss the experimental and methodological details of such a structure analysis or to present detailed results on specific model compounds. For this we refer to the literature, e.g. [19]. We just want to mention that with detailed structural information, we cannot only determine the lattice- and spin structure, but also the charge- and orbital order and can relate them to macroscopic phenomena such as the CMR effect. At first sight it might be surprising that neutron diffraction is able to give us information about charge order. We have learnt in the introductory chapters that neutrons interact mainly through the strong interaction with the nuclei and through the magnetic dipole interaction with the magnetic induction in the sample. So how can neutrons give information about charge order? Obviously charge order is not determined directly with neutrons. However in a transition metal-oxygen bond, the bond length will depend on the charge of the transition metal ion. The higher the positive charge of the transition metal, the shorter will be the bond to the neighbor-ing oxygen, just due to Coulomb attraction. This qualitative argument can be quantified in the so-called bond-valence sum. There is an empirical correlation between the chemical bond length and the bond valence:

$$s_{ij} = e^{\frac{R_0 - R_{ij}}{B}}. \tag{12.6}$$

Here, the R_{ij} are the experimentally determined bond lengths, $B = 0.37$ is a constant, and R_0 are tabulated values for the cation-oxygen bonds, see, e.g., [21]. Table 12.1 reproduces some of these values. Finally the valence or oxidation state of the cation can be determined by the sum of the bond valences around the respective atom i according to

$$V_i = \sum_{ij} s_{ij}. \tag{12.7}$$

Ions	La^{3+}	Pr^{3+}	Nd^{3+}	Sm^{3+}	Eu^{3+}	Gd^{3+}	Tb^{3+}	Dy^{3+}	Er^{3+}
R_0	2.172	2.138	2.105	2.090	2.074	2.058	2.032	2.001	1.988
Ions	Tm^{3+}	Yb^{3+}	Y^{3+}	Ca^{2+}	Sr^{2+}	Ba^{2+}	Mn^{3+}	Mn^{4+}	
R_0	1.978	1.965	2.019	1.967	2.118	2.285	1.760	1.753	

Table 12.1: *R_0 values of cation-oxygen bonds [21] in manganese perovskites needed for the bond valence calculation (12.6).*

Even though this method to determine the valence state is purely empirical, it is rather precise compared to other techniques. The values of the valences found with this method differ significantly from a purely ionic model. Instead of integer differences between charges on different transition metal ions, one finds more likely differences of a few tenth of a charge of an electron, though rare exceptions, where near-integer valence differences were observed, exist [22].

Just like charge order, orbital order is not directly accessible to neutron diffraction since orbital order represents an anisotropic charge distribution and neutrons do not directly interact with the charge of the electron. However, we have seen in the discussion of the Jahn-Teller effect (Figs. 12.8 and 12.9) that an orbital order is linked to a distortion of the local environment visible in different bond lengths within the anion complex surrounding the cation. Thus, by a precise determination of the structural parameters from diffraction, one can determine in favorable cases the ordering patterns of all four degrees of freedom: lattice, spin, charge and orbitals.

Is there a more direct way to determine charge- and orbital order? The scattering cross section of x-rays contains the atomic form factors, which are Fourier transforms of the charge density around an atom. Therefore, one might think that charge and orbital order can be easily determined with x-ray scattering. However, as discussed in the last paragraph, usually only a fraction of an elementary charge contributes to charge- or orbital ordering. Consider the Mn atom: the atomic core has the Ar electron configuration, i.e. 18 electrons are in closed shells with spherical charge distributions. For the Mn^{4+} ion, three further electrons are in t_{2g} levels. Since in scattering, we measure intensities, not amplitudes, these 21 electrons contribute $21^2 r_0^2$ to the scattered intensity (the classical electron radius r_0 is the natural unit of x-ray scattering). If the difference in charge between neighboring Mn ions is $0.2\,e$, this will give an additional contribution to the scattered intensity of $0.2^2 r_0^2$. The relative effect of charge ordering in x-ray scattering is therefore only a tiny $\frac{0.2^2}{21^2} \sim 10^{-4}$, even ignoring that scattering from all other atoms makes the situation worse. There is, however, a way to enhance the scattering from non-spherical charge distributions, the so-called anisotropic anomalous x-ray scattering, first applied for orbital order in manganites by Murakami *et al.* [23]. The principle of this technique is depicted in Fig. 12.12, showing scattering from a hypothetical diatomic 2D compound. Non resonant x-ray scattering is sensitive mainly to the spherical charge distribution. A reconstruction of the charge distribution done from such an experiment might look schematically as shown on the left. The corresponding crystal structure can be described with a primitive unit cell (white lines). To enhance the scattering from the non-spherical part of the charge distribution, an experiment can be done at a synchrotron source, with the energy of the x-rays tuned to the energy of an absorption edge (middle). Now, second order perturbation processes can occur, where a photon induces virtual transitions of an electron from a core level to empty states above the

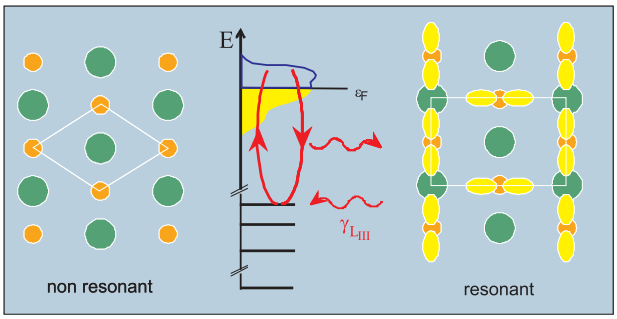

Fig. 12.12: *Anisotropic anomalous x-ray scattering for a hypothetical diatomic 2D compound.* Left*: Reconstruction of the charge distribution from a laboratory x-ray source, sensitive mainly to the spherical charge distribution and corresponding unit cell (white lines).* Middle*: Principles of resonance x-ray scattering in an energy level diagram (see text).* Right*: Charge distribution deduced from such an anomalous x-ray scattering experiment. An orbital ordering pattern is apparent, which could not be detected with non-resonant x-ray scattering. The evidently larger unit cell gives rise to superstructure reflections (at resonance).*

Fermi energy and back with re-emission of a photon of the same energy. As second-order perturbation processes have a resonant denominator, this scattering will be strongly enhanced near an absorption edge. If the intermediate states in this resonant scattering process are somehow connected to orbital ordering, scattering from orbital ordering will be enhanced. Thus in the resonant scattering experiment, orbital order can become visible as indicated on the right. With the shown arrangement of orbitals, the true primitive unit cell of this hypothetical compound is obviously larger than the unit cell that was deduced from the non resonant scattering experiment (left), which was not sensitive enough to determine the fine details of the structure. An increase of the unit cell dimensions in real space is connected with a decrease of the distance of the reciprocal lattice points, leading to additional *superstructure reflections*. The intensity of these reflections has the strong energy dependence expected for a second-order perturbation process. This type of experiment is called anisotropic anomalous x-ray scattering, because it is sensitive to the anisotropic charge distribution around an atom.

So far we have discussed some powerful experimental techniques to determine the various ordering phenomena in complex transition metal oxides. Scattering can give much more information than just on the time averaged structure. Quasi-elastic diffuse scattering gives us information on fluctuations and short range correlations persisiting above the transitions, e.g. short range correlations of polarons, magnetic correlations in the paramagnetic state, local dynamic Jahn-Teller distortions etc. Studying these correlations and fluctuations helps to understand what drives the respective phase transitions into long-range order. The relevant interactions, which give rise to these ordering phenomena, can be determined from inelastic scattering experiments as learnt in the chapter on “Inelastic neutron scattering”. For example, in a new class of iron-based high-temperature superconductors, the involvement in Cooper pairing of lattice vibrations or alternatively magnetic fluctuations is controversial, and both of these can be probed in-depth by inelastic neutron scattering (see, e.g., [24]). Since there is a huge amount of scattering experiments on highly correlated transition metal oxides and chalcogenides, a review of these experiments definitely goes far beyond the scope of this introductory lecture.

12.6 Summary

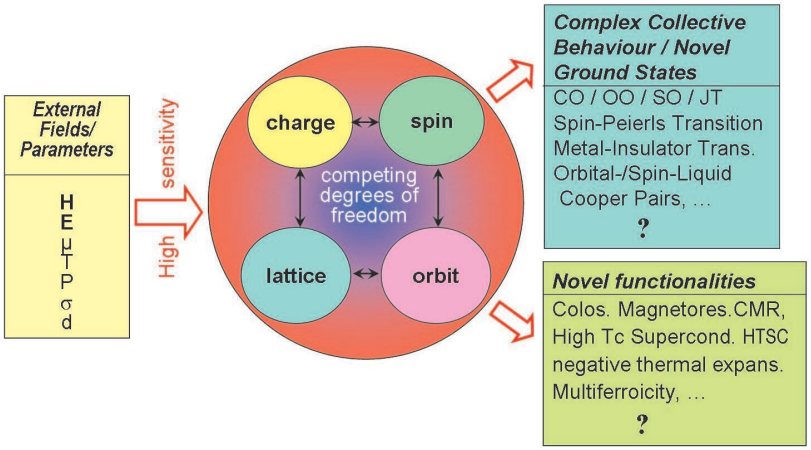

Fig. 12.13: *Illustration of complexity in correlated electron systems.* **H, E***: magnetic and electric field, respectively;* μ*: chemical potential (doping);* T*: temperature;* P*: pressure;* σ*: strain (epitaxial growth);* d*: dimensionality (e.g. bulk versus thin film systems); CO: charge order; OO: orbital order; SO: spin order; JT: Jahn-Teller transition.*

This chapter gave a first introduction into the exciting physics of highly correlated electron systems, exemplified by transition metal oxides and chalcogenides. The main message is summarized in Fig. 12.13. The complexity in these correlated electron systems arises from the competing degrees of freedom: charge, lattice, orbit and spin. The ground state is a result of a detailed balance between these different degrees of freedom. This balance can be easily disturbed by external fields or other thermodynamical parameters, giving rise to new ground states or complex collective behavior. Examples are the various ordering phenomena discussed, Cooper pairing in superconductors, so-called spin-Peierls transitions in 1D systems etc. This high sensitivity to external parameters as well as the novel ground states of the systems gives rise to novel functionalities, such as the colossal magnetoresistance effect, high temperature superconductivity, multiferroicity, and many more. A theoretical description of these complex systems starting from first principles, like Schrödinger equation in quantum mechanics or the maximization of entropy in statistical physics, is bound to fail due to the large number of strongly interacting particles. Entirely new approaches have to be found to describe the emergent behavior of these complex systems. Therefore highly correlated electron systems are a truly outstanding challenge in modern condensed matter physics. We have shown in this lecture that neutron and x-ray scattering are indispensable tools to disentangle this complexity experimentally. They are able to determine the various ordering phenomena as well as the fluctuations and excitations corresponding to the relevant degrees of freedom. No other experimental probe can give so much detailed information on a microscopic level as scattering experiments.

Acknowledgement

This lecture bases largely on material from previous lectures given by Th. Brückel.

References

[1] R. B. Laughlin and D. Pines, *Proc. Natl. Acad. Sci. USA* **97**, 28 (2000).

[2] T. Vicsek, *Nature* **418**, 131 (2002).

[3] J. G. Bednorz and K. A. Müller, *Z. Phys. B* **64**, 189 (1986).

[4] A.-M. Haghiri-Gosnet and J.-P., *J. Phys. D: Appl. Phys.* **36**, R127 (2003).

[5] G. Binasch, P. Grünberg, F. Saurenbach, and W. Zinn *Phys. Rev. B* **39**, 4828 (1989).

[6] M. N. Baibich *et al.*, *Phys. Rev. Lett.* **61**, 2472 (1988).

[7] M. H. Phan and S. C. Yu, *J. Magn. Magn. Mater.* **308**, 325 (2007).

[8] E. J. W. Verwey, *Nature* **144**, 327 (1939).

[9] M. Fiebig, *J. Phys. D.: Appl. Phys.* **38**, R123 (2005).

[10] M. Bibes and A. Barthélémy, *Nat.* **7**, 425 (2008).

[11] G. D. Barrera *et al.*, *J. Phys.: Condens. Mat.* **17**, R217 (2005).

[12] E. Dagotto, *Science* **309**, 257 (2005).

[13] N. W. Ashcroft and N. D. Mermin, *Solid State Physics* (Thomson Brooks/Cole, New York, 1976).

[14] H. Ibach and H. Lüth, *Solid State Physics: An introduction to principles of materials science* (Springer, Berlin, 2010).

[15] J. Bardeeen, L. N. Cooper, and J. R. Schrieffer, *Nobel Prize in Physics in 1972 for a microscopic theory of superconductivity (nowadays called BCS-theory.)*

[16] K. Held *et al.*, *J. Phys.: Condens. Mat.* **20**, 064202 (2008).

[17] N. F. Mott, *Rev. Mod. Phys.* **40**, 677 (1968).

[18] P. Fazekas, *Lecture notes on electron correlation and magnetism* (World Scientific, Singapore, 2003).

[19] T. Chatterji (Ed.), *Colossal magnetoresistive manganites* (Kluwer Academic Publishers, Dordrecht, 2004).

[20] A. Urushibara *et al.*, *Phys. Rev. B* **51**, 14103 (1995).

[21] G. H. Rao, K. Bärner, and I. D. Brown, *J. Phys.: Condens. Mat.* **309**, 257 (2005).

[22] M. Angst *et al.*, *Phys. Rev. Lett.* **99**, 086403 (2007).

[23] Y. Murakami *et al.*, *Phys. Rev. Lett.* **81**, 582 (1998).

[24] R. Mittal *et al.*, *Phys. Rev. Lett.* **102**, 217001 (2009).

Exercises

E12.1 Magnetic order in $EuFe_2As_2$

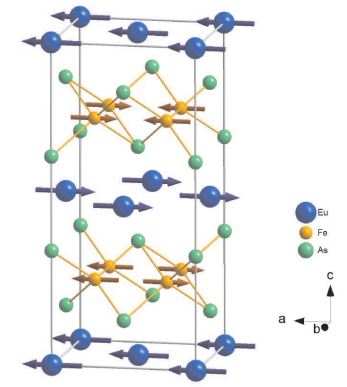

The figure shows the low-temperature crystal and magnetic structure of $EuFe_2As_2$, one of the parent compounds of the new iron based superconductors.

The crystal structure in the magnetically ordered phase is orthorhombic (space group $Fmmm$), with Eu at (000) and Fe at $(\frac{1}{4}\frac{1}{4}\frac{1}{4})$.

a) $\star$ Calculate the magnetic structure factor $\mathbf{F}_{hk\ell}$ (as a function of reciprocal lattice coordinates) for the Eu sublattice. *(Hint: bring all terms that are equal for all atoms of the lattice before the sum. See also chapters 7 and 8).*

b) $\star\star$ As a), but for the Fe sublattice.

c) $\star$ Make a plot of reciprocal spaces in the a^*-c^*-plane indicating the positions, where you expect nuclear and magnetic Bragg peaks to occur – separately for the Fe and Eu sublattices. What are the magnetic propagation vectors for the two sublattices?

d) $\star$ At low temperatures a spin-flop transition from the above antiferromagnetic to a ferromagnetic arrangement can be induced for the Eu sublattice (the Fe sublattice is unaffected) by applying an external magnetic field of $\sim 1\,\mathrm{T}$. Sketch the resulting reflection pattern in the a^*-c^*-plane for magnetic fields applied i) along the c-axis and ii) along the a-axis. Which reflections would you choose to follow this spin-flop transition?

E12.2 Crystal field

Fe has atomic number 26 and in oxides typically has oxidation states $2+$ or $3+$.

a) $\star$ Determine the electronic configuration of free Fe^{2+} and Fe^{3+} ions (hint: the outermost s-electrons are lost first upon ionization).

b) $\star$ From Hund's rules determine the values of the spin S, orbital angular momentum L, and total angular momentum J of Fe^{2+} and Fe^{3+} ions.

(*Hund's rules:*

1. S *max.*
2. *L max consistent with 1.*
3. $J = |L - S|$ *for a less than half filled shell,*
   $J = |L + S|$ *for a more than half filled shell*).

c) $\star$ The effective moment μ_{eff} of a magnetic ion can be determined experimentally by the Curie-Weiss law, and is given by $\mu_{\text{eff}} = g_J\sqrt{J(J+1)}\mu_{\text{B}}$, where the Landé factor is

$$g_J = \frac{3}{2} + \frac{S(S+1) - L(L+1)}{2J(J+1)}\,. \tag{12.8}$$

Calculate the expected effective moment in units of μ_{B} of Fe^{2+} and Fe^{3+} ions, i) assuming S, L, and J as determined in b) and ii) setting $L = 0$ ('quenched orbital momentum'). Compare with the experimental values of $\sim 5.88\,\mu_{\text{B}}$ for Fe^{3+} and $\sim 5.25 - 5.53\,\mu_{\text{B}}$ for Fe^{2+}.

d) $\star\star$ The negatively charged oxygen ions surrounding the Fe ions in an oxide solid influence the energy of the different orbitals. Plot the expected energy level diagram for the case of an octahedral environment of nearest-neighbor O^{2-}. How does the total spin moment of Fe^{2+} change between weak and strong crystal field splittings (relative to intra-atomic "Hund's" exchange)?

e) $\star\star\star$ In a tetrahedral environment the energy levels of the orbitals are reversed compared to an octahedral environment. Determine the spin moment of Fe^{2+} in a tetrahedral environment with strong crystal field splitting. Is an orbital angular momentum possible in this case? How about when a Jahn-Teller-distortion leads to a further splitting of the energy levels?

13 Dynamics of Macromolecules

D. Richter
Jülich Centre for Neutron Science 1
Forschungszentrum Jülich GmbH

Contents

Lecture Notes of the JCNS Laboratory Course Neutron Scattering

13.1 Introduction

Polymeric materials are used because they are durable, cheaply to produce, easily to process and because they exhibit very favourable processing and mechanical properties. Polymers may behave like a viscous fluid or rubber elastic, very tough with high impact strength or even brittle. In the simplest case polymers are long linear chain molecules build from a repeating unit: the monomer. Such polymers are called linear homopolymers. Other than synthetic polymers, biopolymers are highly complex molecular structures with a sharp molecular weight and a uniquely defined sequence of building blocks. They are the molecular manifestations of life with a high variety of structure and specific function. Nevertheless, at least in their denaturated state they exhibit similarities with synthetic materials while in their folded state the specific function evolves. Also the general principles of selfassembly in structure formation are common to both species.

The diffusional motions of long flexible polymers constitute fascinating physics and at the same time represent one of the great challenges of modern material science. The drive towards the molecular understanding of the complex viscoelastic properties of polymer liquids is the focal point of rheology and connects the classical chemical engineering approach with modern physics [1]. There the tube model invented by Doi and Edwards [2] and de Gennes [3] has shown itself as the most successful molecular model describing the topological confinement imposed by the mutually interpenetrating polymer chains in the melt. In terms of this so called reptation model a theory of viscoelasticity has been developed that describes the main features of polymer melt rheology.

Large scale protein motions on the other hand are critical for proteins to coordinate precise biological function. Such dynamics are invoked in regulatory proteins, motor proteins, signalling proteins and structural proteins. Structural studies have documented the conformational flexibility in proteins accompanying their activity. Results from macroscopic studies such as biochemical kinetics and single molecule detection have also shown the importance of conformational dynamics and Brownian thermal fluctuations within the proteins or protein complexes. However, the time dependent dynamic processes that facilitate such protein motions remain poorly understood and experimentally nearly untouched [4].

Neutron spin echo spectroscopy is the highest resolution neutron technique and provides time resolution in the 100ns range, enabling thereby the access to molecular motion on a mesoscopic time scale between the atomic picosecond scales and the macroscopic times [5]. At that scale the molecular motions of the polymers take place that underlie their macroscopic viscoelastic behaviour. Similarly, the large scale motions of bio molecules occur on similar space time frames.

This lecture aims to identify general principles of chain motion on a molecular scale which underpin the macroscopic properties and presents concepts and experimental results on these motional mechanisms in space and time. We will mainly address the

dynamics of homopolymers and give one example for studies of the molecular dynamics of biopolymers.

13.2 Neutron scattering and the large scale motion of macomolecules

Neutron scattering with its space time sensitivity on a molecular and atomic scale unravels the space time occurrence of the molecular motions we are interested in. Commencing at the scale of the single bond, where movements take place at a pace as in normal liquids quasielastic neutronscattering (QENS) provides insight into local relaxation processes – they will be discussed in the lecture of A. Arbe. At larger length scales first the entropy driven Rouse motion and at even larger distances the effect of topological confinement due to the mutual interpenetrating chains come into the observation range. The most powerful technique suitable for these investigations, the neutron spin echo spectroscopy (NSE) operates in the time domain and uncovers a time range from about 2ps to 200ns and accesses a momentum transfer between about 0.01Å^{-1} and 3Å^{-1}.

Coherent, quasi- and inelastic neutronscattering reveals the dynamic structure factor ($S(Q,t)$) or its Fourier transformed counter part $S(Q,\omega)$.

$$S(Q,t) = \frac{1}{N}\sum_{ij}\left\langle \exp\left(-i\underline{Q}\underline{r}_j(t)\right)\exp\left(-i\underline{Q}\underline{r}_i(0)\right)\right\rangle \qquad (13.1)$$

Where $\underline{r}_j(t)$ and $\underline{r}_i(0)$ are the position vectors of the scatterers at time t and time $t = 0$ respectively. N is the number of scatteres, $\hbar Q = \hbar 4\pi/\lambda * \sin(\theta/2)$ is the momentum transfer during scattering (for elastic or nearly elastic scattering) with θ the scattering angle and λ the neutron wavelength. The brackets denote the thermal average. $S(Q,t)$ reflects the pair correlation function and relates to the collective properties of a material. In the neutron cross section it is weighted by the average scattering length $\left|\overline{b}\right|^2$.

Incoherent scattering is related to the scattering length disorder which may either result from spin dependent scattering lengths like in the case of hydrogen or from isotope mixtures of isotopes with different scattering properties. This disorder prevents constructive interference of partial waves scattered at different atoms and reveals the self correlation function . Eq.[1] provides the self correlation function if in the double sum only terms with $i = j$ are considered. In the cross section $S_{inc}(Q,t)$ is weighted by the average scattering length fluctuation $\left(\left\langle b^2\right\rangle - \left|\overline{b}^2\right|\right)$.

In Gaussian approximation which is commonly used for the calculation of neutron dynamic structure factors for polymer dynamics Eq.[1] is approximated by

$$S(Q,t) = \frac{1}{N}\sum_{ij}\exp\left[-\frac{Q^2}{6}\left\langle\left(\underline{r}_i(t)-\underline{r}_j(0)\right)^2\right\rangle\right] \tag{13.2}$$

13.3 Entropy driven dynamics

The dynamics of a generic linear Gaussian chain as described in the Rouse model [6] is the starting point for a standard description of the Brownian dynamics in polymer melts. The Rouse model may be considered as the standard model for polymer dynamics and in many cases serves as a starting part for the treatment of more complex problems. In the Rouse model the conformational entropy of a chain acts as a resource for restoring forces for a chain conformation deviating from thermal equilibrium. In this chapter we deal with this entropy driven dynamics in terms of the Rouse model and present neutron spin echo (NSE) results on the space time evolution of the Rouse relaxation. Because of its fundamental relevance for chain dynamics problems, we present its mathematical treatment in some detail, such that it may be followed in all steps. In the discussion of further models later on for details we refer to the relevant literature.

13.3.1 Gaussian chains

The conformation of a flexible linear polymer chain on scales somewhat larger than the main chain bond length ℓ_0 assumes a random walk. The conformations of such a chain are described by a set of segment vectors $\{\underline{r}(n)\} = (\underline{R}(n) - \underline{R}(n\text{-}1))$ where $\underline{R}(n)$ is the position vector of segment n. Following the central limit theorem the length distribution of a vector $\underline{r}$ connecting segments that have a topological distance of n steps is a Gaussian.

$$\phi(R,n) = \left(\frac{3}{2\pi n\ell^2}\right)^{3/2}\exp\left(-\frac{3R^2}{2n\ell^2}\right) \tag{13.3}$$

with ℓ the segment length. The Rouse model bases on a further idealization of the chain statistics assuming that the bond vector $\underline{\ell}$ of hypothetic connecting points along the chain also has a Gaussian distribution. With $\langle\ell^2\rangle = b^2$. For simplicity throughout the lecture we will take $b^2 = \ell_0^2 C_\infty$. Keeping, however, in mind that the building block of a Gaussian chain may well contain a larger number of main chain bonds. C_∞ is the characteristic ratio accounting for the local stiffness arising from the non-random bond angle distribution of the bonds of length ℓ_0. The conformational probability of a conformation $\{\underline{r}(n)\}$ follows as

$$P\left(\left\{\underline{r}(n)\right\}\right) = \left(\frac{3}{2\pi\ell^2}\right)^{\frac{3}{2}N} \exp\left[-\sum_{n=1}^{N}\frac{3\left(\underline{R}(n)-\underline{R}(n-1)\right)^2}{2\ell^2}\right] \tag{13.4}$$

with n counting the number of segments of the chain. The free energy of a Gaussian chain is entirely described by its conformational entropy

$$S = k_B \ell n\left[P\left(\left\{r(n)\right\}\right)\right] \tag{13.5}$$

The Gaussian chain model yields a spring constant for each Gaussian segment. $k = 3k_BT/\ell^2$ where k_B is the Boltzmann constant. From Eq.[4] the chain extension between arbitrary points along the chain becomes $|n - m|\,\ell^2$.

13.3.2 The Rouse model

The Rouse model starts from a Gaussian chain representing a coarse grained polymer model where springs stand for the entropic forces between hypothetic beats [6] (Fig.1).

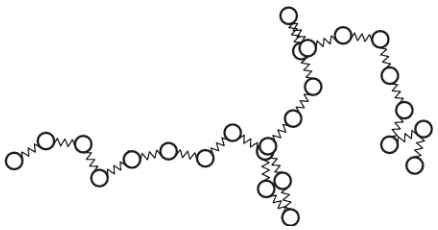

Fig. 1: Spring-bead model of a Gaussian chain as assumed in the Rouse model. The beads are connected by "entropic springs" and are subject to a frictional force $\zeta_0\upsilon$, where υ is the bead velocity and ζ_0 the bead friction coefficient

We are interested in the motion of segments on a length scale $\ell < r < R_E$ where $R_E^2 = N\ell^2$ is the end to end distance of the chain. The segments are subject to an entropic force resulting from the derivative of Eq.[5] (x components).

$$\frac{\partial}{\partial x(n)}\ S = \frac{k_BT}{\ell^2}\left[x(n+1) - 2x(n) + x(n-1)\right] \tag{13.6}$$

And to a stochastic force $f_x(n,t)$ which fulfils $\langle f_x(n,t)\rangle = 0$ and $\left\langle f_\alpha(n,t)\ \ f_\beta(m,0)\right\rangle = 2k_BT\,\zeta_0\ \delta_{nm}\ \delta_{\alpha\beta}\ \delta(t)$. ζ_0 denotes the friction coefficient and α,β the Cartesian components. Regarding the index n as a continuous variable the Langevin equation for segment motion assumes the form

$$\zeta_0\ \frac{\partial x}{\partial t} = \frac{3k_BT}{\ell^2}\ \frac{\partial x^2(n)}{\partial n^2} + f_x(n,t) \tag{13.7}$$

The boundary condition of force free ends requires $\frac{\partial\ x(n)}{\partial n}\ \Big|_{n=0,N} = 0$. The partial differential equations are solved by Cosine Fourier transformation to normal coordinates fulfilling the boundary conditions. In normal coordinates the Langevin Eq.[7] becomes

$$\zeta_p\ \frac{\partial}{\partial t}\ \tilde{x}(p,t) = -k_p\ \tilde{x}(p,t) + \tilde{f}(p,t) \tag{13.8}$$

with $k_p = \frac{2\pi^2 p^2}{N}k$, $\zeta_p = 2N\zeta_0$. For the stochastic force we have

$$\left\langle f_\alpha(p,t)\ f_\beta(q,0)\right\rangle = 2\zeta_p\ k_BT\,\delta_{pq}\ \delta_{\alpha\beta}\ \delta(t) \tag{13.9}$$

Eq.[8] is readily solved by a single exponential

$$\tilde{x}(p,t) = \frac{1}{\zeta_p}\ \int_{-\infty}^{t} dt'\exp\left((t-t')/\tau_p\right)\ \tilde{f}(p,t') \tag{13.10}$$

Where the mode relaxation time τ_p is given by

$$\tau_p = \frac{\zeta_p}{k_p} = \frac{\zeta_0 N^2\ \ell^2}{3\pi^2\ k_BT\ p^2} = \frac{\tau_R}{p^2} = \frac{N^2}{W\pi^2 p^2};\ W = \frac{3k_BT}{\ell^2\zeta_0} \tag{13.11}$$

τR is the Rouse time – the longest time in the relaxation spectrum – and W is the elementary Rouse rate. The correlation function of the normal coordinates is finally obtained to

$$\left\langle \tilde{x}(p,t)\ \tilde{x}(p,0)\right\rangle = \frac{N\ell^2}{6\pi^2 p^2}\ \exp\left(-\frac{t}{\tau_p}\right) \tag{13.12}$$

For the center of mass coordinate one finds

$$\left\langle \tilde{x}(0,t)\ \tilde{x}(0,0)\right\rangle = \frac{2k_BT}{N\zeta_0}t \tag{13.13}$$

Scattering experiments relate to mean square segment correlation functions which are obtained by back transformation of the normal coordinates

$$\begin{aligned} B(n,m,t) = 3\left\langle \left(x(n,t) - x_m(0)\right)^2 \right\rangle &= 6D_R t + |m-n|\,\ell^2 + \frac{4N\ell^2}{\pi^2} \\ \times \sum_{p=1}^{N} \frac{1}{p^2} \cos\left(\frac{p\pi m}{N}\right) \cos\left(\frac{p\pi n}{N}\right) &\left[1 - \exp\left(-\frac{tp^2}{\tau_R}\right)\right] \end{aligned} \tag{13.14}$$

In order to arrive at Eq.[14] we have used $D_R = \frac{3}{6t}\left\langle \left(x(0,t) - x(0,0)\right)^2 \right\rangle$; D_R: Rouse diffusion coefficient and $\sum_{p=1}^{\infty} \frac{1}{p^2}\left[\cos\left(\frac{p\pi m}{N}\right) - \cos\left(\frac{p\pi n}{N}\right)\right]^2 = \frac{\pi^2}{2N}|n-m|$. For the special case of the self correlation function ($n = m$) $B(n,n,t)$ reveals the mean square displacement of a polymer segment. For large p the $\cos^2$ in Eq.[14] is a rapidly oscillating function which may be replaced by the mean value ½. With this approximation we convert the sum into an integral and obtain

$$B(n,n,t) = \left\langle r^2(t)\right\rangle = 2\ell^2\left(\frac{3k_BT\,t}{\pi\,\zeta_0\ell^2}\right)^{1/2} + 6D_R t \tag{13.15}$$

Other than in normal diffusion in the segmental regime the mean square displacement does not grow linearly in time but with its square root. For the translational diffusion coefficient $D_R = \frac{k_BT}{N\ \zeta_0} = \frac{W\ell^4}{3N\ell^2} = \frac{W\ell^4}{3R_E^2}$ is obtained. D_R is inversely proportional to the number of friction performing segments.

The self correlation function relates directly to the mean square displacement of the diffusing segments. In Gaussian approximation, inserting Eq.[15] into Eq.[2], for $t < \tau_R$ we have

$$S_{self}(Q,t) = \exp\left[-Q^2 D_R t\right]\ \exp\left\{-\frac{2}{\sqrt{\pi}}\left(\frac{k_BT\ell^2}{12\zeta_0}Q^4 t\right)^{1/2}\right\} \tag{13.16}$$

For coherent scattering observing the pair correlation function interferences from waves emanating from various segments complicate the scattering function

$$S_{chain}(Q,t) = \frac{1}{N}\exp\ \left[-Q^2 D_R t\right]\ \sum_{n\neq m}\exp\ \left\{-\frac{1}{6}|n-m|\ \ Q^2\ell^2\right\}\ * \tag{13.17}$$

$$\exp\left\{-\frac{2}{3}\frac{R_E^2 Q^2}{\pi^2}\ \sum_p \frac{1}{p^2}\ \left\{\cos\left(\frac{p\pi m}{N}\right)\ \cos\left(\frac{p\pi n}{N}\right)\ \left(1-\exp\ \left(-\frac{tp^2}{\tau_R}\right)\right)\right\}\right\}$$

For small $Q(QR_E < 1)$ the second and third terms are negligible and $S_{chain}(Q,t)$ describes the center of mass diffusion of the chain

$$S_{self}(Q,t) = S_{chain}(Q,t) = \exp\left(-D_R Q^2 t\right) \tag{13.18}$$

For $Q R_E > 1$ and $t < \tau_R$ the internal relaxations dominate. For $t = 0$ we have $S_{chain}(Q,t) = S_{chain}(Q)$ i.e. the structure factor corresponds to a snapshot of the chain structure

$$S_{chain}(Q) = \frac{1}{N}\sum_{n,m}\exp\left(-\frac{1}{6}Q^2\left|n-m\right|\ell^2\right) \tag{13.19}$$

Replacing the summation by integrals and observing the relation $R_g^2 = \frac{1}{6}N\ell^2$ for the radius of gyration Eq.[19] immediately leads to the well known Debye function.

$$\begin{aligned} S_{chain}(Q) &= N f_{Debye}\left(Q^2 R_g^2\right) \\ f_{Debye}(x) &= \frac{2}{x^2}\left(e^{-x} - 1 + x\right) \end{aligned} \tag{13.20}$$

The shape of the Debye function corresponds to the upper most curve in Figure 2.

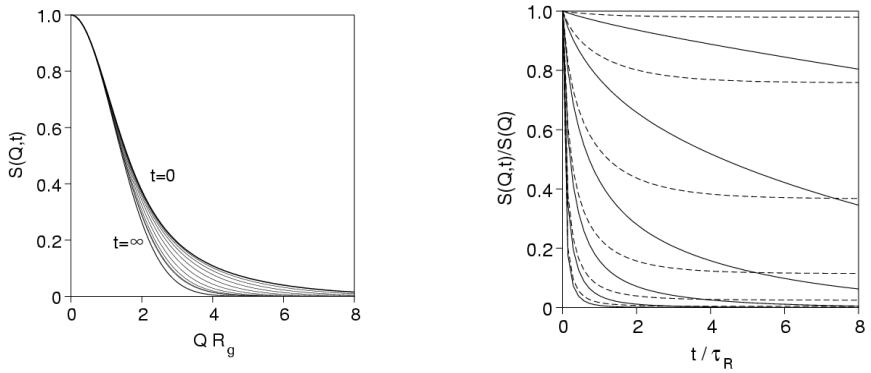

Fig. 2: *Development of S_{chain} (Q,t) for different times (left) and the normalized relaxation function $S_{chain}(Q,t)/S(Q)$ (right) for QR_g = 1, 2, ... 6. The dashed lines contain only the intra-chain relaxation, whereas the solid lines include the center-of-mass diffusion. Note that for short chains, respectively for small Q the translational diffusion dominates the observed dynamics.*

Important scaling properties are revealed by an approximate computation of the high$Q$ behaviour of $S_{chain}(Q,t)$ (Eq.[17]). Replacing sums by integrals and performing some simplifications we get

$$S_{chain}(Q,t) = \frac{12}{Q^2\ell^2}\int_0^\infty du \exp\left\{-u-\left(\Omega_R t\right)^{1/2}\ h\left(u\left(\Omega_R t\right)^{-1/2}\right)\right\}$$
$$h(y) = \frac{2}{\pi}\int_0^\infty dx\ \frac{\cos(xy)}{x^2}\left(1-\exp\left(-x^2\right)\right) \tag{13.21}$$

Note that this equation only depends on one variable: the Rouse variable.

$$\left(\Omega_R t\right)^{1/2} = \frac{Q^2}{6}\sqrt{\frac{3k_B T\,\ell^2 t}{\zeta_0}} = \frac{Q^2\ell^2}{6}\sqrt{Wt} \tag{13.22}$$

The Rouse model does not contain an explicit length scale. Therefore for different momentum transfers the dynamic structure factors are predicted to collapse to a single master curve if they are represented as a function of the Rouse variable.

Further note, that for $t = 0$ Eq.[21] does not resemble the Debye function but yields its high Q limiting behaviour $\approx Q^{-2}$. The approximation is only valid for $QR_g \gg 1$. In that regime the form of Ω_R immediately reveals that the intrachain relaxation increases $\approx Q^4$ in contrast to normal diffusion $\approx Q^2$. Finally, Figure 2 illustrates the time development of the structure factor.

13.3.3 Neutron spin echo results

Recently it became possible to observe directly the incoherent cross section from a protonated chain, thereby measuring the self correlation function. Figure 3 displays the time dependent mean square displacement obtained from a high molecular weight ($M_w = 80000$) monodisperse polyethylene-propylene (PEP) melt at 492K [7]. In Gaussian approximation for negligible translational diffusion Eq.[16] yields

$$\left\langle r^2(t)\right\rangle = -\frac{6}{Q^2}\ell n\ S_{self}(Q,t) \tag{13.23}$$

As may be seen from Figure 3 the mean square displacement (MSD) follows with high accuracy the predicted square root law in time. Since neutron quasielastic scattering resolves dynamic processes in space and time, these measurements give direct information about the segment displacement at a given time. E.g. at 10ns the MSD amounts to 620Å^2 i.e. the average proton has travelled about 25Å during this time interval.

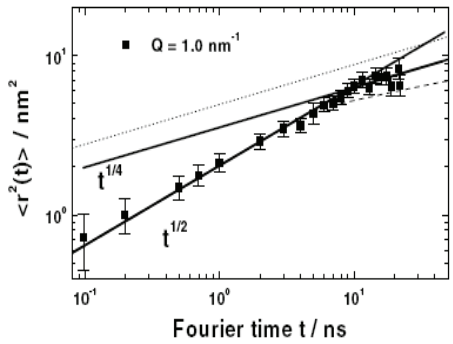

Fig. 3: *Fig. 3: Time dependent mean square displacement of a PEP segment in the melt at 492K. The solid line indicates the prediction of the Rouse model. The slowing down at longer times is an indication of a cross over to local reptation (see ref [7]).*

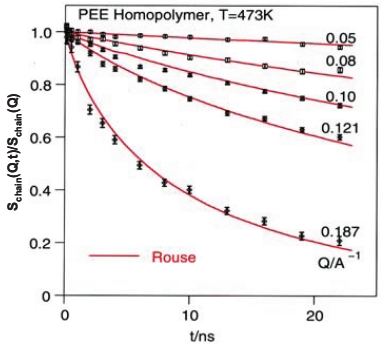

Fig. 4: *Single chain structure factor from a PEE melt at 473K. The numbers along the curves represent the experimental Q-values in [Å^{-1}]. The solid lines are a joint fit with the Rouse model (Eq.[21]).*

The pair correlation function arising from the segment motion within one given chain is observed if some protonated chains are dissolved in a deuterated matrix. Figure 4 displays the observed spectra for polyethylethylene (90% dPEE, 10% hPEE) with the molecular weight of $M_w^h = 21.5 kg/mol$; $M_w^d = 24.5 kg/mol$ and a narrow molecular weight distribution [8]. The solid lines give the predictions of the dynamic structure factor of Eq.[17]. Obviously very good agreement is achieved.

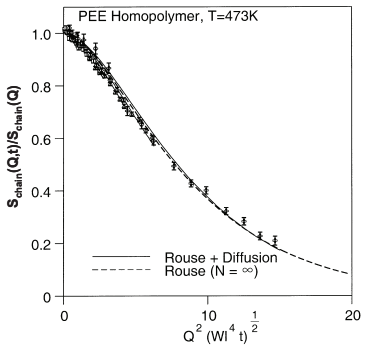

Fig. 5: *Single chain structure factor from PEE melts as a function of the Rouse scaling variable. The dashed line displays the Rouse prediction for infinite chains, the solid lines incorporate the effect of translational diffusion. The different symbols relate to the spectra displayed in Figure 4.*

We now use these data in order to investigate the scaling prediction inherent in Eq.[21]. Figure 5 presents a plot of the data of Figure 4 now as a function of the Rouse scaling variable (Eq.[22]). With satisfactory precision the data follow the scaling prediction. The small deviations are related to the translational diffusion of the chains. This becomes evident from Figure 6 where the obtained relaxation rates $\Omega_R(Q)$ are plotted vs. Q in a double logarithmic fashion. The dashed line gives the Rouse prediction $\Omega_R \approx W\ell^4 Q^4$. While at larger momentum transfer the experimental results follow very well this prediction, towards lower Q a systematic relative increase of the relaxation rate is observed. Including translational diffusion we have

$$\Omega_R(Q) = Q^2\left[D_R + Q^2\frac{W\ell^4}{6}\right] = Q^2 W\ell^2\left[\frac{\ell^2}{3R_E^2} + \frac{Q^2\ell^2}{6}\right] \tag{13.24}$$

The solid lines in Figure 6 represent the predictions of Eq.[24] - perfect agreement is obtained. The above expressions provide a universal description of the dynamics of a Gaussian chain and are valid for real linear polymer chains on intermediate length scales. The specific properties of a polymer enter only in terms of two parameters: $N\ell^2 = R_E^2$ and ℓ^2/ζ_0. The friction parameter is governing the Rouse variable (Eq.[22]). As eluded to in Eq.[24] also the center of mass diffusion coefficient may be expressed in these terms. Since the Rouse model does not contain an inherent length scale the parameter N (chain length) and ℓ^2 (segment length squared) are somewhat arbitrary as long as the physical values ℓ^2/ζ_0 and R_E^2 are constant. The NSE experiments measure directly the friction coefficient/length^2.

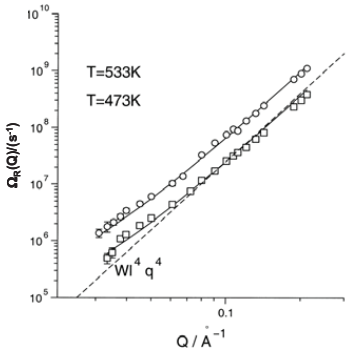

Fig. 6: *Relaxation rates from PEE melts vs. Q for two different temperatures. The dashed line represents the $\Omega_R \sim Q^4$ prediction of the Rouse model. The solid lines include the contribution from translational diffusion (Eq.[24]).*

13.4 Topological confinement: Reptation

The dynamic modulus of a polymer melt is characterized by a plateau in frequency which broadens with increasing chain length. In this plateau regime the polymer melt acts like a rubber where the elastic properties are derived from the entropy elasticity of the chains between permanent cross links. The modulus of a rubber is inversely proportional to the mesh size and proportional to the temperature. In analogy, it is suggestive to assume that the entanglement or topological interactions between the chains in a melt lead to the formation of a temporary network which displays rubber elastic properties. Other than in a rubber for long times the chains may disentangle and the melt flows. This flow process is characterized by a melt viscosity $\eta \approx N^{3.2\ldots3.6}$ and the translational chain diffusion coefficient $D \approx N^{-2\ldots2.3}$ [9]. Using the analogy to the modulus of a rubber we may estimate the distances between entanglement points from the value of the plateau modulus G_N^0. For different polymers they come out to be between 30Å and 100Å. On the basis of such assumptions a number of theories of viscoelasticity have been developed [2,9,10]. The most famous among them is the reptation model by de Gennes [3] and Doi and Edwards [2]. In this model the dominating chain motion is a reptile like creep along the chain profile. The lateral restrictions by the interpenetrating other chains are modelled by a tube with a diameter d parallel to the chain profile. d relates to the plateau modulus of the melt

$$d^2 = \frac{4}{5} \frac{R_E^2}{M} \frac{k_B T}{G_N^0} \tag{13.25}$$

The restrictions of the motion by the presence of the other chains are not effective on a monomer scale but rather permit lateral freedom on intermediate length scales. The experimental observations for viscosity and diffusion can be made directly comprehensible in this simple model.

The viscosity relates to the longest relaxation time in a system. If we consider Rouse diffusion along the tube with a Rouse diffusion coefficient $D_R \approx 1/(N\zeta_0)$ then an initial tube configuration is completely forgotten when the mean square displacement along the tube $\langle r^2(t)\rangle_{\text{tube}}$ = (contour length L)^2. Thus, for the longest relaxation time we obtain

$$\tau_\eta \approx \frac{L^2}{D_R} \approx N^3\zeta_0 \tag{13.26}$$

The diffusion coefficient is found by considering that during this time in real space the MSD just amounts to the end to end distance of the chain squared. Thus, we obtain

$$D_{rep} = \frac{R_E^2}{\tau_\eta} \approx \frac{N}{N^3\zeta_0} \approx \frac{1}{N^2\zeta_0} \tag{13.27}$$

13.3.1 Mean square displacements

We now consider the predictions of the reptation model for the mean square displacements of the chain segments. For short times when the chain segments have not yet realized the topological constraints ($r^2 < d^2$) we expect unrestricted Rouse motion $\langle r^2(t)\rangle \approx t^{1/2}$ (Eq.[15]). Experimentally this was the case for PEP (Figure 4) where for an entangled chain for times up to 20ns and displacements up to 30Å Rouse dynamics was observed. At a time τe, $\tau_e = d^4/(\pi^2 W\ell^4)$ the mean square displacement reaches the order of the tube diameter. τ_e is derived as the Rouse time for polymer strand spanning the tube. Then motional restrictions are expected.

For times $t > \tau_e$ one dimensional curve linear Rouse motion along the tube needs to be considered. Displacements along the tube are described by Eq.[15] where we have to change real space coordinates to coordinates $s(t)$ along the tube. If a segment is displaced along the tube by $\langle(s_n(t) - s_n(0))^2\rangle$ then the mean square displacement in 3-d real space is $d\left\langle\left(s_n(t) - s_n(0)\right)^2\right\rangle^{1/2}$. With that we obtain

$$\left\langle r^2(t)\right\rangle = \begin{cases} 2d\left(\dfrac{k_B T\ell^2 t}{\zeta_0\pi}\right)^{1/4} & \tau_e < t < \tau_R \\ \\ 2d\left(\dfrac{k_B T t}{N\zeta_0}\right)^{1/2} & \tau_R < t < \tau_d \end{cases} \tag{13.28}$$

In Figure 7 the two situations correspond to the second and the third process. The second process where the chain performs Rouse motion along the tube is called local reptation while the creep like diffusion along the tube which eventually leads to a

complete tube renewal is also termed pure reptation. The terminal time τ_d after which the chain has left its original tube determines to a large extend the viscosity of the melt ($\tau_d \approx \tau_\eta$ see Eq.[26]). Beyond that time reptation diffusion prevails.

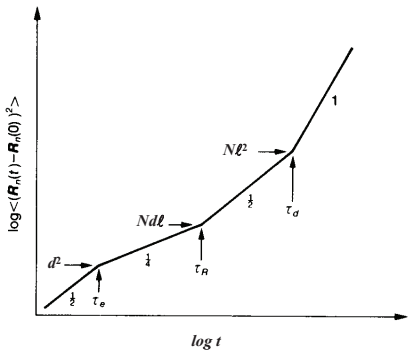

Fig. 7: *Mean-square displacement of a chain segment in the reptation model.*

13.3.2 Self correlation function

In Gaussian approximation the self correlation function of a reptating chain directly relates to the MSD's of chapter 4.1. This supposes that the widths of the Gaussian function after a diffusion time t of the single segment distribution along the 1-dimensional tube contour may be taken for the time dependent displacement. Projecting this on the Gaussian contorted tube then would again correspond to a Gaussian sublinear diffusion in real space.

However, as Fatkullin and Kimmich have shown [11], the real process has to be modelled by projecting the segment probability distribution due to the linear Rouse motion with the curve linear coordinate s on the random walk like contour path of the contorted tube. This leads to a non-Gaussian probability distribution of the segment at times $t > \tau_e$,

$$S_{self}\left(Q, t > \tau_e\right) = \exp\left[\frac{Q^4 d^2}{72}\,\frac{\left\langle r^2(t)\right\rangle}{3}\right] erfc\left[\frac{Q^2 d}{6\sqrt{2}}\sqrt{\frac{\left\langle r^2(t)\right\rangle}{3}}\right] \qquad (13.29)$$

invalidating the Gaussian approximation for times longer than τ_e. We note that Eq.[29] is strictly valid only for $t \gg \tau_e$ when $\langle r^2(t)\rangle \gg d^2$. The effect on the scattering function is that if (wrongly) interpreted in terms of the Gaussian approximation the cross over to local reptation appears to occur a significantly lower values of τ_e. A generic asymptotic $t^{1/4}$ law remains untouched.

In the sense of Eq.[30] the MSD of a chain segment may be directly observed by incoherent quasielastic scattering. In the local reptation regime we expect to observe the predicted cross over of the MSD from a $t^{1/2}$ to a $t^{1/4}$ law (Eq.[28]). Experiments were performed on PE and PEP samples at temperatures where also the dynamic structure factors were studied [7]. Figure 8 displays these data in terms of an effective mean square displacement (Eq.[23]), thereby assuming implicitly the Gaussian approximation.

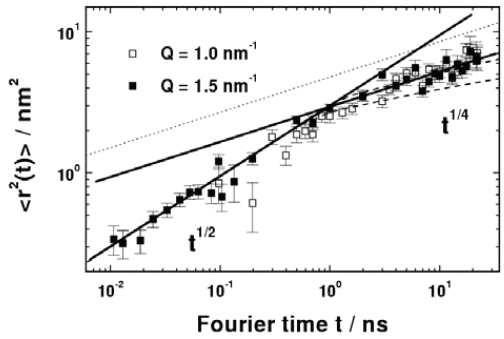

Fig. 8: *NSE data obtained from the incoherent scattering of a fully protonated PE-melt in a representation of -6ℓn[$S_{self}(Q,t)$]/Q^2 which is the mean-square displacement* $\left\langle r^2(t)\right\rangle$ *as long as the Gaussian approximation holds. Solid lines describe the asymptotic power laws* $\left\langle r^2(t)\right\rangle \propto t^{1/2}, t^{1/4}$. *Dotted lines: prediction form the Gaussian approximation, dashed lines: see text.*

Inserting the Rouse rate for PE at 509K, $W\ell^4 = 7 \pm 0.7\text{nm}^4/\text{ns}$ obtained from single chain dynamic structure factor measurements into Eq.[16] the solid line $\approx t^{1/2}$ is obtained. It quantitatively corrobates the correctness of the Rouse descriptions at short times. The data also reveal clearly a transition to a $t^{1/4}$ law, though Eq.[28] would predict the dotted line. The discrepancy explains itself in considering the non-Gaussian character of the curve linear Rouse motion (Eq.[29]). Fixing also the value of the tube diameter to that obtained from single structure factor measurements (see later), the dashed line in Figure 8 presents the prediction of the non-Gaussian treatment. For $Q = 0.1\text{Å}^{-1}$ the unrestricted Rouse regime ($t < \tau_e$) as well as the local reptation regime is perfectly reproduced.

13.3.3 Single chain dynamic structure factor

Now we turn to the single chain dynamic structure factor $S_{chain}(Q,t)$ which is also strongly effected by the topological tube constraints. Qualitatively, we would expect the following behaviour:

(i) At short times $t < \tau_e$ the chain will perform unrestricted Rouse motion and the dynamic structure factor of Eq.[17] and [21] should well describe the dynamics.

This e.g. has been exemplified in earlier measurements of the Rouse dynamic structure factor of entangled PDMS melts - in these materials d is large [14].

(ii) In the regime of local reptation the chain has already explored the tube laterally and further density fluctuations of the labelled chain will only be possible via Rouse relaxation along the tube. Under such circumstances the structure factor to a first approximation will mirror the formfactor of the tube $S_{chain}(Q,\tau_R > t > \tau_e)/S_{chain}(Q) \approx \exp\left(-Q^2d^2/36\right)$. In this regime the experiment should reveal the size of the topological constraints without applying any detailed model.

(iii) In the creep regime $t > \tau_R$ the memory of the tube confinement will be gradually lost and the dynamic structure factor should reveal the fraction of the still confined polymer segments.

(iv) Finally, in the diffusive regime at very small Q ($QR_g \ll 1$) an equivalent to Eq.[18] will be valid where now the reptation diffusion coefficient will be measured. de Gennes [12] and Doi and Edwards [9] have formulated tractable analytic expressions for the dynamic structure factor. Thereby, they neglected the initial Rouse regime i.e. the derived expression is valid only for $t > \tau_e$ once confinement effects become important. The dynamic structure factor is composed from two contributions S^{loc} and S^{esc} reflecting local reptation and escape processes from the tube.

$$\frac{S_{chain}(Q,t)}{S_{chain}(Q)} = \left[1-\exp\left(-\frac{Q^2d^2}{36}\right)\right] S^{loc} + \exp\left(-\frac{Q^2d^2}{36}\right) S^{esc} \tag{13.30}$$

The local reptation part was calculated as

$$S^{loc}(Q,t) = \exp\left(\frac{t}{\tau_0}\right) erfc\left(\sqrt{\frac{t}{\tau_0}}\right) \tag{13.31}$$

Where $\tau_0 = 36/\left(W\ell^4Q^4\right)$ a more general expression for $S^{esc}(Q,t)$ due to pure reptation was given by Doi and Edwards [9]. For short times $S^{chain}(Q,t)$ decays mainly due to local reptation (first term) while for longer times (and low Q) the second term resulting from the creep motion is important. The ratio of the two relevant time scales τ_0 and τ_d is proportional to N^3. Therefore, for long chains at intermediate times a pronounced plateau in $S_{chain}(Q,t)$ is predicted. Such a plateau is a generic signature for confined motion. Beside the reptation model also other models for the description of entanglements have been brought forward.

1. In generalized Rouse models the effect of topological hindrance is described by a memory function. In the boarderline case of long chains the dynamic structure factor can be explicitly calculated in the time domain of the NSE experiment [13].

2. Rubber like models take entanglements as local stress points acting as temporary cross links. de Cloiseaux [14] has proposed such a model where he considered infinite chains with spatially fixed entangled points at intermediate times.
3. Recently in a mode coupling approach a microscopic theory describing the polymer motion in entangled melts has been brought forward. While this theory describes well the different time regimes for a segmental motion, unfortunately as the consequence of the necessary approximations, the dynamic structure factor could not yet been derived [15].

Figure 9 compares the dynamic structure factors from 2 PE melts both studied at 509K for two different molecular weights (9a: M_w = 2kg/mol; 9b: M_w = 12.4kg/mol). The solid lines in Figure 9a display a fit with a Rouse dynamic structure factor according to Eq.[17]. Very good agreement is achieved. Figure 9b presents equivalent results from the higher M_w melt with the solid lights again showing the prediction of the Rouse model.

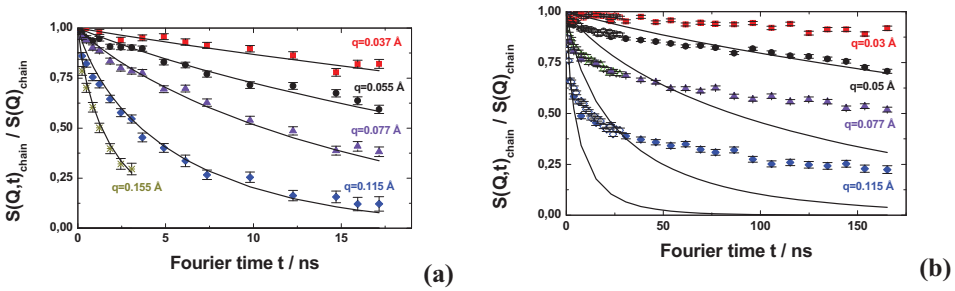

Fig. 9: *Dynamic structure factors from PE-melts at 509K (a) M_w = 2000; (b) M_w = 12400. The solid lines display the predictions of the Rouse model.*

Please note, that the time scale for the 12.4kg/mol sample is extended by one order of magnitude compared to the short chain case. While for the short chain melt the Rouse model describes well the experimental observations, for the longer chains the model fails completely. Only in the short time regime the initial decay of the dynamic structure factor is depicted, while for longer times the relaxation behaviour is strongly retarded signifying the confinement effects.

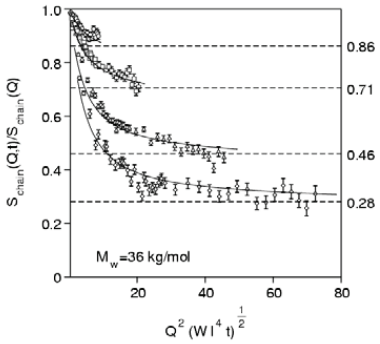

Fig. 10: *Scaling presentation of the dynamic structure factor from a M_w = 36000 PE-melt at 509K as a function of the Rouse scaling variable. The solid lines are a fit with the reptation model (Eq.[30]). The Q-values are from above Q = 0.05, 0.077, 0.115, 0.145Å^{-1}. The horizontal dashed lines display the prediction of the Debye-Waller factor estimate for the confinement size (see text).*

Figure 10 displays the dynamic structure factor from a M_w = 36kg/mol PE-melt as a function of the Rouse variable $Q^2\ell^2\sqrt{Wt}$ (Eq.[22]). Other than in Figure 5, where the scaled data followed a common master curve, here they split into different branches which only at small values of the scaling variable are coming close together. This splitting is a consequence of the existing dynamic length scale invalidating the Rouse scaling properties. We note that this length is of purely dynamical character and cannot be observed in static equilibrium experiments.

In the spirit of Eq.[31] and neglecting the ongoing decay of $S_{chain}(Q,t)$ due to local reptation from the heights of the achieved plateaus we may obtain a first estimate for the amount of confinement. Identifying the plateau levels with a Debye Waller factor description of the confinement, we get d = 46Å, a value which is a lower estimate for the two tube diameter since S^{loc} is not fully relaxed. The horizontal lines in Figure 11 are the predictions from this Debye-Waller factor estimate.

In Figure 11 the same data are presented linearly as a function of time. The figure compares the data with the predictions of the various models. It is evident that these data clearly favour the reptation model. We note that the fits with the reptation model were done with only one free parameter, the entanglement distance d. The Rouse rate $W\ell^4$ was determined earlier through NSE data taken for $t < \tau_e$. With this one free parameter quantitative agreement over the whole range of Q and t using the reptation model with $d = 46 \pm 1.0$Å was found.

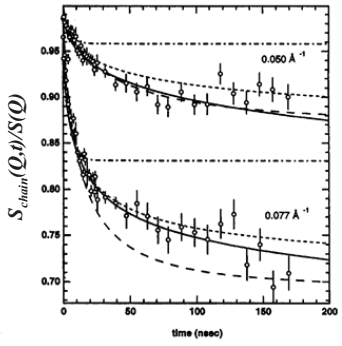

Fig. 11: *Plot of $S_{chain}(Q,t)$ vs. t at Q = 0.050 and 0.077Å^{-1} with a comparison between the predictions of reptation (solid lines) [16], local reptation (dotted lines) [16], the model of des Cloiseaux [14] (dashed lines) and the Ronca model [13] (dot-dashed lines).*

13.5 Large scale dynamics in biopolymers

While the study of the dynamics of synthetic polymers has reached some maturity, the next challenge will be the investigation of the large scale motion of biopolymers. The goal there will be to find out to what extend these dynamics play a role in bio function. On local scales some insight into the conformational dynamics has been gained e.g. by time dependent crystallography [17]. On the other hand, the large scale dynamics such as protein domain motions remain basically untouched experimentally, because of the lack of techniques to study these large scale correlated motions. In this lecture we present a first study on such dynamics on the example of alcohol dehydrogenase (ADH) . The alcohol dehydrogenases are enzymes that are important for many organisms allowing the interconversion between alcohols and ketones. In humans ADH is present as a dimer and catalyzes the oxidation of ethanol allowing thereby the consumption of alcohol in beverages. In yeast on the hand it is at the basis of the fermentation process converting acetaldehyde into ethanol. In the process the cofactor Nicotinamide Adenine Dinucleotide (NAD) is needed assisting the oxidation reaction at the zinc catalytic side.

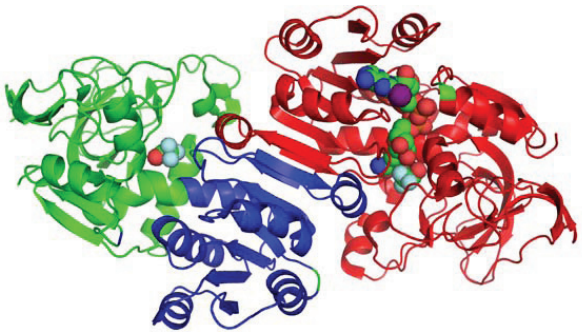

Fig. 12: *Dimer of alcohol dehydrogenase. The molecule presented by spherical caps is the NAD cofactor used in the chemical reaction.*

Figure 13 displays a schematic structure of the dimer based on crystallographic data. The two monomeric units are clearly visible. Each monomer is build from two domains, the catalytic and the binding domain with a small opening in between. For functionary this small cleft between the two domains needs to open in order to allow the cofactor NAD and the ethanol to read the catalytic Mg-atoms at the bottom of the cleft. ADH from yeast forms a tetrameric structure. The crystallographic data suggest a crossed arrangement of the two dimers.

In order to verify whether in solution a similar tetrameric aggregate is present it is important to perform neutron small angle scattering (SANS) experiments. Figure 14 presents SANS data at different concentrations. Let us commence with the insert.

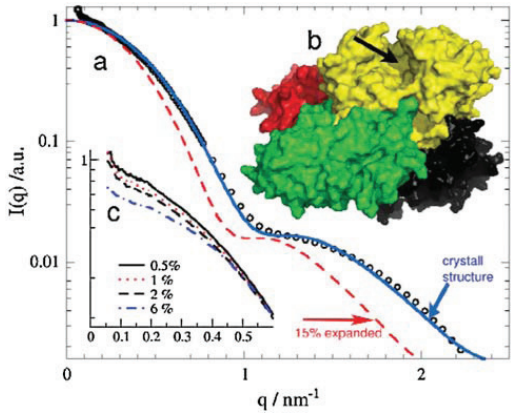

Fig. 13: *SANS results on ADH solutions of different concentration). Insert: concentration dependent results. The solid line in the main figure display the SANS prediction on the basis of the: crystal structure.*

Here for different concentrations the low Q data are presented and there with increasing concentration we observe a decrease of the SANS intensities. This observation results from the repulsive interaction between different tetramers giving rise to an inter tetramer structure factor causing the reduced intensity at low Q.

In the main figure the low concentration data are presented over the full Q range and are compared the crystal structure which appears to be in a very good agreement with the SANS data.

Dynamic light scattering is the proper tool since it investigates the overall dynamics on the proper length scale. Figure 14 displays light scattering results for different ADH concentrations as a function of momentum transfer squared. We note that apparently for all concentrations we observe identical translational diffusion coefficients. At 5°C it amounts to $D_{DLS} = 2.35 \pm 0.2 \times 10^{-2}\text{nm}^2/\text{ns}$. Now we turn to the dynamics. Such a protein complex in solution performs various important motions: (I) translational diffusion, where the whole molecule migrates the solvent (II) rayed body rotational diffusion. There the complex rotates around its center of mass giving rise to important dynamic contribution to the scattering signal as soon as the momentum transfer reads the typical inverse size of the complex and finally (III) there might be contributions from a possible cleft opening dynamics that would also be expected in a Q-range where the rotational dynamics contributes. Thus, in order to identify any large scale internal protein dynamics, one has to sort out all the other important motions.

To separate out the translational diffusion is done in the experiment at very small momentum transfer , where the molecule Appears as a point like object.

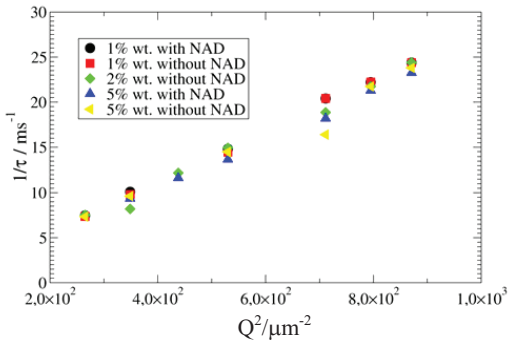

Fig. 14: *Dynamic light scattering results on the translational diffusion of tetrameric ADH in water solution at different concentrations. The characteristic rates* $1/\tau = D*Q^2$ *are plotted vs.* Q^2.

In order to approach the internal dynamics of such an aggregate one has to increase the Q range such that $1/Q$ roughly corresponds to the molecular or aggregate size. This may be achieved implying neutron spin echo spectroscopy to the ADH solutions. Figure 15 displays NSE results for a large number of different momentum transfers Q. The data are presented in a log linear fashion showing directly the single exponential decay observed in all cases. Fits with single exponential decays are included by straight lines. We note however, that at intermediate Q ($Q = 0.68\text{nm}^{-1}$) small but systematic deviations appear indicating a two component structure.

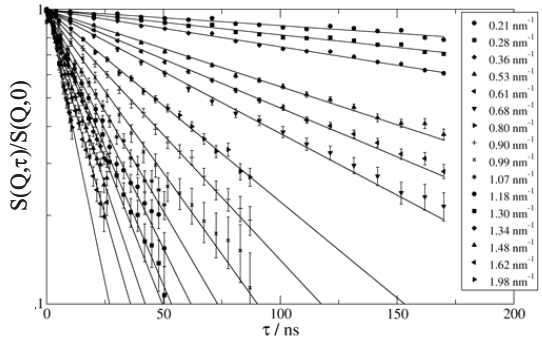

Fig. 15: *Neutron spin echo results on a 5% ADH resolution at 5 °C with cofactor for various momentum transfers.*

Comparing the covered Q range with the SANS data (Figure 13) we realize that the range of the structure factor, where intermolecular interactions are important as well as the regime of internal structure are covered. Now we consider that all data may be described in terms of a single exponential decay. Therefore, we may approximate the spectra in terms of a first cumulant expansion

$$\ell n \frac{S(Q,t)}{S(Q)} = -\Gamma(Q)t + \frac{1}{2}K_2 t^2 \qquad \text{(a)} \qquad (13.32)$$

The decay rate of the dynamic structure factor, also called initial slope, is

$$\Gamma(Q) = -\lim_{t\to 0}\frac{\partial}{\partial t}\,\ell n\left[S(Q,t)\right] \qquad \text{(b)} \qquad (13.33)$$

Using the decay rates $\Gamma(Q)$ we may define an effective diffusion coefficient

$$D_{eff}(Q) = \frac{\Gamma(Q)}{Q^2} \qquad \text{(c)} \qquad (13.34)$$

For the case of a translational diffusion $D_{eff}(Q)$ would be a constant and giving the translational diffusion coefficient.

Figure 16 displays the thus obtained effective diffusion coefficients as a function of Q for the different concentrations with and without the cofactor NAD. The line at low Q indicates the level of the light scattering results.

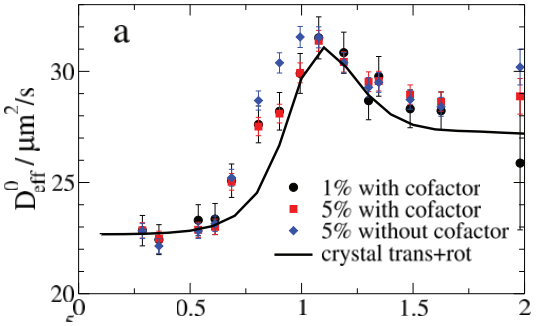

Fig. 16: *Effective diffusion coefficient $D_{eff}(Q)$ for 3 different solutions of ADH, The data were connected for HCQI and S(Q) (see text) Solid line result from a rayed body calculation (see text)*

The experimental results show a strong Q modulation with a maximum around $Q = 1\text{nm}^{-1}$. Furthermore, we realize that at low Q the data are in agreement with the concentration independent light scattering results. We also see that beyond the statistical error in the low Q flank of the 5% data the relaxation without the cofactor NAD is faster than that including the cofactor. We may conclude that in the dynamics of the ADH tetramer on the scale of the aggregate itself we observe significant contributions beyond translational diffusion.

We now want to interpret the data and commence with the low Q data which are affected by the interactions between the molecules. In this regime the effective diffusion coefficient relates to the diffusion coefficient D_0 at infinite dilution by

$$D_{eff}(Q) = D_0 \frac{H(Q)}{S(Q)} \tag{13.35}$$

where $H(Q)$ is the hydrodynamic factor and $S(Q)$ is the interparticle structure factor. The structure factor may be extracted from the SANS data in dividing the concentration dependent results by the lowest concentration results ($C = 0.25\%$). With this experimental structure factor the data needs to be corrected. The hydrodynamic factor cannot be measured directly. A first approximation in terms of a Perkus Yevic model shows that (i) at a 1% level the correction factor $H(Q)/S(Q)$ leaves the experimental data practically untouched and (ii) at 5% the correction is somewhat weaker than the experimentally observed effect. Nevertheless, beyond $Q = 0.6\text{nm}^{-1}$ the ratio of $H(Q)/S(Q)$ remains constant. Thus, the observed higher Q structure is entirely determined by intra aggregate effects.

The prime reason for a Q dependent structure in $D_{eff}(Q)$ are rotational motions of the molecule. In a first cumulant approximation (see Eq.[32]) the effective diffusion coefficient of a rigid boy undergoing translational and rotational diffusion has the form [19]

$$D_{eff}(Q) = \frac{k_B T}{Q^2} \times \frac{\sum_{jK} \left\langle b_j e^{i\underline{Q}\underline{r}_j} \begin{pmatrix} \underline{Q} \\ \underline{Q} \times \underline{r}_j \end{pmatrix} \ddot{H} \begin{pmatrix} \underline{Q} \\ \underline{Q} \times \underline{r}_K \end{pmatrix} b_K e^{-i\underline{Q}\underline{r}_K} \right\rangle}{\sum_{jK} \left\langle b_j e^{i\underline{Q}\underline{r}_j} \; b_K e^{-i\underline{Q}\underline{r}_K} \right\rangle} \tag{13.36}$$

Here $\underline{r}_i$ and $\underline{r}_k$ are the atomic coordinates, b_i and b_k the corresponding neutron scattering length and $\ddot{H}$ the mobility tensor. The sum runs over all atoms of the molecule or molecular aggregate and the pointed brackets indicate an ensemble average. The denominator is the aggregate formfactor. The mobility matrix $\ddot{H}$ is a 6×6 tensor involving translational ($\ddot{T}$) rotational ($\ddot{R}$) parts including a translational rotational coupling ($\overleftrightarrow{TR}$). For the simplest case of an isotropic particle $T = D_{trans}/k_B T$ and $R = D_{rot}/k_B T$. The evaluation of Eq.[34] is importantly complicated by the hydrodynamic interaction between the different parts of the molecule. In the biophysical literature one finds the computer code HYDROPRO which was developed by the group around Garcia de la Torre [20]. In this code a complicated molecule is approximated by a rigid aggregate of little spheres. Its diffusional motion including the hydrodynamic interaction is then calculated by a proper superposition of the motion of the rigidly connected spheres. The calculations with HYDROPRO need as an input the crystallographic coordinates of all atoms. The solid line in Figure 16 displays the result of the HYDROPRO calculations for a rigid molecule. While the line describes the general form of the effective diffusion coefficient data reasonably well, we observe significant deviations at smaller momentum transfers. These differences between the

rotational diffusion expectation for a rigid aggregate and the experimental data are displayed in Figure 17. We note that at Q values below the peak of the rigid body rotational diffusion coefficient significantly faster effective diffusion takes place. This result indicates the presence of internal motion within the molecule which must involve mainly those atoms which are placed in the outer regions of the tetramer emphasizing more strongly the larger distances and within the molecule and therefore giving rise to extra dynamics at low Q.

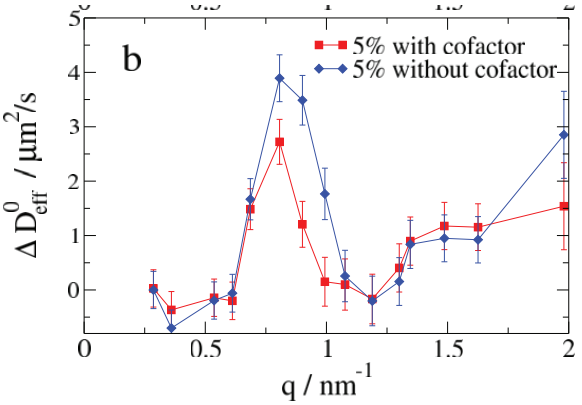

Fig. 17: *Differences between the measured effective Q- dependent diffusion coefficient and expectation from rigid body motion. The lines are guides to the eye.*

A first interpretation of this result may be carried out in terms of a normal mode analysis. For this purpose an elastic network model is used where the complicated bonded and non-bonded interactions are replaced by a pair wise Hookian potential controlled by a single parameter. As has been shown, such a simple formulation is sufficient to describe the anomalous low frequency motion of large proteins [21].

In this model two close enough atoms are connected by a spring, if the equilibrium distance between them is sufficiently small. The elastic forces acting on the particles obey Hookes law and depend only on the change in the distances between them. If $\underline{R}^0_i$ are the equilibrium positions of the particles and $\underline{R}_i(t)$ are their actual coordinates the Hookean Potential has the form

$$E_H = f \sum_{i,j} A_{ij} \left(\left| \underline{R}_i - \underline{R}_j \right| - \left| \underline{R}^0_i - \underline{R}^0_j \right| \right)^2 \qquad (13.37)$$

A is the adjacency matrix with the elements, $A_{ij} = 1$ if $\left| \underline{R}^0_i - \underline{R}^0_j \right| < \ell_0$ and $A_{ij} = 0$ otherwise. In principle the dynamics of such an elastic network is nonlinear because the distances $\left| \underline{R}_i - \underline{R}_j \right|$ are nonlinear functions of the coordinates. Close to the equilibrium the equations of motions can however be linearized yielding to an equation of motion

$$m_i \ddot{\underline{r}}_i = -\sum_j \Lambda_{ij} \underline{r}_j \tag{13.38}$$

where Λ is the $3N \times 3N$ dynamical matrix obtained by the linearization process. In this linear approximation the motions are described by a sum of independent oscillating normal modes.

$$\underline{r}_i(t) = \sum_\alpha k_\alpha \underline{e}_i^\alpha \ (1 - \cos(\omega_\alpha t)) \tag{13.39}$$

With ω_α and $\underline{e}_i^\alpha$ representing nonzero eigenvalues and the respective eigenvectors of the matrix Λ and k_α the amplitude factor of the mode. The large scale slow motions we are interested in, are dominated by the soft modes with small eigenvalues. In the case of overdamped modes which are seen in the experiment the oscillating part needs to be replaced by an exponential $\left(e^{(-\lambda_\alpha t)}\right)$. The relaxation rates λ_α contain the unknown friction factors within the molecule and with the surrounding water molecules.

A first approximation for the dynamic structure factor may be obtained in terms of a one phonon approximation of the cross section. In this approximation the dynamic structure factor reads

$$\begin{aligned} S(Q,t)_{1-phon} &\simeq \sum_{k,\ell} b_k \, b_e \ e^{i\underline{Q}\underline{r}_k} e^{-i\underline{Q}\underline{r}_e} \\ &+ \sum_\alpha \frac{k_B T}{\omega_\alpha^2} e^{-\lambda_\alpha t} \sum_{k,\ell} \frac{b_k \, b_e}{\sqrt{m_k m_l}} \ e^{i\underline{Q}\underline{r}_k} e^{-i\underline{Q}\underline{r}_e} \left(\underline{Q}\,\underline{e}_k^\alpha\right)\left(\underline{Q}\,\underline{e}_\ell^\alpha\right) \end{aligned} \tag{13.40}$$

In first cumulant approximation (Eq.[32]) we have to take the logarithmic derivative with respect to time at time equal zero. Subtracting the translational and rotational part we finally obtain

$$\Delta D_{eff}(Q) = \frac{\sum_\alpha \lambda_\alpha \frac{k_B T}{\omega_\alpha^2} \sum_{k,\ell} \frac{b_k \, b_e}{\sqrt{m_k m_l}} \ e^{i\underline{Q}\underline{r}_k} e^{-i\underline{Q}\underline{r}_e} \left(\underline{Q}\underline{e}_k^\alpha\right) \times \left(\underline{Q}\underline{e}_\ell^\alpha\right)}{Q^2 \sum_{k,\ell} b_k \, b_e \ e^{i\underline{Q}\underline{r}_k} e^{i\underline{Q}\underline{r}_e}} \tag{13.41}$$

describing the dynamic formfactor of the eigenmodes. Finally, Figure 18 presents the outcome of such a harmonic analysis for the tetrameric aggregate of ADH with and without the cofactor. In an exemplary way we present the contributions from the modes 7, 9 and 11 with and without the cofactor. In all cases the low eigenmodes exhibit a formfactor with the strong peak around $Q = 1\text{nm}^{-1}$ comparing with Figure 17 qualitatively the experimental observation and the results of the normal mode analysis resemble each other.

Quantitatively the observed experimental feature is shifted towards smaller Q indicating a more pronounced motion of the outer atoms. This difference is not yet fully

understood but may result from the anharmonicity of the dynamics or the effect inhomogenously distributed friction within the molecule or both.

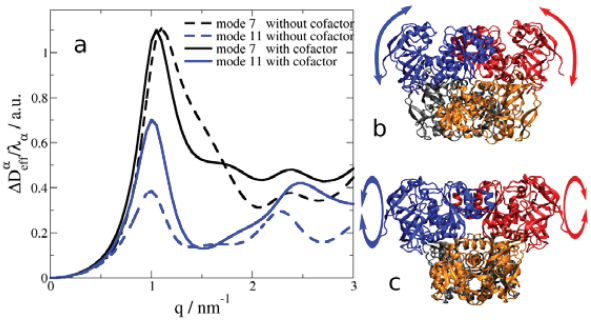

Fig. 18: *Diffusion form factor of the normal modes 7 and 11 for the protein configuration with and without cofactor.* ***b****, Motional pattern of mode 7: Without cofactor the exterior domain (catalytic domain) tilts outwards and opens the cleft. The inner domain with connection points between the monomers remains stiff.* ***c****, Motional pattern of mode 11: With and without bound cofactor the monomers within a dimer exhibit torsional motion around the long dimer axis (in the image plane), which is more pronounced without the cofactor.*

13.6 Conclusion and outlook

We have presented some representative results from neutron spin echo spectroscopy on the dynamics of macromolecules. In the case of synthetic polymers we have displayed recent results on the universal dynamics of flexible polymers from the entropy driven Rouse dynamics to confinement and reptation. In the case of biopolymers we have displayed some first experiments on the intra aggregate motion of alcohol dehydrogenase an important enzyme for fermentation and the oxidation of ethanol. The lecture attempted to transmit a flavour of what can be achieved with high resolution neutron spin spectroscopy which permits to access the molecular motion simultaneously in space and time.

The lecture commenced with a description of the standard model of polymer motion, the entropy driven dynamics covered by the so called Rouse model. In the spatial range where the Rouse approximations are valid, the NSE measurements have confirmed most of the predictions of the Rouse model both for the self- and pair correlation function. We also have shown limitations related to the inter chain interactions which reveal themselves in the center of mass selfdiffusion at short times.

Towards larger scales topological interactions resulting from the mutually interpenetrating chains gain dominating influence and confine the chain motion to a

tube along the chain profile. We have presented measurements on the dynamic structure factor of a reptating chain which unequivocally confirm the picture of local reptation i.e. Rouse relaxation along the contorted tube. A measurement of the self correlation function corrobates the picture.
Compared to the investigations of the dynamics of synthetic polymers the study of the large scale relaxation dynamics of biopolymers is still in its early stages. We have presented some first experimental data on the collective inter aggregate fluctuations of a tetrameric aggregate formed by alcohol dehydrogenase. It became possible to directly measure the Q dependent effective diffusion coefficient which bears information on the detailed rotational diffusion dynamics. Furthermore, additional dynamics appears at low momentum transfers which is related to motions of the outer more flexible parts of each dimer. Employing normal mode analysis these dynamical features have been attributed to the slow large scale collective fluctuations of the domains.

These experiments are a first attempt to directly observe the collective internal dynamics of proteins or protein complexes. In the future experiments will be needed in order to resolve the internal dynamics or further proteins, in order to try to resolve the different relaxation modes. Such experiments need to be accompanied by computer simulations in order to enhance the level of interpretation. Furthermore, the experiments need to address proteins where domain motion is functionally important. We hope that in the future such NSE studies will make an important contribution to a better understanding of protein function based not only on the structure but also on the dynamics.

References

[1] For a recent review see: D. Richter, M. Monkenbusch, A. Arbe, J. Colmenero, Adv. Polymer Sci. 174, Springer, Berlin, Heidelberg, New York (2005)
[2] M. Doi, S.F. Edwards, J. Chem. Soc. Farad. Trans. 274, 1789; 274, 1802; 275, 38 (1978)
[3] P.G. de Gennes, J. Chem. Phys. 55, 572 (1971)
[4] Z. Bu, R. Biehl, M. Monkenbusch, D. Richter, J.E. Callaway, PNAS 102, 17646 (2005)
[5] F. Mezei (Ed.), Neutron spin echo lecture notes in physics 128, Springer, Berlin, Heidelberg, New York (2005)
[6] P.R. Rouse, J. Chem Phys. 21, 1272 (1953)
[7] A. Wischnewski, M. Monkenbusch, L. Willner, D. Richter, B. Farago, G. Kali, Phys. Rev. Lett. 90, 058302 (2003)
[8] H. Montes, M. Monkenbusch, L. Willner, S. Rathgeber, L.J. Fetters, D. Richter, J. Chem. Phys. 110, 10188 (1999)
[9] M. Doi, S.F. Edwards, The theory of polymer dynamics, Clarendon Oxford (1986)
[10] P.G. de Gennes, Scaling concepts in polymer physics, Cornell University Press, Ithaca (1979)
[11] D. Richter, A. Baumgärtner, K. Binder, B. Ewen, J.B. Hayter, Phys. Rev. Lett. 47, 109 (1981)
[12] P.G. de Gennes, J. Phys. (Paris) 42, 735 (1981)
[13] G.J. Ronca, J. Chem. Phys. 79, 79 (1983)
[14] J. des Cloiseaux, Macromolecules 23, 3992 (1990)
[15] K.S. Schweitzer, J. Chem. Phys. 91, 5802; 5822 (1989)
[16] P. Schleger, B. Farago, A. Kollmar, C. Lartigue, D. Richter, Phys. Rev. Lett. 81, 124 (1998)
[17] F. Schotte, M. Lim, T.A. Jackson, A.V. Smirnov, J. Soman, J.S. Olson, G.N. Jr Philips, M. Wulf, P.A. Aminfrud, Science 300, 1944 (2003)
[18] R. Biehl, B. Hoffmann, M. Monkenbusch, P Falus, S. Preost, R. Merkel, D. Richter, Physical Review Letter 101, 138102 (2008)
[19] N. Brown, Dynamic Light Scattering, Monographs of the Physics and Chemistry of Materials, Oxford Science Publications, Oxford 49 (1993)
[20] J. Garcia de la Torre, M.L. Huertas, B. Carrasco, Biophysics J. 78, 719 (2000)
[21] M.M. Tirion, Phys. Rev. Lett. 77, 1905 (1996)

Exercises

E13.1

Silly Putty® is a typical viscoelastic material made from polydimethylsiloxane, silica and oils.

Propose and justify the 3 functions for the following behavior of Silly Putty.
-When left on the table for a long period of time the height, h, decays in the manner of figure "a".
-When rapidly pulled and observed over only shot times the length, l, follows "b".
-When pulled at intermediate speed (1) and then released (2) the behavior of "c" results.

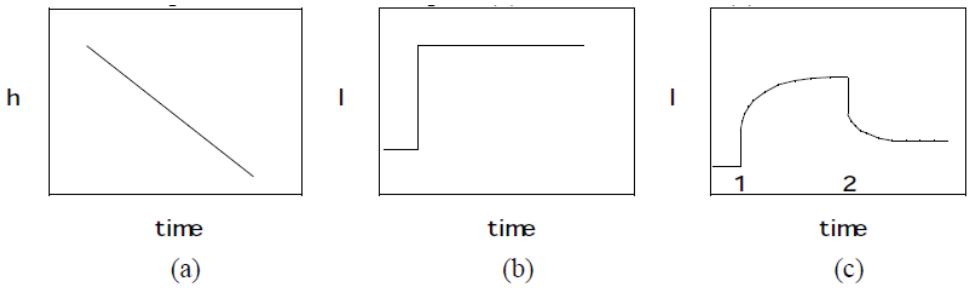

E13.2

The Rouse model represents a polymer coil as a series of beads and springs.
The Rouse spring has a spring constant based on rubber elasticity theory. This is sometimes called the ideal rubber law in analogy to an ideal gas.
-What is the association between an ideal rubber and an ideal gas?

E13.3

In the lecture we have presented a solution for the Rouse Model in Fourier Space of the following form

$$x_p(t) = \frac{1}{2N\xi_0}\int_{-\infty}^{t} dt \exp\left[\left(t-t'\right)/\tau_p\right] f_p(t')$$

The random force obeys the relation $\left\langle f_{p\alpha}\left(t\right) f_{q\beta}\left(t'\right)\right\rangle = 2\delta_{pq}\delta_{\alpha\beta}\xi_p k_B T\delta\left(t-t'\right)$

Calculate the correlation function $\left\langle x_p^{\alpha}\left(t\right) x_q^{\beta}\left(0\right)\right\rangle$

E13.4

The Rouse model is used to construct more complicated models for polymer dynamics that deal with chain entanglements such as the tube (reptation) model. In the tube model the polymer chain retains Rouse dynamics within the confinement of a **rigid** tube of cross-sectional area <d^2>, where d is the tube diameter. For simplicity we take $\left\langle d^2\right\rangle = \ell^2$, where ℓ is the size of a Rouse unit. The tube follows a random walk in 3-D space.

a) If the tube length is $L_p = N_R\ell$, where N_R is the number of Rouse units in a chain, and if the chain in the axial direction of the tube follows Rouse dynamics, with a friction factor of ξ_R for each Rouse unit,

-What is the total chain friction factor **along the tube axis** for the chain in the tube, ξ_p ?

-How does this compare with the Rouse chain friction factor in 3D space?

b) The Einstein relationship tells us that the diffusion coefficent should follow D = kT/ξ.

-What is the diffusion coefficient for the entire chain for motions along the length of the tube (along the tube axis)?

-What is the predicted molecular weight dependence of this diffusion coefficient?

-How does this compare with the Rouse diffusion coefficient?

c) For Brownian motion, such as motion of the chain in the tube, the distance traveled, d, in time, t, is given by $s = \sqrt{Dt}$.

-What is the average time for the chain to move the length of the tube (this is called the reptation time, τ_d)?

-How does τ_d scale with molecular weight?

-How does this compare with the scaling of the Rouse time, τ_R, with molecular weight?

-How does this compare with the observed relaxation time for entangled systems (same as the scaling behavior of η_0 with molecular weight)?

d) The diffusion coefficient for centre of mass motion of a chain in a tube in 3D-space is determined by considering the size of the random walk tube in 3-d space, $R_e = N_R^{1/2}\ell$, and the time required to move the length of the tube. (D = (distance)^2/time)

-What is the molecular weight dependence of the diffusion coefficient for chain motion in 3D-space for a chain confined to a tube?

-How does this compare with the Rouse diffusion coefficient you gave above?

14 Applications of Neutron Scattering - an Overview

Th. Brückel
Jülich Centre for Neutron Science 2
Forschungszentrum Jülich GmbH

Contents

Lecture Notes of the JCNS Laboratory Course Neutron Scattering

14.1 Introduction

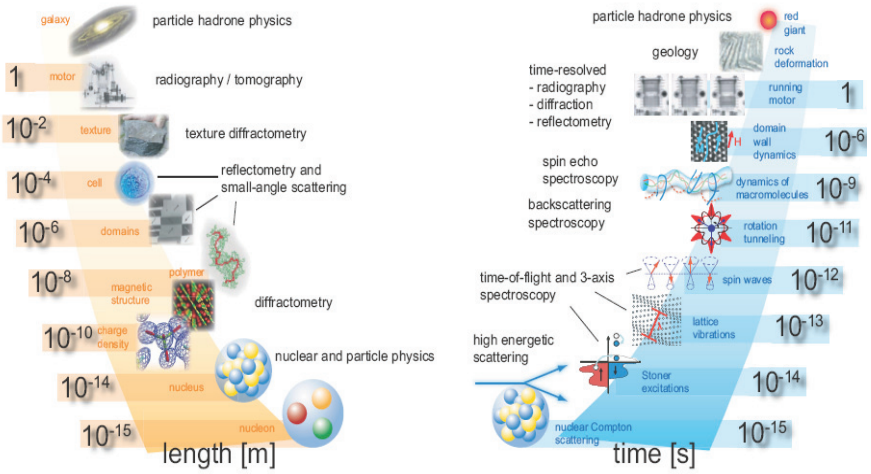

Fig. 14.1: *Length- and time scales covered by research with neutrons giving examples for applications and neutron techniques [1].*

Research with neutrons covers an extraordinary range of length- and time scales as depicted in figure 14.1. The very extremes of length scales - below 10^{-12} m - are the domain of nuclear and particle physics, where e. g. measurements of the charge or electric dipole moment of the neutron provide stringent tests of the standard model of particle physics without the need of huge and costly accelerators. On the other extreme, neutrons also provide information on length- and time scales relevant for astronomical dimensions, e. g. the decay series of radioactive isotopes produced by neutron bombardment give information on the creation of elements in the early universe. In this course, however, we are only concerned with neutrons as a probe for condensed matter research and therefore restrict ourselves to a discussion of neutron scattering. Still, the various neutron scattering techniques cover an area in phase space from picometers pm up to meters and femtoseconds fs up to hours, a range, which probably no other probe can cover to such an extend.

Different specialized neutron scattering techniques are required to obtain structural information on different length scales:

- With *wide angle neutron diffractometry*, magnetization densities can be determined within single atoms on a length scale of ca. 10 pm[1]. The position of at-

[1] In this sense, neutrons are not only nanometer nm, but even picometer pm probes!

oms can be determined on a similar length scale, while distances between atoms lie in the 0.1 nm range[2].

- The sizes of large macromolecules, magnetic domains or biological cells lie in the range of nm to μm or even mm. For such studies of large scale structures, one applies *reflectometry* or *small angle scattering* techniques.
- Most materials relevant for engineering or geo-science occur neither in form of single crystals, nor in form of fine powders. Instead they have a grainy structure, often with preferred orientation of the grains. This so called texture determines the macroscopic strength of the material along different directions. *Texture diffractometry* as a specialized technique allows one to determine this grainy structure on length scales of up to mm.
- Finally, for even larger structures, one uses imaging techniques, such as neutron *radiography* or *tomography*, which give a two dimensional projection or full 3-dimensional view into the interior of a sample due to the attenuation of the neutron beam, the phase shift or other contrast mechanisms.

In a similar way, different specialized neutron scattering techniques are required to obtain information on the system's dynamics on different time scales:

- *Neutron Compton scattering*, where a high energy neutron in the eV energy range makes a deep inelastic collision with a nucleus in so-called impulse approximation, gives us the momentum distribution of the atoms within the solid. Interaction times are in the femtosecond fs time range.
- In magnetic metals, there exist single particle magnetic excitations, so-called Stoner excitations, which can be observed with inelastic scattering of high energy neutrons using the so-called *time-of-flight spectroscopy* or the *triple axis spectroscopy* technique. Typically, these processes range from fs to several hundred fs.
- Lattice vibrations (phonons) or spin waves in magnetic systems (magnons) have frequencies corresponding to periods in the picosecond ps time range. Again these excitations can be observed with *time-of-flight* or *triple axis spectroscopy*.
- Slower processes in condensed matter are the tunneling of atoms, for example in molecular crystals or the slow dynamics of macromolecules. Characteristic time scales for these processes lie in the nanosecond ns time range. They can be observed with specialized techniques such as *backscattering spectroscopy* or *spin-echo spectroscopy*.
- Even slower processes occur in condensed matter on an ever increasing range of lengths scales. One example is the growth of domains in magnetic systems, where domain walls are pinned by impurities. These processes may occur with typical time constants of microseconds μs. Periodic processes on such time scales can be observed with *stroboscopic neutron scattering* techniques.
- Finally, *kinematic neutron scattering* or imaging techniques, where data is taken in consecutive time slots, allow one to observe processes from the millisecond ms to the hour h range.

[2] In what follows, we use as "natural atomic unit" the Ångstrøm, with 1 Å=0.1 nm.

In this chapter, we will overview the various techniques used in neutron scattering and provide some examples for their application. We will start by repeating the properties of the different correlation functions, in order to be able to judge what kind of information we can obtain from a certain neutron scattering experiment. We will introduce neutron scattering techniques used to obtain information on "where the atoms are" (diffractometry) and "what the atoms do" (spectroscopy). We will finish by reviewing the range of applicability of various neutron scattering methods and compare them to other experimental techniques.

14.2 Scattering and correlation functions

This somewhat advanced section can be skipped during first reading, but is given here for completeness.

The neutron scattering cross section for nuclear scattering can be expressed in the following form (for simplicity, we restrict ourselves to a mono-atomic system):

$$\frac{\partial^2\sigma}{\partial\Omega\partial\omega} = \frac{k'}{k}\cdot N\cdot\left[\left(\overline{|b|^2}-|\bar{b}|^2\right)S_{inc}(\underline{Q},\omega)+|\bar{b}|^2\ S_{coh}(\underline{Q},\omega)\right] \tag{14.1}$$

The cross section is proportional to the number N of atoms. It contains a kinematical factor k'/k, i. e. the magnitude of the final wave vector versus the magnitude of the incident wave vector, which results from the phase-space density. The scattering cross section contains two summands: one is the coherent scattering cross section, which depends on the magnitude square of the average scattering length density $|\bar{b}|^2$ and the other one is the incoherent scattering, which depends on the variance of the scattering length $\left(\overline{|b|^2}-|\bar{b}|^2\right)$. The cross section (14.1) has a very convenient form: it separates the interaction strength between probe (the neutrons) and sample from the properties of the system studied. The latter is given by the so-called scattering functions $S_{coh}(\underline{Q},\omega)$ and $S_{inc}(\underline{Q},\omega)$, which are completely independent of the probe and a pure property of the system under investigation [2]. The *coherent scattering function* $S_{coh}(\underline{Q},\omega)$ (also called *dynamical structure factor* or *scattering law*) is a Fourier transform in space and time of the pair correlation function:

$$S_{coh}(\underline{Q},\omega) = \frac{1}{2\pi\hbar}\int G(\underline{r},t)e^{i(\underline{Q}\cdot\underline{r}-\omega t)}d^3r dt \tag{14.2}$$

Here the *pair correlation function* $G(\underline{r},t)$ depends on the time dependent positions of the atoms in the sample:

$$\begin{aligned} G(\underline{r},t) &= \frac{1}{N}\sum_{ij}\int\left\langle\delta(\underline{r}'-\underline{r}_i(0))\cdot\delta(\underline{r}'+\underline{r}-\underline{r}_j(t))\right\rangle d^3r' \\ &= \frac{1}{N}\int\left\langle\rho(\underline{r}',0)\cdot\rho(\underline{r}'+\underline{r},t)\right\rangle d^3r' \end{aligned} \tag{14.3}$$

$\underline{r}_i(0)$ denotes the position of atom *i* at time *0*, while $\underline{r}_j(t)$ denotes the position of another atom *j* at time *t*. The angle brackets denote the thermodynamic ensemble average, the integral extends over the entire sample volume and the sum runs over all atom pairs in the sample. Instead of correlating the positions of two point-like scatterers at different times, one can rewrite the pair correlation function in terms of the particle density as given in the second line of (14.3). Coherent scattering arises from the superposition of the amplitudes of waves scattered from one particle at time *0* and a second particle at time *t*, averaged over the entire sample volume and the thermodynamic state of the sample. In contrast, incoherent scattering arises from the superposition of waves scattered from the same particle at different times. Therefore the *incoherent scattering function* $S_{inc}(\underline{Q},\omega)$ is given in the following form:

$$S_{inc}(\underline{Q},\omega) = \frac{1}{2\pi\hbar}\int G_s(\underline{r},t)e^{i(\underline{Q}\cdot\underline{r}-\omega t)}d^3r dt \tag{14.4}$$

which is the Fourier transform in space and time of the *self correlation function* $G_S(\underline{r},t)$:

$$G_s(\underline{r},t) = \frac{1}{N}\sum_j \int\left\langle \delta(\underline{r}'-\underline{\mathrm{r}}_j(0))\cdot\delta(\underline{r}'+\underline{r}-\underline{\mathrm{r}}_j(t))\right\rangle d^3r' \tag{14.5}$$

We next define the *intermediate scattering function* $S(\underline{Q},t)$ as the purely spatial Fourier transform of the correlation function (here we have dropped the index "coh" and "inc", respectively, as the intermediate scattering function can be defined for coherent as well as for incoherent scattering in the same way):

$$\begin{aligned} S(\underline{Q},t) &:= \int G(\underline{r},t)e^{i\underline{Q}\cdot\underline{r}}d^3r \\ &= S(\underline{Q},\infty) + S'(\underline{Q},t) \end{aligned} \tag{14.6}$$

For reasons, which will become apparent below, we have separated in the second line the intermediate scattering function for infinite time

$$S(\underline{Q},\infty) = \lim_{t\to\infty} S(\underline{Q},t) \tag{14.7}$$

from the time development at intermediate times. Given this form of the intermediate scattering function $S(\underline{Q},t)$, we can now calculate the scattering function as the temporal Fourier transform of the intermediate scattering function:

$$\begin{aligned} S(\underline{Q},\omega) &= \frac{1}{2\pi\hbar}\int_{-\infty}^{+\infty} S(\underline{Q},t)e^{-i\omega t}dt \quad = \frac{1}{2\pi\hbar}\int_{-\infty}^{+\infty}\left[S(\underline{Q},\infty)+S'(\underline{Q},t)\right]e^{-i\omega t}dt \\ &= \underbrace{\frac{1}{\hbar}\delta(\omega)S(\underline{Q},\infty)}_{\text{elastic scattering}} + \underbrace{\frac{1}{2\pi\hbar}\int_{-\infty}^{+\infty} S'(\underline{Q},t)e^{-i\omega t}dt}_{\text{inelastic scattering}} \end{aligned} \tag{14.8}$$

In this way, the scattering function has been separated into one term for frequency *0*, i. e. vanishing energy transfer $\Delta E = \hbar\omega = 0$ and one term for non-vanishing energy transfer. The first term is the purely elastic scattering, which is given by the correlation function at infinite times. Correlation at infinite times is obtained for particles at rest. A prominent example is the Bragg scattering from a crystalline material, which is purely elastic, while the scattering from liquids is purely inelastic, since the atoms in liquids are moving around freely and thus the correlation function vanishes in the limit of infinite time differences.

Often times the energy of the scattered neutron is not discriminated in the detector. In such experiments, where the detector is set at a given scattering angle, but does not resolve the energies of the scattered neutrons, we measure an *integral cross section* for a fixed direction $\hat{\underline{k}}'$ *of* $\underline{k}'$:

$$\left(\frac{d\sigma}{d\Omega}\right)_{coh,\mathrm{int}} = \int \left.\frac{\partial^2\sigma}{\partial\Omega\partial\omega}\right|_{\hat{\underline{k}}'=const} \cdot d\omega \tag{14.9}$$

Momentum and energy conservation are expressed by the following kinematic equations of scattering:

$$\underline{Q} = \underline{k}' - \underline{k} \;\; ; \;\; \hbar\omega = E - E' = \frac{\hbar^2}{2m}\left(k^2 - k'^2\right) \tag{14.10}$$

Due to these kinematic conditions, the scattering vector $\underline{Q}$ will vary with the energy of the scattered neutron E' or the energy transfer $\hbar\omega$ as the integral in (14.9) is performed. The so-called *quasi-static approximation* neglects this variation and uses the scattering vector Q_0 for elastic scattering $(\hbar\omega = 0)$ in (14.9). This approximation is valid only if the energy transfer is small compared to the initial energy. This means that the movements of the atoms are negligible during the propagation of the radiation wave front from one atom to the other. In this case, the above integral can be approximated as follows:

$$\begin{aligned}\left(\frac{d\sigma}{d\Omega}\right)_{coh,QSA} &= \frac{k'}{k}\frac{N}{2\pi\hbar}\int\left(\int G(\underline{r},t)e^{i(\underline{Q}_0\cdot\underline{r}-\omega\cdot t)}d^3r dt\right)d\omega \\ &= \frac{k'}{k}\frac{N}{2\pi\hbar}\int G(\underline{r},t)e^{i\underline{Q}_0\cdot\underline{r}}\delta(t)d^3r dt = \frac{k'}{k}\frac{N}{2\pi\hbar}\int G(\underline{r},0)e^{i\underline{Q}_0\cdot\underline{r}}d^3r\end{aligned} \tag{14.11}$$

which shows that the integral scattering in quasi-static approximation depends on the *instantaneous spatial correlation function* only, i. e. it measures a snapshot of the arrangement of atoms within the sample. This technique is e. g. very important for the determination of short-range order in liquids, where no elastic scattering occurs (see above).

Our discussion on correlation functions can be summarized in a schematic diagrammatic form, see figure 14.2.

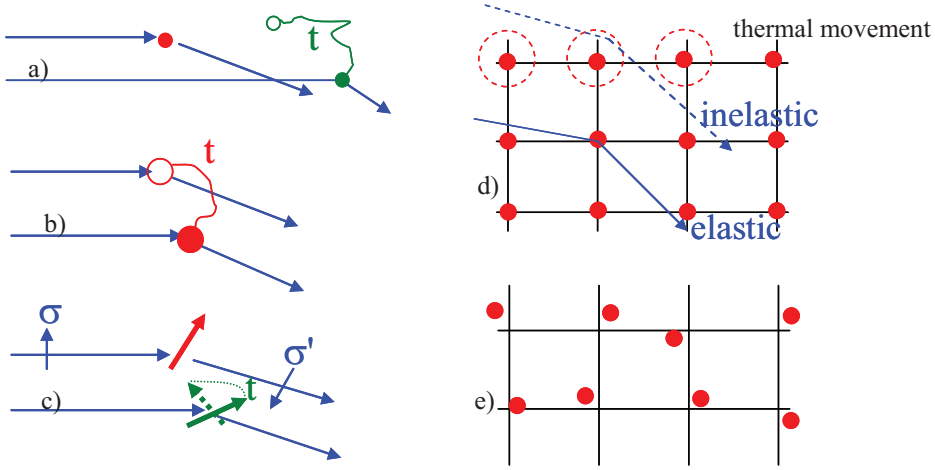

Fig. 14.2: *Schematic diagrams depicting the various scattering processes: a) coherent scattering is connected with the pair correlation function in space-and time; b) incoherent scattering is connected with the self-correlation function; c) magnetic scattering is connected with the spin pair correlation function; d) elastic and inelastic scattering from a crystal measures average positions and movements of the atoms, respectively, e) inelastic scattering in quasistatic approximation sees a snapshot of the sample.*

Figure 14.2 shows that coherent scattering is related to the pair correlation between different atoms at different times (14.2a), while incoherent scattering relates to the one particle self correlation function at different times (14.2b). In analogy to nuclear scattering, magnetic scattering depends on the correlation function between magnetic moments of the atoms. If the magnetic moment is due to spin only, it measures the *spin pair correlation function*. Since the magnetic moment is a vector quantity, this correlation function strongly depends on the neutron polarization. For this reason, in magnetic scattering we often perform a polarization analysis as discussed in the corresponding chapter. Figure 14.2d depicts elastic and inelastic scattering from atoms on a regular lattice. Elastic scattering depends on the infinite time correlation and thus gives us information on the time averaged structure. Excursions of the atoms from their time averaged positions due to the thermal movement will give rise to inelastic scattering, which allows one e. g. to determine the spectrum of lattice vibrations, see chapter on “inelastic neutron scattering”. Finally, an experiment without energy analysis in quasi-static approximation will give us the instantaneous correlations between the atoms, see figure 14.2e. This schematic picture shows a snapshot of the atoms on a regular lattice. Their positions differ from the time averaged positions due to thermal movement.

14.3 The generic scattering experiment

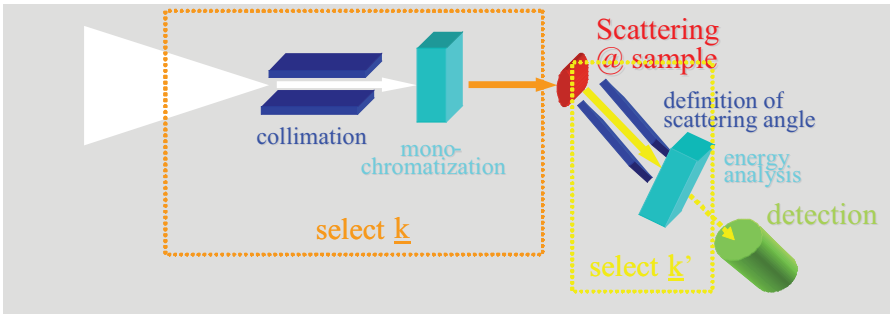

Fig. 14.3: *Schematic diagram of a generic scattering experiment; the primary spectrometer in front of the sample serves to select an incident wave vector distribution by means of collimation and monochromatization; the secondary spectrometer after the sample selects a final wave vector; the number of neutrons for a given distribution of incident wave vector $\underline{k}$ and final wave vector $\underline{k}'$ is counted in the detector.*

A generic scattering experiment is depicted schematically in figure 14.3. The incident beam is prepared by collimators, which define the direction of the beam and monochromators, which define the energy of the incident neutrons. Together these optical elements select an incident wave vector $\underline{k}$. In reality, since these neutron-optical elements are never perfect, a certain distribution of incident wave vectors around an average wave vector is selected in the primary spectrometer. In an analogous manner, a final wave vector - or better a distribution of final wave vectors - is being selected from all scattered waves after the sample by the secondary spectrometer. Finally the scattered neutrons are being counted in the detector. Since our neutron-optical elements are never perfect, the measured intensity in the detector is not simply proportional to the scattering function $S(\underline{Q},\omega)$ (or more precisely, the cross section), but it is proportional to the convolution of the scattering function (or cross section) with the *experimental resolution function R*:

$$I(\underline{Q}_0,\omega_0) \propto \iint S(\underline{Q},\omega) R(\underline{Q}_0 - \underline{Q}, \omega_0 - \omega) d^3Q d\omega \qquad (14.12)$$

Here, the resolution function R appears due to the limited ability of any experimental setup to define an incident or final wave vector $\underline{k}$ or $\underline{k}'$, respectively. R therefore depends purely on the instrumental parameters and not on the scattering system under investigation. The art of any neutron scattering experiment is to adjust the instrument - and with it the resolution function - to the problem under investigation. If the resolution of the instrument is too tight, the intensity in the detector becomes too small and counting statistics will limit the precision of the measurement. If, however, the resolution is too relaxed, the intensity will be smeared out and will not allow one to determine the scattering function properly.

The simplest way to collimate an incident beam is to put two slits with given openings in a certain distance in the beam path and thus define the angular spread of the incident beam. For monochromatization of a neutron beam, usually one of two different methods is applied:

- One can use the wave property of the neutron and diffract the neutron beam from a single crystal. According to Braggs' law $2d\sin\theta = \lambda$, a certain wave length λ is being selected for a given lattice *d*-spacing under a scattering angle 2θ.
- One can use the particle property of the neutron and use the neutron time-of-flight to determine its velocity and thus its kinetic energy. How this is being done technically is discussed in the corresponding section of this course.

Following our discussion of the correlation functions, we will now distinguish two principally different types of neutron scattering instruments:

- Diffractometers: these are scattering instruments, which either perform no energy analysis at all, or which measure only the truly elastic scattering. As discussed in chapter 14.2, the truly elastic scattering allows one to determine the time averaged structure. The prominent example is Bragg scattering from single crystals. If, however, no energy analysis is performed, one usually makes sure that one works in quasistatic approximation to facilitate the interpretation of the scattered intensity distribution. Quasistatic approximation corresponds to a snapshot of the scatterers in the sample and is important for example to determine short-range order in a liquid. Be it elastic scattering or integral scattering in quasistatic approximation, a diffraction experiment allows one to determine the position of the scatterers only. The movement of the scatterers is not (directly) accessible with such a diffraction experiment. Similarly, in a diffraction experiment for magnetic scattering, the arrangement of magnetic moments within the sample, i. e. its magnetic structure, can be determined, while the spin dynamics is not accessible in a diffraction experiment[3].
- Spectrometers: a neutron spectrometer is dedicated to measure inelastic scattering, i. e. to determine the change of the neutrons' kinetic energy $E = \frac{\hbar^2 k^2}{2m}$ during the scattering process. Such an experiment requires the analysis of the energy of the scattered neutrons, in contrast to a conventional diffractometer. Now the intensity measured in the detector depends on momentum- and energy- transfer and is proportional to the convolution of the double differential scattering cross section (14.1) with the resolution function of the instrument (14.12). Therefore a neutron spectrometer gives us information on the scattering functions (coherent or incoherent) and thus on the truly time dependent pair- or self correlation functions. This is why spectrometers are used to determine the dy-

[3] In fact there is a way to access also spin- or lattice- dynamics in a diffraction experiment: lattice vibrations will give rise to diffuse scattering around Bragg peaks, so-called thermal diffuse scattering, which can be modelled and thus the spectrum of excitations can be determined in an indirect, but not model-free direct way.

namics of a system after its structure has been determined in a previous diffraction experiment[4].

14.4 Diffractometers

14.4.1 Wide angle diffraction versus small angle scattering

According to (14.10), the momentum transfer during a scattering experiment is given by $\hbar\underline{Q} = \hbar\underline{k}' - \hbar\underline{k}$. Remembering that $k = \frac{2\pi}{\lambda}$, the magnitude of the scattering vector Q can be expressed in terms of wavelength λ and scattering angle 2θ as:

$$Q = \frac{4\pi}{\lambda}\sin\theta \tag{14.13}$$

As we have seen in chapter 14.2, the scattering cross section is related to the Fourier transform of the spatial correlation function and therefore a reciprocal relation exists between characteristic real space distances d and the magnitude of the scattering vector Q, for which intensity maxima appear:

$$\Delta Q \sim \frac{2\pi}{d} \tag{14.14}$$

Bragg scattering from crystals provides an example for this equation (compare corresponding introductory chapter): the distance between maxima of the Laue function is determined by $\Delta Q \cdot d = 2\pi$, where d is the corresponding real space periodicity. Reflectometry provides another example (see below): the Q-distance between Kiessig fringes is given by the relation $\Delta Q \cdot d \sim 2\pi$ (compare (14.19)), where d is the layer thickness.
(14.14) is central for the choice of an instrument or experimental set-up, since it tells us which Q-range we have to cover in order to get information on a certain length range in real space. (14.13) tells us, at which angles we will observe the corresponding intensity maxima for a given wavelength. This angle has to be large enough in order to separate the scattering event clearly from the primary beam. This is why we need different instruments to study materials on different length scales. Table 14.1 gives two examples.

[4] Of course, spectrometers could also be used to determine the structure, but usually their resolution is not at all adapted to this purpose.

Example	d	ΔQ	2θ (λ=1 Å)	2θ (λ=10 Å)	Technique
Distance between atoms in crystals	2 Å	3.14 $Å^{-1}$	29°	"cut-off"	wide angle diffraction
Precipitates in metals (e.g. Co in Cu)	400 Å	0.016$Å^{-1}$	0.14°	1.46°	small angle scattering

Tab. 14.1: *Examples for scattering from structures on different characteristic real space length scales d. ΔQ is the corresponding characteristic scattering vector according to (14.14), 2θ the scattering angle according to (14.13), calculated for two different wavelength λ.*

1. The study of structures on atomic length scales is typically done with a wavelength of around 1 Å (comparable to the distance between the atoms) and the scattered intensity is observed at rather large angles between 5° and 175°. Therefore one speaks of *wide angle diffraction*, which is employed for the study of atomic structures.
2. For the study of large scale structures (precipitates, magnetic domains, macromolecules in solution or melt) on length scales of 10 up to 10,000 Å (1 up to 1000 nm), the magnitude of the relevant scattering vectors as well as the corresponding scattering angles are small. Therefore one chooses a longer wavelength in order to expand the diffractogram. The suitable technique is *small angle scattering*, which is employed to study large scale structures.

In what follows we will first focus on the study of large scale structures. In the corresponding conceptually very simple instruments, some typical considerations for the design of an instrument can be exemplified. We will distinguish between small angle neutron scattering instruments and reflectometers, discuss the basic instrument concepts and list some possible applications. After having discussed how large scale structures can be studied with neutron diffraction, we will then introduce instruments for wide angle scattering and their possible applications.

14.4.2 Small angle neutron scattering SANS

As mentioned in chapter 14.4.1, small angle scattering is employed whenever structures on length scales between typically 10 Å and 10,000 Å (1 nm and 1,000 nm) are of interest. This range of real space lengths corresponds to a scattering vector of magnitude between about 10^{-1} $Å^{-1}$ and 10^{-4} $Å^{-1}$ ($1\ nm^{-1}$ and 10^{-3} nm^{-1}). In order to observe the scattering events under reasonable scattering angles, one chooses a rather long wavelength. However, due to the moderator spectrum (see chapter on neutron sources), there is very little neutron flux at wavelengths above 20 Å. Therefore typically neutrons of wavelength between 5 and 15 Å are employed for small angle neutron scattering.

Two different principles of small angle neutron scattering will be distinguished in this chapter: the pinhole SANS and the focusing SANS depicted in figures 14.4 and 14.5, respectively. Other types of instruments, e.g. with multi-pinhole grid collimation, are variants of these techniques and will not be discussed here.

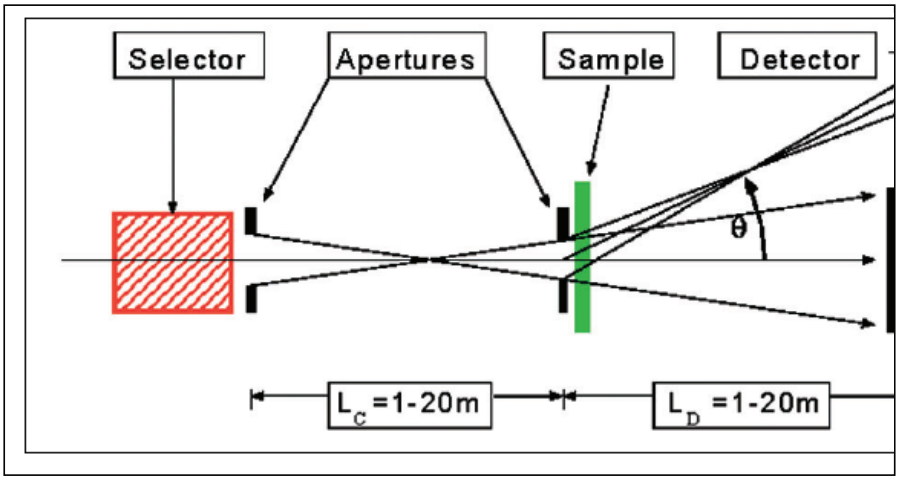

Fig. 14.4: *Schematics of a pinhole SANS, where the incident wave vector is defined through distant apertures (KWS-1 or KWS-2 of JCNS [3]).*

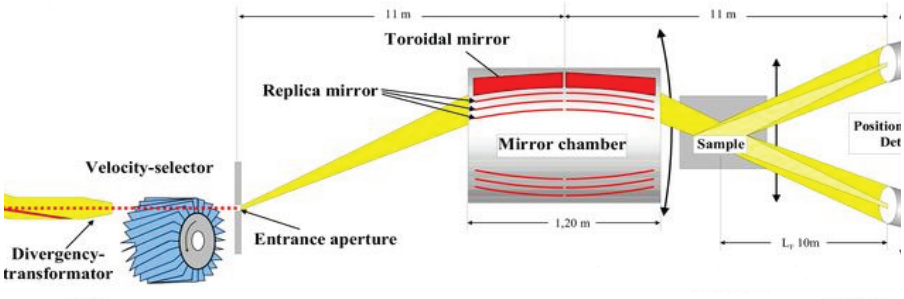

Fig. 14.5: *Schematics of a focusing SANS, where an image of the entrance aperture is produced on the detector by a focusing mirror (KWS-3 of JCNS [3]).*

For both instrument concepts, the wavelength band is usually defined by a so-called velocity selector. Figure 14.6 shows a photo of a velocity selector drum build in Jülich for the instrument KWS-3.

Fig. 14.6: *Photo of the velocity selector drum of the JCNS instrument KWS-3 showing the screw-like twisted channels separated by absorbing walls, which only neutrons of a certain wavelength band can pass when the drum is turning.*

In the pinhole SANS, the incident wave vector $\underline{k}$ is defined by two distant apertures of comparable size. The longer the distance between the diaphragms, the higher is the collimation for a given cross section of the beam. The sample is placed right next to the second aperture and the scattered neutrons are being recorded in a detector, which is at a large distance from the sample; typically the sample-detector distance is comparable to the collimation distance. The overall length of such an instrument can amount to 40 m, up to 80 m.

In contrast to the pinhole SANS, the focusing SANS uses a divergent incident beam and a focusing optical element produces an image of the entrance aperture on the detector. The sample is positioned directly behind the focusing element. Small angle scattering from the sample appears on the position-sensitive area detector around the primary beam spot. Such a set-up with a focusing element would be the natural solution in light optics, where focusing lenses are readily available. Due to the weak interaction of neutrons with matter, the index of refraction for neutrons is very close to one, and it is difficult to produce efficient focusing elements. In case of the focusing SANS realized by Forschungszentrum Jülich [4], a toroidal[5] mirror is employed as focusing element. Locally, the toroidal shape is a good approximation to an ellipsoid with its well-known focusing properties. The challenge in realizing such a device lies in the fact that small angle scattering from the focusing element has to be avoided i.e. the mirror has to be

[5] A torus is a surface of revolution generated by revolving a circle about an axis coplanar with the circle, which does not touch the circle (examples: doughnuts, inner tubes).

flat on an atomic scale (root-mean square roughness of about 3 Å !), which became possible due to the developments of optical industry for x-ray satellites.[6]

As an example of the considerations leading to the design of a neutron scattering instrument, we will now discuss the resolution of a pinhole SANS machine. In general terms, the resolution of an instrument denotes the smearing out of the signal due to the instruments' finite performance (14.12). As neutron scattering is a flux limited technique, there is need for optimization: the better the resolution of the instrument, i. e. the better the angular collimation $\Delta\theta$, the smaller the wavelength spread $\Delta\lambda$, the smaller is the intensity recorded on the detector. Therefore resolution has to be relaxed to such an extent that the features of interest are still measurable and not smeared out entirely by the resolution of the instrument, while at the same time the intensity is maximized. In order to determine the resolution of a SANS instrument, we start from (14.13): $Q = \frac{4\pi}{\lambda}\sin\theta$. The influence of angular- and wavelength spread can be determined by differentiation of this equation, where the different contributions have to be added quadratically:

$$\begin{aligned}\Delta Q^2 &= \left(\frac{\partial Q}{\partial\theta}\right)^2(\Delta\theta)^2 + \left(\frac{\partial Q}{\partial\lambda}\right)^2(\Delta\lambda)^2 = \left(\frac{4\pi}{\lambda}\right)^2\cos^2\theta(\Delta\theta)^2 + \left(\frac{4\pi\sin\theta}{\lambda^2}\right)^2\Delta\lambda^2 \\ &\underset{\theta\to 0}{=} \left(\frac{4\pi}{\lambda}\right)^2\left[(\Delta\theta)^2 + \theta^2\left(\frac{\Delta\lambda}{\lambda}\right)^2\right] = \frac{k^2}{12}\left[\left(\frac{d_D}{L_D}\right)^2 + \left(\frac{d_E}{L_C}\right)^2 + \left(\frac{d_S}{L_C} + \frac{d_S}{L_D}\right)^2 + \theta^2\left(\frac{\Delta\lambda}{\lambda}\right)^2\right]\end{aligned} \tag{14.15}$$

ΔQ^2 is the variance of the scattering vector due to the finite collimation and monochromatization. d_E and d_S are the diameters of the entrance and sample aperture, respectively. d_D denotes the detector pixel size. L_C and L_D are collimation length and sample-detector distance, respectively. An optimization can be achieved, if all terms in (14.15) contribute the same amount, which leads to the condition

$$L_D = L_C \ , \ \ d_E = d_D = 2d_S \tag{14.16}$$

(14.16) shows that a pinhole SANS has to be designed such that sample-to-detector distance L_D is equal to the collimation length L_C. Typical values are $L_D = L_C = 10$ m with openings of $d_E = 3$ cm for the entrance- and $d_S = 1.5$ cm for the sample aperture. Note that one can chose the opening of the entrance aperture to be twice as large as the opening of the sample aperture - or sample size - without sacrificing markedly in resolution, while gaining in neutron count rate! The detector needs a minimum pixel resolution $d_D \approx d_E$; A detector with a radius of about $R_D \approx 30$ cm is necessary to cover the required Q-range up to 0.05 $Å^{-1}$ at $L_D = 10$ m and for $\lambda = 8$ Å. Having defined the incident collimation, we can now determine the appropriate wavelength spread with the same argument as above: the last term in the sum in (14.15), corresponding to the wavelength spread, should contribute the same amount to the variance of the scattering vector as the corresponding terms for the collimation, i. e.:

[6] It should be mentioned that nowadays focusing lenses for neutron scattering have also been realised. These have a very long focal distance, but can be employed to improve intensity or resolution in pinhole SANS.

$$\frac{\Delta\lambda}{\lambda} = \frac{d_E}{L_C} \cdot \frac{L_D}{r_D} \approx \frac{d_E}{r_D} \approx \frac{1}{10} = 10\% \tag{14.17}$$

(14.17) demonstrates that in general for small angle scattering we don't need a very high degree of monochromatization. A 10 % wavelength band is acceptable, since for small angles the smearing due to the wavelength spread is quite comparable to the smearing due to the incident divergence. This is the reason why usually a velocity selector is employed as monochromatizing element for small angle scattering, as it lets a wavelength band of typically 10 % pass.

Let us give a short introduction into the analysis of small angle scattering experiments. As in any scattering experiment, the detected intensity is proportional to the scattering cross section, which in the SANS case is usually normalized to the sample volume and therefore has the unit [cm^{-1}]:

$$\frac{d\Sigma}{d\Omega} = \frac{1}{V_{sample}} \cdot \frac{d\sigma}{d\Omega} \tag{14.18}$$

Here we discuss the so-called “two phase model” only, where homogeneous particles are dispersed in a matrix (e. g. precipitates in metals or nanoparticles in solution etc.). The cross section will then be proportional to the contrast between particles and solution

$$\Delta b = \sum_j b_j \left(\rho_{j,P} - \rho_{j,M} \right) \tag{14.19}$$

where j labels atom species j of scattering length b_j with number density $\rho_{j,P}$ in the particle and $\rho_{j,M}$ in the matrix, respectively. The differential cross section per particle is given by the interference term (note: we use a continuum description for the small Q limit):

$$\begin{aligned} \frac{d\Sigma}{d\Omega}(\underline{Q}) &= \left| \int_V \Delta b \cdot e^{i\underline{Q}\cdot\underline{r}} d^3r \right|^2 \\ &= \Delta b^2 V^2 \underbrace{\left| \frac{1}{V} \int_V e^{i\underline{Q}\cdot\underline{r}} d^3r \right|^2}_{f(\underline{Q})} \end{aligned} \tag{14.20}$$

Here *f(Q)* denotes the *particle form factor* for a homogeneous particle of volume V:

$$f(\underline{Q}) = \frac{1}{V} \int e^{i\underline{Q}\cdot\underline{r}} d^3r \tag{14.21}$$

(14.20) is the differential cross section for a single particle. For very dilute solutions of identical particles, the cross section will be given by (14.20) times the number N of particles (“single particle approximation”). However, in more concentrated solutions, there will be additional interference effects between the particles, which are described by the so-called *structure factor S* and we obtain the modified cross section for dense solutions:

$$\frac{d\sigma}{d\Omega} = N \cdot \Delta b^2 \cdot V^2 \cdot \left| f(\underline{Q}) \right|^2 \cdot S(\underline{Q}) \tag{14.22}$$

where $S(\underline{Q})$ is related to the Fourier Transform of the pair correlation function $g(\underline{R})$ between the single particles at distance $\underline{R}$:

$$S(\underline{Q}) = 1 + \frac{1}{V_{sample}} \int_{V_{sample}} g(\underline{R}) e^{i\underline{Q}\cdot\underline{R}} d^3r \tag{14.23}$$

(Note: for vanishing pair correlations $g(\underline{R}) \equiv 0$, i. e. random distributed particles, the structure factor has to be unity: $S(\underline{Q}) \equiv 1$).

The isotropic form factor of a homogeneous sphere of radius R can be calculated by Fourier transform and is introduced elsewhere in this course:

$$f(Q) = 3\frac{\sin QR - QR\cos QR}{(QR)^3} \tag{14.24}$$

For forward scattering $f(Q=0)=1$ per definition. For small values of the scattering vector, this expression can be approximated by:

"*Guinier Law*" for $QR \leq 2$:

$$\left| f(Q) \right|^2 \approx e^{-\frac{(QR_G)^2}{3}} \approx 1 - \frac{Q^2 R_G^2}{3} \tag{14.25}$$

Here the quantity R_G is the so-called *radius of gyration* of the particle. For a spherical particle $R_G^2 = \frac{3}{5}R^2$, but R_G can defined in a more general way also for non-spherical particles.

For $QR=3$ the form factor squared has dropped to about 10 %. In the larger Q region - neglecting the sharp minima of the form factor (14.24), which are often not visible due to particle size distribution and instrumental resolution - the form factor follows the behavior:

"*Porod Law*" for $QR \geq 4.5$:

$$\left| f(Q) \right|^2 \approx 2\pi \frac{A}{V^2} Q^{-4} \tag{14.26}$$

where $A = 4\pi R^2$ is the surface, and $V = \frac{4\pi}{3}R^3$ the volume of the sphere of radius R. In small angle scattering, often times one does not deal with simple geometrically smooth particles in a second phase. In stochastical growth processes or soft matter system, irregular *fractal* structures can appear, which show self-similarity on multiple length scales. For such structures, power laws with other exponents are observed:

$$\frac{d\sigma}{d\Omega}(mass\ fractal) \sim Q^{-D} = Q^{-1}...Q^{-3}$$
$$\frac{d\sigma}{d\Omega}(surface\ fractal) \sim Q^{D_s-6} = Q^{-3}...Q^{-4} \tag{14.27}$$

where D denotes the so-called *fractal dimension* for porous objects. D is in general smaller than 3 and non-integer. If the particles have a dense core, but a rough self-similar surface, they are called *surface fractals* with a surface area of $A \sim R^{Ds}$. From the above discussion we see that characteristic regions can be distinguished in a small angle scattering experiment:

1. Close to forward direction in the very small Q limit and for dilute solutions, we observe constant scattering proportional to the number of particles N, the square of the particle volume V^2 and contrast (14.19). For known contrast, we can deduce the product $N \cdot V^2$, if the scattering is measured in absolute units by comparing to a known scatterer e. g. water. For dense solutions, the structure factor from correlations between particles becomes apparent.
2. In the region up to $QR \leq 2$, the Guinier Law (14.25) holds for compact particles. From a *Guinier-Plot* $\ln\frac{d\sigma}{d\Omega}$ versus Q^2 one can determine the radius of gyration

$$R_G = \frac{\int_V r^2 \Delta b(r) d^3r}{\int_V \Delta b(r) d^3r} \tag{14.28}$$

3. In the Porod-region $QR \geq 4.5$

$$\frac{d\sigma}{d\Omega} = \Delta b^2 2\pi NAQ^{-4} \tag{14.29}$$

we can, independent of particle shape, determine the total surface area $N \cdot A$ of all particles with sharp surfaces from a *Porod Plot* $\frac{d\sigma}{d\Omega} \cdot Q^4$ versus Q^4.

4. Finally, if Q approaches the value $1/a$ where a corresponds to typical atomic distances, we approach the region of Bragg scattering from atomic structures (wide angle scattering).

Let us now turn to applications of small angle scattering. One example is given in figure 14.7, which is concerned with the self-organization of crystalline amorphous diblock-copolymers [4]. Combining three different instruments, small angle scattering has been observed over ten orders of magnitude in cross section and nearly four orders of magnitude in momentum transfer. In different regions, different power laws apply, corresponding to different structures: the Q^{-2} power law corresponds to *2d* structures on the shortest length scale, the Q^{-1} power law corresponds to the organization of rods in bundles, while the Q^{-3} power law corresponds to a network of bundles with a mass fractal aspect and finally, correlations become visible in the very low Q-range.

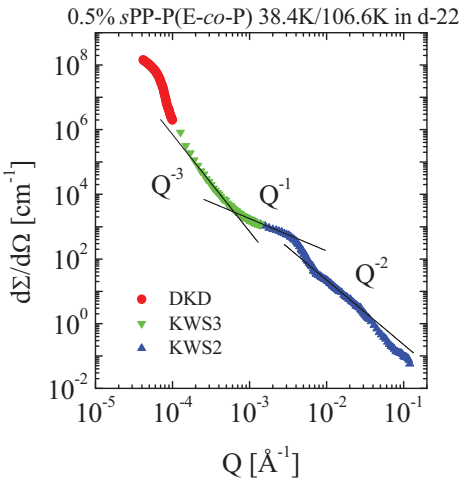

Fig. 14.7: *SANS investigation of the self-organization of a crystalline-amorphous diblock-copolymer measured with three different instruments of different resolution: double crystal diffractometer, focussing SANS and pinhole SANS for the low, medium and larger Q range, respectively. Plotted is the cross section in absolute units versus the magnitude of the scattering vector. For details see [4].*

We will end this short introduction into the principles of small angle scattering by listing some examples for applications of small angle scattering in different fields of science:

- *soft matter*: polymers and colloids, e. g. micelles, dendrimers, liquid crystals, gels, reaction kinetics of mixed systems, …
- *materials science*: phase separation in alloys and glasses, morphologies of superalloys, microporosity in ceramics, interfaces and surfaces of catalysts
- *biological macromolecules*: size and shape of proteins, nucleic acids and of macromolecular complexes, biomembranes, drug vectors
- *magnetism*: ferromagnetic correlations and domains, flux line lattices in superconductors, …

14.4.3 Large scale structures: Reflectometry

As elaborated in chapter 14.4.2, neutron small angle scattering is applied to determine large scale structures, e. g. scattering length density fluctuations on length scales of

some 100 Å in bulk material. There is another type of instrument, which is dedicated to the study of large scale structures in thin film systems, on surfaces and in multilayers. Such an instrument is called a *neutron reflectometer*. This conceptually simple instrument is depicted schematically in figure 14.8.

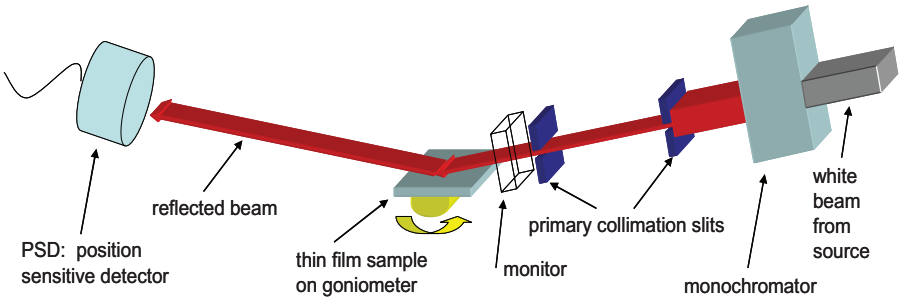

Fig. 14.8: *Schematics of a neutron reflectometer. Monochromatization can be done in many different ways: by a velocity selector, by a crystal monochromator, or by a chopper in a time-of-flight instrument. Collimation slits define the direction of the incident beam. The monitor is a low efficient detector of high transmission, which measures the incident flux on the sample. The reflected neutrons are either detected in a position sensitive detector, or a secondary collimation in front of a point detector selects the direction of the reflected beam. For magnetic samples, a polarizer, a polarization analyzer and guide fields can be inserted for polarization analysis experiments.*

Similar to a pinhole SANS instrument, the incident beam is collimated through a set of two well separated slits. However, since in reflectometry, one is mainly interested in the momentum transfer perpendicular to the planar sample surface, the collimation of a reflectometer is tight only in this direction. Along the sample surface the beam can be wide and have a larger divergence in order to gain intensity. This collimated beam impinges on the sample under a grazing angle (typically fractions of a degree up to a few degrees) and is reflected into a single point detector or a position sensitive detector. To define the angle of exit for a point detector, a secondary collimation is needed between sample and detector. The incident beam is monochromatized using different techniques, depending on the resolution requirements: velocity selector, time-of-flight chopper or crystal monochromator.

With such an instrument, the layer structure of a sample can be determined, such as layer composition, layer thickness and surface- or interfacial roughness. This information is obtained in so-called specular reflection, for which the incident angle is equal to the final angle like in a reflection from a perfect optical mirror. In this case, the momentum transfer of the neutrons is perpendicular to the surface of the sample and thus only laterally averaged information can be obtained. In order to determine lateral correlations within the layers, for example magnetic domain sizes, a momentum transfer within the

layer has to occur, which implies that angle of incidence and final angle have to be different. Short range correlation within the layers will then give rise to so-called off specular diffuse scattering as well know in optics from a bad optical mirror.

The scattering geometry is shown in figure 14.9.

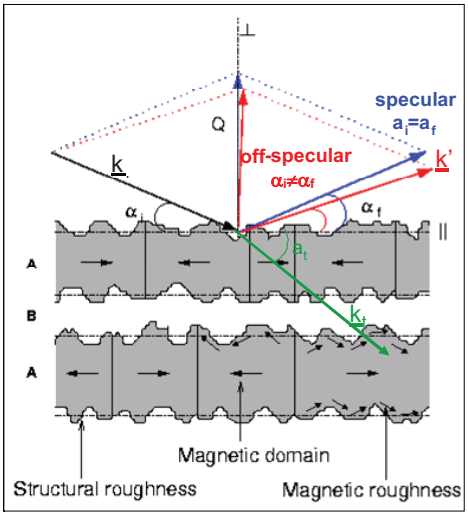

Fig. 14.9: *Scattering geometry for grazing incidence neutron scattering. Specular reflections are obtained, if the angle of incidence equals the final angle $\alpha_i = \alpha_f$. Off-specular scattering is observed at $\alpha_i \neq \alpha_f$.*

In fact, the theoretical description of neutron reflectometry follows exactly along the lines of conventional optics, except that for neutrons in most cases the index of refraction is smaller than one and thus external total reflection occurs for neutrons coming from vacuum towards matter[7]: The index of refraction n of neutrons of wavelength λ from a layer composed of elements with scattering length b_i and number density ρ_i and linear absorption coefficient μ_n is given by:

$$n = 1 - \frac{\lambda^2}{2\pi}\sum_j b_j \rho_j - i\frac{\lambda}{4\pi}\mu_n =: 1 - \delta - i\beta \qquad (14.30)$$

Refraction and total reflection are described by the well-known *Snell's Law* of optics:

[7] This is exactly what happens in neutron guides, evacuated tubes of usually rectangular cross section, where neutrons are totally reflected from the smooth glass side walls, often coated, e.g. with ^{58}Ni, to enhance the angle of total reflection. Since for total reflection conditions, reflectivity is close to 100%, neutrons are transported nearly without loss from the source to the instruments by bouncing back- and forth from the guide side walls.

$$\text{Snells law: } \frac{\cos\alpha_i}{\cos\alpha_t} = \frac{k_t}{k} = n \tag{14.31}$$

$$\text{angle of total reflection: } \cos\theta_c = n \tag{14.32}$$

The intensities of reflected and transmitted beam can be determined from the optical *Fresnel equation* (A_0, A_1, B_0: amplitudes of incident, transmitted and reflected waves, respectively; k_z, k_{tz}: component of wavevector $\underline{k}$ and $\underline{k}_z$, respectively, perpendicular to average surface):
Fresnel equation:

$$\text{Reflectivity } R = \left|\frac{B_0}{A_0}\right|^2 = \left|\frac{k_z - k_{tz}}{k_z + k_{tz}}\right|^2 = \left|\frac{\alpha_i - n\cdot\alpha_t}{\alpha_i + n\cdot\alpha_t}\right|^2 \tag{14.33}$$

$$\text{Transmissivity } T = \left|\frac{A_1}{A_0}\right|^2 = \left|\frac{2k_z}{k_z + k_{t,z}}\right|^2 = \left|\frac{2\alpha_i}{\alpha_i + n\cdot\alpha_t}\right|^2 \tag{14.34}$$

Figure 14.10 shows as an example the reflectivity and transmissivity of a Ni layer.

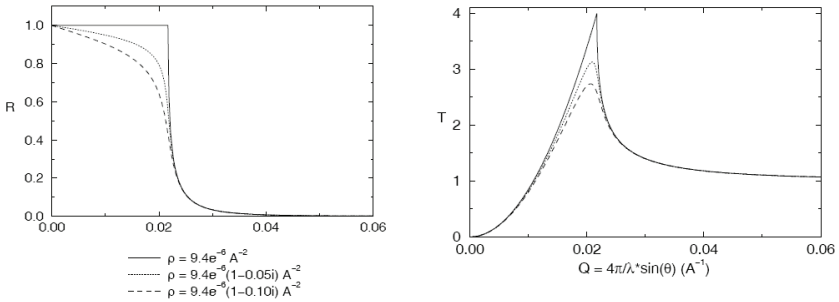

Fig. 14.10: *Reflectivity and transmissivity of neutrons from a Ni surface.*

Here we just want to demonstrate with very simple arguments how interference effects from layered structures arise and how the intensity modulation in Q-space are related to real space length scales. Figure 14.11 shows how interference can occur from a beam being reflected at the surface and at the internal interface of a double layer stack.

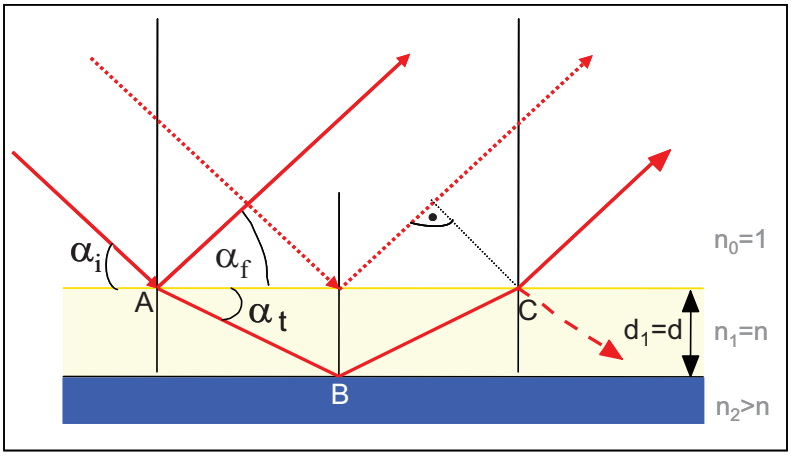

Fig. 14.11: *Schematics of the reflection of a neutron beam from a single layer on a substrate. There exists an optical path length difference Δ between the rays drawn with a solid line and those drawn with a dotted line.*

For simplicity we consider only the case of a specular reflection, i. e. the incident angle α_i is equal to the angle of exit α_f: $\alpha_i = \alpha_f = \alpha$. Interference occurs between beams reflected from the surface (dotted line in figure 14.11) and those first transmitted into the layer, reflected from the interface between layer 1 and substrate and then leaving the layer into vacuum (solid line). To a good approximation, refraction at the top surface can be neglected for incident angles larger than about twice the critical angle of total reflection. In this case $\alpha_t = \alpha_i = \alpha_f = \alpha$ holds. Since the index of refraction for neutrons is very close to one, this approximation is valid even for rather small angles of incidence. Then the optical path length difference for the two beams is:

$$\Delta = 2d \sin\alpha \tag{14.35}$$

Here d is the thickness of the layer 1. We can now determine the distance between interference maxima from the condition that the path length difference has to differ by one wavelength: $\lambda = 2d \cdot \Delta(\sin\alpha) \approx 2d \cdot \Delta\alpha$. With $Q = \frac{4\pi}{\lambda}\sin\alpha \approx \frac{4\pi}{\lambda}\alpha$ we finally obtain:

$$\Delta Q \approx \frac{2\pi}{d} \tag{14.36}$$

Again we can see that the interference phenomena in Q-space are connected with real space length scales in a reciprocal way. (14.36) tells us that there will be a number of interference maxima at distances in Q of $\frac{2\pi}{d}$. These interference phenomena are called "*Kiessig fringes*" and are well known to us in conventional optics for example as the beautiful colors observed in soap bubbles. Figure 14.12 shows as an example the reflectivity of neutrons from a thin nickel layer on a glass substrate, which is nothing else but a section of a neutron guide employed to transport the neutrons from the source to the

instrument over long distances by multiple total reflections. The Kiessig fringes are nicely visible in this example and the thickness of the nickel layer can be determined from the distance between adjacent intensity maxima.

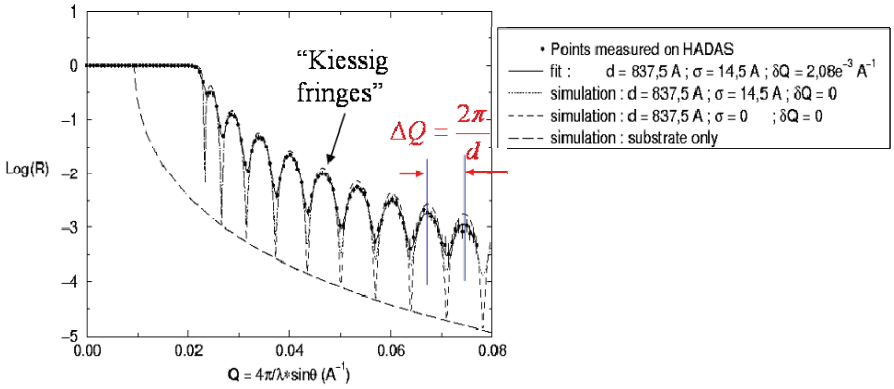

Fig. 14.12: *Reflectivity of neutrons from a nickel layer on glass substrate on a logarithmic scale. Data points were measured on the HADAS reflectometer of the late FRJ-2 reactor. The solid line shows a fit, where the layer thickness was determined to be 837.5 Å with a root mean square roughness of 14.5 Å and where the resolution of the instrument of* $\delta Q = 2.08 \cdot 10^{-3}\,\text{Å}^{-1}$ *has been taken into account; the dotted line shows a simulation for the same structural parameters, but for an ideal instrument without resolution broadening; the short dashed line shows the simulation for the same layer thickness but without roughness; the long dashed line shows the simulation for the glass substrate only.*

Neutron reflectometry has many applications in different fields of science of which we can only list a few:

- *soft matter science*: thin films e. g. polymer films; polymer diffusion, self-organization of diblock copolymers; surfactants; liquid-liquid-interfaces, …
- *life science*: structure of biomembranes
- *materials science*: surface of catalysts; kinetic studies of interface evolution; structure of buried interfaces
- *magnetism*: thin film magnetism e. g. exchange bias, laterally structured systems for magnetic data storage, multilayers of highly correlated electron systems, …

14.4.4 Atomic structures: Single crystal and powder neutron diffraction

As explained in chapter 14.4.1, wide angle scattering with neutrons of wavelength typically 1 Å is applied for the determination of atomic structures. Due to the periodicity of the lattice, Bragg peaks appear under diffraction angles given by the Bragg equation (compare reflectometry: (14.35) and (14.36)!):

$$2d \sin\theta = \lambda \tag{14.37}$$

The intensity of the Bragg peaks is governed by the arrangement of the atoms within the unit cell (structure factor) and the scattering from the single atom (form factor). By collecting a large set of scattered intensities for many Bragg peaks, modeling the atomic structure and refining the parameters in order to get an optimum agreement between calculated and observed intensities, the arrangement of atoms within the unit cell as well as the arrangements of spins for magnetic samples can be determined. Figure 14.13 shows the schematics of a single crystal diffractometer.

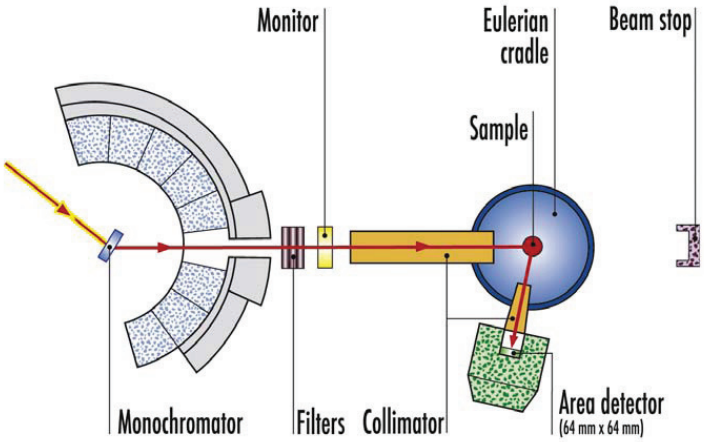

Fig. 14.13: *Schematics of a single crystal diffractometer. The drawing shows the layout of the diffractometer D9 at the Institute Laue-Langevin and has been taken from http://www.ill.eu/.*

In contrast to small angle scattering, where a broad wavelength band is employed to enhance the scattered intensity, a better monochromatization of typically $\frac{\Delta\lambda}{\lambda} \sim 1\%$ has to be achieved for wide angle scattering to avoid the broadening of the Bragg reflections due to the wavelength spread according to (14.37). This monochromatization is typically done by Bragg diffraction from a single crystal. The direction of the incident beam is determined by a set of slits. As Bragg reflections only occur when the corresponding lattice planes have a definite orientation with respect to the incident beam, the single

crystal sample is usually mounted on a so-called Eulerian cradle, which allows one to orient the sample using the three Eulerian angles ω, χ and ϕ. Finally the scattered beam is detected in a point- or small area detector. Care must be taken to collect the entire integrated intensity for a scan through the Bragg reflection.

A conceptually simpler experiment for the determination of atomic structures is the neutron powder diffractometer. In this case, since the powder grains in the sample usually have random orientations with respect to the incident beam, there is no need for orienting the sample with respect to the beam. Scattering will always occur for some of the grains, which by chance fulfill the Bragg condition. As scattering occurs for all allowed Bragg reflections simultaneously, it would be very inefficient to detect it by a single point detector, which would have to be positioned recursively for the correct 2θ values. Therefore in powder diffraction one usually uses a large linear - or even better area - position sensitive detector, which is arranged on a circular arch around the sample position.

While neutron powder diffraction is conceptually simple, it poses the problem that Bragg reflections will overlap for larger unit cells e. g. due to the finite peak width. Among other factors, the peak width is determined by the resolution of the instrument. One can show that the resolution function for a neutron powder diffractometer on a beam being monochromized by a Bragg reflection from a monochromator crystal is given by:

$$\left(\Delta 2\theta\right)^2 = U\tan^2\theta + V\tan\theta + W \tag{14.38}$$

In such a situation, one cannot determine the intensities of the various Bragg reflections separately. The solution to the problem is the so-called *Rietveldt*- or profile refinement, where structural parameters (unit cell metric $a,b,c,\alpha,\beta,\gamma,$ atom positions and site occupations, the Debye-Waller-factors, etc) are refined together with the instrumental parameters (zero point of the scattering angle $2\theta_0$, parameters of the resolution function U, V, W, etc). Assuming a certain peak shape function, this allows one to model the entire powder diffractogram and determine the corresponding parameters from a refinement, which aims at minimizing the weighted sum of the quadratic deviations of calculated and observed intensities for all data points. Figure 14.14 shows an example of such a Rietveldt analysis for data taken from a colossal magnetoresistance manganite.

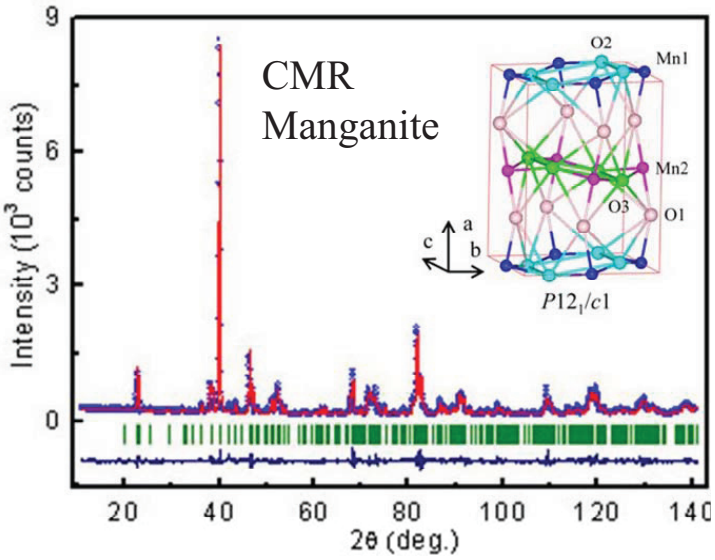

Fig. 14.14: *Powder neutron diffraction from a colossal magnetoresistance manganite. Points represent the measured intensities, the solid line the calculated profile function. The green bars below the diffractogram indicate the positions of the Bragg reflections and the line beneath shows the difference between observed and calculated intensities [5].*

As one can see, there is a very strong overlap of Bragg reflections, especially at larger scattering angles. Still, by using the above mentioned profile refinement technique, the atomic structure of the compound could be determined to a great position.

Applications of wide angle diffractions are manifold:

- *lifescience*: structure of biological macromolecules, e. g. Hydrogen (crystal water!) in protein structures
- *chemistry*: structure determination of new compounds, position of light atoms; time resolved reaction kinetics
- *materials science*: stress-strain determination; texture of materials
- *geo-science*: phase and texture analysis
- *solid state physics*: structure - function relations e. g. in high T_C superconductors; magnetic structures and spin densities, e. g. in molecular magnets

14.5 Spectroscopy

So far, we have only explored the purely elastic - or the quasistatic correlation functions, which give us structural information on various length scales only. We will now

turn to the general case of correlation functions in space and time, which allow us to determine in addition the microscopic dynamics of the sample under investigation. Again, different instrument types exist for different applications. First of all, if we consider the neutron as a particle, we can determine the time of flight it needs to travel from the sample to the detector and thus its velocity or energy after the scattering process. With the knowledge of the incident energy, the energy transfer during the scattering process can be determined. This kind of neutron spectrometer is called a *time-of-flight or TOF spectrometer*. A special case of the TOF spectrometer is the so-called *neutron spin echo spectrometer*, where the time-of-flight of each single neutron is being determined through the Larmor precession of the nuclear spin of the neutron in an external magnetic field. Neutron spin echo spectroscopy has the highest energy resolution and measures the intermediate scattering function directly. Therefore it is well suited to study slow relaxation processes. An alternative approach to spectroscopy is to determine the energy of the scattered neutrons by means of Bragg reflection from an analyzer crystal. Such an instrument is called a *crystal spectrometer* and if the selection of the incident wavelength is done by a crystal monochromator, it is called a *triple axis spectrometer*. A variant of a crystal spectrometer is the high resolution *backscattering spectrometer*. Of course there are various combinations of these techniques, which exist in particular at spallation sources. A discussion of all of the various instrument concepts goes well beyond the scope of this introductory course.

14.5.1 Time-of-Flight or TOF spectroscopy

Figure 14.15 depicts schematically a generic time-of-flight spectrometer.

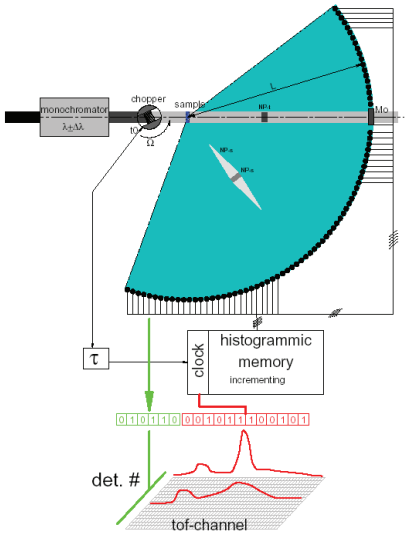

Fig. 14.15: *Generic TOF spectrometer. The neutron beam is monochromatized, either by a crystal monochromator (X-TOF) or by time-of-flight (TOF-TOF) with choppers and / or the pulse from a spallation source. A chopper creates monochromatic neutron beam pulses incident on the sample. The scattered neutrons are collected in an array of detectors surrounding the sample. For each detector pixel, the neutrons are counted into a histogram as a function of their arrival time. These intensity – time histograms can be converted into the scattering function S(Q,ω) by using a reference sample for absolute calibration and simple kinematic relations between scattering angle and flight time on one hand and scattering vector and energy on the other hand.*

Neutrons are being monochromized either by reflection from a monochromator crystal or by time-of-flight techniques (X-TOF or TOF-TOF instruments, respectively). Monochromatic neutron pulses are produced by a chopper, which can be a fast rotating (up to e.g. 600 Hz) disc or drum made from neutron absorbing material, which has a slit that lets neutron pass only during a short time interval of typically some microseconds. This pulsed neutron beam impinges on the sample and is scattered under all possible scattering angles. Neutrons are recorded on a two dimensional position sensitive detector (nowadays, this is often an array of linear position sensitive ^{3}He detector tubes) surrounding the sample typically on the surface of a cylinder. From the arrival time of the neutrons in the detector with respect to the starting time given by the opening of the chopper, an intensity spectrum can be recorded for each scattering angle separately as a function of the arrival time of the neutrons in the detector. Using simple kinematic equations for the neutron as a particle and a calibration obtained by measuring a reference sample, this time-of-flight spectrum can be converted into the scattering function

S(Q,ω). Figure 14.16 illustrates the scattering process in a flight-path versus time diagram.

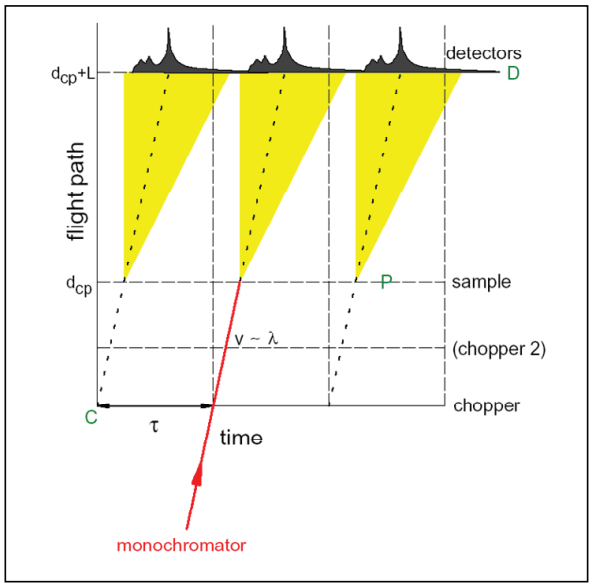

Fig. 14.16: *Flight-path-versus-time-diagram for a generic time-of-flight instrument (see text).* (*Courtesy of Dr. M. Monkenbusch).*

In such a diagram, a monochromatic neutron beam has a certain slope, which can be derived from the de Broglie equation $p = \frac{h}{\lambda} = m \cdot v = m \cdot \frac{s}{t}$:

$$t = \frac{m}{h} \cdot s \cdot \lambda \tag{14.39}$$

Typical velocities for thermal neutrons lie in the range of meter per millisecond. In figure 14.16 the neutrons coming from a monochromator enter the chopper with a certain slope in the path-vs.-time diagram corresponding to the velocity of the monochromatic neutrons. With a repetition rate of $1/\tau$ given by the chopper frequency, pulses of monochromatic neutrons leave the chopper. A second chopper can be applied to suppress higher order reflections. The neutron scattered from the sample can either gain energy, resulting in a steeper slope in the path-vs.-time diagram or loose energy resulting in a shallower slope. The number of neutrons entering the detector in a certain time interval is counted into a histogram with the elastic line usually being strongest and inelastic events being visible in neutron energy gain or -loss.

A nice example for a powder neutron time-of-flight spectrum is given by the excitation spectrum of a molecular magnet, namely Mn_{12} acetat, see figure 14.17 [6]. Here the time-of-flight axis has been converted into an energy scale. Clearly visible are nicely separated excitations, which result in the energy level diagram depicted on the middle of figure 14.17. Transitions between these levels correspond to transitions between different values of the magnetic quantum number of the total spin of the molecule. Modeling this energy level spectrum allows one to determine the magnetic interaction parameters, here mainly the magnetic anisotropy.

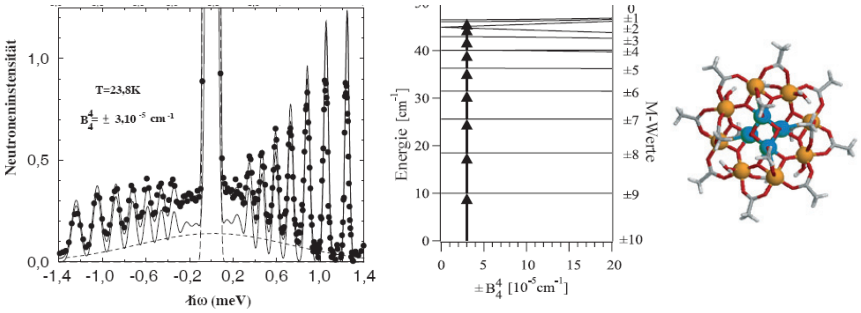

Fig. 14.17: *Left: Time-of-flight spectrum of the molecular magnet Mn_{12} acetat converted into an energy scale; middle: the corresponding energy level diagram; right: the magnetic molecule consisting of an outer ring of 8 Mn atoms with parallel coupled spins and an inner ring of 4 Mn atoms with opposite spin orientation. Taken from [6].*

Typical applications of time-of-flight spectroscopy can be found in various fields of science:

- *soft matter and biology*: dynamics of gels, proteins and biological membranes; diffusion of liquids, polymers; dynamics in confinement
- *chemistry*: vibrational states in solids and adsorbed molecules on surfaces; rotational tunneling in molecular crystals
- *materials science*: molecular excitations in materials of technological interest (e. g. zeolithes) and especially in diluted systems (matrix isolation); local and long range diffusion in superionic glasses, hydrogen-metal systems, ionic conductors
- *solid state physics*: quantum liquids; crystal field splitting in magnetic systems; spin dynamics in high T_C superconductors; phase transitions and quantum critical phenomena; phonon density of states.

14.5.2 Triple axis spectroscopy

An alternative approach for the study of dynamics of condensed matter systems is the so-called *triple axis spectroscopy*. The schematic of a triple axis spectrometer is depicted in figure 14.18.

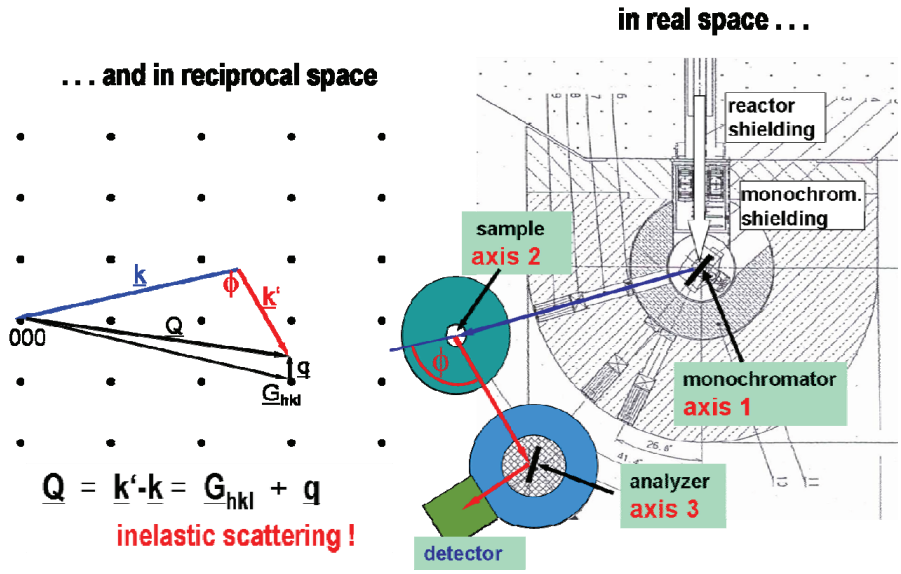

Fig. 14.18: *right: schematics of a triple axis spectrometer showing the three axes; left: scattering diagram in reciprocal space. (Courtesy Dr. H. Conrad).*

In this case the energies of the incident and scattered neutrons are selected by means of a single crystal monochromator and - analyzer, respectively. Also the sample is usually in single crystalline form. These crystals (monochromator, sample, analyser) are on rotation tables, which form axis 1, axis 2 and axis 3 of the triple axis spectrometer. If we compare this instrument with the time-of-flight spectrometer shown in figure 14.15, one difference becomes immediately clear: while the time-of-flight spectrometer with its large detector bank allows one to obtain an overview over the excitation spectrum in reciprocal space, the triple axis spectrometer is the instrument of choice, if a certain narrow region in $\underline{Q}$ and ω is of interest. This is the case, if sharp excitations like lattice vibrations (phonons) or spin waves (magnons) are being investigated. A propagation vector of such an excitation together with a certain energy transfer can be selected by setting monochromator, sample and analyzer to the corresponding values as depicted in the scattering diagram of figure 14.18, left. Here the energy transfer is given by

$\Delta E = \frac{\hbar^2}{2m}(k'^2 - k^2)$, while the momentum transfer is given as $\hbar\underline{Q} = \hbar\underline{k}' - \hbar\underline{k} = \hbar\underline{G}_{hkl} + \hbar\underline{q}$.

Figure 14.19 shows as an example spin wave dispersion relations determined for the garnet $Fe_2Ca_3Ge_3O_{12}$ by triple axis spectroscopy.

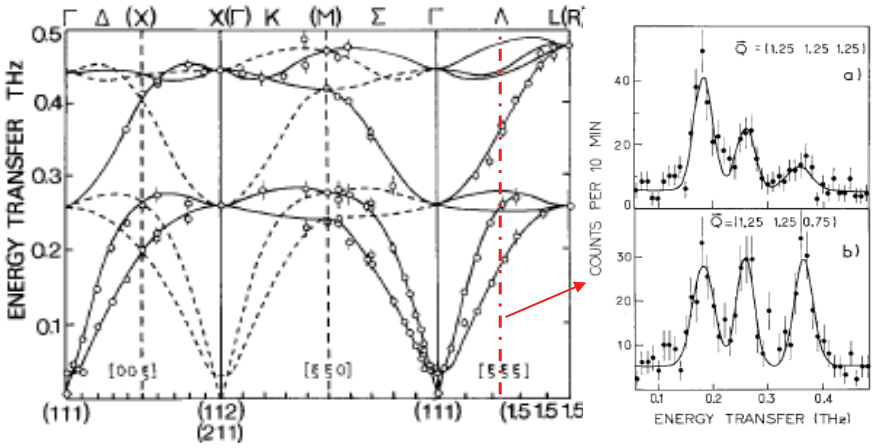

Fig. 14.19: *Spin wave dispersion relations for the garnet $Fe_2Ca_3Ge_3O_{12}$ along main symmetry directions in reciprocal space. The data points are obtained from scans keeping the momentum transfer $\underline{Q}$ constant. The figure on the right shows examples of such "constant Q scans". The solid lines are model calculations, from which the interaction (exchange) parameters between the spins in the unit cells can be determined; figure taken from [7].*

Typical examples of triple axis spectroscopy lie mainly in solid state physics:

- phonon dispersions in crystalline material, from which the interatomic forces can be determined
- spin wave dispersions, which allow one to determine exchange and anisotropy parameters
- dynamics of biological model membranes
- lattice and spin excitations in quantum magnets, superconductors, …
- phase transitions: critical behavior.

14.5.3 High resolution spectroscopy

Both, time-of-flight and triple axis spectroscopy, have typical energy resolutions of a few percent of the incident neutron energy. While such energy resolutions are sufficient in many cases, there is need for higher energy resolutions, for example to investigate the rather slow movements of large macromolecules, the slow spin dynamics of frustrated spin systems, diffusion of atoms or tunneling processes in molecular crystals. In order to improve the energy resolution, one could just narrow the energy band width of the neutrons incident on the sample. However, such an improvement of resolution goes hand-in-hand with the decrease of the signal in the detector and is therefore not practicable. There are, however, alternative approaches to increase the energy resolution: *neutron spin echo spectroscopy* and *backscattering spectroscopy*.

Neutron spin echo spectroscopy can be understood as a further development of the time-of-flight spectroscopy, where the flight time of each single neutron is encoded and thus a broad wavelength band of incident neutron energies can be used. Encoding of the flight-time is done by the Larmor precession of the nuclear spin of the neutrons in an external magnetic field. Loosely speaking "each neutron carries its own clock" to measure its individual time-of-flight. Figure 14.20 demonstrates the principle of neutron spin echo spectroscopy: the incident neutron beam with a broad wavelength band of typically 10 % is being polarized with the polarization along the neutron flight direction. A so-called $\frac{\pi}{2}$-flipper turns the neutron polarization into the vertical direction, just before the neutrons enter a strong magnetic field, which is designed in such a way that the field integral $\int \underline{B}(\underline{s})d\underline{s}$ is identical for all neutron flight paths (an absolute non-trivial requirement!!). In the external filed, the nuclear magnetic moment of the neutron starts to precess in this field with a Larmor precession frequency determined by:

$$\frac{d\underline{s}}{dt} = \gamma \underline{s} \times \underline{B} \tag{14.40}$$

Due to the different neutron velocities and thus different flight times in the magnetic field area, the neutron beam reaching the sample is entirely depolarized. Typical field integrals are in the range of *0.5 T·m* giving rise to some 10,000 precessions of the neutron spin. At the sample, the polarization of each neutron is inverted by a so-called π-flipper. In the second arm of the neutron spin echo spectrometer, the scattered neutrons travel through an identical solenoid as on the incident side. If the neutrons are scattered elastically and the field integrals in the two coils are precisely identical, then the full polarization of the neutron beam will be restored and a full intensity will be recorded in the detector after a further $\frac{\pi}{2}$ flip and a polarization analyzer. This maximum intensity is called the spin echo. This spin echo is due to the fact that in the second coil, each neutron performs as many revolutions as in the first coil and thus has to end up with the initial spin direction. If an inelastic scattering event happens at the sample, the spin echo will be destroyed i. e. the intensity in the detector will be lowered. The echo signal can be measured by scanning the field of the second coil with respect to the field of the first coil. Since the echo signal depends directly on the time-of-flight which neutrons need to travel through the magnetic field region, the spin echo technique directly measures the

intermediate scattering function *S(Q,t)* instead of *S(Q,ω)*. This type of spectroscopy is therefore well suited to measure slow relaxation processes like the magnetization dynamics in spin glasses or the dynamics of large macromolecules.

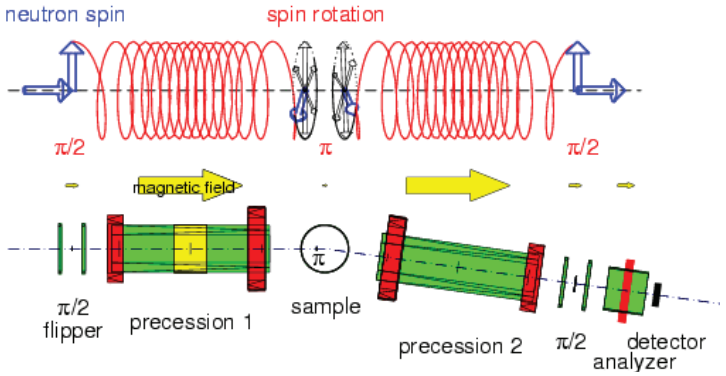

Fig. 14.20: *Schematics of the neutron spin echo spectrometer of JCNS at the FRM II reactor in Munich [3]. The incident neutron beam has wavelength – or energy band of* $\Delta\lambda/\lambda = 10\%$.

Another instrument for high resolution spectroscopy, based on a crystal analyzer and thus related to the triple axis spectrometer, is the so-called neutron *backscattering instrument*. Starting from the Bragg equation $\lambda = 2d\sin\theta$ one can derive the wavelength spread of a Bragg reflection from a monochromator or analyzer crystal by simple derivation:

$$\Delta\lambda = \left(\frac{\partial\lambda}{\partial d}\right)^2 (\Delta d)^2 + \left(\frac{\partial\lambda}{\partial\theta}\right)^2 (\Delta\theta)^2 \Rightarrow \left(\frac{\Delta\lambda}{\lambda}\right)^2 = \left(\frac{\Delta d}{d}\right)^2 + \cot^2\theta\cdot(\Delta\theta)^2 \qquad (14.41)$$

(14.41) shows that the wavelength spread results from two factors: an uncertainty in the lattice d-spacing, which can be minimized for perfect crystals such as silicon or germanium and a term resulting from the divergence of the beam. For backscattering i. e. $2\theta = 180°$ or $\theta = 90°$ this latter contribution vanishes due to the *cot(θ)* dependence. Thus in backscattering, one can work with a very divergent beam and still achieve a very good wavelength- or energy- resolution – of course at the prize of a poor *Q* resolution. This principle is applied for backscattering instruments. An example of such a spectrometer from a neutron spallation source is shown in figure 14.21.

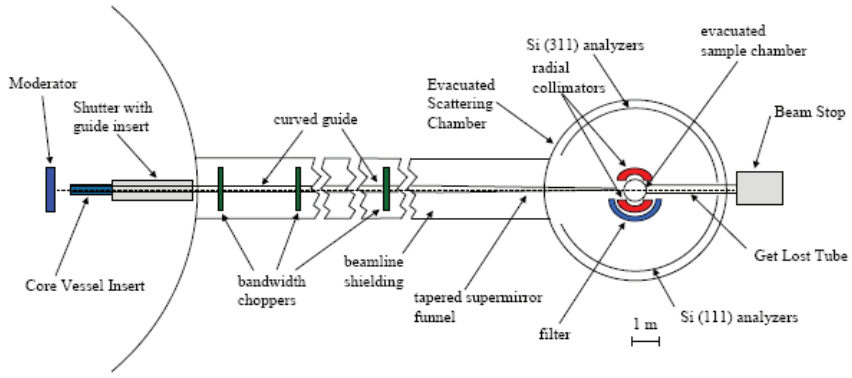

Fig. 14.21: *Schematics of the neutron backscattering spectrometer BASIS at the Spallation Neutron Source SNS in Oak Ridge, USA, taken from [8].*

Neutron pulses are produced in the supercritical hydrogen moderator. These pulses have a width of about *45 μs* for $\lambda = 6.267 Å$ wavelength neutrons (this wavelength corresponds with silicon *(111)* backscattering analyzer). Bandwidth choppers are used to select a certain wavelength band from the pulsed white neutron beam. A long incident flight path of *84 m* between moderator and sample allows one to define with great precision the wavelength of the incident neutrons arriving at the sample at a certain time after the initial neutron pulse. Neutrons are scattered from the sample onto *Si (111)* analyzers, reflected from these analyzers into detectors in a close-to-backscattering geometry. In this way the final neutron wavelength is fixed to *6.267 Å*, while the incident neutron wavelength varies with time after the pulse and thus the energy transfer can be determined like in a time-of-flight instrument. An energy resolution of about *2.2 μeV* can be achieved with the dynamic range of *± 250 μeV*. Typical applications of such a backscattering spectrometer lie in the investigation of tunneling in molecular crystals, spin diffusion or slow spin relaxation in frustrated spin systems, or atomic diffusion processes.

14.6 Summary and conclusions

In this chapter we have given a rough overview over the different neutron scattering techniques and their applications. Many details will be discussed in the practical part of this course. In addition to the instrument concepts presented, there are many variants, which could not be discussed within the scope of this introduction. Besides neutron scattering there are of course many other techniques, which cover similar length and time scales for research in condensed matter. All these techniques are complementary since all of them can only access a certain range of length or time scales and since the contrast mechanisms are quite different for the different techniques. Figures 14.22 and 14.23 depict the relevant length and time scales accessible with the various neutron- and non-neutron techniques.

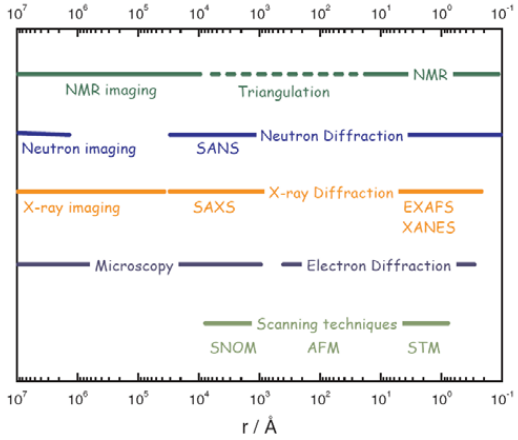

Fig. 14.22: *Experimental techniques with spatial resolution: neutron diffraction compared to other experimental techniques; taken from [9].*

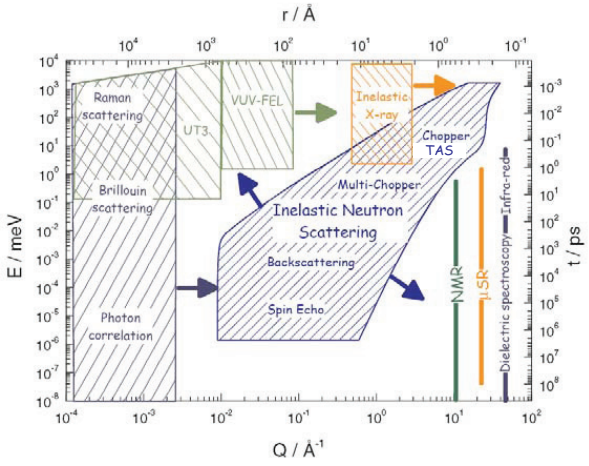

Fig. 14.23: *Experimental techniques with time and energy resolution, respectively: neutron spectroscopy compared to other experimental techniques; taken from [9].*

As these figures clearly demonstrate, neutron techniques cover a very large range of length and time scales relevant for research on condensed matter systems. Together with the typical assets of neutrons - sensitivity to magnetism, gentle non-destructive probe, sensitivity to light elements, contrast for neighboring elements etc. - it is clear why neu-

trons are such an important probe in many fields of research. Figure 14.24 shows how research with neutrons is relevant in many areas of fundamental research and how this in turn is highly relevant for many developments of modern technologies, which are the basis to solve current challenges of mankind.

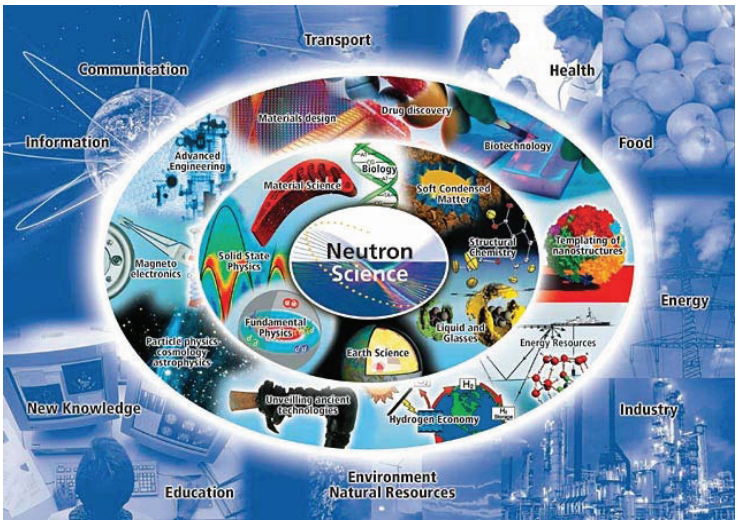

Fig. 14.24: *Significance of research with neutrons in fundamental research and modern technologies, which finally shape our environment and help solve pressing problems of modern societies, like energy supply, transport or communication; taken from [9].*

References

[1] Th. Brückel (Ed.) *Forschung mit Neutronen in Deutschland - Status und Perspektiven* Brochure of the German Committee for Research with Neutrons KFN; 2005
see also http://www.neutronenforschung.de

[2] G.L. Squires *Introduction to the Theory of Thermal Neutron Scattering* Dover Publications Inc.; Reprint 1997 or S.W. Lovesey Theory *of Neutron Scattering from Condensed Matter: Vol. 1 & 2* (International Series of Monographs of Physics) Clarendon Press; 1986

[3] http://www.jcns.info/jcns_instruments/

[4] A. Radulescu, E. Kentzinger, J. Stellbrink, L. Dohmen, B. Alefeld, U. Rücker, M. Heiderich, D. Schwahn, Th. Brückel, D. Richter; *KWS-3: The New (Very) Small-Angle Neutron Scattering Instrument Based on Focusing-Mirror-Optics*; Neutron News 16 (2005), 18 - 21

[5] H. F. Li, Y. Su, Y. Xiao, J. Perßon, P. Meuffels, Th. Brückel; "*Crystal and Magnetic Structure of Single Crystal $La_{1-x}Sr_xMnO_3$ ($x \sim 1/8$)*; European Physical Journal B 67 (2009), 149 - 157

[6] R. Bircher, G. Chaboussant, A. Sieber, H.U. Güdel and H. Mutka; *Transverse magnetic anisotropy in Mn_{12} acetate: Direct determination by inelastic neutron scattering*; Phys. Rev. B 70 (2004), 212413-6

[7] Th. Brückel, B. Dorner, A. Gukasov, V. Plakhty, W. Prandl, E. Shender, O. Smirnow; *Dynamical interaction of antiferromagnetic subsystems: a neutron scattering study of the spinwave spectrum of the garnet $Fe_2Ca_3(GeO_4)_3$*; Z. Phys. B 72 (1988), 477 - 485

[8] http://neutrons.ornl.gov/ ; http://neutrons.ornl.gov/instrument_systems/beamline_02_basis/index.shtml

[9] ESS project reports 2003 and update 2004; http://neutron.neutron-eu.net/n_documentation/n_reports/n_ess_reports_and_more

Exercises

E14.1 Collimation

Assume you have to define the direction of a neutron beam by collimation. The incident beam has a flat angular distribution over an angular range much wider than needed. Employ the following three methods, plot the intensity distribution after your collimating device, comparing shape, width and transmission:

1. two slits with opening S in distance *L*

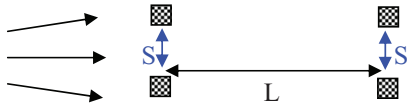

2. a "Soller Collimator" consisting of *N* neutron absorbing plane-parallel plates of thickness *t*, channel width *d* and length *l*:

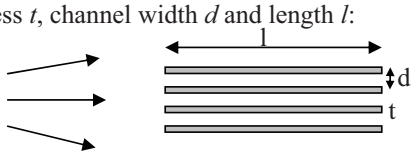

3. a neutron guide of *length L>> width w* coated with ^{58}Ni (*b =14.4 fm*; fcc-structure; a_0 = *3.520 Å*)

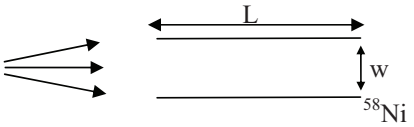

What is the principle difference between method 3 and methods 1 and 2?

E14.2 Monochromatisation

You have now the task to monochromatize your ideally collimated neutron beam (neglect any angular divergence). Again three methods are offered:

a) A velocity selector, see figure 14.6. Take as parameters the thickness of the drums of *10 cm*, an inner radius of the lamella of *6 cm*, a distance between the lamella of *1 cm* and an inclination angle of *10°*. How fast does this selector have to turn to monochromatize neutrons of wavelength *10 Å*? Estimate the wavelength spread in percent.

b) A crystal monochromator made from pyrolytic graphite *PG(002)* reflection with a lattice *d*-spacing of *3.343 Å*. PG is not an ideal crystal, but a mosaic crystal consisting of

many small crystalline blocks slightly canted against each other within an angular width of say *40'*. Calculate the Bragg angle for a wavelength of *2.4 Å* and *10 Å* and estimate the wavelength spread in percent.

c) A sequence of two disk choppers with radius *R* and opening *d* in a distance *L*. Take *L = 3 m*, *R = 20 cm*, *d = 1 cm*. Which wavelength is selected, if the choppers rotate at *200 Hz* with a phase shift of *100°*?

E14.3 TOF-Spectroscopy (optional!)

In a time-of-flight spectrometer, the energy change of the neutrons during scattering is being determined by the neutron time-of-flight:

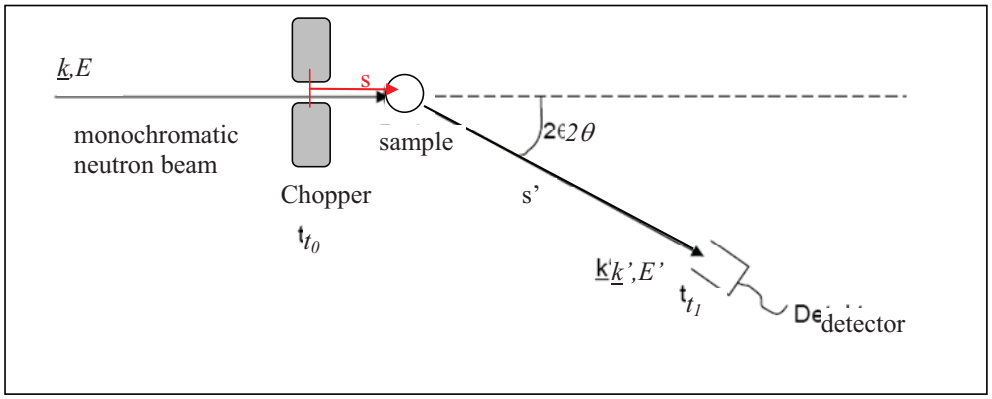

a) Calculate the time-of-flight between chopper and detector for a flight path length *s+s'=3m* for neutrons of wavelength *1 Å* for an elastic scattering process.

b) Determine the relation between the delayed arrival time of neutrons at the detector and the energy loss during inelastic scattering at the sample.

c) Determine the relation between energy transfer $\hbar\omega = E - E'$ and the magnitude of the momentum transfer $\left|\hbar\underline{Q}\right| = \hbar\left|\underline{k}' - \underline{k}\right|$ for a detector with fixed scattering angle 2θ.

Which factors determine the energy resolution of a TOF spectrometer? How does this affect the design of such an instrument?

1. **Soft Matter**
   From Synthetic to Biological Materials
   Lecture manuscripts of the 39th IFF Spring School March 3 – 14, 2008
   Jülich, Germany
   edited by J.K.G. Dhont, G. Gompper, G. Nägele, D. Richter, R.G. Winkler (2008),
   c. 1000 pages
   ISBN: 978-3-89336-517-3

2. **Structural analysis of diblock copolymer nanotemplates using grazing incidence scattering**
   by D. Korolkov (2008), III, 167 pages
   ISBN: 978-3-89336-522-7

3. **Thermal Nonequilibrium**
   Thermal forces in fluid mixtures
   Lecture Notes of the 8th International Meeting on Thermodiffusion,
   9 – 13 June 2008, Bonn, Germany
   edited by S. Wiegand, W. Köhler (2008), 300 pages
   ISBN: 978-3-89336-523-4

4. **Synthesis of CMR manganites and ordering phenomena in complex transition metal oxides**
   by H. Li (2008), IV, 176 pages
   ISBN: 978-3-89336-527-2

5. **Neutron Scattering**
   Lectures of the JCNS Laboratory Course held at the Forschungszentrum Jülich and the research reactor FRM II of TU Munich
   edited by R. Zorn, Th. Brückel, D. Richter (2008), ca. 500 pages
   ISBN: 978-3-89336-532-6

6. **Ultrafast Magnetization Dynamics**
   by S. Woodford (2008), 130 pages
   ISBN: 978-3-89336-536-4

7. **Role of Surface Roughness inTribology: from Atomic to Macroscopic Scale**
   by C. Yang (2008), VII, 166 pages
   ISBN: 978-3-89336-537-1

8. **Strahl- und Spindynamik von Hadronenstrahlen in Mittelenergie-Ringbeschleunigern**
   von A. Lehrach (2008), II, 171 Seiten
   ISBN: 978-3-89336-548-7

9. **Phase Behaviour of Proteins and Colloid-Polymer Mixtures**
   by C. Gögelein (2008), II, 147 pages
   ISBN: 978-3-89336-555-5

10. **Spintronics – From GMR to Quantum Information**
    Lecture Notes of the 40th IFF Spring School March 9 – 20, 2009
    Jülich, Germany
    edited by St. Blügel, D. Bürgler, M. Morgenstern, C. M. Schneider,
    R. Waser (2009), c. 1000 pages
    ISBN: 978-3-89336-559-3

11. **ANKE / PAX Workshop on SPIN Physics**
    JINR, Dubna, Russia / June 22. – 26, 2009
    Org. Committee: A. Kacharava, V. Komarov, A. Kulikov, P. Lenisa, R. Rathmann,
    H. Ströher (2009), CD-ROM
    ISBN: 978-3-89336-586-9

12. **Entwicklung einer Nanotechnologie-Plattform für die Herstellung Crossbar-basierter Speicherarchitekturen**
    von M. Meier (2009), 135 Seiten
    ISBN: 978-3-89336-598-2

13. **Electronic Oxides –**
    Correlation Phenomena, Exotic Phases and Novel Functionalities
    Lecture Notes of the 41st IFF Spring School March 8 – 19, 2010
    Jülich, Germany
    edited by St. Blügel, T. Brückel, R. Waser, C.M. Schneider (2010), ca. 1000 pages
    ISBN: 978-3-89336-609-5

14. **4th Georgian-German School and Workshop in Basic Science**
    Tbilisi, Georgia / May 3 – 7, 2010
    Org. Committee: E. Abrosimova, R. Botchorishvili, A. Kacharava, M. Nioradze,
    A. Prangishvili, H. Ströher (2010); CD-ROM
    ISBN: 978-3-89336-629-3

15. **Neutron Scattering**
    Lectures of the JCNS Laboratory Course held at Forschungszentrum Jülich and the research reactor FRM II of TU Munich
    edited by Th. Brückel, G. Heger, D. Richter, G. Roth and R. Zorn (2010),
    ca 350 pages
    ISBN: 978-3-89336-635-4

16. **Ab *initio* investigations of magnetic properties of ultrathin transition-metal films on *4d* substrates**
    by A. Al-Zubi (2010), II, 143 pages
    ISBN: 978-3-89336-641-5

17. **Investigation of a metal-organic interface realization and understanding of a molecular switch**
    by O. Neucheva (2010), 134 pages
    ISBN: 978-3-89336-650-7

18. **Reine Spinströme in lateralen Spinventilen, *in situ* Erzeugung und Nachweis**
von J. Mennig (2010), V, 95 Seiten
ISBN: 978-3-89336-684-2

19. **Nanoimprint Lithographie als Methode zur chemischen Oberflächenstrukturierung für Anwendungen in der Bioelektronik**
von S. Gilles (2010), II, 169 Seiten
ISBN: 978-3-89336-686-6

20. **Macromolecular Systems in Soft- and Living-Matter**
Lecture Notes of the 42nd IFF Spring School 2011 February 14 – 25, 2011 Jülich, Germany
edited by Jan K.G. Dhont, Gerhard Gompper, Peter R.Lang, Dieter Richter, Marisol Ripoll, Dieter Willbold, Reiner Zorn (2011), ca. 1000 pages
ISBN: 978-3-89336-688-0

21. **The spin structure of magnetic nanoparticles and in magnetic nanostructures**
by S. Disch (2011), V, 342 pages
ISBN: 978-3-89336-704-7

22. **Element-selective and time-resolved magnetic investigations in the extreme ultraviolet range**
by P. Grychtol (2011), xii, 144 pages
ISBN: 978-3-89336-706-1

23. **Spin-Transfer Torque Induced Dynamics of Magnetic Vortices in Nanopillars**
by V. Sluka (2011), 121 pages
ISBN: 978-3-89336-717-7

24. **Adsorption von Phthalocyaninen auf Edelmetalloberflächen**
von I. Kröger (2011), vi, 206 Seiten
ISBN: 978-3-89336-720-7

25. **Time-Resolved Single Molecule FRET Studies on Folding/Unfolding Transitions and on Functional Conformational Changes of Phosphoglycerate Kinase**
by T. Rosenkranz (2011), II, 139 pages
ISBN: 978-3-89336-721-4

26. **NMR solution structures of the MloK1 cyclic nucleotide-gated ion channel binding domain**
by S. Schünke (2011), VI, (getr. pag.)
ISBN: 978-3-89336-722-1

Schriften des Forschungszentrums Jülich
Reihe Schlüsseltechnologien / Key Technologies

27. **Neutron Scattering**
Lectures of the JCNS Laboratory Course held at Forschungszentrum Jülich and the research reactor FRM II of TU Munich
edited by Th. Brückel, G. Heger, D. Richter, G. Roth and R. Zorn (2011),
ca 350 pages
ISBN: 978-3-89336-725-2

Schlüsseltechnologien / Key Technologies
Band / Volume 27
ISBN 978-3-89336-725-2